Habilitationsschrift
(Venia Docendi)

Energy dissipation on Dirac and semimetal surfaces: Understanding surface dynamics on the nano-scale.

for obtaining the Venia Legendi
in Experimental Physics

presented to the
Faculty of Mathematics, Physics and Geodesy
Graz University of Technology

Dr. Anton Tamtögl

Graz University of Technology

Graz, September 2020

EIDESSTATTLICHE ERKLÄRUNG

Ich erkläre an Eides statt, dass ich die vorliegende Arbeit selbstständig verfasst, andere als die angegebenen Quellen/Hilfsmittel nicht benutzt, und die den benutzten Quellen wörtlich und inhaltlich entnommenen Stellen als solche kenntlich gemacht habe.

Graz, am .... (Unterschrift)

STATUTORY DECLARATION

I declare that I have authored this thesis independently, that I have not used other than the declared sources / resources, and that I have explicitly marked all material which has been quoted either literally or by content from the used sources.

Graz, ... (signature)

Abstract

The present thesis provides new insights into the mechanisms of energy dissipation on material surfaces. Dynamical disorder and energy dissipation are key sources of decoherence in quantum devices, yet we understand little about the underlying nature of these mechanisms. Fundamentally, interactions with phonons and electron-hole pairs at the surface determine the lifetime and decoherence rate of quantum states and the mechanisms that control surface dynamical processes.

The first part of this thesis deals with the experimental and theoretical study of various promising material surfaces, so-called Dirac materials. Among these, three-dimensional topological insulators such as Bi_2Te_3 exhibit an insulating gap in the bulk while the surface is electrically conducting. However, in real samples and at finite temperatures, their ideal zero-Kelvin behaviour is perturbed and scattering processes via electron-phonon (e-ph) coupling can give rise to energy losses. In this context it is demonstrated that atom-surface scattering provides a sensitive probe to determine the surface phonon dispersion and the e-ph interaction parameter and several examples of the phonon dispersion and the e-ph coupling of these materials are presented.

The second part illustrates how the lineshape broadening upon inelastic scattering from surfaces can be used to determine the characteristics of energy dissipation during the motion of atoms and molecules. The motion of an adsorbed molecule arises from the rate of energy transfer between the molecule and the surface. The presented experimental data provides information about the role and variety of energy dissipation channels during this process. Moreover, due to the low energy of the probing particle beam delicate adsorbates such as water can be studied without disruption of the motion or dissociation of the molecule.

In general, the study of these surface dynamical processes is a unique and challenging problem for experiments, as it requires both sub-nanometer spatial resolution and fast (pico- to nanosecond) temporal resolution. In an outlook it is shown that ultrahigh-resolution measurements provide experimental access to so-far unexplored concepts such as the lifetime of surface phonon modes. Furthermore, by combining reciprocal space with real space techniques, surface dynamical processes can be measured over 16 orders of magnitude, thus providing experimental data for the rate description of dynamics. The latter is crucial for an understanding of the underlying principles of chemical reactions where the rate prediction from accurate computational calculations suffers from the lack of experimental data.

The presented works thus give quantitative insights into the coupling between the system and its environment with results that provide benchmark data relevant to quantum simulation. It extends the molecular-level understanding of these processes from “classical” surface science systems to novel quantum mechanically designed surfaces.

Zusammenfassung

Die vorliegende Arbeit liefert neue Einblicke in die Mechanismen der Energiedissipation an Oberflächen. Obwohl dynamische Störungen und Energieverluste Dekohärenz in Quantenstrukturbauelementen verursachen, verstehen wir nur sehr wenig der zugrunde liegenden physikalischen und chemischen Prozesse. Prinzipiell bestimmt die Wechselwirkung mit Phononen und Elektron-Loch-Paaren an der Oberfläche sowohl die Lebensdauer und Dekohärenzrate von Quantenzuständen, wie auch die Mechanismen, welche dynamische Prozesse an der Oberfläche kontrollieren.

Der erste Teil dieser Arbeit befasst sich mit der experimentellen und theoretischen Untersuchung verschiedener vielversprechender Materialoberflächen, insbesondere von sogenannten Dirac-Materialien. Innerhalb dieser Gruppe besitzen drei-dimensionale topologische Isolatoren wie Bi_2Te_3 eine Bandlücke im Inneren, während die Oberfläche elektrisch leitend ist. In realen Proben und bei höheren Temperaturen ist deren ideales Null-Kelvin-Verhalten jedoch gestört und Streuprozesse mittels Elektron-Phonon (e-ph) Wechselwirkung können zu Energieverlusten führen. In diesem Zusammenhang wird gezeigt, dass die Atom-Oberflächen-Streuung eine präzise Methode für die Bestimmung der Oberflächen-Phonon-Dispersion und die e-ph Kopplungskonstante darstellt. Es werden mehrere Beispiele für die Phonon-Dispersion und die e-ph Wechselwirkung in diesen Materialien vorgestellt.

Der zweite Teil veranschaulicht, wie anhand der Linienverbreiterung bei inelastischer Streuung an Oberflächen, Eigenschaften der Energiedissipation sich fortbewegender Atome und Moleküle bestimmt werden können. Da sich die Bewegung eines adsorbierten Moleküls aus der Rate des Energieübertrags zwischen dem Molekül und der Oberfläche ergibt, erlauben die vorgestellten experimentellen Daten die Rolle und Vielfalt der Energiedissipationskanäle während dieses Prozesses zu bestimmen. Darüber hinaus können aufgrund der niedrigen Energie des Teilchenstrahls empfindliche Adsorbate wie Wasser untersucht werden, ohne, dass die Bewegung des Moleküls gestört wird oder dieses dissoziiert.

Im Allgemeinen ist die Untersuchung von oberflächendynamischen Prozessen besonders komplex für Experimente, da diese sowohl eine räumliche Auflösung im Sub-Nanometer-Bereich als auch eine schnelle zeitliche (Piko- bis Nanosekunden) Auflösung erfordern. In einem Ausblick wird gezeigt, dass ultrahochauflösende Messungen experimentellen Zugang zu bisher unerforschten Konzepten wie der Lebensdauer von Oberflächen-Phononenmoden bieten. Die Kombination von Streutechniken mit mikroskopischen Techniken erlaubt zudem, oberflächen-dynamische Prozesse über einen Bereich von 16 Größenordnungen zu messen. Damit stehen experimentelle Daten für die Kinetik dieser Prozesse zur Verfügung, was entscheidend für das Verständnis der zugrundeliegenden Prinzipien chemischer Reaktionen ist: Die rechnerische Vorhersage der Reaktionsgeschwindigkeit leidet bisher am Mangel verfügbarer experimentellen Daten.

Die vorgestellten Arbeiten liefern damit quantitative Einblicke in die Kopplung zwischen dem System und seiner Umgebung, mit Ergebnissen, die für quantenmechanische Simulationen relevante Benchmark-Daten liefern. Zudem wird das Verständnis dieser Prozesse auf molekularer Ebene von “klassischen” Oberflächen auf neuartige Materialoberflächen erweitert.

List of abbreviations

AES Auger electron spectroscopy

ARPES angle-resolved photoemission spectroscopy

ASP acoustic surface plasmon

CC close-coupling

CDO charge density oscillation

CE Chudley-Elliott

CMP corrugated Morse potential

CoM centre-of-mass

DFPT density functional perturbation theory

DFT density functional theory

DOS density of states

DW Debye-Waller

e-h electron-hole

e-ph electron-phonon

FT Fourier-transform

GLE generalised Langevin equation

HAS helium atom scattering

hBN hexagonal boron nitride

HeSE helium spin-echo

ISF intermediate scattering function

LEED low-energy electron diffraction

LR longitudinal resonance

MC Monte Carlo

MD molecular dynamics

NSE neutron spin-echo

PEEM photo-emission electron microscopy

PES potential energy surface

QENS quasielastic neutron scattering

QHAS quasielastic helium atom scattering

QL quintuple layer

RW Rayleigh wave

SAR selective adsorption resonance

SF (dynamic) scattering function

SOC spin-orbit coupling

STM scanning tunnelling microscopy

TFSL Thomas-Fermi screening length

TI topological insulator

TMdC transition metal dichalcogenide

TOF time-of-flight

TST transition state theory

UHV ultra-high vacuum

vdW van der Waals

Content

1 Introduction and motivation

Surface science is roughly defined as the study of physical interactions that occur at interfaces and explores various phenomena at the intersection of different phases with the interface between two phases being the focus of interest. Surface science methods have long been used to understand many areas such as materials growth, nanostructures, self-assembly, catalysis, friction, etc. The field has been so successful that surface techniques are nowadays "everywhere". More importantly these are the techniques that underpin much of "nanotechnology" nowadays.
Historically, the motivation in surface science goes back to obtaining a fundamental understanding of heterogeneous catalysis such as e.g. the Haber-Bosch process which has been stated as the most important invention of the twentieth century[1]. In the late 1950s and through the 60s developments in semiconductor technology and microelectronics brought along strong interest in surfaces where the need to build ever smaller structures gives rise to an increasing importance of the interface. Related to the increased importance of surfaces in connection to smaller structures is the field of nanotechnology. The electronic properties of nanostructures are governed by quantum-confinement effects and in some cases, it is even such that surface localised states dominate the electronic properties of a nano-object. In particular new emerging materials such as graphene and topological insulators exhibit peculiar effects at the surface and several works presented in this thesis deal with experimental investigations of these novel materials.
The actuality of the topic is not least confirmed by recently awarded Nobel Prizes, for experiments related to the two-dimensional material graphene (2010) as well as mathematical concepts related to some of the exotic surfaces (2016) presented in this work. The articles selected for this Habilitationsschrift (venia docendi) and the works described below deal with these less studied surfaces and the above mentioned novel materials: semimetals and Dirac materials, including topological insulators (TIs).
In the following, experimental measurements that provide access to the energy and length-scales of dynamical processes on these surfaces are presented. In quantum systems, disorder contributes both to the effectiveness of a device and to the maintenance of coherence. In the latter case, dynamical disorder and coupling to a heat bath is a key source of decoherence, yet we understand little about the underlying mechanisms. Specifically, in the case of molecular systems at or near a surface, interactions with substrate phonons and electron-hole pairs determine the lifetime of quantum states. The same phenomenology controls the mechanisms that control the dynamics of atoms and molecules at surfaces. The here presented works provide quantitative and calibrated insights into the magnitude of the coupling between the system and its environment (the surface), results that provide also benchmark data relevant to quantum simulation. Moreover, while many of the fundamental properties of Dirac and two-dimensional materials have been explored theoretically and experimentally in recent years, future applications require knowledge about a number of so-far unexplored features including energy losses via electron-phonon (e-ph) coupling and property modification upon adsorption of molecules.

1.1 Surface dynamical processes and energy dissipation at surfaces

The present thesis provides new insights into the mechanisms of energy dissipation on material surfaces. Figure 1.1 shows a schematic side-view of a crystal surface, illustrating dynamical processes with surface phonons (ion cores as grey spheres) as well as the movement of adsorbed molecules such as water. Atom-surface scattering provides a sensitive probe to determine the surface phonon energies and energy dissipation considering that electronic transport is coupled to the motion of the ion cores (phonons). Furthermore, lineshape broadening upon inelastic scattering from surfaces can be used to determine the characteristics of energy dissipation during the motion of atoms

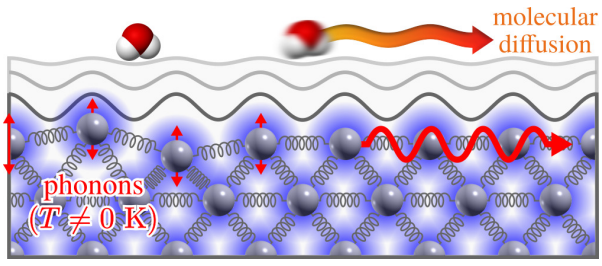

Figure 1.1: Schematic side-view of a crystal surface, illustrating dynamical processes, including lattice vibrations (phonons) at finite temperature as well as the movement of an adsorbed molecule.

and molecules.

Surface dynamics and energy dissipation

Due to the heavy elements in typical TIs such as Bi_2Se_3, the energies of (acoustic) surface lattice vibrations are typically in the low meV energy region and thus measurements of the surface phonon dispersion require high energy resolution as well as surface sensitive probes. Atom-surface scattering provides also access to the electron-phonon (e-ph) coupling strength at surfaces[2,3], a quantity that determines energy losses in surface electronic transport. At finite temperatures, the ideal zero-Kelvin behaviour of TIs is perturbed by e-ph coupling and energy dissipation into the bulk, and electron scattering via e-ph coupling gives rise to energy losses[4–6].
While scattering from defects and other lattice imperfections can possibly be controlled by the quality and a careful growth of crystals and films, phonons will be excited in even the most perfect crystals. Consequently, e-ph coupling should be the dominant scattering mechanism for surface electronic states at finite temperatures and the study of e-ph coupling in TIs, is of paramount importance in assessing potential applications. The presented experiments provide information about the surface phonon dispersion and the e-ph coupling of topological and Dirac materials. Furthermore, insight into the driving mechanism considering phase transitions in peculiar charge density wave systems can be obtained[7].
A better fundamental understanding of the e-ph interaction may guide development of materials with optimal surface transport properties, including low energy losses and large coherence control, which are prerequisites for any solid state quantum sensing or quantum transport devices. The results are relevant for quantum technology applications, where the e-ph coupling plays an active role, e.g., in two-dimensional superconductivity or in opto-acoustic and acousto-electronic signal processing devices.

Molecular diffusion and energy dissipation in surface diffusion

Molecular diffusion at surfaces is of fundamental importance for many dynamical processes, controlling phenomena in physics, chemistry and biology and often determining the kinetics of surface chemical reactions e.g., in catalysis. However, direct studies of the elementary diffusion events, that is the motion of individual atoms and molecules are scarce, as the available techniques are often limited to specific systems. In fact, much of our existing knowledge concerning the microscopic motion of molecules comes from computational simulation[8,9].
Molecular diffusion at the atomic scale is typically described by molecules hopping along the surface (Figure 1.1) while the substrate provides the thermal energy for the motion[10–12]. The motion of the adsorbed molecule arises from the rate of energy transfer between the molecule and the surface and scattering experiments provide information about the role and variety of energy dissipation channels during this process. A central question for this type of motion is in what way the adsorbate dissipates energy to the substrate which may give rise to subsequent decoherence of the motion.
In analogy to motion at the macroscopic scale, energy dissipation during molecular motion can be quantified in terms of an atomic-scale friction. Friction in surface diffusion processes can be caused by a variety of energy dissipation channels, including so-called phononic friction and electronic friction[13] and scattering experiments at the nanoscale allow to address this question.

Methodology

For the presented research, mostly helium atom scattering (HAS) has been used, which provides surface-specific information by scattering a nearly mono-energetic helium beam (8-20 meV) from the electron density at the surface (Figure 2.1(b)). Measuring the angular and energy distribution of the scattered helium atoms, gives access to the static and dynamic properties of the surface under investigation (as described in further detail in chapter 2), while leaving even the most fragile surface structures unchanged. HAS is the only surface characterisation method which is both strictly surface sensitive and equally applicable to insulators, semiconductors and metals[14,15].
Information about the interfacial motion of atoms and molecules comes from a special variant of HAS, namely helium spin-echo (HeSE) spectroscopy as well as from additional measurements with neutron scattering (see chapter 3). In the latter case systems with a high specific surface area are studied, in order

to provide access to surface dynamical processes with an experimental method that otherwise provides mostly information about the bulk.

1.2 Semimetals, topological insulators and Dirac materials

One of the most fascinating aspects when studying surfaces is that their physical and chemical properties can be radically different from those of the corresponding bulk material. E.g., the semimetals Bi and Sb are striking examples for the difference between surface and bulk properties with the surfaces being much better metals than the bulk due to the existence of electronic surface states[16]. There are even more peculiar surface dominated effects when it comes to Dirac materials such as topological insulators as described in 1.2.1. Some basic properties of semimetals, Dirac materials and topological insulator surfaces are outlined in the following.
In terms of their bulk electronic states, almost all investigated surfaces within the course of this work are either characterised as semimetals or semiconductors. A semimetal is a material with a very small overlap between the bottom of the conduction band and the top of the valence band. Hence a semimetal has no band gap, however, in contrast to a "real" metal the density of states (DOS) at the Fermi level is typically much smaller and semimetals exhibit charge carriers of both types (holes and electrons)[17]. A semiconductor, on the other hand, has zero conductivity at zero temperature, whereas the electrical conductivity in a semimetal is always non-zero. For a metal, the conductivity decreases with increasing temperature due to the e-ph interaction while in semimetals and semiconductors where both holes and electrons contribute to the conductivity both the carrier mobilities and carrier concentrations will contribute with different temperature dependencies[17].

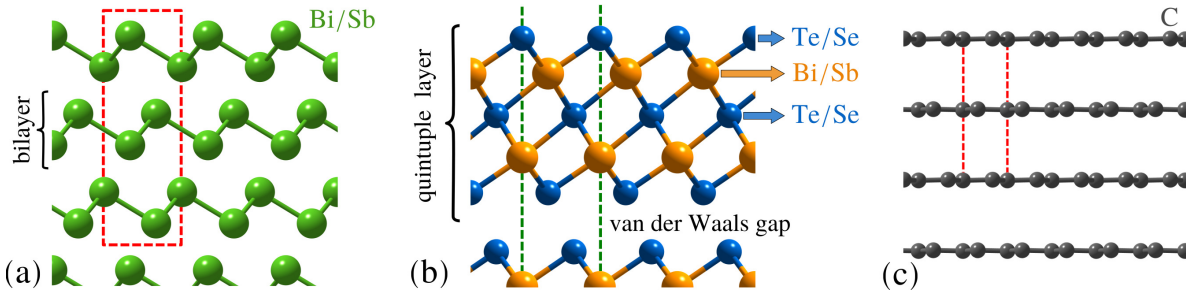

Figure 1.2: Side view of a few characteristic structures of the materials investigated within the course this thesis. (a) The semimetal surfaces Bi(111) and Sb(111) both exhibit a typical bilayer structure with the hexagonal unit cell given by the red dashed line. (b) The binary topological insulators are composed of quintuple layers with the terminating layer being either Te or Se. The hexagonal unit cell (which continues to the top and the bottom) is illustrated by the green dashed lines. (c) The semimetal graphite exhibits also a layered structure (individual layers are called graphene) with bonding in the plane being of covalent character, while bonding between the layers is via weak van der Waals character.

In addition to graphite, an allotrope of carbon, most classic semi-metallic elements belong to group 15 of the periodic table, including Sb and Bi. The side view of a few characteristic structures of the herein investigated material surfaces is shown in Figure 1.2. All materials show a typical layered structure, with intralayer bonding being mostly covalent, whereas the layers are held together by weaker interactions predominantly of van der Waals (vdW) character.
The creation of a surface requires the breaking of atomic bonds and the weak interlayer bonding in Figure 1.2 typically allows for an easy cleavage. In most metals, covalent bonding plays only a minor role and the effect of bond-breaking is small meaning that the surface properties are similar to those of the bulk, although localised electronic surface states may be present[16]. On semiconductors, upon creating the surface usually so-called dangling bonds occur which in turn often give rise to a re-arrangement of the atomic positions so that the dangling bonds are removed and the surface is again a semiconductor and not a metal.
Semimetals such as Sb lie in between these two cases, on the one hand being close to a semiconductor since directional bonding is important, while on the other hand a small overlap between the electronic

bands at some points of the Brillouin zone means that the material is formally a metal[16].

1.2.1 Dirac materials and topological insulators

The unifying framework of the newly emerging class of Dirac materials is an electronic surface state with a linear energy-momentum relationship, a so-called Dirac cone[18]. In typical Dirac materials such as graphene and topological insulators (TIs), low-energy fermionic excitations behave as massless Dirac particles. Figure 1.3(a) shows the calculated electronic dispersion of graphene, while Figure 1.3(b) shows the Dirac cone from an angle-resolved photoemission spectroscopy (ARPES) measurement of the topological insulator Bi_2Te_2Se(111).

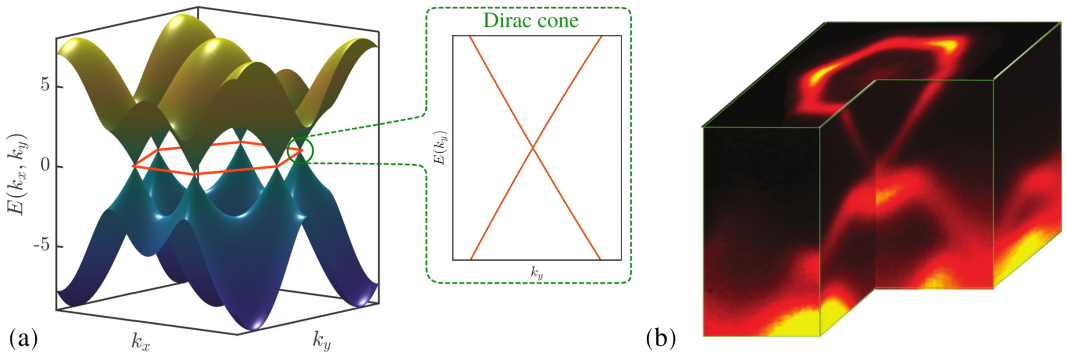

Figure 1.3: (a) Calculated electronic dispersion of graphene, with the corresponding Dirac points at each of the 6 $\overline{\mathrm{K}}$-points (orange hexagon). The inset to the right shows a close-up of the electronic dispersion with the linear energy-momentum relationship. (b) ARPES measurement of the electronic dispersion of the topological insulator Bi_2Te_2Se, showing the Dirac cone.

Among these Dirac materials, three-dimensional TIs such as Bi_2Te_3 or Bi_2Te_2Se exhibit an insulating gap in the bulk while the surface is electrically conducting (see Figure 1.4)[19]. In addition to the linear energy-momentum relationship (Dirac cone) the electronic surface state exhibits no spin degeneracy due to the large spin-orbit splitting (see e.g. Refs.[20,21]). Implications include surface dominated electronic transport and spin-polarised charge transport with intrinsically reduced backscattering[20].

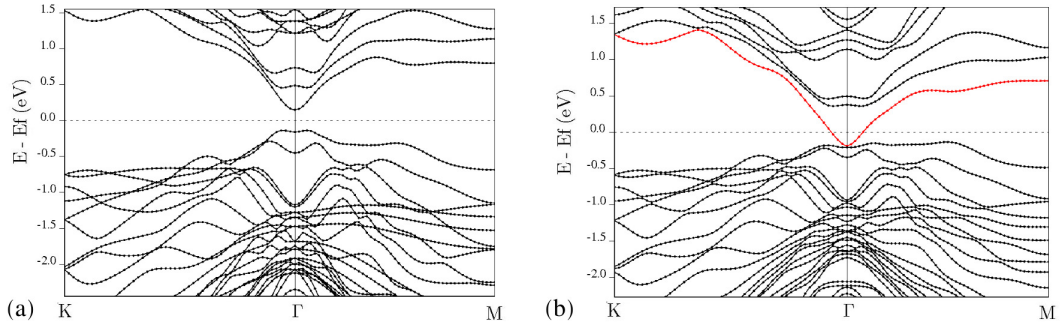

Figure 1.4: Without spin-orbit coupling (SOC), Bi_2Se_3 exhibits a band gap, not only in the bulk but also at the surface with a gap of 0.35 eV as evident from density functional theory (DFT) calculations (a). By including SOC as shown in (b), the electronic band dispersion becomes gap-less, with spin-polarised and Dirac cone shaped surface bands (red line) around the $\overline{\Gamma}$-point in the typical manner of 3D topological insulators.

Three-dimensional TIs, are composed of layered hexagonal structures that are bound by weak vdW forces (Figure 1.3(b)). Aside from the interest in spintronic devices based on TIs, surface dominated transport is a major route towards applications, for instance in quantum sensing by employing electronic changes upon adsorption[22–24] for the realisation of miniature sensors capable of monitoring single atoms or molecules. The electronic properties of TIs have been shown to be tunable by adsorption of atomic or molecular species that can serve as n- or p-type doping agents[22,23].
TIs such as Bi_2Te_3 are also classical thermoelectric materials[25–28] with a large Seebeck coefficient and, as

such, they have been used in thermoelectric refrigeration for a long time. Since the thermoelectric performance is closely related to the phonon dispersion and details of their electronic structure, information on the phonon dispersion and the e-ph coupling is also essential to fully understand their thermoelectric properties[27,29–31].

1.2.2 Two-dimensional materials

The structures shown in Figure 2.3 exhibit similarities with the class of two-dimensional (2D) materials. Since graphene became available by the so-called scotch tape technique, a vast class of 2D materials has been investigated[32]. The common feature of these vdW layered materials is the preparation of thin layers by exfoliation, which also holds for the above described layered class of 3D TIs. Therefore, the crystal samples of TIs can be prepared by *in-situ* cleaving under ultra-high vacuum (UHV) conditions.
Intriguingly and again quite similar to the surface states described above, the well-known physics and chemistry of three-dimensional bulk matter often become irrelevant for 2D materials, revealing exotic phenomena in these vdW layered crystals[32] with first attempts to employ these materials in vdW heterostructures and devices as described e.g. in Ref[33]. Among the most prominent 2D materials, are the semimetal graphene, the insulator hexagonal boron nitride (hBN) and the transition metal dichalcogenides (TMdCs) which tend to be semiconductors.

2 Surface structure and dynamics from helium atom scattering

Experimental measurements of pristine and adsorbate covered surfaces were carried out using helium atom scattering (HAS). The HAS apparatus at the Institute of Experimental Physics in Graz was used for measurements of the surface structure, the atom-surface interaction potential, the surface phonon dispersion relation and the e-ph interaction. Helium spin-echo (HeSE) measurements at the Cavendish Laboratory (3.5) were mostly employed for surface diffusion measurements but also for high-resolution phonon and atom-surface interaction measurements.
HAS provides surface-specific information by scattering a nearly mono-energetic He beam ($8 - 20$ meV) from the electron density at the surface (Figure 2.1(b)). The scattered intensities contain a multitude of experimental information ranging from elastic to inelastic scattering as well as trapping probabilities (as further described below), while providing a completely inert and non-destructive probe. E.g., in the context of TI surfaces, HAS has the advantage that samples are not exposed to any intense ultraviolet illumination which has been reported to trigger energetic shifts of the electronic bands[34].

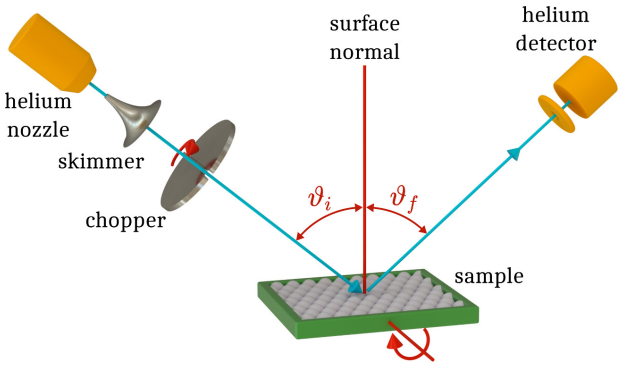

(a) A supersonic helium beam is produced in a source chamber, before scattering from the sample surface. The scattered beam is detected in a mass-spectrometer detector. Momentum transfer ΔK occurs due to scattering of the He beam from the crystal, at a certain incident angle ϑ_i, through a fixed total scattering angle. Energy resolution is optionally added by chopping the He beam with a chopper and measuring the time-of-flight (TOF).

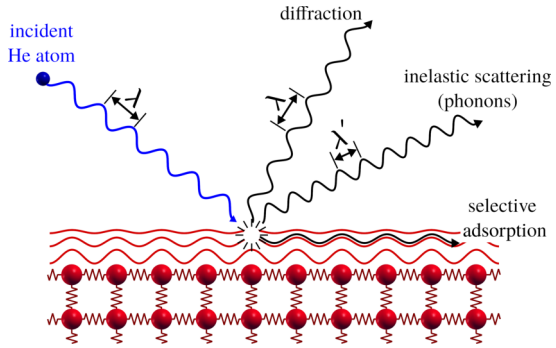

(b) Scattering processes for a monochromatic He beam on a crystal surface. Elastic scattering (no energy exchange) from a periodic surface gives rise to diffraction. Inelastic scattering gives rise to changes of the wavelength, upon creating or annihilating phonons. Finally the He atom can be temporarily trapped on the surface in a so-called selective adsorption process.

Figure 2.1: Schematics of a typical HAS apparatus (a) and graphical representation of the scattering processes (b).

A schematic of a conventional HAS setup is shown in Figure 2.1(a), while further details can be found in various references[35–38]. The scattering chamber of the HAS apparatus in Graz provides also additional surface-specific information via Auger electron spectroscopy (AES) and low energy electron diffraction (LEED) and the chamber is equipped with a sample transfer system which allows *in-situ* cleaving[39] of layered and 2D materials.

2.1 The helium-surface interaction

Figure 2.1(b) shows a schematic diagram of the surface scattering processes with elastic scattering and trapping. An atom of mass m, arriving at the surface with an incident wavevector $\mathbf{k}_i$ and kinetic energy $E_i = \frac{\hbar^2}{2m}\mathbf{k}_i^2$, is scattered by the electron cloud at the surface. The He atom interacts with all atoms of the semi-infinite crystal via a total potential $V(\mathbf{r})$, where the momentary position $\mathbf{r} = (\mathbf{R}, z)$ is expressed in terms of coordinates in the surface plane (capital letters) and along the surface normal z (likewise for the wavevector $\mathbf{k} = (\mathbf{K}, k_z)$, as illustrated in Figure 2.3(a)).
A precise model of this He-surface scattering process is rather complicated, due to the extended nature of the interaction with the surface[12,15]. Conventionally, the potential $V(\mathbf{r})$ is divided into a corrugated short-range repulsive wall and a less corrugated attractive well (typically $5 - 50$ meV) for rare gas atoms. The former arises from the Pauli repulsion of the electrons of the probe atom with the electrons of the surface; the latter is due to dispersion forces resulting from the electrostatic polarisation of the atom induced by the surface charge distribution. The equipotential surface at which the potential $V(\mathbf{R}, z)$

equals the He atom incident energy for the vertical component of motion $E_{iz} = \frac{\hbar^2}{2m} k_{iz}^2$ is given by

$$V(\mathbf{R}, z) = E_{iz} \ , \tag{2.1}$$

where the resulting surface $z = z(\mathbf{R}, E_{iz})$ defines the closest approach of the atom to the surface, i.e., the locus of the classical turning point for the given surface potential and vertical incident energy[15].

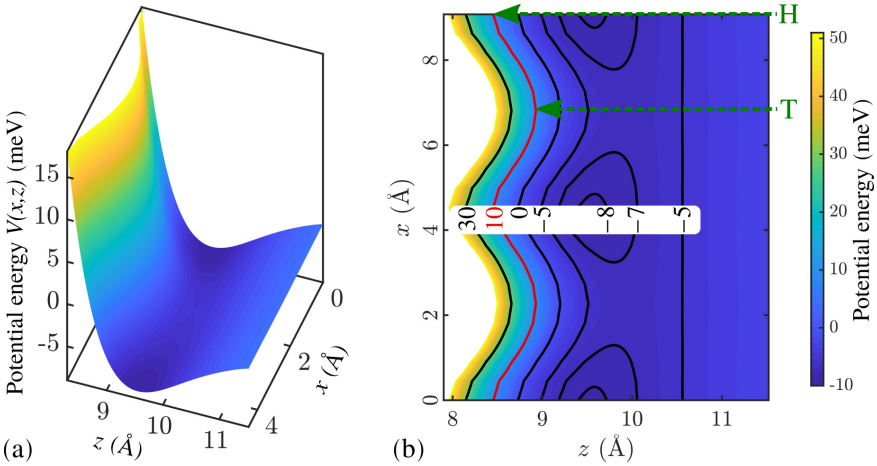

Figure 2.2: Calculated He-surface interaction potential above a Bi(111) surface. (a) shows a surface plot of $V(x, z)$ while (b) shows a contour plot with several equipotential lines. The potential follows the periodicity of the surface along x and has the general z-dependence shown. As illustrated in b), the classical turning point (e.g. for an energy of 10 meV as shown by the red line) depends on the lateral position x, occurring at different distances z from the surface for top (T) and hollow (H) sites, respectively.

Figure 2.2 shows a calculated He-surface interaction potential for Bi(111): (a) shows a surface plot, with the potential energy as a function of the lateral distance x and the distance z with respect to the surface, with the potential rising steeply already at several Å away from the topmost layer. In Figure 2.2(b) a contour plot with equipotential lines is shown, illustrating that the turning point (e.g. for an energy of 10 meV as shown by the red line) depends on the lateral position x. Since the potential follows the two-dimensional periodicity of the surface layer, it is possible to express the static potential in terms of a Fourier series representation[15], which in turn is useful for scattering calculations.

2.2 Elastic scattering: Surface structure and electronic corrugation

The formation of a diffraction pattern upon scattering of a monochromatic atom beam from a periodic surface can be seen in analogy to other scattering methods such as X-ray scattering. As illustrated in Figure 2.3(b), a monochromatic He beam can be described as a plane wave, following the wave-particle duality. Since momentum and wavelength are inversely proportional via the de Broglie relation, He atoms with an incident energy of 10 meV exhibit a wavelength of 1.4 Å[14]. Hence scattering from a surface with periodicity on a similar length scale, will give rise to a diffraction pattern as illustrated in Figure 2.3(b) - quite analogous to X-ray diffraction - although the scattering mechanism itself is quite different (see 2.1) as the classical turning point for a He atom is several Å above the surface.
As stated by Bragg's law, if a wave is scattered by a periodic surface, the change of the wavevector component parallel to the surface, $\mathbf{K}$, must be equal to a surface reciprocal lattice vector, $\mathbf{G}$. The typical scattering geometry in such a HAS experiment is shown schematically in Figure 2.3(a). A diffraction pattern is obtained by varying the polar (incident) angle ϑ_i around the corresponding axis while the scattered beam intensity is detected. For elastic scattering, the momentum transfer parallel to the surface, $\Delta\mathbf{K}$, is then given by

$$|\Delta\mathbf{K}| = |\mathbf{K}_f - \mathbf{K}_i| = |\mathbf{k_i}| \left[\sin\vartheta_f - \sin\vartheta_i\right] = |\mathbf{k_i}| \left[\sin(\vartheta_{SD} - \vartheta_i) - \sin\vartheta_i\right] \ , \tag{2.2}$$

where $\mathbf{k_i}$ is the incident wavevector and ϑ_i and ϑ_f are the incident and final angles with respect to the surface normal, respectively. Note that both types of HAS apparatus used for the studies in this work are based on a fixed source-target-detector geometry, so that $\vartheta_i + \vartheta_f = \vartheta_{SD}$, with ϑ_{SD} the fixed angle between source and detector.

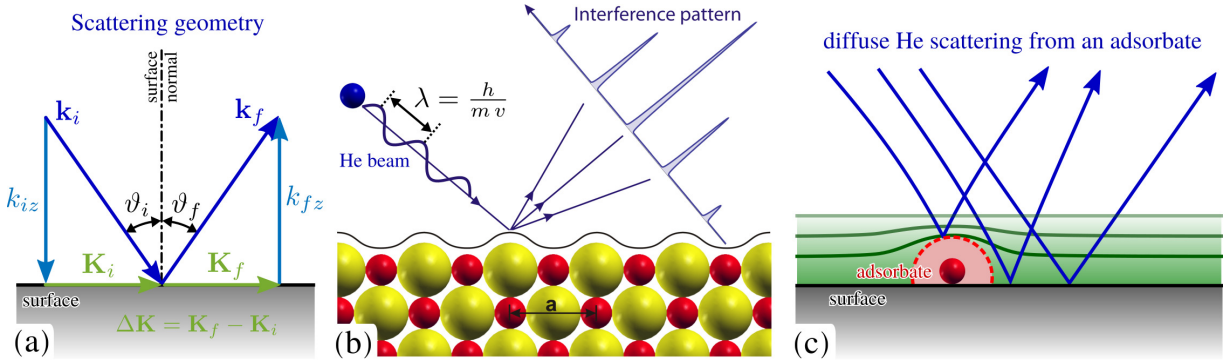

Figure 2.3: (a) Illustration of the scattering geometry in a HAS experiment. The subscripts i, f denote the incident and final states with the incident and scattered wavevectors as $\mathbf{k}_i$ and $\mathbf{k}_f$, respectively. The incident angle ϑ_i is defined with respect to the surface normal while the total scattering angle $\vartheta_{SD} = \vartheta_i + \vartheta_f$ is fixed. By convention, the components parallel to the surface are given in capital letters, $\mathbf{K}_i$ and $\mathbf{K}_f$, with the momentum transfer parallel to the surface becoming $\Delta\mathbf{K} = \mathbf{K}_f - \mathbf{K}_i$. (b) Coherent scattering from a periodic surface gives rise to a diffraction pattern. (c) Scattering from isolated adsorbates typically gives rise to diffuse scattering as illustrated. Isolated adsorbates often exhibit an apparent He scattering cross section which is much larger than its size as illustrated by the dashed red line. It follows from the scattering process since He atoms are scattered from the electron cloud and the He beam exhibits also "refraction" in the vicinity of the adsorbate as illustrated by the blue lines.

Figure 2.4 shows the scattered He intensity versus incident angle ϑ_i for Bi_2Te_3(111) along a high symmetry direction of the crystal. The lattice constants can be determined from the position of the diffraction peaks (illustrated by the horizontal green arrow) while the intensity of the diffraction peaks (red vertical arrow) provides information about the "corrugation" of the surface electron density.
Since He atoms are scattered by the charge distribution at the surface, the shape of this distribution influences the height of the diffraction peaks. The surface charge density as "seen" by He atoms at a certain incident energy can be written as $\xi(\mathbf{R})$ where $\mathbf{R}$ is the lateral position in the surface plane. $\xi(\mathbf{R})$ is referred to as the surface electronic corrugation as it describes a periodically modulated surface (see Figure 2.4(b)) with constant total electron density. In the limit of classical reflection this corresponds to the turning point defined in (2.1).

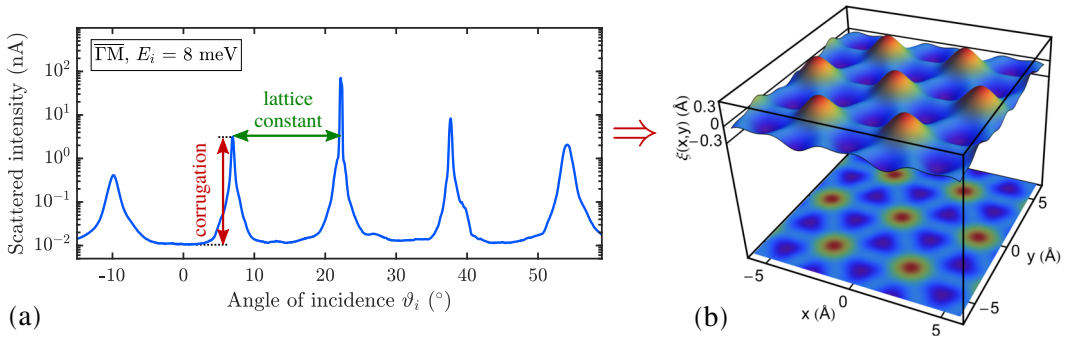

Figure 2.4: The position of the diffraction peaks with respect to the incident angle ϑ_i corresponds directly to the periodic spacing of the sample in real space i.e. to the surface lattice constant (green horizontal arrow). The surface electronic corrugation determines the fraction of the incident beam which is scattered into diffractive channels and thus the diffraction intensities (red vertical arrow). Hence an analysis of the scattering intensities allows to reconstruct the surface electronic corrugation as illustrated in (b).

The electronic corrugation is usually obtained by calculating the expected diffraction probabilities for a certain $\xi(\mathbf{R})$ followed by optimising $\xi(\mathbf{R})$ to obtain the best match between the theoretically and experimentally obtained peak heights. Therefore the diffraction peak intensities upon elastic scattering of a He beam from the surface need to be calculated based on methods described in 2.4.

2.3 Surface order and adsorption/desorption processes from HAS

In addition to diffraction experiments, that reveal information about the surface structure, measurements of the specular He reflectivity can provide information about the degree of order on the surface[14]. The intensity of the specular beam will be greater for a highly ordered surface since less signal is lost in other scattering directions. Hence measuring the proportion of incident He that is scattered into the specular direction is a means of determining the surface quality which is reduced by step edges and defects. Furthermore, monitoring changes in the specularly reflected intensity upon deposition of atoms and molecules provides also a multitude of information about the adsorption process and growth of films at the surface as shortly outlined below.

Degree of surface order In general, the width of the specular peak is determined by the angular broadening of the apparatus and the quality of the crystal. Hence a measurement of the angular spread in the specular peak provides an estimate of the surface quality, since the peak broadening is proportional to the average domain size, also known as the surface coherence length[40]. The measured specular width $\Delta\theta_{exp}$ is a convolution of the angular broadening of the apparatus $\Delta\theta_{app}$ and the domain size broadening $\Delta\theta_w$ given by: $\Delta\theta_{exp}^2 = \Delta\theta_w^2 + \Delta\theta_{app}^2$. The coherence length can then be determined using:

$$l_c = \frac{5.54}{\Delta\theta_w \, k_i \, \cos\vartheta_f} \tag{2.3}$$

with k_i the wavevector of the incoming He beam and ϑ_f the final scattering angle.
As an example, the specular peak ($\vartheta_i = \vartheta_f = 22.2°$) in Figure 2.4 exhibits a full width at half maximum FWHM $= (0.095 \pm 0.005)°$ which corresponds to a width of $0.02\,\text{Å}^{-1}$ in terms of the momentum transfer. Following (2.3), the measured FWHM of the specular peak gives rise to an average domain size of at least $1000\,$Å. As shown in Ref.[40] this example illustrates that TI surfaces can be prepared with an exceptionally good surface quality by in-situ cleaving and are perfectly suited for atom scattering studies.

Adsorption/desorption processes from HAS The processes of adsorption and desorption can be monitored by following in real time the specular beam intensity of He atoms scattered from the crystal surface during the deposition of atoms or molecules. The resulting curve is usually called “uptake” curve[41].
In order to calibrate the coverage and to investigate the adsorption of gases and molecules, the helium specular signal I is measured while dosing or evaporating at fixed surface temperatures. In the low coverage limit, the He scattering cross section, Σ, for isolated adsorbates can be calculated as

$$\Sigma = -\frac{1}{n_s} \cdot \frac{1}{I_0} \cdot \frac{\mathrm{d}I}{\mathrm{d}\Theta}\bigg|_{\Theta=0}, \tag{2.4}$$

where Θ is the coverage given by the number of adsorbates per substrate atom, n_s is the number of substrate atoms per unit area, and I/I_0 is the specular helium beam attenuation at coverage Θ[14]. The fact that the presence of adsorbates on the surface substantially attenuates the specular beam can be used as a measure of the adsorbate coverage. Uptake curves are useful to determine the coverage at a given attenuation of the specular intensity or to study the lateral interactions between adsorbates and to determine when regular overlayer structures occur[14].
As illustrated schematically in Figure 2.3(c), the apparent He scattering cross section, Σ, for isolated adsorbates is often much larger than the adsorbate size due to the scattering process and refractive effects in the vicinity of the adsorbate. Values for small molecules are often in the range of several $100\,\text{Å}^2$, e.g. for water on Bi_2Te_3(111) a cross section $\Sigma = 260\,\text{Å}^2$ was found[41].
While adsorption onto a clean and flat substrate initially reduces the degree of order on the surface, giving rise to a lower reflectivity, upon formation of regular structures the degree of order and thus the He reflectivity increases again. Hence monitoring changes of the specularly scattered intensity allows also to follow processes such as epitaxial growth, as adatoms first form isolated defects before coalescing into complete layers and causing the specular intensity to recover[42].

For non-interacting adsorbates occupying random adsorption sites with large cross sections that overlap, it implies that the specular attenuation as a function of coverage is linear on a logarithmic scale[14]. In a typical measurement, the normalised specular intensity I/I_0 is then related to the adsorbate coverage Θ via:

$$I/I_0 = (1-\Theta)^{n_s \cdot \Sigma/\cos\vartheta_i} \tag{2.5}$$

$$\approx 1 - \Theta \cdot n \cdot \Sigma/\cos\vartheta_i \quad \text{for} \quad \Theta \ll 1 \tag{2.6}$$

where the term $\cos(\vartheta_i)$ accounts for the increase of the apparent scattering cross section since scattering happens at an incident angle ϑ_i[41] and the adsorbate density n_s is given by the monolayer (ML) coverage. In the low coverage limit mentioned above, a linear dependence of the intensity versus Θ can be assumed (2.6) and the scattering cross section Σ can be determined from the initial slope of the adsorption curve.

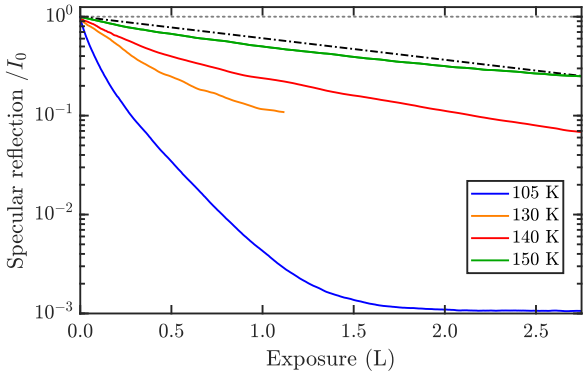

(a) Normalised specular reflection versus exposure for the adsorption of water on Bi_2Te_3(111) at four different surface temperatures.

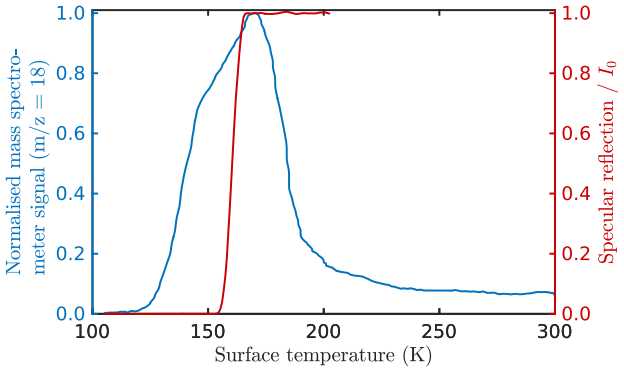

(b) Thermal desorption spectroscopy (left axis) together with the specular He reflection (right axis) for water deposited on Bi_2Te_3(111), prior to heating the sample.

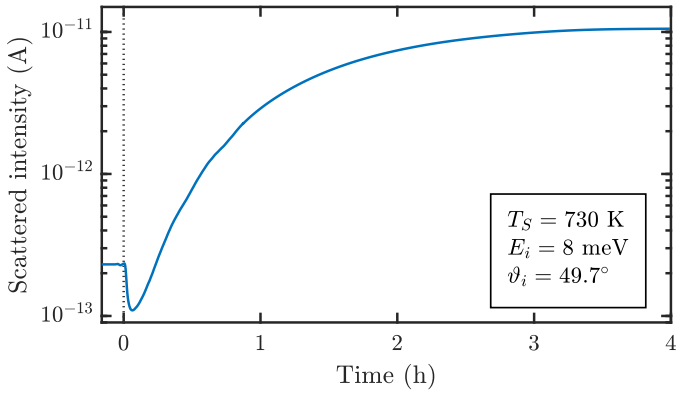

(c) The epitaxial growth of graphene on Ni(111) can be followed by monitoring the first order diffraction peak while dosing ethene (C_2H_4) ($t = 0$ on the abscissa corresponds to starting the dosing). First nickel carbide forms and the intensity drops. As soon as it converts to an ordered graphene layer, the intensity increases since graphene exhibits a larger corrugation than Ni(111).

Figure 2.5: The processes of adsorption and desorption and the formation of regular structures can be monitored by following in real time the specularly scattered He signal during the deposition of adsorbates.

The overlap of giant cross sections with increasing coverage, enables also to obtain information about the adsorbate interatomic forces since both repulsive and attractive forces have distinct signatures[14]. In the case of repulsive forces the scattering cross sections of the individual adsorbates overlap less, increasing the total cross section seen by the He beam compared to that for non-interacting adsorbates and thus the uptake curve falls below the linear line. Attractive interactions on the other hand, will give rise to a larger overlap and the curve rises above linear.
Ideally desorption measurements following the specularly reflected He signal are conducted simultaneously with thermal desorption spectroscopy (TDS) where the m/z ratio on a mass spectrometer is measured. Figure 2.5(b) shows a typical thermal desorption measurement after water had been deposited

on Bi_2Te_3(111). Clearly visible is one dominant peak with a maximum in the TDS spectrum which coincides with a rapid recovery of the specular signal (right axis in Figure 2.5(b)). The Redhead equation can be applied, in order to estimate the desorption energy E_{des}, following:[41]

$$E_{des} \approx k_B \cdot T_m \left[\ln\left(\frac{\nu \cdot T_m}{\beta}\right) - 3.46 \right] , \tag{2.7}$$

with T_m the temperature of the desorption maximum, k_B the Boltzmann constant, β the heating rate and the pre-exponential or frequency factor ν.

2.3.1 From structure to phase transitions at surfaces

The high sensitivity of HAS as compared to other surface probes upon changes of surface structure via scattering from the surface electron density, involves also phenomena such as charge density waves (CDWs). It allows for a precise determination of phase transition temperatures and critical exponents[43,44].
The smallest charge density modulation Δn detectable with HAS can be estimated based on an energy resolution $\Delta E \approx 1$ meV divided by the Esbjerg-Nørskov constant for low-energy He atoms, $A = 750$ eV/atomic units[45], yielding $\Delta n \approx 1.3 \cdot 10^{-6}$ atomic units.
These high sensitivity made the recent observation of CDWs on the surface of Sb(111) possible, which had gone unnoticed by other techniques[46]. Moreover, as recently demonstrated for the 1D topological metal Bi(114), HAS is capable to follow the CDW up to higher temperatures compared to LEED and scanning tunnelling microscopy[47].

2.4 Scattering calculations

The interaction of a helium atom with a surface as introduced in 2.1 is all but simple and in order to precisely calculate the scattering process, one needs to solve the time-dependent Schrödinger equation, with a He-surface interaction potential, of dimension depended on the number of particles in the systems. Such a calculation is impractical for any realistic system of more than a handful of surface atoms. Therefore, the process is often much simplified, by using an analytic atom-surface potential or implying even a hard-wall potential and using approximations such as the Eikonal approximation[14].
A more exact approach is the close-coupling (CC) method[48] which goes beyond the simple hard-wall approximation and has been mainly applied to ionic and metallic surfaces[14]. In the following the elastic variant of the CC formalism is described with a short outlook to the inelastic case (2.6) as it has also been described in Ref[49].
The starting point for the calculation of elastic scattering intensities based on the CC algorithm is the time-(in)dependent Schrödinger equation given by

$$\left[-\frac{\hbar^2}{2m}\nabla^2 + V(\mathbf{r}) - \frac{\hbar^2 \mathbf{k}_\mathrm{i}^2}{2m} \right] \Psi(\mathbf{r}) = 0 , \tag{2.8}$$

with m being the mass of the He atom and $\mathbf{k}_\mathrm{i}$ as the incident wave vector. Due to the periodicity of the surface, the wave function Ψ and the interaction potential V can be written as Fourier series:

$$\Psi(\mathbf{r}) = \sum_{\mathbf{G}} \Psi_{\mathbf{G}}(z) \mathrm{e}^{\mathrm{i}(\mathbf{K}_\mathrm{i}+\mathbf{G})\cdot\mathbf{R}} , \tag{2.9}$$

$$V(\mathbf{r}) = \sum_{\mathbf{G}} V_{\mathbf{G}}(z) \mathrm{e}^{\mathrm{i}\mathbf{G}\cdot\mathbf{R}} . \tag{2.10}$$

Here, $\mathbf{G}$ is the two-dimensional reciprocal lattice vector and $\mathbf{K}_\mathrm{i}$ the projection of the incoming wave vector onto the surface.

Substituting these in (2.8), rearranging the terms and integrating over a single unit cell leads to the CC equations:[48]

$$\left[\frac{\mathrm{d}^2}{\mathrm{d}z^2} + \mathbf{k}^2_{\mathbf{G},z} - V_{\mathbf{0}}(z)\right]\Psi_{\mathbf{G}}(z) = \sum_{\mathbf{G}'\neq\mathbf{G}} V_{\mathbf{G}-\mathbf{G}'}(z)\Psi_{\mathbf{G}'}(z)\ . \tag{2.11}$$

$\mathbf{k}^2_{\mathbf{G},z}$ is the perpendicular energy of the He atom in the scattering channel denoted by the reciprocal lattice vector $\mathbf{G}$ and $V_{\mathbf{G}}$ the Fourier component of the interaction potential with respect to $\mathbf{G}$, with $\mathbf{k}^2_{\mathbf{G},\mathrm{z}} = \mathbf{k}^2_{\mathrm{i}} - (\mathbf{K}_{\mathrm{i}} + \mathbf{G})^2$. $V_{\mathbf{0}}$ in (2.11) is the laterally averaged atom-surface interaction potential.
In cases where $\mathbf{k}^2_{\mathbf{G},\mathrm{z}} > 0$ one speaks of open channels, describing a standard scattering process. If $\mathbf{k}^2_{\mathbf{G},\mathrm{z}} < 0$, the channel is said to be closed and the He atom undergoes a transition into a bound state, if supported by the interaction potential at this specific energy, before leaving the surface again – this process is also called selective adsorption resonance (SAR) and further described in 2.5.
Scattering calculations according to (2.11) require a realistic He-surface interaction potential as introduced in 2.1. In the case of semimetal and TI surfaces, the corrugated Morse potential (CMP) has proven to be a good approximation of the atom-surface interaction potential[38,49] and was applied for the analysis of the here presented surfaces. The CMP can be written as

$$V(\mathbf{R}, z) \;=\; D\left[\frac{1}{\upsilon_0}\mathrm{e}^{-2\chi(z-\xi(\mathbf{R}))} \;-\; 2\mathrm{e}^{-\chi z}\right]\ . \tag{2.12}$$

Here D is the potential well depth, χ is the stiffness parameter, and υ_0 the surface average over $\mathrm{e}^{2\chi\xi(\mathbf{R})}$.
To finally solve the CC equations, all open channels and a selected number of closed channels[49] is included and the system is solved using the Numerov and Fox-Goodwin algorithms[50] with the usual boundary conditions[51] for diffracted waves. The result is the scattering matrix, from which the scattering intensities can be extracted.
The developed CC code was implemented in Python and a short description of how to install a copy on a local computer can be found at www.tugraz.at/en/institutes/iep/research/surfaces/software/.

Diffraction intensities Following these quantum mechanical scattering calculations the intensities in the angular diffraction scans can be determined and compared with the experimental intensities. The elastic CC-calculations further need to be corrected for the Debye-Waller attenuation, using a previously determined Debye-Waller factor / surface Debye temperature Θ_D (Equation 2.22). The comparison of the theoretically evaluated and corrected intensities with the experimental results is usually performed by determining the experimental peak areas. The reason for using the peak areas instead of the peak heights is the need to account for the broadening of the elastic peaks caused by the energy spread of the He beam. Furthermore, additional broadening of the diffraction peaks is caused by the geometry of the apparatus, defects and the domain size effects of the crystal surface.
In principle, the corrugation determines the fraction of the incident beam which is scattered into diffractive channels and thus the diffraction intensities. Thus by optimising $\xi(\mathbf{R})$, a surface corrugation function of the system is obtained. Since $\xi(\mathbf{R})$ follows the periodicity of the surface, it can be written using a simple Fourier ansatz where only the amplitude is varied[38] (see Figure 2.4(b)).
By comparing a data set of several angular scans over the high symmetry directions and at various sample temperatures the value of the corrugation is then iteratively improved. The optimisation is usually performed by minimising a measure of the deviation R:

$$R = \frac{1}{N}\sqrt{\sum_G \left(I_G^{\mathrm{exp}} - I_G^{\mathrm{sim}}\right)^2}\,, \tag{2.13}$$

with I_G^{exp} and I_G^{sim} being the measured and calculated diffraction intensities and N the number of experimentally measured diffraction peaks[14].

Inelastic scattering calculations Extension to inelastic scattering is achieved by starting from the time dependent Schrödinger equation and altering the interaction potential

$$V(\mathbf{r},t) \approx V(\mathbf{R}) + \mathbf{u}(\mathbf{R},t) \cdot \nabla V(\mathbf{r}). \tag{2.14}$$

to include the (time dependent) displacement of the atoms from their respective equilibrium positions. The displacement is then described as

$$\mathbf{u}(\mathbf{R},t) = \sum_{\mathbf{Q},\nu} \mathbf{A}\left(\mathbf{Q},\nu,T\right) \mathrm{e}^{\mathrm{i}\mathbf{Q}\cdot\mathbf{R}} \cos\left[\omega_\nu(\mathbf{Q})t\right], \tag{2.15}$$

with $\omega_\nu(\mathbf{Q})$ as the frequency of a phonon with a wave vector $\mathbf{Q}$ in mode ν and T as surface temperature. $\mathbf{A}\left(\mathbf{Q},\nu,T\right)$ describes the surface temperature dependent amplitude of this motion. Following this approach inelastic effects can be accounted for by adding inelastic scattering channels, as described in a short outlook in 5.1.

2.5 Measurements of the atom-surface interaction potential

The shape of the interaction potential between the surface and atoms can be extracted from atom-surface scattering experiments and several publications presented in this work have followed this approach using HAS from semimetal and TI surfaces[36,52–54].
The He-surface interaction potential as introduced in 2.1 is solely defined through dispersion forces and the Pauli-repulsion and affects the measured elastic and inelastic scattering intensities. Due to the attractive part of the potential, the He atom can be transiently trapped in a bound-state of the interaction potential and travel along the surface until it leaves due to an additional scattering event (Figure 2.6(a)). Intensity fluctuations originating from this effect are called selective adsorption resonances (SAR) and are commonly used to measure the eigenenergies ϵ_n of the interaction potential with high accuracy[14,15,55]. Because of the extremely small adsorption energies of He atoms on surfaces (in the few meV region) and the de-localised nature and mobility of electrons on conducting surfaces, the experimental data can serve as a benchmark for state-of-the-art vdW corrected DFT approaches and the suitability of several vdW approaches[56].
In order to determine an accurate three-dimensional atom-surface interaction potential the analysis of SARs has to be combined with quantum mechanical scattering calculations[42,49,57] as outlined below.

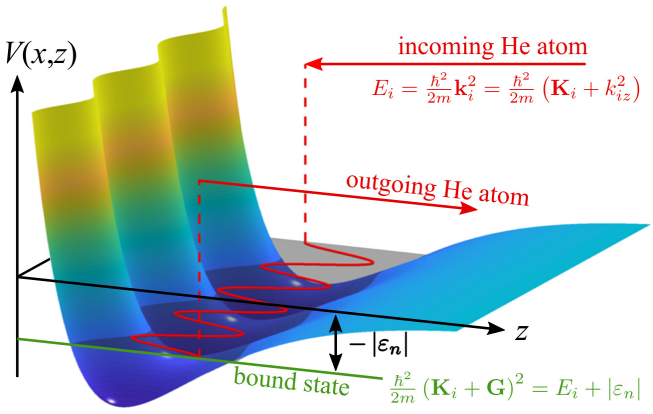

(a) Illustration of a resonance process in which the He atom is trapped in a bound state of the atom-surface potential.

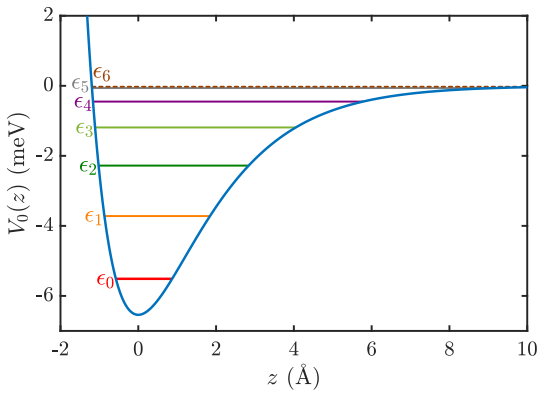

(b) Laterally averaged Morse potential for He-Bi_2Se_3(111) with the bound states (horizontal lines).

Figure 2.6: In the simple semi-classical picture (the free-atom approximation), resonance scattering corresponds to scattering into an evanescent, resonant state that propagates parallel to the surface .

An SAR process occurs when the outgoing wavevector component perpendicular to the surface $k_{f,z}^2$ becomes negative which is a kinematically disallowed state. This appears when the difference between the incident energy and the kinetic energy of the atom moving parallel to the surface matches the binding

energy ϵ_n of an adsorbed atom:[55]

$$E_i = \frac{\hbar^2 \mathbf{k}_i^2}{2m} = \frac{\hbar^2(\mathbf{K}_i + \mathbf{G})^2}{2m} + \epsilon_n(\mathbf{K}_i, \mathbf{G})\,, \tag{2.16}$$

where m is the He mass. The bound state ϵ_n is here defined as a function of the parallel momentum $\mathbf{K}_i$ and the interacting G-vector $\mathbf{G}$. Hence studying the SAR processes on the surface leads to the bound state energies which in succession allows to determine the atom-surface interaction potential.
In the free atom approximation, once the He atom has entered a bound state, it can move freely parallel to the surface as illustrated in Figure 2.6(a). It corresponds to a simplification of (2.16), neglecting the corrugation of the potential: ϵ_n is then the n^{th} bound state of the laterally averaged potential, $V_{\mathbf{0}}(z)$ (ϵ_n in (2.16) becomes independent of $\mathbf{K}_i$ and $\mathbf{G}$). Such an approximation is useful in order to obtain a first "idea" of the potential parameters from the experimental data which can then subsequently be refined using a three-dimensional model potential that is matched to the experimental results.
Following the free-atom approximation one can directly obtain the bound state energies of the laterally averaged interaction potential, $V_0(z) = D\left[e^{-2\kappa z} - 2e^{-\kappa z}\right]$ as shown in Figure 2.6(b). The kinematic condition (2.16) can then be expressed in terms of the incident angle ϑ_i and the incident wave vector k_i:

$$\tfrac{2m}{\hbar^2}|\epsilon_n| = (k_i \sin\vartheta_i + G_\parallel)^2 + G_\perp^2 - k_i^2\,, \tag{2.17}$$

where $\mathbf{G}$ has been split into its parallel and normal component $(G_\parallel, G_\perp)$.
According to the kinematic condition (2.16), one can either vary E_i or the parallel momentum transfer $\mathbf{K}_i$. In a conventional HAS experiment[14], there are three variables: the incident energy, E_i, together with the polar and azimuthal scattering angles, ϑ_i and φ_i. Here, the scattering angles correspond to changes of $\mathbf{K}_i$ as determined by the scattering geometry. Often the energy and azimuthal angle are fixed while the polar angle ϑ_i is varied followed by a simplified analysis.
However, in particular potentials with a large corrugation, derived on the assumption of the free-atom approximation, are inaccurate and the bound-state energies are known to be systematically misplaced. The full picture is analogous to a 2D band structure of nearly-free particles due to the periodic corrugation of the potential, i.e., in the laterally averaged potential, each bound state gives rise to a 2D sub-band of the overall band structure[12]. Hence for an accurate determination of the three-dimensional atom-surface interaction potential, several of the above described experimental variables should be varied, thus providing a larger data set while at the same time solving the elastic scattering problem exactly by using computational methods such as the CC algorithm.

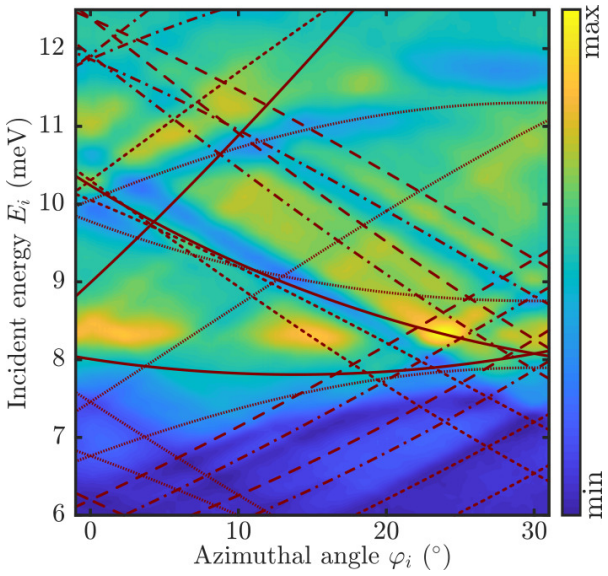

Figure 2.7: Specular intensity for He scattering from Bi(111) at 150 K, obtained from a HAS-FT measurement. The scattered intensity is plotted as a colour map versus incident energy, E_i, and azimuthal angle, φ_i, showing a large number of resonant features which disperse strongly across the plot. The superimposed lines show the kinematic conditions in the free atom approximation.

By using Fourier-transform (FT) HAS, a wide range of incident energies can be studied at once, producing large data-sets over a wide range of kinematic conditions. In FT-HAS, the spread of energies in the incident beam is intentionally broadened as far as possible, and the spin-echo principle (3.5) is then used to analyse the energy distribution of the scattered beam, thus providing energy dependent reflectivity information[12,58] as illustrated in Figure 2.7 for Bi(111): A large number of resonant features can be seen as bright and dark stripes, dispersing across the plot. The advantage of FT HAS with respect to conventional HAS is, that the energy resolution is unaffected by the spread in the incident beam, and the data taking time depends on the required spectral resolution, rather than the spectral range[12]. The superimposed lines in Figure 2.7 show

the kinematic conditions in the free-atom approximation, illustrating that a number of features can be reproduced but there are significant offsets and shifts with respect to the maxima/minima in the experimental data that can only be reproduced when considering the full three-dimensional potential in a quantum mechanical scattering calculation.

2.6 Inelastic scattering and the surface phonon dispersion

Detailed descriptions about lattice vibrations in a solid can be found in most solid state physics textbooks[17,59]. In analogy to surface electronic states, the altered environment at the surface changes also the dynamical properties giving rise to new vibrational modes. These new vibrational modes are called surface phonons due to their localisation at the surface[15]. He atom scattering has long been used to measure the surface phonon dispersion relation of several materials since the combination of relatively high momenta at low energies (compared to photons) and the low atomic mass of He enable the measurement of low frequency surface lattice vibrations with a high scattering cross-section[14,15].
Creation or annihilation of phonons due to inelastic scattering gives rise to an energy loss or gain of the scattered He atom. Thus a determination of the energy change via time-of-flight (TOF) measurements or the spin-echo technique (3.5) allows to determine the involved phonon energies. Employing this method for several incident conditions (momentum transfer ΔK occurs due to scattering from the crystal, at a certain incident angle ϑ_i - see Figure 2.1(a)) allows to reconstruct the entire surface phonon dispersion relation.

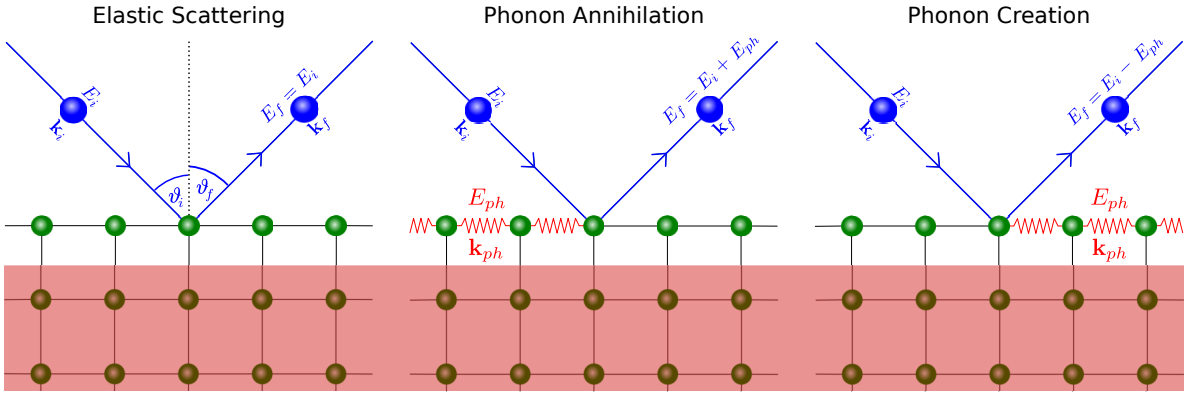

Figure 2.8: Illustration of three possible scattering events: The He atom (in blue) can either be scattered elastically or gain/lose energy via the annihilation/creation of a surface phonon with energy E_{ph}. The fact that the atom cannot penetrate into the bulk is indicated by the region shaded in red.

Figure 2.8 shows a simple illustration for elastic and inelastic scattering of a He beam from a crystal surface, provided that the scattering plane defined by the wavevectors $\mathbf{k}_i, \mathbf{k}_f$ contains the surface normal. The subscripts i, f denote again the incident and final He states and the subscript ph denotes a possible phonon. From conservation of energy and momentum parallel to the surface before and after scattering it follows that $E_f = E_i + \Delta E$ and $K_i = K_f + \Delta K$, with the parallel components of the momentum $K_i = k_i \sin\vartheta_i$ and $K_f = k_f \sin\vartheta_f$. The change in energy ΔE is equal to the change in kinetic energy of the He atom via:

$$\Delta E = E_f - E_i = \frac{\hbar^2}{2m}\left(k_f^2 - k_i^2\right) = \frac{h^2}{2m}\left(\frac{1}{\lambda_f^2} - \frac{1}{\lambda_i^2}\right) . \tag{2.18}$$

The classification into creation/annihilation of phonons is according to the energy change ΔE and the corresponding surface phonon energies are obtained by determining ΔE according to (2.18). In conventional HAS this done by performing TOF measurements and converting TOF data to the energy scale, with energy loss and gain peaks for the creation and annihilation of a phonon, respectively. Spin-echo measurements on the hand directly work in the wavelength domain as described in 3.5.3.

Assuming that the inelastic scattering event corresponds to a single phonon event, the phonon energy $E_{ph} = \hbar\omega$ corresponds directly to ΔE:

$$E_{ph} = \hbar\omega = \frac{h^2}{2m}\left(\frac{1}{\lambda_f^2} - \frac{1}{\lambda_i^2}\right) , \tag{2.19}$$

where λ_i and λ_f are the incoming and outgoing wavelength of the He beam and m is the He mass. To determine the entire phonon dispersion curve up to the Brillouin zone boundary a series of spectra at varying incident angles ϑ_i is measured. The phonon dispersion is then obtained by calculating the parallel momentum transfer $|\Delta K|$ for each extracted phonon energy E_{ph} based on the conservation laws of energy and parallel momentum which provide the so-called scancurve for planar scattering:[60,61]

$$\frac{E_{ph}}{E_i} + 1 = \frac{\sin^2\vartheta_i}{\sin^2\vartheta_f}\left(1 + \frac{\Delta K}{K_i}\right)^2 , \tag{2.20}$$

with incident energy E_i and the scattering geometry $(\vartheta_i\,, \vartheta_f)$ as illustrated in Figure 2.3(a) and Figure 2.8. The phonon parallel momentum is then given by $|\Delta K| + G$, with the surface reciprocal lattice vector G in the scattering plane, needed to bring Q into the first Brillouin zone, accounts for *umklapp* processes.

Finally, on metal, semimetal or semiconductor surfaces, energy-resolved measurements contain information about the e-ph coupling[6,40]: Since the He atom is repelled by the electron density a few Ångströms above the surface, inelastic measurements correspond to lattice vibrations that have communicated through the electron cloud to the impinging He atom (Figure 2.9).

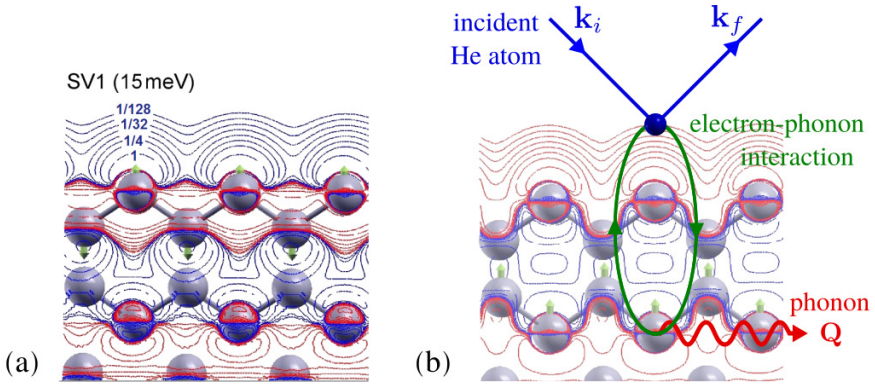

Figure 2.9: Calculated charge density oscillations (CDOs) on Bi(111) induced by the atomic core displacement at zero wave vector. The contour lines show the corresponding increase (red lines) or decrease (blue lines) with respect to the static charge density (in values of $\pm 2^{-n} \cdot 10^{-4}$ atomic units). The core displacement amplitudes are shown by the arrows. Although the SV3 mode in (b) is mostly localised on the 3rd and 4th atomic layer it gives rise to CDOs above the topmost atomic layer, comparable to the first layer mode SV1 in (a), due to the e-ph interaction as schematically illustrated by the green arrows in (b).

Due to this fact, He atoms have a higher chance of interacting with phonon modes possessing a higher e-ph interaction[37,62,63]. Using this information, a simple measurement of inelastic HAS is the first known method, capable of measuring the e-ph interaction parameter $\lambda_{\mathbf{Q},\nu}$ mode-selectively as described in the following.

2.7 The Debye-Waller factor in HAS

Upon scattering on a surface, the thermal vibrations of the surface atoms give rise to inelastic scattering events, which is observed in the thermal attenuation of the coherent diffraction intensities without changes of the peak shape[14,42]. The decay of the diffraction peak intensities with increasing surface temperature T_S is caused by the increasing vibrational amplitude of the surface oscillators.

The Debye-Waller (DW) factor describes this attenuation of the elastically scattered intensity $I(T_S)$ at temperature T_S, with respect to the elastic intensity of the surface at rest, I_0[14,42]. It is a multiplicative factor typically written as an exponential function, $\exp\{-2W(\mathbf{k}_f, \mathbf{k}_i, T_S)\}$, of the final ($\mathbf{k}_f$) and incident ($\mathbf{k}_i$) wavevectors of the scattered atom, i.e.,

$$I(T_S) = I_0\, \mathrm{e}^{-2W(T_S)}\ . \tag{2.21}$$

According to (2.21), the DW exponent can be determined from a plot of the natural logarithm of the intensity $\ln[I(T_S)/I_0]$ versus the surface temperature T_S. For a two-body collision model, where the incident beam directly interacts with the target atom, the DW exponent is simply expressed by $2W(\mathbf{k}_f, \mathbf{k}_i, T) = \left\langle(\Delta\mathbf{k}\cdot\mathbf{u})^2\right\rangle_T$, where $\Delta\mathbf{k} = (\mathbf{k}_f - \mathbf{k}_i)$ is the scattering vector, $\mathbf{u}$ is the phonon displacement experienced upon collision, and $\langle\cdots\rangle_T$ denotes the thermal average.
Note that the concept of the DW factor and the Debye temperature was first derived for X-ray and neutron scattering and later adapted to atom-surface scattering. In the case of HAS, the momentum transfer $\mathbf{\Delta k}$ can be separated into a component parallel and perpendicular to the surface as illustrated in Figure 2.3(a) and the parallel component is given by (2.2).
Within a reasonable approximation for final angles not too different from the incident angle, the DW exponent then reduces to the z-component of $\mathbf{\Delta k}$. Replacing the atom displacement with the relation for a classical harmonic oscillator together with the definition of the Debye temperature gives:

$$2W(T_S) = \frac{3\hbar^2\Delta k_z^2 T_S}{M k_B \Theta_D^2}\ , \tag{2.22}$$

where M is the mass of the surface atom, k_B the Boltzmann constant and Θ_D the surface Debye-temperature. Since we are dealing with comparatively small parallel momentum transfers in the presented HAS experiments, (2.22) can be considered to be approximately correct[37,42]. The presence of the attractive atom-surface interaction in the case of atom-surface scattering can further be corrected for in (2.22) based on (2.25). The surface Debye temperature can then be calculated using the slope of a linear fit of $\ln[I(T_S)/I_0]$ versus T_S.
As long as the Debye model is valid, (2.22) can be used to determine Θ_D, which can further be compared with e.g. the bulk Debye temperature from X-ray and neutron scattering. One caveat of (2.22) is, that a value for the mass of the surface scatterer M has to be assumed. Typically M is chosen to be the mass of the crystal atoms since the surface Debye temperature is related to the motion of the ion cores. However, the ambiguity in this approach is based on its adaptation from other scattering techniques, since He atoms are scattered by the electron density rather than the ion cores[64–66].
Due to the e-ph coupling, the surface Debye temperature is associated with charge density oscillations that are induced by vibrations of the ion cores (see Figure 2.9 and 2.8.1). Hence, strictly speaking, when writing the DW exponent in the usual way as a quantity directly proportional to the surface atom mean-square displacements, one needs to consider an effective surface Debye temperature Θ_D^* and a surface atom effective mass M^*, including contributions arising from the e-ph interaction. Nevertheless, these simple equations have proven to serve as a good approximation in the case of HAS and using the mass of a single surface atom is a reasonable choice in many cases[42].

2.8 Electron-phonon coupling and energy dissipation

Considerable efforts have been made by the condensed matter community to study energy dissipation via e-ph coupling in materials. A convenient parameter to characterise the e-ph coupling strength is the mass-enhancement λ[67]. Following the simple picture introduced in most solid state physics textbooks[17], due to the e-ph coupling the electron dispersion curve is flattened close to the Fermi energy E_F, i.e. the effective electron mass increases according to $m_e^* = m_0(1+\lambda)$ where m_e^* and m_0 are the effective masses with and without e-ph coupling, respectively.
Since the e-ph coupling describes the interaction between the electronic system and the lattice dynamics (phonons), experimental studies at finite temperature can either concentrate on the electronic or the phononic system. The former is mostly available via ARPES measurements by examining the renormal-

isation of the electron energy dispersion in the vicinity of the Fermi surface due to e-ph interactions. The latter can be carried out using HAS, which on the contrary, studies the renormalisation of the surface phonon dispersion due to e-ph interactions. From the above it is apparent that the two methods are complimentary and in order to obtain a complete picture of the e-ph coupling at surfaces, high-resolution measurements of both the electronic and the phononic system are necessary[68]. However, there are also some advantages in tackling the problem by concentrating on the phononic system, as described below.

A typical approach using ARPES is to measure the temperature dependence of the total linewidth Γ. While both electron-electron and defect scattering will influence the total linewidth ($\Gamma = \Gamma_{e-e} + \Gamma_{e-df} + \Gamma_{e-ph}$), typically the e-ph component Γ_{e-ph} is the only one with a strong temperature-dependence[67], which is therefore employed in temperature dependent ARPES measurements of the linewidth[4,69]. Here, the detection energy range of ARPES based on synchrotron radiation is resolution limited to some extend which can be overcome by laser-based ARPES systems[70]. On the other hand, due to the electron mean free path of electrons in the solid, laser-based ARPES exhibits a much larger contribution from bulk states compared to "standard" ARPES.

The ability of HAS to determine the surface averaged e-ph interaction λ, directly from the thermal attenuation of HAS spectra, has the advantage that a wide range of experimental conditions can be used for the evaluation compared to the limited range where e-ph effects are visible in ARPES. Hence in some cases it guarantees a more practical and more accurate determination of the materials λ-value[6]. Finally, the energy-broadening in ARPES is minute compared to the measured absolute (electronic) energies, whereas the phonon energies itself are already in the low meV region and changes due to the e-ph coupling in HAS measurements will be larger in relation to that.

2.8.1 E–ph coupling from the DW factor: The case of metal surfaces

In recent publications[2,63,64,71] and further extensions which are part of this work[6,40,72], it was shown, that the temperature dependence of the DW exponent permits to extract for a conducting surface the mass-enhancement parameter λ (Figure 2.10).

As described in 2.7, the way of writing the DW-factor in terms of the Debye temperature and a surface scattering mass is based on its adaptation from other scattering techniques. Since a meV He beam incident on a conducting surface is exclusively scattered by the surface electron density, the exchange of energy with the phonon gas only occurs via the phonon-induced modulation of the surface free-electron gas, i.e., via the e-ph interaction. Therefore, it is more intuitive, to write the DW factor $W(\mathbf{k}_f, \mathbf{k}_i, T_S)$, which implicitly depends on the scattering wavevectors $(\mathbf{k}_f, \mathbf{k}_i)$, in relation to the e-ph coupling strength λ of the conducting surface.

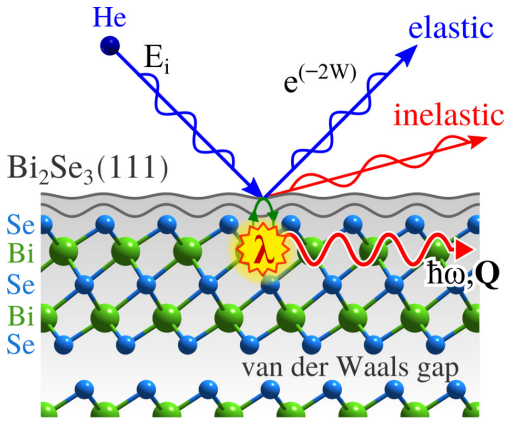

Figure 2.10: The thermal attenuation upon inelastic scattering of a He beam with increasing surface temperature, can be used to determine the electron-phonon coupling constant λ.

Since inelastic scattering corresponds to scattering by phonon-induced charge density oscillations[64,71,73], these oscillations are related to the surface Debye temperature via the e-ph coupling. Upon scattering of a He atom, the probability of creating (or annihilating) a phonon of frequency $\omega_{\mathbf{Q},\nu}$ $\{\mathbf{Q}, \nu\}$ with parallel wavevector $\mathbf{Q}$ and branch index ν, is proportional to the corresponding mode-specific e-ph coupling constant $\lambda_{\mathbf{Q},\nu}$[63,71]. The DW exponent is then expressed as a sum over all contributing phonon modes where each phonon mode $\mathbf{Q}, \nu$ is weighted by the mode-specific $\lambda_{\mathbf{Q},\nu}$. For the simplest case, the specular diffraction peak, Manson *et al.* derived the following DW exponent:[63,74]

$$2W(\mathbf{k_f}, \mathbf{k_i}) \cong 4\mathcal{N}(E_F)\,\frac{m}{m_e^*}\frac{E_{iz}}{\phi}\,\lambda\, k_B\, T_S\ , \tag{2.23}$$

for scattering of an incoming He atom with the wavevector $\mathbf{k_i}$ into a final state of wavevector $\mathbf{k_f}$.

In (2.23) λ expresses now the total e-ph coupling strength with $\mathcal{N}(E_F)$, the density of electron states per unit surface cell at the Fermi level and ϕ, the work function. In addition, m is the mass of the He atom, m_e^* the electron effective mass, E_{iz} is the beam energy E_i normal to the surface ($E_{iz} = E_i \cos\vartheta_i$) and k_B the Boltzmann constant. In the case of a hard-wall potential, as noted below, the normal incident energy E_{iz} needs to include the Beeby correction (2.25), i.e. $E_{iz}^{'} = E_{iz} + D$.
As appears from (2.21) and (2.23), the e-ph coupling constant λ can be directly obtained from the temperature dependence of the HAS specular intensity I using the slope determined from the DW plot, $-\Delta \ln(I/I_0)/\Delta T_S = \ln(I_0/I)/T_S$:

$$\lambda_{HAS} \cong \frac{1}{4\mathcal{N}(E_F)} \frac{m_e^*}{m} \frac{\phi}{k_B\, E_{iz}} \frac{\ln(I_0/I)}{T_S} \,. \tag{2.24}$$

(2.24) was derived in[63,74] for conducting surfaces and shown to provide in the case of ordinary metals and semimetals values of λ in agreement with those known from other sources.
It should be noted that, unlike in the case of low-index metal surfaces, characterised by a soft-wall repulsive potential and negligible corrugation the large surface electronic corrugation found for semimetals and TIs[54] implies a hard-wall potential. In this case one needs to correct E_{iz} (or k_{iz}^2) to account for the acceleration by the attractive part of the potential on the He atom when approaching the surface. The latter is commonly referred to as Beeby correction[14], with the corrected wavevector:

$$k_{iz}^{'2} = k_{iz}^2 + 2mD/\hbar^2 \,, \tag{2.25}$$

where m is the He mass and D the He-surface potential well depth (see 2.5)[54].

2.8.2 E-Ph coupling strength of semiconductors and TIs

Recalling that TIs exhibit metallic surface states, with semiconducting properties in terms of their carrier concentration in the bulk, the above introduced approach for a simple metal surface can be adapted. When applied to the surface of a semiconductor one has to consider that the phonon-induced modulation of the surface charge density only involves electrons near the surface within the Thomas-Fermi screening length (TFSL), λ_{TF}.
Following the same approach as above, the DW-factor originating from the integrated action of all phonons weighted by their respective Bose factors, turns out to be directly proportional, under reasonable approximations, to the mass-enhancement factor λ. The DW exponent is then related to the e-ph coupling λ by the equations:[6]

$$\lambda = \frac{\pi}{2n_s}\iota \,, \quad \iota \equiv \frac{\phi}{A_c\, k_{iz}^2} \frac{\partial \ln I(T_S)}{k_B\, \partial T_S} \,, \tag{2.26}$$

where ϕ is the work function, A_c the surface unit cell area, $I(T_S)$ the He specular intensity, k_{iz} the normal component of the incident wavevector, and n_s the number of conducting layers contributing to phonon-induced modulations of the surface charge density. The latter is estimated to be $n_s = 2\lambda_{TF}/c_0$, where the TFSL λ_{TF} characterises the surface band-bending region. Here c_0 is the quintuple layers (QL) thickness, and the factor 2 considers two metallic sheets per QL. Again, due to the large electronic corrugation, k_{iz} in (2.26) should be replaced according to the Beeby correction (2.25).
Ideally, the Thomas-Fermi screening length λ_{TF} is known from characterisations of the surface band-bending region[75], but it may also be estimated according to the formula reproduced in Refs[72,76] provided that m_e^*, ϵ_r and n_c are known. In the case of a degenerate semiconductor with the Fermi level within the conduction band (as e.g. in the case of Bi_2Te_3[40]), λ_{TF} may also be estimated based on $\lambda_{TF} = (2\epsilon E_F/3e^2 n_0)^{1/2}$, where $\epsilon = \epsilon_r\epsilon_0$, is the static dielectric constant, e the electron charge and n_0 the carrier density in the conduction band[59].

2.8.3 Mode-specific e-ph coupling and Kohn anomalies

In addition to the averaged e-ph coupling λ as described above, HAS allows for a measurement of the mode-specific e-ph coupling strength $\lambda_{\mathbf{Q},\nu}$ as illustrated in Figure 2.9 ($\lambda = \sum_{\mathbf{Q},\nu} \lambda_{\mathbf{Q},\nu}$).
The one-phonon transition probability, for a phonon with energy $E_{\mathbf{Q},\nu}$, is proportional to the corresponding charge-density oscillation via:

$$P(\mathbf{k}_i, \mathbf{k}_f) \propto \frac{k_f}{|k_{iz}|}\left[1 + n_{BE}(\Delta E)\right] A^2 \sum_{\mathbf{Q},\nu} \left|\langle \mathbf{k}_f \left|\delta n(\mathbf{Q}\nu, \mathbf{r})\right| \mathbf{k}_i \rangle\right|^2 \delta\left(\Delta E - E_{\mathbf{Q},\nu}\right) \ , \tag{2.27}$$

where n_{BE} is the Bose-Einstein occupation number, A is the Esbjerg-Nørskov constant and $\delta n(\mathbf{Q}\nu, \mathbf{r})$ is the charge density oscillations at position $\mathbf{r}$. Each surface phonon contribution needs to be weighted by the corresponding e-ph coupling $\lambda_{\mathbf{Q},\nu}$, yielding:

$$P(\mathbf{k}_i, \mathbf{k}_f) \propto f(\Delta E)\ N(E_F) \sum_{\mathbf{Q},\nu} \lambda_{\mathbf{Q},\nu}\ \delta\left(\Delta E - E_{\mathbf{Q},\nu}\right) \ , \tag{2.28}$$

where $f(\Delta E)$ is a purely kinematic factor, given by the experimental conditions and $N(E_F)$ is the electronic DOS at the Fermi level. The intensity of a one-phonon event is then given by the integral over the transition probability, i.e.: $I_{1ph} = \int P(\mathbf{k}_i, \mathbf{k}_f)\mathrm{d}E$. Thus if one measures the intensity of a phonon event in an inelastic HAS measurement and relates that to the intensity of the diffuse elastic peak I_{el}, it simplifies to:

$$I_{1ph}/I_{el} \propto \bar{f}\ N(E_F) \sum_{\mathbf{Q},\nu} \lambda_{\mathbf{Q},\nu} \ . \tag{2.29}$$

Hence the mode specific e-ph coupling strength $\lambda_{\mathbf{Q},\nu}$ can be determined according to (2.29) from HAS measurements provided that the proportionality constant (kinematic factor) $\bar{f}$ is known together with the electronic DOS at the Fermi level (e.g. from calculations).
Thus employing measurements of the mode-specific e-ph coupling allows to determine which phonon mode ν is most responsible for energy dissipation due to e-ph scattering events. In a similar context, when considering conventional superconductors or superconducting thin films one could possibly determine which is the mode that is most responsible for the formation of Cooper pairs.

Kohn anomalies The influence of e-ph coupling shows also up by softening phonon modes at specific values of momentum transfer, a phenomenon known as a Kohn anomaly[5,77,78]. A Kohn anomaly manifests itself as a dip in the phonon dispersion and corresponds to a softening of the phonon mode with the energy $\hbar\omega$ in the vicinity of the nesting condition $q = 2k_F$ based on $\omega^2(q) \propto \ln\left|\frac{q+2k_F}{q-2k_F}\right|$.
Whether Kohn anomalies at a phonon momentum that connects opposite sides of a topological Dirac cone are possible, is still an open question as it would require a phonon-induced transition involving a spin-flip[5,68,77,79]. The latter may become possible by creating or annihilating a phonon which carries an angular momentum of 1 (being a quasiparticle described as a plane wave, see Figure 2.11). While Kohn anomalies have been reported in the lower part of the phonon spectrum of TIs[77,79,80], recent studies presented in this work have shown that the major contribution to e-ph coupling in these materials comes from polar optical modes[6,72,80].

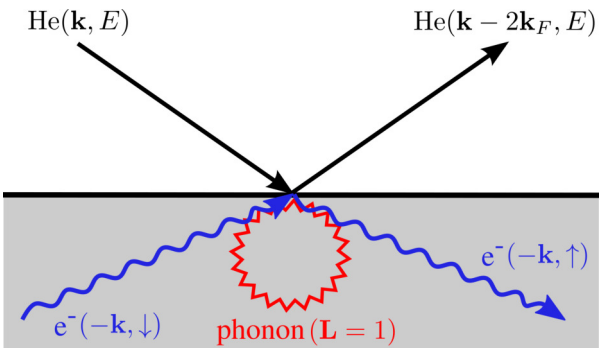

Figure 2.11: Diagram of a possible inelastic Kohn anomaly path enabling a spin-flip transition on a TI surface. The (in this case virtual) phonon supplies its orbital momentum of **L**=1, which in heavy materials (**J**=1) can provide the helicity needed for the spin-flip that is otherwise forbidden by time-reversal symmetry.

3 Surface diffusion measurements based on scattering techniques

While the interfacial motion of atoms and molecules remains a central question to fields as diverse as catalysis, friction, crystal growth and ice nucleation, much of our existing knowledge concerning the microscopic motion still comes from computational simulation[8,9]. In early experimental works, the focus of many techniques was to deduce diffusion constants and make a connection to macroscopic diffusion theory[10–12]. However, only on atomic length-scales the underlying physical behaviour of the diffusion process is revealed. Moreover, only at elevated temperatures, when atoms and molecules move on fast timescales many complicated forms of diffusive motion emerge.
Thus, the study of surface diffusion processes is a unique and challenging problem for experiments, as it requires both sub-nanometer spatial resolution and fast (pico- to nanosecond) temporal resolution as outlined in the following. Consequently, there exists still relatively little experimental knowledge about the fundamental nature of diffusive processes at the molecular level.

3.1 Models of surface diffusion

The process of surface diffusion involves the motion of adatoms, molecules and atomic clusters at material surfaces. For the surface (substrate) being at finite temperature, the diffusing particle is in a continuous thermal motion. Most diffusion concepts are related to the position of the particle, as a function of time, in terms of trajectories. If the trajectories of the individual particles can be "traced" at the atomic level, via measurements or in simulations, the resulting diffusive properties are known as tracer diffusion[10–12]. The concept of tracer diffusion remains also important for finite coverages, as long as the motion of individual species can be distinguished. However, the motion depends on the local configuration of the adsorbed species in a more complicated way and usually, the diffusive process will only in the low coverage regime be mainly determined by the interaction with the substrate.
The term collective or chemical diffusion on the other hand, refers to macroscopic transport of many particles over long distances. Collective diffusion is described by Fick's laws, which applies in the presence of concentration gradients, ceasing as the concentration gradient approaches zero. Note that this should not be confused with correlated tracer motion on the atomic scale - i.e. interactions between the diffusing species - which also has a collective nature[12,41].
A realistic model of collective diffusion requires to account for many physical processes including the diffusion over terraces and step edges as well as over a range of different coverage regimes, in order to make any meaningful comparison with the experiment. The concept of tracer diffusion is much simpler, and typically forms individual building blocks for modelling collective diffusion[10–12].

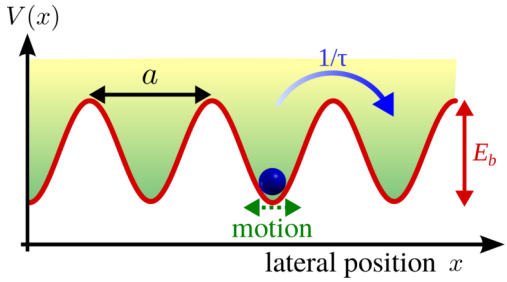

Figure 3.1: Schematic illustration for an atom moving in a one-dimensional lateral potential energy surface (PES). The corrugation of the potential forms an energy barrier, E_b, to diffusive motion. The atom spends most of the time in the well and only occasionally gains enough energy to cross the barrier, giving rise to hopping diffusion. In between these events the atom oscillates around the energy minimum, with the frequency of the vibration being given in terms of a classical motion in a potential well, i.e. by the mass and local curvature of the potential.

The starting point for analytic models, describing the process of atomic-scale diffusion is usually the concept of a particle moving classically in a one-dimensional (1D) lateral potential as shown schematically in Figure 3.1. For low surface temperatures, i.e. if $k_B T \ll E_b$ holds, the adsorbate is mostly confined to the bottom of the adsorption well. The atom gains only occasionally enough energy to cross the barrier, giving rise to hopping motion between adjacent sites.

For such a classical model, the rate Υ how often the hopping occurs, can then be described based on an Arrhenius relationship[11,12],

$$\Upsilon = \Upsilon_0 \exp\left(-\frac{E_b}{k_B T}\right) , \tag{3.1}$$

where E_b is the diffusion barrier and Υ_0 is a pre-exponential factor or attempt frequency. For the hopping rate according to (3.1), Υ_0 is often assumed to be equal to the frustrated translation (T-mode) frequency of the atom in the bottom part of the potential well[11,12].
Note that although $V(x)$ in Figure 3.1 is expected to have the same periodicity a, as the substrate lattice, due to complex adsorbate-surface interactions there exists no general criteria, such as e.g. specific adsorption sites, for the position of the potential minima within a unit cell. In addition, the simple model can be generalised for two dimensions, and corresponding expressions in terms of hopping rates have been obtained, to enable comparison with experiments[10].
Rate theories, which provide estimates of the hopping rate Υ based on the statistical thermodynamic properties of the system, have been widely used. E.g., transition state theory (TST), connects the motion with the transition of the adsorbate from a metastable state over the potential barrier to its adjacent site, as illustrated in Figure 3.1. The underlying idea of TST is to use the ratio of the partition functions in the transition state, Z_s, to the well state, Z_0, to provide an estimate of the hopping rate given by:[11,12]

$$\Upsilon = \frac{k_B T}{h}\frac{Z_s}{Z_0} . \tag{3.2}$$

The concept in traditional TST is quite simple: The hopping rate is related to the rate of passage of the adsorbate through the transition state at the top of the energy barrier. For the simple 1D case described above, the probability for an adsorbate, occupying a certain state in the potential $V(x)$, is given by the Boltzmann distribution which further allows to determine the probability of occupying the transition state in relation to the probabilities of all states within the unit cell. Assuming a very simple potential shape in terms of an harmonic oscillator ($V(x) = \frac{1}{2}kx^2$), the pre-exponential factor in (3.1) is then directly given by the frequency of the harmonic oscillator $\Upsilon_0 = \frac{\omega}{2\pi}$.
However, the problem in assuming the motion of an adsorbate fully classically is that it assumes a free atom kinetic energy for the adsorbate at the transition state, and ignores the possibility of quantum mechanical effects such as tunnelling. Thus, the assumptions of traditional TST ignore the nature of discrete energy states, at which tunnelling processes can occur and significant errors will arise for systems with light adsorbates[81].
More importantly, in addition to quantum mechanical effects which are mostly important for light adsorbates, traditional TST does not account for the rate of energy transfer between the adsorbate and the surface, unlike, for example the Langevin or Fokker-Plank equations[12]. The concept of energy transfer or "friction" refers to energy dissipation from the adsorbate to the substrate which in turn leads to a lower probability of completing a transition to the adjacent site. Thus energy dissipation in surface diffusion is typically represented by a friction coefficient η.
3.6.3 outlines simple types of diffusive motion and their corresponding experimental signatures based on parameters such as η and the diffusion barrier E_b in the Langevin description of dynamics. For example, in ideal Brownian diffusion, where there are no barriers, the hopping rate decreases as the friction η increases.
On the other hand, if the diffusion process is activated, then there exists also a low-friction regime where the hopping rate decreases as η is reduced. The phenomenology is well understood from a theoretical perspective, where it is known as Kramer's turnover theory[82]: In the low friction regime, the adsorbate only gains sufficient energy to escape the adsorption site relatively infrequently. However, once it has gained enough energy to cross the barrier, the rate of energy transfer to the substrate will also be small and thus the low-friction regime includes both single- and multiple-jumps, though single-jumps will always dominate[41].
In the high friction regime the diffusion rate is also reduced since the high rate of energy transfer will reverse adsorbate trajectories and cause barrier recrossing. Consequently, motion in the high-friction regime is dominated by single-jumps and it should be noted that TST is only expected to provide an upper limit of the hopping rate[10,12] corresponding rather to the intermediate friction regime (see also 5.4).

3.2 Langevin description of dynamics

A general approach which considers energy dissipation between the diffusing adsorbate and the substrate together with vibrational motion of the molecules, without requiring large numbers of degrees of freedom, is provided by the Langevin description of dynamics[10–12]. Therefore, the interaction between the adsorbate and the large number of atoms in the surface is approximated by a "frozen" lateral potential energy surface (PES).
The substrate degrees of freedom are integrated out, yielding a 2D potential $V(x, y) = V(\mathbf{R})$, with characteristics similar to the 1D case described above (Figure 3.1). Such an approach is usually reasonable provided that complex forms of atomic motion, such as exchange processes are not present[11]. The two-dimensional motion of adsorbate j with mass m in terms of the Langevin description is then:[12]

$$m\,\ddot{\mathbf{R}}_j \;=\; -\nabla V(\mathbf{R}_j) - \eta\, m\,\dot{\mathbf{R}}_j \;+\; \xi(t) + \sum_{k\neq j} F\left(\mathbf{R}_k - \mathbf{R}_j\right)\;. \tag{3.3}$$

As illustrated in Figure 3.2, according to (3.3) the motion of particle j at position $\mathbf{R}_j$ is determined by the gradient of the adsorbate-surface interaction potential $V(\mathbf{R}_j)$, while the friction coefficient η describes the rate of energy transfer between the adsorbate and the surface and connection to the substrate heat bath is given by the stochastic term $\xi(t)$[11,83]. Thus energy dissipation or friction corresponds to a viscous drag term, while the stochastic term $\xi(t)$ mimics random energy impulses applied to the adsorbate from the substrate heat bath.
Finally, the last term in (3.3) describes possible interaction forces between the adsorbates, with k running over all the adsorbate indices. It accounts for finite coverages, by including the force on each adsorbate due to the presence of k other adsorbates on the surface, due to forces, $\mathbf{F}_{kj}$, between adsorbates. It introduces the possibility of correlated effects, ranging from simple site blocking to attractive and repulsive forces, including possible phase transitions[12].

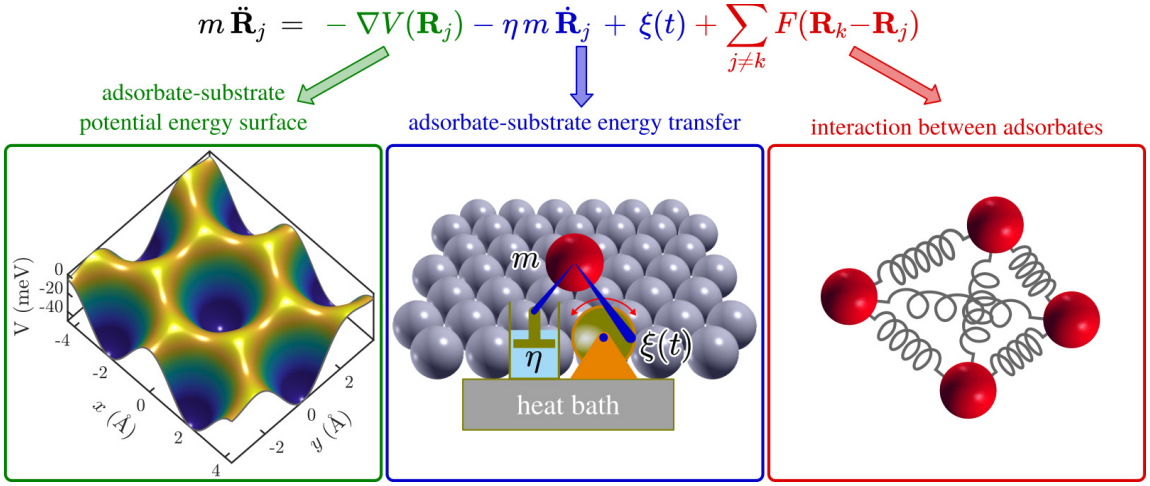

Figure 3.2: Schematic illustration of the three components in the Langevin description of surface diffusion: (i) a (static) adsorbate-substrate potential energy surface, (ii) adsorbate-substrate coupling in terms of the rate of energy transfer (friction η and excitations $\xi(t)$)) and (iii) pairwise interactions between the adsorbates.

While these approximations are entirely classical they work well provided that atoms are not too light and adsorbate-substrate forces are not too strong[11], so that the adsorbate-adsorbate and adsorbate-substrate forces are separable and the pairwise force approximation is valid. Thus the classical approximation is usually good, with the exception of the already above mentioned light particles such as hydrogen, where quantum effects must be accounted for.
It should also be noted that within the classical Langevin equation, the stochastic term $\xi(t)$ is a white noise force term, i.e. it satisfies the fluctuation-dissipation theorem, such that the mean force is zero and

$$\langle \xi\,(t)\,\xi\,(t-\tau)\rangle = 2m\eta k_B T \delta\,(\tau)\;, \tag{3.4}$$

holds[12].

In real systems, the random impulses exerted by the substrate heat bath cannot have a white noise power spectrum and whether the Langevin equation provides a good approximation depends on the mechanism of dissipation. For dissipation governed by electron-hole pair creation and annihilation, the description is plausible since the energy scale of the excitations is generally large compared to the energy scale associated with adsorbate diffusion (e.g. vibrational frequencies in adsorption sites). However, phononic dissipation cannot generally be described via white noise and whenever heat bath excitations above a certain energy are inaccessible, it is reasonable to expect the noise power density to possess a cutoff frequency ω_c , above which the power density is zero or falls rapidly to zero[84]. Such a "coloured" noise spectrum defines the generalised Langevin equation (GLE).
The classical Langevin equation is then simply a special case of the GLE with $1/\omega_c = 0$[83]. For example, the GLE allows to describe diffusive processes where long jumps occur despite the presence of a large friction coefficient. A short description of how to obtain dynamical information from the Langevin equations is given in 3.7 and Ref.[83], while Kramers' turnover theory provides qualitative statements about jump rates and diffusion constants[12,41,85].
From a historic perspective, the very different timescales between surface diffusion measurements (3.3) and measurements of adsorbate vibrations led to the two phenomena being treated quite separately. Yet it has since become clear that the two are intimately linked[12]. The frustrated translation frequency provides an estimate for the pre-exponential factor Υ_0 and can often be used as a guide to the curvature of the potential well around the adsorption site. Moreover, recent works have shown that for the motion of molecules, diffusion may be limited by the excitation of additional vibrational modes, such internal molecular degrees of freedom[86]. The Langevin framework treats both vibration and diffusion equally, making it a tool capable of producing a complete dynamical description, starting with timescales of vibrational periods and extending to longer times.
Finally, it should be noted that models can be used to derive macroscopic diffusion coefficients and those are frequently reported in the literature. However, as outlined by Jardine *et al.*[12] those cannot adequately describe the rich physical behaviour of real systems occurring on the microscopic level and nanoscopic measurements providing detailed information are of paramount importance for benchmarking microscopic theories.

3.3 Experimental approaches to surface diffusion

Several review articles and books provide an overview of experimental methods used to measure surface diffusion at atomic length scales[10,11,87]. Figure 3.3 presents a summary of experimental techniques that can be used to assess surface dynamics, with the techniques being grouped into three general categories, imaging (M), optical (O) and scattering (S). The axes on the figure are logarithmic, ranging from macroscopic length scales of mm to that of individual atoms in Ångstroms and from time scales of seconds to pico-seconds. Generally, imaging techniques occupy the longer timescales while scattering methods such as quasi-elastic neutron scattering (QENS) and quasi-elastic helium atom scattering (QHAS) offer greater potential in the short timescale region as described below.
The first measurements of single-atom diffusion were obtained with field emission and field ionisation microscopy (FIM). However, these early experiments were limited to a few very specific systems and were based on an image-anneal-image approach[87]. More recently scanning tunnelling microscopy (STM) has become the method of choice offering atomic scale resolution with fewer limitations regarding the surfaces that can be studied and allowing for an image-while-hot approach when studying diffusion. Microscopic techniques are attractive for their simplicity of analysis. The simplest method is to correlate successive "frames" of static data into a video of the motion - a method which is also referred to as "video"-STM. More complicated methods, such as those described by Hahne *et al.*[88], determine the residence time of atoms under an STM tip.
The fundamental difference between real and reciprocal space (scattering) techniques lies in the way in which the space and time averaging over the measurements occurs. In the correlation of real-space techniques averaging occurs either over long trajectories or longer times. Hence the real space nature of STM measurements provides valuable insights into the dynamics but the fact that the motion is probed through snapshots does not allow to obtain detailed information about the path of the motion. For ex-

periments utilising scattering techniques, averaging is done in reciprocal space over the whole experiment to increase the signal, while the details of the corresponding motion in real space are maintained. Hence while scattering techniques are more difficult to analyse than their real space counterparts, since they reveal indirect information in reciprocal space, they convey the full breadth of microscopic detail[12].

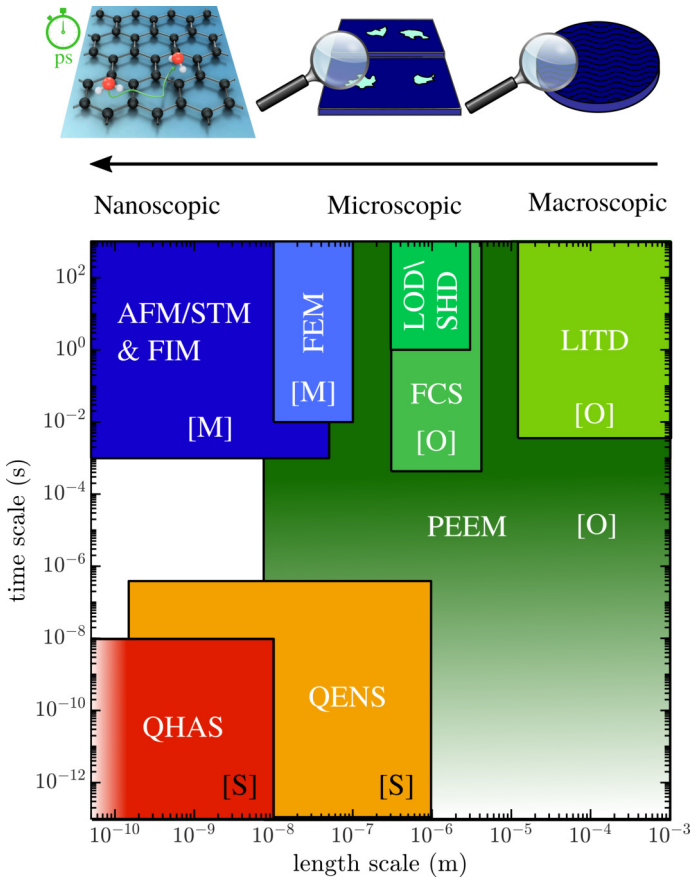

Figure 3.3: Schematic comparison of experimental techniques that can be applied to study surface diffusion with length and timescales of the different methods according to Ref[12] and references therein[**]. Both axes are shown on a logarithmic scale, therefore covering processes over length scales from mm to Å and time scales from seconds to pico-seconds. The colour coding and capital letters are used to group the techniques into imaging techniques (M) in blue, optical techniques (O) in green and scattering (S) in orange and red. The extension of PEEM (shown by the colour gradient) represents the accessibility of sub-femtosecond timescales when using pulse-synchronised methods. Quasi-elastic scattering techniques (quasi-elastic neutron scattering, QENS, and quasi-elastic helium atom scattering, QHAS) are the only techniques which allow studies on both microscopic length scales and on pico- to nanosecond timescales while the system is in true thermal equilibrium. In terms of surface diffusion, QENS can be applied to a number of systems with a high specific surface area (3.4.3) while QHAS is uniquely surface sensitive.

As can be seen in Figure 3.3, quasi-elastic scattering measurements (QENS and QHAS) are the only current experimental methods to continually monitor mobile species on both Å length and ps timescales. Thus they provide detailed microscopic information for comparison with theory under thermodynamic conditions where e.g. the dynamics driving chemical reactions occurs.
When applying scanning probe techniques on the other hand, it is often necessary to work at cryogenic temperatures in order to slow the motion down since the scan time (≈ 5 ms)[89] is often orders of magnitude slower than the dynamic process of interest (pico to nano-seconds) at higher temperatures. For example STM measurements of "molecular cars" which employ chiral molecules as nano-rotors and use electronic excitations by the probe tip as the driving force[89] were collected at 7 K, with partial frames taken at an interval of 5 ms[90]. When the adsorbate-substrate interaction is strong, it may become possible to work at higher temperatures - see e.g. the video of cobalt phthalocyanine molecules on Ag(001) in Ref[91], that was taken at 49 K over an overall scanning time of 5 hours.

[**] LITD: laser induced thermal desorption spectroscopy, FCS: fluorescence correlation spectroscopy, LOD: linear optical diffraction, SHD: second-harmonic diffraction, PEEM: photoemission electron microscopy, FEM: field emission microscopy, FIM: field ion microscopy, AFM: atomic-force microscopy

Figure 3.4 shows a comparison of the rate of diffusion Υ for cobalt-phtalocyanine on a Ag(001), measured using both STM and QHAS. It illustrates the wide range of timescales over which diffusion occurs and highlights the experimental challenge in achieving reliable numerical results. Note that the plot shows the hopping rate Υ versus surface temperature on a log-log axis to highlight the 14 orders of magnitude difference in Υ observed between the two techniques. While STM is sensitive to fractions of hops per second at cryogenic temperatures, the spin-echo variant of QHAS is sensitive to hopping rates of billions of hops per second at room temperature and above.

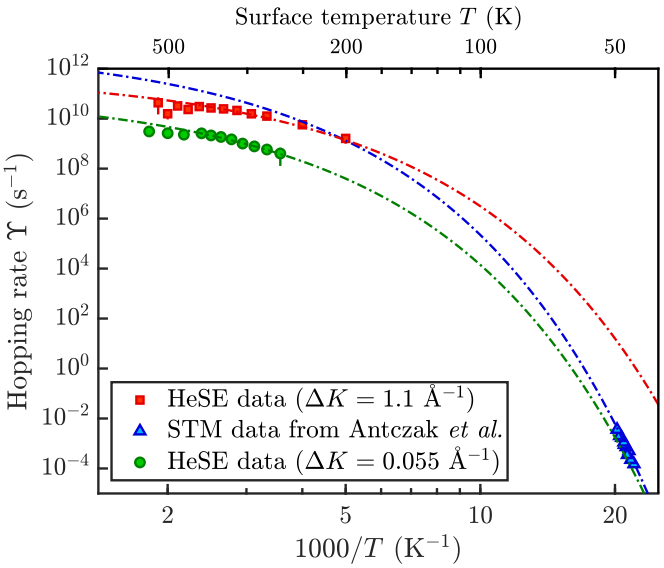

Figure 3.4: Temperature dependence of the rate of hopping Υ of CoPC (cobalt-phtalocyanine) on a Ag(001) surface. Data measured with QHAS shown as red squares/green circles while STM data from Ref.[91] is shown as blue triangles. The dash-dotted lines are fits to the experimental data according to the simple Arrhenius equation (3.1). They have been extrapolated to higher/lower temperatures demonstrating that the diffusive motion cannot be described by (3.1) over the entire temperature range and that in particular an extrapolation of the STM data alone, provides a potentially much larger uncertainty for the calculation of the the pre-exponential factor Υ_0.

The dashed lines in Figure 3.4 represent an Arrhenius law fit to both data-sets. It clearly illustrates that the diffusive process cannot be described by a simple form according to (3.1) when considering the different temperature regimes. It shows that the diffusive motion changes when going from cryogenic to higher temperatures.

While STM measurements are useful to understand the onset of the diffusive motion at low temperatures, QHAS provides insight into the fast processes occurring at ambient and high temperatures. Hence as described in the following, quasi-elastic scattering measurements are a different and complimentary approach to equilibrium surface diffusion measurements providing access to adsorbate dynamics on both atomic length scale and ps timescales.

3.4 Adsorbate dynamics and diffusion in scattering experiments

When a monochromatic particle beam is scattered from a mobile adsorbate, energy exchange occurs similar to inelastic scattering. However, unlike in the case of the creation or annihilation of a phonon or vibrational mode, which corresponds to an energy exchange $\hbar\omega$ of a well defined quanta, the energy changes of the scattered waves are typically much smaller ($\lessapprox$ meV) and occur over a range of different energies centred around the elastic process (0 energy exchange) thus giving rise to a broadening around the elastically scattered peak. Therefore, the process is named quasi-elastic scattering and depending on the beam being composed of neutrons or He atoms, acronymised as QENS and QHAS, respectively.

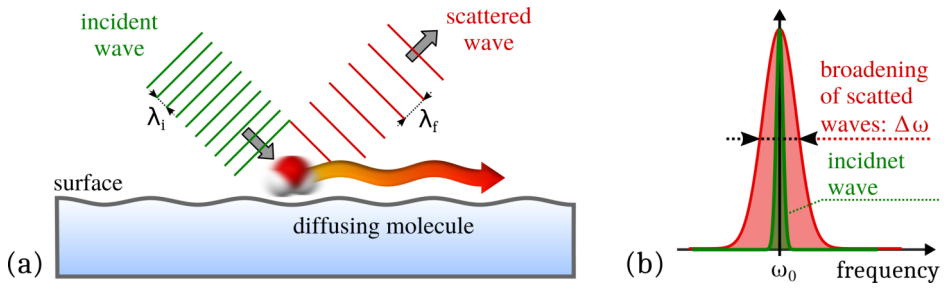

Figure 3.5: Illustration of the linewidth broadening due to scattering of a plane wave from a moving molecule. (a) The frequency of the incident wave changes upon scattering from the moving molecule (water), in analogy to the Doppler effect (exaggerated by the distance between the wavefronts) (b) The wavelength distribution of the scattered waves is broadened ($\Delta\omega$) with respect to the nearly monochromatic incident wave with ω_0.

The effect is analogous to Doppler broadening in atomic physics, where the spectral lines of atoms and molecules in the gas phase are broadened due to the Doppler effect caused by the velocities of the moving atoms. In Figure 3.5 the process is shown in a simple illustration. Scattering of a plane wave from a moving adsorbate, as outlined in Figure 3.5(a), gives rise to a change of the wavelength or frequency. As the moving adsorbates exhibit a distribution of velocities, it gives rise to a broadening in the frequency distribution of the scattered waves as shown in Figure 3.5(b), in comparison with the nearly monochromatic incoming wave at a central frequency ω_0.
The broadening due to the aperiodic motion of the molecules is small but measurable and the specific shape of the the broadening is determined by the diffusion mechanism and the rate of movement. Hence studying the broadening gives access to the diffusive motion itself.

3.4.1 The van Hove formalism

The van Hove formalism was initially developed for thermal neutron scattering[92] and provides a very powerful formalism to understand experimental scattering spectra in terms of their diffusive regimes[93]. It establishes the relation between experimentally accessible functions such as the intermediate scattering function, the scattering function and the generalised correlation function in time and space, also known as van Hove correlation function $G(\mathbf{r}, t)$.
Upon measuring diffusion or the dynamics of a particle in a system, the experiment aims to determine the probability of finding a particle at position $\mathbf{r}$ at time t if the very same particle or a different one was situated at the origin at $t = 0$. This information is known as the van Hove correlation function $G(\mathbf{r}, t)$ with the mathematical definition as:[92]

$$G(\mathbf{r}, t) = \frac{1}{N} \sum_{j,k=1}^{N} \int \left\langle \delta \left[\mathbf{r}' - \mathbf{r}_k(0)\right] \, \delta \left[\mathbf{r}' + \mathbf{r} - \mathbf{r}_j(t)\right] \right\rangle \mathrm{d}\mathbf{r}' \,. \tag{3.5}$$

However, often $G(\mathbf{r}, t)$ cannot be directly measured in an experiment. Alternatively, its Fourier transforms in terms of time or space are measured. The corresponding Fourier transforms are known as (dynamic) scattering function (SF) or intermediate scattering function (ISF) and further described in 3.4.2.

3.4.1.1 Scattering cross sections

The van Hove formalism relates the different observables in scatterings measurements based on a simple theoretical approach with some assumptions that generally hold well for neutrons:

- The incoming beam has a fixed incident wavevector $\mathbf{k}_i$ and therefore a fixed incident energy (which is the equivalent to monochromatisation of the beam).
- The potential for scattering from each nuclei is modelled as a Fermi pseudopotential, which is a delta spike at its position. This condition has to be adapted for HAS (3.4.1.2) as He atoms scatter from the electron clouds).
- A scattered neutron interacts with the bulk potential at most once. Although this assumption neglects the possibility of multiple scattering, it simplifies the theoretical framework considerably[93].

With these assumptions one can directly compute the differential scattering cross section $\frac{\mathrm{d}^2\sigma}{\mathrm{d}\Omega \mathrm{d}(\hbar\omega)}$, defined as the number of neutrons scattered into a solid angle $\mathrm{d}\Omega$ with change of energy $\mathrm{d}(\hbar\omega)$ divided by the flux of incident neutrons:[92]

$$\left(\frac{\mathrm{d}^2\sigma}{\mathrm{d}\Omega d(\hbar\omega)}\right) = \frac{N\sigma}{4\pi}\frac{k_f}{k_i} S(\mathbf{q}, \omega) \,, \tag{3.6}$$

where N is the total number of nuclei, σ is the total scattering cross section, $k_i = |\mathbf{k}_i|, k_f = |\mathbf{k}_f|$ are the magnitudes of the incoming and outgoing scattering wavevectors, $\mathbf{q} = \mathbf{k}_i - \mathbf{k}_f$, $\hbar\omega$ denotes the change in energy and $S(\mathbf{q}, \omega)$ is the scattering function.

3.4.1.2 Extension to HAS

Assuming that there is no correlation between particle dynamics, (3.6) can be adapted to the surface sensitive HAS approach using:[12,94]

$$\frac{\mathrm{d}^2\sigma}{\mathrm{d}\Omega\mathrm{d}\omega} = S(\mathbf{Q},\omega)\cdot|F(\mathbf{Q},\omega)|^2\,. \tag{3.7}$$

Instead of $\mathbf{q}$ used in (3.6), $\mathbf{Q}$ denotes the 2D momentum transfer. Moreover, due to the scattering geometry (see 2.2) the parallel momentum transfer $\Delta\mathbf{K} = \mathbf{K}_f - \mathbf{K}_i$ and $\mathbf{Q} \equiv \Delta\mathbf{K}$ is usually used.
$F(\mathbf{Q},\omega)$ denotes the form factor which takes into account that He atoms are scattered from the electron cloud of the atoms/molecules on the surface in contrast to the nuclear scattering of neutrons. As long as the momentum- and energy-transfer dependence of the scattering form factor is weak, it will not influence any analysis of dynamical data and it is thus usually ignored in QHAS measurements[12].
Since in the present work only 2D cases for neutron scattering are considered and the mechanism of HAS is intrinsically only sensitive to scattering from the surface, the description will be restricted to 2D in the following, as indicated by capital letters such as $\mathbf{R}$ for the position and $\mathbf{Q}$ for the momentum - while many of the original derivations are based on the 3D case and are thus denoted with $\mathbf{r}$.

3.4.2 The scattering functions

As mentioned above, the van Hove correlation function, $G(\mathbf{R},t)$ cannot be directly measured and alternatively, its Fourier transforms in terms of time (energy) or space (momentum transfer) are measured. The corresponding Fourier transforms are known as scattering function $S(\mathbf{Q},\hbar\omega)$ or its Fourier transform in real time/space-momentum transfer, i.e. the intermediate scattering function $I(\mathbf{Q},t)$.

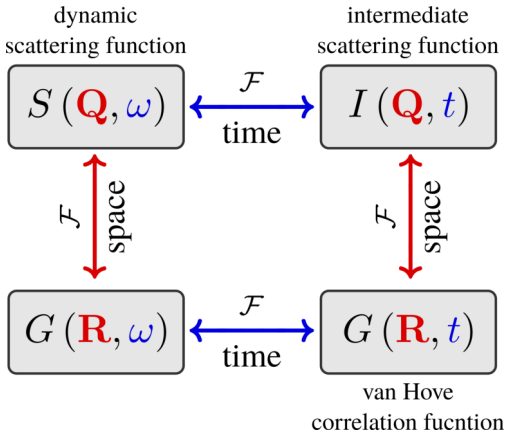

Figure 3.6: Relations between the different scattering functions (top row) accessible in scattering experiments and the van Hove correlation function. The functions are related to each other via the corresponding Fourier transforms in time and space.

Figure 3.6 illustrates a graphical overview of the relations with the top row showing the two measurable scattering functions. The (dynamic) scattering function (SF) $S(\mathbf{Q},\hbar\omega)$, also known as the dynamic structure factor, is measured with a standard scattering spectrometer (TOF) where the dynamical information is encoded in the energy transfer between the probe (a He atom, a neutron or a photon,...) and the targeted system. Conversely, for a spin-echo measurement (using ^{3}He - HeSE, or neutrons - NSE) it can be demonstrated that the final outcome is the intermediate scattering function (ISF):

$$I(\mathbf{Q},t) = \frac{1}{N}\sum_{j,k}^{N}\left\langle \mathrm{e}^{\mathrm{i}\mathbf{Q}\cdot\mathbf{R}_j(t)}\mathrm{e}^{-\mathrm{i}\mathbf{Q}\cdot\mathbf{R}_k(0)}\right\rangle\,, \tag{3.8}$$

where the angle brackets represent an average. According to (3.8) the dynamical information of the particles in the sample is now encoded in real time and reciprocal space. The relation between the ISF

and the van Hove correlation function is the Fourier transform in momentum transfer:[92]

$$G(\mathbf{R},t) = \frac{1}{(2\pi)^3}\int I(\mathbf{Q},t)\mathrm{e}^{-\mathrm{i}\mathbf{Q}\cdot\mathbf{R}}\mathrm{d}\mathbf{Q}\,. \tag{3.9}$$

Finally, the scattering functions SF and ISF, are related by means of the Fourier transformation in time:

$$S(\mathbf{Q},\hbar\omega) = \frac{1}{2\pi\hbar}\int I(\mathbf{Q},t)\mathrm{e}^{-\mathrm{i}\frac{\hbar\omega t}{\hbar}}\mathrm{d}t\,. \tag{3.10}$$

Thus, what makes the van Hove formalism particularly useful is that the two measurable quantities, the SF and the ISF, can be related to the motion of the particles ($G(\mathbf{R},t)$) via multiple Fourier transforms. The correlation function $G(\mathbf{R},t)$ contains information about both self- and collective diffusion. However, if the spatial correlations between particles are negligible, the scattering function is essentially sensitive to the dynamics of a single particle (self-diffusion, see 3.6.1).

3.4.3 QENS and QHAS measurements based on TOF

QENS and QHAS measurements are conventionally conducted by TOF experiments, which involve scattering a pulsed neutron or He beam (produced by a chopper), followed by measuring the scattered velocity distribution via the corresponding arrival times at the detector (and thereby the energy distribution). In TOF-QHAS experiments the nature of the dynamical structure factor can be studied, however, these experiments are limited by the energy resolution. The initial velocity spread of the He beam after the supersonic expansion, limits TOF-QHAS experiments to the study of relatively few, fast moving systems (e.g. Ref.[95]), where the quasi-elastic broadening is comparable to or larger than the beam monochromaticity, such that the measured spectrum can be clearly deconvoluted. In addition, when more than one process contributes to the dynamics, the energy resolution in TOF-QHAS makes it hard to resolve individual processes. The problem can be overcome based on the spin-echo technique, which significantly increases the energy resolution and is described in 3.5.
In terms of neutron TOF measurements the resolution problem is less severe since the beam can be monochromatised as shortly outlined in a typical neutron TOF setup below. On the other hand, using neutron spin-echo experiments, the energy resolution can still be increased: The neutron TOF beamline IN6 achieves an energy resolution of about 100 μeV while with neutron spin-echo (NSE) at the IN11 beamline an energy resolution of about 10 neV is possible[96].
As an example the neutron TOF spectrometer IN6 at the Institute Laue Langevin (which was employed for the work in Refs.[61,97]) is shown in Figure 3.7. The IN6 beamline operates with a continuous white beam of cold neutrons which is monochromatised by three composite graphite monochromators that select only neutrons of a defined wavelength in the range $4.1 - 5.9$ Å via Bragg diffraction. The beam is then cut into pulses by a chopper and collimated before being scattering from the sample. A large panel of detectors, placed in an array spanning about $120°$, enables measurements over a large momentum transfer range. Such a kind of instrument is referred to as a direct geometry spectrometer, since monochromatisation and chopping takes place before the beam scatters from the sample.

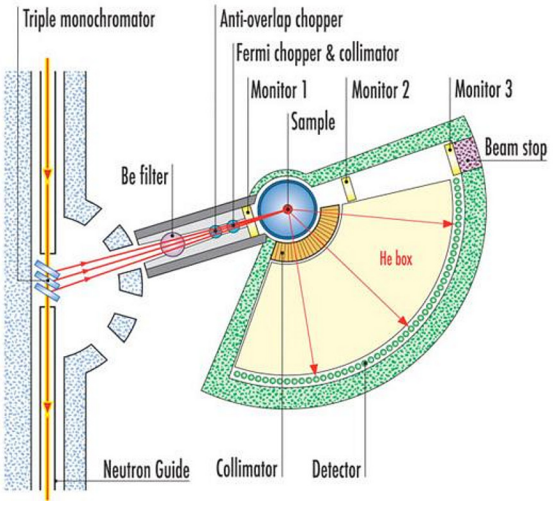

Figure 3.7: Experimental setup of the neutron TOF beamline IN6 (IN6-sharp) at the Institute Laue Langevin, from Ref. [96].

While neutron scattering is usually more concerned with scattering from bulk samples QENS becomes interesting for surface diffusive processes if scattering occurs from samples with a high specific surface area. For example, exfoliated compressed graphite, so called Papyex, exhibits an effective surface area of about 25 $\mathrm{m}^2\,\mathrm{g}^{-1}$ and retains a sufficiently low defect density. Due to its high specific adsorption sur-

face area, it is widely employed for adsorption measurements[61]. In particular the physisorption of carbon based molecules on exfoliated graphite is perfectly suited for QENS measurements, since the weak binding of physisorbed layers gives rise to low frequency external vibrational modes - in contrast to the internal vibrational modes of the molecules - matching the typical energy range accessibly with cold neutrons. More importantly, carbon based molecules such as e.g. benzene (C_6H_6), contain a number of hydrogen atoms meaning that neutron scattering will mostly follow the dynamics of the protons, due to the very large neutron scattering cross-section of the hydrogen nucleus. Thus, QENS provides detailed information about the dynamics of hydrogen-containing molecules adsorbed on exfoliated graphite due to the a pronounced contrast between the scattering cross-section of hydrogen and carbon[97].
For the experiments several exfoliated graphite discs (grade N998 $> 99.8\%$ C, Carbone Lorraine) with a diameter of 2.5 cm are prepared by annealing under vacuum conditions before transferring those into a cylindrical aluminium sample cartridge. The required amount of the adsorbate is added to the graphite discs, either by adding the crystalline powder that is weighed by using a fine balance or by dosing a defined amount from the gas phase. The aluminium sample holder is then hermetically sealed using a lid with a steel knife-edge or, when dosing from the gas phase, the sample cartridge is first sealed by an indium gasket and then connected to a gas sorption system via a stainless steel capillary[61,97]. The graphite samples show a preferential orientation of the basal plane surfaces which can be exploited by orienting those parallel to the scattering plane of the neutron beam meaning that most of the QENS signal comes from the adsorbed layer, in fact mostly from the protons as described above[61].
The usual procedure is to convert the TOF spectra to scattering functions, $S(Q, \hbar\omega)$, where $Q = |\mathbf{Q}| = |\mathbf{k_f} - \mathbf{k_i}|$ is the momentum transfer and $\Delta E = \hbar\omega = E_f - E_i$ is the energy transfer. Figure 3.8(a) shows a two-dimensional contour plot of the dynamic scattering function $S(Q, \hbar\omega)$ for 0.5 ML of $P(C_6H_5)_3$ at a temperature of 500 K. The spectrum shows an intense elastic scattering region around $\Delta E = 0$ meV which is mainly due to scattering from the graphite substrate. The broader feature surrounding the elastic band is the quasi-elastic broadening which appears due to scattering from the diffusing adsorbates.

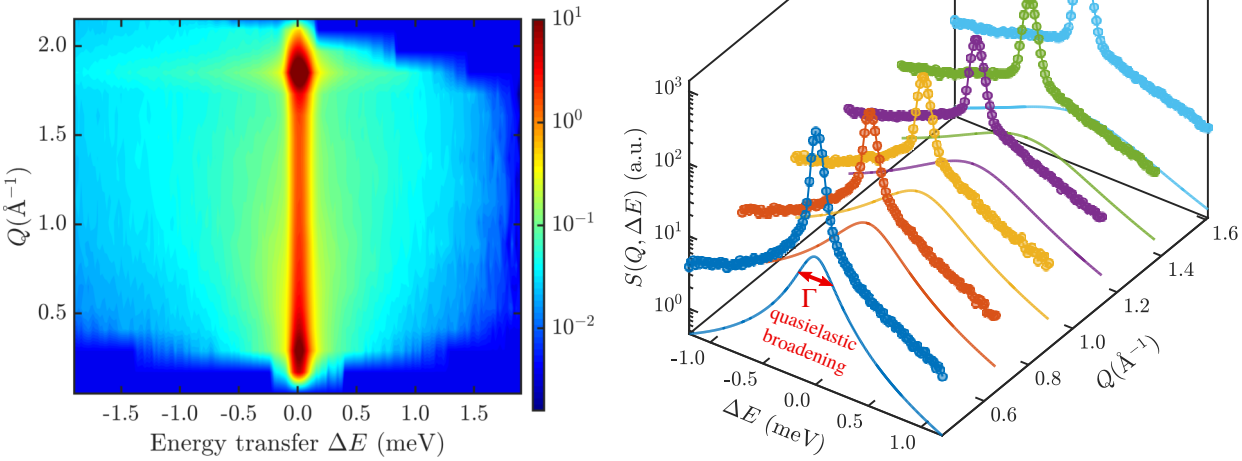

(a) Two-dimensional contour plot of the dynamic scattering function $S(Q, \Delta E)$ that was extracted from neutron TOF data obtained for exfoliated graphite covered by 0.5 ML of $P(C_6H_5)_3$ at 500 K. The intense spot at about $Q = 1.9$ Å^{-1} is due to the (002) Bragg reflection from the basal plane of graphite.

(b) Several dynamic scattering functions $S(Q, \hbar\omega)$ at constant Q as extracted from neutron TOF data plotted as symbols. The solid lines show the fitted quasi-elastic broadening (Γ, note the logarithmic scale) obtained by fitting a Lorentzian peak convoluted with the experimental resolution.

Figure 3.8: Neutron TOF spectra for 0.5 ML of $P(C_6H_5)_3$ adsorbed on graphite, after conversion to $S(Q, \Delta E)$.

Cuts of the scattering function $S(Q, \Delta E)$ at constant values of Q are plotted in Figure 3.8(b) for several temperatures. The quasi-elastic broadening Γ, obtained after fitting the data with a quasi-elastic peak shape convoluted with the experimental resolution, is then used to characterise the diffusion of the adsorbates on the substrate (see 3.6).

3.5 The spin-echo principle

The spin-echo principle was first developed for neutron beams by Mezei in the 1970s to achieve ultra-high energy resolution in neutron scattering experiments and quickly led to the development of the IN11 beamline at the Institut Laue Langevin in Grenoble[98], revolutionising measurements of slow dynamical processes in the bulk[93]. The He spin-echo (HeSE) technique was later realised by a group in Heidelberg[12] by applying the methods used to manipulate the neutron spin to the helium-3 (^{3}He) nucleus and thus combining the benefits of ultra-high energy-resolution with the surface sensitivity of HAS.
The spin-echo method offers a general purpose, ultra-high energy resolution technique for scattering experiments. Essentially, the method uses Larmor precession of the nuclear spin of neutrons or He atoms as an internal timer on each individual particle in the beam. Unlike TOF, which measures the absolute velocity of all scattered particles, spin-echo measures only the energy changes introduced after scattering and hence the initial velocity spread is irrelevant. As a consequence, elastic, inelastic and quasi-elastic scattering all benefit from the improved energy resolution of the method.
While the concept of improved energy resolution helps to relate the spin-echo method to conventional TOF methods, it is more natural to discuss the relationship between adsorbate dynamics and the spin-echo method in the time-domain. As mentioned in 3.4.2, spin-echo measurements provide direct access to the intermediate scattering function $I\left(\Delta\mathbf{K}, t\right)$ (3.8), which is directly related to the van Hove pair correlation function via (3.9).
$I\left(\Delta\mathbf{K}, t\right)$ is a measure of correlation after time t, on the length-scale and direction given by $\Delta\mathbf{K}$. Both variables are adjustable in a spin-echo experiment: $\Delta\mathbf{K}$ is given by the incident beam energy and the scattering geometry (Figure 2.3(a)). The time t, usually referred to as spin-echo time t_{SE}, is determined by the spin manipulation applied in the spin-echo coils, which can be varied by adjusting the current in the winding of the coils[12]. In the following, the concept of HeSE in the time-domain and the relation to adsorbate dynamics in scattering (3.4) is shortly introduced according to the illustration in Figure 3.9. A more thorough description regarding the underlying math is then given in 3.5.1-3.5.3.

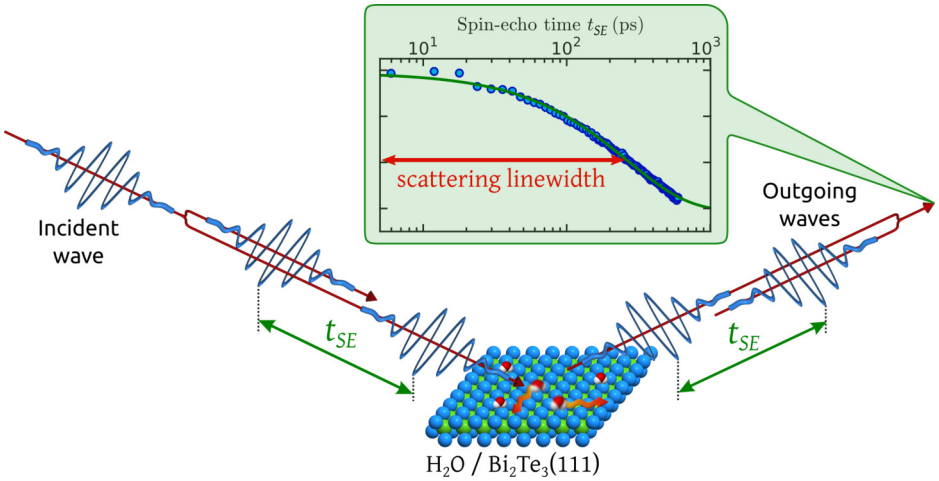

Figure 3.9: Movement on a sample surface can be probed by scattering two wavepackets, spread by a time delay t_{SE}, as explained in 3.5.2. Upon recombination of the two scattered wavepackets a loss in correlation is measured due to a small Doppler broadening when scattering from moving adsorbates. The measured ISF shows an exponential decay in spin polarisation with t_{SE}, from which the decay constant (scattering linewidth) is obtained.

HeSE probes the diffusion of adsorbates by detecting a small energetic Doppler broadening of the He atoms upon scattering from the moving adsorbates. The limitation of the finite monochromaticity of a supersonic He atom beam can be overcome by adopting the principle of spin-echo spectrometers: Using ^{3}He, any energy change is converted to a loss of spin polarisation. The nuclear spin state of the incident ^{3}He is polarised and split into two coherent wave packets, which reach the sample with a time delay t_{SE}, the so-called spin-echo time (Figure 3.9). After scattering, the wave packets are recombined and the resulting polarisation is measured. In the case of dynamic processes on the surface, the wave packets scatter differently and, once recombined, a reduced final beam polarisation is found. As the process is based on self-interference of each ^{3}He atom, the polarisation loss depends only on the change in energy and not the beam energy itself, resolving energy changes that are as small as 20 neV[99]. Because the

impinging He atoms have very low kinetic energies (< 10 meV), they do not affect the observed motion, while at the same time the large He atom scattering cross section provides an outstanding sensitivity[15].

In the following the simple classical description for spin-echo experiments is provided. The semi-classical description given in 3.5.2 uses a quantum description of the measurement process, and provides an intuitive approach to understanding the relation to surface correlations. A full quantum formalism can also be applied but gives only few additional insights[12] and is thus not presented in the current work. Finally, the 2D Fourier transform model is described in 3.5.3, providing a framework within which not only HeSE measurements of quasi-elastic but also inelastic processes can be understood.

3.5.1 The spin-echo concept and the classical model

Traditionally, the spin-echo experiment is described in terms of classical spin precessions: Particle beams with spin $1/2$, such as neutron or ^{3}He beams, can be described by classical Larmor precession as long as the Stern-Gerlach effect is imperceptible[12]. A schematic drawing of the Cambridge spin-echo apparatus is shown in Figure 3.10, while details of the polarisation measurement are discussed in 3.5.1.1. The neutron spin-echo (NSE) spectrometer follows the same principle[100] as shown in Figure 3.10, but includes different elements in terms of the source, spin polarisation and analysis device.
An unpolarised ^{3}He beam is created in the source (top left) via a supersonic expansion, typically giving an energy spread of 5-20%[12]. Since ^{3}He exhibits an overall spin of $1/2$, a strong magnetic field can be used to polarise the beam. By passing the beam through a magnetic spin-polariser, which transmits only one polarisation of the beam, the outgoing atoms are then polarised in a direction perpendicular to the beamline.

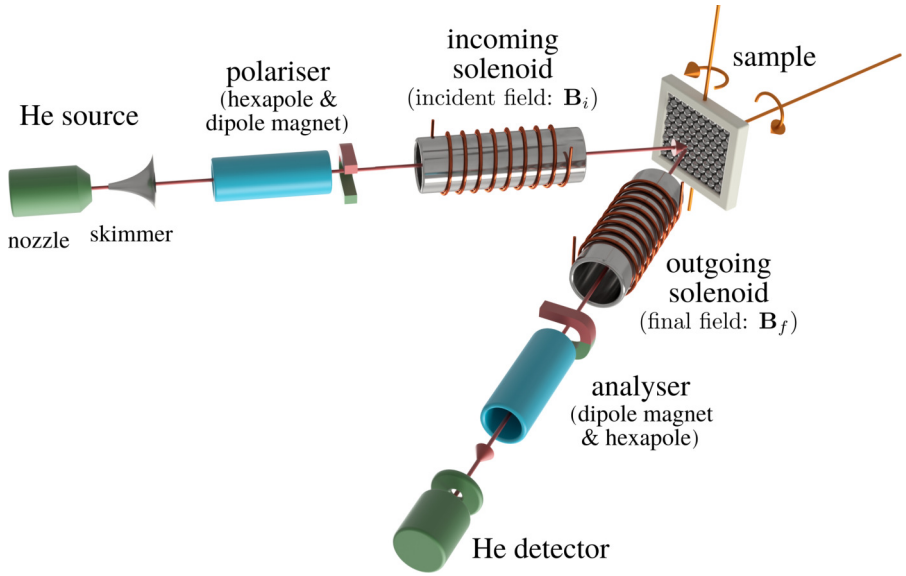

Figure 3.10: Schematic showing the principle parts of the Cambridge spin-echo scattering apparatus. An unpolarised beam of ^{3}He is generated from a supersonic beam source at the top left in a fixed direction. The beam is then passed through a polariser and the aligned nuclear spins are rotated by the incoming solenoid (precession coil) before being scattering from the sample surface. The scattered beam passes back through the identical but reversed field in the outgoing solenoid before being spin-analysed and counted in the detector. The neutron spin-echo spectrometer follows the same principle[100] but includes a different source and spin polarisation principle as well as a different analysis device and spin flippers along the path.

The polarised beam then enters a solenoid field (incoming or incident solenoid) which gives rise to a precession of the spin around the beam axis after which it is scattered from the sample. In the magnetic field of the solenoid, the spin vector, $\mathbf{S}$, undergoes precession according to the classical description,

$$\frac{\mathrm{d}\mathbf{S}}{\mathrm{d}t} = \gamma \mathbf{S} \times \mathbf{B} \,, \tag{3.11}$$

with γ, the gyromagnetic ratio for ^{3}He ($\gamma/2\pi = 32.43$ MHz/T)[12].

Since $\mathbf{B}$ is oriented in the direction of the beam, the spins precess about the beam direction a number of times. The final accumulated precession angle ϕ is then given by the time t_L spent inside the field and thus by the velocity v of the individual atom concerned:

$$\phi = \gamma \int_0^{t_L} B \, \mathrm{d}t = \frac{\gamma}{v} \int_0^L B \, \mathrm{d}l \ , \tag{3.12}$$

with L being the length of the precession field. The "encoded" beam is then scattered from the sample surface and depending on the scattering angle of the outgoing atoms, a portion of the scattered atoms will pass through the second beamline. The scattered atoms reaching the second beamline are again passed through an identical but reversed solenoid field (outgoing or final solenoid) before being spin-analysed and finally counted in a detector. The analyser transmits only a selected polarisation into the detector, (usually the x-component - see 3.5.1.1), which corresponds to the analyser being aligned with the polariser.
Since the rate of precession depends on the time that the atom spent in either of the precession fields and hence the velocity of the atom, the total accumulated precession angle reflects any energy change caused by the scattering at the sample. The total accumulated phase for atoms sequentially passing through the incoming (incident) and outgoing (final) precession fields is then given by

$$\phi \ = \ \phi_i + \phi_f \ = \ \frac{\gamma}{v_i} \int_0^L B_i \, \mathrm{d}l + \frac{\gamma}{v_f} \int_0^L B_f \, \mathrm{d}l \ . \tag{3.13}$$

If the fields B_i and B_f are equal in magnitude but opposite in direction, which is the usual condition for a "standard" spin-echo experiments, (3.13) simplifies to:

$$\phi \ = \ \gamma \left(\frac{1}{v_i} - \frac{1}{v_f} \right) \int_0^L B \, \mathrm{d}l \ = \ \gamma \frac{v_f - v_i}{v_i v_f} \int_0^L B \, \mathrm{d}l \ \approx \ \gamma \frac{\Delta v}{v^2} \int_0^L B \, \mathrm{d}l \ , \tag{3.14}$$

with the last step being valid when the changes in velocity are small and with v now being the mean velocity of the atoms in the beam.
As the energy change for a single He atom is also given by $\hbar\omega = \frac{1}{2} m v_f^2 - \frac{1}{2} m v_i^2 \approx m v \Delta v$ one obtains

$$\phi = \frac{\gamma}{m v^3} \hbar\omega \int_0^L B \, \mathrm{d}l \ . \tag{3.15}$$

Equation 3.15 illustrates that ϕ provides a first order approximation to the energy change experienced by an individual He atom. In real experiments an average over the distribution of energies in the scattered beam is measured. As described above, the averaged polarisation is obtained by passing the beam through the analyser which transmits atoms according to the cosine of their classical spin-phase, with respect to the original polarisation direction.
The averaged polarisation P_x is therefore given by the beam average $P_x = \langle \cos\phi \rangle$.[12] Since the distribution of atoms in the scattered beam is given by the scattering function, $S(\Delta\mathbf{K}, \hbar\omega)$ introduced in 3.4.2, the measured average P_x can be expressed together with the Fourier relation (3.10) as

$$P_x \ = \ \frac{\int S(\Delta\mathbf{K}, \hbar\omega) \cos(\hbar\omega t) \, \mathrm{d}\hbar\omega}{\int S(\Delta\mathbf{K}, \hbar\omega) \, \mathrm{d}\hbar\omega} \ = \ \frac{\mathbb{R}\mathrm{e}\left[I(\Delta\mathbf{K}, t) \right]}{S(\Delta\mathbf{K})} \ = \ \mathbb{R}\mathrm{e}\left[\frac{I(\Delta\mathbf{K}, t)}{I(\Delta\mathbf{K}, 0)} \right] \ , \tag{3.16}$$

with $I(\Delta\mathbf{K}, t)$, the intermediate scattering function (ISF) introduced in 3.4.2 and t, the "spin-echo time" given by

$$t = t_{SE} = \frac{\gamma\hbar}{m v^3} \int_0^L B \mathrm{d}l \ . \tag{3.17}$$

The concept of t_{SE} becomes much clearer when referring to the semi-classical description of the experiment (3.5.2). Following the same phenomenology, it can be shown that the orthogonal polarisation, $P_y = \langle \sin\phi \rangle$, relates to the imaginary part of the normalised ISF, $P_y = \mathbb{I}\mathrm{m}\left[I(\Delta\mathbf{K}, t) / I(\Delta\mathbf{K}, 0) \right]$. Hence for small energy changes during scattering, compared to the mean energy of the He atoms, the

measurement of both polarisation components provides the full (complex) normalised ISF[12].
As $I(\Delta\mathbf{K}, t)$ is the Fourier transform of the van Hove correlation function $G(\mathbf{R}, t)$ (via (3.9)) the measurement provides a complete statistical description of the surface motion, as "seen" by the He beam. In 3.6 it will be outlined how to interpret the scattering functions such as $I(\Delta\mathbf{K}, t)$ in order to understand the motion on surfaces.
As described in the literature[12,101], it is not essential to measure both P_x and P_y in every experiment since a measurement of P_x alone gives the real part of the ISF. For example, in most cases considering the motion of adsorbates it is reasonable to use measurements of P_x alone. However, inelastic processes such as phonon events will generally correspond to an asymmetric form of the SF (see 3.5.3), so both components of the polarisation need to be measured. The latter can be implemented for a HeSE experiment, thus enabling (3.16) to be converted to a complex Fourier transform (see 3.5.3), and an asymmetric energy transfer spectrum to be constructed. There are several approaches that can be used to obtain the sine term[58], with one of those being described in 3.5.1.1.

3.5.1.1 Measurement of the complex polarisation

Inelastic or quasi-elastic scattering from the sample in spin-echo experiments gives rise to a loss in polarisation of a polarised beam. Hence, a crucial part of any spin-echo experiment is to determine the polarisation of the scattered beam which is described in the following. Figure 3.11(a) shows another schematic of the ^{3}He spin-echo apparatus, concentrating now mainly on the direction of the spin polarisation and with the 44.4° scattering geometry removed for simplicity[58].
A beam of ^{3}He is generated with the velocity along the z-direction and the beam passes through a spin polariser, where the nuclear spin is polarised perpendicular to the beamline (along x). The spins perform the above described Larmor precession in the xy-plane where the angle between the ^{3}He spin before and after passing the solenoids depends on the time spent in the magnetic field and hence on its velocity. In the magnetic field of the outgoing solenoid (anti-parallel to the beam axis), the Larmor precession unwinds the spin so that the spin direction at the end of the outgoing coil is the same as at the beginning of the incoming coil (along the x-direction) provided that the scattering event is purely elastic. The final stage of the experiment consists of an analyser that selects components of the beam with the spin aligned along x after which a detector converts the flux into a count rate. An arbitrary polarisation P of the spin in the xy-plane can be conveniently written as a complex number,

$$P = P_x + \mathrm{i}P_y = |P|\cos\delta + \mathrm{i}|P|\sin\delta\ , \tag{3.18}$$

where $P_x = \mathbb{R}\mathrm{e}(P)$ and $P_y = \mathbb{I}\mathrm{m}(P)$ (see also the illustration in the inset of Figure 3.11(a)).
As mentioned above, in principle it is not essential to measure both P_x and P_y in every experiment and e.g. a measurement of P_x alone gives the real part of the ISF $I(\Delta\mathbf{K}, t)$. However, some inelastic processes such as phonon events require the measurement of both components of the polarisation[12,58].
Moreover, even without a magnetic field in the solenoids ($B_i = B_o = 0$) the polarisation may not be entirely real due to practical hardware implementations. These include the misalignment of magnetic elements, small differences between the two coils and their driving circuits as well as external magnetic fields penetrating the beam path.
The issue is illustrated in Figure 3.11(b) which shows schematically a line corresponding to a polarisation measurement under ideal conditions (black, dashed) and a realistic elastic measurement (blue, solid). Hence to obtain the maximum amplitude of the polarisation (due to practical limitations of the apparatus) and the complete information about the underlying dynamical processes both the real and the imaginary part of the polarisation need to be measured[58].
In principle the simplest way of measuring the complex polarisation is to rotate the analyser (in Figure 3.11(a)), by $\pi/2$ which allows independent measurements of the polarisation along the x and the y-axis: P_x and P_y. However, mechanical rotations of magnetic devices are quite complicated and in practice there are simpler solutions. The most convenient approach is to add an additional "phase coil" in the region before the incoming solenoid (see Figure 3.11(a)). The phase coil rotates the spin by a chosen amount depending on the magnetic field B_ϕ.

Thus the ingoing spin vector can be rotated with respect to the outgoing one by a certain (additional) amount, determined by the phase coil current. By measuring a number of discrete points within the period of one full spin rotation the exact polarisation of the spin can be measured. In neutron spin-echo spectroscopy this is typically termed as measurement of the echo-group or as echo-scan[58,98].

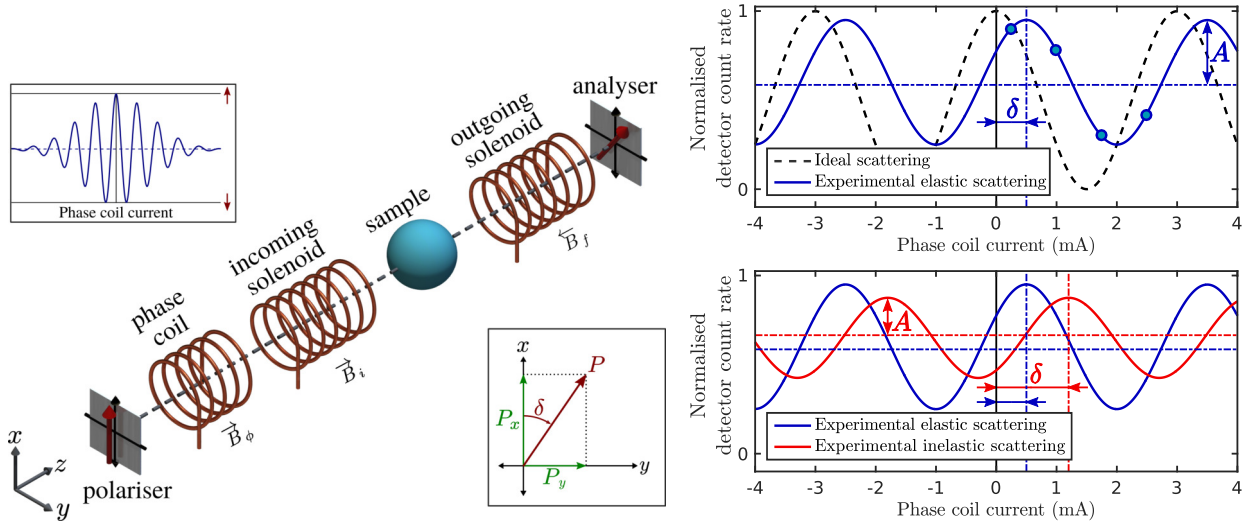

(a) Schematics of the spin-echo experiment, highlighting the polarisation measurement based on an additional phase coil. A beam with velocity along z is generated and the nuclear spin is polarised along x. The beam travels through the magnetic field of the incoming solenoid with the spin performing a Larmor precession in the xy plane. The Larmor precession is effectively unwound in the outgoing solenoid with a magnetic field aligned antiparallel to the incoming one. For quasi- or inelastic scattering a loss of polarisation is observed at the analyser with respect to alignment along x. The phase coil is included before the incoming solenoid and allows the spin to be rotated by an additional chosen amount and can thus be used to determine both the real and complex part of an arbitrary spin polarisation in the xy plane (inset at the bottom right). The top left inset illustrates the spin polarisation versus phase coil current for purely elastic scattering.

(b) Illustration of the 4-point measurement: To determine the polarisation, 4 points are measured over one oscillation when following the variation in polarised intensity versus phase coil current (illustrated by the 4 dots on the blue curve). The upper panel shows the case for scattering from a static sample where an ideal scattering experiment (dashed curve) is compared to a "real" experiment with several non-idealities (solid blue line). By fitting Equation 3.20 to the 4 measured points, A and δ are found which is then used to calculate the real and imaginary part of the polarisation. The lower panel illustrates an inelastic scattering experiment (red line) where motion gives rise to an additional phase shift and a change in amplitude with respect to scattering from a static sample (blue curve).

Figure 3.11: Illustration of the 4-point measurement (b), based on adding an additional phase coil (a), from Ref.[58]

The process is illustrated for four points in Figure 3.11(b): With a current, I, passing through the phase-coil, the spin is rotated by an angle $\Omega_0 I$ where the rotation constant $\Omega_0 = \gamma m B_{\text{eff}} \lambda_0 / \hbar$, depends on the mean wavelength of the particles in the beam, λ_0, the particle mass and the field integral along the beam path $B_{\text{eff}} = \int B \, \mathrm{d}z / I$[12,94,101]. The signal resulting from a fixed polariser in the case of a beam with a Gaussian spread of wavelengths is[58]

$$P_x(I) = A \, \mathrm{e}^{(-I^2/2\sigma^2)} \, \cos\left[\Omega_0 (I - \delta)\right] + C \, . \tag{3.19}$$

In practice the polarisation is measured via the ^{3}He atoms that arrive at the detector where the flux is converted into a count rate

$$n_{det}(I) = A \, \mathrm{e}^{(-I^2/2\sigma^2)} \, \cos\left[\Omega_0 (I - \delta)\right] + \underbrace{C_1 + C_2}_{C} \, . \tag{3.20}$$

The count rate n_{det} in the detector follows (3.20) as the current in the phase coil (I) is changed (see Figure 3.11(b)). The $\cos(\Omega_0 I)$ term describes the rotation of the spin and is determined by the mean wavelength of the particles (via Ω_0) and the current I through the phase coil. The phase shift δ in (3.20) accounts for non-idealities within the ingoing and outgoing spin rotation as discussed above: It describes the effect that the polarisation is not entirely real for $I = 0$ as illustrated in the upper panel of Figure 3.11(b). The spread of wavelengths in the beam is manifest through the Gaussian pre-factor in (3.20),

of width $\sigma = \hbar/\gamma m B_{\text{eff}} \sigma_\lambda$, where σ_λ is the corresponding spread in wavelengths. Finally, the offset C in (3.20) is composed of a background C_1 in the detector and an offset C_2 which is due to the fact that the polarisation of the ^{3}He beam and the selection of a single polarisation by the analyser cannot be perfect in reality. The properties of the beam (Ω_0 and σ in (3.20)) have typically been determined beforehand by measuring the polarisation upon scattering from a static sample by varying the current in the incoming solenoid while the current through the outgoing solenoid is zero.
The polarised intensity can then be measured for a number of different phase coil currents in a single period of the oscillation, as shown by the example blue markers in Figure 3.11(b), which is further used to calculate the complex polarisation of the beam. Hence if the properties of the beam are known, there are three remaining variables in (3.20): A, C and δ. These variables can be determined by measuring at three different phase coil currents I over one oscillation period and solving the resulting set of linear equations. In practice 4 points are measured as described above giving rise to an over constrained set of linear equations which is solved using a least-squares optimisation. The measurement of four points presents a balance of accurate results and high throughput.
Finally after all variables have been determined, (3.20) can be used to calculate the real and the complex part, $\mathbb{R}e(P)$ and $\mathbb{I}\text{m}(P)$ of the spin polarisation. Any changes of the polarisation due to dynamical processes can be determined using this principle. In general, quasi-elastic and inelastic scattering off the sample gives rise to a change of the phase δ and amplitude A of the oscillation with respect to an elastic scattering event, which is illustrated in the lower panel of Figure 3.11(b).
The 4-point measurement is an established method for spin-echo experiments and is convenient when there is little time variation of Ω_0 and σ and the beam properties are easily determined in an infrequent precise measurement. However, other approaches, which involve continuously rotating the spin and measuring its polarisation after being scattered from the sample may provide advantages. First experimental tests of this method on a HeSE machine, have shown that it is working and that it can track changes of the beam properties throughout the experiment[58].

3.5.2 The semi-classical model

The semi-classical approach gives a useful alternative, which provides additional physical insight into the spin-echo process[12]. It considers that the quantitative details of the experimental principle can be described using the quantum mechanical evolution of a spin wavefunction in a magnetic field. Therefore the ^{3}He (spin $1/2$) particle is written with the quantum operator $\mathbf{S}$ describing its spin degree of freedom. Considering the same notation as used before, after the beam has been produced and spin polarised, the atom is found in an eigenstate of S_x. The latter can be written as a superposition of the two $|\pm\rangle_z$ spin eigenstates, parallel and anti-parallel to the field along z, according to:[12]

$$|+\rangle_x = \frac{1}{\sqrt{2}} \left(|+\rangle_z + |-\rangle_z \right) \ . \tag{3.21}$$

The key parameter in a spin-echo experiment is the spin-echo time, t_{SE}, introduced in the classical description above. In the semi-classical description it is defined by the difference in time for the "+" and "-" spin states of the wavepacket to pass through the precession coil. The times can be calculated by considering the different kinetic energies ($\frac{1}{2}mv_0^2 \pm \mu B$) of the two spin components depending on their alignment with the external precession field B, with μ being the magnetic moment.
The magnetic field splits the two components, so that the velocities of the two states inside the magnetic field are given by $v_\pm = v_0 \pm \mu B/mv_0$.[12] The component aligned with the field is accelerated while the other component, which is anti-parallel, is decelerated. Hence the two components take different lengths of time, $t_\pm$, to traverse the solenoid field,

$$t_\pm = \frac{L}{v_0} \pm \frac{\mu}{mv_0^3} \int_0^L B \, \mathrm{d}l \ , \tag{3.22}$$

resulting in the two wavepacket components being separated before they scatter from the sample.

Here L is again the length of the magnetic field, and $\int_0^L B\mathrm{d}l$ is the magnetic field integral. Writing μ in terms of the ^{3}He spin and gyromagnetic ratio, $\gamma\hbar/2$, illustrates that the time difference between the

wavepackets is exactly the spin-echo time introduced in (3.17):

$$t_{SE} = t_+ - t_- = \frac{\gamma\hbar}{m{v_0}^3}\int_0^L B\,\mathrm{d}l\ . \tag{3.23}$$

The concept of the temporal separation of the two spin-components is illustrated by the schematic in Figure 3.9 where the spin-echo principle was introduced: The oscillating blue lines represent the two spin eigenstates of the incoming He wavepacket. The two spin states arrive at the sample with the time spread t_{SE}. After scattering from the surface, the time spread is reversed and the separated wavepackets are recombined. If the surface changes between scattering of the two separated wavepackets, there is a loss of polarisation in the detected beam. The re-combination of the time-separated wavepackets gives the spin-technique its sensitivity to correlations in the surface configuration[12,101].
This picture in the semi-classical approach provides an intuitive way of relating a loss of correlation in scattering measurements to the dynamic motion at the surface (see Figure 3.12). Therefore, scattering of a He wavepacket from a surface can be written in terms of the scattered amplitude from a scattering centre (an adsorbate) at position $\mathbf{R}(t)$ as

$$A \propto \exp\left\{\mathbb{i}\boldsymbol{\Delta K}\cdot\mathbf{R}(t)\right\}\ . \tag{3.24}$$

In an experiment, scattering occurs from a collection of j scattering centres on the surface (coloured spheres in Figure 3.12(a)) and for simplicity it is assumed that the form factors of those are identical. If the scattering centre is found at position $\mathbf{R}_j(t)$ at time t, it may have moved to $\mathbf{R}_j(t+t_{SE})$ at a later time t_{SE}. The total scattered amplitude is then:

$$A\left(\Delta\mathbf{K},t,t_{SE}\right) \propto \sum_j \exp\left\{\mathbb{i}\boldsymbol{\Delta K}\cdot\mathbf{R}_j\left(t\right)\right\} + \exp\left\{\mathbb{i}\boldsymbol{\Delta K}\cdot\mathbf{R}_j\left(t+t_{SE}\right)\right\}\ . \tag{3.25}$$

Since in an experiment the intensity rather than the amplitude is measured, the ISF can be written as:

$$I\left(\Delta\mathbf{K},t,t_{SE}\right) \propto\ AA^*\,, \tag{3.26}$$

with * denoting the complex conjugate.

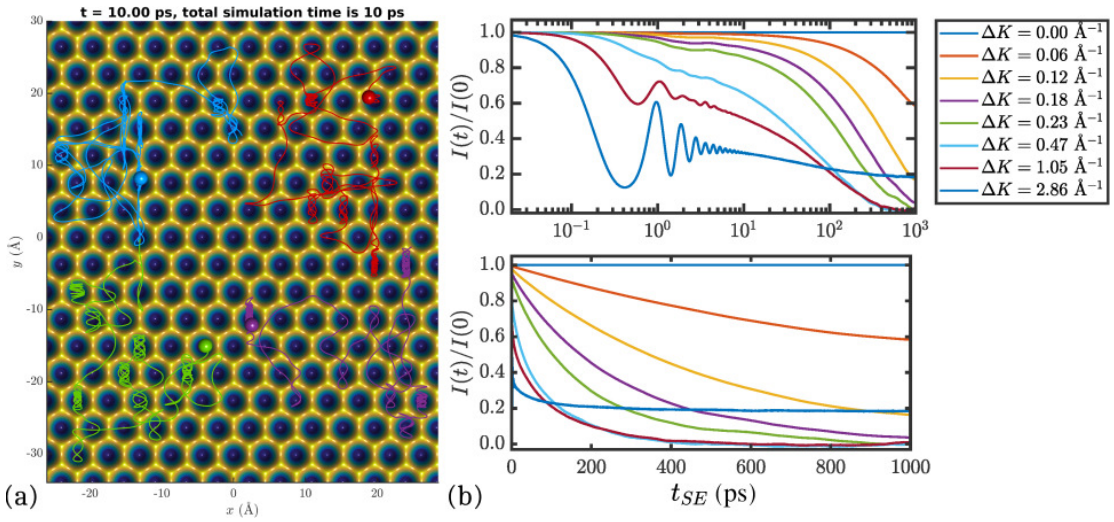

Figure 3.12: (a) Shows the trajectories of several adsorbates (coloured spheres) on top of a potential energy surface, as obtained from a molecular dynamics simulation. (b) shows the corresponding ISF $I(\Delta\mathbf{K},t_{SE})$, for several momentum transfers $\Delta\mathbf{K}$. Measurements of the ISF in a HeSE experiment, provide the loss of correlation with increasing time t_{SE} - a measure for the dynamics at the surface, occurring at a characteristic periodic length scale $2\pi/\Delta\mathbf{K}$. The bottom panel in (b) shows the ISF on a linear x-axis, while the ISF in the top panel is plotted on a log scale. The latter illustrates that vibrations typically occur at shorter times t_{SE}, of the ISF.

Finally the scattered intensity corresponds to the polarisation measurement, $P(\Delta\mathbf{K},t)$, or rather the

magnitude of the polarisation via

$$P = \frac{I_{max} - I_{min}}{I_{max} + I_{min}} \,. \tag{3.27}$$

Here I_{max} occurs at the point when the two wavepackets re-combine constructively at the in-phase condition and I_{min} when they re-combine in the out of phase condition, i.e. destructively. Hence using the complex notation of the polarisation it can be shown that the measured polarisation relates to the ISF and further via (3.9) to the the van Hove correlation function G:[12]

$$P\left(\Delta\mathbf{K}, t_{SE}\right) = \frac{I\left(\Delta\mathbf{K}, t_{SE}\right)}{I\left(\Delta\mathbf{K}, 0\right)} = \frac{\int G\left(\mathbf{R}, t_{SE}\right) \mathrm{e}^{\mathrm{i}\mathbf{K}\cdot\mathbf{R}} \mathrm{d}\mathbf{R}}{\int G\left(\mathbf{R}, 0\right) \mathrm{e}^{\mathrm{i}\mathbf{K}\cdot\mathbf{R}} \mathrm{d}\mathbf{R}} \,. \tag{3.28}$$

From the described semiclassical approach the connection between the decaying ISF and the loss in correlation on the surface, upon movement of the adsorbates (being the scattering centres) becomes clear, as also illustrated schematically in Figure 3.12. The ISF (inset at the top of Figure 3.9 and Figure 3.12(b)) decays as a function of spin-echo time t_{SE} due to the diffusive motion of adsorbates on the surface, and the overall decay can normally be fitted by an exponentially decaying function. The timescale of this measured decay is characteristic for the adsorbate motion (see 3.6).

3.5.3 Spin-echo and periodic dynamical processes: Phonons and the 2D matrix representation

The occurrence of inelastic scattering events, i.e. the creation and annihilation of phonons has so far not been discussed in the description of spin-echo experiments. Therefore a different representation of the spin-echo technique which enables a treatment of both quasi-elastic and inelastic events within the same framework is necessary[94,101]. It represents the spin-echo process as a 2D Fourier transform and is described in the following.

Starting from the accumulated spin phase in one solenoid (3.12), the actual experimental quantity is the solenoid current I, which defines the magnetic field inside the solenoid. With the velocity of the He atom being aligned parallel to the direction of the magnetic field (z) inside the coil, the accumulated phase is:

$$\phi = \frac{\gamma}{v} \int_0^L B(z) \mathrm{d}z = \frac{\gamma}{v} \underbrace{\int_0^L \frac{B(z)}{I} \mathrm{d}z}_{B_{\mathrm{eff}}} I \,, \tag{3.29}$$

where I is the current through the solenoid coil, generating the magnetic field and $B_{\mathrm{eff}} = \int_0^L \frac{B(z)}{I} \mathrm{d}z$. (3.29) assumes that the relationship between the generated field strength B in the solenoids and the current I flowing through the coil is linear, i.e. $B = B_{\mathrm{eff}} \cdot I$, for a coil specific constant B_{eff} which measures the coil sensitivity so that the accumulated phase becomes $\phi = \frac{\gamma}{v} B_{\mathrm{eff}} I$.

Therefore, the total accumulated phase (3.13) after passing through both solenoids becomes:

$$\phi = \phi_i + \phi_f = \gamma B_{\mathrm{eff}} \left(\frac{I_i}{v_i} + \frac{I_f}{v_f} \right) \,, \tag{3.30}$$

assuming that the currents I_i, I_f and velocities v_i, v_f are different but the solenoid length L and the constant B_{eff} are the same.

Inelastic scattering events via the creation and annihilation of phonons according to (2.18) are given in terms of the wavelength of the incoming and scattered particles. Hence in order to describe inelastic (or very broad quasi-elastic) features of spin-echo spectra quantitatively, the nonlinear relationship between wavelength changes and energy changes must be taken into account.

The description in terms of $\hbar\omega$ ((3.16) and (3.10)) suffices for studies of relatively slow diffusion, when the energy transfers are orders of magnitude smaller than the mean incident energy so that changes in energy and changes in wavelength are linearly proportional. However, the time an incoming or outgoing He atom spends in the corresponding solenoid field is proportional to its wavelength λ, and not its energy. Therefore, the spin-echo lineshape is a Fourier transform of the scattering probability in the

wavelength domain $\rho(\lambda_i \rightarrow \lambda_f)$[12,94,101]. Instead of the particle velocity the corresponding wavelength based on the de Broglie relation ($v = \frac{p}{m} = \frac{h}{m\lambda}$) needs to be used. Consequently, (3.30) becomes

$$\phi = \frac{\gamma m B_{\text{eff}}}{h}\left(I_i\lambda_i + I_f\lambda_f\right) . \tag{3.31}$$

Following the same notation as in 3.5.1.1, i.e. the spin polarisation is rotated in the xy-plane and initially polarised in the x-direction, the final (scattered) polarisation at the detector has the form:[12,94]

$$P_x(I_i, I_f) = \langle\cos\phi\rangle_\rho = \int \rho(\lambda_i, \lambda_f)\cos\left(\frac{\gamma m B_{\text{eff}}}{h}\left(I_i\lambda_i + I_f\lambda_f\right)\right)\mathrm{d}\lambda_i\mathrm{d}\lambda_f . \tag{3.32}$$

P_x is the same (experimentally measured) polarisation as introduced in (3.16), with the difference that (3.32) represents now a direct relation between the polarisation and the experimental variables, i.e. the solenoid currents I and the wavelength λ of the incoming and outgoing particles. $\rho(\lambda_i, \lambda_f)$ denotes the wavelength intensity function which describes the distribution of He atoms that reach the final polariser according to their initial and final wavelengths, λ_i and λ_f, respectively.
The full complex polarisation $P = P_x + \mathrm{i}P_y$ is then given by combining the polarisation along the x and y-direction according to (3.32). Therefore, it is more convenient to use the experimentally controllable parameter κ which is proportional to the solenoid current I via:[60,94,101]

$$\kappa \equiv \frac{1}{2\pi h}\gamma m B_{\text{eff}} I . \tag{3.33}$$

Hence the measured complex polarisation of the scattered He beam $P(\kappa_i, \kappa_f)$ is a function of the experimentally adjustable parameters κ_i, κ_f which are proportional to the solenoid currents. The spin-echo process can then be represented by the 2D Fourier transform:[12,94,101]

$$P(\kappa_i, \kappa_f) = \int \rho(\lambda_i, \lambda_f)\, \mathrm{e}^{2\pi\mathrm{i}(\kappa_i\lambda_i + \kappa_f\lambda_f)}\, \mathrm{d}\lambda_i\, \mathrm{d}\lambda_f , \tag{3.34}$$

where $\rho(\lambda_i, \lambda_f)$ is the wavelength intensity matrix which defines the probability of detecting an atom at a given scattering geometry, which had a wavelength λ_i before and a wavelength λ_f after scattering.

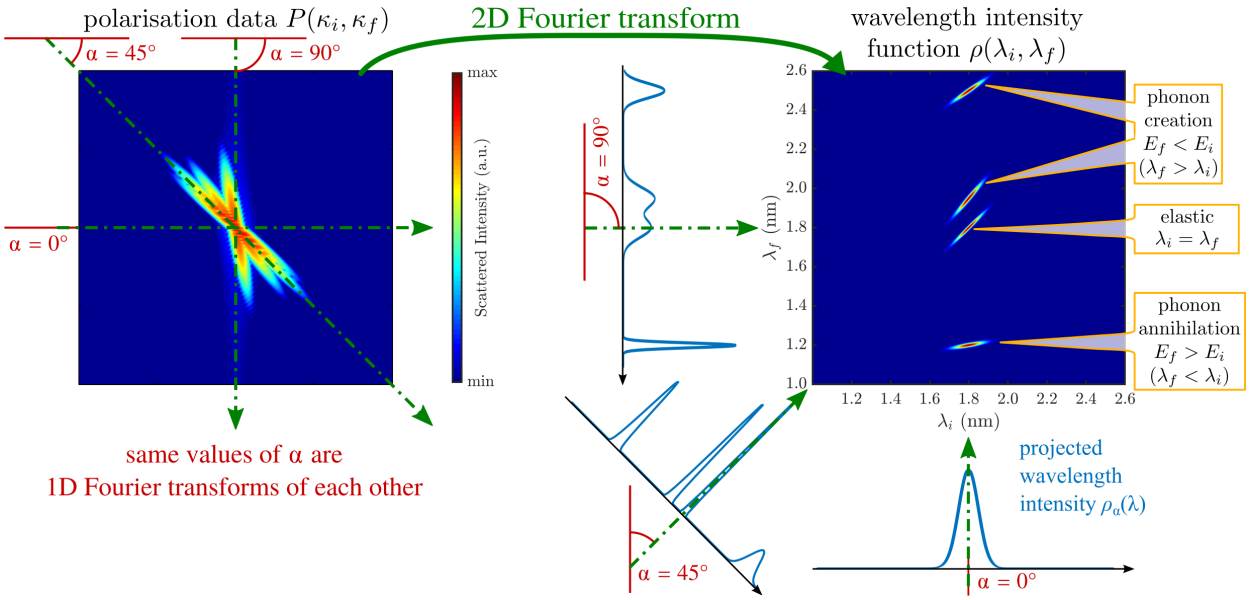

Figure 3.13: The wavelength intensity matrix $\rho(\lambda_i, \lambda_f)$ is the 2D Fourier transform of the (experimentally measured) polarisation data (intensity on a log scale). A typical $\rho(\lambda_i, \lambda_f)$ with key features (quasi-elastic scattering and phonons) is plotted on the right. Illustration of the Fourier slice phenomenon is demonstrated by the green dash-dotted lines which indicate the direction of integration with the corresponding projections as light blue lines. The green dash-dotted lines on the left represent the 1D Fourier transforms of the projections shown on the right.

The matrix $\rho(\lambda_i, \lambda_f)$ contains information about all possible energy transfer processes that are "illuminated" by the wavelength distribution in the incident beam and the underlying physical processes, such as the width (or lifetime) of a particular excitation, can be obtained by examining the shape and width of the features in the matrix (see Ref.[12] and the outlook 5.2).
Since (3.34) is a 2D Fourier transform of the wavelength intensity, $\rho(\lambda_i, \lambda_f)$ can be reconstructed via the inverse Fourier transform of the measured quantity $P(\kappa_i, \kappa_f)$[60,94,101]. This requires full knowledge of the Fourier coefficients satisfying conditions dictated by the Nyquist and resolution limits.
Figure 3.13 shows an example of a wavelength intensity function $\rho(\lambda_i, \lambda_f)$ with possible phonon creation and annihilation events labelled. In the case of elastic scattering ($E_f = E_i$) a peak appears along the diagonal $\lambda_f = \lambda_i$. Quasi-elastic broadening of the elastic peak due to diffusive motion shows up as the width of the peak, perpendicular to the $\lambda_i = \lambda_f$ line. Inelastic scattering events, i.e. phonon creation or annihilation corresponds to energy change of the scattered He atom with the quantised phonon energy E_{ph}. Hence these inelastic scattering events $\lambda_i \rightarrow \lambda_f$, appear above or below $\lambda_i = \lambda_f$ as illustrated in Figure 3.13 and also have an associated width.
According to (3.34), $\rho(\lambda_i, \lambda_f)$ can be reconstructed via the inverse Fourier transform by measuring $P(\kappa_i, \kappa_f)$ for a range of both κ_i and κ_f. However, the two-dimensional nature of $\rho(\lambda_i, \lambda_f)$ and the above mentioned conditions dictated by the Nyquist and resolution limits, require very long acquisition times. On the one hand a new approach which illustrates how to overcome this problem, based on methods known from image reconstruction, is described in Ref.[94].
On the other hand, since the wavelength intensity function is supported around the average initial wavelength it could be viewed as a one-dimensional function that has been smoothed out into two dimensions by the spread of initial wavelengths. If one is only concerned with e.g. the quasi-elastic broadening, measurements are often taken along one line in the (κ_i, κ_f) space.
In practice this means measuring the polarisation along a particular line defined by a constant κ_f/κ_i ratio, i.e. maintaining a constant ratio between the currents in the two solenoids[60,94]. Based on the Fourier slice theorem[94], measurements along a particular line in $P(\kappa_i, \kappa_f)$ space correspond to the Fourier transform of the projection of the entire $\rho(\lambda_i, \lambda_f)$ matrix onto the the equivalent line through $\rho(\lambda_i, \lambda_f)$ space. Considering the projection onto a particular line defined by the angle α, (3.34) reduces to a 1D Fourier transform:

$$P_\alpha(\kappa) = \int \rho_\alpha(\lambda)\, \mathrm{e}^{2\pi \mathrm{i} \kappa \lambda}\, \mathrm{d}\lambda \,, \tag{3.35}$$

with the projected wavelength intensity function $\rho_\alpha(\lambda)$.
Figure 3.13 illustrates how the Fourier slice theorem applies to the wavelength intensity function. Different angles of integration produce different results, especially when it comes to discerning different features.
The simplest measurements are projections with an angle of $\alpha = 0°$ and $\alpha = 90°$, respectively. These correspond to polarisation measurements where only the current through one of the coils is varied whereas the current in the other solenoid is set to zero. Varying only the current through the incoming solenoid (κ_i, $\alpha = 0°$) provides the initial velocity distribution and varying only the current through the outgoing solenoid (κ_f, $\alpha = 90°$) gives rise to the velocity distribution in the scattered beam[12].
In principle it is possible to scan along any other line through $P(\kappa_i, \kappa_f)$ space and the projection angle α can be be adjusted in order to resolve the fundamental linewidth of a specific feature. In general most lines in $\rho(\lambda_i, \lambda_f)$ are curved and only the elastic peak follows a straight line along the $\lambda_i = \lambda_f$ condition. Hence an integration angle of $\alpha = \pi/4$ as illustrated in Figure 3.13 will produce the best result for resolving this feature as a single spike. The latter explains why a conventional spin-echo measurement, which aims to measure the quasi-elastic broadening and scans along the line $I_f = -I_i$ ($\kappa_f = -\kappa_i$), is independent, to first order, of the incoming wavelength distribution λ_i[12].
With the the maximum (λ_0) of the incoming wavelength distribution either being known beforehand or deduced by projecting along $\alpha = 90°$, based on $\lambda_i = \lambda_0$ any projection with an arbitrary angle α can be converted to a function in terms of λ_f only:[94,101]

$$\lambda_f = \lambda_0 \cot\alpha - \lambda_{\mathrm{proj}} \sec\alpha \,, \tag{3.36}$$

where λ_{proj} is a point on the line onto which the projection occurs.

The mentioned curvature of the scattering events in $\rho(\lambda_i, \lambda_f)$ means that no single projection provides an optimum measurement for all events. While, a quasi-elastic measurement, yields the true quasi-elastic linewidth, it will overestimate the width of the inelastic modes. The optimum tilt angle, α, for the curvature of a specific scattering event in $\rho(\lambda_i, \lambda_f)$ space can be found via:[101]

$$\frac{\mathrm{d}\lambda_f}{\mathrm{d}\lambda_i} = -\tan\alpha = -\frac{I_i}{I_f} \tag{3.37}$$

The latter is particularly important if one aims to measure the natural linewidth and thus the lifetime of a phonon mode as described in 5.2.
In order to better understand the technicalities of the experiment and the 2D matrix presentation a modelled measurement created with a simple analytical function will be considered in the following. A typical measurement would include quasi-elastic scattering due to diffusion on the surface as well as inelastic scattering due to surface phonons. The diffusive process gives rise to an exponential decay with increasing current I through the solenoids whereas the phononic process leads to a decaying oscillation. Hence in a simple model the polarisation as a function of the current through the solenoids $P(I)$ takes the following form:

$$P(I) = A_1 \mathrm{e}^{-|I|/\tau} + A_2 \mathrm{e}^{-|I|/\tau_{ph}} \left[\cos\left(\omega_{ph} I\right) + \mathbb{i} \sin\left(\omega_{ph} I\right)\right] \tag{3.38}$$

where τ is the decay of the diffusive process, ω_{ph} the frequency of the phonon mode and τ_{ph} the decay according to the lifetime of the phonon process.
An example of the model function according to (3.38) is presented in Figure 3.14(a). The Fourier spectrum of this model function in the wavelength domain is shown in 3.14(b). The diffusive component gives rise to a broadening of the elastic peak found at the wavelength of the incoming He atoms ($\lambda_i = 1.83$ Å) whereupon the inelastic process leads to a peak that is shifted to larger wavelengths according to ω_{ph}.

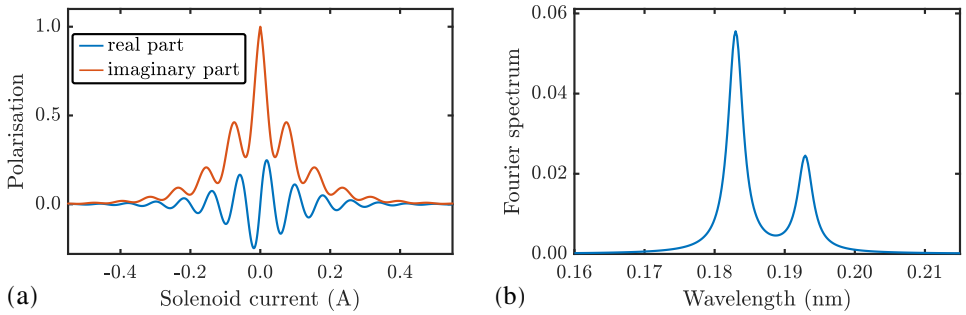

Figure 3.14: Model function according to (3.38): (a) Real and imaginary part of the polarisation as a function of the solenoid current. (b) Fourier transform of the model function in wavelength space showing the quasi-elastic peak at 0.183 nm and the inelastic peak shifted to larger wavelengths.

So far the problem has been considered as a continuous one. In order to apply the inverse Fourier transform to obtain $\rho(\lambda)$ in equation 3.35 this would require knowledge of $P(\kappa)$ at every point κ whereas in the experiment $P(\kappa)$ can only be measured at a finite number of discrete points. Furthermore, the domain of the wavelength intensity $\rho(\lambda)$ is usually discretised so that tools such as the Fast Fourier Transform (FFT) can be used. Hence equation 3.39 becomes a truncated Fourier series expansion.
Since κ and λ are Fourier pairs[12,94], this means that the resolution and the bandwidth of the spectra in wavelength will depend on the maximum value κ_{max} and the spacing $\delta\kappa$ for which $P(\kappa)$ has been measured. Therefore the resolution in terms of the wavelength, $\delta\lambda$, and the maximum wavelength λ_{max} are given by:

$$\delta\lambda = \frac{1}{2\ \kappa_{max}} \quad ; \quad \lambda_{max} = \frac{1}{2\ \delta\kappa}. \tag{3.39}$$

Relation 3.39 shows that increasing the maximum κ improves the wavelength resolution whereas a fine spacing of κ is needed to reconstruct large changes of the wavelength. It implies that a large number of data points has to be measured in order to gain a good resolution and a large bandwidth.

On the other hand we know that due to the events in a typical helium-scattering experiment $\rho(\lambda)$ is zero except for a couple of high intensity features at certain λ[60,101]. Figure 3.14(a) suggests that a larger number of points should be measured at low current whereas no additional information is gained by measuring the polarisation after both processes have decayed[94].

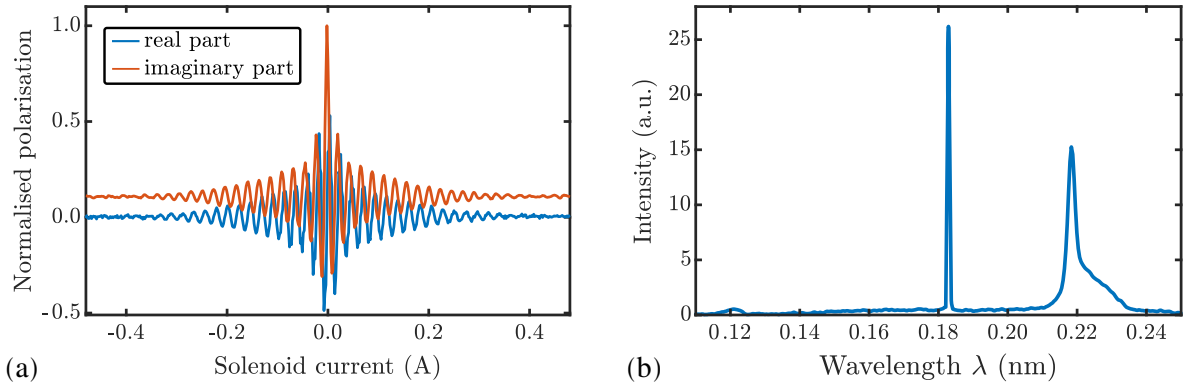

Figure 3.15: A typical HeSE measurement for scattering from a clean Ag(001) surface. (a) shows the real and the imaginary part of the measured polarisation versus the solenoid current. The FFT of the measured data set is shown in (b) where two strong peaks corresponding to elastic and inelastic scattering events can be distinguished.

Based on (3.39) it becomes clear that the resolution $\delta\lambda$ of a quasi-elastic measurement is only limited by the maximum field strength (κ_{max}) that can be applied. A typical ^{3}He spine-echo measurement for scattering from a clean surface illustrated in Figure 3.15 shows that indeed the elastic peak upon Fourier transforming the experimental data appears as a spike with a single point.

3.5.3.1 Changing variables: scattering in terms of wavelengths

After introducing the technicalities of the measurement and the wavelength presentation, in the following the relation between the different scattering functions and the experimentally controllable parameters, in the event of both quasi-elastic and phonon events will be outlined. According to (3.16), for small energy transfers upon scattering, the time domain measurement of $P(\Delta\mathbf{K}, t)$ in a conventional spin-echo experiment (with a projection angle $\alpha = 135°$), provides directly a normalised measurement of the ISF, $I(\Delta\mathbf{K}, t)$.
However, when the energy transfer is comparable to the beam energy, the measured polarisation is not directly proportional to the ISF and a direct change as illustrated in Figure 3.16(a) by the vertical red arrow is no longer possible. In the latter case the presentation in terms of wavelength λ needs to be used and the fact that the polarisation is instead related to the scattering function, S, via a Fourier transform. The necessary steps and relations are outlined in Figure 3.16.
Another important experimental variable, is the parallel momentum transfer $\Delta\mathbf{K}$. So far, measurements of the SF/ISF have been considered for a constant (fixed) $\Delta\mathbf{K}$ which is given by the incident angle ϑ_i. To fully understand the relations between the scattering functions and the wavelength intensity matrix, it is useful to explicitly declare the dependency by considering $\rho(\lambda_i, \lambda_f)$ as $\rho(\vartheta_i, \lambda_i, \lambda_f,)$, as illustrated by the 2D surface plots in Figure 3.16.
The four panels show the polarisation data and scattering functions based on a typical modelled system that exhibits both diffusive motion and surface phonons. The wavelength intensity matrix ρ, here plotted as as a function of the two variables incident angle ϑ_i and outgoing (scattered) wavelength λ, forms the central part as it is related to both the SF $S(\Delta\mathbf{K}, \hbar\omega)$ and the ISF $I(\Delta\mathbf{K}, t)$.
The experimentally obtained data is the polarisation (top-left panel) with the two variables ϑ_i and κ, the latter being proportional to the solenoid current I via (3.33). In a first step the experimental variable (κ) in the polarisation measurement is transferred to λ based on the fact that the the two variables are Fourier pairs, yielding $\rho(\lambda)$. To obtain $S(\Delta\mathbf{K}, \hbar\omega)$ from $P(\vartheta_i, \kappa)$ the Fourier transform is followed by a non-linear scaling to convert wavelength to energy transfer.

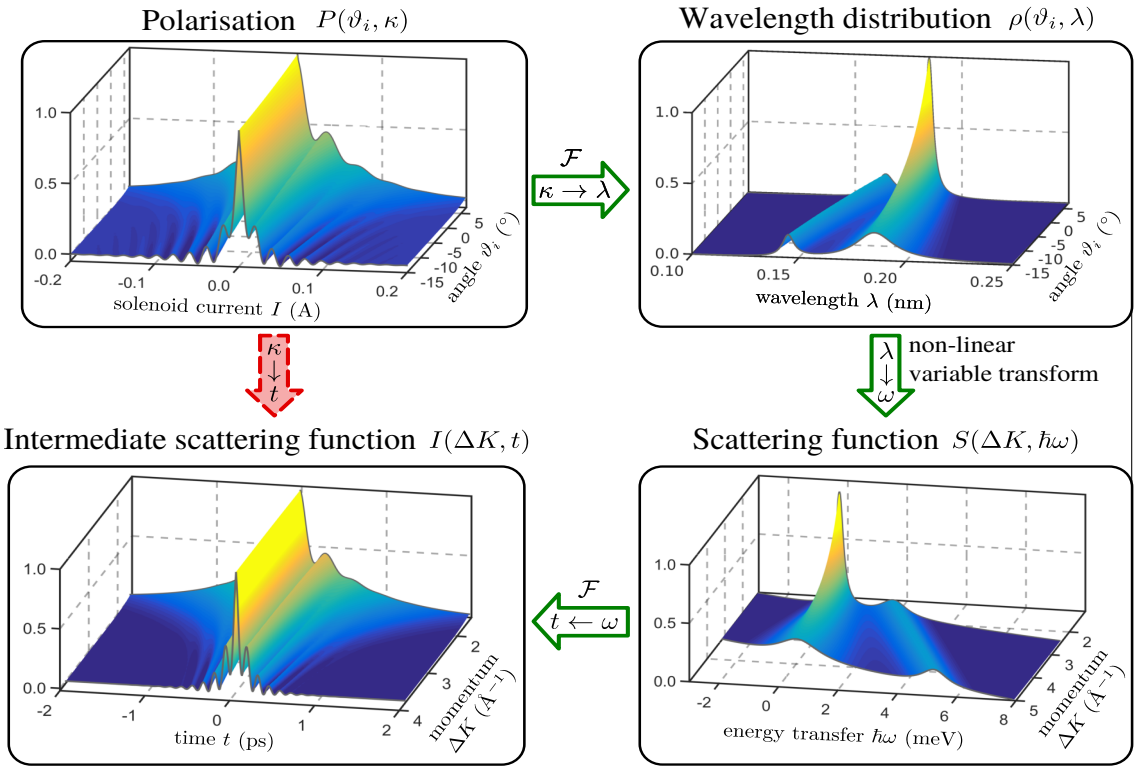

(a) 2D surface plot of the polarisation and scattering functions, in terms of the two experimental variables incident angle ϑ_i and κ (being proportional to the solenoid current I via (3.33)). The direct change from polarisation data to the ISF (red arrow) only holds for small energy changes i.e. in the case of quasi-elastic scattering.

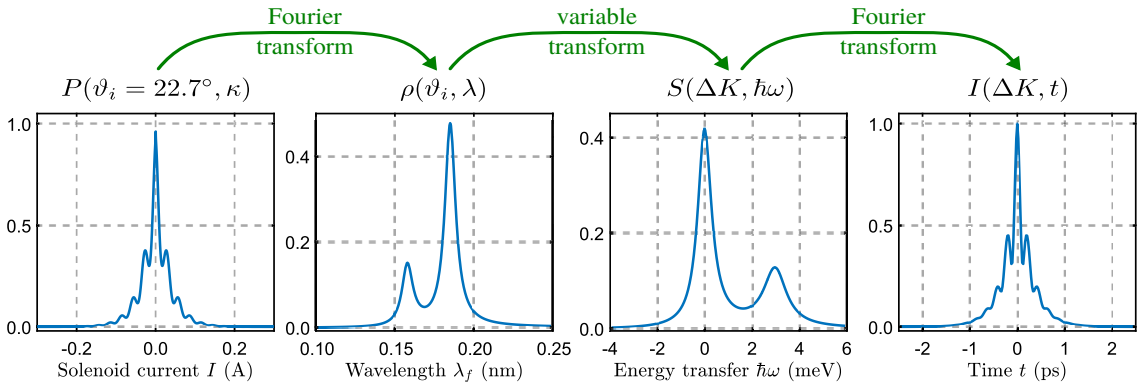

(b) 1D projections/slices of the upper plots with the incident angle ϑ_i kept constant at $22.7°$.

Figure 3.16: Diagram outlining the various stages of data transformation from measurement in polarisation to the ISF. The decaying oscillations in the polarisation/ISF are caused by surface phonons. Surface diffusion gives rise to an exponential decay in the polarisation/ISF and a broadening of the peak at $\Delta E = 0$ of the SF.

The relevant variable in terms of the scattering cross section (3.7) is the momentum transfer parallel to the surface $\Delta\mathbf{K}$. Hence, converting the wavelength intensity matrix $\rho(\vartheta_i, \lambda)$ to the SF $S(\Delta\mathbf{K}, \hbar\omega)$, means that one needs to change variables based on the conservation of energy and momentum (2.18) expressed in terms of wavelength:

$$\begin{aligned} \omega &= \frac{\Delta E}{\hbar} = \frac{\pi h}{m}\left(\frac{1}{\lambda_f^2} - \frac{1}{\lambda_i^2}\right) \\ \Delta K &= \frac{2\pi}{\lambda_f}\sin(\vartheta_{SD} - \vartheta_i) - \frac{2\pi}{\lambda_i}\sin\vartheta_i \ . \end{aligned} \tag{3.40}$$

Here, $\vartheta_{SD} = \vartheta_i + \vartheta_f$ is the fixed source-target-detector angle and considering that $\Delta\mathbf{K}$ is restricted by the source/surface/detector setup a scalar $\Delta K = |\Delta\mathbf{K}|$ is used in (3.40).
Following this approach the wavelength intensity function is converted into a frequency intensity func-

tion, the scattering function $S(\hbar\omega)$. Note that while the resolution of any measurement is uniform in wavelength space, it varies non-linearly with energy transfer. Therefore, the change of variables according to (3.40) requires a multiplication with the corresponding Jacobian, i.e.

$$S(\omega(\lambda_f)) = \rho(\lambda_f) \cdot \left(\frac{\mathrm{d}\omega}{\mathrm{d}\lambda_f}(\lambda_f) \right)^{-1} , \tag{3.41}$$

to preserve the intensity.
Eventually, if necessary the scattering function $S\left(\Delta\mathbf{K}, \hbar\omega\right)$ can be transformed to the ISF $I\left(\Delta\mathbf{K}, t\right)$, based on a Fourier transform of the variable ω, (3.10). One problem, however, is that the paths taken in $(\Delta K, \hbar\omega)$ space, follow the scancurve relation (2.20), along a constant ϑ_i, λ_f-path. These paths are no longer straight lines in terms of parallel momentum transfer ΔK and hence the obtained $I(t)$ should rather be seen as an approximate ISF.
Finally it should be noted that depending on the type of experiment people tend to work either with the SF or the ISF. From Figure 3.16(a), it is clear that the wavelength intensity function ρ forms the central part of the relation between those. $\rho(\lambda_i, \lambda_f)$ is equivalent to the position, shape and width of features in $S\left(\Delta\mathbf{K}, \hbar\omega\right)$, which can also be obtained from TOF experiments, but without the effect of the instrumental resolution. Hence $\rho(\lambda_i, \lambda_f)$ contains much more information than $S\left(\Delta\mathbf{K}, \hbar\omega\right)$, since the latter implicitly assumes that only energy transfers are important, regardless of the incident energy.

3.6 Characterisation of diffusion based on scattering experiments

In the following, the characterisation of surface diffusion and related phenomena based on scattering experiments is described, specifically by employing quasi-elastic helium and neutron scattering. The scattering functions measured in these experiments can be used to obtain comprehensive information about surface dynamical processes at the atomic scale.
However, relating the experimentally obtained scattering functions to physical parameters used to described the system, such as energy barriers for hopping or the potential energy surface, is non-trivial[12].
As outlined in 3.4.1-3.4.2, the underlying framework comes from principles established in neutron scattering[93,94]. These include the Fourier relationships between the scattering functions 3.4.2 and the concept of the pair correlation function, $G\left(\mathbf{R}, t\right)$. Since the pair correlation function, $G\left(\mathbf{R}, t\right)$ contains a full statistical description of the surface dynamics, an experimental approach is to obtain a series of measurements of either the ISF $I\left(\Delta\mathbf{K}, t\right)$ or the SF $S\left(\Delta\mathbf{K}, \hbar\omega\right)$, which can be transformed based on the Fourier relationships to obtain $G\left(\mathbf{R}, t\right)$.
On the one hand, in order to perform this inversion a detailed knowledge of the scattering form factor is needed, which is usually not available. On the other hand, the quasi-elastic broadening and the shape of $S\left(\Delta\mathbf{K}, \hbar\omega\right)$ and $I\left(\Delta\mathbf{K}, t\right)$ can readily be analysed and the way these shapes vary with momentum transfer $\Delta\mathbf{K}$, temperature and adsorbate coverage provide a sensitive measurement of the underlying physical principles of the system.
$G\left(\mathbf{R}, t\right)$ can only be constructed and Fourier transformed for simple models of diffusion and the analysis of QHAS/QENS measurements usually follows the approach to find simple surface dynamical models which reproduce the measurements[12] such as e.g. an underlying lattice and the corresponding hopping rates on which the motion occurs, or a Langevin model with a potential energy surface and friction force that describes the motion.
The models allow for a simplified but realistic experimental description of the system and thus a first characterisation may be followed by more sophisticated methods using e.g. first principles calculations.

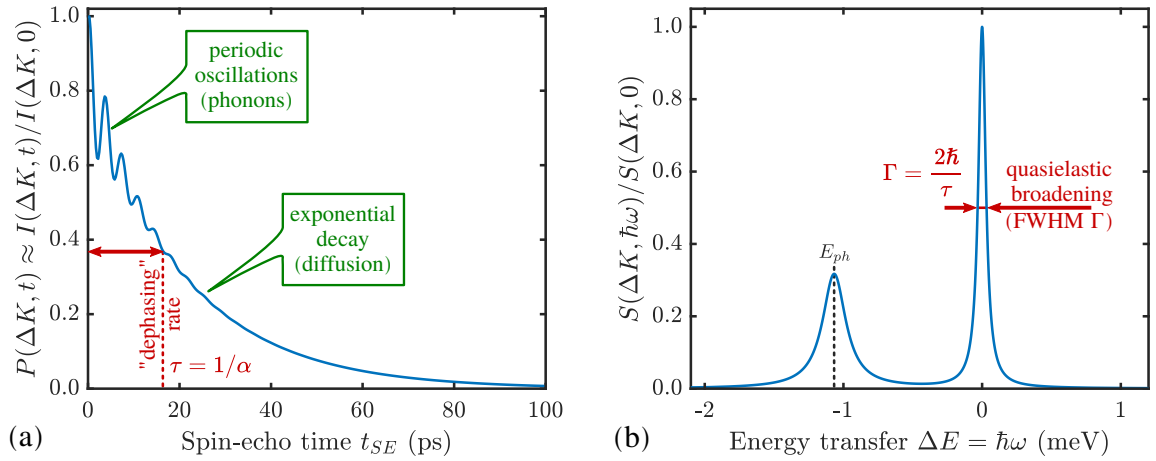

Figure 3.17: Example of typical scattering functions for a system with both phonons and diffusive motion. (a) The intermediate scattering function $I\left(\Delta\mathbf{K}, t\right)$ measured in the time domain, provides a correlation measurement. Periodic motion (phonons) gives rise to oscillations in $I\left(\Delta\mathbf{K}, t\right)$, while aperiodic diffusion gives an overall decay. The "dephasing" rate α is a measure for the loss of correlation with time due to the diffusive motion. (b) shows the scattering function $S\left(\Delta\mathbf{K}, \hbar\omega\right)$ as determined from TOF experiments or after converting the data to the energy domain. Diffusion causes a quasi-elastic energy broadening around zero ($\Delta E = 0$) and periodic oscillations cause a peak at finite energy transfer $E_{ph} = \hbar\omega_{ph}$. Since S is the Fourier transform of I, the FWHM Γ of the quasi-elastic broadening in the energy domain is inversely proportional to the broadening τ in the time domain. Finally, elastic scattering (not shown), from an immobile part of the surface gives rise to a constant background level in I and a delta function at zero energy transfer in S.

In Figure 3.17 the scattering functions of a typical QHAS measurement (based on a simple model such as (3.38)) are plotted, in the time domain (a) and the energy domain (b). As discussed in 3.5.3, for a conventional spin-echo experiment (with a tilt angle $\alpha = 135°$), the time domain measurement of a HeSE experiment yields polarisation as a function of t for a fixed surface-parallel momentum transfer $\Delta\mathbf{K}$ and thus access to the ISF $I(\Delta\mathbf{K}, t)$, provided the energy changes upon scattering are small.
As outlined in the semiclassical description 3.5.2 and schematically illustrated in Figure 3.12, the spin-echo measurement of $I(\Delta\mathbf{K}, t_{SE})$, describes the correlation at the surface after time t_{SE}, for the scattering condition of the beam, $\Delta\mathbf{K}$. Loss of correlation ("dephasing") at $(t_1, \Delta K_1)$, as manifested in the beam intensity, is a measure for the dynamics at the surface during time t_1, with the characteristic periodic length scale $2\pi/\Delta K_1$.
When the adsorbate dynamics follow simple models (such as hopping between adsorption sites that form a Bravais lattice or for Brownian motion), the ISF is known analytically and for a fixed $\Delta\mathbf{K}$ consists of an exponential decay in t with a rate that depends on $\Delta\mathbf{K}$. Allowing for a static offset due to surface defects, $I(\Delta\mathbf{K}, t)$ can then be written as:[12,41]

$$I(\Delta\mathbf{K}, t) = I_0(\Delta\mathbf{K}, 0) \cdot \mathrm{e}^{-\alpha(\Delta\mathbf{K})\cdot t} + C(\Delta\mathbf{K}) \tag{3.42}$$

where α is the dephasing rate and I_0 the amplitude at $t = 0$.
The dynamics are then extracted from the form of $I(\Delta\mathbf{K}, t)$ and the functional dependence of $\alpha(\Delta\mathbf{K})$ on $\Delta\mathbf{K}$. The variation of α with $\Delta\mathbf{K}$ provides a sensitive measurement of the diffusion mechanism (see 3.6.3) together with its variation with temperature and adsorbate coverage.
Periodic oscillations, such as adsorbate vibrations or surface phonons, give rise to additional oscillations in the correlation measurement, as shown in Figure 3.17(a). Following the same intuitive approach in terms of the ISF being a surface correlation measurement, a periodic oscillation means that the correlation comes and goes as a function of t where the periodicity corresponds to the phonon energy and the decay of the oscillations to the lifetime of the phonon.
The energy domain measurement, plotted in Figure 3.17(b), corresponds to the scattering function $S\left(\Delta\mathbf{K}, \hbar\omega\right)$, the observable quantity of a TOF experiment. $S\left(\Delta\mathbf{K}, \hbar\omega\right)$ can be obtained by Fourier a transform of $I\left(\Delta\mathbf{K}, t\right)$ in time[†].

[†] As discussed in 3.5.3.1, $I\left(\Delta\mathbf{K}, t\right)$ is only equal to the measured $P\left(\Delta\mathbf{K}, t\right)$ in the limit of small energy transfers and for larger energy transfers the wavelength domain $\rho(\lambda)$, followed by a non-linear scaling to convert to energy should be used.

In terms of $S(\Delta\mathbf{K}, \hbar\omega)$, the overall decay corresponds to a quasi-elastic broadening of the zero energy transfer peak ($\Delta E = 0$), which exhibits a Lorentzian peak shape in the case of random motion with a FWHM $2\hbar\alpha$ (3.49). Since S is the Fourier transform of I, the FWHM Γ of the quasi-elastic broadening in the energy domain is inversely proportional to the broadening $\tau = 1/\alpha$ in the time domain: $\Gamma = 2\hbar/\tau$[‡].
Periodic oscillations give rise to distinct peaks at finite energy transfer ΔE corresponding the phonon energy $E_{ph} = \hbar\omega_{ph}$.
For a characterisation of the diffusive motion measured with a spin-echo experiment, an analysis in the time domain if often convenient, provided that the vibrational modes and the diffusion are separated in time, i.e. the periodic oscillations have died away before the major decay due to the diffusive motion occurs. In the case of fast diffusion, the two components can overlap substantially and it may be necessary to treat the data in the energy domain[12,100].

3.6.1 Coherent and incoherent scattering

Before considering the actual analysis of the measured scattering functions, the aspects of coherent and incoherent scattering need to be shortly discussed. For finite adsorbate coverages, surface diffusion in terms of the van Hove pair correlation function, $G(\mathbf{R}, t)$, can be written in terms of a self part (S) and a distinct part (D),[12]

$$G(\mathbf{R}, t) = G_S(\mathbf{R}, t) + G_D(\mathbf{R}, t) \ , \tag{3.43}$$

which relates to the correlation of either the same particle, or a distinct particle.
$G_S(\mathbf{R}, t)$ is the self-correlation function, describing the probability of finding the same atom at $\mathbf{R}$ and t given it was at the origin at $t = 0$, and $G_D(\mathbf{R}, t)$ is the distinct correlation function relating the position of two distinct atoms. Following (3.9), the measured ISF (3.28) can then also be written as the sum of a self and a distinct part,

$$I(\Delta\mathbf{K}, t) = I_S(\Delta\mathbf{K}, t) + I_D(\Delta\mathbf{K}, t) \ . \tag{3.44}$$

Since HAS is inherently coherent, a HeSE measurement will always measure the complete function and correlation effects will appear, e.g. if adsorbate interactions become significant at higher coverages. On the other hand, neutron scattering can sometimes be tuned by using isotopes which scatter coherently or incoherently[93].
As discussed in 3.4.3, when using hydrogen containing adsorbates, the largest contribution to the neutron scattering cross section (3.6) comes from the hydrogen atoms which scatter mostly incoherently. Information about the dynamics follows from incoherent scattering from the H-atoms which means that the individual H-atoms inside an adsorbate are indistinguishable.
By using deuterated molecules, i.e. replacing the H-atoms with deuterium (D-atoms) in the adsorbate, scattering becomes mostly coherent. Figuratively speaking this corresponds to each D-atom having an individual "label" and the measured scattering function becomes sensitive to the collective motion rather than the self-diffusion part.
Following this approach, neutron TOF is usually employed to measure incoherent scattering thus yielding the self-diffusion part in terms of dynamics while neutron spin-echo is sensitive to coherent scattering and thus the collective diffusion mechanism[61,93].
In the low coverage limit experimental measurements are often analysed in terms of analytic or numeric models of self-diffusion following the so-called Vineyard approximation, which is valid providing interactions between the adsorbates are not strong enough to introduce correlation effects during the motion[12].
According to this approach it can be shown that the van Hove correlation function $G_D(\mathbf{R}, t)$ can be expressed in terms of the self-correlation function G_S alone, together with the static pair correlation function $g(\mathbf{R}) = G_D(\mathbf{R}, 0)$,

$$G_D(\mathbf{R}, t) = \int g(\mathbf{R}') \, G_S(\mathbf{R} - \mathbf{R}', t) \, \mathrm{d}\mathbf{R}' \ .$$

[‡] Note that the quasi-elastic broadening Γ is sometimes referred to as the half width and sometimes as the full width at half maximum. While the neutron scattering community tends to speak about Γ in terms of the HWHM, the HAS community tends to refer to Γ as the FWHM

It further means that based on the convolution theorem, the complete ISF (3.44) within the Vineyard approximation becomes

$$I\left(\Delta\mathbf{K},t\right)=\left[1+I_D\left(\Delta\mathbf{K},0\right)\right]I_S\left(\Delta\mathbf{K},t\right)=I\left(\Delta\mathbf{K},0\right)I_S\left(\Delta\mathbf{K},t\right)\ ,$$

i.e the effect of the coherent summation over the distribution of distinct scatterers is just to scale the overall intensity and there are no further modulations due to interference[12].

3.6.2 Diffusion barriers

Following the simple relationship in terms of the hopping rate (3.1), a widely used experimental approach is to determine the barrier for the diffusion (activation energy E_a) by measurements at various surface temperatures, while keeping the other experimental conditions constant. Assuming that the diffusion mechanism follows a simple Arrhenius form, for the dephasing rate, α,

$$\alpha=\alpha_0\exp\left(-\frac{E_a}{k_B\,T}\right)\ , \tag{3.45}$$

holds, with the pre-exponential factor α_0. Hence, the activation energy E_a can be extracted from the slope in an Arrhenius plot (plotting $\ln(\alpha)$ versus $1/T$) while the intercept gives α_0[41]. The activation energy E_a provides information about the energy barriers for diffusion and the underlying potential energy surface.
Note however, that E_a does not generally correspond to the true adiabatic energy barrier E_b for diffusion as illustrated in Figure 3.1. Different effective activation energies can be obtained from QHAS measurements depending on the corresponding momentum transfer $\Delta\mathbf{K}$ and as the temperature of the system changes, the underlying mechanism of motion may be subject to changes[12].
For example, the jump length distribution may change with temperature, while the assumption that the diffusion mechanism follows a simple Arrhenius behaviour (3.45) requires an invariant diffusion mechanism over the entire studied temperature range (see also the outlook 5.4). The latter is a difficulty related to the degree of sophistication in the interpretation of the experimental data and the fact that the diffusive motion does not necessarily follow the simple Arrhenius behaviour. Usually the effective activation barrier E_a will be lower than the adiabatic barrier. A better way to extract the adiabatic barrier for diffusion is to run molecular dynamics simulations, as outlined in 3.7, and optimise the adsorbate-substrate PES to obtain agreement with the experimental data set[12].
Furthermore, it should be noted that due to the scattering geometry, QHAS measurements are only sensitive to the projection of the jump length onto the corresponding direction of $\Delta\mathbf{K}$ with respect to the principle lattice direction. Hence Arrhenius activation energies obtained along the principle crystal lattice directions do not correspond to any directional isotropy of the barriers and instead the ratio of the maximum values of α, along the principal directions provides a better estimate of the isotropy of the underlying PES[12,102].

3.6.3 Simple types of diffusive motion and their corresponding experimental signatures

An important question is how one can differentiate between different types of diffusive regimes on a surface based on experimental measurements. The signature of different diffusive regimes is contained in the dependence of the dephasing rate α of the ISF or the quasi-elastic broadening Γ of the SF on the momentum transfer $\Delta\mathbf{K}$[85,93,103].
In the following a short overview of simple two-dimensional modes of diffusion at low coverages (i.e. where adsorbate interactions can be neglected) is given. Examples for the “fingerprint” of different self-diffusive regimes are given in Figure 3.18 with the three basic mechanisms Brownian, ballistic and hopping motion. Following the behaviour in real space based on the van-Hove pair correlation function $G_s\left(\mathbf{R},t\right)$, the different diffusive modes (see the different trajectories $\mathbf{R}_j$ in Figure 3.18) correspond to specific signatures in reciprocal space.

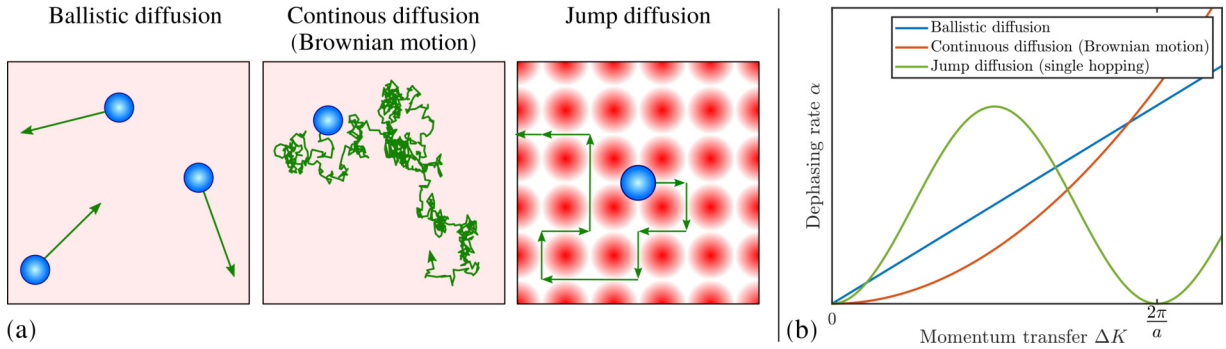

Figure 3.18: Illustration of the quasi-elastic scattering signatures for three simple modes of surface diffusion. In (a) the trajectories are shown schematically as green lines with the blue circles illustrating the moving adsorbates. In the case of jump diffusion the adsorbates move between vacant sites of the underlying surface (illustrated by the red circles) where the potential energy is smallest.
(b) The corresponding dephasing rate α shows a linear/quadratic/periodic dependence upon momentum transfer $\Delta\mathbf{K}$ for ballistic/Brownian/jump motion. Ballistic diffusion gives a Gaussian decay in $I(\Delta\mathbf{K}, t)$, with α varying linearly with $\Delta\mathbf{K}$. Random (Brownian) motion gives an exponential decay in $I(\Delta\mathbf{K}, t)$ with α varying quadratically with $\Delta\mathbf{K}$. For hopping motion the dependence is sinusoidal with a period $2\pi/a$ given by the jump length a.

Ballistic diffusion For a corrugation of the PES that approaches zero compared to the energy of the diffusing adsorbates and a negligible coupling to the substrate, one expects to observe so-called ballistic motion on sufficiently small length and timescales. Ballistic or 2D gas-like motion means that the adsorbates move in a linear fashion over the surface (Figure 3.18). Following the pair correlation function for this case, the corresponding Fourier transforms give a Gaussian lineshape in both the time and energy domain[12,95]. The ISF then becomes,

$$I(\Delta\mathbf{K}, t) = \exp\left[-\frac{k_B T}{2m}\left(\Delta\mathbf{K}\, t\right)^2\right] . \tag{3.46}$$

(3.46) is a Gaussian function whose decay frequency increases linearly with $\Delta\mathbf{K}$, i.e. in addition to the Gaussian lineshape, the variation of the dephasing rate α follows a linear relation as a function of $\Delta\mathbf{K}$ (see Figure 3.18(b)). For the corresponding full width at half-maximum (FWHM) Γ in the energy domain,

$$\Gamma(\Delta\mathbf{K}) = 2\hbar\sqrt{\frac{2\ln(2)k_B T}{m}}\,\Delta\mathbf{K} , \tag{3.47}$$

holds. Hence the slope of the linear behaviour in terms of $\Delta\mathbf{K}$ is directly proportional to the surface temperature T and inversely proportional to the adsorbate mass m.
Note that on small enough length and timescales, all motion appears Ballistic. As shown in one of the recent works[97], at strong enough dilution Brownian dynamics can transform into ballistic motion, i.e., molecular collisions become negligible and molecules move in a linear fashion.

Brownian motion The simplest form of 2D diffusion is continuous random motion, also known as Brownian motion (in other fields such particles in a liquid). Based on $G_s(\mathbf{R}, t)$ in that case[12] and using the Fourier relations introduced in 3.4.2, the corresponding scattering functions become:

$$\begin{aligned} I_S(\Delta\mathbf{K}, t) &= \exp\left(-\Delta\mathbf{K}^2 D\,|t|\right) \\ S(\Delta\mathbf{K}, \hbar\omega) &= \frac{1}{2\pi\hbar}\frac{D\Delta\mathbf{K}^2}{\omega^2 + \left(D\Delta\mathbf{K}^2\right)^2} . \end{aligned} \tag{3.48}$$

According to (3.48) the ISF follows an exponential decay with time t and the SF exhibits a Lorentzian peak shape. The corresponding dephasing rate α in the time domain and the FWHM Γ of the Lorentzian in the energy domain, show a functional dependence in terms of the momentum transfer $\Delta\mathbf{K}$:

$$\Gamma(\Delta\mathbf{K}) = 2\hbar\alpha(\Delta\mathbf{K}) = 2\hbar D\Delta\mathbf{K}^2 . \tag{3.49}$$

The typical signature of continuous random (Brownian) motion is the quadratic dependence of α (or Γ) upon the momentum transfer $\Delta\mathbf{K}$ as illustrated in Figure 3.18. For sufficiently small $\Delta\mathbf{K}$, or in the limit of large length scales in real space, all diffusive motion must conform to this macroscopic limit[12].
Another aspect of Brownian motion is that the curvature of the quadratic dependence of $\alpha\left(\Delta\mathbf{K}\right)$ corresponds directly to the diffusion coefficient D, in fact (3.49) can be used to determine D from an experimental data set[104]. Finally, in the case of Brownian motion the diffusion coefficient is directly related to the atomic-scale friction η via Einstein's relation:[61,104]

$$D = \frac{k_B T}{\eta m} \,, \tag{3.50}$$

where m is the mass of the diffusing adsorbate.

Hopping or jump diffusion For sufficiently low temperatures or large diffusion barriers, the atomic scale motion becomes dominated by the periodic arrangement of the surface atoms and the motion turns into discrete hops or jumps between preferred adsorption sites.
Based on the analysis of neutron scattering data from 3D liquids an analytic model that describes hopping motion was first introduced by Chudley & Elliot[105]. Following that work similar expressions were later developed to describe the hopping of adsorbates on surfaces which is usually referred to as Chudley-Elliott (CE) model[10–12,103,106]. It assumes that an adsorbate instantaneously jumps from one adsorption site to the other, with the probability $p_n = 1/\tau_n$. Starting point is the rate equation[85,93]

$$\frac{\partial}{\partial t} G_S\left(\mathbf{R}, t\right) = \frac{1}{N} \sum_n p_n \left[G_S\left(\mathbf{R} + \mathbf{l}_n, t\right) - G_S(\mathbf{R}, t)\right] \,, \tag{3.51}$$

where $\mathbf{l}_n$ are the jump vectors and p_n is the probability that a jump to the corresponding site occurs. Based on the Fourier relations and assuming that hopping occurs between adsorption sites that form a Bravais lattice, it follows that the ISF is an exponentially decaying function (as illustrated in Figure 3.19(b)) according to $I_S\left(\Delta\mathbf{K}, t\right) = \exp\left[-\alpha\left(\Delta\mathbf{K}\right)|t|\right]$, while in the energy domain a Lorentzian quasi-elastic peak shape is obtained.
The dephasing rate $\alpha\left(\Delta\mathbf{K}\right)$ exhibits then the typical functional dependence in terms of $\Delta\mathbf{K}$:[12,41]

$$\alpha(\Delta\mathbf{K}) = \frac{2}{\tau} \sum_n p_n \sin^2\left(\frac{\Delta\mathbf{K} \cdot \mathbf{l}_n}{2}\right) \,. \tag{3.52}$$

Based on the CE model (3.52), the dephasing rate α follows a sinusoidal dependence ($\sin^2$) versus momentum transfer $\Delta\mathbf{K}$. The amplitude of this sinusoidal shape according to (3.52) is given by $\frac{1}{\tau}$, with τ being the mean residence time between motion from one adsorption site to the other.

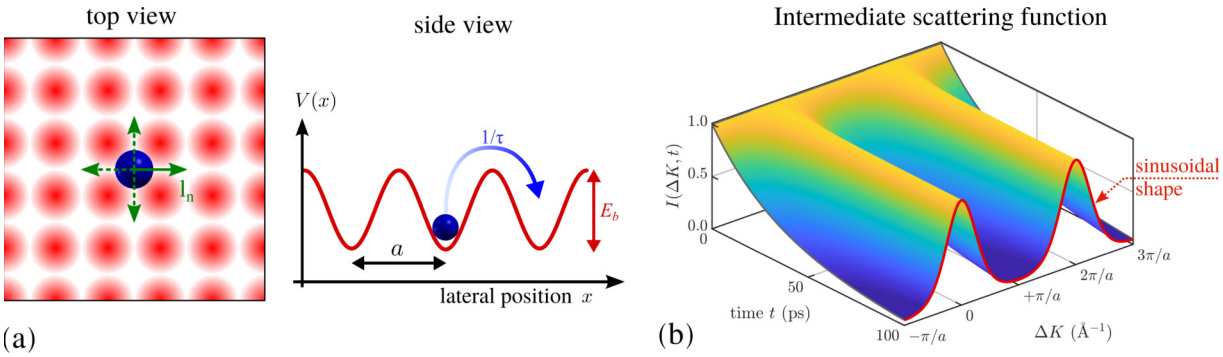

Figure 3.19: (a) Simple illustration for jumps of an adsorbate (blue sphere) on a square lattice. Hopping motion to another adsorption site corresponds to a jump vector $\mathbf{l}_n$ with probability p_n. In its simplest form only "single" jumps, i.e. to the next-nearest adsorption site are possible, though longer jumps can be included as well. For single jumps on a lattice with spacing a, the ISF $I(\Delta\mathbf{K}, t)$ takes the shape as shown in (b). The dephasing rate is then given according to (3.52), following the typical sinusoidal shape as illustrated by the red line in (b).

The surface plot in Figure 3.19(b) illustrates the ISF as a function of both t and $\Delta\mathbf{K}$ for "single" jumps on a lattice with spacing a. For any momentum transfer $\Delta\mathbf{K}$ that corresponds to multiples of the lattice spacing in real space ($2\pi/a$), the ISF remains constant as a function of time t, while in between it decays quickly.
The dephasing rate $\alpha(\Delta\mathbf{K})$ follows the typical $\sin^2$ dependence versus $\Delta\mathbf{K}$ (3.52) as illustrated by the red line in Figure 3.19(b). The position where the ISF remains constant and where (3.52) becomes a minimum in terms of $\Delta\mathbf{K}$ corresponds to the Bragg diffraction peaks for the surface. At a Bragg peak the lattice sites scatter in phase so the amplitudes contributing to $I\left(\Delta\mathbf{K}, t\right)$ are insensitive to jumps between sites, resulting in a dephasing rate, $\alpha = 0$.
When a number of different jump lengths $\mathbf{l}_n$ in (3.52) are possible, these will simply contribute to the overall value of α as a number of Fourier components, while the minima of $\alpha(\Delta\mathbf{K})$ will still be at Bragg peak positions of the substrate lattice. The CE model contains also Brownian diffusion as a long range diffusion limit, i.e. for $\Delta K \to 0$ the broadening converges to a parabola[61] and thus approaches the same $\Delta\mathbf{K}$ dependence as for Brownian motion in (3.49).
Finally, the diffusion coefficient D for 2D motion along a particular surface direction (given by $\Delta\mathbf{K}$), can then be calculated from the hopping rate as determined from the CE model using:[10,12,41]

$$D = \frac{1}{4}\langle l\rangle^2 \Upsilon \tag{3.53}$$

where Υ is the hopping rate and $\langle l\rangle$ is the mean jump length.

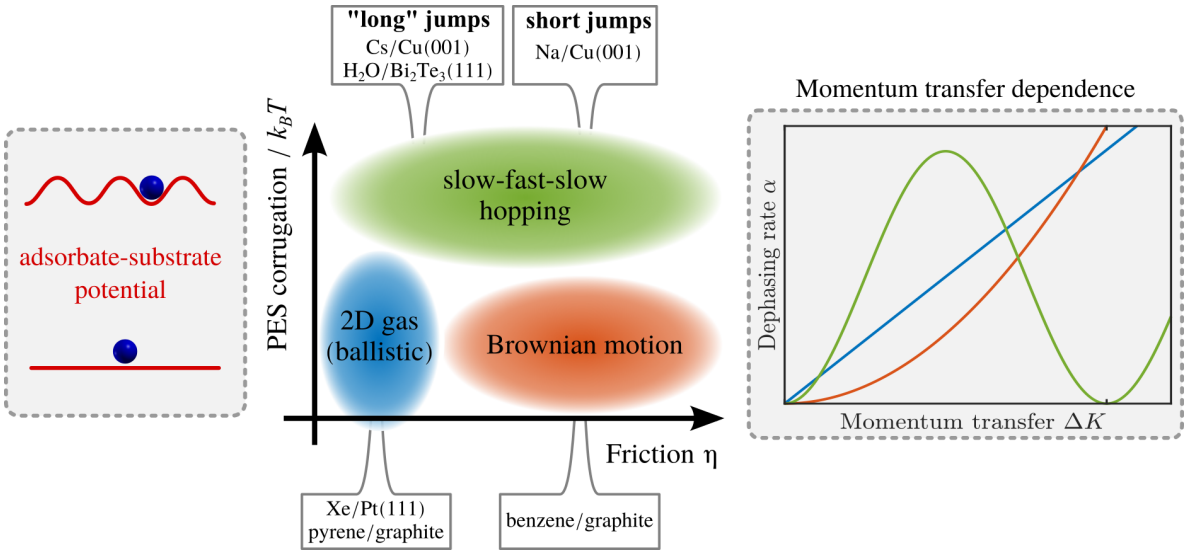

Figure 3.20: Schematic drawing illustrating the three simple models of surface diffusion, with some example systems. The two variables which tend to determine the diffusive motion are the rate of energy transfer to the substrate (friction η on the abscissa) and the corrugation of the adsorbate-substrate potential energy surface (PES) in relation to the thermal energy (k_BT) of the system on the ordinate.
For a negligible corrugation of the PES in relation to k_BT (i.e. a more or less "flat" adsorbate-substrate PES as illustrated on the left) and simultaneously a low friction η, ballistic motion is expected to occur. The characteristic signature is a Gaussian line shape of the quasi-elastic broadening and a linear dependence upon the momentum transfer ΔK as shown on the right (see Refs.[95,97]). Keeping the corrugation of the PES low while increasing the friction η gives rise to continuous random (Brownian) motion with an exponential decay of the ISF and a quadratic dependence of α versus ΔK. (e.g. for benzene on graphite[104]). As soon as the corrugation of the PES becomes significant with respect to k_BT, the diffusive motion tends to follow the periodicity of the underlying PES, giving rise to hopping motion and a periodic shape of $\alpha(\Delta K)$. For jumps on a simple Bravais lattice the ISF exhibits a single exponential decay. In the low friction case, energy dissipation to the substrate is low and "long" jumps can occur (see e.g. Ref.[41]), while for an increasing η generally short (single) jumps dominate (see e.g. Ref.[101]).

The described three simple models and their signatures form the core references for the interpretation of QHAS and QENS experiments, providing a more general insight into the underlying mechanism of surface diffusion. Based on the widely used Langevin framework, two variables tend to determine the diffusive motion as illustrated schematically in Figure 3.20: The rate of energy transfer with the substrate

(friction η) and the corrugation of the adsorbate-substrate potential (PES) in relation to the thermal energy (k_BT) of the system. Depending on the low/high friction and low/high corrugation case, surface diffusion is then broadly divided into four categories as shown in Figure 3.20 - of which each one is again related to one predominant type of motion as described above.
Finally, it should be noted that as described in some of the works of this thesis[41,61,97] real systems hardly show a perfect single mode of motion, since for example "real" jumps do not occur instantaneously, as implicitly assumed in (3.51). Hence while these analytic models allow qualitative statements about the diffusion mechanism, simple combinations of these models often cannot reproduce real data quantitatively[12] and a combination with theoretical approaches such as molecular dynamics or kinetic Monte-Carlo simulations (3.7) in combination with scattering simulations is often required.

Perpendicular and correlated motion The presented simple models do not include, for example, the possibility of an adsorbate motion perpendicular to the surface[12,107].
Moreover, these models consider only translational motion without interaction between the adsorbates. The latter often holds in the low coverage regime though collective motion may also be present at very dilute adsorbate concentrations. In the case of collective motion the dephasing rate typically follows a characteristic shape with a peak at small $\Delta\mathbf{K}$ values followed by a de Gennes narrowing dip. The effect has been described theoretically and observed experimentally for surface diffusion[11,12,107]. The location of the dip corresponds to a peak in the static structure factor[108], verifies the nature of the force and allows also a coverage estimation of the adsorbates.
Further details about these effects in surface diffusion measurements may be found in Refs[41,107].

3.7 Computer simulation methods for surface diffusion

Real systems often contain a combination of the above described signatures and cannot be analysed fully using simple analytical methods. Moreover, the possible internal degrees of freedom in the case of diffusing molecules may further add complexity giving rise to a PES with a number of additional dimensions[86,102]. Hence analysis approaches often include the application of simple calculations based on kinetic Monte-Carlo (MC) or molecular dynamics (MD) simulations. Such simulations provide the trajectories of the adsorbates in real space - thus providing also insight into the real space motion - followed by calculations of the scattering functions which are obtained in the experiment.

MD simulations One of the most common methods for modelling surface dynamics are MD simulations, based on solving the Langevin equation (3.3), introduced in 3.2. The interaction of adsorbates with the substrate atoms is then described by a "frozen" potential energy surface (PES), while the friction coefficient η describes the rate of energy transfer between the adsorbate and the surface and connection to the substrate heat bath is given by the stochastic term $\xi(t)$[11,83].
In comparison to full (micro canonical) MD simulations, which include the interactions of all atoms, Langevin based MD simulations are more economical in terms of the computing time, while offering a comparable quantitative description of the experiment[83]. These MD simulations can thus be treated as a minimalist computational experiment where the simulation parameters are adjusted so that specific features of the experimental data can be understood instead of providing a complete description of the entire degrees of freedom. For example, they are useful to obtain information about the atomic-scale friction η of the system, which directly influences the diffusion as it affects the rate of energy transfer between the adsorbate and the substrate. While for purely Brownian motion, η can be directly extracted with (3.50), this is not possible for hopping motion and instead MD simulations are often employed.
An MD simulation package which was implemented in Simulink and MATLAB based on the GLE, is available from https://doi.org/10.5281/zenodo.2025809 under the GNU/GPL-3.0 license and is described in detail in Ref[83]. To facilitate MD simulations for a further analysis of the experimental data, several MD simulations are run and the output of the MD simulations, the particle trajectories $\mathbf{R}_j(t)$, can then be used to calculate both the coherent and the incoherent $I(\Delta\mathbf{K},t)$[83] which can further be analysed in the same manner as the experimental data.

The simplest approach is to describe only the centre-of-mass (CoM) of the j-th adsorbate parallel to the surface and the MD simulation then follows the configuration of scattering centres imposed on the CoM as they move along the frozen PES with time. Therefore the frozen PES, $V(\mathbf{R})$, is usually described by a Fourier series according to

$$V(\mathbf{R}) = A \sum_n \cos\left(\mathbf{G}_n \cdot \mathbf{R}\right) \ . \tag{3.54}$$

where the $\mathbf{G}_n$ vectors describe the symmetry of the substrate. E.g. for a simple hexagonal Bravais lattice:

$$\begin{aligned} \mathbf{G}_1 &= (0,1)\,\zeta \\ \mathbf{G}_2 &= \left(\tfrac{\sqrt{3}}{2}, -\tfrac{1}{2}\right)\zeta \\ \mathbf{G}_3 &= \left(-\tfrac{\sqrt{3}}{2}, -\tfrac{1}{2}\right)\zeta \end{aligned} \tag{3.55}$$

with $\zeta = 4\pi/(\sqrt{3}a)$ and a being the surface lattice constant.
For an analysis of the rate of barrier crossing based on the Langevin description of dynamics, where the friction η is a direct measure of the coupling between the CoM motion and the heat-bath of the substrate[41], the corrugation of the frozen PES is then chosen to match the experimentally determined activation energy. A plot of such a typical PES is shown in the leftmost panel of Figure 3.2. The remaining parameters in the GLE simulations are then the friction η describing the energy transfer and a cutoff frequency ω_c of the noise power density as mentioned in 3.2.

Kinetic Monte-Carlo simulations Kinetic Monte-Carlo (MC) simulations in combination with the experimentally determined dephasing rates are another way to obtain quantitative insight into the mechanism of diffusion. In contrast to MD simulations, a discrete grid is used and a random sampling over the points means that typically MC simulations are less computationally expensive than the MD simulations described above and can hence be applied to larger systems or to study specific effects which are difficult to simulate with MD simulations.
An example code for kinetic MC simulations employing a modified form of the Metropolis algorithm[11,41] in order to study diffusion a hexagonal lattice is available from https://doi.org/10.5281/zenodo.3240428 under the GNU/GPL-3.0 license.
For example, kinetic MC simulations can be used to provide insight into the mechanism of adsorbate interactions during diffusion[11,41]. Therefore, a periodic grid is used, where adsorbates are initially located on the grid sites at random. The potential energy for an adsorbate at each site of the grid is calculated for the initial configuration, taking into account repulsive/attractive inter-adsorbate interactions based on a pairwise dipole-dipole potential V_{pp} of the form,

$$V_{pp} = \pm\frac{B}{r^3} = \pm\frac{p^2}{4\pi\epsilon_0 r^3} \ , \tag{3.56}$$

where p is the effective value of the dipole moment and r is the distance separating the two dipoles. Allowing for either positive or negative pre-factors provides the ability to explore both repulsive and attractive interactions. Each MC step consists of choosing an adsorbate at random which may then hop to one of its neighbouring sites, with specific probabilities for jumps to first, second and third nearest neighbours. Provided that the adsorbate is not blocked from entering the new site by another molecule, the probabilities are weighted by the difference in the potential of the molecule at the two sites. If several new sites with lower potential energy exist, one of them is chosen at random and the molecule is moved into the new site.
Following this method, a series of kinetic MC simulations can be performed to study the mentioned nature of inter-adsorbate interactions in surface diffusion. The trajectories from the MC simulations are then used to obtain simulated coherence functions and dephasing rates which can further be compared with the $\Delta\mathbf{K}$ resolved experimental data, while also adjusting the simulation to reproduce temperature dependent measurements.

4 Summary

After an introduction into the subject and a description of the used methods, in the following a short summary over a few results is given, followed by a short outlook and finally a reproduction of the articles.

Surface dynamics and structure of semimetals and Dirac materials

Several of the attached papers deal with experimental and theoretical studies regarding the surface structure and dynamics of semimetal and Dirac materials. They demonstrate that atom-surface scattering provides a sensitive probe to determine the surface phonon dispersion and energy dissipation processes in terms of the e-ph interaction parameter on the surfaces of these materials. The obtained experimental data of various TIs[6,40,53,72,80] promises to evolve a more general picture about the surface dynamics and the atom-surface interaction of these peculiar surfaces.
The surface electronic corrugation of the investigated semimetals and binary TIs exhibits a peak to peak corrugation of 6-14% in terms of the lattice constant[40,49,53,54]. An electronic corrugation in the order of 10% of the lattice constant is intermediary between those of metals and semiconductors. In comparison to low-index metal surfaces, the Smoluchowski effect seems to be much reduced on the TI and semimetal surfaces presented in this study, which may originate from the fact that for the described materials only the surface state is metallic and the concentration of surface electrons at specific wavevectors.
The studies of the topological semimetals Sb(111)[46] and Bi(114)[47] investigate charge density waves (CDWs) - periodic modulations of the electron density which are an ubiquitous phenomenon in crystalline metals. The superstructure in measured diffraction spectra of Sb(111) is associated with the surface electron and hole pocket states of the surface electronic band structure. (Unpublished work) regarding elastic HAS measurements of the TI Bi_2Te_2Se(111) show also a number of particularly sharp satellite peaks, aside the diffraction peaks, which are likely to correspond to electronic transitions across the Dirac ring. Taken together the results suggest that HAS may be capable of mapping the surface electronic states at the Fermi level, in the case of narrow electron/hole pockets in reciprocal space as well as the Dirac states of TI surfaces.
The study about the hydrogenation of a graphene surface, including lower bounds on the rates of hydrogen diffusion[109], illustrates the capability of HAS to determine the H-positions at surfaces. The latter is possible due to the large cross section of HAS to isolated adsorbates[110], while the H-positions are hard to determine with other methods (e.g. hydrogen is a weak scatterer for electrons) which also present a severe risk of damaging the H-layer. Surface dynamics measurements of graphene grown on Ni(111)[42] illustrate that for a single layer of metal-supported graphene, the surface phonon dispersion remains basically the one from the substrate.
Together with the ability of HAS to investigate the e-ph interaction at surfaces, the corresponding low energy excitations of CDWs could be identified on the surface of Sb(111)[46]. Further results about the surface dynamics of Bi_2Se_3(111)[72] show that low-energy collective electronic excitations can be measured with HAS, implying that HAS may be used as a choice spectroscopy for the investigation of surface electronic excitations in the terahertz domain.
Investigations of the archetypal TI Bi_2Te_3(111)[80] show a prominent surface acoustic mode that may have important implications in layered and nanoscale devices. Moreover, thanks to the high resolution experimental data, it is shown in comparison with *ab-initio* calculations that the inclusion of vdW interactions is necessary for an exact theoretical description of application-relevant issues like the thermal conductivity of layered structures in general[80].

Surface diffusion and energy dissipation on the nanoscale

The characteristics of energy dissipation during the motion of atoms and molecules can be determined from the lineshape broadening upon inelastic scattering from surfaces. In fact inelastic helium and neutron scattering are the only known methods capable of determining surface diffusive processes at timescales of ps to ns with atomic resolution. Moreover, due to the low energy of the probing particle beam delicate adsorbates such as water can be studied without disruption of the motion or dissociation of the molecule.

Results about the diffusion of pyrene on the semimetal graphite provide the first unequivocal proof of molecular motion in the ballistic regime:[97] At strong enough dilution, Brownian dynamics can transform into ballistic motion, i.e., molecular collisions where linear and angular momentum is exchanged become negligible and molecules move in a linear fashion. The diffusion of ammonia on graphite[61] reveals hopping motion of the ammonia molecules with an unusually fast molecular transport.

Since the experimental observation of dynamical processes on surfaces implies fast data acquisition, Ref[94] describes how new findings in the field of image reconstruction and compressed sensing can be implemented. Within an inter-disciplinary collaboration with the department of mathematics the presented novel approach allows to reduce significantly the quantity of data which is actually measured while preserving the statistical quality of the measurement.

In a study of the diffusion of water on the TI Bi_2Te_3(111)[41], the mechanisms underlying the molecular motion of water are specified and by comparison with first-principle calculations, aspects of its adsorption geometry are identified, as well as the energy landscape for the motion. The experimental data shows evidence for repulsive interactions between the molecules, contrary to the expectation that attractive interactions dominate the behaviour and aggregation of water. A qualitative assessment of the rates of energy transfer between water molecules and the TI on which they move is made. The latter is discussed in terms of the nanoscale-friction affecting the motion, where a TI is particularly interesting since certain friction mechanisms are disallowed by the topological character of the substrate.

5 Outlook

This last chapter contains a selection of plans and ideas for future research, dealing with a number of so-far unexplored features. 5.1 describes how quantum mechanical scattering calculations can be extended to "realistically" include inelastic effects. The following sections then discuss, based on unpublished or preliminary experimental results how, e.g. upon pushing the resolution limits effects such as the linewidth and lifetime of surface phonons can be determined (5.2), ideas about tuning the vdW bonding strength between absorbed molecules and the substrate (5.3) and ways to verify rate theory upon studying surface diffusion (5.4).

5.1 Inelastic quantum mechanical scattering calculations

Extension to inelastic quantum mechanical scattering calculations can be achieved by starting from the time dependent Schrödinger equation together with the (time dependent) displacement of atoms from their respective equilibrium positions as in (2.15). Following this approach, inelastic effects can be accounted for by adding inelastic scattering channels allowing to simultaneously take into account effects such as inelastic broadenings, e.g. the linewidth of selective adsorption resonances from a theoretical point of view.
Therefore, $\mathbf{A}\left(\mathbf{Q},\nu,T\right)$ as a whole needs to be used as fitting parameter, but as a start often a simpler form which was originally derived for copper surfaces is assumed:[111]

$$\mathbf{A}\left(\mathbf{Q},\nu,T\right)=\frac{1}{aQ_{\mathrm{c}}}\sqrt{\frac{384\hbar^{2}\pi T}{Mk_{\mathrm{b}}\Theta_{\mathrm{D}}^{2}}}\,. \tag{5.1}$$

Here Q_{c} is a cut-off factor for the harmonic motion, a is the lattice constant, M the mass of the surface atoms and Θ_{D} is the surface Debye temperature[49].
Taking periodicity in space and time into account, the potential and wave function can be written as Fourier series and inserted into the Schrödinger equation, again leading to a coupled set of equations:

$$\begin{aligned}\left[\frac{\mathrm{d}^{2}}{\mathrm{d}z^{2}}+\mathbf{k}_{\mathbf{G}+\mathbf{Q},\mathrm{n}_{\mathbf{Q},\nu},\mathrm{z}}^{2}-V_{\mathbf{0}}(z)\right]\Psi_{\mathbf{G}+\mathbf{Q},\mathrm{n}_{\mathbf{Q},\nu}}(z)&=\sum_{\mathbf{G}'\neq\mathbf{G}}V_{\mathbf{G}-\mathbf{G}'}(z)\Psi_{\mathbf{G}'+\mathbf{Q},\mathrm{n}_{\mathbf{Q},\nu}}(z)\\&+\tfrac{1}{2}\mathbf{A}(\mathbf{Q},\nu,T)\cdot\sum_{\mathbf{G}'}\left[\mathbf{F}_{\mathbf{G}-\mathbf{G}'-\mathbf{Q}}(z)+\mathbf{F}_{\mathbf{G}-\mathbf{G}'+\mathbf{Q}}(z)\right]\\&\times\left[\Psi_{\mathbf{G}+\mathbf{Q},\mathrm{n}_{\mathbf{Q},\nu}+1}(z)+\Psi_{\mathbf{G}+\mathbf{Q},\mathrm{n}_{\mathbf{Q},\nu}-1}(z)\right]\end{aligned} \tag{5.2}$$

(5.2) includes elastic scattering processes as well as contributions from phonon creation $(\mathrm{n}_{\mathbf{Q},\nu}+1)$ and annihilation $(\mathrm{n}_{\mathbf{Q},\nu}-1)$ events, respectively. The channels are now said to be dressed by a phonon field and all channels within one active mode form a so called Floquet block.
In the case of single-phonon scattering three Floquet blocks have to be used, representing elastic scattering and creation/annihilation of a single phonon. Extension to multi-phonon scattering is achieved by adding more Floquet blocks.
However, to the best of my knowledge and at the time of writing this thesis no publication or implementation of an inelastic CC-code that takes into account the "full" phonon dispersion relation was available. In order to ease the calculations, typically phonons are instead given zero momentum and a Debye model is assumed for the surface[49]. Hence, an implementation that considers phonons in a more realistic way, thus allowing to describe inelastic effects in the experiments, seems to be timely.

5.2 Phonon lifetimes

The phonon lifetimes of bulk modes are accessibly with high-resolution inelastic neutron scattering and are thus a very active area of research[112,113]. However, measurements of the linewidth and thus the lifetime of surface modes have been mainly resolution limited. In a similar manner, measurements of anharmonic effects (phonon energy shifts with temperature) in the bulk are again accessible by inelastic neutron scattering[112] while classical HAS can provide the necessary resolution for surface modes in a few cases[114].
Finally, in terms of phase transitions to e.g. superconducting phases, changes on the phonon lineshape and lifetime are also expected, which again up to now have only been addressed in the bulk[115].
If experimental data is available for surface phonon modes, it has either been measured at the Brillouin zone boundary[116] or in the frequency domain (i.e. for optical modes) by means of high-resolution Raman scattering experiments[117]. In general, experimental information on the lifetimes of acoustic surface phonons remains limited by resolution effects due to the typically low phonon energies and the thus required high energy resolution in order to resolve the linewidth (≈ tens of μeV).

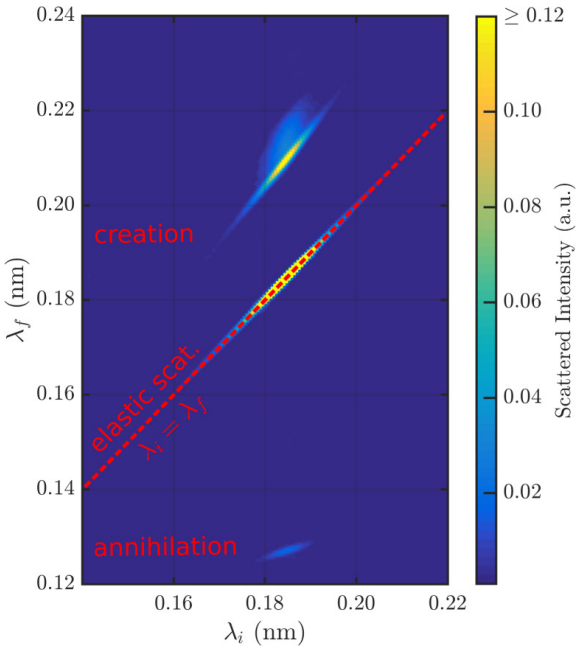

Figure 5.1: Measurement of the wavelength intensity function $\rho(\lambda_i, \lambda_f)$ at $\vartheta_i = 19.2°$ where the linewidth measurements are performed, allow to determine the optimum tilting angle as $\alpha = 140.77°$.

Consequently, there are no reports about the lifetime of surface phonon modes and further subtle effects, if measured close to Γ instead of the Brillouin zone boundary. It has, however, been demonstrated experimentally for Cu(001)[118] and is outlined in the following for Ag(001) that the latter is experimentally possible when employing He spin-echo spectroscopy.

Phonon measurements of Ag(001)

Surface phonon energies were obtained by performing spin-echo measurements over a wide range of spin-echo times (including both real and imaginary components of the beam polarisation). Therefore the solenoid current was varied from -1 to $+1$ A, with 1025 equally spaced points (top panel in Figure 5.2(a)). Oscillations in the polarisation correspond to surface atoms vibrating with a characteristic period, i.e. to a particular surface phonon mode. Hence Fourier transforming the data to the wavelength domain and converting to the energy scale gives rise to spectra which are analogous to TOF spectra, with energy loss and gain peaks for the creation and annihilation of phonons, respectively[60,61] (lower panel in Figure 5.2(a)). The phonon energy $E_{ph} = \hbar\omega$ is then given via (2.19) with λ_i and λ_f, the incoming and outgoing wavelength of the He beam and m the ^{3}He mass.
To determine the entire phonon dispersion curve up to the Brillouin zone boundary a series of spin-echo spectra at varying incident angles ϑ_i was measured. The phonon dispersion was then obtained by calculating the parallel momentum transfer $|\Delta K|$ for each extracted phonon energy ΔE based on the conservation laws of energy and parallel momentum which provide the so-called scancurve for planar scattering (2.20).
Figure 5.2(b) shows the extracted phonon dispersion of Ag(001) in the energy region of acoustic phonons with the measurements performed at room temperature. While the longitudinal resonance (LR) is difficult to resolve close to $\overline{\Gamma}$, because it appears in the spectra mainly as a weak shoulder next to the Rayleigh wave (RW), the bulk band edge seems to give rise to a distinct peak throughout the measurements - where only a few points are found in the literature[119]. The black dashed line in Figure 5.2(b) shows a comparison with the RW mode determined by high-resolution electron energy loss spectroscopy[116], which seems to be slightly lower in energy when approaching the Brillouin zone boundary.

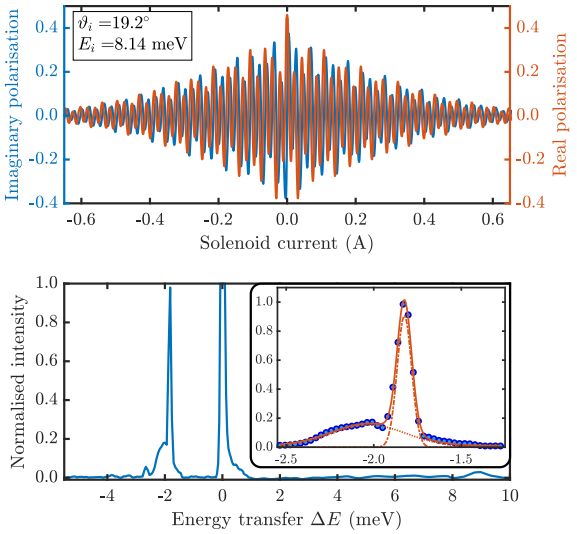

(a) The top panel shows an ISF for a typical example measurement at 135 K, while in the bottom panel the data has been converted to the energy transfer scale. The inset shows the fitting of the RW mode and the LR with two Gaussians.

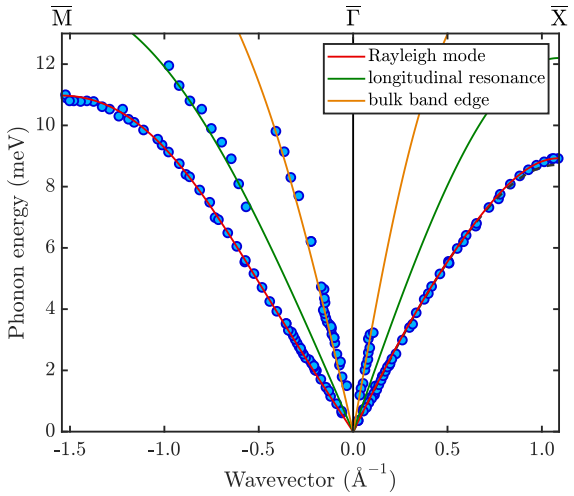

(b) The extracted phonon dispersion of Ag(001) in the energy region of acoustic phonons, performed with the sample at room temperature.

Figure 5.2: HeSE surface phonon dispersion measurements of Ag(001).

On the one hand the quality of the crystal surface and the presence of defects such as steps will increase the height of the diffuse elastic peak (at $\Delta E = 0$). Usually, the energy resolution of the apparatus will add to the width of the peak, however, in the spin-echo setup, tuned for measurements of the quasi-elastic peak (around $\Delta E = 0$), the measurement is only limited by the maximum Fourier time of the instrument. Under this measurement condition, the finite energy transfer peaks are also broadened by the projection of the feature in the wavelength intensity transfer matrix[94].
Measurements of the wavelength intensity function $\rho(\lambda_i, \lambda_f)$ as described in 3.5.3 and plotted in Figure 5.1 allow to determine the optimum tilting angle 3.37 in order to measure the natural linewidth of a phonon event. Here, the optimum tilt to resolve the width of the creation event is determined as $\alpha = 140.77°$, i.e. it differs by about $+6°$ from the optimum tilt angle for elastic scattering ($\alpha = 135°$).

Anharmonicity of the Rayleigh wave

The position and linewidth of the RW mode was measured in the temperature range from 135 K to 750 K. Figure 5.3(a) shows the extracted position of the RW mode as a function of sample temperature. In accordance to previous bulk and surface phonon measurements the energy of the mode reduces with increasing temperature[112,114,120,121]. The decay is however very subtle, with the slope of a linear fit (red dash-dotted line in Figure 5.3(a)) being 210 neV/K and a phonon energy of 1.86 meV when extrapolating to $T = 0$ K. Most previous temperature dependent measurements and calculations were typically performed at much higher momentum transfers, often at the Brillouin zone boundary[116].
The mode softening seen in Figure 5.3(a), i.e. the anharmonic shift of the surface phonon energy $E_{ph} = \hbar\omega$ with temperature T is typically assumed in a first approximation to be proportional to the harmonic energy of the corresponding oscillator, as for molecular vibrations:[114]

$$\hbar\omega(T) = \hbar\omega_0 - \chi_e \hbar\omega_0 (2n_0 + 1)\,, \tag{5.3}$$

where χ_e it the anharmonicity parameter and the occupation of the mode n_0 is $n_0 = \exp(\hbar\omega_0/k_B T) - 1$. Fitting the experimental data according to (5.3) (red dash-dotted line) yields an anharmonicity parameter $\chi_e = (1.23 \pm 0.02) \cdot 10^{-3}$.

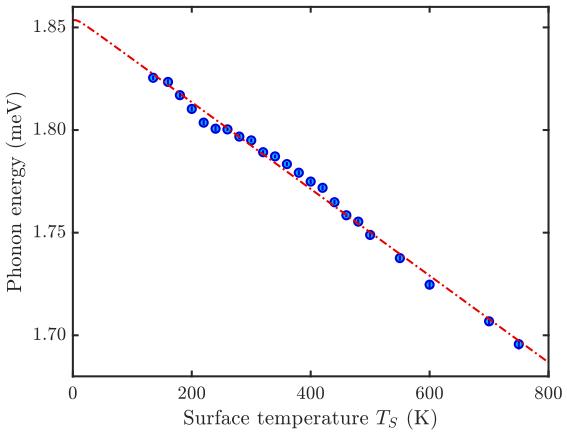

(a) Temperature dependence of the phonon energy E_{ph} for the RW mode at $\Delta K = 0.15$ Å^{-1}. In a first approximation, the mode softening with increasing temperature can be fitted according to (5.3) (red dash-dotted line).

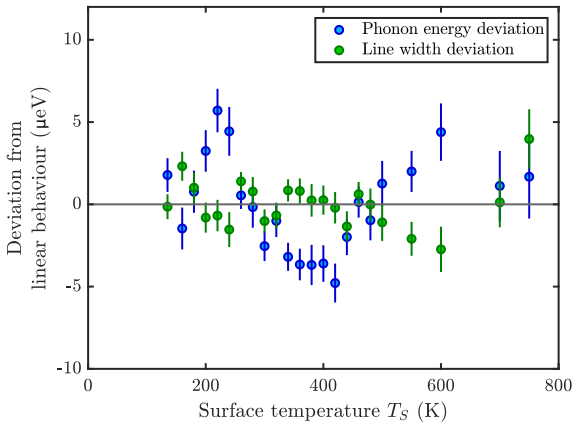

(b) A plot of the deviations from the linear fit shows that there seem to be systematic differences with respect to the linear behaviour both for the phonon energy as well as for the linewidth of the RW mode.

Figure 5.3: Anharmonicity of RW mode and systematic deviations of the energy / linewidth from the linear behaviour.

Linewidth and lifetime of the Rayleigh wave

Several resolution effects can add to the natural linewidth of a phonon mode. First, the energy broadening in the incident beam needs to be accounted for - which can be directly taken care of by choosing the right tilt angle in the measurement ($\alpha = 140.77°$, see Figure 5.1 and (3.37)).

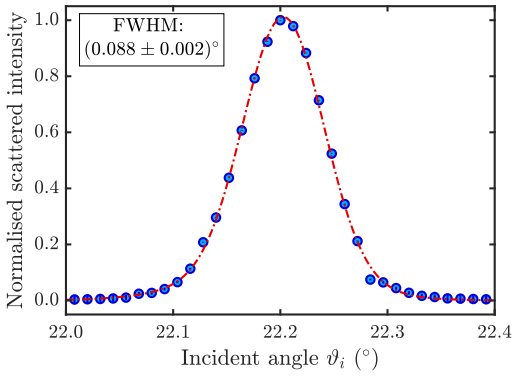

(a) Measured angular broadening of the specular peak for scattering of Ag(001).

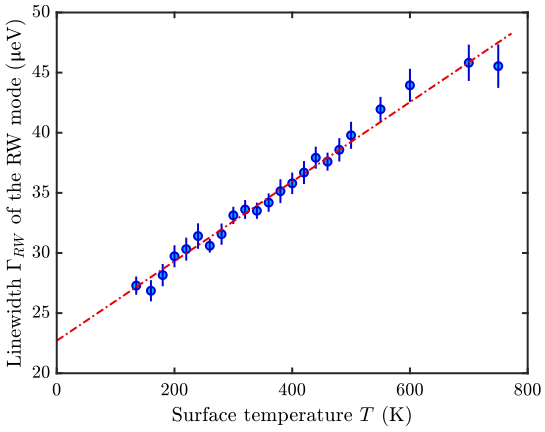

(b) Natural linewidth Γ_{RW} of the RW phonon mode at $\Delta K = 0.15$ Å^{-1} versus surface temperature.

Figure 5.4: Temperature dependence of the natural linewidth of the RW mode on Ag(001)

Any remaining broadening in the current experimental setup is then due to the angular broadening of the apparatus. The angular broadening of the apparatus is estimated based on the angular broadening of the specular peak (HWHM = $0.044°$, Figure 5.4(a)). Using this angular broadening together with the phonon dispersion in the scancurve (2.20) gives an energy broadening (HWHM) $\Delta E_{app} = 30$ μeV due to the apparatus.
The "natural" linewidth of the phonon mode is then given via $(\Gamma_{RW})^2 = (\Gamma_{total})^2 - (\Gamma_{app})^2$ where Γ_{total} is the total energy broadening as determined from measurements such as Figure 5.2(a). Following this procedure, the natural linewidth Γ_{RW} of the RW phonon mode at $\Delta K = 0.15$ Å^{-1} is obtained and the temperature dependence of Γ_{RW} is plotted in Figure 5.4(b). The intercept of the linear fit, corresponds to an extrapolation of the lifetime $\tau_{RW} = \hbar/\Gamma_{RW}$ to $T = 0$ K with:

$$\tau_{RW} = (29 \pm 1)\,\text{ps}\ .$$

5.3 Tuning the van der Waals bonding strength

Preliminary neutron scattering experiments suggest that the vdW bonding strength of adsorbed molecules with the substrate can be tuned and may affect the energy dissipation channels during nanoscale diffusion, i.e. the amount of electronic friction. By replacing some of the C atoms in benzene (C_6H_6) with N atoms (see Figure 5.5(a)), as done in the described measurements, experimental data can be compared to those with the dynamics of aromatics having similar geometry, but different aromaticity and electronic structure.
The introduction of N atoms into the ring reduces the electronic density around the carbon atoms of the molecule and decreases the repulsion between the π-orbitals of the ring and the substrate, giving rise to a stronger bonding to the substrate, because the intensity of the vdW interactions is tuned by the polarisability and electrophilic character of the π-systems of the molecules interacting with the π-system of graphite[21,122,123].

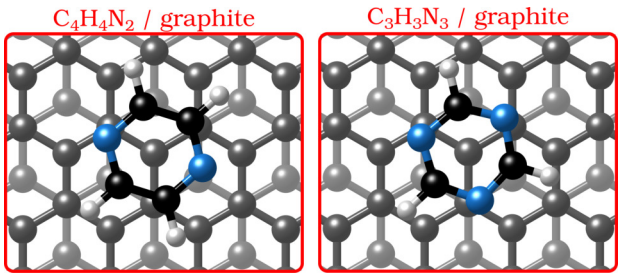

(a) Graphical impression of the heterocyclic organic molecules pyrazine ($C_4H_4N_4$) and s-triazine ($C_3H_3N_3$) on graphite.

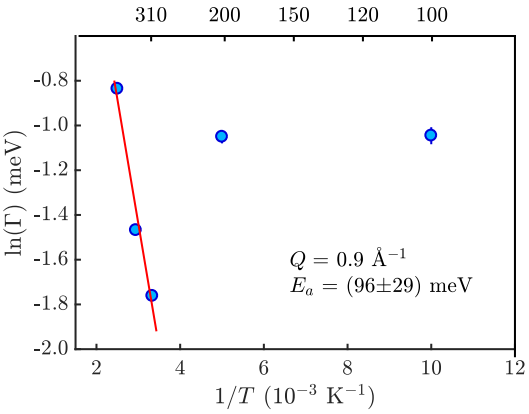

(b) Arrhenius plot for the extracted quasi-elastic broadening $\Gamma(Q)$ for 0.5 ML $C_3H_3N_3$ on graphite.

Figure 5.5: Preliminary neutron scattering experiments suggest that the vdW bonding strength to the substrate can be tuned by replacing some of the C atoms in benzene with N atoms.

The QENS measurements are concerned with the diffusion of pyrazine ($C_4H_4N_2$) and s-triazine ($C_3H_3N_3$) on exfoliated graphite. The project builds on previous results about the dynamics of hydrocarbons and small molecules on graphite[61,97,104,124] where in particular for benzene (C_6H_6), very detailed spectroscopy data is available[104,124]. Benzene adsorbs in a flat (face-face) configuration on graphite and follows Brownian diffusion on this substrate as shown in previous neutron scattering experiments[104,124].
Contrary to benzene, the behaviour of nitrogen containing heterocyclic compounds such as pyrazine and triazine on carbon surfaces is much less understood, although previous theoretical studies confirm that, similarly to benzene, these N-containing molecules adsorb with a horizontal configuration at a distance of $3.00-3.21$ Å[122]. Triazine exists in three different isomeric forms and the study deals with the behaviour of the most common and more symmetrical isomer, $1,3,5-$triazine which is also known as s-triazine. S-triazine is essentially as aromatic as benzene, though less polarisable, whereas pyrazine is slightly less aromatic. While the adsorption geometry of the molecules remains the same for all three adsorbates, the intensity of the vdW-interactions is tuned by the number of nitrogen atoms in the ring[21,122,123].
NSE measurements were performed for a 0.5 ML sample of $C_4D_4N_2$ adsorbed on exfoliated graphite. Dynamics is already observable starting from low temperatures (100 K) up to 400 K but it appears that there exist two different dynamical regimes, with the second dynamic process setting in at $T > 300$ K and thus giving rise to larger quasi-elastic amplitudes at higher temperatures.
The diffusion of $C_3H_3N_3$ was then measured with neutron TOF, with a first initial test run of 0.5 ML $C_3H_3N_3$ on IN6, followed by a test run of both 0.2 and 0.5 ML $C_3H_3N_3$ on IN5. Again there is evidence for two dynamic regimes / processes as observed in the NSE data of $C_4D_4N_2$. It appears that for the data below 300 K, the quasi-elastic broadening Γ is almost constant with respect to Q which could e.g. be due to rotations of the molecule. From $300-400$ K the broadening shows a much clearer trend in terms of the momentum transfer dependence.
The Arrhenius plot (Figure 5.5(b)), extracted for the measurement at $Q = 0.9$ Å^{-1} illustrates that at about

300 K an activated process seems to set in with an activation energy of about 100 meV. Hence the first preliminary analysis of the QENS data shows that indeed the substitution of C atoms with N atoms in the benzene ring gives rise to a different diffusive motion. The activated process starting to set in at about 300 K and probably related to the actual mass transport on the surface, appears at much higher temperatures compared to benzene diffusion (Refs.[104,124]).

5.4 The range of dynamics: Verifying rate theory

Predicting the rates of dynamical processes based on accurate computational calculations is crucial for an understanding of the underlying principles of chemical reactions. However, the rate description of dynamics often suffers from the lack of experimental data which covers the entire range of relevant timescales and temperatures.
Based on experimental data regarding the surface diffusion of cobalt phthalocyanine (CoPc, $C_{32}H_{16}CoN_8$) on a Ag(001) substrate, it can be demonstrated that microscopy provides information in the low temperature regime, while only inelastic atom-surface scattering can follow the diffusive process at high temperatures. By combining both experimental techniques, the rate of translational motion can be followed over 16 orders of magnitude.

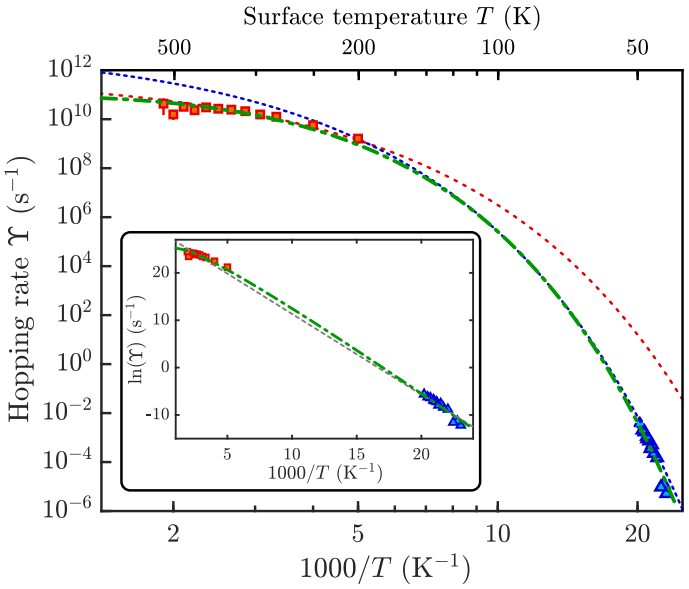

Figure 5.6: Comparison of STM jump rates (from Antczak *et al.*[91]) and HeSe jump rates obtained in the current study (temperature on a log scale). The green dash-dotted line shows a fit with a temperature dependent pre-exponential factor. The inset shows the same data in a "conventional" Arrhenius plot.

Figure 5.6 nicely proves the complementary nature of the techniques for surface diffusion studies. STM provides insight into surface diffusion at low temperatures close to the onset temperature of surface diffusion. Within this temperature range, surface diffusion is dominated by single jumps. However, it is difficult to gain a detailed insight into long jumps with STM. This is due to a loss of the tracking ability within the finite time needed to probe one line of the STM image and STM can only observe long jumps for very specific systems[125].
Between the two studies of the dynamics of CoPc motion on Ag(100) in Figure 5.6 lies a range of jump rates (10^{-6} s^{-1} to 10^{10} s^{-1}) which may well be completely unprecedented for any rate process involving atoms and molecules. It is found that the activation energy for lateral diffusion changes from 150 meV at $45 - 50$ K to 100 meV at $250 - 500$ K, and that the process goes from exclusively single jumps at low temperatures to predominantly multiple jumps at high temperatures. Hence upon comparing scenarios for the same process over such widely divergent time scales, one does indeed see different things. Again, this is an unprecedented result and provides rare benchmark data for the evaluation of rate theory.
As illustrated by the dotted blue line in Figure 5.6, a fit of the STM data based on a simple Arrhenius form

such as (3.1) cannot describe the diffusion over the entire temperature range and an extrapolation of the STM data alone, provides a pre-exponential factor Υ_0 which is far too large. The importance of the pre-factor is often underestimated due to the lack of accurate experimental references, since it mathematically refers to extrapolating the rate to infinitely high temperatures. The scattering data taken at high temperatures allows for a better comparison of the pre-exponential factor in the rate description with theoretical predictions.
Only the green dash-dotted line in Figure 5.6, which shows an Arrhenius fit with a temperature dependent pre-exponential factor, allows for a reasonable description of the experimental data over the entire dynamical range, thus illustrating that the assumptions of classical transition state theory cannot describe the full range of dynamics in terms of experimental diffusion rates.

Bibliography

1. Smil, V. Detonator of the population explosion. *Nature* **400,** 415–415 (1999).
2. Benedek, G., Miret-Artés S., S., Toennies, J. P. & Manson, J. R. Electron–Phonon Coupling Constant of Metallic Overlayers from Specular He Atom Scattering. *J. Phys. Chem. Lett.* **9,** 76–83 (2018).
3. Benedek, G., Manson, J. R. & Miret-Artés, S. The Electron-Phonon Interaction of Low-Dimensional and Multi-Dimensional Materials from He Atom Scattering. *Adv. Mater.* **32,** 2002072 (2020).
4. Pan, Z.-H., Fedorov, A. V., Gardner, D., Lee, Y. S., Chu, S. & Valla, T. Measurement of an Exceptionally Weak Electron-Phonon Coupling on the Surface of the Topological Insulator $\mathrm{Bi_2Se_3}$ Using Angle-Resolved Photoemission Spectroscopy. *Phys. Rev. Lett.* **108,** 187001 (2012).
5. Zhu, X., Santos, L., Howard, C., Sankar, R., Chou, F. C., Chamon, C. & El-Batanouny, M. Electron-Phonon Coupling on the Surface of the Topological Insulator $\mathrm{Bi_2Se_3}$ Determined from Surface-Phonon Dispersion Measurements. *Phys. Rev. Lett.* **108,** 185501 (2012).
6. Benedek, G., Miret-Artés, S., Manson, J. R., Ruckhofer, A., Ernst, W. E. & Tamtögl, A. Origin of the Electron-Phonon Interaction of Topological Semimetal Surfaces Measured with Helium Atom Scattering. *J. Phys. Chem. Lett.* **11,** 1927–1933 (2020).
7. Grüner, G. The dynamics of charge-density waves. *Rev. Mod. Phys.* **60,** 1129–1181 (1988).
8. Tocci, G., Joly, L. & Michaelides, A. Friction of Water on Graphene and Hexagonal Boron Nitride from *Ab Initio* Methods: Very Different Slippage Despite Very Similar Interface Structures. *Nano Lett.* **14,** 6872–6877 (2014).
9. Ma, M., Tocci, G., Michaelides, A. & Aeppli, G. Fast diffusion of water nanodroplets on graphene. *Nat. Mater.* **15,** 66–71 (2016).
10. Barth, J. Transport of adsorbates at metal surfaces: from thermal migration to hot precursors. *Surf. Sci. Rep* **40,** 75–149 (2000).
11. Ala-Nissila, T., Ferrando, R. & Ying, S. C. Collective and single particle diffusion on surfaces. *Adv. Phys.* **51,** 949–1078 (2002).
12. Jardine, A., Hedgeland, H., Alexandrowicz, G., Allison, W. & Ellis, J. Helium-3 spin-echo: principles and application to dynamics at surfaces. *Prog. Surf. Sci.* **84,** 323 (2009).
13. Rittmeyer, S. P., Bukas, V. J. & Reuter, K. Energy dissipation at metal surfaces. *Adv. Phys.* **3,** 1381574 (2018).
14. Farías, D. & Rieder, K.-H. Atomic beam diffraction from solid surfaces. *Rep. Prog. Phys.* **61,** 1575 (1998).
15. Benedek, G. & Toennies, J. P. *Atomic Scale Dynamics at Surfaces* (Springer, Berlin, Heidelberg, 2018).
16. Hofmann, P. The surfaces of bismuth: Structural and electronic properties. *Prog. Surf. Sci.* **81,** 191–245 (2006).
17. Kittel, C. *Introduction to solid state physics* (John Wiley & Sons Inc, 2005).
18. Wehling, T., Black-Schaffer, A. & Balatsky, A. Dirac materials. *Adv. Phys.* **63,** 1–76 (2014).
19. Barreto, L., Kühnemund, L., Edler, F., Tegenkamp, C., Mi, J., Bremholm, M., Iversen, B. B., Frydendahl, C., Bianchi, M. & Hofmann, P. Surface-Dominated Transport on a Bulk Topological Insulator. *Nano Lett.* **14,** 3755–3760 (2014).
20. Moore, J. Topological insulators: The next generation. *Nature Phys.* **5,** 378–380 (2009).
21. Qi, X.-L. & Zhang, S.-C. Topological insulators and superconductors. *Rev. Mod. Phys.* **83,** 1057–1110 (2011).

22. Hsieh, D., Xia, Y., Qian, D., Wray, L., Dil, J. H., Meier, F., Osterwalder, J., Patthey, L., Checkelsky, J. G., Ong, N. P., Fedorov, A. V., Lin, H., Bansil, A., Grauer, D., Hor, Y. S., Cava, R. J. & Hasan, M. Z. A tunable topological insulator in the spin helical Dirac transport regime. *Nature* **460,** 1101–1105 (2009).
23. Caputo, M. *et al.* Manipulating the Topological Interface by Molecular Adsorbates: Adsorption of Co-Phthalo-cyanine on Bi_2Se_3. *Nano Lett.* **16,** 3409–3414 (2016).
24. Schoop, L. M., Pielnhofer, F. & Lotsch, B. V. Chemical Principles of Topological Semimetals. *Chem. Mat.* **30,** 3155–3176 (2018).
25. Rittweger, F., Hinsche, N. F., Zahn, P. & Mertig, I. Signature of the topological surface state in the thermoelectric properties of Bi_2Te_3. *Phys. Rev. B* **89,** 035439 (2014).
26. Kadel, K., Kumari, L., Li, W., Huang, J. Y. & Provencio, P. P. Synthesis and Thermoelectric Properties of Bi_2Se_3 Nanostructures. *Nanoscale Res Lett* **6,** 57 (2010).
27. Snyder, G. J. & Toberer, E. S. Complex thermoelectric materials. *Nat. Mater.* **7,** 105–114 (2008).
28. Mishra, S. K., Satpathy, S. & Jepsen, O. Electronic structure and thermoelectric properties of bismuth telluride and bismuth selenide. *J. Phys.: Condens. Matter* **9,** 461 (1997).
29. Minnich, A. J., Dresselhaus, M. S., Ren, Z. F. & Chen, G. Bulk nanostructured thermoelectric materials: current research and future prospects. *Energy Environ. Sci* **2,** 466–479 (2009).
30. Liang, J., Cheng, L., Zhang, J., Liu, H. & Zhang, Z. Maximizing the thermoelectric performance of topological insulator Bi_2Te_3 films in the few-quintuple layer regime. *Nanoscale* **8,** 8855–8862 (2016).
31. Hsiung, T.-C., Mou, C.-Y., Lee, T.-K. & Chen, Y.-Y. Surface-dominated transport and enhanced thermoelectric figure of merit in topological insulator $Bi_{1.5}Sb_{0.5}Te_{1.7}Se_{1.3}$. *Nanoscale* **7,** 518–523 (2015).
32. Duong, D. L., Yun, S. J. & Lee, Y. H. van der Waals Layered Materials: Opportunities and Challenges. *ACS Nano* **11,** 11803–11830 (2017).
33. Liu, Y., Weiss, N. O., Duan, X., Cheng, H.-C., Huang, Y. & Duan, X. Van der Waals heterostructures and devices. *Nat. Rev. Mater* **1,** 16042 (2016).
34. Frantzeskakis, E., Ramankutty, S. V., de Jong, N., Huang, Y. K., Pan, Y., Tytarenko, A., Radovic, M., Plumb, N. C., Shi, M., Varykhalov, A., de Visser, A., van Heumen, E. & Golden, M. S. Trigger of the Ubiquitous Surface Band Bending in 3D Topological Insulators. *Phys. Rev. X* **7,** 041041 (2017).
35. Tamtögl, A., Mayrhofer-Reinhartshuber, M., Balak, N., Ernst, W. E. & Rieder, K. Elastic and inelastic scattering of He atoms from Bi(111). *J. Phys.: Condens. Matter* **22,** 5 (2010).
36. Kraus, P., Tamtögl, A., Mayrhofer-Reinhartshuber, M., Benedek, G. & Ernst, W. E. Resonance-enhanced inelastic He-atom scattering from subsurface optical phonons of Bi(111). *Phys. Rev. B* **87,** 245433 (2013).
37. Tamtögl, A., Kraus, P., Mayrhofer-Reinhartshuber, M., Campi, D., Bernasconi, M., Benedek, G. & Ernst, W. E. Surface and subsurface phonons of Bi(111) measured with helium atom scattering. *Phys. Rev. B* **87,** 035410 (2013).
38. Mayrhofer-Reinhartshuber, M., Tamtögl, A., Kraus, P. & Ernst, W. E. Helium atom scattering investigation of the Sb(111) surface. *J. Phys.: Condens. Matter* **25,** 395002 (2013).
39. Tamtögl, A., Carter, E. A., Ward, D. J., Avidor, N., Kole, P. R., Jardine, A. P., Ellis, J. & Allison, W. Note: A simple sample transfer alignment for ultra-high vacuum systems. *Rev. Sci. Instrum.* **87,** 066108 (2016).
40. Tamtögl, A., Kraus, P., Avidor, N., Bremholm, M., Hedegaard, E. M. J., Iversen, B. B., Bianchi, M., Hofmann, P., Ellis, J., Allison, W., Benedek, G. & Ernst, W. E. Electron-Phonon Coupling and Surface Debye Temperature of Bi_2Te_3(111) from Helium Atom Scattering. *Phys. Rev. B* **95,** 195401 (2017).

41. Tamtögl, A., Sacchi, M., Avidor, N., Calvo-Almazán, I., Townsend, P. S. M., Bremholm, M., Hofmann, P., Ellis, J. & Allison, W. Nanoscopic diffusion of water on a topological insulator. *Nat. Commun.* **11,** 278 (2020).

42. Tamtögl, A., Bahn, E., Zhu, J., Fouquet, P., Ellis, J. & Allison, W. Graphene on Ni(111): Electronic Corrugation and Dynamics from Helium Atom Scattering. *J. Phys. Chem. C* **119,** 25983–25990 (2015).

43. Benedek, G., Brusdeylins, G., Heimlich, C., Miglio, L., Skofronick, J. G., Toennies, J. P. & Vollmer, R. Shifted surface-phonon anomaly in 2H-$TaSe_2$. *Phys. Rev. Lett.* **60,** 1037–1040 (1988).

44. Brusdeylins, G., Heimlich, C., Skofronick, J. G., Toennies, J. P., Vollmer, R. & Benedek, G. Determination of the Critical Exponent for a Charge Density Wave Transition in 2H-$TaSe_2$ by Helium Atom Scattering. *EPL* **9,** 563 (1989).

45. Esbjerg, N. & Nørskov, J. K. Dependence of the He-Scattering Potential at Surfaces on the Surface-Electron-Density Profile. *Phys. Rev. Lett.* **45,** 807–810 (1980).

46. Tamtögl, A., Kraus, P., Mayrhofer-Reinhartshuber, M., Benedek, G., Bernasconi, M., Dragoni, D., Campi, D. & Ernst, W. E. Statics and dynamics of multivalley charge density waves in Sb(111). *npj Quantum Mater.* **4,** 28 (2019).

47. Hofmann, P., Ugeda, M. M., Tamtögl, A., Ruckhofer, A., Ernst, W. E., Benedek, G., Martínez-Galera, A. J., Stróżecka, A., Gómez-Rodrıguez, J. M., Rienks, E., Jensen, M. F., Pascual, J. I. & Wells, J. W. Strong-coupling charge density wave in a one-dimensional topological metal. *Phys. Rev. B* **99,** 035438 (2019).

48. Sanz, A. & Miret-Artés, S. Selective adsorption resonances: Quantum and stochastic approaches. *Phys. Rep.* **451,** 37–154 (2007).

49. Kraus, P., Tamtögl, A., Mayrhofer-Reinhartshuber M .and Apolloner, F., Gösweiner, C., Miret-Artés, S. & Ernst, W. E. Surface Structure of Bi(111) from Helium Atom Scattering Measurements. Inelastic Close-Coupling Formalism. *J. Phys. Chem. C* **119,** 17235–17242 (2015).

50. Fox, L. *The Numerical Solution of Two-point Boundary Value Problems* (Oxford University Press, 1957).

51. Wolken, G. Theoretical studies of atom-solid elastic scattering: He+LiF. *J. Chem. Phys* **58,** 3047–3064 (1973).

52. Mayrhofer-Reinhartshuber, M., Kraus, P., Tamtögl, A., Miret-Artés, S. & Ernst, W. E. Helium-surface interaction potential of Sb(111) from scattering experiments and close-coupling calculations. *Phys. Rev. B* **88,** 205425 (2013).

53. Tamtögl, A., Pusterhofer, M., Bremholm, M., Hedegaard, E. M., Iversen, B. B., Hofmann, P., Ellis, J., Allison, W., Miret-Artés, S. & Ernst, W. E. A Helium-Surface Interaction Potential of Bi_2Te_3(111) from Ultrahigh-Resolution Spin-Echo Measurements. *Surf. Sci.* **678,** 25–31 (2018).

54. Ruckhofer, A., Tamtögl, A., Pusterhofer, M., Bremholm, M. & Ernst, W. E. Helium-Surface Interaction and Electronic Corrugation of Bi_2Se_3(111). *J. Phys. Chem. C* **123,** 17829–17841 (2019).

55. Hoinkes, H. The Physical Interaction Potential of Gas Atoms with Single-Crystal Surfaces, Determined from Gas-Surface Diffraction Experiments. *Rev. Mod. Phys.* **52,** 933–970 (1980).

56. De Lara-Castells, M. P., Fernández-Perea, R., Madzharova, F. & Voloshina, E. Post-Hartree-Fock Studies of the He/Mg(0001) Interaction: Anti-Corrugation, Screening, and Pairwise Additivity. *J. Chem. Phys* **144,** 244707 (2016).

57. Martinez-Casado, R., Usvyat, D., Mallia, G., Maschio, L., Casassa, S., Ellis, J., Schütz, M. & Harrison, N. M. Diffraction of Helium on MgO(100) Surface Calculated from First-Principles. *Phys. Chem. Chem. Phys.* **16,** 21106–21113 (2014).

58. Tamtögl, A., Davey, B., Ward, D. J., Jardine, A. P., Ellis, J. & Allison, W. Polarisation in spin-echo experiments: Multi-point and lock-in measurements. *Rev. Sci. Instrum.* **89,** 023902 (2018).
59. Ashcroft, N. W. & Mermin, N. D. *Solid State Physics* (Harcourt College Publishing, 1976).
60. Kole, P. R., Jardine, A. P., Hedgeland, H. & Alexandrowicz, G. Measuring surface phonons with a ^{3}He spin echo spectrometer: a two-dimensional approach. *J. Phys.: Cond. Matt.* **22,** 304018 (2010).
61. Tamtögl, A., Sacchi, M., Calvo-Almazán, I., Zbiri, M., Koza, M. M., Ernst, W. E. & Fouquet, P. Ultrafast molecular transport on carbon surfaces: The diffusion of ammonia on graphite. *Carbon* **126,** 23–30 (2018).
62. Sklyadneva, I. Y., Benedek, G., Chulkov, E. V., Echenique, P. M., Heid, R., Bohnen, K.-P. & Toennies, J. P. Mode-Selected Electron-Phonon Coupling in Superconducting Pb Nanofilms Determined from He Atom Scattering. *Phys. Rev. Lett.* **107,** 095502 (2011).
63. Manson, J. R., Benedek, G. & Miret-Artés, S. Electron-Phonon Coupling Strength at Metal Surfaces Directly Determined from the Helium Atom Scattering Debye-Waller Factor. *J. Phys. Chem. Lett.* **7,** 1016–1021 (2016).
64. Tamtögl, A., Mayrhofer-Reinhartshuber, M., Kraus, P. & Ernst, W. E. Surface Debye temperature and vibrational dynamics of antimony(111) from helium atom scattering measurements. *Surf. Sci.* **617,** 225–228 (2013).
65. Hayes, W. W. & Manson, J. R. Argon scattering from Ru(0001): Calculations and comparison with experiment. *Phys. Rev. B* **75,** 113408 (11 2007).
66. Al Taleb, A., Anemone, G., Farías, D. & Miranda, R. Acoustic surface phonons of graphene on Ni(111). *Carbon* **99,** 416–422 (2016).
67. Grimvall, G. *The Electron-Phonon Interaction in Metals* (North-Holland Pub. Co., 1981).
68. Howard, C. & El-Batanouny, M. Connecting electron and phonon spectroscopy data to consistently determine quasiparticle-phonon coupling on the surface of topological insulators. *Phys. Rev. B* **89,** 075425 (2014).
69. Hatch, R. C., Bianchi, M., Guan, D., Bao, S., Mi, J., Iversen, B. B., Nilsson, L., Hornekær, L. & Hofmann, P. Stability of the Bi_2Se_3(111) topological state: Electron-phonon and electron-defect scattering. *Phys. Rev. B* **83,** 241303 (2011).
70. Kondo, T., Nakashima, Y., Ota, Y., Ishida, Y., Malaeb, W., Okazaki, K., Shin, S., Kriener, M., Sasaki, S., Segawa, K. & Ando, Y. Anomalous Dressing of Dirac Fermions in the Topological Surface State of Bi_2Se_3, Bi_2Te_3, and Cu-Doped Bi_2Se_3. *Phys. Rev. Lett.* **110,** 217601 (21 2013).
71. Benedek, G., Bernasconi, M., Bohnen, K.-P., Campi, D., Chulkov, E. V., Echenique, P. M., Heid, R., Sklyadneva, I. Y. & Toennies, J. P. Unveiling mode-selected electron-phonon interactions in metal films by helium atom scattering. *Phys. Chem. Chem. Phys.* **16,** 7159 (2014).
72. Ruckhofer, A., Campi, D., Bremholm, M., Hofmann, P., Benedek, G., Bernasconi, M., Ernst, W. E. & Tamtögl, A. Terahertz surface modes and electron-phonon coupling on Bi_2Se_3(111). *Phys. Rev. Research* **2,** 023186 (2020).
73. Senet, P., Toennies, J. P. & Benedek, G. Theory of the He-phonon forces at a metal surface. *EPL* **57,** 430 (2002).
74. Manson, J. R., Benedek, G. & Miret-Artés, S. Correction to "Electron-Phonon Coupling Strength at Metal Surfaces Directly Determined from the Helium Atom Scattering Debye-Waller Factor". *J. Phys. Chem. Lett.* **7,** 1691–1691 (2016).
75. Bianchi, M., Guan, D., Bao, S., Mi, J., Iversen, B. B., King, P. D. & Hofmann, P. Coexistence of the topological state and a two-dimensional electron gas on the surface of Bi_2Se_3. *Nat. Commun.* **1,** 128 (2010).

76. Anemone, G., Taleb, A. A., Benedek, G., Castellanos-Gomez, A. & Farías, D. Electron-Phonon Coupling Constant of 2H-MoS_2(0001) from Helium-Atom Scattering. *J. Phys. Chem. C* **123,** 3682–3686 (2019).

77. Zhu, X., Santos, L., Sankar, R., Chikara, S., Howard, C. ., Chou, F. C., Chamon, C. & El-Batanouny, M. Interaction of Phonons and Dirac Fermions on the Surface of Bi_2Se_3: A Strong Kohn Anomaly. *Phys. Rev. Lett.* **107,** 186102 (2011).

78. Kalish, S., Chamon, C., El-Batanouny, M., Santos, L. H., Sankar, R. & Chou, F. C. Contrasting the Surface Phonon Dispersion of $Pb_{0.7}Sn_{0.3}Se$ in Its Topologically Trivial and Nontrivial Phases. *Phys. Rev. Lett.* **122,** 116101 (2019).

79. Howard, C., El-Batanouny, M., Sankar, R. & Chou, F. C. Anomalous behavior in the phonon dispersion of the (001) surface of Bi_2Te_3 determined from helium atom-surface scattering measurements. *Phys. Rev. B* **88,** 035402 (2013).

80. Tamtögl, A., Campi, D., Bremholm, M., Hedegaard, E. M. J., Iversen, B. B., Bianchi, M., Hofmann, P., Marzari, N., Benedek, G., Ellis, J. & Allison, W. Nanoscale surface dynamics of Bi_2Te_3(111): observation of a prominent surface acoustic wave and the role of van der Waals interactions. *Nanoscale* **10,** 14627–14636 (2018).

81. McIntosh, E. M., Wikfeldt, K. T., Ellis, J., Michaelides, A. & Allison, W. Quantum Effects in the Diffusion of Hydrogen on Ru(0001). *J. Phys. Chem. Lett* **4,** 1565–1569 (2013).

82. Ianconescu, R. & Pollak, E. A study of Kramers' turnover theory in the presence of exponential memory friction. *J. Chem. Phys* **143,** 104104 (2015).

83. Avidor, N., Townsend, P., Ward, D., Jardine, A., Ellis, J. & Allison, W. PIGLE - Particles Interacting in Generalized Langevin Equation simulator. *Comput. Phys. Commun.* **242,** 145–152 (2019).

84. Townsend, P. S. M. & Ward, D. J. The intermediate scattering function for quasi-elastic scattering in the presence of memory friction. *J. Phys. Commun.* **2,** 075011 (2018).

85. Miret-Artés, S. & Pollak, E. The dynamics of activated surface diffusion. *J. Phys.: Condens. Matter* **17,** S4133–S4150 (2005).

86. Lechner, B. A. J., de Wijn, A. S., Hedgeland, H., Jardine, A. P., Hinch, B. J., Allison, W. & Ellis, J. Atomic scale friction of molecular adsorbates during diffusion. *J. Chem. Phys* **138,** 194710 (2013).

87. Antczak, G. & Ehrlich, G. *Surface diffusion: metals, metal atoms, and clusters* (Cambridge University Press, 2010).

88. Hahne, S., Ikonomov, J., Sokolowski, M. & Maass, P. Determining molecule diffusion coefficients on surfaces from a locally fixed probe: Analysis of signal fluctuations. *Phys. Rev. B* **87,** 085409 (2013).

89. Kudernac, T., Ruangsupapichat, N., Parschau, M., Maciá, B., Katsonis, N., Harutyunyan, S. R., Ernst, K.-H. & Feringa, B. L. Electrically driven directional motion of a four-wheeled molecule on a metal surface. *Nature* **479,** 208–211 (2011).

90. Akimov, A. V., Williams, C. & Kolomeisky, A. B. Charge Transfer and Chemisorption of Fullerene Molecules on Metal Surfaces: Application to Dynamics of Nanocars. *J. Phys. Chem. C* **116,** 13816–13826 (2012).

91. Antczak, G., Kamiński, W., Sabik, A., Zaum, C. & Morgenstern, K. Complex Surface Diffusion Mechanisms of Cobalt Phthalocyanine Molecules on Ag(100). *J. Am. Chem. Soc.* **137,** 14920–14929. eprint: `http://dx.doi.org/10.1021/jacs.5b08001` (2015).

92. Squires, G. L. *Introduction to the Theory of Thermal Neutron Scattering* (Cambirdge University Press, 1978).

93. Bée, M. *Quasielastic Neutron Scattering* (CRC Press, 1988).

94. Jones, A., Tamtögl, A., Calvo-Almazán, I. & Hansen, A. Continuous Compressed Sensing for Surface Dynamical Processes with Helium Atom Scattering. *Sci. Rep.* **6,** 27776 (2016).

95. Ellis, J., Graham, A. P. & Toennies, J. P. Quasielastic Helium Atom Scattering from a Two-Dimensional Gas of Xe Atoms on Pt(111). *Phys. Rev. Lett.* **82,** 5072–5075 (1999).

96. Büttner, H., Lelievre-Berna, E. & Pinet, F. *The yellow book. Guide to neutron research facilities at the ILL* (Institut Laue-Langevin, Grenoble, 2008).

97. Calvo-Almazán, I., Sacchi, M., Tamtögl, A., Bahn, E., Koza, M. M., Miret-Artés, S. & Fouquet, P. Ballistic diffusion in poly-aromatic hydrocarbons on graphite. *J. Phys. Chem. Lett.* **7,** 5285–5290 (2016).

98. Mezei, F., Pappas, C. & Gutberlet, T. *Neutron spin echo spectroscopy: basics, trends, and applications* (Springer, Berlin, New York, 2003).

99. Jardine, A. P., Dworski, S., Fouquet, P., Alexandrowicz, G., Riley, D. J., Lee, G. Y. H., Ellis, J. & Allison, W. Ultrahigh-resolution spin-echo measurement of surface potential energy landscapes. *Science* **304,** 1790 (2004).

100. Fouquet, P., Hedgeland, H. & Jardine, A. P. Surface Diffusion Studies Using Neutron and Helium Spin-echo Spectroscopy. *Z. Phys. Chem* **224,** 61–81 (2010).

101. Alexandrowicz, G. & Jardine, A. P. Helium spin-echo spectroscopy: studying surface dynamics with ultra-high-energy resolution. *J. Phys.: Cond. Matt.* **19,** 305001 (2007).

102. Alexandrowicz, G., Jardine, A. P., Fouquet, P., Dworski, S., Allison, W. & Ellis, J. Observation of Microscopic CO Dynamics on Cu(001) Using ^{3}He Spin-Echo Spectroscopy. *Phys. Rev. Lett.* **93,** 156103 (2004).

103. Vega, J. L., Guantes, R. & Miret-Artés, S. Quasielastic and low vibrational lineshapes in atom-surface diffusion. *J. Phys.: Condens. Matter* **16,** S2879–S2894 (2004).

104. Hedgeland, H., Fouquet, P., Jardine, A. P., Alexandrowicz, G., Allison, W. & Ellis, J. Measurement of single-molecule frictional dissipation in a prototypical nanoscale system. *Nature Phys.* **5,** 561–564 (2009).

105. Chudley, C. T. & Elliott, R. J. Neutron Scattering from a Liquid on a Jump Diffusion Model. *Proc. Phys. Soc.* **77,** 353 (1961).

106. Martínez-Casado, R., Vega, J. L., Sanz, A. S. & Miret-Artés, S. Generalized Chudley-Elliott vibration-jump model in activated atom surface diffusion. *J. Chem. Phys* **126,** 194711 (2007).

107. Alexandrowicz, G., Jardine, A. P., Hedgeland, H., Allison, W. & Ellis, J. Onset of 3D Collective Surface Diffusion in the Presence of Lateral Interactions: $\mathrm{Na/Cu(001)}$. *Phys. Rev. Lett.* **97,** 156103 (2006).

108. Serra, A. & Ferrando, R. An efficient method for computing collective diffusion in a strongly interacting lattice gas. *Surf. Sci* **515,** 588–596 (2002).

109. Bahn, E., Tamtögl, A., Ellis, J., Allison, W. & Fouquet, P. Structure and dynamics investigations of a partially hydrogenated graphene/Ni(111) surface. *Carbon* **114,** 504–510 (2017).

110. Kraus, P., Gösweiner, C., Tamtögl, A., Apolloner, F. & Ernst, W. E. Adhesion properties of hydrogen on Sb(111) probed by helium atom scattering. *Europhys. Lett.* **114,** 56001 (2016).

111. Miret-Artés, S. Resonant inelastic scattering of atoms from surfaces. *Surf. Sci.* **339,** 205–220 (1995).

112. Ma, J., Delaire, O., May, A. F., Carlton, C. E., McGuire, M. A., VanBebber, L. H., Abernathy, D. L., Ehlers, G., Hong, T., Huq, A., Tian, W., Keppens, V. M., Shao-Horn, Y. & Sales, B. C. Glass-like phonon scattering from a spontaneous nanostructure in $AgSbTe_2$. *Nat. Nanotechnol.,* 445 (2013).

113. Lory, P.-F. *et al.* Direct measurement of individual phonon lifetimes in the clathrate compound $Ba_{7.81}Ge_{40.67}Au_{5.33}$. *Nat. Commun.* **8,** 491 (2017).

114. Benedek, G. & Toennies, J. P. Systematic trends in the normal enhancement of the phonon anharmonicity at the surface of metals. *Phys. Rev. B* **46,** 13643–13646 (1992).

115. Weber, F. & Pintschovius, L. Superconductivity-induced distortions of phonon lineshapes in niobium. *Phys. Rev. B* **82,** 024509 (2010).

116. Kostov, K. L., Polzin, S. & Widdra, W. High-resolution phonon study of the Ag(100) surface. *J. Phys.: Condens. Matter* **23,** 484006 (2011).

117. Menéndez, J. & Cardona, M. Temperature dependence of the first-order Raman scattering by phonons in Si, Ge, and $\alpha - \mathrm{Sn}$: Anharmonic effects. *Phys. Rev. B* **29,** 2051–2059 (1984).

118. Alexandrowicz, G. *Helium Spin Echo Spectroscopy: Measuring the Dynamics of Atoms, Molecules and Surfaces* PhD thesis (University of Cambridge, 2005).

119. Bunjes, N., Luo, N. S., Ruggerone, P., Toennies, J. P. & Witte, G. Surface-phonon dispersion curves and the longitudinal resonance in Ag(001) observed by helium-atom scattering. *Phys. Rev. B* **50,** 8897–8900 (1994).

120. Gester, M., Kleinhesselink, D., Ruggerone, P. & Toennies, J. P. Combined helium-atom-scattering and molecular-dynamics study of aluminum surface-phonon anharmonicities and linewidths. *Phys. Rev. B* **49,** 5777–5780 (1994).

121. Bracco, G., Bruschi, L., Pedemonte, L. & Tatarek, R. Temperature dependence of the Ag(110) surface phonons. *Surf. Sci.* **377–379,** 325–329 (1997).

122. Scott, A. M., Gorb, L., Burns, E. A., Yashkin, S. N., Hill, F. C. & Leszczynski, J. Toward Accurate and Efficient Predictions of Entropy and Gibbs Free Energy of Adsorption of High Nitrogen Compounds on Carbonaceous Materials. *J. Phys. Chem. C* **118,** 4774–4783 (2014).

123. Zarudnev, E., Stepanian, S., Adamowicz, L. & Karachevtsev, V. Noncovalent Interaction of Graphene with Heterocyclic Compounds: Benzene, Imidazole, Tetracene, and Imidazophenazines. *ChemPhysChem* **17,** 1204–1212 (2016).

124. Calvo-Almazán, I., Bahn, E., Koza, M., Zbiri, M., Maccarini, M., Telling, M., Miret-Artés, S. & Fouquet, P. Benzene diffusion on graphite described by a rough hard disk model. *Carbon* **79,** 183–191 (2014).

125. Schunack, M., Linderoth, T. R., Rosei, F., Lægsgaard, E., Stensgaard, I. & Besenbacher, F. Long Jumps in the Surface Diffusion of Large Molecules. *Phys. Rev. Lett.* **88,** 156102 (2002).

6 Publications

Articles on
Energy dissipation on Dirac and semimetal surfaces:
Understanding surface dynamics at the nanoscale.

In the following peer-reviewed publications of the last five years, dealing with the nano-scale surface dynamics of the described systems appear in chronological order.

Within this period fall also two rather technical papers, which deal with experimental improvements and have not been reprinted below but shall be mentioned at this point:

1. Tamtögl, A., Carter, E. A., Ward, D. J., Avidor, N., Kole, P. R., Jardine, A. P., Ellis, J. & Allison, W. Note: A simple sample transfer alignment for ultra-high vacuum systems. *Rev. Sci. Instrum.* **87,** 066108 (2016).
2. Tamtögl, A., Davey, B., Ward, D. J., Jardine, A. P., Ellis, J. & Allison, W. Polarisation in spin-echo experiments: Multi-point and lock-in measurements. *Rev. Sci. Instrum.* **89,** 023902 (2018).

Moreover, the following manuscripts had been submitted to a peer-review journals at the time of writing this thesis:

1. Ward, D. J., Raghavan, A., Tamtögl, A., Jardine, A. P., Bahn, E., Ellis, J., Miret-Artés, S. & Allison, W. Inter-adsorbate forces and coherent scattering in helium spin-echo experiments. *Phys. Chem. Chem. Phys.* submitted (2020).
2. Ruckhofer, A., Halbritter, S., Lund, H. E., Holt, A. J. U., Bianchi, M., Bremholm, M., Benedek, G., Hofmann, P., Ernst, W. E. & Tamtögl, A. Inelastic helium atom scattering from Sb_2Te_3(111): Surface phonon dispersion, kinematical focusing and surfing. *Phys. Chem. Chem. Phys.* submitted (2020).
3. Tamtögl, A., Bahn, E., Sacchi, M., Zhu, J., Ward, D. J., Jardine, A. P., Jenkins, S. J., Fouquet, P., Ellis, J. & Allison, W. Interfacial motion in water reveals the molecular origin of a barrier to ice formation. *submitted.* arXiv: 1810.00650 [cond-mat.mtrl-sci] (2020).

6.1 Publication A

Kraus, P., Tamtögl, A., Mayrhofer-Reinhartshuber M .and Apolloner, F., Gösweiner, C., Miret-Artés, S. & Ernst, W. E. Surface Structure of Bi(111) from Helium Atom Scattering Measurements. Inelastic Close-Coupling Formalism. *J. Phys. Chem. C* **119,** 17235–17242 (2015)

contributions	
funding	A. Tamtögl, W. E. Ernst
preparation / setup	A. Tamtögl
data acquisition	A. Tamtögl, M. Mayrhofer-Reinhartshuber
theory and calculations	P. Kraus
data analysis	A. Tamtögl, P. Kraus, F. Apolloner, Ch. Gösweiner
interpretation	P. Kraus, S. Miret-Artés
publication writing	A. Tamtögl, P. Kraus

Reprinted from:

Kraus, P., Tamtögl, A., Mayrhofer-Reinhartshuber M .and Apolloner, F., Gösweiner, C., Miret-Artés, S. & Ernst, W. E. Surface Structure of Bi(111) from Helium Atom Scattering Measurements. Inelastic Close-Coupling Formalism. *J. Phys. Chem. C* **119,** 17235–17242 (2015)

THE JOURNAL OF PHYSICAL CHEMISTRY C

Article

pubs.acs.org/JPCC

Surface Structure of Bi(111) from Helium Atom Scattering Measurements. Inelastic Close-Coupling Formalism

P. Kraus,*[,†] A. Tamtögl,[†] M. Mayrhofer-Reinhartshuber,[†] F. Apolloner,[†] Ch. Gösweiner,[†] S. Miret-Artés,[†,‡] and W.E. Ernst[†]

[†]Institute of Experimental Physics, Graz University of Technology, Petersgasse 16, 8010 Graz, Austria

[‡]Instituto de Física Fundamental (IFF-CSIC), Serrano 123, 28006 Madrid, Spain

ABSTRACT: Elastic and inelastic close-coupling (CC) calculations have been used to extract information about the corrugation amplitude and the surface vibrational atomic displacement by fitting to several experimental diffraction patterns. To model the three-dimensional interaction between the He atom and the Bi(111) surface under investigation, a corrugated Morse potential has been assumed. Two different types of calculations are used to obtain theoretical diffraction intensities at three surface temperatures along the two symmetry directions. Type one consists of solving the elastic CC (eCC) and attenuating the corresponding diffraction intensities by a global Debye−Waller (DW) factor. The second one, within a unitary theory, is derived from merely solving the inelastic CC (iCC) equations, where no DW factor is necessary to include. While both methods arrive at similar predictions for the peak-to-peak corrugation value, the variance of the value obtained by the iCC method is much better. Furthermore, the more extensive calculation is better suited to model the temperature induced signal asymmetries and renders the inclusion for a second Debye temperature for the diffraction peaks futile.

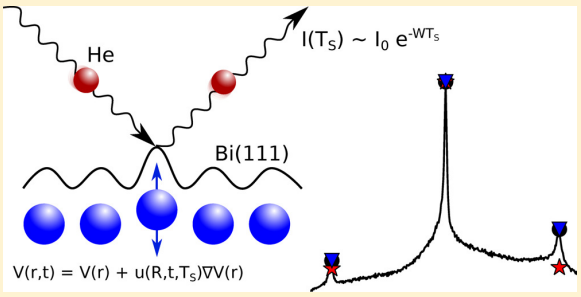

INTRODUCTION

The electronic density structure of a surface determines its chemical behavior. While on surfaces like platinum, which is widely used as a catalyst, the effects of crystal face, surface steps, and kinks are well-known, more complicated electronic surface structures still lack a detailed treatment. Recently, the (111) surfaces of the semimetals bismuth (Bi) and antimony (Sb) have raised a lot of interest. Not only do they represent the two main ingredients of topological insulators,[1,2] but they also both present a fairly strong electronic surface density corrugation despite exhibiting conducting surface states.[3,4] The temperature dependence of these peculiar electronic structures may change the binding character of adsorbed species remarkably;[5] thus, it is essential to determine a complete picture of an electronic surface structure before conducting adsorbate experiments on them. Helium atom scattering (HAS) experiments provide a low-energetic, completely nondestructive means of investigation to measure the pure surface properties of materials. The inert neutral helium atoms are already repelled from the electronic density corrugation above the surface, probing only surface effects. Close-coupling (CC) calculations[6] provide a significant improvement compared to oversimple approximate methods. While the essential accurate knowledge of the interaction potential requires numerous measurements and a careful analysis, the effort may be worthwhile because the quantum mechanical treatment of the scattering procedure provides by far better insight into the scattering processes. Earlier CC investigations included the Debye−Waller (DW) factor to account for the thermal attenuation of scattering intensities. Heavy materials like bismuth, however, exhibit very low surface Debye temperatures, indicating an extremely fast decay of scattering intensities with the surface temperature. The inclusion of inelastic channels into the standard CC equations[7] provides a natural extension within this theoretical framework, and as a result, the attenuation of the diffraction intensities arises automatically. When the number of diffraction channels (elastic and inelastic) is increased, the number of exiting channels increases and the initial flux of He atoms has to be redistributed among them, the elastic peaks being reduced in intensity. This fact implies that we do not have to add any ad hoc global factor, as the DW factor, to account for such an attenuation. Even more, within the inelastic CC (iCC) formalism, the theory is unitary. The unitarity in the elastic CC (eCC) calculations is lost when the DW factor is used to attenuate the diffraction intensities. In this work, we are going to use the iCC equations to extract information about the interaction potential. In general, the number of fitting parameters for this type of scattering is quite high and settles around five in this specific case. For surface temperatures around 300 K, the number of total channels playing a role in

Received: May 26, 2015
Revised: July 8, 2015
Published: July 9, 2015

this scattering is also quite high, typically more than 200. On the other hand, when working on a fixed geometry experimental setup, the whole experimental diffraction pattern is not fitted at once by solving a complete set of iCC equations (up to numerical convergence). Each experimental diffraction peak of the corresponding pattern has to be fitted by solving a complete set of those equations. As a result, the fitting procedure becomes rather cumbersome. To circumvent the expensive high-dimensional fitting procedure, previously fitted eCC potential parameters have been assumed as given and fixed.

BISMUTH SURFACE STRUCTURE AND EXPERIMENTAL SETUP

Bulk bismuth, like all of the heavier pnictogens, crystallizes in the rhombohedral A7 structure with two atoms per unit cell (space group $R\bar{3}m$). A typical structural property of this crystal structure is the existence of puckered bilayers of atoms perpendicular to the [111] direction, as illustrated in Figure 1a.

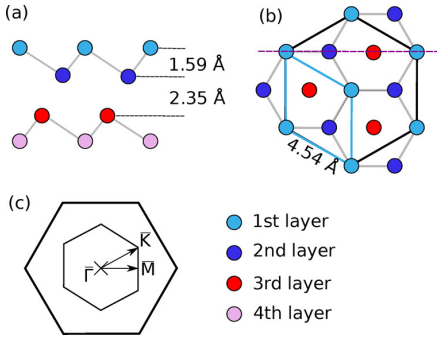

Figure 1. (a) Side view of the (111) surface along the dashed magenta line in (b). (b) Top view of the Bi(111) surface as determined by Mönig et al.[8] (c) First Brillouin zone of the topmost layer with the two high symmetry directions.

The bonding of the atoms within these bilayers is of a strong covalent type, while the interbilayer bonding is closer to a van der Waals type. This is reflected in the relative distances between the layers, as labeled in Figure 1a. Because of this strong contrast in binding energies, bismuth crystals preferably cleave perpendicular to the [111] direction. The topmost layer of this prepared crystal reveals a 6-fold symmetry, as illustrated in Figure 1b. Despite the crystal's 3-fold symmetry, the Bi(111) surface can be treated as being 6-fold symmetric in low energy HAS experiments.[9,10] The lattice constant of this hexagonal-like surface structure has been determined to be a = 4.538 Å by LEED and HAS measurements.[3,8] This hexagonal surface structure leads to two distinguishable high symmetry directions in reciprocal space that are commonly denoted as $\overline{\Gamma M}$ and $\overline{\Gamma K}$, as illustrated in Figure 1c. The reciprocal directions in Figure 1c correspond with the real-space directions in Figure 1b.

All measurements mentioned above and used in this work have been carried out on a helium atom scattering apparatus with a fixed source-target-detector angle of 91.5° that has been described in a previous publication.[11] The helium-atom beam is produced via supersonic expansion of He-gas through a cooled nozzle at 50 bar which is followed by a skimmer creating a spatially and energetically narrow beam ($\Delta E/E \approx 2\%$). The bismuth sample is positioned on a 7-axis manipulator in the main chamber at a base pressure of 10^{-11} mbar. The sample can be cooled using LN_2 or heated using a button heater while the temperature is measured by a type K thermocouple. The scattered He atoms are then detected by a quadrupole mass spectrometer followed by a multichannel analyzer. Angular elastic scans can be carried out by rotating the manipulator leading to diffraction spectra (0.1° resolution). Time-of-flight measurements allow us to record inelastic scattering spectra and are realized using a pseudo-random chopper disk with subsequent deconvolution of the measured signal. The disk-shaped Bi(111) single crystal sample with a diameter of 15 mm and a thickness of 2 mm has been cleaned using several cycles of Ar^+ sputtering followed by annealing at 150 °C. Surface cleanliness and contamination were checked via Auger electron spectroscopy (AES) and the intensity of the diffuse elastic peak, its orientation has been aligned using a low energy electron diffraction (LEED) system. Experiments can be carried out within a beam energy range of 15−25 meV with the sample cooled (113 K) or at room temperature in the two main symmetry directions of the crystal surface.

THEORETICAL BACKGROUND

Inelastic Close-Coupling Equations. The CC formalism provides a method for calculating the diffraction intensities of scattering experiments exactly (up to numerical convergence) in the elastic as well as in the inelastic regime.[6] The helium atom is considered to be a structureless and nonpenetrating particle, the one-phonon approximation is assumed, and the surface corrugation is described by a static as well as a dynamic time-dependent contribution. The time-dependent Schrödinger equation for a structureless particle is written as

$$i\hbar \frac{\partial \Psi(\mathbf{r}, t)}{\partial t} = [-\nabla^2 + V(\mathbf{r}, t)]\Psi(\mathbf{r}, t) \quad (1)$$

where squared wave vector quantities are given in energy units with $\hbar^2/2m = 1$, with m being the mass of the incident particle. The standard notation is also used here where capital letters are for vectors parallel to the surface (2D) and small letters are for vectors in 3D. The gas−surface interaction potential, V, turns out to be dependent on time through the instantaneous position of the surface atoms, $\mathbf{R} + \mathbf{u}(\mathbf{R},t)$, with $\mathbf{u}(\mathbf{R},t)$ being the deviation or displacement from the equilibrium position. If this displacement is considered to behave as a Gaussian function within the unit cell, it can be written along each surface degree of freedom as[7]

$$\mathbf{u}(\mathbf{x}, t) = \mathbf{u}_{\mathbf{z},0} \exp(-x^2/\sigma_c^2) \cos \omega t \quad (2)$$

$$\mathbf{u}(\mathbf{y}, t) = \mathbf{u}_{\mathbf{z},0} \exp(-y^2/\sigma_c^2) \cos \omega t$$

with $\mathbf{u}_{\mathbf{z},0}$ the initial amplitude, ω the frequency of the active phonon mode, and σ_c the parameter describing the width of the Gaussian function. As long as the relative displacements $\mathbf{u}$ are small compared to the lattice constant, the interaction potential can be Taylor expanded up to first order (within the so-called single-phonon approximation) as[12]

$$V(\mathbf{r}, t) \simeq V(\mathbf{r}) + \mathbf{u}(\mathbf{R}, t)\cdot\nabla V(\mathbf{r}) \quad (3)$$

From the layer description of lattice dynamics, it is well-known that the $\mathbf{u}$ displacement can be, in general, written as

$$\mathbf{u}(\mathbf{R}, t) = \sum_{\mathbf{Q},\nu} \mathbf{A}(\mathbf{Q}, \nu, T)\, e^{i\mathbf{Q}\cdot\mathbf{R}} \cos[\omega_\nu(\mathbf{Q})t] \quad (4)$$

DOI: 10.1021/acs.jpcc.5b05010
J. Phys. Chem. C 2015, 119, 17235−17242

where the amplitude **A** includes the phonon polarization vector and the dependence on the surface temperature and ω_ν ($\mathbf{Q}$) is the frequency of the surface mode with quantum numbers ($\mathbf{Q},\nu$). For most practical purposes, only displacements of atoms on the first layer significantly contribute to the interaction potential.

In the Taylor expansion given by eq 3, the zero order or static part of the interaction, $V(\mathbf{r})$, is evaluated at zero displacements. Considering the periodicity of the lattice surface, this function can then be expanded into a Fourier series as

$$V(\mathbf{r}) = \sum_{\mathbf{G}} V_{\mathbf{G}}(z)\, e^{i\mathbf{G}\cdot\mathbf{R}} \tag{5}$$

with **G** being the 2D reciprocal lattice vector.

On the other hand, the wave function $\Psi(\mathbf{r},t)$ has to take into account the double periodicity given by the Hamiltonian, in space and time. Thus, according to the Bloch theorem, $\Psi(\mathbf{r},t)$ can be expanded as

$$\Psi(\mathbf{r},t) = e^{-i\mathbf{k}_i^2 t/\hbar} \sum_{\mathbf{G},\mathbf{Q},\nu,n_{\mathbf{Q}\nu}} \Psi_{\mathbf{G}+\mathbf{Q},n_{\mathbf{Q}\nu}}(z)\cdot e^{i(\mathbf{K}_i+\mathbf{G}+\mathbf{Q})\cdot\mathbf{R}}\, e^{in_{\mathbf{Q}\nu}\omega_\nu(\mathbf{Q})t} \tag{6}$$

where $n_{\mathbf{Q}\nu}$ stands for the number of phonons of the mode ($\mathbf{Q},\nu$). In this work, we exclusively consider the inelastic effects on the elastic intensities. As commonly known, the Bragg law (for $\mathbf{Q} = 0$) is written as

$$\Delta\mathbf{K} = \mathbf{K}_f - \mathbf{K}_i = \mathbf{G} \tag{7}$$

Moreover, we also assume that only one mode is active in the scattering process and the coupling among phonons is neglected within the harmonic approximation. Thus, we can drop the subindex ($\mathbf{Q},\nu$) in $n_{\mathbf{Q}\nu}$ for the number of phonons, writing only n. Similarly, for the frequency of the active mode, we can simply write ω. After substituting eqs 3, 5, and 6 into eq 1, multiplying the resulting expression by $\exp[-i(\mathbf{K}_i + \mathbf{G})\cdot\mathbf{R}]$ and $\exp[-in\omega t]$, and then integrating over both time and the area of a single unit cell, one obtains[7] the following set of coupled differential equations for the diffracted waves

$$\left[\frac{d^2}{dz^2} + \mathbf{k}_{\mathbf{G},n,z}^2 - V_{\mathbf{0}}(z)\right]\Psi_{\mathbf{G},n}(z) = \sum_{\mathbf{G}'\neq\mathbf{G}} V_{\mathbf{G}-\mathbf{G}'}(z)\Psi_{\mathbf{G}',n}(z) + \mathbf{A}\sum_{\mathbf{G}'\neq\mathbf{G}} \mathbf{F}_{\mathbf{G}-\mathbf{G}'}(z)\,[\Psi_{\mathbf{G},n+1}(z) + \Psi_{\mathbf{G},n-1}(z)] \tag{8}$$

and

$$\left[\frac{d^2}{dz^2} + \mathbf{k}_{\mathbf{G},n+1,z}^2 - V_{\mathbf{0}}(z)\right]\Psi_{\mathbf{G},n+1}(z) = \sum_{\mathbf{G}'\neq\mathbf{G}} V_{\mathbf{G}-\mathbf{G}'}(z)\Psi_{\mathbf{G}',n+1}(z) + \mathbf{A}\sum_{\mathbf{G}'\neq\mathbf{G}} \mathbf{F}_{\mathbf{G}-\mathbf{G}'}(z)\,[\Psi_{\mathbf{G},n+2}(z) + \Psi_{\mathbf{G},n}(z)] \tag{9}$$

where

$$\mathbf{k}_{\mathbf{G},n,z}^2 = \mathbf{k}_i^2 - (\mathbf{K}_i + \mathbf{G})^2 - n\hbar\omega \tag{10}$$

is the z component of the kinetic energy for the (n,**G**)-diffracted wave and

$$\mathbf{F}_{\mathbf{G}-\mathbf{G}'}(z) \equiv [i(\mathbf{G}-\mathbf{G}')V_{\mathbf{G}-\mathbf{G}'}(z),\, V_{\mathbf{G}-\mathbf{G}'}'(z)] \tag{11}$$

is the contribution of the gradient of the interaction potential or vector force field (V' represents the first derivative with respect to z); the first term represents the (x,y) components of the force, and the second one is its z component.

The iCC equations are solved numerically by imposing the standard boundary conditions given elsewhere.[6] The theory is unitary; that is, the sum of diffraction probabilities (forming the diffraction pattern), for a given incident energy and angle, is equal to 1.

Inelastic and Elastic Channels: Floquet Blocks. Within this theoretical scheme, each diffraction channel is then represented by an effective potential formed by $V_{\mathbf{0}}(z)$ plus the asymptotic energy, given by

$$(\mathbf{K}_i + \mathbf{G})^2 + n\hbar\omega \tag{12}$$

and is called an inelastic diffraction channel. Thus, any inelastic event, annihilation or creation, is represented by the transition from the entrance (or specular) channel to one of the channels with $(n-1)$ or $(n+1)$. Similarly, the wave functions associated with the discrete spectrum (bound states, labeled by v) of each channel are denoted by $|\mathbf{K}_i + \mathbf{G}, n, v\rangle$ and those associated with the continuum one (diffracted beams) by $|\mathbf{K}_i + \mathbf{G}, n, \mathbf{k}_{\mathbf{G},n,z}^2\rangle$. In the literature, it is also said that the inelastic channels are *dressed* by the phonon field. The number of channels dressed by a given number of phonons form a block, called a *Floquet block*. Thus, if only single-phonon scattering is considered, at least three Floquet blocks must be included in the calculation: the blocks dressed by minus and plus one phonon of the active mode and the block dressed by zero phonons or pure elastic channels (those used for an eCC calculation). The number of diffraction channels within a given Floquet block is formed at least by those used to obtain numerical convergence in an elastic CC calculation. Multiphonon contributions of the same active mode are taken into account by including more Floquet blocks—those dressed by two, three, or more phonons by following the staircase structure of eqs 8 and 9 through $n \pm 1$.

Intrablock and Interblock Couplings. Furthermore, two coupling terms of very different nature are now present: $V_{\mathbf{G}-\mathbf{G}'}(z)$ is responsible for the intrablock coupling, and the scalar function

$$\mathbf{A}(T)\cdot\mathbf{F}_{\mathbf{G}-\mathbf{G}'}(z) \tag{13}$$

for the interblock one. The latter is responsible for the thermal attenuation of the diffraction intensities (see the second term on the right-hand part of eqs 8 and 9) described many times from a phenomenological viewpoint by a DW factor. In previous publications on the phonon dispersion of the Bi(111) surface,[9,10] the lowest lying, isolated Rayleigh mode was identified as the shear-vertical mode corresponding to the sole phonon dispersion line in the Debye model. According to the shear-vertical polarization of the suggested mode, the horizontal displacement of the lattice atoms can be neglected, simplifying the force term eq 11 to the vertical term

$$\mathbf{F}_{\mathbf{G}-\mathbf{G}'}(z) \simeq V_{\mathbf{G}-\mathbf{G}'}'(z) \tag{14}$$

and consequently the inelastic coupling term to

$$\mathbf{A}(T)\cdot\mathbf{F}_{\mathbf{G}-\mathbf{G}'}(z) \simeq A_z(T)\cdot V_{\mathbf{G}-\mathbf{G}'}'(z) \tag{15}$$

The average thermal displacement $A_z(T)$ is related to the effective mean square displacement and has been estimated[7] to be

DOI: 10.1021/acs.jpcc.5b05010
J. Phys. Chem. C 2015, 119, 17235−17242

$$A_z(T) \simeq \frac{1}{aQ_c}\sqrt{\frac{384\hbar^2\pi T}{Mk_B\Theta_D^2}} \tag{16}$$

with T the actual surface temperature, Θ_D the surface Debye temperature, M the mass of a surface particle, a the lattice constant, k_B the Boltzmann constant, and Q_c is a fitting parameter for the Gaussian cutoff factor given by $Q_c = 2/\sigma_c$ with σ_c being the width parameter introduced in eq 2.

Averaging over Phonon Frequencies. On the other hand, when solving the iCC equations, frequency-dependent diffraction intensities are obtained, and these have to be averaged by assuming a density of phonons in order to compare with the experimental ones. The corresponding integration over phonon frequencies can be weighted by the Debye spectral density given by

$$\rho(\omega) = \frac{3\omega^2}{\omega_D^3} \tag{17}$$

with ω_D the Debye frequency. Thus, the final diffraction intensities are due to virtual phonon events only; no real phonon events are taken into account since the corresponding momenta are not involved in Bragg's law. The term "virtual events" denotes that when the phonon is created in the dynamics it has to be annihilated in order to have a net energy balance equal to zero. The origin of the attenuation in the iCC formalism is precisely due to these virtual phonon events since they are responsible for the appearance of the new inelastic channels. Note that the quadratic dependence on phonon frequency is strictly speaking only valid for the bulk; the surface would be better represented by a linear dependence. However, the quadratic term was chosen since the Debye model that the simulation is compared to is built upon the bulk description of the material. A simulation comparing the intensities using a linear and a quadratic term for the Debye spectral density yielded no mentionable difference for the relative elastic diffraction intensities.

Debye–Waller Attenuation Factor. As previously mentioned, an alternative way to obtain diffraction intensities from the eCC equations that can be compared with the temperature-dependent experimental results and iCC calculations is by including a global attenuating factor, the DW factor.[13] By doing this, the unitarity of the attenuated eCC intensities is lost. This is an important theoretical inconsistency of this procedure. As observed in earlier measurements,[3] diffraction peak intensities are surface-temperature dependent. As known, the DW factor relates the intensity $I(T_S)$ of diffraction peaks at temperature T_S to the eCC intensity I_0 at zero surface temperature by means of

$$I(T_S) = I_0\, e^{-2W(T_S)} \tag{18}$$

where $\exp(-2W(T_S))$ represents the DW factor. Although the theoretical basis for the DW factor has been developed for neutron and X-ray diffraction,[14] a reasonable approximation for surfaces can be given by

$$2W(T_S) \simeq \langle u_z^2\rangle(\Delta k_z)^2 \tag{19}$$

assuming zero parallel momentum transfer to the surface and final angles near the specular angle. In this expression, $\langle u_z^2\rangle$ describes the average squared displacement of the atom perpendicular to the surface and Δk_z is the momentum transfer perpendicular to the surface during the scattering event. Assuming a harmonic oscillator within the Debye model, $W(T_S)$ becomes[14,15]

$$W(T_S) = \frac{3(\hbar^2\Delta k_z^2)T_S}{2Mk_B\Theta_D^2} \tag{20}$$

The applicability of the conventional DW factor which was introduced for X-ray diffraction in atom-surface scattering model,[16,17] has been discussed extensively in theory as well as in experiments. Different models have been discussed by Levi,[18] who, for example, predicts an increase of diffraction intensities for soft potentials. Deviations from the predicted temperature dependencies of DW factors especially at high surface temperatures have been experimentally observed on the He–Cu(001) system. These deviations have been analyzed with special focus on the role of the interaction potentials and scattering from surface defects.[19] Multiphonon and resonance effects concerning the dependency of the initial particle energy on the DW-factor for a coupled channel approach which cannot be described by the Born approximation are described in a comparative work by Brenig.[20] Multiphonon effects in the evolution of the DW factor have already been observed on standard scattering targets like LiF[21] and still lack a proper treatment in the standard DW model. The surface Debye temperature of Bi(111) has been determined to be Θ_D = 71(+7/−5) K using LEED and Θ_D = (84 ± 8) K using the specular beam in HAS experiments.[3,8] The surface Debye temperature determined from the attenuation of the first-order diffraction peaks was Θ_D' = (75 ± 8) K. In the literature, the appearance of two different values for the surface Debye temperature for specular and scattered contributions has been justified because the DW factor relies on scattering processes without momentum transfer parallel to the surface. In particular, the specular HAS value reproduces the theoretical approximation of van Delft[22] that estimates the surface Debye temperature to be lower than the bulk value, which is 120 K,[23,24] by a multiplicative factor of $1/\sqrt{2}$.

Static Surface Corrugation. For antimony, the elastic coupling parameters for a lattice with the same surface periodicity have been calculated in a previous publication[25] for a corrugation represented as a sum of cosine functions from a Fourier expansion up to the second term, such as

$$\xi(x,y) = \xi_0\left(\cos\left[\frac{2\pi}{a}\left(x - \frac{y}{\sqrt{3}}\right)\right] + \cos\left[\frac{2\pi}{a}\left(x + \frac{y}{\sqrt{3}}\right)\right]\right) + \xi_0\cos\left[\frac{2\pi}{a}\frac{2y}{\sqrt{3}}\right] + h.o \tag{21}$$

with ξ_0 as the corrugation amplitude. The same corrugation function is, with a different lattice constant, assumed for the Bi(111) surface.

By assuming a corrugated Morse potential written as

$$V(\mathbf{r}) = D(e^{-2\kappa(z-\xi(\mathbf{R}))} - e^{-\kappa z}) \tag{22}$$

the intrablock coupling is given by

$$V_{\mathbf{G}-\mathbf{G}'}(z) = D\frac{\nu_{n,m}}{\nu_{0,0}}e^{-2\kappa z} \tag{23}$$

where D is the well depth of the Morse potential, κ the stiffness parameter, and the $G(n,m)$-specific coupling constants $\nu_{n,m}$ are expressed in terms of the modified Bessel function of the first kind, I_k, as[26]

DOI: 10.1021/acs.jpcc.5b05010
J. Phys. Chem. C 2015, 119, 17235–17242

$$\nu_{n,m} = \frac{\sqrt{3}}{2}\frac{a^2}{\pi}\frac{1}{2}\sum_{k=-\infty}^{\infty} I_k(\alpha)(I_{k+n}(\alpha)I_{k-m}(\alpha) + I_{k-n}(\alpha)I_{k+m}(\alpha)) \quad (24)$$

where $\alpha = 2\kappa\xi_0$. Equation 24 is only exact for a corrugated Morse interaction potential. While modified versions of the interaction potential describe the long-range interaction more accurately, the sole change of V_0 in eqs 8 and 9 to a hybrid potential poses a certain inconsistency. As the inclusion of inelastic effects seems to eliminate the limitations of the Morse potential to model second-order diffraction intensities,[4,25] the usage of the plain Morse potential avoids these inconsistencies while producing excellent results. A more in-depth analysis of a more complicated potential structure calculated numerically from ab initio simulations might further improve the results.

RESULTS AND DISCUSSION

Inelastic TOF and Interaction Potential. Previous investigations of the He−Bi(111) interaction potential[27] revealed three well-defined bound state energies when a 9−3 interaction potential model was used. However, preceding close-coupling studies using various potential shapes on Sb(111)[25] suggest that Morse- or Morse-like potential functions are much more suitable for representing the bound state energies of semimetal surfaces.

To propose a more accurate Morse-like interaction potential, features resulting from inelastic resonance effects in time-of-flight (TOF) spectra were analyzed to identify an additional bound state level at smaller bound state energies. Figure 2 illustrates one of the spectra with an isolated feature originating from the fourth identified bound state as listed in Table 1.

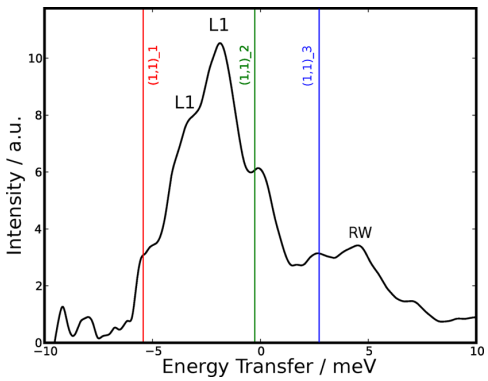

Figure 2. Time-of-flight spectrum of Bi(111) in $\overline{\Gamma M}$ direction at an incident angle of 54.9° and an incident energy of 17.5 meV. The suggested bound state energy level coincides with an observed increase in intensity around an energy transfer of +3 meV. L1 and RW indicate the suggested positions of the longitudinal resonance as well as the Rayleigh branch, while the features marked with $(n,m)\_l$ label possible inelastic bound state resonance positions of the reciprocal vector (n,m) with the bound state level l.

The last line of Table 1 lists the obtained bound state energy levels of the fitted first Fourier coefficient of the corrugated Morse potential

$$V_{00}^{M}(z) = D[e^{-2\kappa z} - 2e^{-\kappa z}] \quad (25)$$

Table 1. Measured and Fitted Bound State Energy Levels for the He−Bi(111) Interaction Potential[a]

level no.	0	1	2	3
measured (meV)	6.18	3.49	1.42	0.327
morse-fit (meV)	6.20	3.43	1.47	0.327

[a]The first three measured values were taken from Kraus et al.[27].

with a potential depth D of (7.898 ± 0.126) meV and a potential stiffness κ of (0.884 ± 0.024) Å^{-1}. With the highest identified bound state level much closer to the threshold, the attractive part of the fitted potential may be considered to describe the real interaction more accurately.

eCC and iCC Analysis of Bi(111). Previous investigations[3] treated the electron density corrugation of the Bi(111) surface from the helium atom scattering (HAS) data using the GR method and the Eikonal approximation, including the Beeby correction. Thermal attenuation effects were included using the DW factor, with two different surface Debye temperatures to account for the two different attenuation features obtained from the measurements. Because the surface Debye temperature is an intrinsic surface property, given by the maximum energy of the phonons in the Debye model, it seems unsatisfactory to include a second temperature in order to account for the different attenuation of the scattering channels. Thus, all of the diffraction intensities issued from the eCC calculations plus the DW factor (eCC+DW) were achieved using only one surface Debye temperature Θ_D = 85 K.

As mentioned previously, in order to reduce the number of fitting parameters in the CC calculations, only the surface corrugation amplitude was considered in the eCC calculations, while in the iCC calculations the parameter space was extended to include also the Gaussian cutoff value Q_c. All six angular diffraction spectra (three temperatures at the two distinguishable high-symmetry directions $\overline{\Gamma M}$ and $\overline{\Gamma K}$) were fitted separately using both methods. In all cases, the overall deviation of the measured diffraction intensities from the calculated intensities

$$\sigma = \frac{1}{N}\sqrt{\sum_{n=1}^{N}(I_n^{calc} - I_n^{exp})^2} \quad (26)$$

with N being the total number of scattering intensities considered per fit was minimized. The optimization algorithm is terminated after a relative accuracy of 0.1% in all of the considered parameters and conditions.

Figure 3 displays the experimental diffraction intensities as well as the best-fitting eCC + DW (red stars) and iCC results (blue downward triangles). To obtain comparable values, the experimental diffraction peak areas were normalized to their respective specular peak area for each spectrum separately. As can be seen in both directions, but especially at the high-temperature measurement in the $\overline{\Gamma K}$ direction, the iCC method can almost perfectly account for the emerging asymmetry at varying temperatures, a feature that is vastly impossible for DW-attenuated features. In Table 2, for comparison, the corrugation amplitudes averaged over the three measured surface temperatures for each high symmetry direction given in percentage of the lattice length are listed for both applied calculation methods.

The corrugation amplitude values calculated by both methods are significantly lower than the ones obtained by approximate methods,[3] with the GR method assuming around

DOI: 10.1021/acs.jpcc.5b05010
J. Phys. Chem. C 2015, 119, 17235−17242

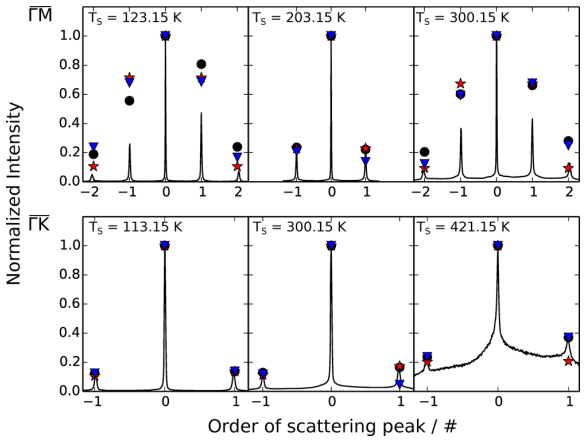

Figure 3. Measured and calculated diffraction peak intensities in both distinguishable lattice directions at three surface temperatures and a beam energy of 17 meV. Black dots signify measured peak areas, red stars signify calculated peak intensities using elastic close-coupling with a DW attenuation, and blue downward triangles signify calculated peak intensities using the inelastic close-coupling approach. The "order" of the scattering peak refers to the number of reciprocal lattice vectors needed when fulfilling the Bragg condition (eq 7). Upper panel: Angular scans in $\overline{\Gamma M}$ direction at three different surface temperatures. Lower panel: Angular scans in $\overline{\Gamma K}$ direction at three different surface temperatures.

Table 2. Comparison of Fitted Peak-to-Peak Corrugation Values as Well as Gaussian Cutoff Parameters in the Case of the Two Applied Calculation Methods[a]

	eCC + DW		iCC			
	ξ_{PP} (% a)	$\Delta\xi_{PP}$ (% a)	ξ_{PP} (% a)	$\Delta\xi_{PP}$ (% a)	Q_c (Å^{-1})	ΔQ_c (Å^{-1})
$\overline{\Gamma M}$	3.96	0.62	4.97	0.21	0.6286	0.0511
$\overline{\Gamma K}$	5.31	0.90	4.85	0.33	0.6638	0.1471
avg $\overline{\Gamma M}$ and $\overline{\Gamma K}$	4.63	1.01	4.97	0.68	0.6462	0.1115

[a]Fitted values are averaged over all available temperature points. Peak-to-peak corruation heights are given in percentage of the lattice constant a.

10% and the Eikonal approximation settling around 11% of the lattice constant a. While both methods when averaged over both directions assume a peak-to-peak corrugation height of around 4.5−5.0%, the variance of the simple elastic model is somewhat higher. In addition, the direction-specific corrugation heights differ significantly from each other in the case of the eCC + DW calculations, while both calculations performed with the iCC method settle around the same corrugation value. The cutoff value implies a width of 3.1 Å, around two-thirds the value of the lattice constant, which justifies the use of the expansion in eq 4 within the single phonon approximation.

The inelastic calculations were carried out using 150 scattering channels in three Floquet blocks in a grid going from −7 to +16 Å. The shortest wavelength of the open channels is always described by 100 points. The phonon frequency average is carried out by integration via a simple weighted Legendre quadrature from zero frequency to the Debye frequency with 10 evaluated roots. All parameters were tested for convergence for each of the scattering spectra involved. In particular for the highest temperature involved, the extension to five Floquet blocks was evaluated and found to present no advantage. While the small Debye temperature of Bi(111) influences both the DW factor and the inelastic coupling constant, the iCC approach is the only one that can account for deviation from the strict exponential characteristic of the elastic diffraction peaks with the surface temperature assumed up to now.

Figure 4 shows the temperature-dependent attenuation as calculated by the iCC method in comparison with a simple DW factor for both specular and first-order diffraction intensities. The parallel but shifted behavior confirms a DW-like attenuation of the diffraction peaks with the same Debye temperature as for the specular. This also poses as an internal test of our iCC calculation. The left panel of Figure 4 confirms that the attenuation of the specular contribution in both directions follow a DW behavior with a Debye temperature of 85.9 K even though the set Debye temperature of the system introduced in the inelastic coupling constants in eq 16 was 85 K.

The experimental condition of a constant source-detector angle causes the angular spectrum to be recorded while changing the angle of incidence. This so-called "moving threshold" situation causes the beam on one side of the specular contribution to encounter a different scattering scheme

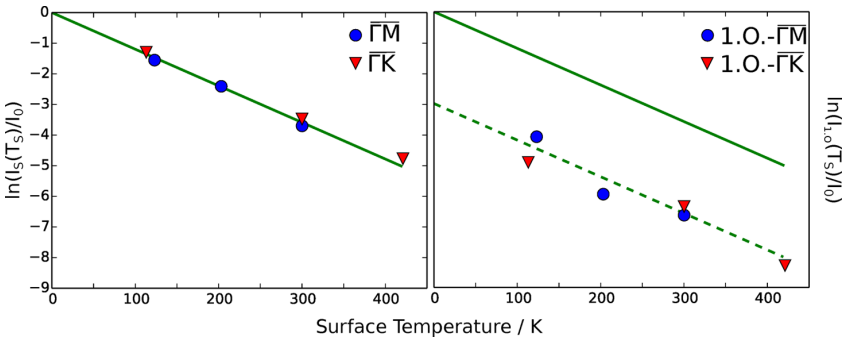

Figure 4. Natural logarithm of the calculated intensities divided by the elastic (unattenuated) specular intensity. Left panel: Attenuation of the specular contribution in both high-symmetry directions. The green line corresponds to a fit of a simple DW-like attenuation with a Debye temperature of Θ_D = 85.9 K. Right panel: Attenuation of the calculated first-order diffraction peaks in both high-symmetry directions. The parallel but shifted behavior confirms a DW-like attenuation of the diffraction peaks with the same Debye temperature as for the specular.

DOI: 10.1021/acs.jpcc.5b05010
J. Phys. Chem. C 2015, 119, 17235−17242

as on the other side, enabling the iCC calculation with its higher adaptability due to the inclusion of inelastic contributions to also model some of the experimentally encountered peak asymmetries as for example in the 400 K surface temperature measurement in $\overline{\Gamma K}$ direction depicted in Figure 3. Obviously, there are other experimental sources of asymmetry, as, for example, sample alignment or the changing visible surface area from the detector while rotating the sample.

An extension of the coupling calculations, including a complete treatment of the overall force eq 11 and the correct geometry on the scattered helium atom in surface parallel directions, could account for the different polarization directions and improve the quality of the calculated scattering intensities even further. The overall ability of the iCC calculations to model the measured scattering features could be vastly improved if previously determined interaction potential parameters would also enter the fitting procedure directly, instead of being predetermined solely from bound state feature fittings. However, expanding the included parameter space to four dimensions (corrugation height, Gaussian cutoff, potential depth, potential stiffness) becomes prohibitive. Furthermore, including a more realistic interaction potential shape as well as mode-dependent lattice displacements, probably determined by ab initio approaches, would promote the iCC method into a remarkable tool for simulating the effects of inelastic scattering contributions in temperature dependent measurements. A further, essential advancement will be the inclusion of finite phonon momentum in the iCC calculations, extending the Bragg condition to $\mathbf{K}_i - \mathbf{K}_f = \mathbf{G} + \mathbf{Q}$. A so-enhanced inelastic scattering code could predictably be used to model the experimental time-of-flight spectra and extract information about the mode-specific electron−phonon interaction on conducting surfaces. Using the inelastic close-coupling approach to simulate the scattering from surfaces with finite temperatures clearly renders the inclusion of an additional surface Debye temperature futile. By not being bound to an exponential attenuation characteristic, the method is more adaptive and thus better suited to describe the temperature-dependent scattering behavior.

AUTHOR INFORMATION

Corresponding Author

*E-mail: patrick.kraus@tugraz.at. Tel: +43 (0)316 873-8143.

Notes

The authors declare no competing financial interest.

ACKNOWLEDGMENTS

This research was supported by the European Commission and the Styrian Government within the ERDF program. S.M.A. acknowledges MICINN (Spain) through Grant No. FIS2011-29596-C02-01. A.T. acknowledges financial support provided by the FWF (Austrian Science Fund) within the project J3479-N20.

REFERENCES

(1) Hsieh, D.; Xia, Y.; Wray, L.; Qian, D.; Pal, A.; Dil, J. H.; Osterwalder, J.; Meier, F.; Bihlmayer, G.; Kane, C. L.; et al. Observation of Unconventional Quantum Spin Textures in Topological Insulators. *Science* **2009**, *323*, 919.

(2) Zhang, H.; Liu, C.-X.; Qi, X.-L.; Dai, X.; Fang, Z.; Zhang, S.-C. Topological Insulators in Bi_2Se_3, Bi_2Te_3 and Sb_2Te_3 with a Single Dirac Cone on the Surface. *Nat. Phys.* **2009**, *5*, 438.

(3) Mayrhofer-Reinhartshuber, M.; Tamtögl, A.; Kraus, P.; Rieder, K. H.; Ernst, W. E. Vibrational Dynamics and Surface Structure of Bi(111) from Helium Atom Scattering Measurements. *J. Phys.: Condens. Matter* **2012**, *24*, 104008.

(4) Mayrhofer-Reinhartshuber, M.; Kraus, P.; Tamtögl, A.; Miret-Artés, S.; Ernst, W. E. Helium-Surface Interaction Potential of Sb(111) from Scattering Experiments and Close-Coupling Calculations. *Phys. Rev. B: Condens. Matter Mater. Phys.* **2013**, *88*, 205425.

(5) Somorjai, G. A. In *Chemistry in two Dimensions: Surfaces*; Somorjai, G. A., Ed.; Cornell University: Ithaca, NY, 1981.

(6) Sanz, A.; Miret-Artés, S. Selective Adsorption Resonances: Quantum and Stochastic Approaches. *Phys. Rep.* **2007**, *451*, 37−154.

(7) Miret-Artés, S. Resonant Inelastic Scattering of Atoms from Surfaces. *Surf. Sci.* **1995**, *339*, 205−220.

(8) Mönig, H.; Sun, J.; Koroteev, Y. M.; Bihlmayer, G.; Wells, J.; Chulkov, E. V.; Pohl, K.; Hofmann, P. Structure of the (111) Surface of Bismuth: LEED Analysis and First-Principles Calculations. *Phys. Rev. B: Condens. Matter Mater. Phys.* **2005**, *72*, 085410.

(9) Tamtögl, A.; Kraus, P.; Mayrhofer-Reinhartshuber, M.; Campi, D.; Bernasconi, M.; Benedek, G.; Ernst, W. E. Surface and Subsurface Phonons of Bi(111) Measured with Helium Atom Scattering. *Phys. Rev. B: Condens. Matter Mater. Phys.* **2013**, *87*, 035410.

(10) Tamtögl, A.; Kraus, P.; Mayrhofer-Reinhartshuber, M.; Campi, D.; Bernasconi, M.; Benedek, G.; Ernst, W. E. Erratum: Surface and Subsurface Phonons of Bi(111) Measured with Helium Atom Scattering. *Phys. Rev. B: Condens. Matter Mater. Phys.* **2013**, *87*, 159906(E).

(11) Tamtögl, A.; Mayrhofer-Reinhartshuber, M.; Balak, N.; Ernst, W. E.; Rieder, K. H. Elastic and Inelastic Scattering of He Atoms from Bi(111). *J. Phys.: Condens. Matter* **2010**, *22*, 30419.

(12) Eichenauer, D.; Harten, U.; Toennies, J.; Celli, V. Interaction Potential for One-Phonon Inelastic He-Cu(111) and He-Ag(111) Scattering. *J. Chem. Phys.* **1987**, *86*, 3693.

(13) Krishnaswamy, S.; Derry, G.; Wesner, D.; O'gorman, T.; Frankl, D. Debye-Waller Effects in Atom-Surface Scattering. *Surf. Sci.* **1978**, *77*, 493−504.

(14) Farias, D.; Rieder, K.-H. Atomic Beam Diffraction from Solid Surfaces. *Rep. Prog. Phys.* **1998**, *61*, 1575.

(15) Manson, J. R. Inelastic scattering from surfaces. *Phys. Rev. B: Condens. Matter Mater. Phys.* **1991**, *43*, 6924−6937.

(16) Gumhalter, B. Different Aspects of the Debye-Waller Factor in Various Atom-Surface Scattering Theories. *Surf. Sci.* **1996**, *347*, 237−248.

(17) Johansson, P. K.; Persson, B. N. J. On the Debye-Waller Factor in Molecular Beam Scattering Experiments. *Solid State Commun.* **1980**, *36*, 271−273.

(18) Levi, A. C.; Suhl, H. Quantum Theory of Atom-Surface Scattering: Debye-Waller Factor. *Surf. Sci.* **1979**, *88*, 221−254.

(19) Šiber, A.; Gumhalter, B. Debye-Waller Factor in He → Cu(001) Collisions Revisited: The Role of the Interaction Potentials. *Surf. Sci.* **1997**, *385*, 270−280.

(20) Brenig, W. Multiphonon Resonances in the Debye-Waller Factor of Atom Surface Scattering. *Phys. Rev. Lett.* **2004**, *92*, 056102.

(21) Vidali, G.; Hutchings, C. Measurement of the Debye-Waller Factor for He-LiF(001). *Phys. Rev. B: Condens. Matter Mater. Phys.* **1988**, *37*, 10374.

(22) van Delft, F. C. M. J. M. Bulk and Surface Debye Temperatures in Relation to Cohesive Energy and Lennard-Jones Potentials. *Surf. Sci.* **1991**, *251/252*, 690−695.

(23) Goodman, R. M.; Somorjai, G. A. Low-Energy Electron Diffraction Studies of Surface Melting and Freezing of Lead, Bismuth and Tin Single-Crystal Surfaces. *J. Chem. Phys.* **1970**, *52*, 6325−6331.

(24) Ramanathan, K. G.; Srinivasan, T. M. Specific Heat of Bismuth at Liquid Helium Temperatures. *Phys. Rev.* **1955**, *99*, 442.

(25) Kraus, P.; Mayrhofer-Reinhartshuber, M.; Gösweiner, C.; Apolloner, F.; Miret-Artés, S.; Ernst, W. E. A Comparative Study of the He-Sb(111) Interaction Potential from Close-Coupling Calculations and Helium Atom Scattering Experiments. *Surf. Sci.* **2014**, *630*, 208−215.

DOI: 10.1021/acs.jpcc.5b05010
J. Phys. Chem. C 2015, 119, 17235−17242

(26) Gradshteyn, I.; Ryzhik, I. In *Table of Integrals, Series and Products*, 7th ed.; Jeffrey, A., Zwillinger, D., Eds.; Academic Press: New York, 2007.
(27) Kraus, P.; Tamtögl, A.; Mayrhofer-Reinhartshuber, M.; Benedek, G.; Ernst, W. E. Resonance-Enhanced Inelastic He-atom Scattering from Subsurface Optical Phonons of Bi(111). *Phys. Rev. B: Condens. Matter Mater. Phys.* **2013**, *87*, 245433.

DOI: 10.1021/acs.jpcc.5b05010
J. Phys. Chem. C 2015, 119, 17235−17242

6.2 Publication B

Tamtögl, A., Bahn, E., Zhu, J., Fouquet, P., Ellis, J. & Allison, W. Graphene on Ni(111): Electronic Corrugation and Dynamics from Helium Atom Scattering. *J. Phys. Chem. C* **119,** 25983–25990 (2015)

contributions	
funding	A. Tamtögl, W. Allison, J. Ellis, P. Fouquet
preparation / setup	A. Tamtögl, J. Zhu
data acquisition	A. Tamtögl, E. Bahn
data analysis	A. Tamtögl
interpretation	A. Tamtögl
publication writing	A. Tamtögl

Reprinted from:

Tamtögl, A., Bahn, E., Zhu, J., Fouquet, P., Ellis, J. & Allison, W. Graphene on Ni(111): Electronic Corrugation and Dynamics from Helium Atom Scattering. *J. Phys. Chem. C* **119,** 25983–25990 (2015)

Note that in equation (7), a factor 2 is missing, i.e. it should read $2W(T_S) = \frac{24M}{m} \cdots$. However, all numbers and results presented in the paper remain correct as they have been obtained based on the correct equation.

THE JOURNAL OF PHYSICAL CHEMISTRY C

Article

pubs.acs.org/JPCC

Graphene on Ni(111): Electronic Corrugation and Dynamics from Helium Atom Scattering

Anton Tamtögl,*[,†] Emanuel Bahn,[‡] Jianding Zhu,[†] Peter Fouquet,[‡] John Ellis,[†] and William Allison[†]

[†]Cavendish Laboratory, J. J. Thompson Avenue, Cambridge CB3 0HE, United Kingdom

[‡]Institut Laue-Langevin, 71 Avenue des Martyrs, 38000 Grenoble, France

ABSTRACT: Using helium atom scattering, we have studied the structure and dynamics of a graphene layer prepared in situ on a Ni(111) surface. Graphene/Ni(111) exhibits a helium reflectivity of ~20% for a thermal helium atom beam and a particularly small surface electron density corrugation ((0.06 ± 0.02) Å peak to peak height). The Debye−Waller attenuation of the elastic diffraction peaks of graphene/Ni(111) and Ni(111) was measured at surface temperatures between 150 and 740 K. A surface Debye temperature of θ_D = (784 ± 14) K is determined for the graphene/Ni(111) system and θ_D = (388 ± 7) K for Ni(111), suggesting that the interlayer interaction between graphene and the Ni substrate is intermediary between those for strongly interacting systems like graphene/Ru(0001) and weakly interacting systems like graphene/Pt(111). In addition we present measurements of low frequency surface phonon modes on graphene/Ni(111) where the phonon modes of the Ni(111) substrate can be clearly observed. The similarity of these findings with the graphene/Ru(0001) system indicates that the bonding of graphene to a metal substrate alters the dynamic properties of the graphene surface strongly and is responsible for the high helium reflectivity of these systems.

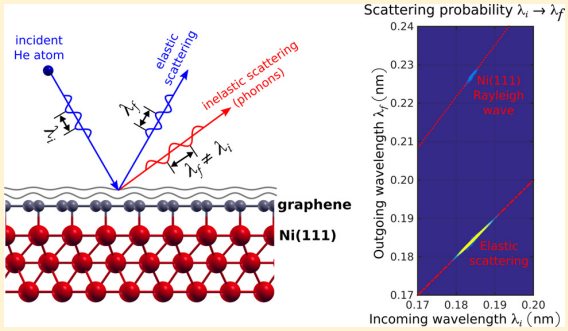

INTRODUCTION

Metal−graphene interfaces are attracting much attention due to the possibility of synthesizing large area graphene films on metals by chemical vapor deposition.[1] During deposition the metal substrate acts as a catalyst for the dehydrogenation of hydrocarbon precursors, which leaves carbon at the surface. The quality of graphene layers grown in this way is in general very high allowing us to investigate the elastic properties of these systems and the interaction strength between the graphene layer and the metallic substrate.[2,3] Moreover, graphene−metal systems are excellent model systems in order to understand the interaction between organic semiconductors and metal electrodes which is vital in organic electronics.[4] Since the interaction between an organic molecule and the substrate is weak compared with conventional metallic or covalent bonding, techniques such as X-ray scattering and high-energy electron diffraction can often turn out to be destructive. Neutral He atom beams with energies of typically 10 meV are perfectly suited to probe these systems in an inert, completely nondestructive manner.[4−6] In addition, helium atom scattering (HAS) provides an accurate description of the surface charge density corrugation as seen by He atoms at thermal energies and the excellent surface sensitivity of this technique has been used to determine structural and vibrational properties of molecular adsorbates.[4,5] More importantly, HAS can be used to obtain information about the weak interactions between substrates and a molecular overlayer: As recently shown by Shichibe et al.,[4] by measuring the surface Debye temperature the interlayer bonding can be quantified, which is rather difficult to probe with other conventional techniques.

Graphene on Ni is considered to be one of the "strong binding" systems, like graphene/Ru(0001), while graphene/Pt(111) is a weakly binding system in which the graphene binding is about the same as it is for pure graphite.[1,4] It has been suggested that graphene/Ni should be highly reflective to He atom scattering, because of its strong binding, similar to the case of graphene/Ru.[5] Our measurements of the helium reflectivity and the Debye−Waller factor provide an excellent test of this theory.

Furthermore, we present measurements of the surface phonon modes in the very low energy regime which were previously limited to higher phonon energies in the case of graphene/Ni(111).[1] These phonon modes hold important information about the thermal conductivity of graphene which is dominated by contributions from acoustic phonons near room temperature. It also shows the importance of the graphene−substrate interaction which has the potential to modify the corresponding phonon dispersion curves.

Received: August 25, 2015
Revised: October 22, 2015
Published: October 22, 2015

DOI: 10.1021/acs.jpcc.5b08284
J. Phys. Chem. C 2015, 119, 25983−25990

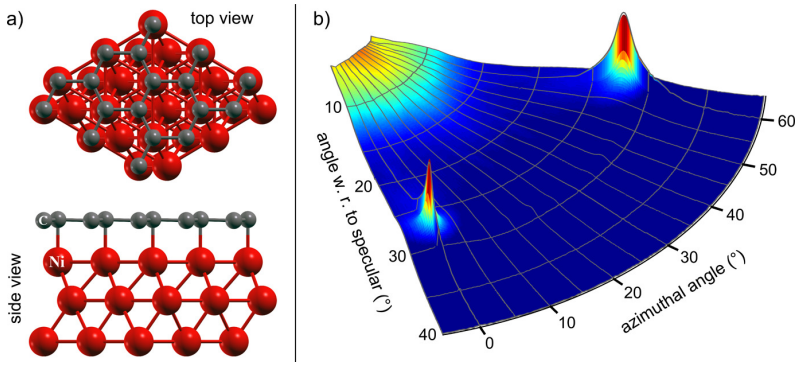

Figure 1. (a) Top and side view of the graphene/Ni(111) surface structure (according to refs 10 and 11). (b) Three-dimensional polar plot of the scattered He intensity for graphene/Ni(111) where the *z*-axis corresponds to the scattered intensity on a logarithmic scale. The scan was taken with an incident beam energy of E_i = 8 meV and the surface at 150 K. The two diffraction peaks which are contained in the scanned azimuthal range are clearly visible. The specular peak is not shown in the plot due the high intensity compared to the diffraction peaks.

EXPERIMENTAL DETAILS

All measurements of this work were conducted on the Cambridge helium-3 spin−echo apparatus.[7] In this setup a nearly monochromatic beam of ^{3}He is scattered of the sample surface in a fixed 44.4° source-target-detector geometry. Energy changes of the scattered He beam can be determined using the spin−echo principle. The setup of the whole apparatus has been described in greater detail elsewhere.[7,8] The described measurements were carried out using an incident beam energy of 8 meV.

The Ni(111) single crystal used in the study was a disc with a diameter of 10 mm and a thickness of 1 mm. The crystal was mounted on the sample holder which can be heated using a radiative heating from a filament on the backside of the crystal or cooled down to 100 K using liquid nitrogen. The sample temperature was measured using a chromel−alumel thermocouple. Prior to the measurements, the surface was cleaned by Ar^+ sputtering and annealing to 870 K.

RESULTS AND DISCUSSION

Preparation and HAS from Graphene/Ni(111). A monolayer of graphite on Ni(111) was grown by dosing ethene (C_2H_4) while heating the Ni crystal (730 K) over several hours.[9,10] The resulting graphene layer is epitaxial and not rotated with respect to the substrate. The formation of a single domain of the graphitic lattice causes a diffraction pattern which exhibits the same symmetry as the hexagonal Ni(111) surface.

Figure 1 shows a three-dimensional polar plot of the scattered intensity from the prepared graphene/Ni(111) surface. Here the radial coordinate corresponds to the incident angle θ_i, and the polar angle corresponds to the azimuthal orientation of the crystal. The *z*-axis indicates the scattered intensity which is plotted on a logarithmic scale. One can clearly see the two diffraction peaks which are contained in the scanned azimuthal range. They are located at the same position as the peaks of the Ni substrate, hence suggesting a (1 × 1) structure on the underlying Ni(111) surface in accordance with prior studies.[9,10]

Recent density functional theory (DFT) calculations suggest that the lowest energy configuration for graphene/Ni(111) is the top-fcc structure (see Figure 1a)) followed by the top-hcp structure which is less favorable.[12−14] The energy difference between these two structures has been reported to be quite small, and domains with both configurations have been observed in experiments,[13,14] even though Gamo et al. clearly favored the top-fcc structure.[10] We are unable to distinguish the two configurations from our diffraction data. However, based on about 20% He reflectivity of the graphene covered surface and the small width of the specular peak, we expect to have predominantly one configuration since the number of defects and domain boundaries must be small in order to achieve this reflectivity.[6]

Note in particular that the specular reflectivity for He is comparable to the graphene/Ru(0001) system where a reflectivity of up to 23% was reported.[5,15] Graphene/Ni(111) not only exhibits a high He reflectivity as recently predicted,[5] its reflectivity remains also unchanged after O_2 exposure at 2 × 10^{-7} mbar for 15 min similar to the graphene/Ru(0001) system.[15] The reflectivity of the clean Ni(111) surface is ∼35% but Ni immediately starts picking up oxygen when exposed to O_2, and its reflectivity decreases to almost 0 after the same exposure. By using the Debye−Waller factor which is determined later in this work, the reflectivity of graphene/Ni(111) measured at room temperature can be extrapolated to a reflectivity of ∼30% at 0 K.

Figure 2 displays the scattered intensity versus the incident angle θ_i for both Ni(111) and graphene/Ni(111) along the $\overline{\Gamma M}$ azimuth. On the graphene covered surface the intensity of the diffraction peak is increased by 2 orders of magnitude, indicating a larger corrugation of the surface electron density compared to the clean Ni(111) surface. According to the peak area, the intensity of the first order diffraction peak is only 0.003% of the specular intensity for Ni(111) and 1% for graphene/Ni(111), respectively.

Using a purely elastic close-coupling calculation with a corrugated Morse potential,[16] the peak-to-peak height of the surface electron density corrugation for graphene/Ni(111) is 2.5% of the Ni surface lattice constant and 0.22% in case of the pristine Ni surface, respectively. A calculation based on the eikonal approximation would give similar results. Hence the surface electron density corrugation for graphene/Ni(111) which corresponds to a peak to peak height of 0.06 Å is considerably larger than the one on clean Ni. However, it is still comparable to the findings of some metal surfaces[6] and even smaller than the corrugation on graphite (0.21 Å[17,18]). Compared to graphene/Ru(0001) (0.15 Å[19]) and graphene/

DOI: 10.1021/acs.jpcc.5b08284
J. Phys. Chem. C 2015, 119, 25983−25990

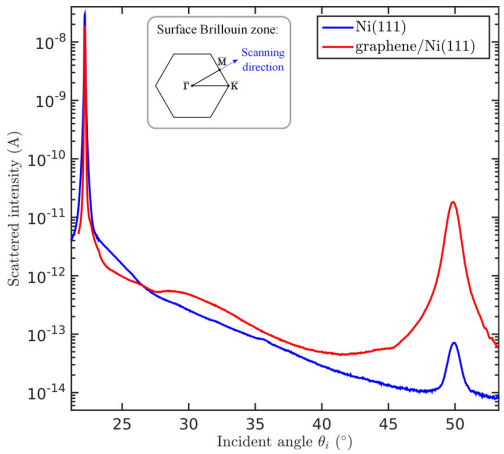

Figure 2. Comparison of the scattered intensities for graphene/Ni(111) and clean Ni(111) versus incident angle θ_i. Both scans were taken along the $\overline{\Gamma M}$ azimuth with the crystal at room temperature and a beam energy of 8 meV. The intensity of the diffraction peak is increased on the graphene covered surface which indicates a larger corrugation of the surface electron density compared to the pristine Ni surface. The inset shows the surface Brillouin zone and the scanning direction.

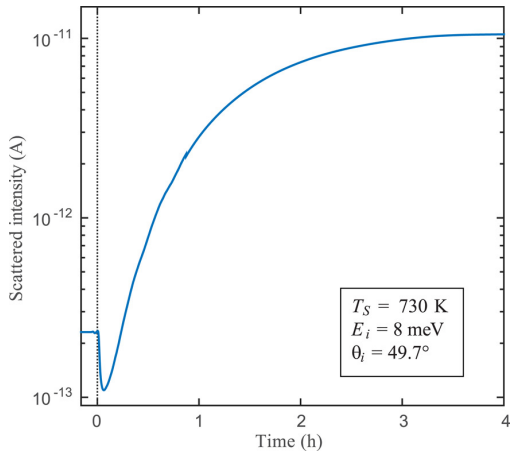

Figure 3. Growth of graphene on Ni(111) can be followed by monitoring the first order diffraction peak while dosing ethene (C_2H_4). Here the time t = 0 on the abscissa corresponds to starting the dosing of ethene. First nickel carbide forms and the intensity drops. As soon as this converts to graphene, the intensity increases since graphene exhibits a larger corrugation than Ni(111). The whole growth process continues over several hours.

Rh(111) (0.9 Å[20]), this is the smallest surface electron density corrugation that has been reported for graphene/metal systems so far (see also Table 1).

Table 1. Comparison of the Surface Debye Temperatures and the Surface Charge Density Corrugation for Different Graphene/Metal Systems and Highly Oriented Pyrolytic Graphite (HOPG)[a]

	surface Debye temperature (K)	electronic corrugation (Å)
graphene/Ru(0001)[15,19]	1045 ± 25	0.15
graphene/Ni(111)	784 ± 14	0.06
graphene/Pt(111)[4]	580 ± 70	
HOPG[4,17]	480 ± 70	0.21

[a]The values for graphene/Ni(111) have been determined within the framework of this study. The surface Debye temperature of graphene/Ni(111) lies between those for graphene/Ru(0001) and graphene/Pt(111). The electron density corrugation of graphene/Ni(111) is the smallest one of all listed systems (except for graphene/Pt(111) where no reported value for HAS exists to our knowledge).

Gamo et al.[10] showed that the graphene ion cores have a very small corrugation of 0.05 Å in low energy electron diffraction (LEED) measurements. Scanning tunnelling microscopy (STM) measurements revealed an atomic corrugation of 0.1−0.15 Å for epitaxial graphene/Ni(111), which is roughly a factor of 3 larger than the height profile measured on bare Ni(111).[21] A similar atomic corrugation with a peak-to-peak height of 0.2 Å is observed in STM measurements of moiré patterns that form in the case of a rotated graphene phase on Ni(111).[1] When comparing values, it is important to remember that the corrugation determined by HAS is the surface charge density corrugation as seen by an 8 meV He beam.

The fact that the graphene covered surface has a larger electron density corrugation than the Ni(111) surface can also be used to monitor the graphene growth. Figure 3 shows how the intensity of the first order diffraction peak develops during growth. The intensity drops initially, upon formation of nickel carbide domains[9] and later increases, upon conversion to graphene. The diffraction intensity saturates at a value above the initial intensity when the graphene layer is completed and the whole process terminates after a complete monolayer has been formed. The growth process itself is relatively slow and proceeds over a time scale of a few hours. However, this gives rise to very high quality graphene layers as also observed in previous studies, whereas at higher surface temperatures (>500 °C) rotated graphene phases are much more likely.[9]

Surface Debye Temperatures. The thermal attenuation of the diffraction peaks provides information about both the surface vibrational dynamics as well as the bonding strength of the graphene layer to the underlying substrate.[4] The onset of thermal vibrations of the surface atoms at finite temperatures causes inelastic scattering of the incoming particles. This can be observed in the thermal attenuation of the coherent diffraction intensities whereupon the peak shape does not change.[6]

The inset in Figure 4 shows the decay of the zero order peak for He scattered from graphene/Ni(111) at an incident beam energy E_i = 8 meV. Scans of the scattered intensity versus the incident angle θ_i were collected, while the crystal temperature was varied between 150 and 740 K. The decay of the peak intensity with increasing surface temperature T_S is caused by the increasing vibrational amplitude of the surface oscillators, which can be described by the Debye−Waller factor. The Debye−Waller factor $\exp[-2W(T_S)]$ relates the diffraction intensity $I(T_S)$ of a sample at temperature T_S to the intensity I_0 of a sample at rest by[6]

$$I(T_S) = I_0 \cdot e^{-2W(T_S)} \quad (1)$$

The Debye−Waller factor is described using

$$2W(T_S) = \langle (\mathbf{u}\cdot\Delta\mathbf{k})^2 \rangle_{T_S} \quad (2)$$

where $\mathbf{u}$, is the displacement of a lattice atom out of its equilibrium position and $\Delta\mathbf{k}$ the momentum transfer. Here, the

DOI: 10.1021/acs.jpcc.5b08284
J. Phys. Chem. C 2015, 119, 25983−25990

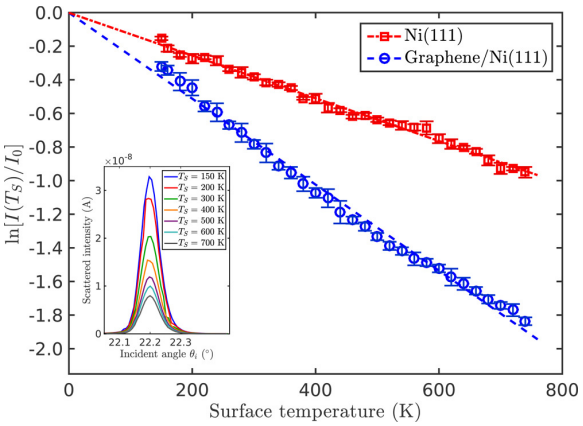

Figure 4. Decay of the logarithmic specular peak intensity $\ln[I(T_S)]$ versus surface temperature T_S using an incident beam energy of 8 meV for the Ni(111) surface and for graphene/Ni(111). In the inset, scans over the specular peak of graphene/Ni(111) are depicted for a couple of different temperatures.

outer brackets denote the thermal average.[6] Equation 2 can be decomposed into contributions from perpendicular momentum transfer Δk_z and parallel momentum transfer $|\mathbf{\Delta K}|$:[22,23]

$$2W = \Delta k_z^2 \langle u_z^2 \rangle + |\mathbf{\Delta K}| \langle U^2 \rangle \tag{3}$$

For elastic scattering the momentum transfer is given by $|\mathbf{\Delta K}| = |\mathbf{k}_i| (\sin(\theta_i) - \sin(\theta_f))$ with the incident wave vector $\mathbf{k}_i$ and θ_i and θ_f the incident and final angle with respect to the surface normal, respectively. Assuming that the momentum transfer parallel to the surface is zero (i.e., for the specular geometry $\theta_i = \theta_f$) eq 3 reduces to

$$2W(T_S) = \langle u_z^2 \rangle \cdot (\Delta k_z)^2 \tag{4}$$

with $\langle u_z^2 \rangle$, the average square displacement of a crystal atom perpendicular to the surface. When using the relation $1/2M\omega^2\langle u^2 \rangle = 3/2k_BT$ for a classical harmonic oscillator and applying the Debye model with the definition of the Debye temperature[24] in terms of the Debye frequency ω_D: $\hbar\omega_D/k_BT = \theta_D/T$, eq 4 becomes

$$2W(T_S) = \frac{3\hbar^2 \Delta k_z^2 T_S}{M k_B \theta_D^2} \tag{5}$$

where M is the mass of the surface atom and θ_D the surface Debye temperature.

It should be noted that eq 5 is not generally valid and problems arise in the application to atom-surface scattering due to the relatively long-range of the interaction potential and because the collisions are often no longer fast enough to be considered impulsive.[25−27] Levi and Suhl[28] have proposed corrections that account for the long interaction time with respect to the vibrational phonon periods and the presence of the attractive atom−surface interaction can be included using the Beeby correction.[29] The first correction requires the knowledge of the surface phonon spectrum and is rather involved. Since we are dealing with comparatively small parallel momentum transfers (8 meV beam) in the presented HAS experiments, eq 5 can be considered to be approximately correct[6,15,30,31] and will form the basis for the following analysis. The latter correction is accounted for as described in the following.

The attractive part of the atom−surface interaction potential can be taken into account by using the Beeby correction. Because of the attractive part of the potential, the incoming He atoms are first accelerated, and the scattered atoms are then decelerating as they leave the surface. Consequently, this effect of the attractive well is considered by replacing the perpendicular momentum transfer Δk_z by[6,30]

$$\Delta k_z' = k_i \left[\sqrt{\cos^2(\theta_f) + \frac{D}{E_i}} + \sqrt{\cos^2(\theta_i) + \frac{D}{E_i}} \right] \tag{6}$$

which assumes an attractive part of the potential with a spatially uniform well of depth D, where values in the range of 4−16 meV are typical for HAS.[6]

In the case of the specular geometry, $\theta_i = \theta_f$ holds and the Debye−Waller factor (eq 5) together with the Beeby correction simplifies to

$$2W(T_S) = \frac{12m[E_i \cos^2(\theta_i) + D]T_S}{M k_B \theta_D^2} \tag{7}$$

where m is the impinging particle mass and the momentum is now replaced by the incident beam energy E_i using $k_i^2 = 2m E_i/\hbar^2$.

According to eq 1, a plot of the natural logarithm of the intensity $\ln[I(T_S)/I_0]$ versus the surface temperature T_S gives rise to a linear decay within the Debye model whereupon the surface Debye temperature can be calculated from the slope. Figure 4 shows the decay of the specular peak intensity versus the surface temperature for both graphene/Ni(111) and the pristine Ni(111) surface.

Equation 7, together with eq 1, is used to determine the surface Debye temperature (θ_D) from the experimental data. The potential well depth D for graphite and graphene/metal systems is typically 15−16 meV,[4,17,32] and, in the present analysis, we used a value of 15.7 meV.[32] (The sensitivity of the Debye temperature θ_D to changing D by 1 meV is relatively small and falls within the experimental uncertainty of θ_D.) While there are no reported values for Ni(111) in the literature, D has been determined to be 6.6 meV for Cu(111) and 7 meV for Ag(111).[33] Hence we have used D = 6.6 meV, assuming that the well depth is similar to that of Cu(111).

One must also assume a value for the mass M which is typically the mass of the crystal atoms since the surface Debye temperature and vibration amplitudes are usually related to the motion of the ion cores. However, He atoms are scattered by the electron density; i.e., in the case of inelastic scattering this corresponds to a scattering by phonon-induced charge density oscillations.[34,35] While the association of these charge density oscillations with the surface Debye temperature is possible due to the electron−phonon coupling the value for M is not necessarily the mass of a single atom.[4]

Recently it has been suggested that the Debye−Waller factor in atom scattering is better expressed in terms of the electron−phonon interaction parameters for simple metal surfaces.[36] This approach has the advantage that it does not include the mass of the surface scatterer. However, the method has not been extended to more complicated surfaces than simple metals so far. Moreover, even though there is some ambiguity connected with the mass of the surface scatterer, these simple equations have proven to serve as a good approximation in the case of HAS,[6,15,30] and using the mass of a single surface atom is a reasonable choice in most cases.[4,15]

DOI: 10.1021/acs.jpcc.5b08284
J. Phys. Chem. C 2015, 119, 25983−25990

Using the best-fit results a surface Debye temperature θ_D = (784 ± 14) K is obtained for the graphene/Ni(111) system and θ_D = (388 ± 7) K for Ni(111). Here we have set M in eq 7 equal to the mass of a single carbon or nickel atom, respectively. In Table 1 the surface Debye temperatures for various graphene/metal systems and for highly oriented pyrolytic graphite (HOPG) are listed in descending order. The surface Debye temperature for graphene/Ni can be found in a region that is between the values found for strongly interacting graphene (graphene/Ru(0001)[4,15]) and weakly interacting graphene (graphene/Pt(111)[4]). While the low surface electron density corrugation suggests an interaction with the Ni(111) substrate that is not large enough to cause any rippling of the graphene layer, it is still greater than for weakly interacting systems, hence explaining the high He reflectivity.

In the case of Ni(111) the surface Debye temperature has been determined with LEED previously, yielding a value of θ_D = (370 ± 5) K.[37] Even though precaution must be taken when comparing HAS measurements with LEED experiments due to the different nature of the scattering processes, our findings are in very good agreement with the value obtained from LEED.

In order to confirm the consistency of our measurements, we apply the same analysis to the first order diffraction peaks measured along the $\overline{\Gamma M}$ azimuth. A plot of $\ln[I(T_S)]$ versus the surface temperature T_S for the first order diffraction peak is depicted in Figure 5. Using the slope of the linear fits, the

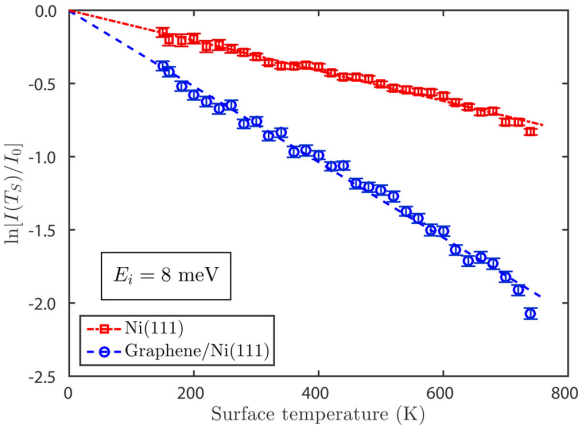

Figure 5. Decay of the logarithmic peak intensity $\ln[I(T_S)]$ with increasing surface temperature T_S of the first order diffraction peak along $\overline{\Gamma M}$. The plot shows the decay for both Ni(111) and graphene/Ni(111), measured at an incident beam energy of 8 meV.

Debye temperature can be calculated using eq 5. Since the mirror condition $\theta_i = \theta_f$ no longer holds, the perpendicular momentum transfer is calculated using eq 6 with the same parameters for the well depth as before.

The surface Debye temperature from the analysis of the first order diffraction peak intensities is θ_D = (760 ± 30) K for graphene/Ni(111) and θ_D = (410 ± 22) K for Ni(111). Both values are in very good agreement with the Debye temperatures determined from the specular peak.

Phonon Spectra for Graphene/Ni(111). The phonon spectra which have been recorded along the $\overline{\Gamma M}$ azimuth suggest that there is no significant difference in the surface phonon dispersion relation for Ni(111) and the graphene covered surface within the energy range accessible with a 8 meV beam. In Figure 6 the 2D wavelength intensity matrix[8] for

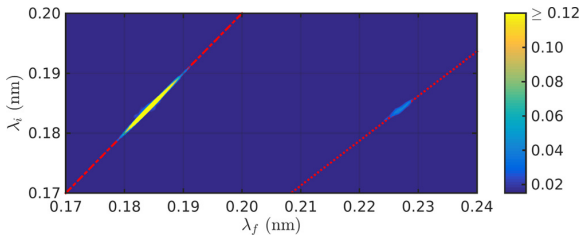

Figure 6. 2D wavelength intensity matrix for graphene/Ni(111) along $\overline{\Gamma M}$ recorded at θ_i = 18.2°, a beam energy of 8 meV, and a sample temperature of 150 K. The plot shows the measured probability for detecting a scattered He atom with wavelength λ_f versus the incoming wavelength λ_i (see refs 8 and 38 for details). The only two visible features are the elastic peak (at $\lambda_f = \lambda_i$) and the Rayleigh mode on the creation side (at larger λ_f). This is also highlighted by the red dash-dotted line which corresponds to elastic scattering ($\lambda_f = \lambda_i$) and the red dotted line which corresponds to the phonon dispersion of the Rayleigh wave of Ni(111).

graphene/Ni(111) at an incident angle of 18.2° is displayed with λ_i being the incident wavelength and λ_f the final wavelength, respectively. The only noticeable feature except for the elastic peak at $\lambda_f = \lambda_i$ is the Rayleigh mode of Ni(111) on the phonon creation side (at larger λ_f).

At first glance, one might expect to detect phonon modes similar to the ones in graphite[39,40] or graphene[41,42] on graphene/Ni(111). The three acoustic modes (ZA, TA, and LA) should be at a detectable energy within the vicinity of the $\overline{\Gamma}$-point. However, previous measurements of the graphene/Ni have only covered phonon events at energies greater than 20 meV.[1,2,43,44] The experiments in the present work have been performed for in plane scattering along the $\overline{\Gamma M}$ azimuth of the crystal. For this geometry, the scattering plane, defined by the incoming and scattered He beam, coincides with a mirror plane of the surface. Hence the TA mode cannot be excited since it is antisymmetric with respect to the scattering plane.[45,46] As shown by de Juan et al.,[45] the symmetry is not broken by bonding of the graphene layer to the substrate in the case of Ni(111). However, because of the bonding to a perfectly commensurate triangular substrate the ZA mode becomes much stiffer for wavevectors close to $\overline{\Gamma}$ lifting its energies to values above 20 meV,[45] which brings the ZA mode out of the detectable energy range of our instrument.

Hence the LA mode is the only phonon mode present in graphene/Ni(111) that is experimentally accessible within the framework of the present study. The LA mode has the largest slope of the acoustic phonon modes and would only be detectable close to $\overline{\Gamma}$. While in the current spectra there are no indications for this mode, it would require a more thorough investigation at specific scattering conditions to make any final conclusions since low energy phonon modes have been found on other graphene/metal systems.[3,5,47] Nevertheless, an important result of this study is that the Rayleigh mode and the longitudinal resonance of the Ni(111) substrate[48,49] are observable on the graphene covered surface, even though the Ni atoms are screened out by the graphene sheet.

A typical phonon spectrum is shown in Figure 7 together with a spectrum taken on Ni(111) under the same experimental conditions. Both spectra have been normalized by the area

DOI: 10.1021/acs.jpcc.5b08284
J. Phys. Chem. C 2015, 119, 25983−25990

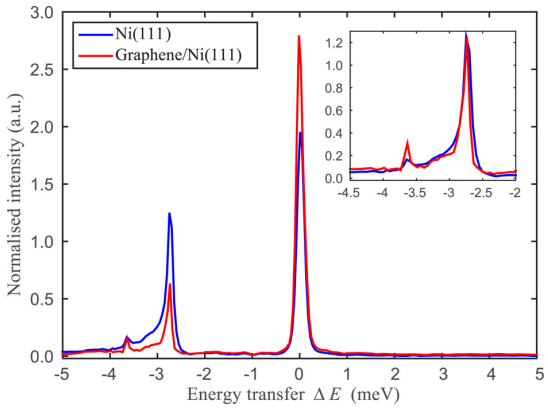

Figure 7. Comparison of the phonon spectra for graphene/Ni(111) and Ni(111). The spectrum was taken along the $\overline{\Gamma M}$ azimuth at an incident angle $\theta_i = 18.2°$, $E_i = 8$ meV, and the sample was cooled down to 150 K. Both spectra have been normalized by the area under each spectrum. Despite the diffuse elastic peak at 0 energy transfer, both the Rayleigh mode at −2.7 meV and the longitudinal resonance at −3.6 meV can clearly be seen. The intensity of the Rayleigh mode is smaller on the graphene covered surface. In the inset the spectrum of the graphene covered surface has been scaled so that the Rayleigh mode exhibits the same height as on the pristine surface. This illustrates that the scattering cross section for the longitudinal resonance at −3.6 meV is enhanced with respect to the intensity of the Rayleigh mode on the graphene covered surface.

under each individual spectrum. This is based on the fact that the overall scattered intensities including elastic scattering due to static defects and inelastic scattering are roughly the same on both surfaces at this incident angle. We have investigated other normalization methods and ensured that our conclusions are robust. In Figure 7 the Rayleigh mode and the longitudinal resonance can be seen on the creation side. The intensity of the Rayleigh mode is clearly reduced on the graphene covered surface with respect to the intensity on Ni(111). The same trend can be seen when comparing intensities of several spectra throughout the $\overline{\Gamma M}$ direction.

As we are observing low frequency phonon modes, i.e., long wavelength modes, one would expect that the whole graphene layer can move up and down with the Ni substrate since the graphite atoms are much lighter than the Ni atoms, provided a relatively strong bonding to the substrate. Note in our experiment it is difficult to obtain an absolute experimental ratio of the phonon cross-section in graphene and nickel. The fact that the static electron density corrugation is significantly different will certainly affect the phonon intensities. However, there are also important changes in the relative intensities of the two main phonon modes. The inset in Figure 7 shows that the scattering cross section of the longitudinal resonance seems to be enhanced on the graphene covered surface when related to the intensity of the Rayleigh mode.

Since this mode appears at higher energies (and smaller momentum transfer) compared to the Rayleigh mode, the so-called "quantum sonar" effect[50] may play an important role: By this we mean that inelastic scattering of He atoms is due to phonon-induced charge density oscillations with subsurface phonon modes being made accessible due to the electron−phonon coupling. The electron−phonon coupling parameters λ found for graphite and graphene/metal systems have been reported to be close to 1,[51] which is similar to values reported for other systems where subsurface phonon modes could be detected with HAS.[35,52]

Furthermore, the observation of the Rayleigh mode from the substrate is consistent with measurements of graphene/Ru(0001) where a strong intensity of the Rayleigh mode from the Ru(0001) substrate was found.[5] Maccariello at el. demonstrated that surface charge density oscillations are the main contribution for this observation on graphene/Ru, although the graphene layer also oscillates with the underlying Ru surface due to the strong bonding to the substrate.[5]

SUMMARY AND CONCLUSION

Graphene/Ni(111) was prepared under ultrahigh vacuum conditions and studied using helium-3 spin−echo spectroscopy. The epitaxial graphene layer exhibits an electron density corrugation with a peak to peak height of 0.06 Å upon scattering of ^{3}He with a beam energy of 8 meV. This corrugation is smaller than the values reported for graphene/Ru(0001) (0.15 Å) and graphite (0.21 Å). The graphene/Ni(111) surface shows a high He reflectivity of ∼20%, similar to the value reported for graphene/Ru(0001).

The thermal attenuation in the diffraction of He from graphene/Ni(111) and Ni(111) was studied in a temperature range between 150 and 740 K. Both systems show a typical Debye−Waller behavior and a surface Debye temperature of θ_D = (784 ± 14) K is determined for the graphene/Ni(111) system and θ_D = (388 ± 7) K for Ni(111). The surface Debye temperature for graphene/Ni(111) lies between those for strongly interacting systems (graphene/Ru(0001)) and weakly interacting systems (graphene/Pt(111)).

Measurements of the surface phonon modes in the low energy region show the same modes as on the pristine Ni surface. Two of the three acoustic phonon modes of graphene are not accessible in our setup. The observation of the Ni(111) surface modes can be explained in terms of a relatively strong binding to the substrate and the lighter mass of the graphite atoms compared to the substrate. In addition, the ability of HAS to detect subsurface phonon modes due to the electron−phonon coupling can also enhance the scattered intensity from these substrate modes, even though the Ni substrate is covered by the graphene monolayer. In general, the intensity of the Rayleigh mode is smaller on the graphene coated surface compared to the Ni surface.

Our findings confirm that graphene/Ni(111) can be created with very high quality and forms an ideal support system for the study of interactions between metals, carbon, and eventually adsorbate atoms. The similarity of our results with atom scattering results from graphene/Ru[5] perfectly confirms the theory that graphene−metal systems with a relatively strong bonding to the substrate should give rise to a high He reflectivity.

AUTHOR INFORMATION

Corresponding Author

*E-mail: tamtoegl@gmail.com.

Notes

The authors declare no competing financial interest.

ACKNOWLEDGMENTS

The authors would like to thank Robert Weatherup and Daniel Farías for their advice on the graphene growth procedure. The authors are also grateful to J. R. Manson for many helpful

DOI: 10.1021/acs.jpcc.5b08284
J. Phys. Chem. C 2015, 119, 25983−25990

discussions. One of us (A.T.) acknowledges financial support provided by the FWF (Austrian Science Fund) within the Project J3479-N20. E.B. would like to thank the Ecole Doctorale de Physique of the Université de Grenoble for funding.

REFERENCES

(1) Dahal, A.; Batzill, M. Graphene-nickel interfaces: a review. *Nanoscale* **2014**, *6*, 2548−2562.
(2) Allard, A.; Wirtz, L. Graphene on metallic substrates: suppression of the Kohn anomalies in the phonon dispersion. *Nano Lett.* **2010**, *10*, 4335−4340.
(3) Politano, A.; Marino, A. R.; Chiarello, G. Phonon dispersion of quasi-freestanding graphene on Pt(111). *J. Phys.: Condens. Matter* **2012**, *24*, 104025.
(4) Shichibe, H.; Satake, Y.; Watanabe, K.; Kinjyo, A.; Kunihara, A.; Yamada, Y.; Sasaki, M.; Hayes, W. W.; Manson, J. R. Probing interlayer interactions between graphene and metal substrates by supersonic rare-gas atom scattering. *Phys. Rev. B: Condens. Matter Mater. Phys.* **2015**, *91*, 155403.
(5) Maccariello, D.; Campi, D.; Al Taleb, A.; Benedek, G.; Farías, D.; Bernasconi, M.; Miranda, R. Low-energy excitations of graphene on Ru(0001). *Carbon* **2015**, *93*, 1−10.
(6) Farías, D.; Rieder, K.-H. Atomic beam diffraction from solid surfaces. *Rep. Prog. Phys.* **1998**, *61*, 1575.
(7) Jardine, A.; Hedgeland, H.; Alexandrowicz, G.; Allison, W.; Ellis, J. Helium-3 spin-echo: principles and application to dynamics at surfaces. *Prog. Surf. Sci.* **2009**, *84*, 323.
(8) Alexandrowicz, G.; Jardine, A. P. Helium spin-echo spectroscopy: studying surface dynamics with ultra-high-energy resolution. *J. Phys.: Condens. Matter* **2007**, *19*, 305001.
(9) Patera, L. L.; Africh, C.; Weatherup, R. S.; Blume, R.; Bhardwaj, S.; Castellarin-Cudia, C.; Knop-Gericke, A.; Schloegl, R.; Comelli, G.; Hofmann, S.; et al. In situ observations of the atomistic mechanisms of Ni catalyzed low temperature graphene growth. *ACS Nano* **2013**, *7*, 7901−7912.
(10) Gamo, Y.; Nagashima, A.; Wakabayashi, M.; Terai, M.; Oshima, C. Atomic structure of monolayer graphite formed on Ni(111). *Surf. Sci.* **1997**, *374*, 61−64.
(11) Wintterlin, J.; Bocquet, M.-L. Graphene on metal surfaces. *Surf. Sci.* **2009**, *603*, 1841−1852.
(12) Bianchini, F.; Patera, L. L.; Peressi, M.; Africh, C.; Comelli, G. Atomic scale identification of coexisting graphene structures on Ni(111). *J. Phys. Chem. Lett.* **2014**, *5*, 467−473.
(13) Zhang, W.-B.; Chen, C.; Tang, P.-Y. First-principles study for stability and binding mechanism of graphene/Ni(111) interface: Role of vdW interaction. *J. Chem. Phys.* **2014**, *141*, 044708.
(14) Parreiras, D. E.; Soares, E. A.; Abreu, G. J. P.; Bueno, T. E. P.; Fernandes, W. P.; de Carvalho, V. E.; Carara, S. S.; Chacham, H.; Paniago, R. Graphene/Ni(111) surface structure probed by low-energy electron diffraction, photoelectron diffraction, and first-principles calculations. *Phys. Rev. B: Condens. Matter Mater. Phys.* **2014**, *90*, 155454.
(15) Politano, A.; Borca, B.; Minniti, M.; Hinarejos, J. J.; Vázquez de Parga, A. L.; Farías, D.; Miranda, R. Helium reflectivity and Debye temperature of graphene grown epitaxially on Ru(0001). *Phys. Rev. B: Condens. Matter Mater. Phys.* **2011**, *84*, 035450.
(16) Mayrhofer-Reinhartshuber, M.; Kraus, P.; Tamtögl, A.; Miret-Artés, S.; Ernst, W. E. Helium-surface interaction potential of Sb(111) from scattering experiments and close-coupling calculations. *Phys. Rev. B: Condens. Matter Mater. Phys.* **2013**, *88*, 205425.
(17) Boato, G.; Cantini, P.; Tatarek, R. Study of gas-graphite potential by means of helium atom diffraction. *Phys. Rev. Lett.* **1978**, *40*, 887−889.
(18) Oh, J. P.; Kondo, T.; Hatake, D.; Nakamura, J. Elastic and inelastic scattering components in the angular intensity distribution of He scattered from graphite. *Surf. Sci.* **2009**, *603*, 895−900.
(19) Borca, B.; Barja, S.; Garnica, M.; Minniti, M.; Politano, A.; Rodriguez-García, J. M.; Hinarejos, J. J.; Farías, D.; Parga, A. L. V. d.; Miranda, R. Electronic and geometric corrugation of periodically rippled, self-nanostructured graphene epitaxially grown on Ru(0001). *New J. Phys.* **2010**, *12*, 093018.
(20) Gibson, K.; Sibener, S. J. Helium atom scattering from graphene grown on Rh(111). *J. Phys. Chem. C* **2014**, *118*, 29077−29083.
(21) Dzemiantsova, L. V.; Karolak, M.; Lofink, F.; Kubetzka, A.; Sachs, B.; von Bergmann, K.; Hankemeier, S.; Wehling, T. O.; Frömter, R.; Oepen, H. P.; Lichtenstein, A. I.; Wiesendanger, R.; et al. Multiscale magnetic study of Ni(111) and graphene on Ni(111). *Phys. Rev. B: Condens. Matter Mater. Phys.* **2011**, *84*, 205431.
(22) Bracco, G.; Ward, M. D.; Scoles, G. Atomic diffraction study of the interaction of helium atoms with the surface of an organic single crystal: The (001) cleavage planes of guanidinium methanesulfonate. *J. Chem. Phys.* **2003**, *118*, 8405.
(23) Lapujoulade, J.; Perreau, J.; Kara, A. The thermal attenuation of elastic scattering of helium from copper single crystal surfaces. *Surf. Sci.* **1983**, *129*, 59.
(24) Kittel, C. *Introduction to Solid State Physics*; John Wiley & Sons Inc: New York, 2005.
(25) Gumhalter, B. Different aspects of the Debye-Waller factor in various atom-surface scattering theories. *Surf. Sci.* **1996**, *347*, 237−248.
(26) Siber, A.; Gumhalter, B. Debye-Waller factor in He-Cu(001) collisions revisited: the role of the interaction potentials. *Surf. Sci.* **1997**, *385*, 270−280.
(27) Daon, S.; Pollak, E.; Miret-Artés, S. Communication: Semi-classical perturbation theory for the quantum diffractive scattering of atoms on thermal surfaces. *J. Chem. Phys.* **2012**, *137*, 201103.
(28) Levi, A. C.; Suhl, H. Quantum theory of atom-surface scattering: Debye-Waller factor. *Surf. Sci.* **1979**, *88*, 221−254.
(29) Beeby, J. L. The scattering of helium atoms from surfaces. *J. Phys. C: Solid State Phys.* **1971**, *4*, L359−L362.
(30) Becker, J. S.; Brown, R. D.; Johansson, E.; Lewis, N. S.; Sibener, S. J. Helium atom diffraction measurements of the surface structure and vibrational dynamics of CH_3-Si(111) and CD_3-Si(111) surfaces. *J. Chem. Phys.* **2010**, *133*, 104705.
(31) Tamtögl, A.; Mayrhofer-Reinhartshuber, M.; Kraus, P.; Ernst, W. E. Surface Debye temperature and vibrational dynamics of antimony(111) from helium atom scattering measurements. *Surf. Sci.* **2013**, *617*, 225−228.
(32) Boato, G.; Cantini, P.; Salvo, C.; Tatarek, R.; Terreni, S. Atomic vibrations at the (0001) graphite surface studied by He atom scattering. *Surf. Sci.* **1982**, *114*, 485−497.
(33) Eichenauer, D.; Harten, U.; Toennies, J. P.; Celli, V. Interaction potential for one-phonon inelastic He-Cu(111) and He-Ag(111) scattering. *J. Chem. Phys.* **1987**, *86*, 3693−3710.
(34) Benedek, G.; Bernasconi, M.; Chis, V.; Chulkov, E.; Echenique, P. M.; Hellsing, B.; Toennies, J. P. Theory of surface phonons at metal surfaces: recent advances. *J. Phys.: Condens. Matter* **2010**, *22*, 084020.
(35) Tamtögl, A.; Kraus, P.; Mayrhofer-Reinhartshuber, M.; Campi, D.; Bernasconi, M.; Benedek, G.; Ernst, W. E. Surface and subsurface phonons of Bi(111) measured with helium atom scattering. *Phys. Rev. B: Condens. Matter Mater. Phys.* **2013**, *87*, 035410.
(36) Manson, J. R.; Benedek, G.; Miret-Artés, S. A new approach to atom scattering from conducting surfaces, unpublished 2015.
(37) Krupski, A. Debye temperature of the Pb layers on Ni(111). *Phys. Status Solidi B* **2006**, *243*, 467−472.
(38) Kole, P. R.; Jardine, A. P.; Hedgeland, H.; Alexandrowicz, G. Measuring surface phonons with a ^{3}He spin echo spectrometer: a two-dimensional approach. *J. Phys.: Condens. Matter* **2010**, *22*, 304018.
(39) Benedek, G.; Brusdeylins, G.; Heimlich, C.; Toennies, J.; Valbusa, U. Surface phonons in graphite (001). *Surf. Sci.* **1986**, *178*, 545−552.
(40) Oshima, C.; Aizawa, T.; Souda, R.; Ishizawa, Y.; Sumiyoshi, Y. Surface phonon dispersion curves of graphite (0001) over the entire energy region. *Solid State Commun.* **1988**, *65*, 1601−1604.
(41) Yan, J.-A.; Ruan, W. Y.; Chou, M. Y. Phonon dispersions and vibrational properties of monolayer, bilayer, and trilayer graphene:

DOI: 10.1021/acs.jpcc.5b08284
J. Phys. Chem. C 2015, 119, 25983−25990

Density-functional perturbation theory. *Phys. Rev. B: Condens. Matter Mater. Phys.* **2008**, *77*, 125401.
(42) Michel, K. H.; Verberck, B. Theory of the evolution of phonon spectra and elastic constants from graphene to graphite. *Phys. Rev. B: Condens. Matter Mater. Phys.* **2008**, *78*, 085424.
(43) Shikin, A.; Farías, D.; Adamchuk, V.; Rieder, K.-H. Surface phonon dispersion of a graphite monolayer adsorbed on Ni(111) and its modification caused by intercalation of Yb, La and Cu layers. *Surf. Sci.* **1999**, *424*, 155−167.
(44) Aizawa, T.; Souda, R.; Ishizawa, Y.; Hirano, H.; Yamada, T.; Tanaka, K.-I.; Oshima, C. Phonon dispersion in monolayer graphite formed on Ni(111) and Ni(001). *Surf. Sci.* **1990**, *237*, 194−202.
(45) de Juan, F.; Politano, A.; Chiarello, G.; Fertig, H. A. Symmetries and selection rules in the measurement of the phonon spectrum of graphene and related materials. *Carbon* **2015**, *85*, 225−232.
(46) Yanagisawa, H.; Tanaka, T.; Ishida, Y.; Matsue, M.; Rokuta, E.; Otani, S.; Oshima, C. Analysis of phonons in graphene sheets by means of HREELS measurement and ab initio calculation. *Surf. Interface Anal.* **2005**, *37*, 133−136.
(47) Politano, A.; Marino, A. R.; Campi, D.; Farrías, D.; Miranda, R.; Chiarello, G. Elastic properties of a macroscopic graphene sample from phonon dispersion measurements. *Carbon* **2012**, *50*, 4903−4910.
(48) Menezes, W.; Knipp, P.; Tisdale, G.; Sibener, S. J. Surface phonon spectroscopy of Ni(111) studied by inelastic electron scattering. *Phys. Rev. B: Condens. Matter Mater. Phys.* **1990**, *41*, 5648.
(49) Ditlevsen, P. D.; Nørskov, J. K. Vibrational properties of aluminum, nickel and copper surfaces. *Surf. Sci.* **1991**, *254*, 261−274.
(50) Benedek, G.; Bernasconi, M.; Bohnen, K.-P.; Campi, D.; Chulkov, E. V.; Echenique, P. M.; Heid, R.; Sklyadneva, I. Y.; Toennies, J. P. Unveiling mode-selected electron-phonon interactions in metal films by helium atom scattering. *Phys. Chem. Chem. Phys.* **2014**, *16*, 7159.
(51) Mazzola, F.; Wells, J. W.; Yakimova, R.; Ulstrup, S.; Miwa, J. A.; Balog, R.; Bianchi, M.; Leandersson, M.; Adell, J.; Hofmann, P.; Balasubramanian, T.; et al. Kinks in the σ band of graphene induced by electron-phonon coupling. *Phys. Rev. Lett.* **2013**, *111*, 216806.
(52) Kraus, P.; Tamtögl, A.; Mayrhofer-Reinhartshuber, M.; Benedek, G.; Ernst, W. E. Resonance-enhanced inelastic He-atom scattering from subsurface optical phonons of Bi(111). *Phys. Rev. B: Condens. Matter Mater. Phys.* **2013**, *87*, 245433.

DOI: 10.1021/acs.jpcc.5b08284
J. Phys. Chem. C 2015, 119, 25983−25990

6.3 Publication C

Jones, A., Tamtögl, A., Calvo-Almazán, I. & Hansen, A. Continuous Compressed Sensing for Surface Dynamical Processes with Helium Atom Scattering. *Sci. Rep.* **6,** 27776 (2016)

A. Tamtögl and A. Jones are joint first authors of the paper.

contributions	
funding	A. Tamtögl, A. Hansen, I. Calvo-Almazán
data acquisition	A. Tamtögl
theory / mathematical background	A. Jones
data analysis	A. Tamtögl, I. Calvo-Almazán
interpretation	A. Tamtögl, A. Jones, I. Calvo-Almazán
publication writing	A. Tamtögl, A. Jones, I. Calvo-Almazán

Reprinted from:

Jones, A., Tamtögl, A., Calvo-Almazán, I. & Hansen, A. Continuous Compressed Sensing for Surface Dynamical Processes with Helium Atom Scattering. *Sci. Rep.* **6,** 27776 (2016)

www.nature.com/scientificreports

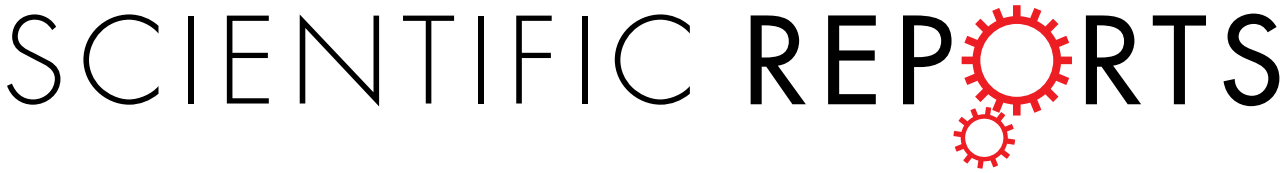

OPEN

Continuous Compressed Sensing for Surface Dynamical Processes with Helium Atom Scattering

Received: 02 February 2016
Accepted: 11 May 2016
Published: 15 June 2016

Alex Jones[1,*], Anton Tamtögl[2,*], Irene Calvo-Almazán[2] & Anders Hansen[1]

Compressed Sensing (CS) techniques are used to measure and reconstruct surface dynamical processes with a helium spin-echo spectrometer for the first time. Helium atom scattering is a well established method for examining the surface structure and dynamics of materials at atomic sized resolution and the spin-echo technique opens up the possibility of compressing the data acquisition process. CS methods demonstrating the compressibility of spin-echo spectra are presented for several measurements. Recent developments on structured multilevel sampling that are empirically and theoretically shown to substantially improve upon the state of the art CS techniques are implemented. In addition, wavelet based CS approximations, founded on a new continuous CS approach, are used to construct continuous spectra. In order to measure both surface diffusion and surface phonons, which appear usually on different energy scales, standard CS techniques are not sufficient. However, the new continuous CS wavelet approach allows simultaneous analysis of surface phonons and molecular diffusion while reducing acquisition times substantially. The developed methodology is not exclusive to Helium atom scattering and can also be applied to other scattering frameworks such as neutron spin-echo and Raman spectroscopy.

Helium atom scattering has proven to be an invaluable technique to study the structure and dynamics of a wide variety of surfaces ranging from simple metals to reactive and metastable surfaces[1–3]. Helium Spin-Echo (HeSE) spectrsocopy is a novel technique[4,5] which combines the surface sensitivity and the inert, completely non-destructive nature of He atom scattering with the unprecedented energy resolution of the spin-echo method[6]. HeSE is the ideal tool for studying surface dynamical processes within a time window from sub-pico second up to nanosecond time scales. This involves atoms and molecules diffusing on the surface[7,8], phonon vibrations[9,10], etc. Thanks to the work of Van Hove *et al.*[11] a theoretical framework exists which describes the dynamics of atoms and molecules through the relation of position and time ($\mathbf{r}$, t) to momentum and energy transfer ($\Delta\mathbf{K}$, ΔE) as a Fourier pair.

In this paper we present a Compressed Sensing (CS) approach for compressing this measurement process, showing that the time needed to reconstruct HeSE spectra can be reduced by several orders of magnitude compared to standard Discrete Fourier Transform (DFT) reconstruction techniques. CS, pioneered by Candès, Donoho, Tao *et al.*[12–15] has long been associated with Nuclear Magnetic Resonance (NMR) based applications such as Magnetic Resonance Imaging[15,16] and NMR Spectroscopy[17]. Recently, compressed sensing has also seen applications focusing on Raman spectroscopy measurements[18] and in molecular dynamics simulations[19].

Spin-echo spectroscopy shares clear similarities with these fields, such as Fourier transforms arising naturally in data acquisition, however there are also significant differences. In particular, one of the goals of spin-echo spectroscopy is to determine dynamical processes by monitoring the change of polarisation data. Here we consider the whole process of data processing, from polarisation data measurements to the extraction of the molecular dynamics information. Unlike NMR and many other spectroscopy-based applications, after we have performed compression on the initial Fourier transform step we cannot directly use the output data, it must instead undergo several further transforms. Crucially, this includes a non-linear change of variables to momentum/energy space ($\Delta\mathbf{K}$, ΔE). This precludes the use of standard DFT-based CS techniques as this transform distorts the (necessarily discrete) set of values that we can solve for.

[1]Centre for Mathematical Sciences, University of Cambridge, United Kingdom. [2]Cavendish Laboratory, J. J. Thompson Avenue, Cambridge CB3 0HE, United Kingdom. *These authors contributed equally to this work. Correspondence and requests for materials should be addressed to A.T. (email: tamtoegl@gmail.com)

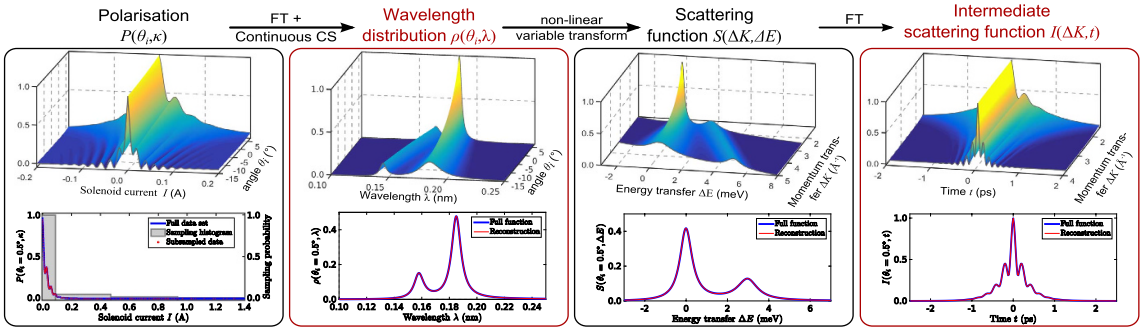

Figure 1. Diagram outlining the various stages of data transformation from measurement in polarisation to the intermediate scattering function (ISF). The upper plots denote the full 2D data while the lower plots are 1D projections/slices with one variable kept constant. The decaying oscillations in the polarisation/ISF are caused by surface phonons. Surface diffusion gives rise to an exponential decay in the polarisation/ISF and a broadening of the peak at $\Delta E = 0$ of the scattering function. The stages highlighted in red correspond to the target data we wish to reconstruct. The plotted intensities are in consistent arbitrary units (a.u.). Current spacing/resolution is $2.7 \cdot 10^{-4}$A/10233 points and 930 points (≈9%) are subsampled. The experimental variable κ is proportional to current I according to (9).

Instead a new *continuous* CS approach, recently introduced by Adcock, Hansen *et al.*[20–22], is used to reconstruct a continuous approximation that avoids discretising entirely. With this method one has the freedom of evaluating the reconstructed function at any point they desire while still having the speed-up benefits of compressive sampling. Such an approach could be used to handle other inverse problems that require further transformations after reconstruction. Moreover, as demonstrated in refs 20–22 the continuous model avoids the so-called wavelet and inverse "crimes" and hence provides superior reconstructions compared to the classical approach.

Figure 1 shows the process of converting sampled polarisation data to the intermediate scattering function (ISF) $I(\Delta K, t)$ alongside the application of this new CS technique. Note that CS reconstructions in red for the wavelength intensity and scattering functions match the true signal with 9% of the data traditionally used to reconstruct such spectra using direct Fourier inversion without compression.

Moreover, in standard NMR experiments the smallest group of data that is taken in one measurement is typically a line (or path) of data points in k-space, with the exception of new realisations such as electron spin echo envelope modulation[23]. However, in HeSE each measurement corresponds to a single point. This gives us an additional degree of freedom in the data acquisition process which makes the application of CS particularly effective, as one can utilize the new approach of structured multilevel sampling in[21] to its fullest to boost performance. In particular, by also taking the structure of the signal into account when designing the sampling strategy one can outperform the classical compressed sensing results (see refs 24 and 25 for experimental validation) that are dictated by the estimate on the number of samples m to be

$$m \gtrsim s \ \log(N),$$

where s is the number of non-zero or important coefficients and N is the dimension of the vector (The notation $f(\cdot) \gtrsim g(\cdot)$ means there is a universal constant $C > 0$ such that $f(\cdot) \geq Cg(\cdot)$).

However, if a signal has $s = M_1 + s_2 + \ldots + s_r$ non-zero coefficients where M_1 denotes the number of the first consecutive non-zero coefficients in the first levels of a wavelet expansion and s_j is the number of non-zero coefficients in the j-th level of the wavelet structure then, by using a multilevel sampling procedure[21], one needs only

$$m \gtrsim M_1 + (s_2 + s_3 + \ldots + s_r)\log(N).$$

measurements[21]. Typically, the coefficients corresponding to M_1 are the most important, and most of the energy in the signal is contained in these. This is very convenient as we do not have to pay a log factor for these coefficients. In practice this means substantial gain over the standard approaches as demonstrated in recent puplications[24,25].

Compressing Spin-Echo Spectra

To understand how continuous CS differs from conventional DFT CS we start with a typical 1D Fourier problem where we measure Fourier samples P of a wavelength intensity function ρ we want to reconstruct:

$$P(\kappa) = \int \rho(\lambda) e^{2\pi i \kappa \cdot \lambda} \, \mathrm{d}\lambda, \quad \lambda, \kappa \in \mathbb{R}. \tag{1}$$

From the above it is immediately recognised that P is a Fourier Transform of ρ and therefore ρ can be obtained by the inverse Fourier transform of P. For a general function ρ this would require knowing $P(\kappa)$ at every point $\kappa \in \mathbb{R}$ which is unrealistic.

In practice however, the wavelength intensity function ρ is treated as a periodic function

$$\tilde{\rho}(\lambda) = \sum_{l\in\mathbb{Z}} \rho(\lambda + (b-a)l), \tag{2}$$

over a fixed interval $[a, b]$. This is convenient because it permits changing the problem to one of handling a Fourier transform to that of handling a Fourier series expansion:

$$\begin{aligned} \tilde{\rho}(\lambda) &= \sum_{l\in\mathbb{Z}} \langle \rho, \chi_{l,\varepsilon}\rangle \chi_{l,\varepsilon}(\lambda), \quad \lambda \in [a, b], \\ \chi_{l,\varepsilon}(\lambda) &= \varepsilon^{1/2} \exp(-2\pi \mathrm{i}\varepsilon l \cdot \lambda), \quad l \in \mathbb{Z}, \quad \varepsilon = (b-a)^{-1}, \\ \langle \rho, \chi_{l,\varepsilon}\rangle &= \int_{\mathbb{R}} \rho(\lambda)\overline{\chi_{l,\varepsilon}(\lambda)} d\lambda = P(l\varepsilon)\varepsilon. \end{aligned} \tag{3}$$

The upshot of (3) is that we now only need the values $P(l\varepsilon)$, $l \in \mathbb{Z}$, to obtain the wavelength intensity function ρ, rather than $P(\kappa)$, $\kappa \in \mathbb{R}$.

Typically the next step is to truncate the Fourier series expansion, meaning that one makes the approximation

$$\tilde{\rho}(\lambda) \approx \tilde{\rho}_N(\lambda) = \sum_{l=-N}^{N} \langle \rho, \chi_{l,\varepsilon}\rangle \chi_{l,\varepsilon}(\lambda), \quad \lambda \in [a, b], \tag{4}$$

for some fixed $N \in \mathbb{N}$. The problem is now feasible as only finitely many data points l are required to determine $\tilde{\rho}_N$.

Up to this point both continuous CS and conventional DFT CS agree. Conventional DFT CS then breaks up the interval $[a, b]$ into a uniform grid of N points

$$\lambda_{j,N} = a + \frac{b-a}{2N+1} j \tag{5}$$

and solves for $\tilde{\rho}_N(\lambda_{j,N})$, $j = 1, \ldots, 2N+1$. The advantage of doing this is that (4) becomes a vector-matrix equation of the form $g = Af$ where $g_j = \tilde{\rho}_N(\lambda_{j,N})$, A is a DFT matrix and f corresponds to samples of P. This can be inverted to give $f = A^{-1} g$ where A^{-1} is still a DFT matrix, and therefore an isometry, which facilitates the application of CS.

The drawback of this approach is that important information could be lost by only considering $\tilde{\rho}_N(\lambda_{j,N})$, $j = 1, \ldots, 2N+1$ instead of (4). The Fourier series approximation could have been evaluated at any point in the interval $[a, b]$ and suddenly the best we can do is reconstruct the $\tilde{\rho}_N(\lambda_{j,N})$, even though we are still working with the same number of Fourier samples. Do we really have to pay this price in order to be able to compress this problem? The answer is: no.

Motivated by the Fourier series (4), one can try approximating ρ in terms of a new *Reconstruction Basis* σ_n, $n \in \mathbb{N}$

$$\tilde{\rho}(\lambda) \approx \sum_{n=1}^{M} \langle \rho, \sigma_n\rangle \sigma_n(\lambda), \quad \lambda \in [a, b]. \tag{6}$$

Apart from the benefit of keeping the problem continuous, one also has the freedom to *choose* which basis σ_n to work with, making the approach more versatile than a straight DFT approach. Note that this is similar in spirit to the work on finite rate of innovation[26] as well as to the concept suggested by Markovich *et al.*[27].

Since one is still sampling data that corresponds to Fourier coefficients of ρ, it is impossible to exclusively work with their choice of basis σ_n. Instead one has to convert Fourier series coefficients into coefficients in the basis σ_n. This is achieved by working with the infinite change of basis matrix for the two bases:

$$B_{l,n} = \langle \sigma_n, \chi_{l,\varepsilon}\rangle, \quad n \in \mathbb{N}, \quad l \in \mathbb{Z}. \tag{7}$$

Using this matrix to reconstruct the coefficients $\langle \rho, \sigma_n\rangle$, $n = 1, \ldots, M$ we can then use (6) to approximate $\tilde{\rho}(\lambda)$. As long as we assume the σ_n form an orthonormal basis then the matrix B is an infinite-dimensional isometry which also allows the application of CS thanks to the work of refs 20 and 22.

This continuous approach has two significant advantages:

- The approximation $\tilde{\rho}$ is now a continuous function (as opposed to discrete) that can be evaluated at any point and hence this allows the non-linear change of variables going from the wavelength distribution to the scattering function S (as shown in Fig. 1). Such a transform is not possible with conventional discrete CS techniques.
- The approximation $\tilde{\rho}$ is computed with the actual coefficients in the new expansion of the wavelength function, and hence this approximation has the characteristics of the approximation in the new basis rather than the truncated Fourier series. This means reducing Gibbs ringing and other artefacts coming from Fourier approximations (see refs 20–22 for details).

Details on the theoretical background of CS, what basis to use, the convex optimisation problems we solve and how to subsample the Fourier data are provided later on in the paper.

Paper Outline. After a short introduction into HeSE spectroscopy and compressed sensing/continuous compressed sensing we focus on the first Fourier transform step shown in Fig. 1. CS is used to demonstrate the compressibility of phonon detection.

In Surface Diffusion Using Continuous CS, we consider the full cycle of transforms shown in Fig. 1, from polarisation data to the determination of diffusion processes. Thereafter we elaborate on the advantages of the continuous CS technique in order to measure processes that appear on different energy scales.

Helium Spin-Echo Spectroscopy

The principle of the Helium spin-echo apparatus is the following: A beam of thermal ^{3}He is generated from the source in a fixed direction. The nuclear spins are polarised and then rotated by the initial or incoming solenoid before being scattered from the target crystal surface. Afterwards any scattered He atoms heading in the direction of the detector are then rotated by the final or outgoing solenoid and passed through another polarisation filter. Thereby the apparatus achieves an energy resolution of 3 μeV and dynamical processes within a time window spanning from the sub-picosecond regime up to nanoseconds can be observed. While a schematic sketch of the machine used at the Cavendish laboratory can be found in the Supplementary Information further details can be found in Jardine *et al.*[4].

Key variables that the operator can freely adjust include:

- The currents I_i, I_f that run through the initial and final solenoid respectively.
- The scattering geometry, namely the angle of the surface normal relative to the source/detector setup.

The incoming monochromatic He beam can be viewed as a plane wave with propagation wavevector $\mathbf{k} \in \mathbb{R}^3$ and angular frequency ω:

$$\psi(\mathbf{r}, t) = \exp(\mathrm{i}(\mathbf{k} \cdot \mathbf{r} - \omega t)), \quad \mathbf{r} \in \mathbb{R}^3, \quad t \in \mathbb{R}. \tag{8}$$

Here, $\mathbf{r}$ denotes position and t is time. The wavevector $\mathbf{k}$ and wavelength λ are related to particle's momentum $\mathbf{p}$ by the de Broglie relations via $\mathbf{p} = \hbar\mathbf{k}$ and $|\mathbf{p}| = p = 2\pi/\lambda$. Furthermore, the frequency ω is related to the particle energy E by the relation $E = \hbar\omega$. Using these relations we can treat $\mathbf{k}$ as representing momentum and ω as energy. Notice that by Formula (8) we have identified two Fourier pairs $(\mathbf{k}, \mathbf{r})$, (ω, t).

Upon scattering from a dynamic surface, the wavevector $\mathbf{k}$ and the energy of the He atom E before and after the scattering will typically change. By measuring the probability of a He atom to go from an initial state i to a final state f information about the surface dynamical processes can be gained. Therefore, we need to measure the properties of the initial and final He beam which is in practice done by changing the current through the solenoids.

In the following we show how the solenoid currents are related to the scattering wavelengths (λ_i, λ_f). This section follows closely the review of Alexandrowicz and Jardine[5] and a more detailed description can be found in the Supplementary Information.

Solenoid Currents and Spin Polarisation. The solenoid currents (I_i, I_f) and scattering wavelengths (λ_i, λ_f) share a direct Fourier relationship. Recall that we have two solenoids that generate magnetic fields which rotate the polarisation of the He beam. The solenoid current determines the strength of the magnetic field but it is more convenient to use the experimentally controllable parameter κ which is proportional to the current in the solenoids via:

$$\kappa_i = \frac{m\gamma B_{\mathrm{eff}} I_i}{2\pi h}, \quad \kappa_f = \frac{m\gamma B_{\mathrm{eff}} I_f}{2\pi h}, \tag{9}$$

where γ is the gyromagnetic ratio of the He atom, m is its mass and B_{eff} is an apparatus specific constant. The polarisation of the He beam in terms of amplitude and phase can be conveniently written as a complex number. When using the scaled variables of (9) the measured polarisation of the He beam in the detector can be represented as the two-dimensional Fourier transform of $\rho(\lambda_i, \lambda_f)$:

$$P(\boldsymbol{\kappa}) = \int \rho(\boldsymbol{\lambda}) e^{2\pi \mathrm{i} \boldsymbol{\kappa} \cdot \boldsymbol{\lambda}} \mathrm{d}\boldsymbol{\lambda}, \quad \boldsymbol{\lambda} = (\lambda_i, \lambda_f), \boldsymbol{\kappa} = (\kappa_i, \kappa_f) \in \mathbb{R}^2. \tag{10}$$

Here $\rho(\lambda_i, \lambda_f)$ denotes the *Wavelength Intensity Function* describing the distribution of He atoms that reach the detector according to initial and final wavelengths.

The change in wavelength can be caused by the creation or annihilation of surface phonons. A short description of the scattering upon surface vibrations can be found in the Supplementary Information. An example of a wavelength intensity function is displayed on the right-hand side of Fig. 2a showing four prominent features. Assuming the features in the plot originate from phonon phenomena on the crystal surface, the classification into creation/annihilation/elastic is according to the energy change ΔE[28]:

$$\Delta E = E_f - E_i = \frac{\hbar^2}{2m}(k_f^2 - k_i^2) = \frac{h^2}{2m}\left(\frac{1}{\lambda_f^2} - \frac{1}{\lambda_i^2}\right). \tag{11}$$

Looking at Fig. 2a as an example, we see that the key features of the wavelength intensity function can be broken down into lines of various slants which suggests that treating the function as one-dimensional would be advantageous. It is precisely because of this decomposition into slanted regions that the two-dimensional problem is often reduced to a one-dimensional one using the Fourier slice theorem: Instead of the two-dimensional (λ_i, λ_f)

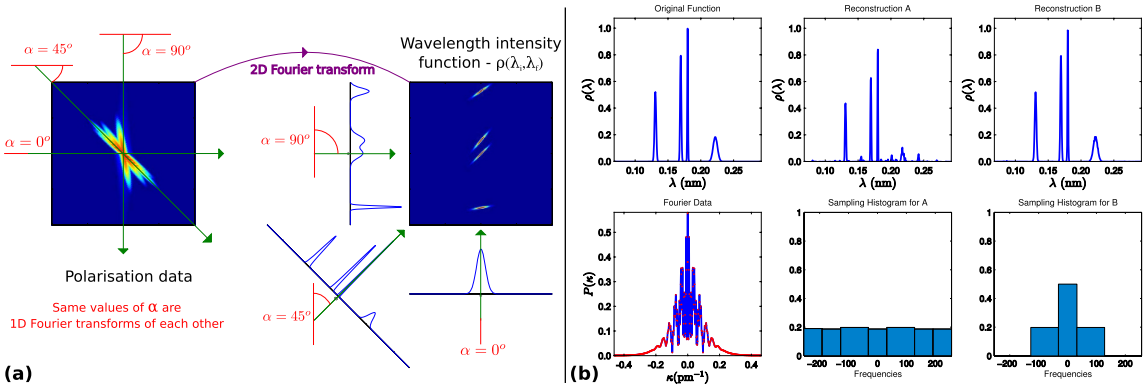

Figure 2. Illustration of a typical wavelength intensity function and the Fourier slice theorem (left panel). The right panel shows a demonstration of the CS for a 1D example shown on the left. (**a**) The wavelength intensity function (on the right) is the two-dimensional Fourier transform of the polarisation data (on the left). The Fourier slice phenomenon is demonstrated by the green lines on the right which indicate the direction of integration with the corresponding projections shown as lines in blue. The green lines on the left hand side represent the one-dimensional Fourier transforms of the projections shown on the right. The polarisation data intensity is shown on a log scale for the sake of readability. (**b**) Demonstrating CS for the 1D 45° projection shown in Fig. 2a, using uniform and multilevel sampling. Samples are taken from the Fourier data according to the sampling histograms shown. (Note that the frequency term in the sampling histogram relates to the values of κ at which $P(\kappa)$ is sampled). Sampling pattern A is unreliable in reconstructing the rightmost feature as it is the least sparse of the four peaks while sampling pattern B remedies this by taking more of the lower frequency values that it depends upon. Reconstructions are at a resolution of 512 data points.

space one considers the projection onto a particular line defined by the angle α. By restricting the measurement of P along the line $\{(\kappa \cos\alpha, -\kappa \sin\alpha), \quad \kappa \in \mathbb{R}\}$ the Fourier transform (10) becomes:

$$P(\kappa_i \cos\alpha, -\kappa_i \sin\alpha) = \int \rho_\alpha(\tau_1) \exp(2\pi i \kappa_i \tau_1)\, d\tau_1, \tag{12}$$

where $\rho_\alpha(\tau_1)$ denotes the integral of $\rho(\lambda)$ along the line $\{R_\alpha(\tau_1, \tau_2): \tau_2 \in \mathbb{R}\}$. For a more detailed derivation of the Fourier slice theorem please refer to the Supplementary Information.

Figure 2a shows how the Fourier slice theorem applies to the wavelength intensity function. Notice that different angles of integration produce different results, especially when it comes to discerning different features. Since we know beforehand that an elastic peak lies along the line $\lambda_i = \lambda_f$ we expect that an integration angle of $\alpha = \pi/4$ will produce the best results for resolving this feature as a single spike.

With this projection, we can treat the problem (12) as a one-dimensional version of (10) with a new wavelength intensity function $\rho_\alpha(\lambda)$

$$P_\alpha(\kappa) = \int_a^b \rho_\alpha(\lambda) e^{2\pi i \kappa\cdot\lambda}\, d\lambda, \quad \lambda, \kappa \in \mathbb{R}. \tag{13}$$

Compressed Sensing. In this section we shall assume that we have already reduced the problem to one dimension and write P_α, ρ_α from (13) as P, ρ.

One can discretise (13) by breaking up the interval $[a, b]$ into a uniform grid of N points $\lambda_{j,N}$ as in (5), leading to the following matrix equation:

$$g_j = \sum_{l=-N}^{N} A_{j,l} f_l, \quad j = 0, \ldots, 2N, \quad g_j = \tilde{\rho}_N(\lambda_{j,N}), \tag{14}$$

where $f_l = \text{Constant}(l) \cdot P(l\varepsilon)$ and A is a DFT matrix.

Currently, to obtain the full vector $(g_j)_{j=0,\ldots,2N}$ we need to know the entire vector $(f_l)_{l=-N,\ldots,N}$. If we only had knowledge of a fraction of the entries of f we can no longer use (14) to determine g directly as the problem is now underdetermined. Therefore, the problem is not well posed and has to be modified.

The matrix equation (14) can be inverted to give

$$f_j = \sum_{l=0}^{2N} A^{-1}_{j,l} g_l, \quad j = -N, \ldots, N. \tag{15}$$

Now suppose that $\Omega \subset \{-N, \ldots, N\}$ denotes the set of indices corresponding to the samples of f that are measured and $P_\Omega f$ denotes the projection onto these samples. With this notation $P_\Omega f$ denotes the vector of samples that are measured. Therefore when we subsample from $\{-N, \ldots, N\}$ equation (15) becomes

$$P_\Omega f = P_\Omega A^{-1} g. \tag{16}$$

The classical CS approach is to solve this problem via the now well established ℓ^1 recovery problem

$$\min_{g\in\mathbb{C}^N} \|Wg\|_{\ell^1} \quad \text{subject to} \quad P_\Omega f = P_\Omega A^{-1} g, \tag{17}$$

where W is some transformation that should make g sparse. Typically this is a wavelet transformation. We can then solve this kind of problem quickly and conveniently using convex solvers such as the (SPGL1) algorithm[29].

The classical idea of CS is that Ω should be chosen uniformly at random. In this case the number of samples $m = |\Omega|$ must satisfy

$$m \gtrsim N \cdot \mu(A^{-1}W^{-1}) \cdot s \cdot \log(N), \tag{18}$$

in order to guaranty successful recovery with high probability, where $\mu(B) = \max_{1\le i,j\le N} |B_{i,j}|^2$. In the case where $B = A^{-1}W^{-1}$ as above with any wavelet transform W we have that $\mu(B) = 1$. In this case, as well as many others, uniform random sampling may give suboptimal results and one has to sample with (structured) variable density sampling, see[21] and references therein. The key problem is that the optimality of variable density sampling depends on the signal itself[21,24,25], and thus designing the best sampling pattern is a very delicate task. We will give a short demonstration below.

How to do structured sampling. The key to understanding structured sampling is to understand the structure of the signal. For example, the coefficients of a signal in a wavelet basis typically have a very specific level structure. This is known as sparsity in levels.

Sparsity in levels. Let x be a $\mathbb{C}^N$ vector. For $r \in \mathbb{N}$ let $\mathbf{M} = (M_1, \ldots, M_r) \in \mathbb{N}^r$ with $1 \le M_1 < \ldots < M_r$ and $\mathbf{s} = (s_1, \ldots, s_r) \in \mathbb{N}^r$, with $s_l \le M_l - M_{l-1}$, $l = 1,\ldots, r$, where $M_0 = 0$. We say that x is $(\mathbf{s}, \mathbf{M})$-sparse if, for each $l = 1,\ldots, r$, $\Delta_k := \mathrm{supp}(x) \cap \{M_{l-1}+1, \ldots, M_l\}$, satisfies $|\Delta_l| \le s_l$. This known structure can be utilised when designing the sampling strategy and is the motivation behind multilevel sampling.

Multilevel sampling. Let $r \in \mathbb{N}$, $\mathbf{N} = (N_1, \ldots, N_r) \in \mathbb{N}^r$ with $1 \le N_1 < \ldots < N_r$, $\mathbf{m} = (m_1, \ldots, m_r) \in \mathbb{N}^r$, with $m_l \le N_l - N_{l-1}$, $l = 1, \ldots, r$, and suppose that $\Omega_l \subseteq \{N_{l-1}+1,\ldots, N_l\}$, $|\Omega_l| = m_l$, $l = 1, \ldots, r$, are chosen uniformly at random, where $N_0 = 0$. We refer to the set $\Omega = \Omega_{\mathbf{N},\mathbf{m}} = \Omega_1 \cup \ldots \cup \Omega_r$ as an $(\mathbf{N}, \mathbf{m})$-multilevel sampling scheme. The key is that in the case of Fourier sampling, represented by the B above, combined with a wavelet transform W such that the recovery problem becomes (17), the multilevel sampling should match the level structure of the wavelets. More precisely, $\mathbf{N} = \mathbf{M}$. In this case, if x is $(\mathbf{s}, \mathbf{M})$-sparse with total sparsity $s = s_1 + \ldots + s_r$ and $s_1 = M_1 = m_1$, then the total number of samples needed is

$$m = m_1 + \ldots + m_r \gtrsim s_1 + (s_2 + s_3 + \ldots + s_r)\log(N). \tag{19}$$

In particular, by utilizing the level structure in the sampling, one can outperform the standard CS results. For a more in-depth analysis and explanation see refs 21 and 25. See also refs 14 and 30 for early versions of this kind of sampling.

Continuous Compressed Sensing. The motivations behind continuous CS are: (i) to obtain a continuous approximation in the CS reconstruction, as opposed to a discrete approximation, as this allows for an easy non-linear change of variables to obtain the scattering function and the intermediate scattering function. (ii) If an alternative basis to the Fourier representation yields a better representation of the function to be recovered, one wants the freedom to use that. In particular, one can try approximating the wavelength intensity function ρ in terms of a new *Reconstruction Basis* σ_n, $n \in \mathbb{N}$:

$$\tilde{\rho}(\lambda) \approx \sum_{n=1}^{N} \langle \rho, \sigma_n \rangle \sigma_n(\lambda), \qquad \lambda \in [a, b]. \tag{20}$$

For technical reasons, one often requires these functions to form an orthonormal basis of $L^2[a, b]$, e.g. Legendre polynomials, splines, wavelets etc., although this condition can be relaxed to other groups of functions like frames[31]. For this paper we shall be using Daubechies wavelets[32] exclusively as our reconstruction basis. Let us quickly discuss *why* one would want to work with another basis.

Apart from the benefit of keeping the problem continuous, one also has the freedom to *choose* which basis σ_n to work with, making the approach more versatile than a straight DFT approach, where we are essentially forced to work with a pixel basis every time.

Furthermore, the notion of *sparsity* is now in terms of the coefficients $\langle \rho, \sigma_n \rangle$, which means we have the additional advantage of choosing a basis that makes the function ρ sparse. As we shall see, this opens up the possibility of using compressed sensing where traditional sparsity does not hold. In addition, this approach is closer to the philosophy that ρ being sparse should relate to ρ having low information content; a choice of basis σ_n that makes ρ sparse tells us how to (approximately) express the function ρ with a few non-zero coefficients.

Since one is still sampling data that corresponds to Fourier coefficients of ρ, it is impossible to exclusively work with their choice of basis σ_n. Instead one has to convert Fourier series coefficients into coefficients in the basis σ_n. This is achieved by working with the infinite change of basis matrix for the two bases:

$$B_{l,n} = \langle \sigma_n, \chi_{l,\varepsilon} \rangle, \quad n \in \mathbb{N}, \quad l \in \mathbb{Z}. \tag{21}$$

As opposed to (17), we now end up solving the infinite dimensional convex optimisation problem of finding

$$h^* \in \underset{h \in \ell^2(\mathbb{N})}{\operatorname{argmin}} \{ \|h\|_1 : P_\Omega B h = P_\Omega f \}, \tag{22}$$

Again P_Ω denotes the projection onto the samples we have taken. In practice we cannot solve for the infinite solution to (22), therefore we truncate the reconstruction basis in a similar fashion to how we truncate the Fourier basis. This means we end up computing

$$h^* \in \underset{h \in \mathbb{C}^N}{\operatorname{argmin}} \{ \|h\|_1 : P_\Omega B P_N h = P_\Omega f \}, \tag{23}$$

where P_N denotes the projection onto the first N functions in the reconstruction basis. This problem is now numerically feasible since the submatrix $P_\Omega B P_N$ is now finite (see[21] for estimates on how to choose N). The solution to (23), let's say h^*, is recognised as the (approximate) wavelet coefficients of the intensity function. We can then use these wavelet coefficients to compute an approximation to ρ evaluated at any point on the interval $[a, b]$ by following (20):

$$\rho(\lambda) \approx \sum_{n=1}^{N} h_n^* \sigma_n(\lambda), \quad \lambda \in [a, b]. \tag{24}$$

From here one can use the same multilevel sampling techniques as the discrete case to reconstruct $(\mathbf{s}, \mathbf{M})$-sparse coefficients. Moreover, the sampling rule (19) also applies in this case. Note, however, that solving (23) is very different from solving (17). Indeed, B in (21) is an infinite matrix, moreover $P_\Omega B P_N \neq P_\Omega A^{-1} W^{-1}$ where we recall A^{-1} and W^{-1} from (17). Both approaches, (23) and (17), are approximations to the true continuous problem (22), however, the discretisation is done differently. The discretisation in (17) turns out to be suboptimal, which can be seen as follows. As discussed in Compressing Spin-Echo Spectra, if $g = Af$, where f is a finite vector consisting of the samples of P from (1), then g is a vector that is a rasterised version of the truncated Fourier series approximation to ρ (the true solution we are seeking). Thus, if we apply a discrete wavelet transform W to g, we see that the result $\tilde{h} = Wg$ is precisely the vector of the wavelet coefficients of the truncated Fourier series approximation to ρ. This means that whatever artefacts the truncated Fourier series approximation suffers from, such as Gibbs ringing, are also transferred to Wg. Hence, by solving (17) we will, at best, recover the wavelet coefficients of the truncated Fourier series that may be a suboptimal approximation. The wavelet coefficients of the truncated Fourier series are of little interest. What we want are the wavelet coefficients of the true solution ρ. This can be formulated via the infinite linear system $\tilde{f} = Bh$, where $\tilde{f}$ is the infinite vector of all samples of the values $P(l\varepsilon)$, $l \in \mathbb{Z}$, and h is the infinite vector of all the true wavelet coefficients of ρ. In comparison, the discretisation based on the DFT yields $f = A^{-1} W^{-1} \tilde{h}$, where $\tilde{h}$ is the vector of wavelet coefficients of the truncated Fourier series. Note that (22) is an infinite-dimensional problem, thus, we need to approximate it via (23). However, as N grows, any solution to (23) converges to a solution to (22).

(23) is not based on the traditional DFT, however, it is possible to find a fast $n \log(n)$ implementation for applying the matrix $P_\Omega B P_N$, the finite section of the infinite matrix B, to any vector. For further explanation and numerical examples demonstrating the benefits of the continuous approach and the differences with the discrete approach, see[20–22].

CS for Phonon Detection

In this section we look at the performance of the CS approach described in the previous section by looking at examples of phonon detection. We shall first look at its effects on the one-dimensional projections shown previously and then focus on a real ^{3}He spectrum for scattering of gold where more exotic signal behaviour is present.

Simulated 1D Example. For consistency with previous sections we shall first work with the 45° projection shown earlier. Although this is a simplified model it clearly demonstrates some of the basic properties of compressed sensing. Reconstructions are shown in Fig. 2b.

Recall that we project along a 45° angle in an attempt to reduce the spread caused by the inaccuracy of the wavelength of the incident He^3 beam. In particular, since we know that there will always be an elastic feature in the wavelength intensity function which itself is slanted at 45°, this choice is seen as ideal for refocusing the various phonon features to be closer to that of a delta spike. Not only is this useful in preventing features from overlapping each other but this also increases sparsity which is ideal for compressed sensing; if features are sparse then by the rule (18) we can subsample to a great degree since the signal itself is very sparse. In this case, a change of basis may not be needed.

If one goes for a uniformly random approach to subsampling (as in Reconstruction A), as opposed to multilevel sampling discussed above, then there is only so far that one can go before problems occur. At around 20% subsampling, the reconstruction becomes unreliable in recovering the least sparse of the features on the far right. With 30% the rightmost feature is typically reconstructed but it is nonetheless unreliable. There is however an even more effective way of reliably reconstructing the rightmost feature by using multilevel sampling (as in Reconstruction B). The theory on how to design optimal structured multilevel sampling strategies is very new[21,24,25] and this is a highly unexplored topic. We do not attempt to seek optimality here, as this paper is about establishing the effectiveness of CS in HeSE. Note that, since there is no wavelet change of basis ($W = I$, the

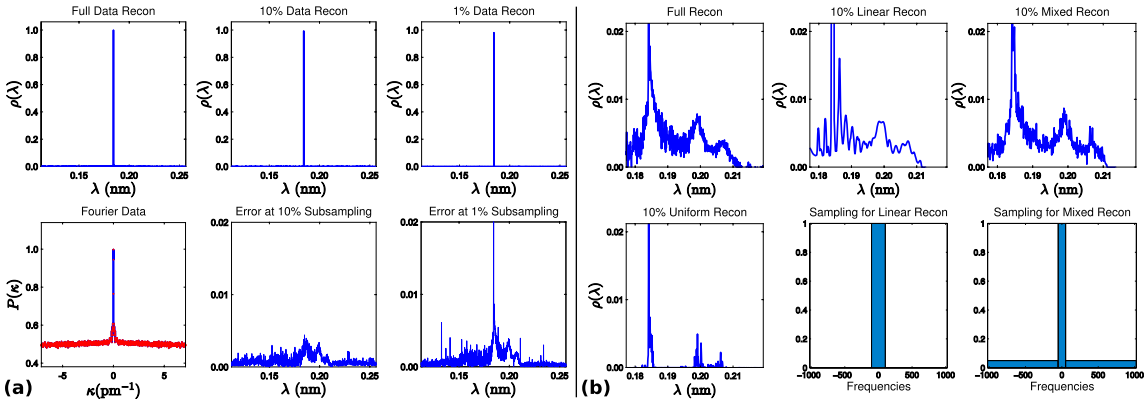

Figure 3. Compressed sensing reconstructions for a measured gold(111) phonon spectrum. (**a**) Compressed sensing reconstructions for a gold phonon spectrum (a.u.): With this choice of viewing range, only the elastic peak can be clearly seen. In this figure the sampling is performed uniformly at random which recovers the highly sparse central peak. This is suboptimal compared to the multilevel sampling in Fig. 3b. Frequencies sampled are from the range $\{-1024, ..., 1023\}$ and reconstructions are at a resolution of 2048. (**b**) Compressed sensing reconstructions for the same gold phonon spectrum as in Fig. 3a, zoomed in so that features beside the elastic peak are visible. Notice that the smaller features shown here are over 200 times smaller than the elastic peak. Reconstructions shown here are not only uniform (as in the bottom left graph) but also linear (i.e. straight Fourier series) and non-linear examples using roughly the same number of samples across each.

identity, in (17)) in this case, the theoretical understanding of the effect of multilevel sampling is not fully understood. This is still work in progress together with optimality conditions.

Real Phonon Spectrum. As we have already mentioned, real phonon spectra contain more exotic features than the simulation given in the previous example. Naturally noise adds to the data due to some experimental uncertainties of the measurement, but more unusual are the relative sizes and shapes of the various features.

In Fig. 3a we have uniform sampling reconstructions for a typical gold(111) spectrum (for more details see Supplementary Information) with projection at 45° to focus on the elastic peak, which is the only clearly visible feature in the graphs. The peak is extremely fine and is in fact even smaller than the pixel resolution used for reconstruction (2048) which can be determined from the observation that the Fourier data has yet to decay to zero near the highest frequencies. Consequently this is an ideal situation for CS since this feature is almost as sparse as can be. Hence, one can subsample to a much greater degree (e.g. 1%) than in the previous example.

However, what has happened to the other inelastic features in this spectrum? At first one might come to the conclusion that they are not there at all, but, focusing on a small part of this spectrum reveals features that are over 200 times smaller than the measured intensity of the large elastic spike. Figure 3b shows various CS reconstructions zoomed in on this region. Notice that we still have the elastic peak visible, along with a couple of more (and less sparse) features. Like in the previous example, we expect the smooth features to be more dependent upon the lower frequency samples. Therefore, when we attempt to take just the first 10% of samples all from the lowest frequencies (the *linear* reconstruction) we find that these features are at the very least present, unlike the 10% uniform sampling approach where only the central peak remains. On the other hand, the central peak suffers from Gibbs artifacts which manifests themselves as wave like features near the central peak as well as broadening of the peak itself.

Instead, one can opt for a mix of these methods by taking the first 5% of samples from the lowest frequencies and the other 5% taken uniformly from the rest. This approach empirically performs the best out of the three methods, resolving the low resolution features without the Gibbs artefacts of the linear approach. Note that, as demonstrated in[21,24], the optimal sampling procedure is signal structure dependent. How to choose optimal multilevel sampling is beyond the scope of this paper, and we have deliberately chosen a simple two-level sampling pattern, which is a reasonable all rounder, in order to demonstrate the effectiveness of the sampling technique.

Comparing CS Techniques. In this section we look at an example of how the continuous wavelet approach to compressed sensing can be used to tackle problems that are beyond the capabilities of the traditional compressed sensing approach described earlier.

Prior to data acquisition the spacing in current (equivalent to spacing in κ) must be chosen, which in turn determines the length of the wavelength window $[a, b]$ that the wavelength intensity function ρ is constructed over. If ρ is not truly supported on this window, then by (2) we instead reconstruct the periodised version of ρ. In particular, if peaks in the intensity function decay particularly slowly relevant to the window then the intensity function will stay considerably above zero throughout that window. Because of this, the traditional compressed sensing approach applied earlier cannot be used successfully here as the function is maximally non-sparse.

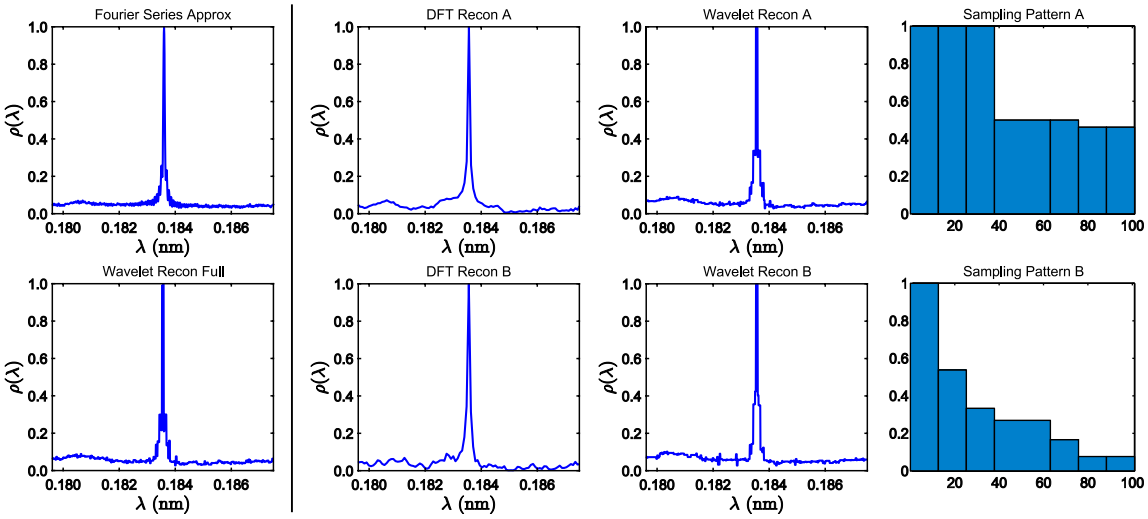

Figure 4. (Continuous vs discrete CS) Reconstructions of a spin-echo spectrum (a.u.) of CoPc molecules deposited on Ag(001) with a noticeable baseline feature. (See Supplementary Information for details on the sample preparation). In the DFT reconstructions the baseline level of around 0.1 is no longer flat leaving bumpy artefacts while the wavelet reconstructions preserve this flat feature. As we are only subsampling from 101 frequency points, considerable Gibbs artefacts are present in the Fourier series approximation. The DFT reconstructions have a resolution of 101 points, while the continuous Fourier series and wavelet reconstructions have been rasterised at a resolution ten times this number.

However, if one recalls the wavelet reconstruction bases that are used, then one quickly notices that they both have a constant function as the first basis function. This effectively means that the base level caused by slow decay is captured by this single basis function, which keeps the function sparse in these bases.

Figure 4 compares the two compression techniques for the diffusion of cobalt phthalocyanine (CoPc) on Ag(001) with an observable baseline feature. The full set of polarisation data points only corresponds to the first 101 frequencies and therefore there are noticeable Gibbs artefacts around the elastic peak in the Fourier series approximation. This strongly suggests that the Fourier series approximation here is not a particularly accurate approximation to the true intensity function.

Furthermore, the wavelet approximation aims to reconstruct the true underlying continuous wavelength intensity function, unlike the DFT approach which attempts to reconstruct a discretised form of the Fourier series approximation. Consequently, even with full sampling, the wavelet reconstruction is noticeably different to the Fourier series approximation. This reflects the fact that, as we are handling real data, we cannot directly compare to the true underlying wavelength intensity function.

Regardless we clearly observe that the baseline feature is preserved under subsampling using wavelets where the DFT approach clearly fails, matching predictions based on sparsity observations earlier. Note that both techniques use exactly the same samples. While we are able to subsample to a reasonable degree here (≈33%), one should ideally work with a larger range of frequencies to truly exploit the benefits of this approach, i.e. subsampling from polarisation data with thousands of points rather than hundreds.

Surface Diffusion Using Continuous CS. Surface diffusion, in contrast to phonon studies, deals with species (atoms, molecules) adsorbed on surfaces which diffuse over large distances. It aims to identify the main mechanisms governing the motion on surfaces (i.e. the energetic landscape governing the adsorbate dynamics) and, therefore, to characterize their diffusive behaviour.

The Van Hove formalism of correlation functions in time and space[11], initially developed for neutron scattering (see Sec. S.5 in the Supplementary Information for more details), provides us with a theoretical formalism to understand and interpret the experimentally determined ISF $I(\mathbf{K}, t)$ in terms of diffusive regimes. (Here we have omitted the Δ in the notation of the momentum transfer $\Delta\mathbf{K}$ for the sake of simplicity.) The Van Hove correlation contains all the information related to the dynamics of particles in the system but it cannot be directly measured. However, its properties can be inferred from partial knowledge of the SF/ISF (see Fig. 5). In particular, different diffusive regimes can be identified through the *dephasing rate* $\alpha(\mathbf{K})$, which describes the decay in time t of the ISF as a function of $\mathbf{K}$[33]:

$$\alpha(\mathbf{K}) = \inf\{t > 0 : |I(\mathbf{K}, t)| = e^{-1}|I(\mathbf{K}, 0)|\}. \tag{25}$$

Its Fourier pair is the so-called *quasi-elastic broadening* $\Gamma(\mathbf{K})$ and is defined as the half-width-half-maximum of the quasi-elastic profile in the SF, i.e in the peak centred around $\Delta E = 0$ of the SF in Fig. 5.

Therefore, it is essential to determine the "true" ISF from the measured polarisation $P(\kappa)$. The processing of the data from $P(\kappa)$ to the ISF requires to go through a series of Fourier transformations and change of variables as

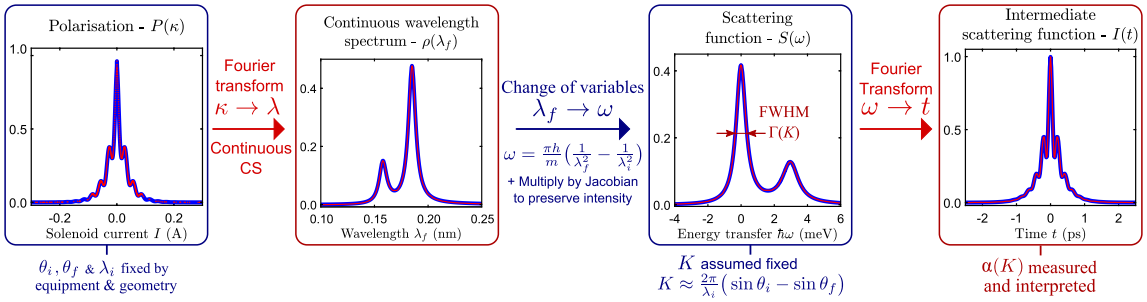

Figure 5. A detailed 1D description of the full loop presented in Fig. 1. Blue lines denote the true underlying signal and red lines denote the reconstructions (except for the left panel where the red dots denote the sampling points). Sampling points are taken according to the sampling histogram present in Fig. 1. Note that there is no comparison with standard discrete CS here as the change of variable technique is impossible in the discrete setup. This can only be done in the continuous case.

shown in Fig. 5. The drawback is that the change from wavelength to energy in (11) is incompatible with the standard DFT based CS methods because the uniform grid of coordinates in wavelength space is transformed onto a non-uniform grid in (**K**, ΔE)-space (see Sec. S.6 in the Supplementary Information for more details on this variable transform). With continuous CS one can work backwards, first specifying a uniform grid in (**K**, ΔE)-space which is converted to a non-uniform grid in wavelength space. As a result, since the reconstructed solution of (22) is a function rather than a vector, one can directly sample the wavelength intensity function on this non-uniform grid and compute the SF on a uniform energy grid. This allows to apply the standard DFT algorithm to obtain the final ISF.

Measuring Diffusion and Phonons in One Go. Through the different sections of this paper we have seen that the HeSE technique can explore dynamical processes spanning from phonon measurements in the sub-picosecond time window up to diffusion in the cents of picoseconds scale. Yet the continuous CS approach enables us not only to reduce the measurement times, it is also a powerful method to circumvent the experimental complications when trying to capture very different dynamical processes within a single set of data.

Firstly, the capability to reconstruct the spectrum out of a subsampled set of measured currents allows to cover a very large current window with a high resolution in a reasonable measurement time. This provides us with a very broad and highly resolved energy window where we can separate accurately the phonon (the inelastic peak in the spectrum) from the diffusive contribution (the quasi-elastic peak centered at $\Delta E = 0$ meV). Secondly, the flexibility of the continuous CS approach allows us to evaluate the reconstructed signal in any desired wavelength grid which greatly simplifies the application of the standard DFT algorithm linking the last two stages of the data processing, from the SF to the ISF in Fig. 5.

Hence the CS approach provides us with a flexible framework where the different physical processes contained in a single data set can be disentangled and analysed in the energy domain (where inelastic features such as phonons can be easily investigated) or in the time domain (where diffusive processes are easier to characterise).

Conclusion and Summary

We have used compressed sensing (CS) techniques to measure and reconstruct surface dynamical processes with a helium spin-echo spectrometer. This work demonstrates that in particular the continuous CS approach can be used to reduce measurement times by at least an order of magnitude whilst capturing both phonon and diffusion processes simultaneously.

Continuous CS allows us to reconstruct spectra with a very broad and highly resolved energy window in a reasonable measurement time so that we can separate accurately phonon events and diffusion processes measured in a single data set. Since the continuous CS approach allows to evaluate the reconstructed signal on any desired grid this makes it easy to switch between the energy and the time domain and to analyse the underlying physical processes. Not only has this made current helium spin-echo experiments more convenient, but this has also brought forward future projects that were originally deemed too time-consuming to measure. Eventually the final goal is to capture the entire scattering function over all of (**K**, ΔE)-space using a two-dimensional continuous CS method.

The developed methodology can also be applied to other scattering frameworks and the authors hope that these advances will be quickly brought to the attention of the neutron scattering and X-ray communities.

References

1. Farías, D. & Rieder, K.-H. Atomic beam diffraction from solid surfaces. *Rep. Prog. Phys.* **61,** 1575 (1998).
2. Benedek, G. & Toennies, J. P. Helium atom scattering spectroscopy of surface phonons: genesis and achievements. *Surf. Sci.* **299,** 587–611 (1994).
3. Tamtögl, A. *et al.* Graphene on Ni(111): Electronic Corrugation and Dynamics from Helium Atom Scattering. *J. Phys. Chem. C* **119,** 25983–25990 (2015).
4. Jardine, A. P., Hedgeland, H., Alexandrowicz, G., Allison, W. & Ellis, J. Helium-3 spin-echo: Principles and application to dynamics at surfaces. *Prog. Surf. Sci.* **84,** 323–379 (2009).
5. Alexandrowicz, G. & Jardine, A. P. Helium spin-echo spectroscopy: studying surface dynamics with ultra-high-energy resolution. *J. Phys.: Condens. Matter* **19,** 305001 (2007).

6. Mezei, F. Neutron Spin Echo: Proceedings of a Laue-Langevin Institut Workshop Grenoble, October 15–16, 1979, chap. The principles of neutron spin echo, 1–26 (Springer, 1980).
7. Jardine, A. P., Alexandrowicz, G., Hedgeland, H., Allison, W. & Ellis, J. Studying the microscopic nature of diffusion with helium-3 spin-echo. *Phys. Chem. Chem. Phys.* **11,** 3355–3374 (2009).
8. Hedgeland, H. *et al.* Measurement of single-molecule frictional dissipation in a prototypical nanoscale system. *Nat. Phys.* **5,** 561–564 (2009).
9. Harten, U., Toennies, J. P. & Woll, C. Helium Time-of-flight Spectroscopy of Surface-phonon Dispersion Curves of the Noble Metals. *Faraday Discuss. Gem. Soc.* **80,** 137–149 (1985).
10. Kole, P. R., Jardine, A. P., Hedgeland, H. & Alexandrowicz, G. Measuring surface phonons with a ^{3}He spin echo spectrometer: a two-dimensional approach. *J. Phys. Condens. Matter* **22,** 304018 (2010).
11. Hove, L. V. Correlations in space and time and born approximation scattering in systems of interacting particles. *Phys. Rev.* **95,** 249 (1954).
12. Candès, E. J., Romberg, J. & Tao, T. Robust uncertainty principles: exact signal reconstruction from highly incomplete frequency information. *IEEE Trans. Inf. Theory* **52,** 489–509 (2006).
13. Candès, E. J. An introduction to compressive sensing. *IEEE Signal Process. Mag.* **25,** 21–30 (2008).
14. Donoho, D. L. Compressed sensing. *IEEE Trans. Inf. Theory* **52,** 1289–1306 (2006).
15. Lustig, M., Donoho, D. L., Santos, J. M. & Pauly, J. M. Compressed sensing mri. *IEEE Signal Process. Mag.* **25,** 72–82 (2008).
16. Guerquin-Kern, M., Häberlin, M., Pruessmann, K. & Unser, M. A fast wavelet-based reconstruction method for magnetic resonance imaging. *IEEE Trans. Med. Imag.* **30,** 1649–1660 (2011).
17. Holland, D. J., Bostock, M. J., Gladden, L. F. & Nietlispach, D. Fast multidimensional nmr spectroscopy using compressed sensing. *Angew. Chem. Int. Ed.* **50,** 6548–6551 (2011).
18. Galvis-Carreño, D. F., Meijía-Melgarejo, Y. & Arguello-Fuentes, H. Efficient reconstruction of raman spectroscopy imaging based on compressive sensing. *DYNA* **81,** 116–124 (2014).
19. Andrade, X., Sanders, J. N. & Aspuru-Guzik, A. Application of Compressed Sensing to the Simulation of Atomic Systems. *Proc. Natl. Acad. Sci. USA* **108,** 13928–13933 (2012).
20. Adcock, B. & Hansen, A. Generalized sampling and infinite dimensional compressed sensing. *Found. Comp. Math.* 1–61 (2015).
21. Adcock, B., Hansen, A. C., Poon, C. & Roman, B. Breaking the coherence barrier: A new theory for compressed sensing arXiv:1302.0561 (2014).
22. Adcock, B., Hansen, A. C., Roman, B. & Teschke, G. Generalized sampling: stable reconstructions, inverse problems and compressed sensing over the continuum. *Adv. in Imag. and Electr. Phys.* **182,** 187–279 (2014).
23. Scheuer, J. *et al.* Accelerated 2D magnetic resonance spectroscopy of single spins using matrix completion. *Sci. Rep.* **5,** 17728 (2015).
24. Roman, B., Adcock, B. & Hansen, A. On asymptotic structure in compressed sensing, arXiv:1406.4178 (2014).
25. Adcock, B., Hansen, A. C. & Roman, B. *Compressed Sensing and its Applications: MATHEON Workshop 2013,* chap. The Quest for Optimal Sampling: Computationally Efficient, Structure-Exploiting Measurements for Compressed Sensing, 143–167 (Springer, 2015).
26. Vetterli, M., Marziliano, P. & Blu, T. Sampling signals with finite rate of innovation. *IEEE Trans. Signal Process.* **50,** 1417–1428 (2002).
27. Markovich, T. *et al.* More accurate and efficient bath spectral densities from super-resolution arXiv:1307.4407 (2013).
28. McIntosh, E. M. *et al.* Measurement of the phason dispersion of misfit dislocations on the au(111) surface. *Phys. Rev. Lett.* **110,** 086103 (2013).
29. Berg, E. & Friedlander, M. Probing the pareto frontier for basis pursuit solutions. *SIAM J. Sci. Comput.* **31,** 890–912 (2008).
30. Studer, V. *et al.* Compressive fluorescence microscopy for biological and hyperspectral imaging. *Proc. Natl. Acad. Sci. USA* **109,** E1679–E1687 (2011).
31. Mallat, S. *A wavelet tour of signal processing* (Elsevier Academic Press, 2008), 3 edn.
32. Daubechies, I. Orthonormal bases of compactly supported wavelets. *Comm. Pure Appl. Math.* **41,** 909–996 (1988).
33. Bée, M. *Quasielastic Neutron Scattering*, chap. Long-range Translational Diffusion, 148–175 (CRC Press, 1988).

Acknowledgements

A. Jones acknowledges EPSRC grant EP/H023348/1, A. Tamtögl acknowledges support by the FWF (project J3479-N20), I. Calvo-Almazán acknowledges support from the Ramón Areces Institution and A. Hansen acknowledges support from a Royal Society University Research Fellowship as well as EPSRC grant EP/L003457/1. The authors would like to thank W. Allison for many helpful discussions.

Author Contributions

A.J. implemented the main parts of the compressed sensing and wavelet reconstruction algorithms and A.T. performed the experimental measurements. I.C.-A. implemented the post-processing of the measured data, in particular the transformation steps from the measured data up to the intermediate scattering function. A.J., I.C.-A. and A.T. analysed the data and prepared the figures. All authors were involved in preparing and revising the manuscript.

Additional Information

Supplementary information accompanies this paper at http://www.nature.com/srep

Competing financial interests: The authors declare no competing financial interests.

How to cite this article: Jones, A. *et al.* Continuous Compressed Sensing for Surface Dynamical Processes with Helium Atom Scattering. *Sci. Rep.* **6**, 27776; doi: 10.1038/srep27776 (2016).

6.4 Publication D

Kraus, P., Gösweiner, C., Tamtögl, A., Apolloner, F. & Ernst, W. E. Adhesion properties of hydrogen on Sb(111) probed by helium atom scattering. *Europhys. Lett.* **114,** 56001 (2016)

	contributions
funding	A. Tamtögl, W. E. Ernst
data acquisition	Ch. Gösweiner, F. Apolloner
data analysis	A. Tamtögl, Ch. Gösweiner, P. Kraus
interpretation	A. Tamtögl, P. Kraus
publication writing	A. Tamtögl, P. Kraus

A Letters Journal Exploring the Frontiers of Physics

June 2016

EPL, **114** (2016) 56001
doi: 10.1209/0295-5075/114/56001

www.epljournal.org

Adhesion properties of hydrogen on Sb(111) probed by helium atom scattering

P. Kraus, Ch. Gösweiner, A. Tamtögl, F. Apolloner and W. E. Ernst

Institute of Experimental Physics, Graz University of Technology - Petersgasse 16, 8010 Graz, Austria

received 18 February 2016; accepted in final form 7 June 2016
published online 28 June 2016

PACS 68.43.-h – Chemisorption/physisorption: adsorbates on surfaces
PACS 68.49.Bc – Atom scattering from surfaces (diffraction and energy transfer)
PACS 34.35.+a – Interactions of atoms and molecules with surfaces

Abstract – We have carried out a series of helium atom scattering measurements in order to characterise the adsorption properties of hydrogen on antimony(111). Molecular hydrogen does not adsorb at temperatures above 110 K in contrast to pre-dissociated atomic hydrogen. Depending on the substrate temperature, two different adlayer phases of atomic hydrogen on Sb(111) occur. At low substrate temperatures (110 K), the deposited hydrogen layer does not show any ordering while we observe a perfectly ordered (1×1) H/Sb(111) structure for deposition at room temperature. Furthermore, the amorphous hydrogen layer deposited at low temperature forms an ordered overlayer upon heating the crystal to room temperature. Hydrogen starts to desorb at $T_m = 430$ K which corresponds to a desorption energy of $E_{des} = (1.33 \pm 0.06)$ eV. Using measurements of the helium reflectivity during hydrogen exposure at different surface temperatures, we conclude that the initial sticking coefficient of atomic hydrogen on Sb(111) decreases with increasing surface temperature. Furthermore, the scattering cross-section for the diffuse scattering of helium from hydrogen on Sb(111) is determined as $\Sigma = (12 \pm 1)$ Å^2.

Introduction. – The semimetal antimony (Sb), one of the essential components in the newly discovered group of topological insulators [1], has gained wide attention recently. While antimony itself is a topological semimetal [2], Sb nanofilms are proposed to be topological insulators [3] and are often stated as interesting candidates for applications in spintronics [4]. Recently, first-principles calculations showed that the adsorption of hydrogen (H) on antimony thin films is capable of modulating the topological surface states: Adsorption of H on Sb induces a huge band gap and a quantum phase transition from an ordinary insulator to a non-trivial topological phase [5].

The adsorption of hydrogen on metal surfaces has been the subject of many experimental and theoretical efforts in the last decades. Hydrogen, by virtue of its single electron, provides also an ideal system for modelling gas-surface interactions [6,7]. However, very little experimental data exists for the adsorption properties of semimetal surfaces apart from graphene [8] and to our knowledge there are no experimental studies upon the adsorption of atomic hydrogen on Sb(111).

It has been shown via scanning tunneling microscopy (STM) [9], low electron energy diffraction (LEED) [10,11] and helium atom scattering (HAS) [12,13], that neither reconstructions nor mentionable relaxations occur at the (111) surface of Sb. Moreover, it has been claimed that antimony is chemically highly inert [14], with the only exception of surface oxidation occurring at elevated temperatures $> 260\,^{\circ}$C [15].

We present helium atom scattering measurements which allow us to characterise the adsorption behaviour of Sb(111) with respect to atomic and molecular hydrogen. Neutral He atom beams with energies of typically 10–20 meV are perfectly suited to probe this system in an inert, completely non-destructive manner [16]. HAS provides an accurate description of the surface charge density corrugation as seen by He atoms at thermal energies [17,18], whereas, *e.g.*, electron scattering is not well suited to detect hydrogen overlayers due to the very small cross-section of hydrogen atoms for electrons [19].

Experiment. – All measurements presented in this manuscript have been conducted on the local helium atom scattering apparatus [20]. An energetically narrow ($< 2\%$ E_0) helium beam is produced via supersonic

expansion from a high-pressure chamber (50 bar) into the source chamber vacuum ($\sim 10^{-7}$ mbar).

The surface can be modified by hydrogen exposure using either thermal molecular hydrogen or an atomic hydrogen source. The source produces a beam of atomic hydrogen from molecular hydrogen which flows through a heated tungsten capillary where it dissociates (see [21] for a characterisation of the source). The main chamber additionally features a quadrupole mass analyser for accurate residual gas analysis and a combined LEED and Auger-electron-spectroscopy (AES) apparatus for surface analysis.

The initial scattering angle of the helium on the so-prepared surface can be controlled by mounting the sample on a seven-axis manipulator, centred in the main chamber of the apparatus. The angular intensity of scattered helium atoms can be detected along a fixed total scattering angle using a quadrupole mass analyser.

Sb(111) substrate. The substrate used for the hydrogen adsorption in this study was an Sb(111) single crystal. The properties of the clean Sb(111) crystal surface have thoroughly been investigated by our group using HAS and Close-Coupling (CC) simulations [12,13,22,23]. Bulk antimony exhibits the rhombohedral A7 structure, with puckered bilayers perpendicular to the [111] direction. The resulting (111) surface can be described using a hexagonal unit cell with a lattice constant of $a = (4.3084 \pm 0.0002)$ Å [9,11]. The surface has two high-symmetry directions, $\overline{\Gamma M}$ and $\overline{\Gamma K}$. All HAS measurements within this study were performed with the scattering direction aligned parallel to the $\overline{\Gamma M}$-direction. As in the present study, all HAS experiments were carried out keeping the clean sample at a base pressure of 10^{-10} mbar to avoid the adsorption of residual gas atoms.

Results. –

Molecular hydrogen adsorption. Angular HAS scans were performed for the clean Sb(111) surface as well as after hydrogen exposure. Figure 1 displays the resulting data along the $\overline{\Gamma M}$ direction. Hydrogen adsorption was initiated by flooding the measurement chamber up to a total pressure of $1.2 \cdot 10^{-7}$ mbar for 4 minutes (22 langmuir) as well as for 15 minutes (81 langmuir) with the sample at room temperature. As can be seen in fig. 1, neither the scattering intensities nor the peak positions changed significantly, indicating the total lack of adsorbed hydrogen on the antimony surface. The same holds when the surface is cooled down to 110 K and exposed to H_2 (lower panel in fig. 1). Hence we can exclude the adsorption of molecular hydrogen at temperatures above 110 K for timescales relevant in single-atom scattering experiments. Shorter sticking timescales for hydrogen on Sb(111) can be probed by directly scattering hydrogen molecules from the clean Sb(111) surface as has been done on several other metal surfaces [16]. The Sb(111) surface seems to be largely inert with respect to molecular hydrogen adsorption —as has been indicated by Shan *et al.* [14]— and hydrogen needs

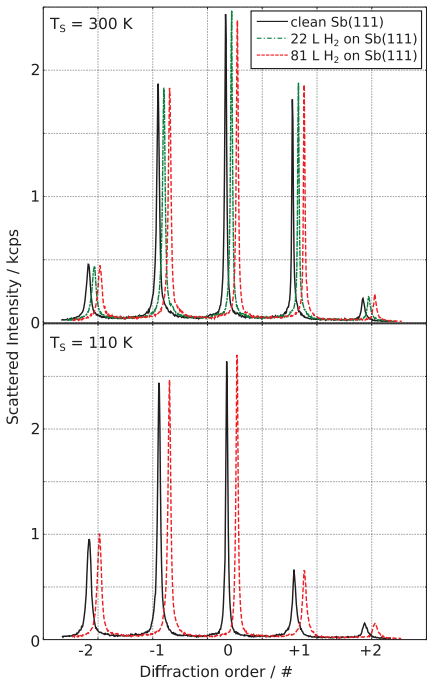

Fig. 1: (Colour online) Angular scattering spectra of the clean Sb(111) surface and after exposure to H_2 along the $\overline{\Gamma M}$ direction and at two surface temperatures. The surface seems largely inert to application of even large amounts of molecular hydrogen. The recorded spectra have been shifted by several degrees to facilitate the presentation. The asymmetry in the 110 K measurement originates from a slight azimuthal alignment shift due to the sample temperature change.

to be pre-dissociated before adsorption on the Sb(111) surface. Furthermore, since dissociation does not occur on the Sb(111) surface, this means that the upper limit for the H-Sb binding energy must be half the H_2 binding energy of 4.52 eV.

Atomic hydrogen adsorption. To study the effect of atomic hydrogen adsorption on the Sb(111) surface, the H_2 was thermally dissociated by heating the tungsten nozzle of the hydrogen source up to 1450 °C using electron bombardment. For a first analysis —starting with a clean sample— angular reference scans were performed at 300 K and 110 K. A large amount of atomic hydrogen (> 1000 L) was then dosed onto the cooled surface and immediately analysed by another angular scattering scan. The thus-obtained surface was then heated up to 300 K and again monitored by an angular scan.

The scans are depicted in fig. 2. After treating the cold surface with atomic hydrogen, the characteristic Sb(111) diffraction peaks are completely absent and only the diffuse multi-phonon background remains. This indicates a totally unordered, amorphous surface structure. Most likely the hydrogen atoms stick at the site where they

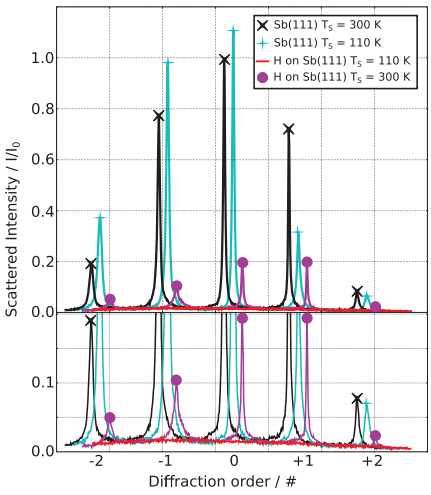

Fig. 2: (Colour online) Angular scattering spectra after several stages of atomic hydrogen exposure along the $\overline{\Gamma M}$ direction of Sb(111). After dosing atomic hydrogen onto Sb(111) at 110 K the diffraction peaks are completely absent (red line), indicating a non-ordered overlayer. Upon heating the surface to 300 K, the diffraction pattern is recovered but with smaller different peak intensities (purple curve).

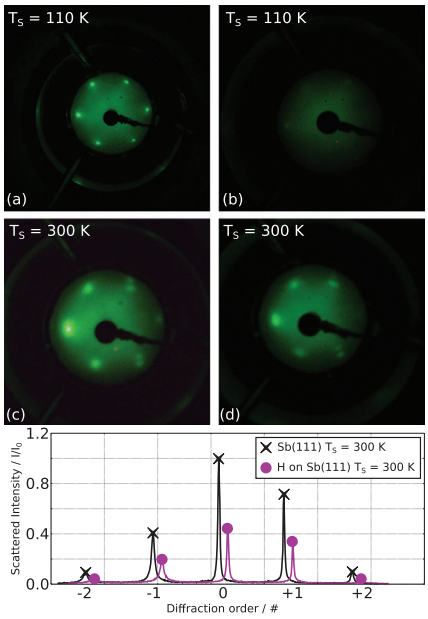

Fig. 3: (Colour online) Top: LEED images after dosing atomic hydrogen at two different surface temperatures. (a) Clean Sb(111) surface at $T_S = 110$ K. (b) Loss of structure after atomic hydrogen exposure at $T_S = 110$ K. (c) Clean Sb(111) surface at $T_S = 300$ K. (d) Almost no change in the LEED pattern, aside from a slight intensity loss after atomic hydrogen exposure at $T_S = 300$ K. Bottom: after dosing atomic hydrogen onto the surface at $T_S = 300$ K, the resulting angular HAS scan reproduces the same pattern as observed after heating the hydrogen-covered surface up to room temperature (see fig. 2). This indicates the organisation of the hydrogen overlayer into an ordered structure.

arrive on the surface and the formation of any ordered structure is kinetically hindered.

Upon re-heating the surface to 300 K, distinct diffraction peaks re-appear, with lower intensity but in the very same spots as the Sb(111) peaks. This can either indicate the partial desorption of adsorbed hydrogen, leaving parts of the clean Sb(111) surface behind, or the formation of an ordered (1×1) H overlayer. Since we obtain the same diffraction peaks upon heating the deposited H-layer (fig. 2) and dosing atomic H with the crystal held at room-temperature (lower panel of fig. 3), the formation of an ordered layer of hydrogen seems more likely. Furthermore, LEED measurements presented in the upper panel of fig. 3 support the interpretation of this behaviour.

The diffraction peak intensities of the ordered H layer and the clean Sb(111) surface are within the same order of magnitude. However, it is difficult to provide a quantitative comparison of the electronic corrugation without calculations of the diffraction peak intensities. The angular diffraction spectra lack pronounced resonance features in the inelastic background between the elastic scattering peaks. Such features, as observed on the clean Sb(111) surface previously [13] could be used to determine the atom-surface interaction potential and allow a detailed corrugation analysis using a close-coupling approach. Note that the electronic corrugation of the clean Sb(111) surface (0.6 Å [23]) is already larger than the corrugation of most hydrogen-covered metal surfaces [24,25].

Thermal organisation and desorption. To determine the stability of the amorphous hydrogen layer as well as the binding energy of the crystalline hydrogen layer, the specular helium scattering intensity was recorded during the heating process. The surface under observation was sputtered and annealed before large amounts of atomic hydrogen (> 1000 L) were dosed onto the cold surface at $T_S = 110$ K. As the machine is usually not prepared for conducting thermal desorption spectroscopy (TDS) experiments, the heating rate available was limited to $0.035\,\mathrm{K} \cdot \mathrm{s}^{-1}$. Figure 4 presents the two temperature drift measurements performed. Already after a small increase of the sample temperature, a continuous rise in the specular reflection commences. This dynamic enhancement of helium reflectivity reaches its maximum rate at around 250 K and slows down significantly before reaching room temperature (fig. 4(a)). The initial rise represents the onset for the transition from a disordered hydrogen overlayer to an ordered structure which has been characterised in the previous section. Once the diffusion of hydrogen on the surface is no longer kinetically hindered, the hydrogen atoms are able to reach their preferred adsorption sites until at 300 K the transition is almost complete.

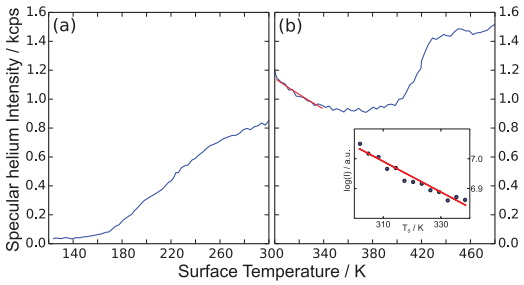

Fig. 4: (Colour online) Intensity of the specular helium reflection from a hydrogen-covered Sb(111) crystal *vs.* surface temperature. The starting point represents an amorphous hydrogen layer which had been deposited prior to the measurement. (a) At a surface temperature of ≈ 150 K, the signal slowly starts its continuous rise, indicating the start of an ordering process among the hydrogen atoms. (b) Further heating of the fully ordered hydrogen overlayer gives rise to a decline due to the Debye-Waller attenuation which is followed by a sudden increase in intensity at around 430 K. This sudden change indicates the desorption of the hydrogen layer.

In order to allow the overlayer to form the fully ordered structure, the system was kept at constant conditions for 8 hours. Upon further heating of the ordered hydrogen overlayer at 300 K (fig. 4(b)), the specular signal first drops according to the Debye-Waller attenuation as the surface temperature is raised, but exhibits a sharp rise around 430 K. Since we expect that the hydrogen overlayer is in a completely ordered state by now, the feature can only be explained by thermal desorption of the hydrogen atoms, leaving the clean Sb(111) surface behind. Using this transition temperature together with the Redhead concept for first-order desorption [26], the desorption energy E_{des} can be estimated. The Redhead's equation reads as follows:

$$E_{des} = k_B \cdot T_m \left[\ln\left(\frac{\nu \cdot T_m}{\beta} \right) - 3.46 \right], \qquad (1)$$

with T_m the temperature of the desorption maximum, k_B the Boltzmann constant, β the heating rate and the pre-exponential or frequency factor ν. Using $T_m = 430\,\mathrm{K}$ as measured in fig. 4 and $\nu = 10^{13}\,\mathrm{s}^{-1}$ [7] we obtain a desorption energy of about $(1.33 \pm 0.06)\,\mathrm{eV}$.

The inset in fig. 4 shows the logarithm of the specularly reflected intensity as a function of T_S in the range 300–350 K for the (1×1)-H saturated surface. Even though only a limited temperature window is available the slope can be used to determine an estimate of the Debye temperature [16]. Hence the Debye temperature of the H-covered surface is $\theta_D = (530 \pm 20)\,\mathrm{K}$ compared to $\theta_D = (155 \pm 3)\,\mathrm{K}$ for the pristine Sb(111) surface [22]. This indicates the different vibrational properties of the hydrogen-covered surface and is in accordance with other studies, *e.g.,* the deuterium or hydrogen-covered Ru(0001) surface, where the Debye temperature of the adsorbate-covered surface is even increased by a factor of 5 and 8, respectively [27].

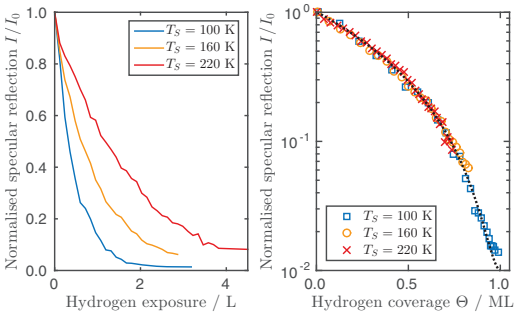

Fig. 5: (Colour online) Left panel: normalised specular reflection I/I_0 *vs.* exposure for the adsorption of atomic hydrogen on Sb(111) at three different surface temperatures and an incident beam energy of 16.2 meV. Right panel: I/I_0 *vs.* coverage plotted on a logarithmic scale. The coverage has been determined from the exposure using the sticking coefficients listed in table 1. The dashed line corresponds to eq. (2) with $\Sigma = 12\,\text{Å}^2$.

Atomic hydrogen uptake. In order to investigate the adsorption of hydrogen on Sb(111), the helium specular signal I was measured while dosing atomic hydrogen for several different surface temperatures T_S. The left panel in fig. 5 shows the relative He specular peak height I/I_0 as a function of H exposure during adsorption for T_S = 100, 160 and 220 K. The different slopes at the beginning clearly point to differences in the adsorption behaviour at these three temperatures. Furthermore, we notice that the curve at 100 K decays to almost zero, whereas at higher temperatures, in particular at 220 K, I/I_0 levels off at a constant value greater than zero. Subsequent diffraction measurements after the dosing had stopped show that the intensity remains constant provided the surface is held at a constant temperature. The behaviour at 100 K is typical if no ordered structure forms, whereas at higher surface temperatures an ordered hydrogen overlayer forms which confirms the result of the diffraction measurements in the previous section.

The fact that the presence of hydrogen on the surface substantially attenuates the specular beam indicates that the hydrogen-covered parts of the surface do not contribute to the specular intensity. Hence the attenuation of the specular intensity during the adsorption of hydrogen can be used as a direct measure of the probability of diffuse scattering [28]. In other words, the adsorbed hydrogen atoms scatter the He beam diffusively and the specular intensity arises exclusively from substrate areas not covered by hydrogen. The normalised specular intensity I/I_0 can then be related to the hydrogen coverage Θ via

$$I/I_0 = (1-\Theta)^{n\cdot\Sigma/\cos\vartheta_i} \qquad (2)$$

$$\approx 1 - \Theta \cdot n \cdot \Sigma/\cos\vartheta_i, \quad \text{for} \quad \Theta \ll 1, \qquad (3)$$

where n is the adsorbate density at monolayer (ML) coverage, Σ is the helium scattering cross-section and the term $\cos(\vartheta_i)$ accounts for the increase of the apparent scattering

Table 1: Temperature dependence of the initial sticking coefficient for the adsorption of atomic hydrogen on Sb(111) relative to the sticking coefficient at 100 K.

Surface temperature T_S (K)	100	160	220
Initial sticking coefficient $S_0(T_S)/S_0(T_S = 100\,\mathrm{K})$	1.0	0.54	0.32

cross-section since scattering occurs at an incident angle $\vartheta_i = 45.7°$. Equation (2) follows a strict geometrical overlap approach of the scattering cross-sections and assumes no interaction between the adsorbates (random adsorption of the adsorbates) [16,28].

In the case of low coverage and no adsorbate-adsorbate interaction, a linear dependence of the intensity on the coverage can be assumed (eq. (3)) and the scattering cross-section Σ can be determined from the initial slope of the adsorption curve [16]. Hence the different slopes in fig. 5 suggest that either the helium scattering cross-section changes with temperature or the sticking coefficient decreases with temperature. Since it is unlikely that Σ changes with surface temperature we assume that the sticking coefficient becomes smaller with increasing surface temperature.

The right panel in fig. 5 shows I/I_0 *vs.* coverage where the surface coverage Θ has been determined from the exposure using an initial sticking coefficient of 1 for adsorption at 100 K. Note that this assumption can only serve as an upper bound and is based on the fact that the sticking coefficient for atomic hydrogen on metal surfaces is often close to one [29].

Monolayer coverage consists of one hydrogen atom per unit cell (as also confirmed by the diffraction data in the previous section) which corresponds to an adsorbate density $n = 0.108\,\text{Å}^{-2}$. The surface coverage is related to the surface exposure which is defined as the impinging flux of adsorbates on the surface integrated over the time of exposure. For this purpose, the dosing pressure was corrected according to [29], to obtain the number of hydrogen atoms impinging on the surface compared to the pressure readout. Furthermore we have used a Langmuir adsorption model where adsorption is limited to one monolayer, all adsorption sites are equivalent and only one particle can reside in an adsorption site. Therefore, the sticking coefficient is given by $S(\Theta) = (1 - \Theta)S_0$, where S_0 is the initial sticking coefficient for the uncovered surface.

In order to maintain a constant helium scattering cross-section, S_0 needs to decrease with increasing temperature. The results for S_0 which give rise to the same initial slope are given in table 1. As can be seen from the right panel in fig. 5 the hereby determined adsorption curves at different surface temperatures are now on top of each other.

Finally, the dashed line in fig. 5 corresponds to a fit according to eq. (2) where we have added a small offset at monolayer coverage. The best fit value of the helium scattering cross-section Σ is $(12 \pm 1)\,\text{Å}^2$. While for hydrogen on Fe(110) $\Sigma = 3.5\,\text{Å}^2$ (for 63 meV beam energy [16]), the scattering cross-section for hydrogen on transition metal surfaces as well as on metal oxide surfaces is typically around 10–12 Å^2 (for 11–40 meV beam energy [19,28]), which is in good agreement with our result.

Conclusion. – We have carried out a series of helium atom scattering experiments in order to characterise the adsorption properties of hydrogen on Sb(111). Initial HAS spectra show that molecular hydrogen does not spontaneously dissociate and adsorb on the Sb(111) surface. The astonishing inertness of the Sb(111) surface towards the adsorption of molecular hydrogen explains why the Sb(111) surface remains exceptionally clean in UHV environments where the main residual gas contribution is molecular hydrogen.

Depending on the substrate temperature while dosing pre-dissociated atomic hydrogen onto the antimony surface, two different adlayer phases were observed. At low substrate temperatures (experiments performed at $T_S = 110\,\mathrm{K}$), the resulting hydrogen overlayer observed by HAS and LEED does not show any ordering. The same experiments performed with the surface at room temperature revealed a perfectly ordered (1×1) H/Sb(111) structure. Furthermore, the hydrogen layer deposited at low temperature appears to re-organize upon heating the crystal to room temperature.

When monitoring the specular He reflection upon heating of the hydrogen-covered surface, hydrogen starts to desorb at $T_m = 430\,\mathrm{K}$ which corresponds to a desorption energy of $E_{des} = (1.33 \pm 0.06)\,\mathrm{eV}$. The attenuation of the specular He reflection during the adsorption of atomic hydrogen can also be used as a measure of the hydrogen coverage. At low surface temperature (100 K), the specular intensity is completely attenuated after large exposures, whereas at higher surface temperatures, it levels off at a constant value. This is another proof for the formation of an amorphous overlayer at low temperatures and an ordered structure at higher crystal temperatures.

Moreover, from the different slopes of the adsorption curves we conclude that the initial sticking coefficient of atomic hydrogen on Sb(111) decreases with increasing surface temperature. The scattering cross-section for the diffuse scattering of helium from hydrogen on Sb(111) is determined with $\Sigma = (12 \pm 1)\,\text{Å}^2$, which is in good agreement for hydrogen on other surfaces.

* * *

We would like to thank A. Winkler from the Institute of Solid State Physics (Graz University of Technology) for providing us with the atomic hydrogen source and for his advice on molecular hydrogen dissociation. One of us (AT) acknowledges financial support provided by the FWF (Austrian Science Fund) within the project J3479-N20.

REFERENCES

[1] Zhang H., Liu C.-X., Qi X.-L., Dai X., Fang Z. and Zang S.-C., *Nat. Phys.*, **5** (2009) 438.

[2] Hsieh D., Xia Y., Wray L., Qian D., Pal A., Dil J. H., Osterwalder J., Bihlmayer F. M. G., Kane C. L., Hor Y. S., Cava R. J. and Hasan M. Z., *Science*, **323** (2009) 919.

[3] Zhang P. F., Liu Z., Duan W., Liu F. and Wu J., *Phys. Rev. B*, **85** (2012) 201410.

[4] Bian G., Wang X., Liu Y., Miller T. and Chiang T.-C., *Phys. Rev. Lett.*, **108** (2012) 176401.

[5] Wang D., Chen L., Liu H., Wang X., Cui G., Zhang P., Zhao D. and Ji S., *Phys. Chem. Chem. Phys.*, **17** (2015) 3577.

[6] Christmann K., *Prog. Surf. Sci.*, **48** (1995) 15.

[7] Christmann K., *Surf. Sci. Rep.*, **9** (1988) 1.

[8] Lin C., Feng Y., Xiao YI., Dürr M., Huang X., Xu X., Zhao R., Wang E., Li X.-Z. and Hu Z., *Nano Lett.*, **15** (2015) 903.

[9] Stegemann B., Ritter C., Kaiser B. and Rademann K., *Phys. Rev. B*, **69** (2004) 155432.

[10] Jona F., *Surf. Sci.*, **8** (1967) 57.

[11] Bengió S., Wells J. W., Kim T. K., Zampieri G., Petaccia L., Lizzit S. and Hofmann PH., *Surf. Sci.*, **601** (2007) 2908.

[12] Mayrhofer-Reinhartshuber M., Tamtögl A., Kraus P. and Ernst W. E., *J. Phys.: Condens. Matter*, **25** (2013) 395002.

[13] Mayrhofer-Reinhartshuber M., Kraus P., Tamtögl A., Miret-Artés S. and Ernst W. E., *Phys. Rev. B*, **88** (2013) 205425.

[14] Shan J., Chakradar A., Yu Z. and Burghaus U., *Chem. Phys. Lett.*, **517** (2011) 46.

[15] Rosenberg A. J., Menna A. A. and Turnbull T. P., *J. Electrochem. Soc.*, **107** (1960) 196.

[16] Farías D. and Rieder K.-H., *Rep. Prog. Phys.*, **61** (1998) 1575.

[17] Tamtögl A., Bahn E., Zhu J., Fouquet P., Ellis J. and Allison W., *J. Phys. Chem. C*, **119** (2015) 25983.

[18] Kraus P., Tamtögl A., Mayrhofer-Reinhartshuber F., Apolloner M., Gösweiner Ch., Miret-artés S. and Ernst W. E., *J. Phys. Chem. C*, **119** (2015) 17235.

[19] Wöll C., *J. Phys.: Condens. Matter*, **16** (2004) S2981.

[20] Tamtögl A., Mayrhofer-Reinhartshuber M., Balak N., Ernst W. E. and Rieder K. H., *J. Phys.: Condens. Matter*, **22** (2010) 304019.

[21] Eibl C., Lackner G. and Winkler A., *J. Vac. Sci. Technol. A*, **16** (1998) 2979.

[22] Tamtögl A., Mayrhofer M., Kraus P. and Ernst W. E., *Surf. Sci.*, **617** (2013) 225.

[23] Kraus P., Mayrhofer-Reinhartshuber M., Gösweiner Ch., Apolloner F., Miret-Artés S. and Ernst W. E., *Surf. Sci.*, **630** (2014) 208.

[24] Lee J., Cowin J. P. and Wharton L., *Surf. Sci.*, **130** (1983) 1.

[25] Gross G. and Rieder K. H., *Surf. Sci.*, **241** (1991) 33.

[26] Redhead P. A., *Vacuum*, **12** (1962) 203.

[27] Mcintosh E. M., *Adsorption and dynamics of interacting surface systems*, PhD Thesis University of Cambridge (2013).

[28] Poelsema B. and Comsa G., *Scattering of Thermal Energy Atoms from Discordered Surfaces*, *Springer Tracts Mod. Phys.*, Vol. **115** (Springer, Berlin) 1989.

[29] Winkler A., *Appl. Phys. A*, **67** (1998) 637.

6.5 Publication E

Calvo-Almazán, I., Sacchi, M., Tamtögl, A., Bahn, E., Koza, M. M., Miret-Artés, S. & Fouquet, P. Ballistic diffusion in poly-aromatic hydrocarbons on graphite. *J. Phys. Chem. Lett.* **7,** 5285–5290 (2016)

contributions	
funding	A. Tamtögl, I. Calvo-Almazán
preparation / setup	A. Tamtögl, I. Calvo-Almazán
data acquisition	A. Tamtögl, I. Calvo-Almazán, M. M. Koza, P. Fouquet
theory (*ab initio*) calculations	M. Sacchi
data analysis	A. Tamtögl, I. Calvo-Almazán
interpretation	A. Tamtögl, I. Calvo-Almazán, S. Miret-Artés
publication writing	A. Tamtögl, I. Calvo-Almazán

THE JOURNAL OF PHYSICAL CHEMISTRY Letters

Letter

pubs.acs.org/JPCL

Ballistic Diffusion in Polyaromatic Hydrocarbons on Graphite

Irene Calvo-Almazán,*[,†] Marco Sacchi,[‡] Anton Tamtögl,[†] Emanuel Bahn,[§] Marek M. Koza,[§] Salvador Miret-Artés,[∥] and Peter Fouquet[§]

[†]Cavendish Laboratory, University of Cambridge, J. J. Thomson Avenue, CB3 0HE Cambridge, United Kingdom

[‡]Department of Chemistry, University of Surrey, GU2 7XH Guildford, United Kingdom

[§]Institut Laue-Langevin, 71 Avenue des Martyrs, CS 20156, F-38042 Grenoble Cedex 9, France

[∥]Instituto de Física Fundamental, Consejo Superior de Investigaciones Científicas, Serrano 123, E-28006 Madrid, Spain

Supporting Information

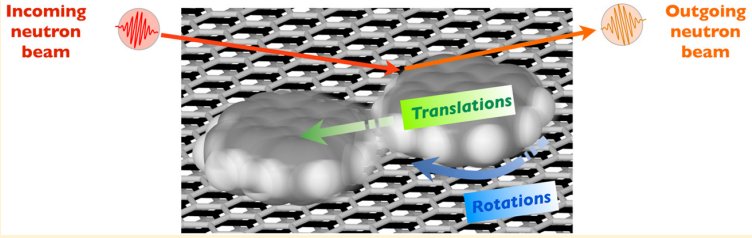

ABSTRACT: This work presents an experimental picture of molecular ballistic diffusion on a surface, a process that is difficult to pinpoint because it generally occurs on very short length scales. By combining neutron time-of-flight data with molecular dynamics simulations and density functional theory calculations, we provide a complete description of the ballistic translations and rotations of a polyaromatic hydrocarbon (PAH) adsorbed on the basal plane of graphite. Pyrene, $C_{16}H_{10}$, adsorbed on graphite is a unique system, where at relative surface coverages of about 10−20% its mean free path matches the experimentally accessible time/space scale of neutron time-of-flight spectroscopy (IN6 at the Institut Laue-Langevin). The comparison between the diffusive behavior of large and small PAHs such as pyrene and benzene adsorbed on graphite brings a strong experimental indication that the interaction between molecules is the dominating mechanism in the surface diffusion of polyaromatic hydrocarbons adsorbed on graphite.

Carbon-based materials play a central role in the search for low-friction building blocks in nanotechnology.[1−4] The high economical impact of wear, friction (energy dissipation), and lubrication in industry and transport[5] has fostered intensive research in friction-free or superdiffusive systems.[6] Superdiffusivity has been observed in systems involving graphitic compounds: fullerenes,[7,8] metallic clusters,[9] or graphene flakes adsorbed on graphite.[10,11] The existence of quadrupole or higher order interactions may cause the superdiffusivity between graphene and graphite observed with atomic force microscopy (AFM).[10,12,13] Interactions of the same nature exist in polyaromatic hydrocarbons (PAHs) adsorbed on graphitic substrates,[14,15] which are characterized by a very low energy barrier for lateral diffusion[16] and can act as nanosized lubricants.[2]

Scattering techniques such as quasi-elastic helium atom scattering (QHAS) and quasi-elastic neutron scattering (QENS) are powerful tools to investigate very fast molecular dynamics (picosecond time scale and atomistic length scale).[17] Their combination provided the first unambiguous experimental observation of Brownian diffusion of molecules adsorbed on surfaces (benzene/graphite) as well as the first precise measurement of the kinetic friction parameter.[16,18] The sensitivity of QENS and QHAS to the dynamics of adsorbates on weakly corrugated surfaces (diffusion energy barrier in the millielectronvolt range) turns them into the ideal probe for research into the origin of energy dissipation on graphite.[17,19,20]

At strong dilution, Brownian dynamics can transform into ballistic motion, that is, molecular collisions where linear and angular momentum is exchanged, become negligible and molecules move in a linear fashion. Hints of ballistic dynamics were already found at very low relative coverages of benzene on graphite (0.1 monolayers (ML), corresponding to 10% occupancy of the effective surface adsorption sites).[18] However, the observation of the pure ballistic regime requires an even lower density of adsorbates, which, in turn, requires the use of molecules with a bigger size and a large scattering cross section to preserve an adequate signal-to-noise ratio. In the present work, we explore the diffusion of pyrene ($C_{16}H_{10}$) on graphite in the low coverage regime of 0.1 and 0.2 ML and for temperatures between 80 and 350 K. We compare its diffusive behavior to benzene (C_6H_6) on graphite at equivalent relative coverages and temperatures. By combining the experimental

Received: October 6, 2016
Accepted: December 2, 2016
Published: December 2, 2016

DOI: 10.1021/acs.jpclett.6b02305
J. Phys. Chem. Lett. 2016, 7, 5285−5290

The Journal of Physical Chemistry Letters Letter

Table 1. Summary of the Relevant Physical Parameters for Benzene and Pyrene Adsorbed on Graphite for a Relative Coverage of θ = 0.2 ML

physical parameter	C_6H_6	$C_{16}H_{10}$
area: σ (Å^2)[a]	37	~85
molecule radius: $a = \sqrt{\sigma/\pi}$ (Å)[b]	3.5	5.2
pair correlation: $g(d_+)$[c]	2.6	2.6*
molecular density: $\rho = \theta g(d_+)/(\sigma)$ (molecules·Å^{-2})[d]	1.4×10^{-2}	0.6×10^{-2}
mean free path: $\bar{l} = 1/(2\sqrt{2}\rho a)$ (Å)	7.2	10.9
corresponding momentum transfer: $Q_{ball} = 2\pi/\bar{l}$ (Å^{-1})	0.9	0.6
energy for adsorption (eV)[e]	−0.64	−1.56
energy barrier for diffusion (eV)[e]	0.012	0.011

[a]Value for the area occupied by a molecule lying flat on the basal plane of graphite σ (see ref 22 for benzene and DFT calculations for pyrene). [b]Radius a of the adsorbed molecule. [c]Pair correlation value at the first neighbor distance $g(d_+)$ (*we assume that benzene and pyrene have the same pair correlation; see ref 18). [d]Molecule density at the contact distance ρ. [e]Energy for adsorption and the barrier for diffusion have been calculated with DFT.

data with density functional theory (DFT) calculations, molecular dynamics (MD) simulations, and a new analytical model, which predicts the signature of ballistic translations and rotations in QENS data, we achieve a full characterization of pyrene's diffusive behavior.

QENS measurements of 0.2 ML of pyrene and benzene at equivalent kinetic temperatures (where the ratio temperature to mass, T/m, is the same) show how the molecular size allows us to adjust the mean free path $\bar{l}$ for ballistic diffusion to the time and length scale covered by the neutron spectrometer. The values for the molecular radius and the mean free path expected for 0.2 ML of pyrene and benzene are summarized in Table 1. Accordingly, benzene's ballistic diffusion will be visible at momentum transfers of $Q_{ball} > 0.9$ Å^{-1}, while pyrene's ballistic diffusion is already visible at $Q_{ball} > 0.6$ Å^{-1}. Figure 1 displays the distribution of neutron intensity, the so-called scattering function $S(Q,\Delta E)$ (SF),[21] as a function of the energy transfer ΔE, at a momentum transfer of $Q = 0.8$ Å^{-1} for 0.2 ML of benzene (at 60 and 140 K) and 0.2 ML of pyrene (at 160 and 320 K), respectively.

The molecule's diffusive behavior can be characterized qualitatively by analyzing the energy profile of the scattering function: A Gaussian form of the quasi-elastic spectrum is characteristic for ballistic diffusion. Conversely, a Lorentzian-like profile of the energy transfer is the signature of Brownian diffusion.[20] To quantify the degree of ballistic/Brownian diffusion (Gaussian/Lorentzian like quasi-elastic profile), we fit the experimental SF to the convolution of the experimental resolution function (the vanadium scattering function) with a model function for diffusion on a flat potential energy surface[23]

$$S_{inc}(Q,\Delta E) = y_0 + S_{res}(Q,\Delta E)\otimes \left[\exp[\chi^2(Q)] \times A(Q) \sum_{n=0}^{\infty} \frac{(-\chi^2(Q))^n}{\pi n!} \frac{(n+\chi^2(Q))\eta}{[(n+\chi^2(Q))\eta]^2 + \Delta E^2}\right] \quad (1)$$

Here y_0 is the background arising from processes that are too fast to be observed in the current time window (phonons for instance) and instrumental noise; $A(Q)$ is the global amplitude of the quasi-elastic signal, $\chi(Q) = \sqrt{\langle v^2\rangle}\, Q/\eta$ is the shape parameter, defined as the ratio between the mean square velocity $\langle v^2\rangle$ and the friction parameter η.[23] Its value determines the energy dependence of the quasi-elastic profile:[23] (i) For large η (Brownian diffusion), $\chi \ll 1$, and only the first term $n = 0$ of the summation in eq 1 contributes to the scattering function. (ii) Conversely, if η is very small and $\chi \gg 1$, then eq 1 can be approximated by a Gaussian function, which is the typical signature of ballistic diffusion.[20]

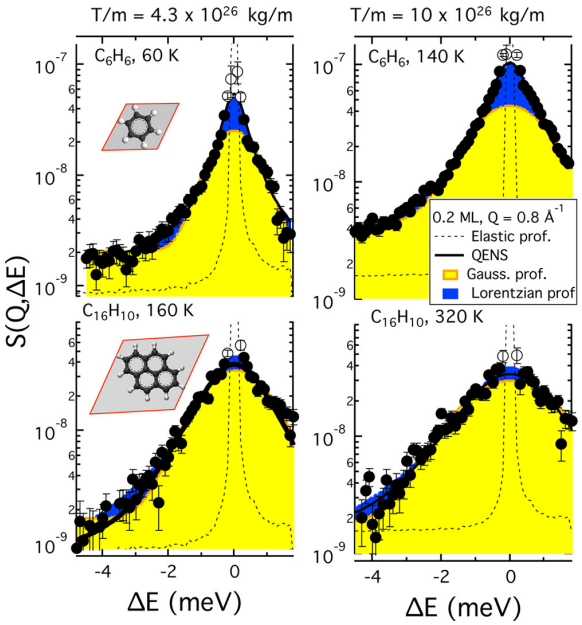

Figure 1. Comparison of the experimental scattering function $S(Q = 0.8$ Å^{-1}, $\Delta E)$ for 0.2 ML of benzene at 60 (top left) and 140 K (top right) and 0.2 ML of pyrene at 160 (bottom left) and 320 K (bottom right). On the top of each graph, we indicate the temperature/mass ratio: 4×10^{26} K·kg^{-1} (left) and 10×10^{26} K·kg^{-1} (right). The thick black line is the fitting of the experimental data to eq 1. The yellow area is the fit of the experimental data to a Gaussian function, and the blue area is the fit of the experimental data to a Lorentzian function. The dotted black line is the elastic profile. The open circles mark the data points excluded from the GoF calculation.

Table 2 summarizes the result of the best fit while Figure 1 shows the best fit for each experimental profile in comparison with a single Lorentzian and Gaussian function (further details can be found in the Supporting Information). We observe that the fitted shape parameter χ for pyrene is equal to one, while for benzene it is clearly below. Accordingly, the benzene quasi-elastic profile is best-fitted by a Lorentzian function and the pyrene quasi-elastic profile could be fitted with either a Gaussian or a Lorentzian function. Both options yield a very similar goodness of fit, GoF, in the range of energies, which

DOI: 10.1021/acs.jpclett.6b02305
J. Phys. Chem. Lett. 2016, 7, 5285−5290

The Journal of Physical Chemistry Letters Letter

Table 2. Summary of the Fit Results of the Benzene and Pyrene Experimental SFs under Equivalent Experimental Conditions and for a Relative Coverage of θ = 0.2 ML and a Momentum Transfer of Q = 0.8 Å^{-1}

physical parameter	C_6H_6		$C_{16}H_{10}$	
temperature (K)	60	140	160	320
shape parameter: $\chi(Q = 0.8$ Å$^{-1})$	$0.3^{+0.5}_{-0.3}$	$0.3^{+0.5}_{-0.3}$	0.9 ± 0.4	1.0 ± 0.3
GoF[a] for eq 1	1.2	2.9	2.0	2.1
GoF for Lorentzian function fit	1.0	1.5	1.6	1.7
GoF for Gaussian function fit	2.6	2 0.5	1.8	1.9

[a]Goodness of fit.

excludes the points within [−0.2,0.2] meV, where the elastic signal dominates over the quasi-elastic signal. Therefore, benzene diffuses in a Brownian fashion (significant value of η), while pyrene displays hints of ballistic diffusion at Q = 0.8 Å^{-1} ($\eta \ll 1$ and high degree of Gaussian-like quasi-elastic profile). In addition, the very low corrugation of the substrate potential energy surface calculated by DFT for both molecules suggests that the role of the substrate in the friction dissipative process is small. The observation of a ballistic diffusive behavior in a dilute system (pyrene) and a Brownian diffusive regime in a denser system (benzene) supports the hypothesis that the origin of friction in PAH adsorbed on graphite is mostly due to collisions between molecules, which act as rough hard disks and exchange linear and angular momentum.[18] The main channel for the translational kinetic energy dissipation is therefore the conversion of linear motion into rotations and other internal degrees of freedoms: tumbling for benzene and internal vibrations for pyrene (see the last section of the Supporting Information). In the following paragraph we attempt to fully characterize pyrene's diffusive behavior.

Figure 2 displays the quasi-elastic neutron spectra measured in pyrene/graphite samples at two different relative coverages: 0.1 and 0.2 ML, at 320 K, and calculated from molecular dynamics simulations of a full molecule and its center of mass (CoM) trajectories. The energy profiles are fitted to a model that combines an elastic peak (in the case of experimental data), a quasi-elastic peak arising from ballistic translations and rotations, and an inelastic contribution whose origin we explore with DFT calculations as shown in the Supporting Information. Note that for the experimental data, eq 2 needs to be convoluted with the resolution function, the vanadium scattering function: $S_{res}(\mathbf{Q},\Delta E) \otimes S_{fit}(\mathbf{Q},\Delta E)$.

$$S_{fit}(\mathbf{Q}, \Delta E) = y_0 + \left[A_{el}(Q)\delta(\Delta E)A(Q) + A(Q)S_{BTR}(\mathbf{Q}, \Delta E) + \frac{A_p(Q)}{(\Delta E - \Delta E_p(Q))^2 + \Gamma_p(Q)^2} \right] \quad (2)$$

The free parameters in the fitting are the flat background y_0, the elastic peak amplitude $A_{el}(Q)$ (in the case of the experimental data), the global amplitude of the quasi-elastic profile $A(Q)$, the energy $\Delta E_p(Q)$, the amplitude $A_p(Q)$, and the width $\Gamma_p(Q)$ of the inelastic peak. $S_{BTR}(\mathbf{Q},\Delta E)$ stands for the ballistic translational rotational (BTR) model consisting in the convolution of a classical Gaussian function, typical for ballistic translations, with an adaptation of the scattering function for uniaxial rotational diffusion[24] to the ballistic regime (see eq 14 in the Supporting Information)

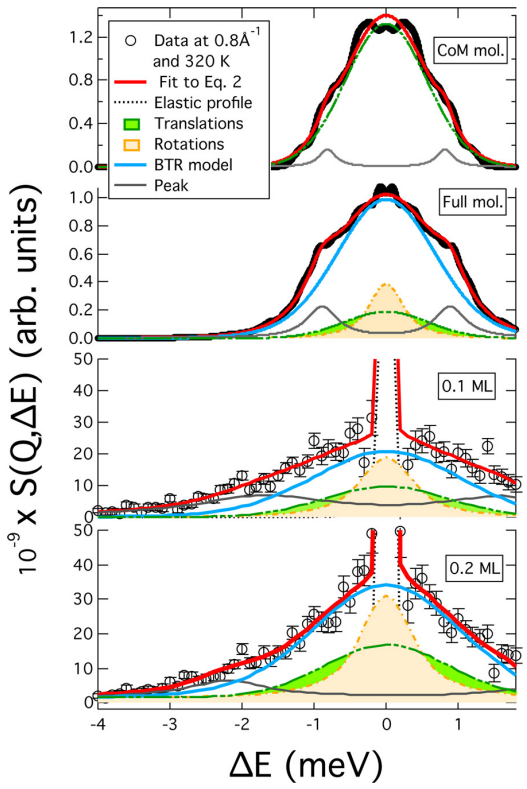

Figure 2. Simulated and experimental scattering functions (SFs) at a momentum transfer of 0.8 Å^{-1} and at 320 K. First and second panels: Simulated SFs extracted from the center of mass (CoM) and the full-molecule trajectories in the MD simulation, respectively. Third and fourth panels: Experimental SFs of 0.1 and 0.2 ML of pyrene/graphite.

$$S_{BTR}(\mathbf{Q}, \Delta E) = S_T(\mathbf{Q}, \Delta E) \otimes S_R(\mathbf{Q}, \Delta E) = \sum_{k=1}^{N_H} [J_0^2(Qa_k)S_T(Q, \Delta E) + 2\sum_{l=1}^{\infty} J_l^2(Qa_k)S_T(Q, \Delta E) \otimes S_R(l, \Delta E)] \quad (3)$$

The ballistic rotational scattering function is a summation of Gaussian profiles $S_R(l,\Delta E)$, whose half width at half-maximum (hwhm) is determined by the angular mean square velocity (by analogy to the translational case) but is independent of the momentum transfer (due to confinement[24,25]). Each term of the sum is weighted by the cylindrical Bessel function $J_l(Qa_k)$ of

DOI: 10.1021/acs.jpclett.6b02305
J. Phys. Chem. Lett. 2016, 7, 5285−5290

the lth order, which takes into account the geometry of the motion. a_k is the radius of the circle on which each scatterer moves when the molecule rotates. In the case of hydrogenated pyrene, $C_{16}H_{10}$, the scattering intensity is dominated by the incoherent scattering cross section of the protons; therefore, k accounts only for the N_H hydrogen atoms in the molecule.[20]

The fit of the experimental data to the model (eq 3) yields an excellent agreement for the values of $\langle v^2 \rangle$ and $\langle \omega^2 \rangle$ predicted by the equipartition theorem for 2D translations and uniaxial rotation: 2.69 Å^2 ps^{-2} and 0.18 ps^{-2}, respectively. The translational and rotational quasi-elastic profiles have a distinct hwhm due to their different time scale: ∼15 ps for a 2π rotation of the molecule versus ∼5 ps for a distance of 8 Å (corresponding to $Q \approx 0.8$ Å^{-1}). The MD simulations show a similar behavior where translations and rotations also display separable time scales. The values obtained for $\langle v^2 \rangle$ and $\langle \omega^2 \rangle$, 1.26 ± 0.02 Å^2 ps^{-2} and 0.075 ± 0.001 ps^{-2} respectively, are smaller than the predictions of the equipartition theorem, but their ratio of 16.8 is in accordance with the theoretical ratio of 13.6, which is determined by the ratio between the mass and the moment of inertia of pyrene. Therefore, we obtain qualitatively the same behavior of the quasi-elastic profile for simulated and experimental data.

The signature of the molecular diffusive regime can also be found in the quasi-elastic broadening Γ,[20] taken as the hwhm of the quasi-elastic profile. Figure 3 shows the quasi-elastic broadenings extracted from the fit of 0.1, 0.2 ML and simulations to eq 2 as a function of coverage, the momentum transfer (panels A and B), and temperature (panel C). (The error in the quasi-elastic broadening is calculated by evaluating eq 2 in the limits of the confidence band of the fitted parameters. The resulting error bar is of the size of the symbol.) It also compares them with the predictions of the BTR model. Panel D shows a scheme of the translational-rotational dynamics of the molecules generated from the MD-simulated trajectories.[26]

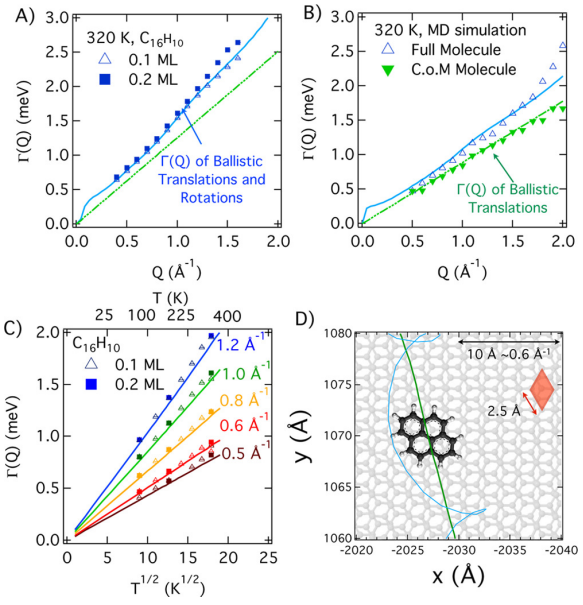

Figure 3. (A) Quasi-elastic broadening versus the momentum transfer, extracted from the fitted profile of the experimental data to eq 2. (B) Quasi-elastic broadenings extracted from the fit to eq 2 of the simulated SF. (C) Experimental quasi-elastic broadening for 0.1 and 0.2 ML versus the temperature. In all three panels, the solid lines are the prediction for the quasi-elastic broadening of the BTR model. (D) Schematic representation of the dynamics of the molecule as observed in the MD simulation;[26] with a green line, we represent the center of mass motion, and with a blue line, we represent the trajectory of one of the protons of the molecule. The red area represents the graphite unit cell.

We observe the following: (i) The quasi-elastic broadening is independent of coverage, in the entire momentum transfer range (panel A) and also in a very wide thermal range (panel C). (ii) Panel A shows how rotations deviate the quasi-elastic broadening dependence on Q from the linear law. (iii) Panel C confirms that the quasi-elastic broadening is proportional to $\sqrt{T}$. Thus we conclude that the main part of the quasi-elastic intensity comes from the ballistic translations and rotations of the pyrene molecules on the surface and is well-reproduced by the BTR model. Panel B displays the quasi-elastic broadenings extracted from the fit of the MD-simulated scattering functions to eq 2. Qualitatively, the MD simulations deliver a picture of the diffusive behavior of a single pyrene molecule matching the experimental observations. The CoM of the molecule follows a linear law of the momentum transfer, as expected for ballistic translations, while the total quasi-elastic broadening (calculated from the trajectories of the full molecule) deviates from the linear law of Q and follows the BTR model. Note that for the MD simulations the agreement with the model is achieved by considering either an effective mass and an effective momentum of inertia, which are larger than the real values of the pyrene molecule, or an effective temperature that is below 320 K.

Finally, we consider several possibilities for the origin of the inelastic feature in the quasi-elastic spectrum of pyrene. The inelastic feature may be caused by the low-energy phonons of graphite along the [0001] direction,[27] which are observed due to the misalignment of graphite crystallites in the Papyex substrate.[28] We have also explored the effect of molecular tumbling (librations around the x or y axes resulting in a motion along the z axis). DFT calculations provide a potential well for the tilting of pyrene with respect to the substrate plane (see the Supporting Information). From the quadratic part of the well, we estimate the frequency of an oscillatory motion along the z axis, whose ground energy is $\Delta E = \hbar\omega/2 = 0.4$ meV. Another possibility is external vibrations of the whole molecule with respect to the surface, which can also give rise to vibrations within this energy range as observed on metal substrates.[29]

In summary, we have studied the diffusive behavior of pyrene adsorbed on exfoliated graphite using quasi-elastic neutron scattering over a large thermal range (80 up to 320 K) and for a coverage of 0.1 and 0.2 ML. The dependency of the quasi-elastic signal on energy, momentum transfer, coverage, and temperature suggests that pyrene diffuses ballistically on the basal plane of graphite. The comparison with the Brownian diffusion observed for benzene under equivalent experimental conditions brings a strong support for the description of friction processes in PAH/graphite systems as a result of molecular collisions: We observe how surface friction vanishes at strong dilution.

To fully characterize the ballistic diffusive regime of the pyrene molecule on the basal plane of graphite, we have developed a new model (BTR) to identify the experimental signature of friction free-translations and rotations. DFT calculations complement the interpretation of the experimental

DOI: 10.1021/acs.jpclett.6b02305
J. Phys. Chem. Lett. 2016, 7, 5285−5290

data by providing a very low energy barrier for diffusion of 11 meV and a potential well for the tumbling of the molecule on the substrate. Finally, MD simulations of a single pyrene molecule on graphite qualitatively reproduce the experimental observations and allow us to separate the purely translational part from the rotational part of the scattering function.

Thus the study of PAH on graphitic surfaces represents a wide territory for the investigation of different diffusive motions. The present work leaves several open questions that we hope will encourage further studies of the surface dynamics of weakly physisorbed systems: The role of tumbling in the friction dissipation process of PAH's kinetic energy is still an open issue. Moreover, measurements of even larger PAH such as coronene could provide a deep insight into the role of size and rotations in the diffusion of PAH on graphite.

EXPERIMENTAL PROCEDURE

The measurements were performed at the IN6 time-of-flight spectrometer of the ILL. The incoming neutron wavelengths was set to 5.12 Å with an energy resolutions at full width at half-maximum of 70 μeV. The neutron scattering signal of the adsorbate molecules was enhanced by using Papyex exfoliated graphite substrates (grade N998, >99.8% C, Carbone Lorraine), which have a high specific surface area on the order of 23 m^2 g^{-1} [28] and a preferential orientation of the graphite crystallites with their basal plane parallel to the scattering plane (in-plane scattering geometry).[28,30] In addition, the coherent length of the crystallites extracted from the X-ray diffraction pattern is, on average, 600 Å.[28] Hence we expect the impact of edges and defects to be negligible for the diffusion process given that the pyrene mean free path is of 10 Å. The specific surface area of the samples was verified by the Brunauer–Emmett–Teller (BET) nitrogen adsorption isotherms. We used liquid He cryostats as sample environment to control the temperature within the range of 1.7–320 K. We have performed measurements of 0.1 and 0.2 ML pyrene in the thermal range of 80 to 320 K and of 0.2 ML of benzene at 60 and 140 K. In addition, we have also measured the scattering function of the clean graphite substrate (before adsorption) as reference for substrate contributions, and the resolution function of the instrument using a sample of vanadium with the same geometry as the actual sample.

ASSOCIATED CONTENT

Supporting Information

The Supporting Information is available free of charge on the ACS Publications website at DOI: 10.1021/acs.jpclett.6b02305.

Details of the sample preparation, the MD simulations, and the DFT calculations; description of the ballistic translational-rotational analytical model, the fit of the experimental data, and the MD simulated trajectories; results of the DFT calculations. (PDF)

AUTHOR INFORMATION

Corresponding Author

*E-mail: ic314@cam.ac.uk. Tel: +44 (0)1223 337279

ORCID

Irene Calvo-Almazán: 0000-0002-3448-9831

Notes

The authors declare no competing financial interest.

ACKNOWLEDGMENTS

I.C.-A. is grateful to the Ramón Areces foundation for the funding of her postdoctoral research position. She is also very grateful to Dr. W. Allison, Dr. N. Avidor, and Dr. M. A. Gonzalez for many helpful discussions. M.S. thanks the U.K.'s HEC Materials Chemistry Consortium, which is funded by EPSRC (EP/L000202); this work used the ARCHER U.K. National Supercomputing Service. E.B. acknowledges financial support by the graduate college of the Université de Grenoble (France) and A.T. thanks the FWF (Austrian Science Fund) for financial support within the project J3479-N20. S.M.-A. acknowledges the funding from the project FIS2014-52172-C2-1-P, from Ministerio de Economia y Competitividad (Spain). We acknowledge the generous provision of neutron beam time at ILL, the support by technicians, and the CS laboratory where the MD simulations have been carried out.

REFERENCES

(1) Barreiro, A.; Rurali, R.; Hernández, E. R.; Moser, J.; Pichler, T.; Forró, L.; Bachtold, A. Subnanometer Motion of Cargoes Driven by Thermal Gradients Along Carbon Nanotubes. *Science* **2008**, *320*, 775–778.

(2) Scharf, T.; Prasad, S. Solid Lubricants: a Review. *J. Mater. Sci.* **2013**, *48*, 511–531.

(3) Krim, J. Friction and Energy Dissipation Mechanisms in Adsorbed Molecules and Molecularly Thin Films. *Adv. Phys.* **2012**, *61*, 155–323.

(4) Browne, W. R.; Feringa, B. L. Making Molecular Machines Work. *Nat. Nanotechnol.* **2006**, *1*, 25–35.

(5) Persson, B. N. J. *Sliding Friction. Physical Principles and Applications*, 2nd ed.; Springer: Berlin, 2000.

(6) Zheng, Q.; Liu, Z. Experimental Advances in Superlubricity. *Friction* **2014**, *2*, 182–192.

(7) Legoas, S. B.; Giro, R.; Galvão, D. S. Molecular Dynamics Simulations of C60 Nanobearings. *Chem. Phys. Lett.* **2004**, *386*, 425–429.

(8) Miura, K.; Kamiya, S.; Sasaki, N. C-60 Molecular Bearings. *Phys. Rev. Lett.* **2003**, *90*, 055509–4.

(9) Guerra, R.; Tartaglino, U.; Vanossi, A.; Tosatti, E. Ballistic Nanofriction. *Nat. Mater.* **2010**, *9*, 634–637.

(10) Dienwiebel, M.; Verhoeven, G. S.; Pradeep, N.; Frenken, J. W. M.; Heimberg, J. A.; Zandbergen, H. W. Superlubricity of Graphite. *Phys. Rev. Lett.* **2004**, *92*, 126101–4.

(11) Lebedeva, I. V.; Knizhnik, A. A.; Popov, A. M.; Ershova, O. V.; Lozovik, Y. E.; Potapkin, B. V. Diffusion and Drift of Graphene Flake on Graphite Surface. *J. Chem. Phys.* **2011**, *134*, 104505–14.

(12) Verhoeven, G. S.; Dienwiebel, M.; Frenken, J. W. M. Model Calculations of Superlubricity of Graphite. *Phys. Rev. B: Condens. Matter Mater. Phys.* **2004**, *70*, 165418–10.

(13) Yang, J.; Liu, Z.; Grey, F.; Xu, Z.; Li, X.; Liu, Y.; Urbakh, M.; Cheng, Y.; Zheng, Q. Observation of High-Speed Microscale Superlubricity in Graphite. *Phys. Rev. Lett.* **2013**, *110*, 255504–5.

(14) Vernov, A.; Steele, W. A. Computer Simulations of Benzene Adsorbed on Graphite. 1. 85 K. *Langmuir* **1991**, *7*, 3110–3117.

(15) Vernov, A.; Steele, W. A. Computer Simulations of Benzene Adsorbed on Graphite. 2. 298 K. *Langmuir* **1991**, *7*, 2817–2820.

(16) Hedgeland, H.; Fouquet, P.; Jardine, A. P.; Alexandrowicz, G.; Allison, W.; Ellis, J. Measurement of Single Molecule Frictional Dissipation in a Prototypical Nanoscale System. *Nat. Phys.* **2009**, *5*, 561–564.

(17) Jardine, A. P.; Hedgeland, H.; Alexandrowicz, G.; Allison, W.; Ellis, J. Helium-3 Spin-Echo: Principles and Application to Dynamics at Surfaces. *Prog. Surf. Sci.* **2009**, *84*, 323–379.

(18) Calvo-Almazán, I.; Bahn, E.; Koza, M.; Zbiri, M.; Maccarini, M.; Telling, M.; Miret-Artés, S.; Fouquet, P. Benzene Diffusion on Graphite Described by a Rough Hard Disk Model. *Carbon* **2014**, *79*, 183–191.

DOI: 10.1021/acs.jpclett.6b02305
J. Phys. Chem. Lett. 2016, 7, 5285–5290

(19) Alexandrowicz, G.; Jardine, A.; Fouquet, P.; Dworski, S.; Allison, W.; Ellis, J. Observation of Microscopic CO Dynamics on Cu(001) Using He-3 Spin-Echo Spectroscopy. *Phys. Rev. Lett.* **2004**, *93*, 156103−4.
(20) Bée, M. *Quasielastic Neutron Scattering*; Adam Hilger: Bristol, U.K., 1988.
(21) Fouquet, P.; Calvo-Almazán, I.; Koza, M.; Tamtögl, A. *Diffusion of Pyrene Molecules: the Transition to Ballistic Diffusion*; Institut Laue-Langevin (ILL), 2015. DOI: 10.5291/ILL-DATA.7-05-440.
(22) Bardi, U.; Magnanelli, S.; Rovida, G. LEED Study of Benzene and Naphthalene Monolayers Adsorbed on the Basal Plane of Graphite. *Langmuir* **1987**, *3*, 159−163.
(23) Martínez-Casado, R.; Vega, J. L.; Sanz, A. S.; Miret-Artes, S. Quasi-Elastic Peak Lineshapes in Adsorbate Diffusion on Nearly Flat Lurfaces at Low Coverages: the Motional Narrowing Effect in Xe on Pt(111). *J. Phys.: Condens. Matter* **2007**, *19*, 176006.
(24) Dianoux, A. J.; Volino, F.; Hervet, H. Incoherent Scattering Law for Neutron Quasi-Elastic Scattering in Liquid Crystals. *Mol. Phys.* **1975**, *30*, 1181−1194.
(25) Volino, F.; Dianoux, A. Neutron Incoherent Scattering Law for Diffusion in a Potential of Spherical Symmetry: General Formalism and Application to Diffusion Inside a Sphere. *Mol. Phys.* **1980**, *41*, 271−279.
(26) *Jmol: an open-source Java viewer for chemical structures in 3D*. http://www.jmol.org/.
(27) Wirtz, L.; Rubio, A. The Phonon Dispersion of Graphite Revisited. *Solid State Commun.* **2004**, *131*, 141−152.
(28) Gilbert, E. P.; Reynolds, P. A.; White, J. W. Characterisation of a Basal-Plane-Oriented Graphite. *J. Chem. Soc., Faraday Trans.* **1998**, *94*, 1861−1868.
(29) Witte, G. Low Frequency Vibrational Modes of Adsorbates. *Surf. Sci.* **2002**, *502*−*503*, 405−416.
(30) Bockel, C.; Coulomb, J.; Dupont-Pavlovsky, N. Comparison of the Adsorptive Properties of Papyex and Uncompressed Exfoliated Graphite. *Surf. Sci.* **1982**, *116*, 369−379.

DOI: 10.1021/acs.jpclett.6b02305
J. Phys. Chem. Lett. 2016, 7, 5285−5290

6.6 Publication F

Bahn, E., Tamtögl, A., Ellis, J., Allison, W. & Fouquet, P. Structure and dynamics investigations of a partially hydrogenated graphene/Ni(111) surface. *Carbon* **114,** 504–510 (2017)

contributions	
funding	A. Tamtögl, W. Allison, J. Ellis, P. Fouquet
preparation / setup	A. Tamtögl
data acquisition	A. Tamtögl, E. Bahn
data analysis	A. Tamtögl, E. Bahn
interpretation	A. Tamtögl, E. Bahn
publication writing	A. Tamtögl, E. Bahn

Carbon 114 (2017) 504–510

Contents lists available at ScienceDirect

Carbon

journal homepage: www.elsevier.com/locate/carbon

Structure and dynamics investigations of a partially hydrogenated graphene/Ni(111) surface

Emanuel Bahn [a, b, *], Anton Tamtögl [b, c, **], John Ellis [b], William Allison [b], Peter Fouquet [a, ***]

[a] Institut Laue-Langevin, 71 Avenue des Martyrs, 38042, Grenoble Cedex 9, France
[b] Cavendish Laboratory, 19 J J Thomson Avenue, Cambridge, CB3 0HE, United Kingdom
[c] Institute of Experimental Physics, Graz University of Technology, Petersgasse 16, 8010, Graz, Austria

ARTICLE INFO

Article history:
Received 22 September 2016
Received in revised form
30 November 2016
Accepted 19 December 2016
Available online 21 December 2016

Keywords:
Graphene
Ni(111)
Hydrogenation
Helium atom scattering

ABSTRACT

Using helium-3 atom scattering, we have studied the adsorption kinetics, the structure and the diffusional dynamics of atomic hydrogen on the surface of a graphene monolayer on Ni(111). Diffraction measurements reveal a 4° rotated rectangular hydrogen overstructure. Hydrogen adsorption and desorption exhibit activation barriers of $E_a = (89\pm7)$ meV and $E_d = (1.8\pm0.2)$ eV, respectively. Helium-3 spin-echo measurements showed no decay of the spatial correlation function (or intermediate scattering function) within the time range of the spectrometer. Hence, we are able to set lower limits for a possible hydrogen surface diffusion rate.

1. Introduction

The existence of an ordered hydrogenation of graphene remains an open question to date although it is of fundamental interest for the tuning of graphene properties [1]. The existence of a stable fully hydrogenated graphene [2,3] layer (graphane) was theoretically predicted almost a decade ago [4], but the synthesis of an almost perfect graphane layer has only recently been reported [5]. A review on graphane and hydrogenated graphene has been published by Pumera et al. [6]. In perfect graphane, one hydrogen atom binds to each carbon atom in an sp^3 hybridised state in an alternating manner, with the hydrogen atom being located either above or below the 2D plane. This leads to four different possible conformations: the chair, boat, twisted-chair, and twisted-boat conformations [6].

The first successful hydrogenation of graphene was reported by Elias et al. [7], where free-standing graphene and graphene on a SiO_2 substrate were used. On top of a substrate, only single-sided hydrogenation of graphene is possible, which has been predicted to create a disordered material [7]. A graphene layer that is fully hydrogenated on one side is being referred to as graphone. Graphone has recently been successfully synthesised from graphene/Ni(111) in a reversible manner [8]. The partial one-sided hydrogenation of a graphene sheet has also recently been achieved by splitting of intercalated water in the graphene/Ni(111) system at room temperature [9].

Before the theoretical discovery of graphane and graphone, the hydrogenation of the graphite(0001) surface had been studied intensely for various interests, such as the mechanism of H_2 formation in the interstellar medium. A disordered formation of hydrogen dimers on graphite was observed at low hydrogen coverage [10,11], while at high coverage the appearance of a triangular structure was observed that occupies only one of the two trigonal sublattices, into which the (0001) surface can be separated [12]. This preferential sublattice adsorption is also found in the hydrogenation of metal supported graphene, where the underlying metal lattice often plays an important role.

Ng et al. have shown that on the weakly interacting metal-graphene systems such as graphene/Ir(111) and graphene/Pt(111) H atoms form a graphone-like structure in the valleys of the moiré

* Corresponding author. Institut Laue-Langevin, 71 Avenue des Martyrs, 38042, Grenoble Cedex 9, France.
** Corresponding author. Institute of Experimental Physics, Graz University of Technology, Petersgasse 16, 8010, Graz, Austria.
*** Corresponding author.
E-mail addresses: em.bahn@gmail.com (E. Bahn), tamtoegl@gmail.com (A. Tamtögl), fouquet@ill.eu (P. Fouquet).

http://dx.doi.org/10.1016/j.carbon.2016.12.055
0008-6223/

pattern [13] which is caused by a lattice mismatch between the graphene and the metal lattice. On the strongly bound and lattice matched graphene/Ni(111) system, however, a blocking of not only one sublattice, but also of nearest neighbour adsorption sites of the same sublattice has been observed [13]. This is in good agreement with our findings, as will be discussed later. On the other hand, on the same graphene/Ni(111) system, a full hydrogenation of one sublattice, and therefore the synthesis of graphone was found in a different study [8]. The major difference between the two studies is that in the latter one, hydrogenation took place at a much lower temperature (170 K compared to 300 K).

On graphene/SiC, dimer formation at low coverage and disordered cluster formation at high coverage have been observed. In contrast to the graphite(0001) surface, hydrogen monomers were also found on graphene/SiC, suggesting a stronger binding to the surface in this case [14,15]. On graphene/Cu(111), a structural arrangement has been observed by scanning tunnelling microscopy (STM) [1], where three different configurations were found, all with a preference to sublattice adsorption. Such a sublattice configuration is predicted to cause ferromagnetism in graphene [16]. These effects are linked to the fact that the adsorption of an H atom on a graphene surface creates a distortion in both electron and spin density that exhibits a $(\sqrt{3} \times \sqrt{3})\mathbf{R}30^\circ$ overstructure and that extends over several nm, as shown by ab-initio calculations and STM/atomic-force microscopy (AFM) measurements [17–19].

Directly connected to the question of an ordered hydrogenation is the question if a diffusion of H adatoms on the graphene/Ni(111) surface is in general possible (i.e., if the diffusion barrier is lower than the desorption barrier) and, if possible, at what rates it would occur. On the graphene/Ni(111) surface, density-functional theory (DFT) calculations predict a diffusion barrier of 1.9 eV, which is lower than the desorption barrier for a single H atom of 2.25 eV [8]. Quantum transition-state theory (TST) calculations predict H atom diffusion on a free-standing graphene surface with a diffusion barrier of 0.71 eV [20]. DFT calculations predict a diffusion barrier of 1.25 eV for single H atoms, but only 0.46 eV for an H atom in the vicinity of a second atom [21]. On a graphene bilayer, Kinetic Monte Carlo (KMC) calculations predict dimer formation via diffusion and subsequent desorption within a few minutes [22].

Here, we present our findings from helium atom scattering (HAS). Various pristine graphene/metal systems have been studied successfully with HAS previously, where precise values for the surface Debye temperature, electronic corrugation, or possible moiré patterns could be determined [23–29]. Notably, neutral He atom beams with energies in the order of 5–10 meV are perfectly suited to probe H overlayers in an inert, completely non-destructive manner. HAS provides, furthermore, a precise probe for both adsorbate coverage and adsorbate structure due to the very large scattering cross section of surface defects and adsorbed molecules [30]. This allowed us to study both, hydrogen sorption kinetics and structural adsorbate ordering. In addition, the spin-echo technique allowed us to gain information on surface dynamics in a time range from sub-picoseconds to about 1 ns. We made use of this to exclude a diffusion of H atoms over a large time scale.

2. Experimental details

2.1. Hydrogenation of graphene/Ni(111)

All measurements have been performed on the Cambridge helium-3 spin-echo spectrometer (HeSE) [31,32]. We have published the characterisation and growth of the graphene layer on a Ni(111) surface elsewhere [33]. Briefly, the nickel (Ni) (111) single crystal used in the study was a disc with a diameter of 10 mm and a thickness of 1 mm. The crystal was mounted on a sample holder, which can be heated using radiative heating from a filament on the backside of the crystal or cooled down to 100 K using liquid nitrogen or 45 K using liquid helium, respectively. The sample temperature was measured using a chromel-alumel thermocouple. Prior to the measurements, the surface was cleaned by Ar^+ sputtering and annealing at 870 K. A monolayer of graphene on Ni(111) was grown by dosing ethene (C_2H_4) while heating the Ni crystal (730 K) over several hours.

In a series of experiments, the graphene/Ni(111) sample was heated to different temperatures and hydrogen gas was injected into the vacuum chamber using a microcapillary array beam doser at a distance of 50 mm to the sample. A cracking filament (4 A, 1 V DC) was used to produce atomic hydrogen. A mass spectrometer was routinely used during all measurements to exclude possible contaminations of the chamber.

We studied the hydrogen adsorption kinetics by monitoring the attenuation of the specular helium-scattering signal during hydrogenation of the graphene surface. Adsorption was monitored at 400–700 K at a dosing pressure at the surface of $3 \cdot 10^{-6}$ mbar. Subsequently, isothermal desorption was monitored at different temperatures using the same approach.

2.2. Diffraction and spin-echo measurements

After a maximum possible hydrogenation of the graphene surface (confirmed by a maximum attenuation of the specular scattering signal), helium diffraction studies were performed in the fixed 44.4° source – detector scattering geometry of the HeSE apparatus. The surface temperature of 400 K was chosen because a contamination through intercalation at defect sites cannot be ruled out at room temperature, although the graphene/Ni(111) surface is highly inert. In the case of HAS, the momentum transfer $\Delta\mathbf{k}$ can be separated into a component parallel to the surface and perpendicular to the surface (designated by subscript z): $\Delta\mathbf{k} = (\Delta\mathbf{K}, \Delta k_z)$. For a diffraction scan the momentum transfer parallel to the surface, given by $|\Delta\mathbf{K}| = |\mathbf{k_i}|(\sin(\gamma_f) - \sin(\gamma_i))$, is varied by changing the incident angle γ_i. Here, $\mathbf{k_i}$ is the incident wave vector and γ_i and γ_f are the incident and final angle with respect to the surface normal, respectively.

Helium spin-echo measurements were subsequently performed in the same set-up at temperatures of 400, 500 and 600 K, respectively. At 500 and 600 K, a constant H overpressure was applied to ensure a constant surface coverage despite desorption. In spin-echo spectroscopy the intermediate scattering function (ISF), $I(\Delta K, t)$, is directly measured in form of a polarisation amplitude [34]. Structural reconfigurations of the surface from e.g. adsorbate diffusion cause a decay of $I(\Delta K, t)$ over the spin-echo time, t. For simple diffusional processes this decay bears the shape of an exponential decay [35].

3. Results and discussion

3.1. Isothermal hydrogen adsorption

Adsorption measurements were performed by monitoring the specularly reflected helium signal in real time while exposing the graphene surface to a constant partial pressure of atomic hydrogen, that had been dissociated by a cracking filament. This was repeated at different surface temperatures in the range 400–700 K. Adsorption was observed up to temperatures below 600 K, above which an adsorption-desorption equilibrium was rapidly reached and thus no substantial scattering-signal attenuation occurred.

Fig. 1 shows the specularly reflected helium-scattering signal during adsorption of atomic hydrogen on the graphene/Ni(111) surface for three different temperatures: 400 K, 500 K, and 550 K. In

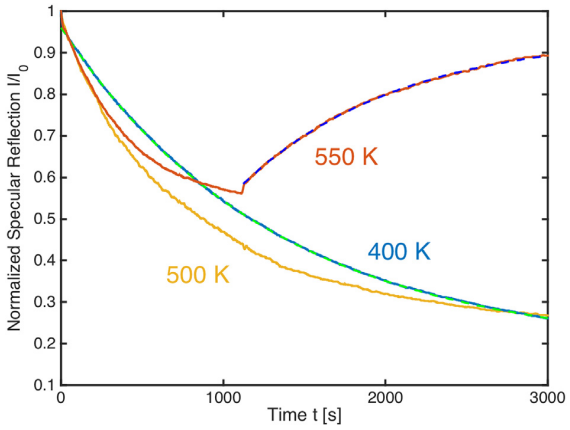

Fig. 1. Normalised specular helium-scattering signal I/I_0 as a function of time during exposure of the graphene/Ni(111) surface to atomic hydrogen in the temperature range 400–550 K. Green dashed line: exponential decay fitted to the scattering signal at 400 K during adsorption; blue dashed line: exponential recovery fitted to the scattering signal at 550 K during desorption (the hydrogen overpressure was turned off after about 1100 s). Instant jumps of the scattering signal appear at the start of dosing (0 s) and after the dosing has been stopped (1100 s) due to attenuation of the helium beam from ambient hydrogen gas. (A colour version of this figure can be viewed online.)

this range, a single exponential decay of the scattering signal was observed, as shown for the 400 K data by a dashed green line. The perfect exponential behaviour indicates a lack of reorientation of adsorbed atoms due to attractive or repulsive interaction with other adatoms, resulting in a slower-than-exponential or a faster-than-exponential decay, respectively [36].

In contrast to the high temperature adsorption of atomic hydrogen, dosing molecular hydrogen through a microcapillary array beam doser at surface temperatures above 100 K does not give rise to any changes of the specularly reflected He signal. This indicates the total lack of adsorbed molecular hydrogen on the graphene/Ni(111) surface. Only upon cooling the surface to temperatures between 45 and 80 K a significant change in the specular helium reflection was observed. In subsequent diffraction scans no additional diffraction peaks were observed for molecular hydrogen adsorbed on graphene/Ni(111). Hence we can exclude the adsorption of molecular hydrogen at temperatures above 100 K. The graphene/Ni(111) surface seems to be largely inert with respect to the adsorption of molecular hydrogen and H_2 needs to be predissociated before adsorption at higher temperatures occurs.

Since we have no absolute calibration of the cracking filament efficiency, we cannot deduce the flux of atomic hydrogen to the surface from the monitored H_2 background pressure. We therefore have to rely on existing information on the helium scattering cross section from single H atoms in order to relate the specularly reflected signal to a surface coverage. The helium scattering cross section Σ of H on transition metal and semimetal surfaces is typically around $10-12$ Å^2 [36–38]. Since Σ is comparable to the graphene/Ni(111) unit cell size (5.4 Å^2), we expect the effect of overlap to be negligible. Indeed, all measured H adsorption isotherms exhibit the shape of an exponential decay over time at constant partial H pressure, as would be expected from the Langmuir adsorption model where adsorption is limited to one monolayer, all adsorption sites are equivalent and only one adparticle can reside in an adsorption site. We observed the highest attenuation of about 80% at 400 K, where we expect desorption to be negligible. Assuming an approximative scattering cross section of 11 Å^2, this would correspond to one H atom per 2–3 graphene unit cells or an H/C ratio of about 20%. The fact that the adsorption curves at higher temperature (500 K and 550 K) exhibit a slightly steeper initial slope with respect to the curve at 400 K indicates that there exists a small activation energy for the adsorption of atomic hydrogen. Fig. 2 shows the rates of exponential decay of the specularly reflected signal during adsorption as a function of the inverse temperature in an Arrhenius plot. The errorbars indicate an approximative relative statistical error of 8% which was obtained by comparing repeated measurements. We expect the source of this error to lie in a gradual misalignment of the sample with respect to specular and/or in a fluctuating efficiency of the hydrogen cracking filament. The linear dependence indicates an activation barrier to adsorption. From the slope of a fitted straight line we can deduce an adsorption barrier, $E_a = (89\pm7)$ meV. DFT calculations on free-standing graphene and graphite predict an adsorption barrier for a single H atom of 0.14 eV [19], 0.2 eV [39,40], 0.25 eV [41] and a reduced barrier down to 0 eV, when the adsorption happens in the neighbourhood of an adsorbed H atom and on the same sublattice, since local magnetization reduces the adsorption barrier [19,41]. Our observation of a relatively low adsorption barrier might therefore hint towards a preferential sublattice adsorption.

We subsequently monitored isothermal desorption from the surface by monitoring the recovery of the specular helium-scattering signal from a covered surface at different constant surface temperatures. In the range 500–600 K, rapid desorption from the covered surface was observed in the form of an exponential recovery of the scattering-signal. Fig. 1 shows the specular scattering signal recovery during isothermal desorption at 550 K (hydrogen dosing was switched off after $\simeq$1100 s) together with a fitted exponential curve, shown by a blue dashed line. Due to gradual misalignment of the sample away from the specular position over time (which stems from thermal expansion of the sample environment at elevated temperatures), the specular signal does not recover entirely to its initial value. Re-aligning the crystal to the specular reflection condition after the measurement restored the original intensity of the clean surface. Since this behaviour does not cause significant changes of the observed decay rates we did not apply any corrections.

With respect to conventional temperature programmed desorption (TPD) this method has the advantage that it is very sensitive to small changes of the hydrogen coverage due to the large scattering cross section of single adsorbates on a surface. Conventional TPD is often limited to studies of D^2 adsorption/

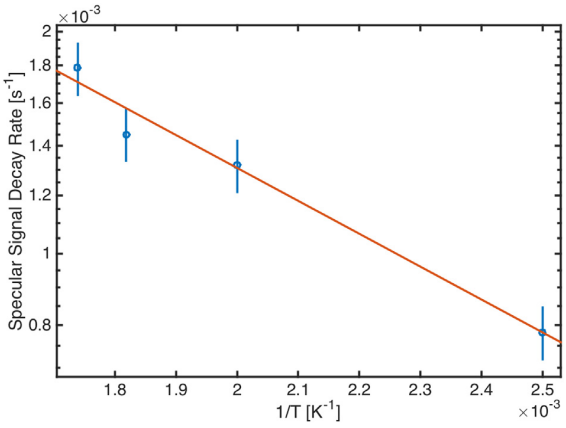

Fig. 2. Arrhenius plot of the specular scattering-signal decay rate during isothermal hydrogen adsorption versus inverse temperature. The slope of the linear fit returns an adsorption barrier $E_a = (89\pm7)$ meV. (A colour version of this figure can be viewed online.)

desorption since there is typically always a rather high amount of H_2 in the residual gas and the mass of D_2 allows a better distinction from the background. Fig. 3 shows an Arrhenius plot of the isothermal hydrogen desorption rates, obtained by fitting an exponential decay to the specular signal recovery during isothermal desorption. Down to a temperature of about 550 K, a straight line can be fitted to the data, which corresponds to activated behaviour for desorption. From this we obtain an activation energy for desorption $E_d = (1.8\pm0.2)$ eV. This agrees well with results from TPD measurements from a hydrogenated graphene/Ni(111) surface, where two desorption processes with 1.0 eV and 1.8 eV desorption barriers were found [8]. Since the lower energy process would lead to rapid desorption already at room temperature, it is probable that we observed only the high-barrier desorption. The authors argue with the support of DFT calculations that the desorption with a barrier of about 1.8 eV is mediated by diffusion towards a meta-dimer as a rate-limiting step, while at higher coverage, diffusion is no longer necessary. TPD spectra from highly covered graphite surfaces found conflicting values for the desorption barrier of hydrogen with 0.6 eV [42] and 1.3–1.6 eV [10], respectively. On the other hand, based on DFT calculations, adsorption energies of 1.5–1.7 eV where found, depending on the number of graphene layers [43], which agrees very well with our experimental findings. Note however, that precaution must be taken when comparing values calculated for free-standing graphene with measurements on graphene/Ni(111) due to the relatively strong binding of graphene to the Ni substrate.

Moreover, DFT calculations predict a barrier of 1.25 eV for diffusion of a single H atom and 2.8 eV for recombination of two neighbouring H atoms [21]. Under ultra-high vacuum conditions, recombinative desorption via the Eley-Rideal mechanism is not possible and it is more likely that individual hydrogen atoms recombine to desorb as molecular hydrogen. Therefore, the question about a possible surface diffusion leading to recombinative desorption arises.

3.2. Structure

We have performed HAS diffraction scans of a fully (up to saturation) hydrogenated graphene/Ni(111) surface along the off-specular angle γ and the azimuthal angle α. Fig. 4 shows the diffraction pattern as a polar plot with γ along the radial axis and α along the angular component ($\alpha = 0$ corresponds to the $\overline{\Gamma M}$ azimuthal direction). Bright diffraction peaks are visible at the same positions as the first order diffraction peaks of the graphene layer and of the underlying Ni(111) surface. In addition, a large number of smaller diffraction peaks have appeared upon hydrogenation.

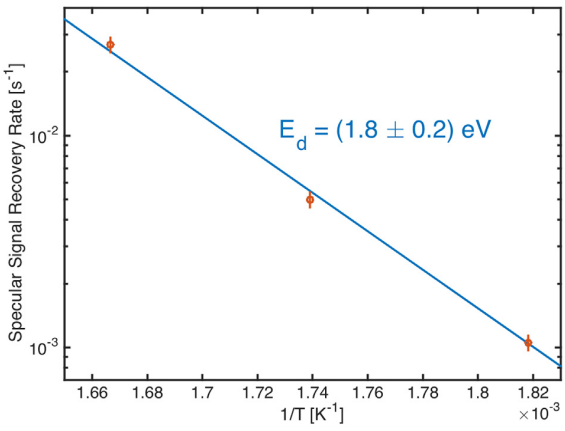

Fig. 3. Arrhenius plot of the specular scattering-signal recovery rate during isothermal hydrogen desorption versus inverse temperature. Errorbars indicate the standard error obtained from the exponential fits of the isothermal decays. The straight line shows a linear fit to the data points. The slope of the linear fit returns an activation energy of desorption $E_d = (1.8\pm0.2)$ meV. (A colour version of this figure can be viewed online.)

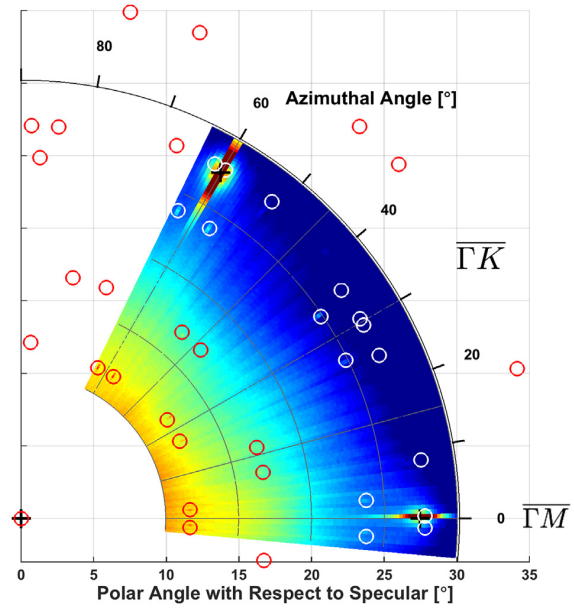

Fig. 4. Two-dimensional colour plot of the helium diffraction signal where warmer colours correspond to a higher scattering intensity. The radial axis corresponds to the angle of incidence, with the specular (mirror) scattering geometry in the centre. The region around the specular position is not shown because of its high intensity. The polar axis corresponds the azimuthal scattering angle, with $\alpha = 0$ corresponding to the $\overline{\Gamma M}$ azimuth. Black crosses: position of graphene/Ni(111) first order diffraction peaks; red/white circles: theoretical positions of the 4° rotated rectangular overstructure; grey dashed arrows: unit cell vectors of the overstructure. Some of the additional peaks due to the hydrogenation are difficult to spot in the contour plot, however, they are definitely present as can be seen in the one-dimensional scans presented in Fig. 5. (A colour version of this figure can be viewed online.)

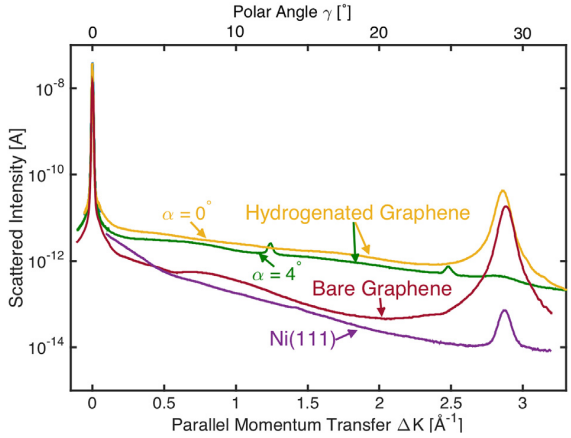

Fig. 5. Comparison of the scattered intensities for hydrogenated graphene/Ni(111), bare graphene/Ni(111) and clean Ni(111) versus momentum transfer ΔK. For better orientation, the off-specular polar scattering angle γ is indicated on the top axis. All scans were taken at a He beam energy of 8 meV. Graphene/Ni(111) and the pristine Ni(111) surface were scanned at 300 K, the hydrogenated graphene at 400 K. (A colour version of this figure can be viewed online.)

Fig. 5 shows a comparison of diffraction scans along γ at the azimuthal angle $\alpha = 0^\circ$ for the Ni(111) surface, the bare, and the hydrogenated graphene surface. In addition, a diffraction scan through the peaks at 4° is shown. For all scans, the scattering signal is plotted against the parallel momentum transfer ΔK (on the bottom axis). The corresponding off-specular scattering angles γ are indicated on the top axis. Note that we did not pursue any corrugation analysis based on close-coupling calculations at this point, since the angular diffraction scans lack bound state resonances which could be used to determine the atom-surface interaction potential [44].

Via the condition of elastic diffractive scattering we could determine the geometry of the hydrogenated graphene surface from the positions of the diffraction peaks: The positions of the bright peaks could either stem from bare graphene or from graphone-like regions, which cause diffraction peaks at the same position [1]. The positions of the smaller peaks are well reproduced by different domains of an $\alpha = \pm 4^\circ$ rotated rectangular superstructure with $a' = (1.98 \pm 0.06) \cdot a = (4.93 \pm 0.15)$ Å and $b' = (1.9 \pm 0.06) \cdot b = (4.73 \pm 0.14)$ Å unit cell size ($a = b = 2.49$ Å are the moduli of the basis vectors of the graphene/Ni(111) unit cell). This structure is surprising since it is much larger than the boat- and chair-conformation. However, on graphene/Ni(111), photoemission spectroscopy measurements have predicted an adsorption barrier that prevents adsorption on neighbouring C atoms on the "on top" sublattice, resulting in a minimum distance between two adsorbed H atoms of $\sqrt{3}a$, assuming that the H atoms adsorb directly on top of the C atoms [13]. This effect could lead to a long-range ordered hydrogenation of the graphene/Ni(111) layer. Two overstructures would be plausible in this picture, a trigonal ($\sqrt{3}$ x$\sqrt{3}$)**R**30° structure and a rectangular $\begin{pmatrix} 2 & 1 \\ 0 & 2 \end{pmatrix}$ structure: the latter is close to what we observe here. Fig. 6 shows an illustration of this rectangular structure (green dots denote the positions of the H atoms), which matches relatively well our observations (green rectangle). For comparison, the graphene unit cell is illustrated by an orange rhombus. Our findings predict a structure that is 14% longer in the $\overline{\Gamma M}$ direction and 5% shorter in the $\overline{\Gamma K}$ direction, compared to the positions of the corresponding C atoms on a pristine graphene/Ni(111) layer. *Ab initio* calculations of the hydrogenation of a free-standing graphene lattice predict a stretching of the C–C bonds by about 5–8% due to a change from sp^2 to sp^3 bonding [4,45]. A change in bond length should thus not be sufficient to explain the observed unit cell length of the overstructure. However, considering the underlying geometry of the graphene lattice, we find the proposed structure to be the only plausible explanation.

The rotation of the observed superstructure by 4° appears somewhat puzzling at first glance. However, rotated graphene structures have also been observed in bilayer graphene [46] and rotations of superstructures along non-symmetry angles have been observed, e.g., for physisorbed noble gas layers on graphite [47–49] and for chemisorbed alkali layers on metal substrates [50–52]. Moreover, graphene grown above 500 °C by chemical vapour deposition on the Ni(111) surface exhibits also rotated domains [53], and since the adsorption energy in the eV range of an H atom is considerably larger than the calculated adsorption energy per C atom in the graphene layer of about 0.16 eV [54], the hydrogenation may cause a reorientation of the graphene layer.

Ab inito calculations would be a helpful tool to test the proposed structure; yet the size of the resulting supercell required for a periodic DFT calculation would be at the border of what is possible in terms of computational feasibility at present. Other possibilities include running a calculation for the hydrogenated graphene

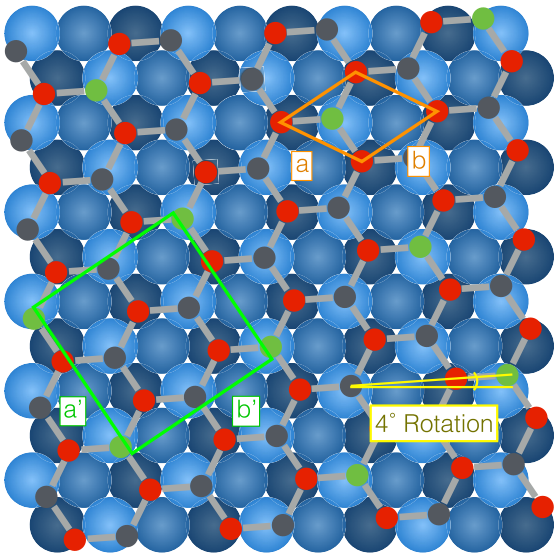

Fig. 6. Illustration of the proposed 4° rotated structure of hydrogenated graphene/Ni(111). Green rectangle: unit cell of observed diffraction pattern; orange rhombus: graphene/Ni(111) unit cell for comparison; Blue spheres in background: Ni(111) surface; Hexagonal structure: graphene layer, 4° rotated but undistorted; green dots: C Atoms favourable for H adsorption; dark red dots: fcc sublattice that is energetically unfavourable for H adsorption; grey dots: C atoms of same sublattice as adsorption sites, but energetically unfavourable as next-nearest neighbours of adsorption sites. The relative position of the graphene layer on-top of the Ni(111) surface is chosen arbitrarily since our diffraction measurements allow no conclusions on this matter. Please note that probable distortions of the graphene layer due to hydrogenation have not been taken into account in this illustration. (A colour version of this figure can be viewed online.)

modelled as a non-periodic graphene island. However, the dimension of the island and the consequent overall offset with the Ni substrate would inevitably be arbitrary and it might be difficult to obtain completely reliable results.

Our proposed rectangular overstructure would correspond to a theoretical H/C ratio of 12.5%. This is much lower than the 20% deduced from the attenuation of the specular reflection. Since diffraction from the rectangular structure is much weaker than diffraction found at the position of the graphene peaks, it seems reasonable to assume that a substantial part of the adsorbed hydrogen is either arranged in a graphone-like geometry or in a disordered manner and is therefore not observable for us via diffraction. (Such a graphone-like structure has been observed by STM e.g. for graphene on copper [1].) This would also explain why the observed H/C ratio is higher than the theoretical ratio of the rectangular structure. An H/C ratio of 16% has been previously observed on GR/Ni(111), which corresponds to a (trigonal) ($\sqrt{3} \times \sqrt{3}$)**R**30° superstructure [13] whereas we did not observe such a trigonal structure. The ratio observed in our study is also much lower than the 50% ratio that was found in an X-ray photoelectron spectroscopy/TPD study of the same system [8]. However, in the latter publication, hydrogenation was performed at low temperature (170 K), while the low coverage saturation was observed after hydrogenation at room temperature.

Unfortunately, we did not perform adsorption or diffraction measurements at such low temperatures since we did not expect to observe any hydrogenation within reasonable times at such low temperatures (extrapolating the signal decay rate to 170 K predicts a characteristic time of adsorption of $\simeq 4.1 \cdot 10^4$ s). The overall picture is thus that of a hydrogenation that depends on both,

surface temperature and coverage, where large overstructures appear at room temperature and low coverage, while at high coverage, a denser structure is likely to form.

3.3. Dynamics

Helium spin-echo studies reveal information about surface diffusion. One of the aims of this study was to gain information about a possible diffusion of the adsorbed H atoms on the graphene lattice. Since the accessible spin-echo time range of the HeSE apparatus is restricted to about 1.2 ns, a time window that is considerably shorter than the expected time scale of H atom diffusion, we can only extrapolate the available data to set a lower limit on the characteristic time τ between jumps of a hydrogen atom.

Spin-echo measurements were performed at 400 K, 500 K and 600 K, respectively, at a momentum transfer $\Delta K = 1$ Å^{-1}. At 500 K and 600 K, a constant overpressure of atomic hydrogen was applied in order to ensure a constant surface coverage of about 0.08 ML during the spin-echo scans, which was deduced by monitoring the specularly reflected scattering signal.

The jump diffusion process is described by the Chudley-Elliott model [55]: The incoherent ISF obtains the form of an exponential decay:

$$I(\Delta\mathbf{K}, t)_{inc} = I_{inc}(\Delta\mathbf{K}, 0)\exp[-\Gamma(\Delta\mathbf{K})t], \quad (1)$$

with the decay rate

$$\Gamma(\Delta\mathbf{K}) = \frac{1}{n\tau}\sum_{\mathbf{l}_j}\left[1 - \exp(-i\Delta\mathbf{K}\cdot\mathbf{l}_j)\right]. \quad (2)$$

Here, $\mathbf{l}_j$ is the vector that connects beginning and end of the jth possible jump. In the geometry of jumps between neighbouring on-top adsorption sites, along the $\overline{\Gamma M}$ direction the decay rate can be approximately given by the form for a hexagonal Bravais lattice:

$$\Gamma(\Delta K) = \frac{1}{3\tau}\left[\sin^2(\Delta K\, l/2) + 2\sin^2(\Delta K\, l/4)\right]. \quad (3)$$

For stability reasons we fitted a linearised model function to the data, using a linear least squares fitting algorithm.

From this we obtained lower bounds for the fitting parameter τ, which is the inverse jump rate, or characteristic time between two jumps of a hydrogen atom. The lower bounds for τ are listed in Table 1, within the corresponding one-sided confidence intervals of 1 σ (84.2%) and 2 σ (97.8%). While at 400 K, we could deduce a lower bound for τ of 75 ns, at 600 K this lower limit is at 4 ns since with increasing temperature the polarisation amplitude experiences a stronger initial drop due to surface phonon processes. We also list the inverse jump rates predicted by path integral molecular dynamics (PIMD) calculations by Herrero et al. [20] for comparison. Our experimental findings are not sufficient to draw further conclusions since the predicted jump times are about two orders of magnitude longer than the observed lower limits, but our findings are in line with present theory.

Table 1
Lower limits for the characteristic time τ between jumps at different temperatures, demanding statistical confidences of 1 and 2 σ. Also listed are the values for τ predicted by PIMD calculations by Herrero et al. [20].

Temperature	400 K	500 K	600 K
Prediction according to [20]	73000 ns	1300 ns	93 ns
84.2% confidence	1000 ns	200 ns	6 ns
97.8% confidence	75 ns	45 ns	4 ns

4. Summary and conclusion

Graphene/Ni(111) was hydrogenated under ultra high vacuum conditions and studied by helium-3 diffraction and spin-echo spectroscopy. By measuring isothermal sorption rates, activation barriers for adsorption, $E_a = (89\pm7)$ meV, and for desorption, $E_d = (1.8\pm0.2)$ eV, were found. Diffraction scans revealed an ordered hydrogenation of the graphene surface creating a 4° rotated rectangular structure. Spin-echo studies allowed us to set lower limits on the jump times τ for hydrogen diffusion at temperatures in the range 400–600 K which are in accordance with PIMD calculations [20].

Acknowledgements

The authors would like to thank R. Weatherup and D. Farías for their advice on the graphene growth procedure as well as M. Sacchi for many useful discussions regarding DFT calculations. This work is part of the Ph.D. project of E. Bahn who would like to thank the Ecole Doctorale de Physique of the Université de Grenoble for funding. A. Tamtögl acknowledges financial support provided by the FWF (Austrian Science Fund) (Grant number: J3479-N20) within the project J3479-N20.

References

[1] C. Lin, Y. Feng, Y. Xiao, M. Dürr, X. Huang, X. Xu, et al., Direct observation of ordered configurations of hydrogen adatoms on graphene, Nano Lett. 15 (2015) 903–908, http://dx.doi.org/10.1021/nl503635x.
[2] K.S. Novoselov, A.K. Geim, S.V. Morozov, D. Jiang, Electric field effect in atomically thin carbon films, Science 306 (2004) 666–669, http://dx.doi.org/10.1126/science.1102896.
[3] A.K. Geim, K.S. Novoselov, The rise of graphene, Nat. Mat. 6 (2007) 183–191, http://dx.doi.org/10.1038/nmat1849.
[4] J.O. Sofo, A.S. Chaudhari, G.D. Barber, Graphane: a two-dimensional hydrocarbon, Phys. Rev. B 75 (2007), http://dx.doi.org/10.1103/PhysRevB.75.153401, 153401–1–4.
[5] Y. Yang, Y. Li, Z. Huang, X. Huang, (c1.04H)n: a nearly perfect pure graphane, Carbon 107 (2016) 154–161, http://dx.doi.org/10.1016/j.carbon.2016.05.066.
[6] M. Pumera, C.H.A. Wong, Graphane and hydrogenated graphene, Chem. Soc. Rev. 42 (2013) 5987–5995, http://dx.doi.org/10.1039/c3cs60132c.
[7] D.C. Elias, R.R. Nair, T. Mohiuddin, S.V. Morozov, Control of graphene's properties by reversible hydrogenation: evidence for graphane, Science 323 (2009) 610–613, http://dx.doi.org/10.1126/science.1092905.
[8] W. Zhao, J. Gebhardt, F. Späth, K. Gotterbarm, C. Gleichweit, H.P. Steinrück, et al., Reversible hydrogenation of graphene on ni(111)-synthesis of "graphone", Chem. Eur. J. 21 (2015) 3347–3358, http://dx.doi.org/10.1002/chem.201404938.
[9] A. Politano, M. Cattelan, D.W. Boukhvalov, D. Campi, A. Cupolillo, S. Agnoli, et al., Unveiling the mechanisms leading to h2 production promoted by water decomposition on epitaxial graphene at room temperature, ACS Nano 10 (4) (2016) 4543–4549, http://dx.doi.org/10.1021/acsnano.6b00554.
[10] L. Hornekær, Ž. Šljivančanin, W. Xu, R. Otero, E. Rauls, I. Stensgaard, et al., Metastable structures and recombination pathways for atomic hydrogen on the graphite (0001) surface, Phys. Rev. Lett. 96 (2006), http://dx.doi.org/10.1103/PhysRevLett.96.156104, 156104–1–4.
[11] L. Hornekær, E. Rauls, W. Xu, Ž. Šljivančanin, R. Otero, I. Stensgaard, et al., Clustering of chemisorbed h(d) atoms on the graphite (0001) surface due to preferential sticking, Phys. Rev. Lett. 97 (2006), http://dx.doi.org/10.1103/PhysRevLett.97.186102, 186102–1–4.
[12] L. Hornekær, W. Xu, R. Otero, E. Lægsgaard, F. Besenbacher, Long range orientation of meta-stable atomic hydrogen adsorbate clusters on the graphite(0001) surface, Chem. Phys. Lett. 446 (2007) 237–242, http://dx.doi.org/10.1016/j.cplett.2007.08.064.
[13] M.L. Ng, R. Balog, L. Hornekær, A.B. Preobrajenski, N.A. Vinogradov, N. Mårtensson, et al., Controlling hydrogenation of graphene on transition metals, J. Phys. Chem. C 114 (2010) 18559–18565, http://dx.doi.org/10.1021/jp106361y.
[14] N.P. Guisinger, G.M. Rutter, J.N. Crain, P.N. First, J.A. Stroscio, Exposure of epitaxial graphene on SiC(0001) to atomic hydrogen, Nano Lett. 9 (2009) 1462–1466, http://dx.doi.org/10.1021/nl803331q.
[15] R. Balog, B. Jørgensen, J.W. Wells, E. Lægsgaard, P. Hofmann, F. Besenbacher, et al., Atomic hydrogen adsorbate structures on graphene, J. Am. Chem. Soc. 131 (2009) 8744–8745, http://dx.doi.org/10.1021/ja902714h.
[16] J. Zhou, Q. Wang, Q. Sun, X.S. Chen, Y. Kawazoe, P. Jena, Ferromagnetism in semihydrogenated graphene sheet, Nano Lett. 9 (2009) 3867–3870, http://dx.doi.org/10.1021/nl9020733.

[17] P. Ruffieux, O. Gröning, P. Schwaller, L. Schlapbach, Hydrogen atoms cause long-range electronic effects on graphite, Phys. Rev. 84 (2000) 4910–4913, http://dx.doi.org/10.1103/PhysRevLett.84.4910.

[18] O.V. Yazyev, L. Helm, Defect-induced magnetism in graphene, Phys. Rev. B 75 (2007), http://dx.doi.org/10.1103/PhysRevB.75.125408, 125408–1–5.

[19] S. Casolo, O.M. Lovvik, R. Martinazzo, Understanding adsorption of hydrogen atoms on graphene, J. Chem. Phys. 130 (2009), http://dx.doi.org/10.1063/1.3072333, 054704–1–10.

[20] C.P. Herrero, Vibrational properties and diffusion of hydrogen on graphene, Phys. Rev. B 79 (2009), http://dx.doi.org/10.1103/PhysRevB.79.115429, 115429–1–8.

[21] Y. Ferro, F. Marinelli, A. Allouche, Density functional theory investigation of the diffusion and recombination of h on a graphite surface, Chem. Phys. Lett. 368 (2003) 609–615, http://dx.doi.org/10.1126/science.1102896.

[22] M. Moaied, J.A. Moreno, M.J. Caturla, F. Ynduráin, Theoretical study of the dynamics of atomic hydrogen adsorbed on graphene multilayers, Phys. Rev. B 91 (2015), http://dx.doi.org/10.1103/PhysRevB.91.155419, 155419–1–8.

[23] B. Borca, S. Barja, M. Garnica, M. Minniti, A. Politano, J.M. Rodriguez-Garc i a, et al., Electronic and geometric corrugation of periodically rippled, self-nanostructured graphene epitaxially grown on ru (0001), New J. Phys. 12 (9) (2010), http://dx.doi.org/10.1088/1367-2630/12/9/093018, 093018–1–15.

[24] A. Politano, B. Borca, M. Minniti, J.J. Hinarejos, Helium reflectivity and debye temperature of graphene grown epitaxially on ru (0001), Phys. Rev. B 84 (2011), http://dx.doi.org/10.1103/PhysRevB.84.035450, 035450–1–6.

[25] K.D. Gibson, S.J. Sibener, Helium atom scattering from graphene grown on rh (111), J. Phys. Chem. C 118 (2014) 29077–29083, http://dx.doi.org/10.1021/jp504024t.

[26] A. Politano, Probing growth dynamics of graphene/ru(0001) and the effects of air exposure by means of helium atom scattering, Surf. Sci. 634 (C) (2015) 44–48, http://dx.doi.org/10.1016/j.susc.2014.10.012.

[27] H. Shichibe, Y. Satake, K. Watanabe, A. Kinjyo, A. Kunihara, Y. Yamada, et al., Probing interlayer interactions between graphene and metal substrates by supersonic rare-gas atom scattering, Phys. Rev. B 91 (2015), http://dx.doi.org/10.1103/PhysRevB.91.155403, 155403–1–8.

[28] A. Al Taleb, H.K. Yu, G. Anemone, D. Farías, A.M. Wodtke, Helium diffraction and acoustic phonons of graphene grown on copper foil, Carbon 95 (2015) 731–737, http://dx.doi.org/10.1016/j.carbon.2015.08.110.

[29] D. Maccariello, A. Al Taleb, F. Calleja, A.L. Vázquez de Parga, P. Perna, J. Camarero, et al., Observation of localized vibrational modes of graphene nanodomes by inelastic atom scattering, Nano Lett. 16 (2016) 2–7, http://dx.doi.org/10.1021/acs.nanolett.5b02887.

[30] D. Farías, K.H. Rieder, Atomic beam diffraction from solid surfaces, Rep. Prog. Phys. 61 (1998) 1575–1664, http://dx.doi.org/10.1088/0034-4885/61/12/001.

[31] A.P. Jardine, G. Alexandrowicz, H. Hedgeland, W. Allison, J. Ellis, Studying the microscopic nature of diffusion with helium-3 spin-echo, Phys. Chem. Chem. Phys. 11 (2009) 3355–3374, http://dx.doi.org/10.1039/b810769f.

[32] P. Fouquet, A.P. Jardine, S. Dworski, G. Alexandrowicz, W. Allison, J. Ellis, Thermal energy [sup 3]he spin-echo spectrometer for ultrahigh resolution surface dynamics measurements, Rev. Sci. Instrum. 76 (2005), http://dx.doi.org/10.1063/1.1896945, 053109–1–13.

[33] A. Tamtögl, E. Bahn, J. Zhu, P. Fouquet, Graphene on ni (111): electronic corrugation and dynamics from helium atom scattering, J. Phys. Chem. C 119 (2015) 25983–25990, http://dx.doi.org/10.1021/acs.jpcc.5b08284.

[34] F. Mezei, Neutron spin echo: a new concept in polarized thermal neutron techniques, Z Phys. 255 (1972) 146–160, http://dx.doi.org/10.1007/BF01394523.

[35] G. Alexandrowicz, A.P. Jardine, Helium spin-echo spectroscopy: studying surface dynamics with ultra-high-energy resolution, J. Phys. Cond. Mat. 19 (2007) 305001–305026, http://dx.doi.org/10.1088/0953-8984/19/30/305001.

[36] G. Comsa, B. Poelsema, Scattering of Thermal Energy Atoms from Disordered Surfaces, vol. 115, Springer, Heidelberg, 1989, http://dx.doi.org/10.1007/BFb0045229 of Springer Tracts in Modern Physics.

[37] B. Poelsema, G. Mechtersheimer, G. Comsa, The interaction of hydrogen with platinum (s) 9 (111) (111) studied with helium beam diffraction, Surf. Sci. 111 (1981) 519–544, http://dx.doi.org/10.1016/0039-6028(81)90406-4.

[38] P. Kraus, A. Tamtögl, M. Mayrhofer-Reinhartshuber, Resonance-enhanced inelastic he-atom scattering from subsurface optical phonons of bi (111), Phys. Rev. B 87 (2013), http://dx.doi.org/10.1103/PhysRevB.87.245433, 245433–1–7.

[39] L. Jeloaica, V. Sidis, Dft investigation of the adsorption of atomic hydrogen on a cluster-model graphite surface, Chem. Phys. Lett. 300 (1999) 157–162, http://dx.doi.org/10.1016/S0009-2614(98)01337-2.

[40] X. Sha, B. Jackson, First-principles study of the structural and energetic properties of h atoms on a graphite (0001) surface, Surf. Sci. 496 (2002) 318–330, http://dx.doi.org/10.1016/S0039-6028(01)01602-8.

[41] Ž. Šljivančanin, E. Rauls, L. Hornekær, W. Xu, F. Besenbacher, B. Hammer, Extended atomic hydrogen dimer configurations on the graphite(0001) surface, J. Chem. Phys. 131 (2009), http://dx.doi.org/10.1063/1.3187941, 084706–1–6.

[42] T. Zecho, A. Güttler, X. Sha, B. Jackson, J. Küppers, Adsorption of hydrogen and deuterium atoms on the (0001) graphite surface, J. Chem. Phys. 117 (2002) 8486–8492, http://dx.doi.org/10.1063/1.1511729.

[43] D.W. Boukhvalov, M.I. Katsnelson, A.I. Lichtenstein, Hydrogen on graphene: electronic structure, total energy, structural distortions and magnetism from first-principles calculations, Phys. Rev. B 77 (2008), http://dx.doi.org/10.1103/PhysRevB.77.035427, 035427–1–7.

[44] M. Mayrhofer-Reinhartshuber, P. Kraus, A. Tamtögl, Helium-surface interaction potential of sb (111) from scattering experiments and close-coupling calculations, Phys. Rev. B 88 (2013), http://dx.doi.org/10.1103/PhysRevB.88.205425, 205425–1–11.

[45] O. Leenaerts, H. Peelaers, A.D. Hernández-Nieves, B. Partoens, First-principles investigation of graphene fluoride and graphane, Phys. Rev. B 82 (2010), http://dx.doi.org/10.1103/PhysRevB.82.195436, 195436–1–6.

[46] R. Zhao, Y. Zhang, T. Gao, Y. Gao, N. Liu, L. Fu, et al., Scanning tunneling microscope observations of non-ab stacking of graphene on ni films, Nano Res. 4 (2011) 712–721, http://dx.doi.org/10.1007/s12274-011-0127-8.

[47] C.G. Shaw, S.C. Fain Jr., M.D. Chinn, Observation of orientational ordering of incommensurate argon monolayers on graphite, Phys. Rev. Lett. 41 (1978) 955–957, http://dx.doi.org/10.1103/PhysRevLett.41.955.

[48] S.C. Fain, M.D. Chinn, R.D. Diehl, Commensurate-incommensurate transition of solid krypton monolayers on graphite, Phys. Rev. B 21 (1980) 4170–4172, http://dx.doi.org/10.1103/PhysRevB.21.4170.

[49] S. Calisti, J. Suzanne, J.A. Venables, A leed study of adsorbed neon on graphite, Surf. Sci. 115 (1982) 455–468, http://dx.doi.org/10.1016/0039-6028(82)90381-8.

[50] D.L. Doering, S. Semancik, Low temperature ordering of sodium overlayers on ru (001), Surf. Sci. 129 (1983) 177–191, http://dx.doi.org/10.1016/0039-6028(83)90101-2.

[51] D.L. Doering, S. Semancik, Orientational ordering in a strongly chemisorbed system: Na on ru (001), Phys. Rev. Lett. 53 (1984) 66–69, http://dx.doi.org/10.1103/PhysRevLett.53.66.

[52] T. Aruga, H. Tochihara, Y. Murata, Rotational epitaxy of chemisorbed k monolayers on cu (001), Phys. Rev. Lett. 52 (1984) 1794–1797, http://dx.doi.org/10.1103/PhysRevLett.52.1794.

[53] C. Africh, R.S. Weatherup, R. Blume, S. Bhardwaj, C. Castellarin-Cudia, A. Knop-Gericke, et al., In situ observations of the atomistic mechanisms of ni catalyzed low temperature graphene growth, ACS Nano 7 (2013) 7901–7912, http://dx.doi.org/10.1021/nn402927q.

[54] F. Bianchini, L.L. Patera, M. Peressi, Atomic scale identification of coexisting graphene structures on ni (111), J. Phys. Chem. Lett. 5 (2014) 467–473, http://dx.doi.org/10.1021/jz402609d.

[55] C.T. Chudley, R.J. Elliott, Neutron scattering from a liquid on a jump diffusion model, Proc. Phys. Soc. 77 (1961) 353–361, http://dx.doi.org/10.1088/0370-1328/77/2/319.

6.7 Publication G

Tamtögl, A., Kraus, P., Avidor, N., Bremholm, M., Hedegaard, E. M. J., Iversen, B. B., Bianchi, M., Hofmann, P., Ellis, J., Allison, W., Benedek, G. & Ernst, W. E. Electron-Phonon Coupling and Surface Debye Temperature of Bi_2Te_3(111) from Helium Atom Scattering. *Phys. Rev. B* **95,** 195401 (2017)

contributions	
funding	A. Tamtögl, W. Allison, J. Ellis, P. Hofmann, W. E. Ernst
sample synthesis	E. M. J. Hedegaard, M. Bremholm, B. B. Iversen
preparation / setup	A. Tamtögl, N. Avidor, M. Bianchi
data acquisition	A. Tamtögl
data analysis	A. Tamtögl, P. Kraus
interpretation	A. Tamtögl, G. Benedek
publication writing	A. Tamtögl, G. Benedek

Tamtögl, A., Kraus, P., Avidor, N., Bremholm, M., Hedegaard, E. M. J., Iversen, B. B., Bianchi, M., Hofmann, P., Ellis, J., Allison, W., Benedek, G. & Ernst, W. E. Electron-Phonon Coupling and Surface Debye Temperature of Bi_2Te_3(111) from Helium Atom Scattering. *Phys. Rev. B* **95,** 195401 (2017)

PHYSICAL REVIEW B **95**, 195401 (2017)

Electron-phonon coupling and surface Debye temperature of $Bi_2Te_3(111)$ from helium atom scattering

Anton Tamtögl,[1,2,*] Patrick Kraus,[2] Nadav Avidor,[1] Martin Bremholm,[3] Ellen M. J. Hedegaard,[3] Bo B. Iversen,[3] Marco Bianchi,[4] Philip Hofmann,[4] John Ellis,[1] William Allison,[1] Giorgio Benedek,[5,6] and Wolfgang E. Ernst[2]

[1]*Cavendish Laboratory, J. J. Thompson Avenue, Cambridge CB3 0HE, United Kingdom*

[2]*Institute of Experimental Physics, Graz University of Technology, 8010 Graz, Austria*

[3]*Center for Materials Crystallography, Department of Chemistry and iNANO, Aarhus University, 8000 Aarhus, Denmark*

[4]*Department of Physics and Astronomy, Interdisciplinary Nanoscience Center (iNANO), Aarhus University, 8000 Aarhus, Denmark*

[5]*Dipartimento di Scienza dei Materiali, Università degli Studi di Milano-Bicocca, 20125 Milano, Italy*

[6]*Donostia International Physics Center (DIPC), University of the Basque Country (EHU-UPV), 20018 Donostia, San Sebastian, Spain*

(Received 1 August 2016; revised manuscript received 11 October 2016; published 4 May 2017)

We have studied the topological insulator $Bi_2Te_3(111)$ by means of helium atom scattering. The average electron-phonon coupling λ of $Bi_2Te_3(111)$ is determined by adapting a recently developed quantum-theoretical derivation of the helium scattering probabilities to the case of degenerate semiconductors. Based on the Debye-Waller attenuation of the elastic diffraction peaks of $Bi_2Te_3(111)$, measured at surface temperatures between 110 and 355 K, we find λ to be in the range of 0.04–0.11. This method allows us to extract a correctly averaged λ and to address the discrepancy between previous studies. The relatively modest value of λ is not surprising even though some individual phonons may provide a larger electron-phonon interaction. Furthermore, the surface Debye temperature of $Bi_2Te_3(111)$ is determined as $\Theta_D = (81 \pm 6)$ K. The electronic surface corrugation was analyzed based on close-coupling calculations. By using a corrugated Morse potential a peak-to-peak corrugation of 9% of the lattice constant is obtained.

DOI: 10.1103/PhysRevB.95.195401

I. INTRODUCTION

Bi_2Te_3 is a layered narrow-gap ($\approx$0.2 eV) semiconductor which is widely studied as a thermoelectric material [1]. The excellent thermoelectric performance of Bi_2Te_3 has been attributed to the details of the electronic structure and a low lattice thermal conductivity similar to ordinary glass. Many recent advances in enhancing the thermoelectric figure of merit are linked with nanoscale phenomena found in bulk samples with nanoscale constituents as well as in nanoscale samples and thin-film devices [2,3].

More recently, Bi_2Te_3 has been classified as a topological insulator [4], a recently discovered class of materials with an insulating bulk electronic structure and protected metallic surface states [5,6]. Surface-dominated transport is a major objective on the way to technical applications of these materials [7], however, the detailed scattering channels for the surface-state electrons may impose constraints for potential applications. In particular, the electron-phonon (e-ph) interaction may introduce a strong scattering mechanism at finite temperatures [8–10]. The e-ph coupling constant λ is a convenient and effective parameter to characterize the strength of interaction between electrons and phonons on these surfaces.

While the e-ph coupling on topological insulator surfaces has been widely studied recently [10–14], conflicting values of λ have been reported for the surface of $Bi_2Te_3(111)$ [9,14,15]. The large variability of the mass-enhancement factor λ from different experimental and theoretical sources depends on the balance of the two kinds of charge carriers, i.e., on the actual position of the Fermi level: If the Fermi level falls into the gap (ordinary semiconductor), surface Dirac states dominate, whereas for a degenerate semiconductor the surface conduction electrons dominate. Even when the Fermi level falls into the gap, the doping for a specific surface can be expected to play an important role as well: While the phase space for scattering can be quite large for a strongly doped sample, it shrinks to nearly zero when the doping is such that the Dirac point is placed at the Fermi level.

We attempt to clarify this discrepancy among the experimental results by applying a different approach which allows us to extract the correctly averaged λ [16]. Our approach is based on helium atom scattering (HAS) from $Bi_2Te_3(111)$, where in the degenerate n-type semiconductor case, the contribution of the surface two-dimensional electron gas (2DEG) overwhelms that of the Dirac states.

He atoms at thermal energies are scattered directly by the surface charge density corrugation rather than the ion cores. In the case of inelastic scattering, this corresponds to a scattering by phonon-induced charge density oscillations. This means in turn that the measured intensity of a phonon mode can be used to infer information about the e-ph coupling strength for a specific phonon [17,18], resulting in a mode-specific λ. Recently Manson *et al.* [16] showed that the Debye-Waller (DW) exponent in atom scattering from a conducting surface can be directly related to the e-ph coupling constant λ. Since the DW exponent contains the sum over all contributing phonon modes, this theory can be used to determine the average e-ph coupling λ.

We use this approach, originally formulated for a 3D electron gas model, in a formulation adapted to the surface of a degenerate semiconductor to extract the e-ph coupling strength from temperature-dependent He atom scattering measurements. Furthermore, we present a study of the surface

*tamtoegl@gmail.com

Debye temperature of $Bi_2Te_3(111)$. Finally, diffraction peak intensities are used to extract the surface electronic corrugation upon scattering of a thermal energy He beam.

II. EXPERIMENTAL DETAILS

All measurements were performed on the Cambridge helium-3 spin-echo apparatus which generates a nearly monochromatic beam of ^{3}He that is scattered off the sample surface in a fixed 44.4° source-target-detector geometry. The detailed setup of the apparatus has been described in greater detail elsewhere [19,20]. The reported measurements were carried out using an incident-beam energy of 8 meV.

The crystal structure of Bi_2Te_3 is rhombohedral, consisting of quintuple layers (QLs) bound to each other through weak van der Waals forces which gives easy access to the (111) surface by cleavage [21]. The (111) cleavage plane is terminated by Te atoms and exhibits a hexagonal structure ($a = 4.386$ Å) [8]. The Bi_2Te_3 single crystals used in the study were attached onto a sample holder using electrically and thermally conductive epoxy. The sample holder was then inserted into the chamber using a load-lock system [22] and cleaved *in situ*. The sample holder can be heated using a radiative heating filament on the backside of the crystal or cooled down to 100 K using liquid nitrogen. The sample temperature was measured using a chromel-alumel thermocouple.

Angle-resolved photoemission spectroscopy (ARPES) data were taken at the SGM-3 beamline of the synchrotron radiation facility ASTRID2 in Aarhus [23]. The combined energy resolution of beamline and analyzer was better than 30 meV, and the experimentally determined angular resolution was better than 0.2°. The sample temperature was 100 K for all ARPES data shown here.

III. RESULTS AND DISCUSSION

A. Helium diffraction from $Bi_2Te_3(111)$

Figure 1 displays the scattered He intensity versus the incident angle ϑ_i on $Bi_2Te_3(111)$ for both high-symmetry directions of the crystal. The crystal was held at 110 K for both measurements and the intensity is shown on a logarithmic scale. The lattice constant as determined from the diffraction peak positions in Fig. 1 is $a = (4.36 \pm 0.02)$ Å. This is in good agreement with the reported values in literature ($a = 4.386$ Å at room temperature [8]) and has also been used for the calculations presented in Sec. III B. The specular peak ($\vartheta_i = \vartheta_f = 22.2°$) in Fig. 1 exhibits a full width at half maximum (FWHM) $= (0.095 \pm 0.005)°$ which corresponds to a width of 0.02 Å^{-1} in terms of the momentum transfer.

In general the width of the specular peak is determined by the angular broadening of the apparatus and the quality of the crystal [24–26]. Hence a measurement of the angular spread in the specular peak provides an estimate of the surface quality. This is possible since the peak broadening is proportional to the average domain size, also known as the surface coherence length. The measured specular width $\Delta\theta_{\text{expt}}$ is a convolution of the angular broadening of the apparatus $\Delta\theta_{\text{app}}$ and the domain size broadening $\Delta\theta_w$ given by $\Delta\theta^2_{\text{expt}} = \Delta\theta^2_w + \Delta\theta^2_{\text{app}}$. The

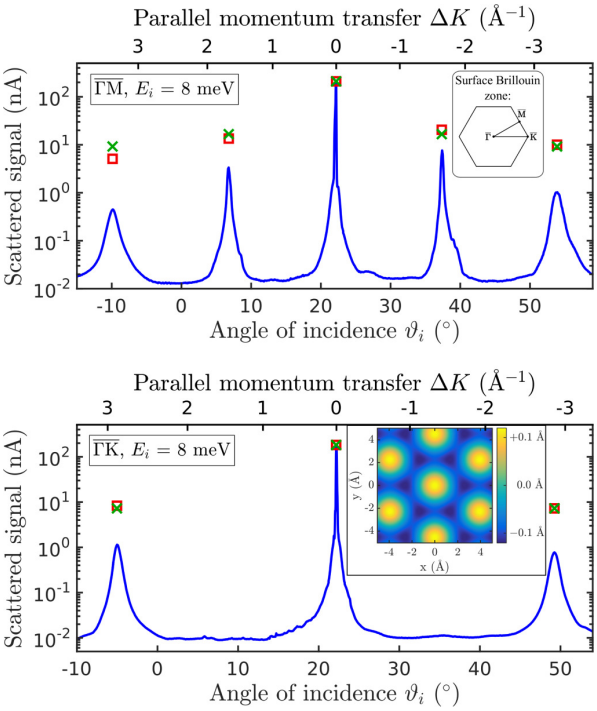

FIG. 1. Scattered He intensities (logarithmic scale) for $Bi_2Te_3(111)$ vs incident angle ϑ_i for the two high-symmetry directions. The upper panel shows a scan along the $\overline{\Gamma M}$ azimuth and the lower panel shows a scan along $\overline{\Gamma K}$. The upper abscissa shows the corresponding parallel momentum transfer. In both cases the crystal was kept at 110 K and an incident beam energy of 8 meV was used. The inset in the upper panel shows the surface Brillouin zone and the scanning directions. The red squares show the peak areas determined from measurements (scaled relative to the specular intensity). They are in good agreement with best-fit results from close-coupling calculations (green crosses), except for a slight asymmetry in the angular scan along $\overline{\Gamma M}$. The inset in the lower panel shows a contour plot of the surface corrugation as obtained by the best-fit results from the close-coupling calculation.

coherence length can then be determined using

$$l_c = \frac{5.54}{\Delta\theta_w \, k_i \, \cos\vartheta_f} \tag{1}$$

with k_i the wave vector of the incoming He beam and ϑ_f the final scattering angle [24–26]. The angular broadening $\Delta\theta_{\text{app}}$ of the He spin-echo apparatus is almost the same size as the experimental broadening. Nevertheless, we can use the experimentally determined broadening $\Delta\theta_{\text{expt}}$ together with (1) to obtain an estimate (lower limit) for the quality of the crystal. The measured FWHM of the specular peak gives rise to an average domain size of at least 1000 Å. This illustrates that topological insulator surfaces can be prepared with an exceptionally good surface quality by *in situ* cleaving and are perfectly suited for atom scattering studies. Compared to previous HAS experiments [15] the FWHM of the specular peak is much smaller (by a factor of approximately 20) which indicates the high quality of the investigated surface.

B. Electronic corrugation

Since He atoms are scattered by the charge distribution at the surface, the shape of this distribution influences the height of the diffraction peaks. The surface charge density as "seen" by He atoms at a certain incident energy can be written as $\xi(\mathbf{R})$ where $\mathbf{R}$ is the lateral position in the surface plane. $\xi(\mathbf{R})$ is referred to as the electronic surface corrugation as it describes a periodically modulated surface with constant total electron density (see the inset in the lower panel of Fig. 1).

The electronic corrugation is usually obtained by calculating the expected diffraction probabilities for a certain $\xi(\mathbf{R})$ and then optimizing $\xi(\mathbf{R})$ to get the best match between the theoretically and experimentally obtained peak heights.

The elastic diffraction peaks of He scattered from $Bi_2Te_3(111)$ were calculated using the exact close-coupling (CC) method [27] which goes beyond the simple hard-wall approximation and has been mainly applied to ionic and metallic surfaces [28]. An exact description of the CC formalism can be found in the literature [27] and its application to a hexagonal semimetal surface is described in Mayrhofer-Reinhartshuber *et al.* [29], so we will only shortly describe the concept: In a purely elastic-scattering scheme, the scattering process can be described by the time-independent Schrödinger equation. The atom-surface interaction potential is considered to be statically corrugated and periodic. Due to the surface periodicity, the interaction potential as well as the wave function can be Fourier expanded. Substitution into the Schrödinger equation results in a set of coupled second-order differential equations which are solved [27,29].

The corrugated Morse potential (CMP) has proven to be a good approximation of the atom-surface interaction potential in the case of semimetal surfaces [29,30] and was applied for a first analysis of $Bi_2Te_3(111)$. The CMP can be written as

$$V(\mathbf{R},z) = D\left[\frac{1}{\upsilon_0}e^{-2\chi(z-\xi(\mathbf{R}))} - 2e^{-\chi z}\right], \qquad (2)$$

with the position $\mathbf{R}$ parallel to the surface and z perpendicular to the surface. Here D is the potential well depth, χ is the stiffness parameter, and υ_0 the surface average over $e^{2\chi\xi(\mathbf{R})}$. By optimizing $\xi(\mathbf{R})$ as described above, a surface corrugation function of the system He-$Bi_2Te_3(111)$ is obtained. Hereby $\xi(\mathbf{R})$ follows the hexagonal periodicity of the surface and can be written using a simple Fourier ansatz where only the amplitude is varied [29] (see the inset in the lower panel of Fig. 1).

The calculated purely elastic intensities are corrected with the DW attenuation using the Debye temperature as determined later in this work before comparison with the experimental results. The comparison of the theoretically evaluated and corrected intensities with the experimental results was performed by determining the experimental peak areas (red squares in Fig. 1). The reason for using the peak areas instead of the peak heights is the need to account for the broadening of the elastic peaks caused by the energy spread of the He beam. Furthermore, additional broadening of the diffraction peaks is caused by the geometry of the apparatus, defects, and the domain size effects of the crystal surface.

Using a well depth $D = 5.8$ meV and stiffness $\chi = 0.88\,\text{Å}^{-1}$ [31] we obtain the best fit to the experimental data for a peak to peak corrugation of 0.39 Å or 9% in terms of the lattice constant, respectively. The results from the CC calculation illustrated by the green crosses in Fig. 1 are in good agreement with the measured peak areas, except for a slight asymmetry in the angular scan along $\overline{\Gamma M}$ which is probably due to a not totally perfect alignment.

An electronic corrugation with a peak to peak height of 9% of the lattice constant is considerably larger than the values found for most low-index metal surfaces [28,32]. The low corrugation on metal surfaces is due to the metallic charge density that smears itself out in order to lower its energy (Smoluchowski effect). This effect seems to be much reduced on the topological insulator $Bi_2Te_3(111)$. Indeed the same has been observed for the single-component semimetal surfaces of Bi(111) and Sb(111) which yielded a similar electronic corrugation [29,30]. Since both are semimetals in the bulk with metallic surface states [33,34] as well as essential components in the group of topological insulators a similar electronic corrugation for $Bi_2Te_3(111)$ may be anticipated. Moreover, the electronic corrugation of $Bi_2Te_3(111)$ is still smaller than the corrugation of semiconductor surfaces that have been reported so far [28,35–38]. Hence the reported value is intermediary between those of metals and semiconductors which may originate in the fact that only the surface state is metallic and the concentration of surface electrons at relatively small momentum. To our knowledge, there are no previous experimental reports on the electronic corrugation of other topological insulator surfaces and previous He atom scattering measurements [15] could not provide an appropriate signal-to-noise ratio for a detailed analysis.

C. Debye-Waller factor in scattering

Upon scattering on a surface, the thermal vibrations of the surface atoms give rise to inelastic-scattering events. This can be observed in the thermal attenuation of the coherent diffraction intensities without changes of the peak shape [28,32]. The decay of the diffraction peak intensities with increasing surface temperature T_S is caused by the increasing vibrational amplitude of the surface oscillators. Its effect on the scattered intensity can be described by the DW factor, $\exp[-2W(T_S)]$, which relates the diffraction intensity $I(T_S)$ of a sample at temperature T_S to the intensity I_0 for the sample at rest by [28,32]

$$I(T_S) = I_0 e^{-2W(T_S)}. \qquad (3)$$

Hence the thermal attenuation of the diffraction peaks provides information about the surface vibrational dynamics.

According to (3), the DW exponent can be determined from a plot of the natural logarithm of the intensity $\ln[I(T_S)/I_0]$ versus the surface temperature T_S. Figure 2 shows the decay of the specular peak intensity versus the surface temperature for $Bi_2Te_3(111)$ which gives rise to a linear decay as expected within the Debye model. Therefore, scans of the scattered intensity versus the incident angle ϑ_i were collected while the crystal temperature was varied between 110 and 355 K. Several of these angular scans are depicted in the inset of Fig. 3 showing the decay of the first order diffraction peak for He scattered from $Bi_2Te_3(111)$ at an incident beam energy $E_i = 8$ meV.

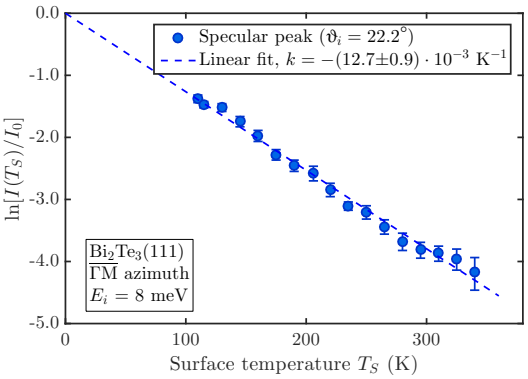

FIG. 2. Decay of the logarithmic specular peak intensity $\ln[I(T_S)]$ vs surface temperature T_S using an incident-beam energy of 8 meV for Bi_2Te_3(111).

The observed linearity within the measured temperature range supports also the use of the high-temperature approximation as applied by Manson *et al.* [16,39], which leads to (8), later used in this work. Only upon a careful inspection of the data shown in Fig. 2 one might anticipate a slight change of the slope at about 300 K, which may be interpreted as due to the switch-on of optical phonons at higher temperatures. However, this trend is still within the uncertainty of the measurements and we can safely employ a linear fit to the present data.

D. Surface Debye temperature of Bi_2Te_3(111)

We consider first the surface Debye temperature classically derived for x-ray and neutron scattering and later adapted to surface scattering. The DW exponent is given by the displacement $\mathbf{u}$ of the lattice atoms out of their equilibrium position and the momentum transfer $\Delta\mathbf{k}$ via

$$2W(T_S) = \langle(\mathbf{u}\cdot\Delta\mathbf{k})^2\rangle_{T_S}, \tag{4}$$

where the outer brackets denote the thermal average. Since a detailed derivation of the DW factor for HAS can be found in the literature [28], it is only briefly outlined below.

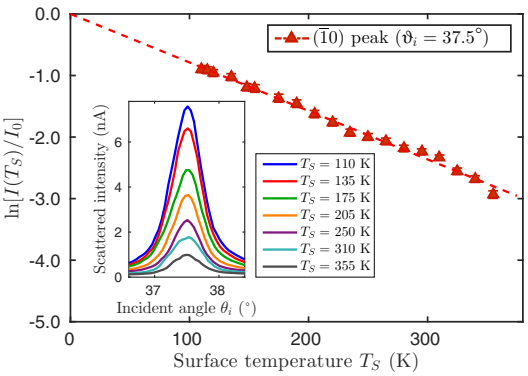

FIG. 3. Decay of the logarithmic peak intensity $\ln[I(T_S)]$ with increasing surface temperature T_S of the first-order diffraction peak along $\overline{\Gamma M}$ measured at an incident-beam energy of 8 meV. In the inset, angular scans over the peak are depicted for a selection of different temperatures.

In the case of HAS, the momentum transfer $\Delta\mathbf{k}$ can be separated into a component parallel to the surface and perpendicular to the surface (designated by subscript z): $\Delta\mathbf{k} = (\Delta\mathbf{K}, \Delta k_z)$. For elastic scattering the momentum transfer parallel to the surface is given by $|\Delta\mathbf{K}| = |\mathbf{k_i}|[\sin(\vartheta_f) - \sin(\vartheta_i)]$ with the incident wave vector $\mathbf{k_i}$ and ϑ_i and ϑ_f the incident and final angle with respect to the surface normal, respectively. Within a reasonable approximation for final angles not too different from the incident angle, (4) reduces to the z component. Replacing the atom displacement with the relation for a classical harmonic oscillator together with the definition of the Debye temperature gives

$$2W(T_S) = \frac{3\hbar^2\Delta k_z^2 T_S}{M k_B \Theta_D^2}, \tag{5}$$

where M is the mass of the surface atom, k_B is the Boltzmann constant, and Θ_D is the surface Debye temperature. Since we are dealing with comparatively small parallel momentum transfers (8 meV beam) in the presented HAS experiments, Eq. (5) can be considered to be approximately correct [32,40] and will form the basis for the following analysis.

However, it should be noted that (5) is not generally valid for atom-surface scattering [41–43] and corrections regarding the surface phonon spectrum [44] and the presence of the attractive atom-surface interaction might be necessary for other kinematic conditions. The influence of the attractive part of the atom-surface potential upon scattering can be considered by the Beeby correction [45]. The perpendicular momentum transfer Δk_z is then replaced by [28]

$$\Delta k_z' = k_i\left[\sqrt{\cos^2(\vartheta_f) + \frac{D}{E_i}} + \sqrt{\cos^2(\vartheta_i) + \frac{D}{E_i}}\right], \tag{6}$$

which assumes an attractive part of the potential with a spatially uniform well of depth D. In the case of the specular geometry, $\vartheta_i = \vartheta_f$ holds and the DW exponent (5) together with the Beeby correction further simplifies to

$$2W(T_S) = \frac{24m[E_i\cos^2(\vartheta_i) + D]T_S}{M k_B \Theta_D^2}, \tag{7}$$

where m is the impinging particle mass and the momentum has been replaced by the incident-beam energy E_i using $k_i^2 = 2mE_i/\hbar^2$.

The surface Debye temperature can then be calculated using the slope of a linear fit of $\ln[I(T_S)/I_0]$ versus the surface temperature T_S. We can again make use of Fig. 2 which shows the decay of the natural logarithm of the specular peak intensity versus the surface temperature for Bi_2Te_3(111). Equation (7), together with (3), is used to determine the surface Debye temperature (Θ_D) from the experimental data. We have used a value of $D = 5.8$ meV for the potential well depth in the present analysis as already mentioned in Sec. III A. (The sensitivity of the Debye temperature Θ_D to changing D by 1 meV is relatively small and falls within the experimental uncertainty of Θ_D.)

One must also assume a value for the mass M which is typically the mass of the crystal atoms since the surface Debye temperature is related to the motion of the ion cores. There is some ambiguity connected with the mass of the surface

scatterer, since this concept was adapted from other scattering techniques and He atoms are scattered by the electron density rather the ion cores as described above [17,46,47]. Due to the e-ph coupling, the surface Debye temperature is associated with charge-density oscillations that are induced by vibrations of the ion cores which will be discussed in Sec. III E. Hence, strictly speaking, when writing the DW exponent in the usual way as a quantity directly proportional to the surface atom mean-square displacements, one needs to consider an effective surface Debye temperature Θ_D^* and a surface atom effective mass M^*, which includes contributions arising from the e-ph interaction. Nevertheless, these simple equations have proven to serve as a good approximation in the case of HAS [24,28,48] and using the mass of a single surface atom is a reasonable choice in most cases [32,48,49].

Using the best-fit result of Fig. 2, a surface Debye temperature $\Theta_D = (81 \pm 6)$ K is obtained for the specular geometry. Here we have set M in (7) equal to the mass of a single Te atom.

In order to confirm the consistency of our measurements we apply the same analysis to the first-order diffraction peak measured along the $\overline{\Gamma M}$ azimuth. A plot of $\ln[I(T_S)]$ versus the surface temperature T_S for the first-order diffraction peak is depicted in Fig. 3. Using the slope of the linear fit, the Debye temperature can be calculated with (5). Since the mirror condition $\vartheta_i = \vartheta_f$ no longer holds, the perpendicular momentum transfer is calculated using (6) with the same parameters for the well depth as before. The surface Debye temperature from the analysis of the first-order diffraction peak intensities is $\Theta_D = (97 \pm 8)$ K. The value is slightly larger but still in reasonable agreement with the Debye temperature determined from the specular peak.

Both values are significantly reduced with respect to the bulk value which has been determined as ≈145 K [50]. This is in good agreement with simple theoretical approximations that estimate a reduction by a factor of $1/\sqrt{2}$ with respect to the bulk value [51]. Furthermore, the surface Debye temperature of $Bi_2Te_3(111)$ is very similar to the surface Debye temperature of Bi(111) [33,52].

E. Electron-phonon coupling from the Debye-Waller factor

As already mentioned above, in the case of HAS the He atoms are not scattered by the vibrating ion cores. Here, inelastic scattering corresponds to a scattering by phonon-induced charge-density oscillations [17,18,53]. These charge-density oscillations are related to the surface Debye temperature via the e-ph coupling.

Upon scattering of a He atom, the probability of creating (or annihilating) a phonon of frequency $\omega_{\mathbf{Q},\nu}$ with parallel wave vector $\mathbf{Q}$ and branch index ν is proportional to the corresponding mode-specific e-ph coupling constant $\lambda_{\mathbf{Q},\nu}$ [16,18]. The DW exponent is then expressed as a sum over all contributing phonon modes where each phonon mode $\mathbf{Q},\nu$ is weighted by the mode-specific $\lambda_{\mathbf{Q},\nu}$. For the simplest case, the specular diffraction peak, Manson *et al.* derived the following DW exponent [16,39]:

$$2W(\mathbf{k_f},\mathbf{k_i}) \cong 4\mathcal{N}(E_F)\,\frac{m}{m_e^*}\,\frac{E_{iz}}{\phi}\,\lambda\,k_B\,T_S \tag{8}$$

for scattering of an incoming He atom with the wave vector $\mathbf{k_i}$ into a final state of wave vector $\mathbf{k_f}$. Here $\mathcal{N}(E_F)$ is the density of electron states per unit surface cell at the Fermi level and ϕ is the work function. m is the mass of the ^{3}He atom, m_e^* is the electron effective mass, and the mass enhancement factor λ expresses now the total e-ph coupling strength. E_{iz} is the beam energy E_i normal to the surface ($E_{iz} = E_i \cos\vartheta_i$) and k_B is the Boltzmann constant. As explained above, the normal incident energy E_{iz} needs to include the Beeby correction, i.e., to be replaced by $E_{iz}' = E_{iz} + D$.

As appears from (3) and (8), the e-ph coupling constant λ can be directly obtained from the temperature dependence of the HAS specular intensity I using the slope determined from the DW plot [Fig. 2, $-\Delta\ln(I/I_0)/\Delta T_S = \ln(I_0/I)/T_S$]:

$$\lambda_{\mathrm{HAS}} \cong \frac{1}{4\mathcal{N}(E_F)}\,\frac{m_e^*}{m}\,\frac{\phi}{k_B\,E_{iz}}\,\frac{\ln(I_0/I)}{T_S}. \tag{9}$$

This expression has been derived in [16,39] for conducting surfaces and shown to provide for the surfaces of ordinary metals and semimetals values of λ in agreement with those known from other sources.

When applied to the surface of a *degenerate* semiconductor with the Fermi level within the conduction band (as in the present case according to [3,21,54]) one has to consider that the phonon-induced modulation of the surface charge density only involves electrons near the surface within the Thomas-Fermi screening length (TFSL), $k_0^{-1} = (2\epsilon E_F/3e^2 n_0)^{1/2}$, where $\epsilon = \epsilon_r\epsilon_0$, is the static dielectric constant, e is the electron charge, and n_0 is the carrier density in the conduction band [55]. $\mathcal{N}(E_F)$ is then written as $\mathcal{N}(E_F) = 3n_0A_c/2E_Fk_0$ where A_c is the surface unit-cell area, and the Fermi energy E_F is referred to the conduction-band minimum. With the substitutions $n_0 = k_{F\parallel}^2 k_{F\perp}/3\pi^2$, valid for an anisotropic 3D free-electron gas, where $k_{F\parallel}$ and $k_{F\perp}$ are the Fermi wave vectors of the conduction electrons parallel and normal to the surface, and $E_F = \hbar^2 k_{F\parallel}^2/2m_e^*$ it is found that

$$\mathcal{N}(E_F) = \frac{m_e^* A_c}{\pi\hbar^2}\,\frac{k_{F\perp}}{\pi k_0}. \tag{10}$$

The first factor is easily recognized as the 2DEG Fermi-level density of states referred to the surface unit cell. As to the second factor, since in n-Bi_2Te_3 and similar materials ϵ is very large [e.g., $\epsilon_r = 290$ in n-$Bi_2Te_3(111)$ [56]], it is in general $k_{F\perp}/\pi k_0 \gg 1$. Thus the major contribution to $\mathcal{N}(E_F)$ effective in the total surface e-ph interaction comes from the surface-projected density of states (DOS) of the conduction electron states above the conduction-band minimum (CBm, Fig. 4) rather than from the Dirac states. As appears from ARPES data on the 3D material [21] the conduction band in the normal direction is rather flat and $k_{F\perp}$ is hard to extract.

Thus λ_{HAS} is more conveniently expressed in terms of k_0, $k_{F\parallel}$, and n_0, the latter being known from transport measurements:

$$\lambda_{\mathrm{HAS}} \cong \alpha\,\frac{k_{F\parallel}^2\,k_0}{6n_0} = \alpha\,\frac{m_e^*}{\hbar^2}\sqrt{\frac{E_F\,e^2}{6\,\epsilon\,n_0}},$$
$$\alpha \equiv \frac{\phi\,\ln(I_0/I)}{A_c\,k_{iz}^2\,k_B\,T_S}, \tag{11}$$

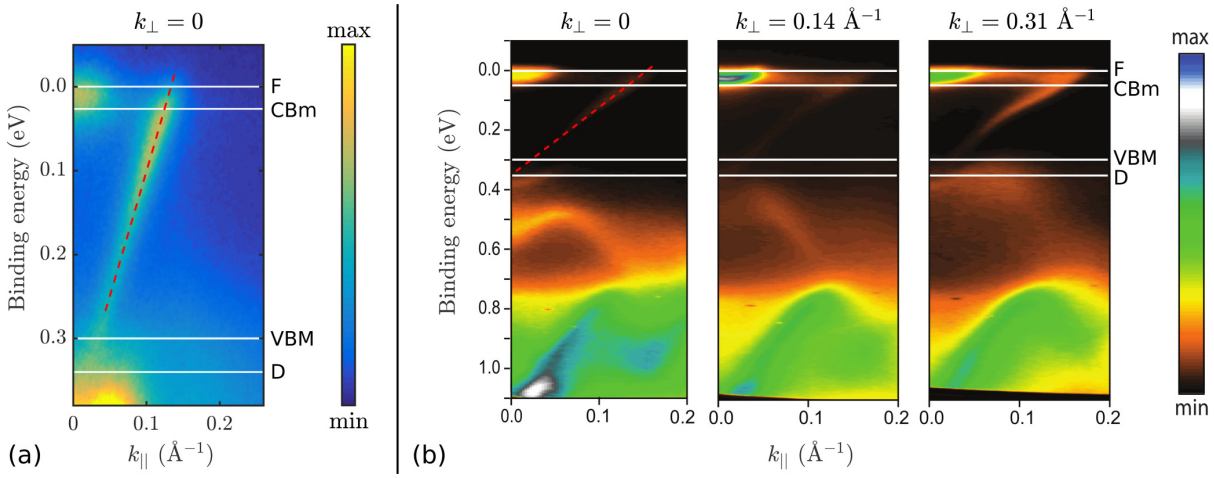

FIG. 4. Photoemission intensity for Bi_2Te_3(111) along $\overline{\Gamma M}$ of (a) the sample of the present HAS study and (b) the sample measured by Michiardi *et al.* (adapted figure with permission from [21], Copyrighted by the American Physical Society) at three different values of the normal momentum transfer (with the zero conventionally set at the $\overline{\Gamma}$ point). The positions of the Fermi level (F), the conduction-band minimum (CBm), the valence-band maximum (VBM), and the Dirac point (D) are indicated by the horizontal lines. The dashed red lines show the quasilinear dispersion of the surface Dirac states.

where $k_{iz} = \sqrt{2mE_{iz}'}/\hbar$ is the normal component of the He incident wave vector including the Beeby correction. Using the slope determined from the linear fit in Fig. 2, together with $\phi = 4.9$ eV [54] and $A_c = 16.5$ Å^2 (using the lattice constant a determined from the diffraction data in Sec. III A) gives $\alpha = 2.38$. With $E_F = 0.025$ eV, as suggested by ARPES data on the present sample [Fig. 4(a)] and reported by Suh *et al.* for unirradiated samples [54] and $m_e^* = 0.07m_e$ (from Huang *et al.* [57]), (11) gives

$$\lambda_{\mathrm{HAS}} \cong 0.11/\sqrt{n_0} \tag{12}$$

with n_0 given in units of 10^{20} cm^{-3}. As discussed by Suh *et al.* [54], unirradiated n-Bi_2Te_3 thick films show a conduction electron density of about 7×10^{18} cm^{-3}. Note that the ARPES measurements by Michiardi *et al.* [21] of the 3D band structure for a similar sample, reproduced in Fig. 4(b) for the $\overline{\Gamma M}$ direction, indicate a Fermi level above the CBm of ≈0.05 eV, which would give $\lambda_{\mathrm{HAS}} \cong 0.15/\sqrt{n_0}$.

The carrier concentration from Hall measurements in the present sample is 6.44×10^{18} cm^{-3}, in agreement with the data of Suh *et al.* [54], for unirradiated n-Bi_2Te_3 thick films (7×10^{18} cm^{-3}). This would give $\lambda_{\mathrm{HAS}} \cong 0.42$ for $E_F = 0.025$ eV (our sample) or $\lambda_{\mathrm{HAS}} \cong 0.57$ for $E_F = 0.05$ eV. However, as shown in the work by Suh *et al.* [54], the carrier concentration rapidly increases with decreasing thickness of the samples, due to the increasing weight of the surface accumulation layer in the region within the TFSL where the downward band bending occurs [3]. As explained above, it is the carrier density near the surface, the one within the TFSL, which enters (12). Hence a carrier density in the range of 10^{20} cm^{-3}, corresponding to $\lambda_{\mathrm{HAS}} \cong 0.1$ or less, appears to be more appropriate.

Indeed recent *ab initio* calculations by Huang [8] for three QLs found $\lambda = 0.05$ in agreement with Heid *et al.* [58] which obtain for a calculation of 5 QLs as a function of the Fermi energy the same value when E_F is 0.35 eV above the Dirac point (as in Fig. 4). This value of λ would require an average density of $n \approx 4 \times 10^{20}$ cm^{-3} for the 2DEG in the surface band bending region.

A listing of the e-ph coupling on Bi_2Te_3(111) obtained from both experimental methods and calculations can be found in Table I. It is immediately apparent that there exists a large variation in the e-ph coupling constants determined for Bi_2Te_3(111), in particular between a mode-selected e-ph coupling associated with some prominent Kohn anomaly, as obtained from inelastic HAS [15,59] and the value of λ averaged over the whole phonon spectrum as derived from ARPES measurements [9]. One reason for this discrepancy is that the rather large values for a specific phonon mode [15,59] cannot be compared with ARPES measurements where one typically integrates over all phonon modes. Furthermore, the exceptionally large value determined by Kondo *et al.* [14] is dominated by the contribution from a theoretically proposed spin plasmon [14].

The great variability of λ values reported for Bi_2Te_3 and similar materials largely depends on their complex electronic structure and the fact that different e-ph dependent properties actually enucleate different aspects of the e-ph interaction. In insulators and nondegenerate semiconductors the e-ph interaction is related to the polarization of valence electrons due to phonon displacements and related electric fields, and essentially involves virtual electronic excitations across the gap. In metals and degenerate semiconductors the phonon-induced electronic transitions between states near the Fermi level play the major role. In conducting chalcogenides with large anion polarizabilities both aspects of e-ph interaction can be equally important. In narrow-gap topological insulators with only surface Dirac states crossing the Fermi level, the role of valence electrons in λ is important, even more so if they are degenerate semiconductors with the Fermi level lifted above the CBm as a consequence of doping or surface defects, as in the present case.

TABLE I. Comparison of the electron-phonon coupling constants λ for $Bi_2Te_3(111)$ obtained from both experimental methods and calculations. The mode-specific λ for the low-lying surface optical mode is much larger than the average λ as listed in the second part of the table. We obtain a λ of $0.11/\sqrt{n_0}$ (with n_0 in 10^{20} cm^{-3}) which corresponds to a range of 0.04–0.11 for a charge-carrier density of the order of 10^{20} cm^{-3}.

Sample	Methods	Ref.	λ
Cleaved	ARPES[a]	[14]	3
Theory semi-∞	PCM + LRT[b]	[59]	2
Cleaved	HAS[c]	[15]	1.44
Cleaved n-type	ARPES	[9]	0.19
Theory semi-∞	IEC[d]	[60]	0.13
Cleaved n-type	HAS[e]		$0.11/\sqrt{n_0}$
Theory 3 QL	DFPT + SOC[f]	[8]	0.05
Theory 5 QL	DFPT + SOC[g]	[58]	0.05
Cleaved p-type	ARPES	[9]	0.0

[a]With the contribution from both the e-ph coupling and the electron-spin-plasmon coupling [14].
[b]Mode-selected e-ph coupling for the low-lying surface optical mode using a pseudocharge model (PCM). for lattice dynamics and linear-response theory.
[c]Mode-selected e-ph coupling for the surface optical mode originating at 5.8 meV at the $\overline{\Gamma}$ point.
[d]Isotropic elastic continuum (IEC) model for lattice dynamics.
[e]Present work with the carrier density n_0 in 10^{20} cm^{-3}.
[f]Density functional perturbation theory (DFPT) with spin-orbit coupling (SOC).
[g]For a Fermi level 0.35 eV above the Dirac point.

In all these complex cases better information would be obtained from electron state-selected e-ph interaction, as from ARPES or recent Heid *et al. ab initio* studies [58], or phonon mode-selected e-ph coupling constants, as from inelastic HAS [18]. However, both the mode-selected ($\lambda_{\mathbf{Q},\nu}$) and the average (λ) e-ph constants derived from HAS contain the contribution of all electronic transitions producing a modulation of the surface charge density. Even in an insulating surface such as Xe(111) a quantum-sonar effect is observed with HAS, which is a manifestation of e-ph interaction due to the large polarizability of Xe atoms [61]. Thus in the general case of different contributions to the e-ph interaction, the temperature dependence of the HAS DW exponent provides a complete information on λ at the surface by directly measuring the electron charge-density oscillations induced by the entire surface-projected phonon spectrum.

Hence, combined with ARPES data, the approach based on the DW attenuation in He scattering enables us to extract the correctly averaged λ for a given surface [16]. Furthermore, the measurement of the thermal attenuation is a robust and reliable experimental method to extract the e-ph coupling. In contrast, the determination of the e-ph coupling directly from ARPES requires high-resolution measurements due to the small momentum space and energy window relevant for this process [9] and it remains difficult to exclude effects from bulk states [10].

When considering the average λ of $Bi_2Te_3(111)$, our measurements suggest a rather modest e-ph coupling in agreement with other studies (Table I). While it is difficult to directly relate superconducting states with the e-ph coupling of a surface, the fact that Bi_2Te_3 does not exhibit a superconducting phase under "normal" conditions [62,63] supports our results. Hence our finding of a modest λ is not surprising even though some individual phonons may provide a much larger e-ph interaction as reported by Howard *et al.* [15].

IV. SUMMARY AND CONCLUSION

We have studied the topological insulator $Bi_2Te_3(111)$ by means of helium atom scattering. The exact close-coupling method was applied to determine the electronic surface corrugation from the diffraction peak intensities. Hereby $Bi_2Te_3(111)$ exhibits an electron density corrugation with a peak to peak height of 0.39 Å (9% of the surface lattice constant) upon scattering of ^{3}He with a beam energy of 8 meV. The obtained electronic corrugation is intermediary between those of metal and semiconductor surfaces as well as comparable to studies of semimetal surfaces. The thermal attenuation in the diffraction of He from $Bi_2Te_3(111)$ was studied in a temperature range between 110 and 335 K. The system shows a typical Debye-Waller behavior with a surface Debye temperature of $\Theta_D = (81 \pm 6)$ K.

By adapting a recently developed quantum-theoretical derivation of the He scattering probabilities to the case of a degenerate semiconductor, we are able to extract the e-ph coupling strength from temperature-dependent He atom scattering measurements. The Debye-Waller attenuation, which is directly related to the e-ph coupling λ, allows us to extract a correctly averaged λ for a given surface. Hence we obtain a λ in the range of 0.04–0.11 for $Bi_2Te_3(111)$ for a charge-carrier density of the order of 10^{20} cm^{-3}. This relatively modest value of λ is not surprising even though some individual phonons may provide a larger e-ph interaction. Our results of the e-ph coupling are consistent with other theoretical and experimental results and suggest that previous inconsistencies were found when relating mode-specific values with an average λ.

With respect to potential applications, the obtained weak electron-phonon coupling indicates that the Bi_2Te_3 system may be useful in achieving high electron mobilities. In particular the growth of defect-free ultrathin films offers a route towards fast devices based on any small-gap semiconductors such as Bi_2Te_3 due to the high electron mobilities (small m_e^*) and a long mean-free path (small e-ph interaction).

ACKNOWLEDGMENTS

The authors would like to thank J. R. Manson, S. Miret-Artès, and E. V. Chulkov for many helpful discussions. One of us (A.T.) acknowledges financial support provided by the FWF (Austrian Science Fund) within Project No. J3479-N20. The authors are grateful for financial support by the Blavatnik Foundation, the Aarhus University Research Foundation, VILLUM FONDEN via the Centre of Excellence for Dirac Materials (Grant No. 11744), and the SPP1666 of the DFG (Grant No. HO 5150/1-1). M.B., E.M.J.H., and B.B.I. acknowledge financial support from the Center of Materials Crystallography (CMC) and the Danish National Research Foundation (DNRF93).

[1] H. J. Goldsmid, Materials **7**, 2577 (2014).
[2] G. J. Snyder and E. S. Toberer, Nat. Mater. **7**, 105 (2008).
[3] M. T. Pettes, J. Maassen, I. Jo, M. S. Lundstrom, and L. Shi, Nano Lett. **13**, 5316 (2013).
[4] Y. L. Chen, J. G. Analytis, J.-H. Chu, Z. K. Liu, S.-K. Mo, X. L. Qi, H. J. Zhang, D. H. Lu, X. Dai, Z. Fang, S. C. Zhang, I. R. Fisher, Z. Hussain, and Z.-X. Shen, Science **325**, 178 (2009).
[5] M. Z. Hasan and C. L. Kane, Rev. Mod. Phys. **82**, 3045 (2010).
[6] J. Moore, Nat. Phys. **5**, 378 (2009).
[7] L. Barreto, L. Kühnemund, F. Edler, C. Tegenkamp, J. Mi, M. Bremholm, B. B. Iversen, C. Frydendahl, M. Bianchi, and P. Hofmann, Nano Lett. **14**, 3755 (2014).
[8] G. Q. Huang, Europhys. Lett. **100**, 17001 (2012).
[9] C. Chen, Z. Xie, Y. Feng, H. Yi, A. Liang, S. He, D. Mou, J. He, Y. Peng, X. Liu *et al.*, Sci. Rep. **3**, 2411 (2013).
[10] J. A. Sobota, S.-L. Yang, D. Leuenberger, A. F. Kemper, J. G. Analytis, I. R. Fisher, P. S. Kirchmann, T. P. Devereaux, and Z.-X. Shen, Phys. Rev. Lett. **113**, 157401 (2014).
[11] X. Zhu, L. Santos, C. Howard, R. Sankar, F. C. Chou, C. Chamon, and M. El-Batanouny, Phys. Rev. Lett. **108**, 185501 (2012).
[12] R. C. Hatch, M. Bianchi, D. Guan, S. Bao, J. Mi, B. B. Iversen, L. Nilsson, L. Hornekær, and P. Hofmann, Phys. Rev. B **83**, 241303 (2011).
[13] Z.-H. Pan, A. V. Fedorov, D. Gardner, Y. S. Lee, S. Chu, and T. Valla, Phys. Rev. Lett. **108**, 187001 (2012).
[14] T. Kondo, Y. Nakashima, Y. Ota, Y. Ishida, W. Malaeb, K. Okazaki, S. Shin, M. Kriener, S. Sasaki, K. Segawa, and Y. Ando, Phys. Rev. Lett. **110**, 217601 (2013).
[15] C. Howard, M. El-Batanouny, R. Sankar, and F. C. Chou, Phys. Rev. B **88**, 035402 (2013).
[16] J. R. Manson, G. Benedek, and S. Miret-Artés, J. Phys. Chem. Lett. **7**, 1016 (2016).
[17] A. Tamtögl, P. Kraus, M. Mayrhofer-Reinhartshuber, D. Campi, M. Bernasconi, G. Benedek, and W. E. Ernst, Phys. Rev. B **87**, 035410 (2013).
[18] G. Benedek, M. Bernasconi, K.-P. Bohnen, D. Campi, E. V. Chulkov, P. M. Echenique, R. Heid, I. Y. Sklyadneva, and J. P. Toennies, Phys. Chem. Chem. Phys. **16**, 7159 (2014).
[19] G. Alexandrowicz and A. P. Jardine, J. Phys.: Condens. Matter **19**, 305001 (2007).
[20] A. Jardine, H. Hedgeland, G. Alexandrowicz, W. Allison, and J. Ellis, Prog. Surf. Sci. **84**, 323 (2009).
[21] M. Michiardi, I. Aguilera, M. Bianchi, V. E. de Carvalho, L. O. Ladeira, N. G. Teixeira, E. A. Soares, C. Friedrich, S. Blügel, and P. Hofmann, Phys. Rev. B **90**, 075105 (2014).
[22] A. Tamtögl, E. A. Carter, D. J. Ward, N. Avidor, P. R. Kole, A. P. Jardine, J. Ellis, and W. Allison, Rev. Sci. Instrum. **87**, 066108 (2016).
[23] S. V. Hoffmann, C. Søndergaard, C. Schultz, Z. Li, and P. Hofmann, Nucl. Instrum. Methods Phys. Res. A **523**, 441 (2004).
[24] J. S. Becker, R. D. Brown, E. Johansson, N. S. Lewis, and S. J. Sibener, J. Chem. Phys. **133**, 104705 (2010).
[25] G. Comsa, Surf. Sci. **81**, 57 (1979).
[26] J. Lapujoulade, Y. Lejay, and G. Armand, Surf. Sci. **95**, 107 (1980).
[27] A. Sanz and S. Miret-Artés, Phys. Rep. **451**, 37 (2007).
[28] D. Farías and K.-H. Rieder, Rep. Prog. Phys. **61**, 1575 (1998).
[29] M. Mayrhofer-Reinhartshuber, P. Kraus, A. Tamtögl, S. Miret-Artés, and W. E. Ernst, Phys. Rev. B **88**, 205425 (2013).
[30] P. Kraus, A. Tamtögl, M. Mayrhofer-Reinhartshuber, F. Apolloner, C. Gösweiner, S. Miret-Artés, and W. E. Ernst, J. Phys. Chem. C **119**, 17235 (2015).
[31] A. Tamtögl, M. Pusterhofer, P. Kraus, M. Bremholm, E. M. J. Hedegaard, B. B. Iversen, M. Bianchi, P. Hofmann, J. Ellis, W. Allison, and W. E. Ernst (unpublished).
[32] A. Tamtögl, E. Bahn, J. Zhu, P. Fouquet, J. Ellis, and W. Allison, J. Phys. Chem. C **119**, 25983 (2015).
[33] P. Hofmann, Prog. Surf. Sci. **81**, 191 (2006).
[34] K. Sugawara, T. Sato, S. Souma, T. Takahashi, M. Arai, and T. Sasaki, Phys. Rev. Lett. **96**, 046411 (2006).
[35] D. Farías, G. Lange, K. H. Rieder, and J. P. Toennies, Phys. Rev. B **55**, 7023 (1997).
[36] M. Cardillo, G. Becker, S. Sibener, and D. Miller, Surf. Sci. **107**, 469 (1981).
[37] W. R. Lambert, P. L. Trevor, M. J. Cardillo, A. Sakai, and D. R. Hamann, Phys. Rev. B **35**, 8055 (1987).
[38] R. B. Laughlin, Phys. Rev. B **25**, 2222 (1982).
[39] J. R. Manson, G. Benedek, and S. Miret-Artés, J. Phys. Chem. Lett. **7**, 1691 (2016).
[40] A. Tamtögl, M. Mayrhofer-Reinhartshuber, P. Kraus, and W. E. Ernst, Surf. Sci. **617**, 225 (2013).
[41] B. Gumhalter, Surf. Sci. **347**, 237 (1996).
[42] A. Siber and B. Gumhalter, Surf. Sci. **385**, 270 (1997).
[43] S. Daon, E. Pollak, and S. Miret-Artés, J. Chem. Phys **137**, 201103 (2012).
[44] A. C. Levi and H. Suhl, Surf. Sci. **88**, 221 (1979).
[45] J. L. Beeby, J. Phys. C **4**, L359 (1971).
[46] W. W. Hayes and J. R. Manson, Phys. Rev. B **75**, 113408 (2007).
[47] A. al Taleb, G. Anemone, D. Farías, and R. Miranda, Carbon **99**, 416 (2016).
[48] A. Politano, B. Borca, M. Minniti, J. J. Hinarejos, A. L. Vázquez de Parga, D. Farías, and R. Miranda, Phys. Rev. B **84**, 035450 (2011).
[49] H. Shichibe, Y. Satake, K. Watanabe, A. Kinjyo, A. Kunihara, Y. Yamada, M. Sasaki, W. W. Hayes, and J. R. Manson, Phys. Rev. B **91**, 155403 (2015).
[50] P. A. Walker, Proc. Phys. Soc. **76**, 113 (1960).
[51] F. C. M. J. M. van Delft, Surf. Sci. **251**, 690 (1991).
[52] M. Mayrhofer-Reinhartshuber, A. Tamtögl, P. Kraus, K. H. Rieder, and W. E. Ernst, J. Phys.: Condens. Matter **24**, 104008 (2012).
[53] P. Senet, J. P. Toennies, and G. Benedek, Europhys. Lett. **57**, 430 (2002).
[54] J. Suh, D. Fu, X. Liu, J. K. Furdyna, K. M. Yu, W. Walukiewicz, and J. Wu, Phys. Rev. B **89**, 115307 (2014).
[55] N. W. Ashcroft and N. D. Mermin, *Solid State Physics*, 2nd ed. (Holt Rinehart & Winston, Austin, TX, 2002).
[56] W. Richter and C. R. Becker, Phys. Status Solidi B **84**, 619 (1977).

[57] B.-L. Huang and M. Kaviany, Phys. Rev. B **77**, 125209 (2008).
[58] R. Heid, I. Y. Sklyadneva, and E. V. Chulkov, Sci. Rep. **7**, 1095 (2017).
[59] C. Howard and M. El-Batanouny, Phys. Rev. B **89**, 075425 (2014).
[60] S. Giraud and R. Egger, Phys. Rev. B **83**, 245322 (2011).
[61] D. Campi, M. Bernasconi, G. Benedek, and J. P. Toennies, J. Phys. Chem. C **119**, 14579 (2015).
[62] K. Matsubayashi, T. Terai, J. S. Zhou, and Y. Uwatoko, Phys. Rev. B **90**, 125126 (2014).
[63] P. H. Le, W.-Y. Tzeng, H.-J. Chen, C. W. Luo, J.-Y. Lin, and J. Leu, APL Materials **2**, 096105 (2014).

6.8 Publication H

Tamtögl, A., Sacchi, M., Calvo-Almazán, I., Zbiri, M., Koza, M. M., Ernst, W. E. & Fouquet, P. Ultrafast molecular transport on carbon surfaces: The diffusion of ammonia on graphite. *Carbon* **126,** 23–30 (2018)

contributions	
funding	P. Fouquet, A. Tamtögl, W. E. Ernst
preparation / setup	A. Tamtögl, I. Calvo-Almazán
data acquisition	A. Tamtögl, M. M. Koza, P. Fouquet, M. Zbiri
theory (*ab initio*) calculations	M. Sacchi
data analysis	A. Tamtögl
interpretation	A. Tamtögl, I. Calvo-Almazán
publication writing	A. Tamtögl

Carbon 126 (2018) 23–30

Contents lists available at ScienceDirect

Carbon

journal homepage: www.elsevier.com/locate/carbon

Ultrafast molecular transport on carbon surfaces: The diffusion of ammonia on graphite

Anton Tamtögl [a, *], M. Sacchi [b], I. Calvo-Almazán [c, d], M. Zbiri [e], M.M. Koza [e], W.E. Ernst [a], P. Fouquet [e]

[a] Institute of Experimental Physics, Graz University of Technology, Petersgasse 16, 8010, Graz, Austria
[b] Department of Chemistry, University of Surrey, GU2 7XH, Guildford, United Kingdom
[c] Material Science Division, Argonne National Laboratory, Argonne, 60439, Illinois, United States
[d] Cavendish Laboratory, University of Cambridge, J. J. Thomson Avenue, CB3 0HE, Cambridge, United Kingdom
[e] Institut Laue-Langevin, 71 Avenue des Martyrs, CS 20156, F-38042, Grenoble Cedex 9, France

ARTICLE INFO

Article history:
Received 17 July 2017
Received in revised form
26 September 2017
Accepted 29 September 2017
Available online 30 September 2017

Keywords:
Ammonia
Graphite
Diffusion
Neutron scattering
DFT
Adsorption

ABSTRACT

We present a combined experimental and theoretical study of the self-diffusion of ammonia on exfoliated graphite. Using neutron time-of-flight spectroscopy we are able to resolve the ultrafast diffusion process of adsorbed ammonia, NH_3, on graphite. Together with van der Waals corrected density functional theory calculations we show that the diffusion of NH_3 follows a hopping motion on a weakly corrugated potential energy surface with an activation energy of about 4 meV which is particularly low for this type of diffusive motion. The hopping motion includes further a significant number of long jumps and the diffusion constant of ammonia adsorbed on graphite is determined with $D = 3.9 \cdot 10^{-8}$ m^2/s at 94 K.

1. Introduction

The diffusion of ammonia on graphite is particularly interesting for potential applications of graphene and graphitic material surfaces. Those include chemical doping of graphene, e.g., n-doping of graphene by thermal annealing in the presence of ammonia gas [1,2]. Furthermore, the modification of the electronic structure of graphene upon adsorption of ammonia has been employed for quantum sensing/gas sensor applications [3–6]. It was shown that it is possible to use graphene as a gas sensor with high sensitivity and high accuracy for detecting ammonia groups due to the fact that ammonia adsorbed on graphene induces the appearance of new substrate electronic states [7–9]. The changes to the graphene electronic states could be reverted by annealing, where in particular desorption is often dominated by the kinetic processes on the surface. Moreover, the gas adsorption and diffusion on the graphene surface basically determines the sensitivity of these graphene based gas sensors [10].

The adsorption and diffusion of molecular species on graphene and graphitic materials is also of fundamental interest in various fields. Several studies on the dynamics and the structure of physisorbed molecular species on graphite have been carried out, including molecular hydrogen [11], alkanes [12–17] and aromatic hydrocarbons [18–20]. The diffusion of adsorbates and clusters on carbon-based materials has also been subject to intensive research, in search for low-friction and superdiffusive systems [21–24] as well as for studying elementary dynamic processes such as atomic-scale friction [25,26] and the development of nanometer size motorization systems [27].

However, little experimental data exists for the diffusion of ammonia (NH_3) on graphite. This is quite surprising, given that NH_3 represents one of the simplest heteroatomic molecules. Experimental results about the ammonia/graphite system are mainly based on thermal desorption studies of ammonia on graphitic surfaces and some very early neutron and nuclear magnetic resonance (NMR) diffusion data [28]. While ammonia on highly oriented pyrolytic graphite (HOPG) starts to desorb at 90 K [29], slightly higher desorption temperatures (111 K) have been found

* Corresponding author.
E-mail address: tamtoegl@gmail.com (A. Tamtögl).

https://doi.org/10.1016/j.carbon.2017.09.104
0008-6223/

for graphene/metal systems [9]. According to density functional theory (DFT) calculations, NH_3 adsorbs in the centre of the carbon hexagon ($E_a = 31 - 48$ meV), almost invariant to rotations around the axis perpendicular to the surface and through the nitrogen atom [7,30,31]. On the other hand, the adsorption energy from thermal desorption spectroscopy (TDS) is $E_a = (260 \pm 20)$ meV [29] and DFT calculations have predicted that the barrier for translational diffusion is about 10 meV [7,28].

Here we present a combined neutron scattering and density functional theory (DFT) study of the diffusion of ammonia on exfoliated graphite. Scattering techniques such as quasi-elastic neutron scattering (QENS) and quasi-elastic helium atom scattering (QHAS) are powerful techniques to study very fast molecular dynamics, allowing to follow the atomic-scale motion of atoms and molecules and resolving diffusion processes on timescales from ns to sub-ps [20,32–34]. Ammonia on graphite is a fast diffusing system, accessible within the time-window of neutron time-of-flight spectroscopy. Together with van der Waals (vdW) corrected DFT calculations we show that ammonia follows a jump motion on a weakly corrugated potential energy surface.

2. Experimental and computational details

2.1. Sample preparation

We used exfoliated compressed graphite, *Papyex*, a material that is widely employed for adsorption measurements due to its high specific adsorption surface area. It exhibits an effective surface area of about 25 $m^2\ g^{-1}$ and retains a sufficiently low defect density [35,36]. In addition, exfoliated graphite samples show a preferential orientation of the basal plane surfaces. We exploited this and oriented the basal planes parallel to the scattering plane of the neutrons. We used 7.39 g of Papyex exfoliated graphite of grade N998 (> 99.8% C, Carbone Lorraine, Gennevilliers, France). The prepared exfoliated graphite disks were heated to 973 K under vacuum for 4 days before transferring them into a cylindrical aluminium sample cartridge. The sample cartridge was sealed by an indium gasket and connected to a gas sorption system via a stainless steel capillary.

The sample temperature was controlled using a standard liquid helium cryostat. The sample was initially cooled down to 4 K and the quantity corresponding to 0.5 monolayer (ML) and 0.9 ML of ammonia gas, respectively, was dosed through the stainless steel capillary which was connected to a pressure control monitor. At monolayer coverage the area occupied by one NH_3 molecule corresponds to $\Sigma = 10.8$ Å^2 (see Ref. [37]). Throughout the entire experiment, connection to a 500 cm^3 reservoir at room temperature was maintained, for safety and monitoring purposes. In using this set-up any desorbed ammonia rises to the reservoir, where the desorbed quantity can be deduced through pressure monitoring (Fig. 1).

2.2. Instrumental details

The measurements were performed at the IN6 time-of-flight (TOF) neutron spectrometer and the IN11 neutron spin-echo (NSE) spectrometer of the ILL [38]. The incoming neutron wavelengths were set to 5.12 Å and 5.5 Å, respectively, with energy resolutions at full width at half maximum of 70 μeV (IN6) and 1 μeV (IN11). Neutron scattering TOF spectra of NH_3/graphite were obtained over a large range of temperatures: 4 K, 15 K, 25 K, 37 K, 85 K, 94 K (at 0.5 ML and 0.9 ML NH_3 coverages) and 105 K (only at 0.9 ML NH_3 coverage). Previous to the adsorption of NH_3, the scattering function of the graphite substrate was measured at 4 K, in order to obtain an elastic scattering resolution of the clean graphite sample.

The TOF spectra were converted to scattering functions, $S(Q, \Delta E)$, where $Q = |\mathbf{Q}| = \left|\mathbf{k_f} - \mathbf{k_i}\right|$ is the momentum transfer and $\Delta E = E_f - E_i$ is the energy transfer. Fig. 2a shows a two-dimensional contour plot of the dynamic scattering function $S(Q, \Delta E)$ for 0.9 ML

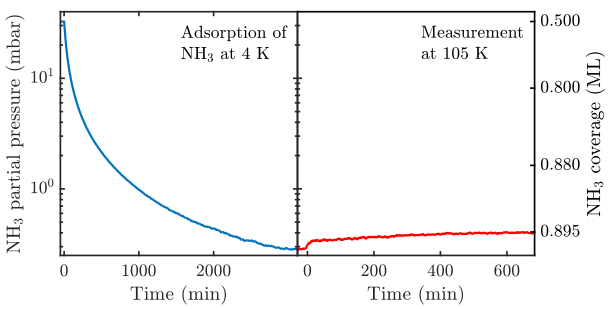

Fig. 1. The adsorption process of NH_3 on exfoliated graphite can be followed by monitoring the pressure in the connected reservoir. Left panel: Uptake during dosing from 0.5 to 0.9 ML coverage at a sample temperature of 4 K. Right panel: During the measurements at 105 K desorption slowly starts to commence. However, the pressure rise corresponds to a loss of less than 1% of the original coverage, so we can still safely assume a coverage of 0.9 ML. (A colour version of this figure can be viewed online.)

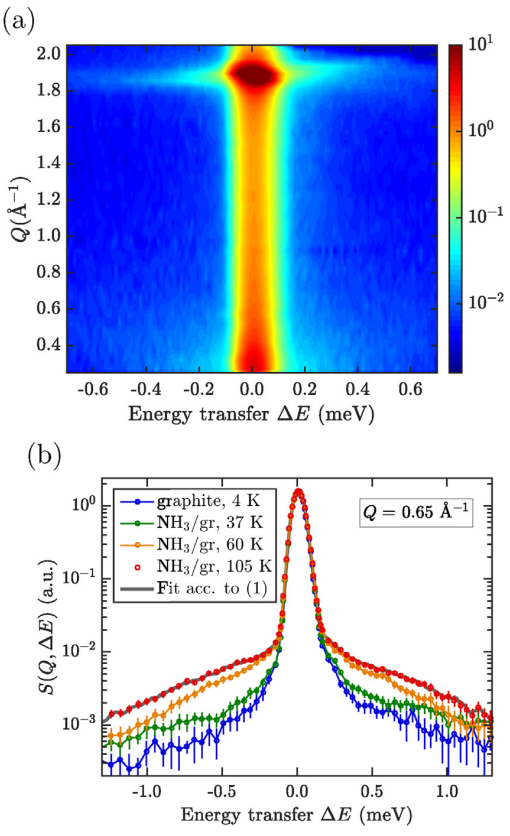

Fig. 2. Neutron TOF spectra for 0.9 ML of NH_3 on graphite, converted to the dynamic scattering function $S(Q, \Delta E)$. (a) Two-dimensional contour plot of the dynamic scattering function S(Q, ΔE) that was extracted from neutron TOF data obtained for exfoliated graphite covered by 0.9 ML of NH_3 at 94 K. The intense spot at about Q = 1:9 A^{-1} is due to the (002) Bragg reection from the basal plane of graphite. (b) Comparison of the scattering functions S(Q, ΔE) at a momentum transfer of Q = 0:65 A^{-1} for several temperatures with the clean graphite measured at 4 K. (A colour version of this figure can be viewed online.)

of NH_3 at a temperature of 94 K. The spectrum shows an intense elastic scattering region around $\Delta E = 0$ meV which is mainly due to scattering from the graphite substrate. The broader feature surrounding the elastic band is the quasi-elastic broadening which appears due to scattering from the diffusing ammonia adsorbates.

A cut of the scattering function $S(Q,\Delta E)$ at $Q = 0.65$ Å^{-1} is displayed in Fig. 2b for several temperatures. Fig. 2b shows that the quasi-elastic broadening increases with sample temperature. Up to a sample temperature of 37 K the broadening is relatively small and it is not possible to extract the quasi-elastic broadening with a reliable fit of the measured data. However, in the temperature range from 60 K to 105 K we observe a clearly discernible quasi-elastic broadening which will be used in the following to extract information about the diffusion of ammonia on exfoliated graphite.

2.3. Computational details

The DFT calculations were performed using CASTEP [39], a plane wave periodic boundary condition code. The Perdew Burke Ernzerhof [40] exchange-correlation functional, with the dispersion force corrections developed by Tkatchenko and Scheffler (TS method) [41], was employed for the calculations presented in this work. The plane wave basis set was truncated to a kinetic energy cutoff of 360 eV. We have used (4×4) and (2×2) graphene unit cells composed of a three-layer graphene sheet to model the adsobate system at two coverages. A vacuum spacing of 20 Å was imposed above the graphite surface in order to avoid interactions with the periodically repeated supercells. The substrate is frozen during the calculation and the Brillouin zone of the two unit cells are sampled with regular $(4 \times 4 \times 1)$ and $(8 \times 8 \times 1)$ k-point Monkhorst-Pack grids. The electron energy was converged up to a tolerance of 10^{-8} eV while the force tolerance for structural optimizations was set to 0.05 eV/Å.

3. Results and discussion

The experimentally measured scattering function $S(Q,\Delta E)$ was fitted using a convolution of the resolution function of the neutron TOF spectrometer $S_{res}(Q,\Delta E)$ with an elastic term $I_{el}(Q)\delta(\Delta E)$ and the quasi-elastic contribution $S_{inc}(Q,\Delta E)$:

$$\begin{aligned} S(Q,\Delta E) &= S_{res}(Q,\Delta E) \otimes [I_{el}(Q)\delta(\Delta E) + S_{inc}(Q,\Delta E)] \\ &= S_{res}(Q,\Delta E) \otimes \left[I_{el}(Q)\delta(\Delta E) + A(Q)\frac{1}{2\pi}\frac{\Gamma(Q)}{[\Gamma(Q)]^2 + \Delta E^2} \right]. \end{aligned} \quad (1)$$

Here, δ represents the Dirac delta and the quasi-elastic broadening is modelled by a Lorentzian function, where $I_{el}(Q)$ is the intensity of the elastic scattering and $A(Q)$ is the intensity of the quasi-elastic scattering. $\Gamma(Q)$ is the half width at half maximum (HWHM) of the Lorentzian. We write $S_{inc}(Q,\Delta E)$ because the quasi-elastic part of the scattering function is nearly identical to the incoherent scattering function since the coherent scattering of the graphite substrate in the considered Q range is weak and the scattering of the ammonia is strongly dominated by the H atoms [19,33]. An exemplary fit is illustrated by the thick grey line in Fig. 2b.

The hereby extracted quasi-elastic broadening $\Gamma(Q)$ at a temperature of 94 K is plotted versus the momentum transfer Q in Fig. 3. The error bars in Fig. 3 represent the confidence intervals of the least squares fits. The error bars at small momentum transfers are invisible in the plot, since they are smaller than the size of the symbols, but for momentum transfers $Q > 0.6$ Å^{-1} they grow rapidly as Γ approaches the widths of the spectroscopic window of the spectrometer.

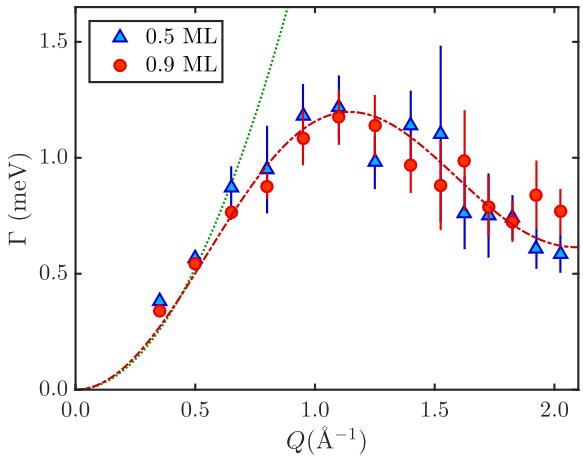

Fig. 3. Extracted quasi-elastic broadening $\Gamma(Q)$ for 0.5 and 0.9 ML NH_3 at 94 K versus momentum transfer Q. The momentum transfer dependence can be described by the 2D isotropic Chudley Elliot model, Eq. (3), with $l = 1.4 \cdot a_{gr}$ (red dash dotted curve). $\Gamma(Q)$ shows hardly any change with coverage apart from a slightly reduced broadening at small Q with increasing coverage. The green dotted line shows the theoretical $\Gamma(Q)$ for Brownian motion. (A colour version of this figure can be viewed online.)

For the case that the diffusion of the adsorbate is governed by the interaction of the molecule with a corrugated surface, its motion can be well described by the Chudley-Elliott (CE) model of jump diffusion [42,43]. The CE model assumes that a particle rests for a time τ at an adsorption site, before it moves instantaneously to another adsorption site. In the simplest case, this motion happens on a Bravais lattice and the HWHM $\Gamma(Q)$ can be expressed as:

$$\Gamma(Q) = \frac{\hbar}{N\tau}\sum_{n=1}^{N}\left[1 - e^{-i\mathbf{Q}\cdot\mathbf{l}_n}\right], \quad (2)$$

where $\mathbf{l}_n$ are the corresponding jump vectors. In the case of scattering from a polycrystalline sample, isotropic angular averaging has to be performed since the scattered neutron signal "sees" the jumping adsorbate from all possible directions. In the case of 2D isotropy, integration in the scattering plane (over the azimuth φ) yields:

$$\Gamma(Q) = \frac{\hbar}{\tau}[1 - J_0(Q \cdot l \cdot \sin\theta)], \quad (3)$$

where $J_0(Q \cdot l \cdot \sin\theta)$ is the zeroth order cylindrical Bessel function and l is the average jump length. $Q \cdot \sin\theta$ is the component of the scattering vector in the plane of diffusion, and θ the angle between $\mathbf{Q}$ and the normal to this plane [44]. Papyex consists of planes with an inclination that is normally distributed around $\theta = 90°$ with a HWHM of about 15° [35]. This has been taken into account by numerical integration of (3).

It should be noted that the isotropic averaging is only an approximation and it omits the fact that for a correct isotropic averaging one needs to integrate over the $S(Q,\Delta E)$ rather than the broadening $\Gamma(Q)$, which produces in general a non-Lorentzian QENS broadening [33,45]. However, the deviation from the Lorentz distribution is mainly caused due to scattering processes which occur almost perpendicular to the plane of diffusion. While this contribution should not be neglected in the case of three-dimensional polycrystalline materials, in the case of Papyex the scattering vector $\mathbf{Q}$ is approximately parallel to the (0001) basal plane of graphite as mentioned above. Hence we will rely on the

approximate solution (3), which produces very good results. (3) is then fitted to the experimentally determined broadening $\Gamma(Q)$ using an iterative generalized least squares algorithm with weights (and a numerical integration over θ). The red dash-dotted line in Fig. 3 shows that (3) fits the data very well for $l = (3.45\pm0.02)$ Å and $\tau = (0.85\pm0.08)$ ps. From the momentum transfer dependence we can clearly exclude other types of motion. E.g. ballistic diffusion, which represents a two dimensional ideal gas, is characterised by a linear dependence of $\Gamma(Q)$. Moreover, Brownian diffusion which describes a continuous motion, is characterised by a square law dependence of the momentum transfer (green dotted line in Fig. 3) and cannot reproduce the momentum transfer dependence of the broadening.

Note that the average jump distance ($l = 3.45$ Å) corresponds to 1.4 a_{gr} where a_{gr} is the graphite lattice constant. Hence the average jump length suggests that a significant number of long jumps occurs at this temperature. Using the residence time τ and the average jump length l Einstein's equation for diffusion (in the two-dimensional case) can be used to determine the diffusion constant D [43]:

$$D = \frac{\langle l \rangle^2}{4\tau} \tag{4}$$

with the mean jump length $\langle l \rangle$. Using (4) we obtain a diffusion constant of $D = (3.9\pm0.4)\cdot10^{-8}$ m^2/s at 94 K. The diffusion constant for ammonia adsorbed on graphitized carbon black has been determined to range from $D = 0.6\cdot10^{-8}$ m^2/s at 180 K to $D = 6\cdot10^{-8}$ m^2/s at 230 K using NMR [46] with similar values at 205 K using neutron scattering [47]. Considering that these values were determined at much higher temperatures (where ammonia on graphite will already have been completely desorbed) and for a different substrate, the diffusion constants are within the same order of magnitude compared to our results.

The diffusion of small molecules on graphite and graphene has been mainly treated by theoretical approaches where typically a fast diffusion process is predicted [48,49]. E.g. Ma et al. [48] report that H_2O adsorbed on graphene undergoes an ultra-fast diffusion process at 100 K with $D = 6\cdot10^{-9}$ m^2/s. The value determined for ammonia in our study is even one order of magnitude larger showing that the diffusion of ammonia on graphite is a very rapid process. Compared to other experimental studies it is about the same size compared to the jump diffusion of molecular hydrogen (H_2) on graphite [33,50] and again one order of magnitude larger than the diffusion constant found for benzene (C_6H_6) on graphite [20].

As a next step we consider the coverage and temperature dependence of the diffusion process. Unfortunately, the signal-to-noise ratio and the difference between the scattering function and the resolution function is too small for the data measured at 0.5 ML coverage to extract a reliable quasi-elastic broadening. The only exception is the highest temperature (94 K), measured at this coverage. This is due to the fact that with increasing temperature the broadening becomes larger, as one would expect for an activated motion. Fig. 3 shows a comparison of the quasi-elastic broadening $\Gamma(Q)$ for 0.5 and 0.9 ML of NH_3 coverage as a function of momentum transfer Q. One may anticipate a slightly reduced broadening at the higher coverage and thus a smaller hopping rate, which is however, only discernible at small Q due to the uncertainties. In general the experiments show no significant coverage dependence within the experimental uncertainties. Hence we cannot quantify the respective contributions of the molecule-molecule collisions or the molecule-surface interactions to the diffusion process.

In Fig. 4a the quasi-elastic broadening $\Gamma(Q)$ is plotted for all

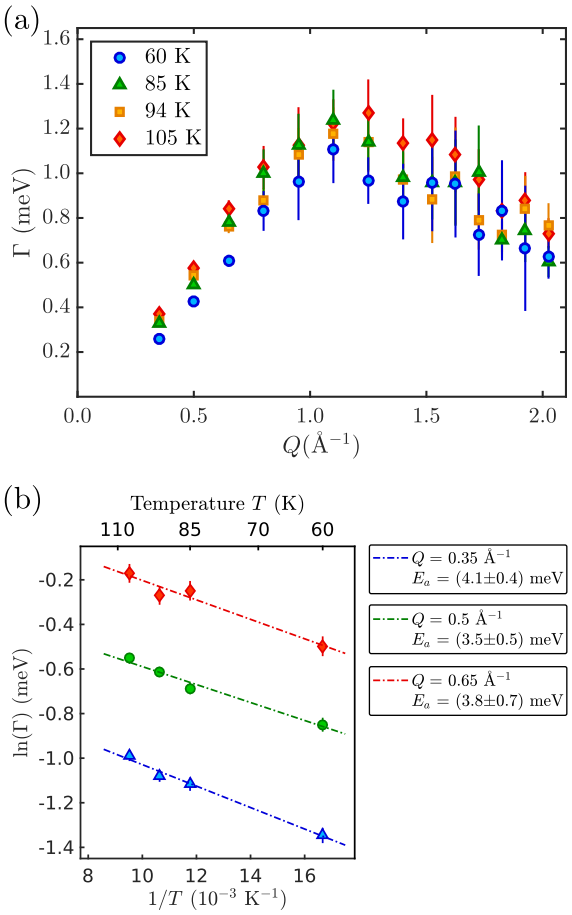

Fig. 4. Temperature dependence of the quasi-elastic broadening for 0.9 ML of NH_3 on graphite. (a) Temperature dependence of the quasielastic broadening $\Gamma(Q)$ at 0.9 ML coverage. While the speed of the diffusion changes with temperature, the overall dependence upon Q remains constant. (b) Arrhenius plot showing the temperature dependence of the broadening Γ at small Q. The activation energy for diffusion, E_a, is extracted from the slope of the linear fit. (A colour version of this figure can be viewed online.)

temperatures measured at an NH_3 coverage of 0.9 ML. The broadening and hence the hopping rate becomes larger with increasing temperature, but the overall dependence upon Q, i.e., the hopping distance, remains largely constant.

While at high Q the uncertainties in Fig. 4a are too large to extract a meaningful temperature dependence, we can use the temperature dependence of Γ at small Q, i.e., for long range diffusion, to obtain a diffusion barrier. For a thermally activated processes, Arrhenius' law predicts a temperature dependence of the broadening Γ, as:

$$\Gamma = \Gamma_0 \, e^{-\frac{E_a}{k_B T}}, \tag{5}$$

where Γ_0 is the pre-exponential factor, E_a is the activation energy for diffusion, k_B the Boltzmann constant and T the sample temperature. Taking the natural logarithm of (5) results in a linear relationship between the inverse of the temperature, $1/T$, and the natural logarithm of the broadening Γ.

Fig. 4b shows such an Arrhenius plot of the broadening Γ for the three lowest momentum transfers Q. The activation energy, extracted from the linear fit varies between 3.5 and 4.1 meV giving

rise to a mean value of $E_a = (3.8 \pm 0.7)$ meV.

Note that the hereby determined diffusion barrier is smaller than the thermal energy (k_BT) of the substrate, while on the other hand the thermal energy is still significantly below the desorption energy. Other experimental examples for the occurrence of jump-like diffusion in the case of a very low potential energy barrier include the case of Cs on Cu(001) [51]. Nevertheless, it is quite unusual to observe hopping motion for a system with such a weakly corrugated potential energy surface. It suggests that substantial energy dissipation channels must be present in the ammonia/graphite system (e.g., by molecular collisions or by energy dissipation to the surface), in contrast to the diffusion of flat hydrocarbons such as pyrene on graphite [18].

In general, at temperatures higher than the diffusion barrier height, the time spent by the adsorbate near the minimum of the adsorption potential is comparable to the time in the in-between regions. In this case both diffusive and vibrational motions, associated with a temporary trapping of an adsorbate inside the surface potential well, contribute to the quasielastic broadening and are coupled [52]. As theoretically proposed by Martínez-Casado et al. [53] in a generalised model for the quasi-elastic broadening, a combination of both cases should give rise to a more complicated dependence of the broadening on the momentum transfer due to the diffusive hopping motion and the friction parameter η. As shown by Jardine et al. [54], friction may become more apparent in the broadening due to these vibrational motions, whereas the contribution of the effect to energy dissipation during diffusion cannot be decoupled due to the final energy resolution of the instrument. The internal degrees of freedom of the adsorbed molecule may even further complicate the underlying microscopic processes [55].

However, based on the approach by Martínez-Casado et al. [53], we can use the fact that the CE model contains Brownian diffusion as a long range diffusion limit, to obtain a crude estimate for the friction. For $Q \rightarrow 0$ the broadening converges to a parabola, i.e. the broadening approaches the same momentum transfer dependence as for Brownian motion, where the atomic-scale friction η can be directly extracted using Einstein's relation [32] as used in the fluctuation-dissipation theorem by Kubo [19,32]:

$$D = \frac{k_B T}{\eta m}, \tag{6}$$

where m is the mass of the ammonia molecule. Using this approximation we obtain an estimate of the atomic-scale friction of $\eta = 1.2$ ps^{-1} from the data in Fig. 3, which is a medium value for the atomic-scale friction compared to previous studies [51,54,55].

We would like to stress that the result should be taken with care and can only serve as a crude estimate. Friction in surface diffusion processes can be caused by a variety of energy dissipation channels, including also interactions between the adsorbates and interaction with the substrate. Since the measurements were performed close to the monolayer regime, the friction parameter extracted from the fitting of the quasi-elastic broadening to a parabola at low momentum transfers cannot be written as a simple sum of contributions to the energy dissipation [56]. It is rather an averaged friction parameter which is related to the energy dissipation frequency of a single molecule diffusing on the basal plane of graphite and interacting with the surface phonon bath and its neighbouring molecules.

Nonetheless it suggests that friction plays a significant role in the NH_3/graphite system. Indeed, for a system with non-negligible friction, one would expect that for each single jump an energy equivalent to the height of the barrier is dissipated [57,58]. Therefore energy dissipation via frictional coupling is likely to be responsible for the occurrence of the hopping motion. On the other hand with increasing thermal energy compared to the potential energy surface, more and more long jumps start to set in during jump diffusion [58–61], which is evident from the experimental data, since the best fit Chudley-Elliott model gives an average jump length of 1.4 a_{gr}.

Note that a similar motion was observed for molecular hydrogen on graphite with jump diffusion and also a very low activation energy [33,50,62]. Although the role of atomic-scale friction was not explicitly discussed in those cases, it suggests together with the results presented in our study, that friction may be partly caused by the geometry of the molecule when compared to the flat-lying polycyclic aromatic hydrocarbons which closely resemble the structure of the graphite substrate [18,20,63].

Finally, the occurrence of long jumps makes the determination of a meaningful activation energy challenging since under these circumstances jumps start to become correlated as shown in theoretical studies [57,64]. In the case of exfoliated graphite this is further complicated by the azimuthal averaging as described above. Nevertheless we will use this value as a rough estimate for the diffusion of ammonia on graphite and attempt in the following to compare our experimental results with DFT calculations.

3.1. DFT results

We have studied the adsorption of NH_3 on graphite for a large number of different adsorption geometries. Those include 6 different adsorption sites within the graphite unit cell, the orientation of the molecule with the hydrogen atoms pointing upwards (U) or downwards (D) as well as three different rotations around the axis perpendicular to the surface. Fig. 5 shows the energetically most favourable adsorption site, with the molecule located at the C

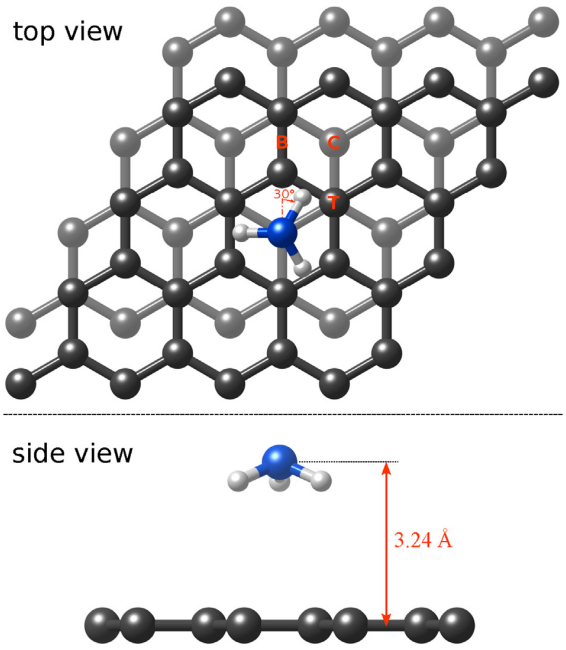

Fig. 5. Geometry of the NH_3/graphite system investigated in this study. The high symmetry adsorption positions with respect to the graphite lattice are labelled as T: on-top; B: onbond or bridge and C: centre. The most favourable adsorption site according to vdW corrected DFT is for NH_3 at the centre position with the rotation axis perpendicular to the surface and the hydrogen atoms directed towards the onbond sites. (A colour version of this figure can be viewed online.)

site (centre) and the H-atoms pointing towards the surface, directed towards the onbond sites.

Based on the vdW corrected DFT calculations the adsorption energy of a single NH_3 molecule on graphite is 173 meV, which is slightly reduced to 151 meV in the high coverage regime (about 1 ML). Note that the adsorption energy is much closer to the experimentally found values from TDS than in previous DFT calculations which yielded adsorption energies in the order of 25–30% of the experimentally determined value. Hence it shows the importance of vdW interactions in this system and that previous DFT results (without vdW interactions) should be taken cautiously when trying to make predictions.

Interestingly Böttcher et al. [9] obtain a similar adsorption energy of 146 meV for NH_3 on graphene/Ni(111) from vdW corrected DFT, however, the molecule is adsorbed in the upwards configuration on graphene/Ni(111). On the other hand, recent X-ray absorption spectroscopy measurements provided evidence for a chemical contribution to the adsorption bond in the case of NH_3 adsorbed on graphene/Ni(111) [65]. Hence it is possible that due to the present metal substrate the adsorption geometry of the ammonia molecule on graphene/Ni(111) changes compared to ammonia adsorbed on graphite.

Table 1 summarises six arrangements where the molecule is placed in the high symmetry positions (T, B, and C) at a rotation of 30° for an ammonia coverage of about 1 ML. For the complete set (including all considered adsorption geometries and coverages) please refer to the supplementary information, where a video, visualising the diffusion process of ammonia molecules on the graphite surface based on force field molecular dynamics simulation can be found as well. We conclude from Table 1 that the downwards configuration is definitively favoured with respect to the upwards configuration, regardless of the adsorption site. For the down configuration the energy differences between different adsorption sites are in general extremely small. Moreover, the distance of the molecule with respect to the surface does not vary significantly, e.g., for a given rotation angle and downwards orientation the minimum distance is 3.24 Å at the C site and the maximum is 3.26 Å at the B site.

Hence, the DFT calculations confirm that the diffusion of ammonia on graphite should be governed by a weakly corrugated potential energy surface. It can also be seen from Fig. 6 which shows a contour plot of the potential energy surface for NH_3 adsorbed on different positions of the graphite substrate. The adsorption energies for both the upwards and the downwards configuration are illustrated, as extracted from the vdW corrected DFT calculations with the minimum energy rotation of 30° and at a coverage of approximately 1 ML NH_3. For the downwards configuration, Fig. 6a the top site located above the second layer carbon atom is energetically less favourable by a significant amount but all other adsorption positions vary only by several meV. Based on the "static snapshots" i.e. the energy differences between the adsorption sites from vdW corrected DFT (Table 1 and Fig. 6a) the diffusion barrier would be 6 meV, which is in good agreement with the value extracted from the experimental data. According to this the most likely trajectory would be from the C site via the B site to the next C site.

Table 1
The adsorption energy E_a and the energy difference ΔE_a relative to the most favourable adsorption site for NH_3 on graphite. The six different adsorption geometries are with the H-atoms pointing upwards (U) or downwards (D) and the centre (C), top (T) and bridge (B) adsorption site.

Orientation	Position	E_a (eV)	ΔE_a (meV)
D	T	−0.144	7
D	B	−0.145	6
D	C	−0.151	0
U	T	−0.089	62
U	B	−0.095	56
U	C	−0.113	38

Furthermore, we have also calculated the energy difference for nitrogen inversion (the umbrella or symmetric deformation vibration mode) on graphite. Here, the energy difference between the up and down NH_3 configuration in a given position can only serve as a lower limit to the "real" inversion barrier and gives 38 meV for 1 ML of NH_3 in our case. Therefore we have also calculated the transition state structure for NH_3 inversion on the global minimum for both the (2×2) and (4×4) cells. At lower coverage the barrier is 157 meV (starting from the down configuration) and 142 meV (starting from the up configuration). At higher coverage, the barriers are reduced to 132 meV and 94 meV, respectively. Since the down and up configurations are not symmetrical, there is a slight difference in the barrier from the down and up structures.

There is quite a substantial activation energy change when going to the higher coverage. We suspect that this change may be caused by repulsive steric interactions between the hydrogen atoms of two adjacent NH_3 molecules. In general the barrier is in line with the values reported for other systems with adsorbed ammonia. E.g the energy of this mode is typically between 130 and 145 meV for NH_3 adsorbed on metal surfaces [66,67]. For NH_3 on HOPG the umbrella mode could only be observed in the multilayer case where the value is similar to the one for solid ammonia [68] upon adsorption on graphite.

3.2. Spin-echo measurements

The neutron spin-echo experiments for deuterated ammonia (ND_3) at a surface coverage of 0.9 ML were conducted on IN11 for sample temperatures of 2 K (resolution) and for 60 K, 85 K, 94 K and 105 K. The NSE measurement delivers the development of the space correlation function with time t, i.e., the normalised intermediate scattering function $S(Q,t)/S(Q,0)$[32,69]. This function can also be obtained by Fourier transforming the scattering function $S(Q,\Delta E)$. Converting the quasi-elastic broadening determined in section 3 to a broadening in time gives rise to $\tau \approx 1$ ps at $Q = 0.5$ Å^{-1}. This is below the spectral acceptance window of IN11 and the corresponding decay does not appear in the IN11 spectra. Nevertheless, the spin-echo measurements show that there is no additional motion at longer timescales, confirming the fast diffusion process seen in the TOF measurements (see also the supplementary information).

4. Summary and conclusion

We have studied the diffusion of ammonia on exfoliated graphite using quasi-elastic neutron scattering. The dependency of the quasielastic broadening on the momentum transfer shows that ammonia follows a hopping motion on the basal plane of graphite. The diffusion constant at 94 K was determined as $D = (3.9 \pm 0.4) \cdot 10^{-8}$ m^2/s suggesting that the diffusion of ammonia on graphite is a very rapid process, comparable to the diffusion of molecular hydrogen and much faster than the diffusion of larger molecules, such as benzene. Considering in particular the mass of the molecule, together with the unusual tilted NH–π bonding, makes the observed diffusion in this system uniquely fast. In terms of possible applications for gas sensing purposes, it implies that after adsorption the kinetics on the surface should not be the limiting factor.

The activation energy extracted from the temperature dependence of the quasielastic broadening is about 4 meV. The

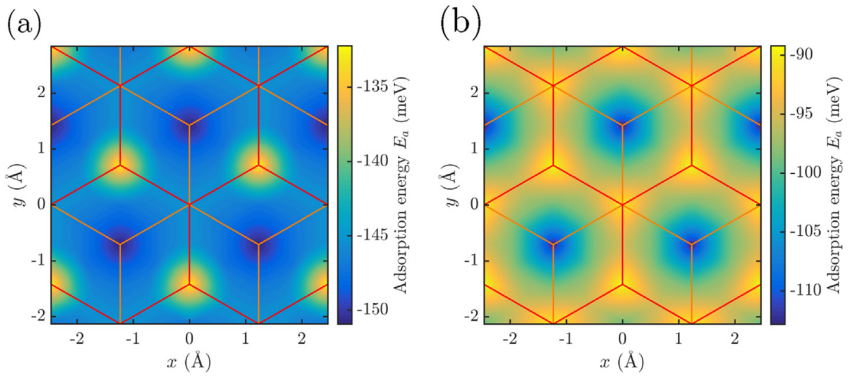

Fig. 6. Comparison of the potential energy surface as obtained by the vdW corrected DFT for NH_3 in the downwards and upwards configuration. Both calculations are for the minimum energy rotation of 30° and at a coverage of approximately 1 ML NH_3. The red and orange lines represent the first and second layer of the graphite substrate, respectively. (a) Downwards conguration. (b) Upwards configuration. (A colour version of this figure can be viewed online.)

combination of jump diffusion and a low activation energy suggests that NH_3/graphite is a system with a rather unusual combination of a weakly corrugated potential energy surface together with a significant friction. The combination of jump diffusion and a low activation energy suggests that NH_3/graphite is a system with a rather unusual combination of a weakly corrugated potential energy surface together with a significant friction. Indeed, preliminary molecular dynamics studies suggest that the ammonia molecules show a peculiar rolling pattern of motion (see data in supplementary information). We hope that our work will initiate further theoretical investigations in order to address this interesting finding.

The calculated potential energy surfaces is extremely flat for a given orientation of the molecule. The configuration of the adsorbate with the reverse polarity (NH bonds pointing upwards) is energetically unfavourable, therefore breaking the symmetry of the umbrella inversion mode. Furthermore, the adsorption energy of ammonia on graphite is determined as 173 meV from DFT, much closer to the experimental value compared to previous DFT calculations without dispersion corrections. The close agreement between the calculated adsorption energy, diffusion barrier and the experimental results confirm the accuracy of the TS dispersion corrections scheme for vdW bonded systems on graphite.

Acknowledgement

One of us (A.T.) acknowledges financial support provided by the FWF (Austrian Science Fund) within the project J3479-N20. We thank Francesco Marino for the molecular dynamics simulations which are shown in the supplementary information. The authors would like to thank E. Bahn for many helpful discussions. M.S. is grateful for the support from the Royal Society. This work used the ARCHER UK National Supercomputing Service via the membership of the UK's HEC Materials Chemistry Consortium which is funded by the EPSRC (EP/L000202). The authors acknowledge the generous provision of neutron beam time at the ILL.

Appendix A. Supplementary data

Supplementary data related to this article can be found at https://doi.org/10.1016/j.carbon.2017.09.104.

References

[1] H. Liu, Y. Liu, D. Zhu, Chemical doping of graphene, J. Mater Chem. 21 (2011) 3335–3345, https://doi.org/10.1039/C0JM02922J.
[2] X. Wang, X. Li, L. Zhang, Y. Yoon, P.K. Weber, H. Wang, et al., N-doping of graphene through electrothermal reactions with ammonia, Science 324 (5928) (2009) 768–771, https://doi.org/10.1126/science.1170335.
[3] H.E. Romero, P. Joshi, A.K. Gupta, H.R. Gutierrez, M.W. Cole, S.A. Tadigadapa, et al., Adsorption of ammonia on graphene, Nanotechnology 20 (24) (2009) 245501, https://doi.org/10.1088/0957-4484/20/24/245501.
[4] R.K. Paul, S. Badhulika, N.M. Saucedo, A. Mulchandani, Graphene nanomesh as highly sensitive chemiresistor gas sensor, Anal. Chem. 84 (19) (2012) 8171–8178, https://doi.org/10.1021/ac3012895.
[5] W. Yuan, G. Shi, Graphene-based gas sensors, J. Mater Chem. A 1 (2013) 10078–10091, https://doi.org/10.1039/C3TA11774J.
[6] Z.B. Aziza, Q. Zhang, D. Baillargeat, Graphene/mica based ammonia gas sensors, Appl. Phys. Lett. 105 (25) (2014) 254102, https://doi.org/10.1063/1.4905039.
[7] Z. Zhang, X. Zhang, W. Luo, H. Yang, Y. He, Y. Liu, et al., Study on adsorption and desorption of ammonia on graphene, Nanoscale Res. Lett. 10 (1) (2015) 1–8, https://doi.org/10.1186/s11671-015-1060-7.
[8] F. Schedin, A.K. Geim, S.V. Morozov, E.W. Hill, P. Blake, M.I. Katsnelson, et al., Detection of individual gas molecules adsorbed on graphene, Nat. Mater. 6 (9) (2007) 652–655, https://doi.org/10.1038/nmat1967.
[9] S. Böttcher, M. Weser, Y.S. Dedkov, K. Horn, E.N. Voloshina, B. Paulus, Graphene on ferromagnetic surfaces and its functionalization with water and ammonia, Nanoscale Res. Lett. 6 (1) (2011) 1–7, https://doi.org/10.1186/1556-276X-6-214.
[10] C. Sun, B. Bai, Gas diffusion on graphene surfaces, Phys. Chem. Chem. Phys. 19 (2017) 3894–3902, https://doi.org/10.1039/C6CP06267A.
[11] M. Bienfait, P. Zeppenfeld, R.C. Ramos, J.M. Gay, O.E. Vilches, G. Coddens, Isotopic ordering in adsorbed hydrogen monolayers, Phys. Rev. B 60 (1999) 11773–11782, https://doi.org/10.1103/PhysRevB.60.11773.
[12] R. Thomas, Neutron scattering from adsorbed systems, Prog. Solid State Chem. 14 (1) (1982) 1–93, https://doi.org/10.1016/0079-6786(82)90002-4.
[13] S.M. Clarke, Neutron diffraction and incoherent neutron scattering from adsorbed layers, Curr. Opin. Colloid Interface Sci. 6 (2) (2001) 118–125, https://doi.org/10.1016/S1359-0294(01)00069-3.
[14] T. Arnold, R.K. Thomas, M.A. Castro, S.M. Clarke, L. Messe, A. Inaba, The crystalline structures of the even alkanes hexane, octane, decane, dodecane and tetradecane monolayers adsorbed on graphite at submonolayer coverages and from the liquid, Phys. Chem. Chem. Phys. 4 (2002a) 345–351, https://doi.org/10.1039/B108190J.
[15] T. Arnold, C.C. Dong, R.K. Thomas, M.A. Castro, A. Perdigon, S.M. Clarke, et al., The crystalline structures of the odd alkanes pentane, heptane, nonane, undecane, tridecane and pentadecane monolayers adsorbed on graphite at submonolayer coverages and from the liquid, Phys. Chem. Chem. Phys. 4 (2002b) 3430–3435, https://doi.org/10.1039/B201988B.
[16] L.W. Bruch, R.D. Diehl, J.A. Venables, Progress in the measurement and modeling of physisorbed layers, Rev. Mod. Phys. 79 (2007) 1381–1454, https://doi.org/10.1103/RevModPhys.79.1381.
[17] T. Arnold, S.M. Clarke, Diffraction from physisorbed layers, Curr. Opin. Colloid Interface Sci. 17 (1) (2012) 23–32, https://doi.org/10.1016/j.cocis.2011.11.003.
[18] I. Calvo-Almazán, M. Sacchi, A. Tamtögl, E. Bahn, M.M. Koza, S. Miret-Artés, et al., Ballistic diffusion in poly-aromatic hydrocarbons on graphite, J. Phys. Chem. Lett. 7 (24) (2016) 5285–5290, https://doi.org/10.1021/acs.jpclett.6b02305.
[19] I. Calvo-Almazán, E. Bahn, M. Koza, M. Zbiri, M. Maccarini, M. Telling, et al., Benzene diffusion on graphite described by a rough hard disk model, Carbon 79 (2014) 183–191, https://doi.org/10.1016/j.carbon.2014.07.058.
[20] H. Hedgeland, P. Fouquet, A.P. Jardine, G. Alexandrowicz, W. Allison, J. Ellis,

Measurement of single-molecule frictional dissipation in a prototypical nanoscale system, Nat. Phys. 5 (8) (2009) 561–564, https://doi.org/10.1038/nphys1335.
[21] L. Bardotti, P. Jensen, A. Hoareau, M. Treilleux, B. Cabaud, Experimental observation of fast diffusion of large antimony clusters on graphite surfaces, Phys. Rev. Lett. 74 (1995) 4694–4697, https://doi.org/10.1103/PhysRevLett.74.4694.
[22] K. Miura, S. Kamiya, N. Sasaki, C_{60} molecular bearings, Phys. Rev. Lett. 90 (2003) 055509, https://doi.org/10.1103/PhysRevLett.90.055509.
[23] R. Guerra, U. Tartaglino, A. Vanossi, E. Tosatti, Ballistic nanofriction, Nat. Mater 9 (8) (2010) 634–637, https://doi.org/10.1038/nmat2798.
[24] S. Kawai, A. Benassi, E. Gnecco, H. Söde, R. Pawlak, X. Feng, et al., Superlubricity of graphene nanoribbons on gold surfaces, Science 351 (6276) (2016) 957–961, https://doi.org/10.1126/science.aad3569.
[25] A.S. de Wijn, Internal degrees of freedom and transport of benzene on graphite, Phys. Rev. E 84 (2011) 011610, https://doi.org/10.1103/PhysRevE.84.011610.
[26] R. Pawlak, S. Kawai, T. Meier, T. Glatzel, A. Baratoff, E. Meyer, Single-molecule manipulation experiments to explore friction and adhesion, J. Phys. D. Appl. Phys. 50 (11) (2017) 113003, https://doi.org/10.1088/1361-6463/aa599d.
[27] W.R. Browne, B.L. Feringa, Making molecular machines work, Nat. Nanotechnol. 1 (1) (2006) 25–35, https://doi.org/10.1038/nnano.2006.45.
[28] J. Tabony, Nuclear magnetic resonance studies of molecules physisorbed on homogeneous surfaces, Prog. Nucl. Magn. Reson Spectrosc. 14 (1) (1980) 1–26, https://doi.org/10.1016/0079-6565(80)80001-X.
[29] H. Ulbricht, R. Zacharia, N. Cindir, T. Hertel, Thermal desorption of gases and solvents from graphite and carbon nanotube surfaces, Carbon 44 (14) (2006) 2931–2942, https://doi.org/10.1016/j.carbon.2006.05.040.
[30] O. Leenaerts, B. Partoens, F.M. Peeters, Adsorption of H_2O, NH_3, CO, NO_2, and NO on graphene: a first-principles study, Phys. Rev. B 77 (12) (2008) 125416, https://doi.org/10.1103/PhysRevB.77.125416.
[31] X. Lin, J. Ni, C. Fang, Adsorption capacity of H_2O, NH_3, CO, and NO_2 on the pristine graphene, J. Appl. Phys. 113 (3) (2013) 034306, https://doi.org/10.1063/1.4776239.
[32] P. Fouquet, H. Hedgeland, A.P. Jardine, Surface diffusion studies using neutron and helium spin-echo spectroscopy, Z Phys. Chem. 224 (224) (2010) 61–81, https://doi.org/10.1524/zpch.2010.6092.
[33] E. Bahn, O. Czakkel, B. Nagy, K. László, S. Villar-Rodil, J.M. Tascón, et al., Diffusion of molecular hydrogen in carbon aerogel, Carbon 98 (2016) 572–581, https://doi.org/10.1016/j.carbon.2015.11.034.
[34] E. Bahn, A. Tamtögl, J. Ellis, W. Allison, P. Fouquet, Structure and dynamics investigations of a partially hydrogenated graphene/Ni(111) surface, Carbon 114 (2017) 504–510, https://doi.org/10.1016/j.carbon.2016.12.055.
[35] E.P. Gilbert, P.A. Reynolds, J.W. White, Characterisation of a basal-plane-oriented graphite, J. Chem. Soc. Faraday Trans. 94 (13) (1998) 1861–1868, https://doi.org/10.1039/A801303I.
[36] Y. Finkelstein, D. Nemirovsky, R. Moreh, G. Kimmel, Study of the Papyex structure using neutron Compton scattering, Phys. B Condens Matter 291 (12) (2000) 213–218, https://doi.org/10.1016/S0921-4526(99)01876-1.
[37] P. Rowntree, G. Scoles, J. Xu, The structure of ammonia overlayers physisorbed onto the surface of single crystal graphite, determined by means of atomic beam diffraction, J. Chem. Phys. 92 (6) (1990) 3853–3857, https://doi.org/10.1063/1.457842.
[38] A. Tamtögl, I. Calvo-Almazán, P. Fouquet, M. Koza, M. Zbiri, Diffusion of Ammonia on Exfoliated Graphite, Institut Laue-Langevin (ILL), 2016, https://doi.org/10.5291/ILL-DATA.7-05-458.
[39] S.J. Clark, M.D. Segall, C.J. Pickard, P.J. Hasnip, M.I.J. Probert, K. Refson, et al., First principles methods using CASTEP, Z Krist. Cryst. Mater 220 (5–6) (2005) 567–570, https://doi.org/10.1524/zkri.220.5.567.65075.
[40] J.P. Perdew, K. Burke, M. Ernzerhof, Generalized gradient approximation made simple, Phys. Rev. Lett. 77 (18) (1996) 3865–3868, https://doi.org/10.1103/PhysRevLett.77.3865.
[41] A. Tkatchenko, M. Scheffler, Accurate molecular van der Waals interactions from ground-state electron density and free-atom reference data, Phys. Rev. Lett. 102 (7) (2009) 073005, https://doi.org/10.1103/PhysRevLett.102.073005.
[42] C.T. Chudley, R.J. Elliott, Neutron scattering from a liquid on a jump diffusion model, Proc. Phys. Soc. 77 (2) (1961) 353, https://doi.org/10.1088/0370-1328/77/2/319.
[43] M. Bée, Quasielastic Neutron Scattering, Adam Hilger, Bristol, 1988.
[44] R. Lechner, Effects of low-dimensionality in solid-state protonic conductors, Solid State Ionics 77 (1995) 280–286, https://doi.org/10.1016/0167-2738(94)00308-F.
[45] H. Jobic, Diffusion à longue distance, Le J. de Physique IV 10 (PR1) (2000) Pr1–Pr77, https://doi.org/10.1051/jp4:2000106.
[46] J. Tabony, T. Cosgrove, Diffusion coefficients of small molecules at the gas-solid interface as measured by the nuclear magnetic resonance pulsed field gradient method, Chem. Phys. Lett. 67 (1) (1979) 103–106, https://doi.org/10.1016/0009-2614(79)87115-8.
[47] P.H. Gamlen, R.K. Thomas, T.D. Trewern, G. Bomchil, N.M. Harris, M. Leslie, et al., Structure and dynamics of ammonia absorbed on graphitized carbon black. Part 3.-Neutron quasielastic and inelastic spectra, J. Chem. Soc. Faraday Trans. 1 75 (1979) 1553–1569, https://doi.org/10.1039/F19797501553.
[48] J. Ma, A. Michaelides, D. Alfè, L. Schimka, G. Kresse, E. Wang, Adsorption and diffusion of water on graphene from first principles, Phys. Rev. B 84 (2011) 033402, https://doi.org/10.1103/PhysRevB.84.033402.
[49] S. Tang, Z. Cao, Adsorption of nitrogen oxides on graphene and graphene oxides: insights from density functional calculations, J. Chem. Phys. 134 (4) (2011) 044710, https://doi.org/10.1063/1.3541249.
[50] O.E. Haas, J.M. Simon, S. Kjelstrup, Surface self-diffusion and mean displacement of hydrogen on graphite and a PEM fuel cell catalyst support, J. Phys. Chem. C 113 (47) (2009) 20281–20289, https://doi.org/10.1021/jp902491s.
[51] A.P. Jardine, G. Alexandrowicz, H. Hedgeland, R.D. Diehl, W. Allison, J. Ellis, Vibration and diffusion of Cs atoms on Cu(001), J. Phys. Condens Matter 19 (30) (2007) 305010, https://doi.org/10.1088/0953-8984/19/30/305010.
[52] L.Y. Chen, S.C. Ying, Dynamics of adatoms on solid surfaces, Phys. Rev. B 49 (1994) 13838–13847, https://doi.org/10.1103/PhysRevB.49.13838.
[53] R. Martínez-Casado, J.L. Vega, A.S. Sanz, S. Miret-Artés, Generalized Chudley-Elliott vibration-jump model in activated atom surface diffusion, J. Chem. Phys. 126 (19) (2007) 194711, https://doi.org/10.1063/1.2735586.
[54] A.P. Jardine, J. Ellis, W. Allison, Effects of resolution and friction in the interpretation of QHAS measurements, J. Chem. Phys. 120 (18) (2004) 8724–8733, https://doi.org/10.1063/1.1695320.
[55] B.A.J. Lechner, A.S. de Wijn, H. Hedgeland, A.P. Jardine, B.J. Hinch, W. Allison, et al., Atomic scale friction of molecular adsorbates during diffusion, J. Chem. Phys. 138 (19) (2013) 194710, https://doi.org/10.1063/1.4804269.
[56] R. Martínez-Casado, A. Sanz, J. Vega, G. Rojas-Lorenzo, S. Miret-Arttés, Linear response theory of activated surface diffusion with interacting adsorbates, Chem. Phys. 370 (1) (2010) 180–193, https://doi.org/10.1016/j.chemphys.2010.02.013.
[57] G. Boisvert, L.J. Lewis, Self-diffusion on low-index metallic surfaces: Ag and Au (100) and (111), Phys. Rev. B 54 (1996) 2880–2889, https://doi.org/10.1103/PhysRevB.54.2880.
[58] E. Hershkovitz, P. Talkner, E. Pollak, Y. Georgievskii, Multiple hops in multi-dimensional activated surface diffusion, Surf. Sci. 421 (1) (1999) 73–88, https://doi.org/10.1016/S0039-6028(98)00820-6.
[59] T.R. Linderoth, S. Horch, E. Lægsgaard, I. Stensgaard, F. Besenbacher, Surface diffusion of Pt on Pt(110): Arrhenius behavior of long jumps, Phys. Rev. Lett. 78 (1997) 4978–4981, https://doi.org/10.1103/PhysRevLett.78.4978.
[60] J. Ferrón, R. Miranda, J.J. de Miguel, Atomic jumps during surface diffusion, Phys. Rev. B 79 (2009) 245407, https://doi.org/10.1103/PhysRevB.79.245407.
[61] S. Miret-Artés, E. Pollak, The dynamics of activated surface diffusion, J. Phys. Condens Matter 17 (49) (2005) S4133, https://doi.org/10.1088/0953-8984/17/49/009.
[62] J. Petucci, C. LeBlond, M. Karimi, G. Vidali, Diffusion, adsorption, and desorption of molecular hydrogen on graphene and in graphite, J. Chem. Phys. 139 (4) (2013) 044706, https://doi.org/10.1063/1.4813919.
[63] S.Y. Guo, S.J. Jenkins, W. Ji, Z. Ning, J.C. Polanyi, M. Sacchi, et al., Repulsion-induced surface-migration by ballistics and bounce, J. Phys. Chem. Lett. 6 (20) (2015) 4093–4098, https://doi.org/10.1021/acs.jpclett.5b01829.
[64] J. Ferrón, L. Gómez, J.J. de Miguel, R. Miranda, Nonstochastic behavior of atomic surface diffusion on Cu(111) down to low temperatures, Phys. Rev. Lett. 93 (2004) 166107, https://doi.org/10.1103/PhysRevLett.93.166107.
[65] S. Böttcher, H. Vita, M. Weser, F. Bisti, Y.S. Dedkov, K. Horn, Adsorption of water and ammonia on graphene: evidence for chemisorption from x-ray absorption spectra, J. Phys. Chem. Lett. 8 (15) (2017) 3668–3672, https://doi.org/10.1021/acs.jpclett.7b01085.
[66] J.E. Parmeter, Y. Wang, C.B. Mullins, W.H. Weinberg, Electron energy loss spectroscopy of ammonia on Ru(001), J. Chem. Phys. 88 (8) (1988) 5225–5236, https://doi.org/10.1063/1.454597.
[67] J.I. Pascual, N. Lorente, Z. Song, H. Conrad, H.P. Rust, Selectivity in vibrationally mediated single-molecule chemistry, Nature 423 (6939) (2003) 525–528, https://doi.org/10.1038/nature01649.
[68] A. Bolina, W. Brown, Studies of physisorbed ammonia overlayers adsorbed on graphite, Surf. Sci. 598 (1–3) (2005) 45–56, https://doi.org/10.1016/j.susc.2005.08.025.
[69] F. Mezei, Neutron Spin Echo: Proceedings of a Laue-langevin Institut Workshop Grenoble, October 15–16, 1979; Chap. The Principles of Neutron Spin Echo, Springer, 1980, pp. 1–26.

6.9 Publication I

Tamtögl, A., Campi, D., Bremholm, M., Hedegaard, E. M. J., Iversen, B. B., Bianchi, M., Hofmann, P., Marzari, N., Benedek, G., Ellis, J. & Allison, W. Nanoscale surface dynamics of Bi_2Te_3(111): observation of a prominent surface acoustic wave and the role of van der Waals interactions. *Nanoscale* **10,** 14627–14636 (2018)

contributions	
funding	A. Tamtögl, W. Allison, J. Ellis, N. Marzari, P. Hofmann
sample synthesis	E. M. J. Hedegaard, M. Bremholm, B. B. Iversen
preparation / setup	A. Tamtögl, M. Bianchi
data acquisition	A. Tamtögl
theory (*ab initio*) calculations	D. Campi
data analysis	A. Tamtögl
interpretation	A. Tamtögl, D. Campi, G. Benedek
publication writing	A. Tamtögl, D. Campi

Reprinted from:

Tamtögl, A., Campi, D., Bremholm, M., Hedegaard, E. M. J., Iversen, B. B., Bianchi, M., Hofmann, P., Marzari, N., Benedek, G., Ellis, J. & Allison, W. Nanoscale surface dynamics of Bi_2Te_3(111): observation of a prominent surface acoustic wave and the role of van der Waals interactions. *Nanoscale* **10,** 14627–14636 (2018)

with permission from The Royal Society of Chemistry.

Nanoscale

PAPER

View Article Online
View Journal

Cite this: DOI: 10.1039/c8nr03102a

Nanoscale surface dynamics of Bi_2Te_3(111): observation of a prominent surface acoustic wave and the role of van der Waals interactions

Anton Tamtögl, *[a,b] Davide Campi, [c] Martin Bremholm, [d] Ellen M. J. Hedegaard,[d] Bo B. Iversen, [d] Marco Bianchi, [e] Philip Hofmann, [e] Nicola Marzari,[c] Giorgio Benedek, [f,g] John Ellis[a] and William Allison[a]

We present a combined experimental and theoretical study of the surface vibrational modes of the topological insulator Bi_2Te_3. Using high-resolution helium-3 spin-echo spectroscopy we are able to resolve the acoustic phonon modes of Bi_2Te_3(111). The low energy region of the lattice vibrations is mainly dominated by the Rayleigh mode which has been claimed to be absent in previous experimental studies. The appearance of the Rayleigh mode is consistent with previous bulk lattice dynamics studies as well as theoretical predictions of the surface phonon modes. Density functional perturbation theory calculations including van der Waals corrections are in excellent agreement with the experimental data. Comparison of the experimental results with theoretically obtained values for films with a thickness of several layers further demonstrate, that for an accurate theoretical description of three-dimensional topological insulators with their layered structure the inclusion of van der Waals corrections is essential. The presence of a prominent surface acoustic wave and the contribution of van der Waals bonding to the lattice dynamics may hold important implications for the thermoelectric properties of thin-film and nanoscale devices.

Received 16th April 2018,
Accepted 14th July 2018

DOI: 10.1039/c8nr03102a

rsc.li/nanoscale

Introduction

Bi_2Te_3 is one of the most studied topological insulators (TI),[1] a class of materials which exhibit protected metallic surface states and an insulating bulk electronic structure.[2,3] The interaction of surface phonons with electrons on Bi_2Te_3 has been mainly focused on determinations of the electron–phonon (e–ph) coupling constant λ.[4–7] Since scattering channels for the surface state electrons may impose constraints for potential applications such as surface-dominated transport, λ is a convenient parameter to characterise the e–ph interaction strength.[8]

However, very limited experimental data exists for the surface phonon dispersion of Bi_2Te_3(111) as well as for the region of acoustic phonon modes on topological insulator surfaces in general. Information on the surface phonon dispersion is also essential to fully understand the thermoelectric properties of Bi_2Te_3 thin films and nanoscale devices[9–11] and the low lattice thermal conductivity of Bi_2Te_3, one of the most studied and efficient thermoelectric materials.[12,13] Previously, the excellent thermoelectric performance of Bi_2Te_3 has been attributed to the details of the electronic structure and a low lattice thermal conductivity similar to ordinary glass.[13,14] While the vibrational properties of Raman active modes have been studied,[15,16] a systematic experimental investigation of the acoustic phonons in these materials is still missing.

Here we use the helium spin-echo technique which is capable of measuring surface phonon spectra with very high resolution.[17] He atom beams with energies of typically 10 meV are perfectly suited to probe all kind of surfaces in an inert, completely nondestructive manner.[18] In the context of TI surfaces, helium atom scattering (HAS) has also the advantage that the samples are not exposed to any intense ultraviolet illumination which has been reported to trigger energetic shifts of the electronic bands near the surface of a TI crystal after cleav-

[a]Cavendish Laboratory, J. J. Thompson Avenue, Cambridge CB3 0HE, UK. E-mail: tamtoegl@gmail.com; Tel: +43 680 3171626
[b]Institute of Experimental Physics, Graz University of Technology, 8010 Graz, Austria
[c]Theory and Simulation of Materials (THEOS) and National Centre for Computational Design and Discovery of Novel Materials (MARVEL), École Polytechnique Fédérale de Lausanne, Lausanne CH-1015, Switzerland
[d]Center for Materials Crystallography, Department of Chemistry and iNANO, Aarhus University, 8000 Aarhus, Denmark
[e]Department of Physics and Astronomy, Interdisciplinary Nanoscience Center (iNANO), Aarhus University, 8000 Aarhus, Denmark
[f]Dipartimento di Scienza dei Materiali, Universitá di Milano-Bicocca, Via R. Cozzi 53, 20125 Milano, Italy
[g]Donostia international Physics Center (DIPC), University of the Basque Country (EHU-UPV), Donostia, San Sebastian, Spain

View Article Online

Paper Nanoscale

ing.[19] Since He atoms at thermal energies are scattered directly by the surface charge density corrugation,[20] inelastic scattering results from coupling to phonon-induced charge density oscillations (CDOs). Therefore, inelastic HAS can also be used to infer information about the corresponding e–ph coupling strength.[4,21]

While previous experimental studies claimed that the Rayleigh wave (RW) is absent on Bi_2Te_3(111),[22] theoretical studies showed that the e–ph interaction cannot account for this absence.[23,24] Moreover, the low energy region of surface acoustic waves (≈0–5 meV) has not been subject to an experimental study up to now and we show, that the RW is not only present but also the dominant feature in the inelastic scattering spectra in this energy region.

Furthermore, we compare the experimentally determined surface phonon dispersion with density functional perturbation theory (DFPT) calculations detailing the role of van der Waals (vdW) interactions and spin–orbit coupling (SOC). As demonstrated recently, many-body vdW interactions can substantially affect vibrational properties leading to the appearance of low-frequency phonon modes which may even favour the thermal stability of a certain crystal structure.[25,26] The inclusion of vdW interactions becomes increasingly important for layered TIs[27] and two-dimensional materials such as *e.g.* hexagonal boron nitride[28,29] or for a correct description of hydrogenated graphene.[30,31]

Experimental and computational details

The reported measurements were performed on the Cambridge helium-3 spin-echo apparatus which generates a nearly monochromatic beam of ^{3}He that is scattered off the sample surface in a fixed 44.4° source-target-detector geometry. For a detailed description of the apparatus please refer to ref. 32 and 33.

The rhombohedral crystal structure of Bi_2Te_3 consists of quintuple layers (QLs) which are connected by weak vdW forces.[34] The hexagonal unit cell of the Bi_2Te_3 crystal is shown in Fig. 1 which consists of 3 QLs. Each quintuple layer (QL) is terminated by Te atoms, giving rise to the (111) cleavage plane that exhibits a hexagonal structure (a = 4.36 Å,[4] see Fig. 1(b)). The Bi_2Te_3 single crystal used in the study was attached onto a sample cartridge using electrically and thermally conductive epoxy. The sample cartridge was then inserted into the scattering chamber using a load-lock system[35] and cleaved *in situ*. The sample can be heated using a radiative heating filament on the backside of the crystal or cooled down to 110 K *via* a thermal connection to a liquid nitrogen reservoir. The sample temperature was measured using a chromel–alumel thermocouple.

All scattering spectra were taken with the crystal cooled down to 115 K. The incident He beam energy was set to 8 meV with the exception of a few spectra that were measured at an incident beam energy of 12 meV.

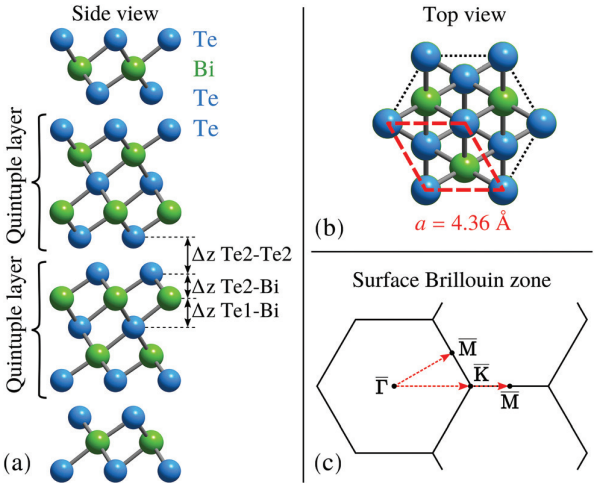

Fig. 1 Crystal structure of Bi_2Te_3. (a) Side view of the conventional hexagonal unit cell containing three quintuple layers of which each one is terminated by a Te layer. (b) Top view of the (111) surface of Bi_2Te_3 where the red rhombus highlights the hexagonal surface unit cell. (c) Surface Brillouin zone with the two scanning directions.

Computational details

The dynamical properties of Bi_2Te_3 were studied by means of density functional perturbation theory (DFPT)[36] as implemented in the Quantum-ESPRESSO package.[37] The surface phonon dispersion of Be_3(111) was calculated using a slab consisting of 3 QLs separated from its periodic replica by 30 Å of vacuum. For an accurate calculation of the surface lattice vibrations, in principle both SOC and a proper treatment of vdW corrections are necessary. The presence of heavy elements in Bi_2Te_3 requires the inclusion of SOC while at the same time the inclusion of vdW interactions is necessary for a correct description of the weak bonding between the individual quintuple layers.[27] To asses the importance of SOC and vdW interactions we performed the calculations using a standard Perdew–Burke–Ernzerhof (PBE) functional[38] and two flavours of vdW correction, a semi-empirical DFT-D3 correction[39] and a nonlocal vdW-DF2-C09 functional.[40–42] The first two were performed with the inclusion of SOC while the latter only without SOC due to the limitations of the current implementation in Quantum-ESPRESSO. Hermann *et al.*[43] provide a recent discussion about the advantages and limitations of existing vdW-inclusive methods.

Effects of SOC were treated self-consistently with fully relativistic pseudopotentials and the formalism for noncollinear spin magnetisation. We used scalar relativistic and fully relativistic norm conserving pseudopotentials from the PseudoDojo library with an energy cutoff of 80 Ry. The surface Brillouin zone (SBZ) was sampled using a 9 × 9 × 1 uniform k-point grid.[44]

Due to the topologically non-trivial nature of Bi_2Te_3 the inclusion of SOC leads to the formation of Dirac cones in the surface electronic structure. To deal with this metallic nature, a Gaussian smearing of 0.01 Ry was introduced in the occupation of states. The topologically protected Dirac cone forms

a small Fermi circle around the Γ-point which cannot be properly described with a coarse mesh and a large smearing resulting in the impossibility to capture subtle effects, such as the proposed Kohn anomaly[22] with a standard calculation. For this reason we also performed calculations using a non-uniform k-point grid with a density equal to a 90 × 90 × 1 grid around Γ and a 9 × 9 × 1 grid far away from it with a reduced smearing of 0.001 Ry. Due to the high computational cost these calculations were performed only at the Γ-point and at a single q-point corresponding to the nesting vector of the Fermi surface $q_{\mathrm{Nest}} = 2k_{\mathrm{F}} = 0.28$ Å^{-1} where the Kohn anomaly is expected. To reproduce the experimental nesting vector, determined by the self-doping of the sample, a fraction of 0.016 electrons was added to the simulation.

Results and discussion

Surface phonon energies were obtained by performing spin-echo measurements over a wide range of spin-echo times (including both real and imaginary components of the beam polarisation). Therefore the solenoid current was varied from −1 to +1 A with 2049 equally spaced points (top panel in Fig. 2). Oscillations in the polarisation correspond to surface atoms vibrating with a characteristic period, *i.e.* to a particular surface phonon mode. Hence Fourier transforming the data to the wavelength domain and converting to the energy scale gives rise to spectra which are analogous to time-of-flight (TOF) spectra, with energy loss and gain peaks for the creation and annihilation of a phonon, respectively[17,33] (lower panel in Fig. 2). The phonon energy $\Delta E = \hbar\omega$ is then given *via*:

$$\Delta E = \hbar\omega = \frac{h^2}{2m}\left(\frac{1}{\lambda_{\mathrm{f}}{}^2} - \frac{1}{\lambda_{\mathrm{i}}{}^2}\right). \quad (1)$$

where λ_{i} and λ_{f} are the incoming and outgoing wavelength of the He beam and m is the ^{3}He mass.

To determine the entire phonon dispersion curve up to the Brillouin zone boundary a series of spin-echo spectra at incident angles between the first-order diffraction peaks was measured. The phonon dispersion was then obtained by calculating the parallel momentum transfer $|\Delta K|$ for each extracted phonon energy ΔE from the conservation laws of energy and parallel momentum, providing the so-called scancurve for planar scattering:[17,45]

$$\frac{\Delta E}{E_{\mathrm{i}}} + 1 = \frac{\sin^2\vartheta_{\mathrm{i}}}{\sin^2\vartheta_{\mathrm{f}}}\left(1 + \frac{\Delta K}{K_{\mathrm{i}}}\right)^2 \quad (2)$$

where E_{i} is the energy of the incident beam and K_{i} is the parallel component of the incident wavevector. Here, ϑ_{i} and ϑ_{f} are the incident and final angle with respect to the surface normal, respectively. The phonon parallel momentum is then given by $|\Delta K| + G$, where the surface reciprocal lattice vector G in the scattering plane, needed to bring Q into the first Brillouin zone, accounts for umklapp processes.

Fig. 3 shows a collection of 40 inelastic scattering spectra measured along $\overline{\Gamma\mathrm{M}}$ with an incident beam energy of 8 meV. Each spectrum was converted to energy ΔE and parallel momentum ΔK using (1) and (2) and the intensity is plotted as a function of (ΔK, ΔE). The region around $\Delta E = 0$ is not shown

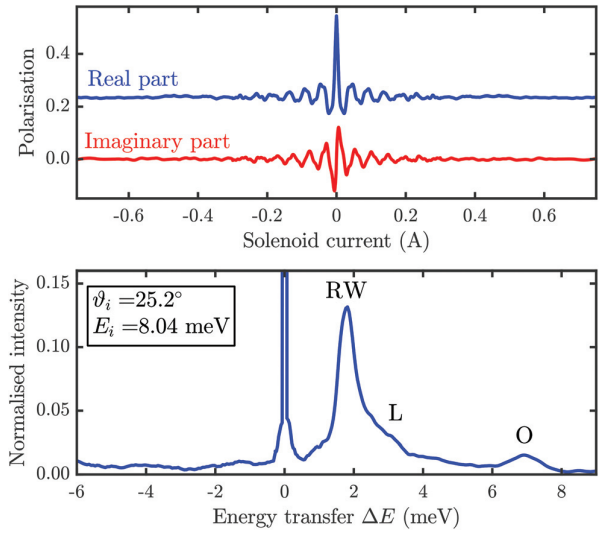

Fig. 2 A typical ^{3}He spin-echo measurement performed along the $\overline{\Gamma\mathrm{M}}$ azimuth with the crystal at 115 K. The upper panel shows the real and imaginary components of the complex polarisation. The oscillations are due to phonon scattering events which becomes evident after Fourier transforming and converting to the energy transfer scale (lower panel). The peak at $\Delta E = 0$ is due to diffuse elastic scattering, and the phonon modes are now visible as finite energy transfer peaks with the Rayleigh wave (RW), the longitudinal resonance (L) and an optical mode (O). The most dominant phonon peak corresponds to the Rayleigh mode and appears at $\Delta E \approx +1.8$ meV in the spectrum.

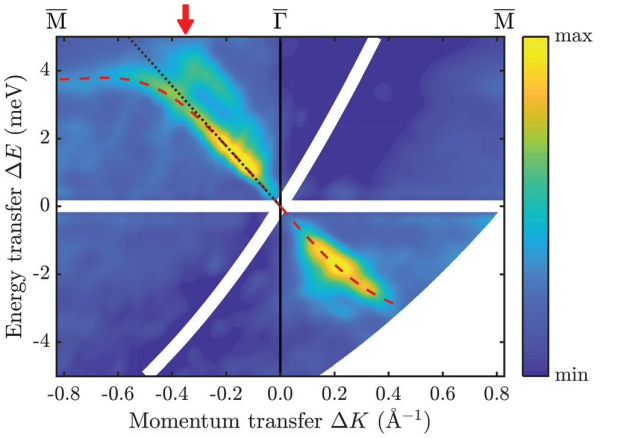

Fig. 3 Collection of several experimental spectra along $\overline{\Gamma\mathrm{M}}$ with an incident beam energy of 8 meV. The intensity is shown as a function of energy and parallel momentum transfer. The region around $\Delta E = 0$ is not shown due to the large intensity of the elastic peak compared to the phonon modes. The red dashed line is plotted as a guide to the eye to show the dispersion of the Rayleigh mode. The black dotted line represents the group velocity of the Rayleigh mode.

due to the large intensity of the elastic peak compared to the phonon modes, as well as the region corresponding to (ΔK, ΔE) very close to the specular condition ($\vartheta_i = \vartheta_f$). Most intensity is found along the dashed line and is associated with the RW, while the weaker intensity above the RW, corresponding to the shoulder labelled L in the lower panel of Fig. 2, is attributed to the longitudinal resonance.[46]

Such a prominent RW could not be observed on TI surfaces in previous experiments and it was instead claimed that the RW mode is absent on Bi_2Te_3(111) in a study by Howard *et al.*[22] However, the mentioned previous experimental study[22] was rather concentrated on phonon events with higher energies and in the presence of a broad diffuse elastic peak, individual phonon peaks with small energy transfers (as the low-lying RW) are difficult to separate. Moreover, the quality of the crystal surface (as indicated by the diffraction spectra[4]) and the presence of defects such as steps will increase the height of the diffuse elastic peak. Finally, the energy resolution of the apparatus will add to the width of the peak, emphasising the advantage of the spin-echo technique in this context: in a standard spin-echo measurement, tuned for the quasi-elastic peak (around $\Delta E = 0$), the resolution is only limited by the maximum Fourier time of the instrument.[47] Note however, that under this measurement condition, the finite energy transfer peaks are also broadened by the projection of the features in the wavelength intensity transfer matrix.[17,47] It should also be mentioned that it is often difficult to directly compare intensities obtained *via* TOF measurements (as performed by Howard *et al.*[22]) with those from spin-echo measurements obtained after Fourier transforming the data.

Indeed the presence of the RW is in line with the fact that the anisotropy of the elastic constants of Bi_2Te_3 is not strong at all[48–50] and later theoretical studies about the electron–phonon interaction of Bi_2Te_3.[23,24,51] The bulk phonon properties of Bi_2Te_3 have been studied by Raman spectroscopy[15,16,52,53] and an early neutron scattering study performed by Wagner *et al.*[54] Based on these experimental results together with lattice dynamical shell model calculations, Kullmann *et al.*[48] showed that in terms of the bulk lattice dynamics the typical properties of a three-dimensional crystal dominate: Kullmann *et al.* concluded that the layered quintuple structure of Bi_2Te_3 gives rise to much less characteristic features of low dimensional crystal structures[48] compared to two-dimensional materials such as graphene[55].

The group velocity $v_g = \partial\omega/\partial K$ of an acoustic phonon mode corresponds to the speed of sound along a certain crystal direction in the long wavelength limit (close to $\bar{\Gamma}$, see the black dotted line in Fig. 3). Using the slope close to $\bar{\Gamma}$ we obtain for the speed of sound of the Rayleigh wave at 115 K and along both azimuthal directions:

$$\overline{\Gamma M}: \; v_{RW} = 1300\,\mathrm{m\,s^{-1}} \tag{3}$$

$$\overline{\Gamma K}: v_{RW} = 1600\,\mathrm{m\,s^{-1}}. \tag{4}$$

In general the speed of surface acoustic waves is lower than the speed of the slowest bulk wave. The speed of sound in the bulk can be obtained from the elastic constants[56,57] as determined from ultrasonic measurements at room temperature in the case of Bi_2Te_3.[49,50] The values for shear vertical (SV) and shear horizontal (SH) polarisation along both azimuthal directions are:

$$\overline{\Gamma M}: v_{SV} \approx v_{SH} = 1740\,\mathrm{m\,s^{-1}} \tag{5}$$

$$\overline{\Gamma K}: v_{SV} = 2290\,\mathrm{m\,s^{-1}}, \tag{6}$$

similar to the values found in later studies.[58–60] The v_{RW}/v_{SV} ratio for the surface modes as given by the two velocities along $\overline{\Gamma M}$ and $\overline{\Gamma K}$, is about 0.72. It is interesting to note that this value is similar to the ratio $v_{RW}/v_{SV} = 0.83$ which would be obtained for the (001) surface of a cubic crystal with the same elastic constant ratios $C_{12}/C_{44} = 0.795$ and $C_{11}/C_{44} = 2.24$ of Bi_2Te_3 (see ref. 56). Moreover, v_{RW} from the present study is somewhat smaller than that recently measured with Brillouin scattering in Bi_2Te_3 thin films grown on a stiffer substrate and with the RW penetration depths comparable to the film thickness.[61]

Note also, that an important aspect of the surface dynamics of Bi_2Te_3 is that the above described RW is, technically, a pseudo-surface wave (PSW), because there exists a bulk acoustic branch which is even softer.[61] From ultrasonic experiments[48–50] it is known that an additional low lying bulk mode with shear horizontal (SH) polarisation exists (with a group velocity of about 1250 m s^{-1} along $\overline{\Gamma K}$ as obtained from the elastic constants[49,50,62]). In any direction where the sagittal plane (defined by the incident wave vector and the surface normal) has a mirror symmetry, the RW is orthogonal to the SH modes and therefore there is no mixing, and its localisation is ensured. However, any small deviation from the mirror-symmetry direction yields a coupling to bulk SH modes and the RW becomes a resonance, acquiring an oscillating factor on top of the exponential decay inside the bulk. Thus in experiments, where the angular acceptance angle cannot be zero, PSWs always have a resonance width and the peaks always show an intrinsic broadening with respect to ordinary localised RWs, due to the mixing with the SH modes.

DFPT dispersion curves and comparison with experiment

The entire set of data-points obtained from the measurements within the irreducible Brillouin zone is plotted in Fig. 4, superimposed onto the DFPT calculations (grey lines) as obtained for 3 QLs with the inclusion of vdW interactions. Along the $\overline{KM}$ azimuth there are no data points shown since when scanning along $\overline{\Gamma KM}$ the intensity of the inelastic features becomes very small for incident angles which are more than approximately 9° off the specular condition. Hence it is difficult to retrieve spectra with a sufficient signal-to-noise ratio for momentum transfers in the $\overline{\Gamma KM}$ region.

The experimental data points in Fig. 4 are plotted as different symbols where each symbol is likely to correspond to a different phonon mode. The majority of the extracted data points corresponds to the RW mode (red crosses) followed by the longitudinal resonance (blue circles) and two further low-

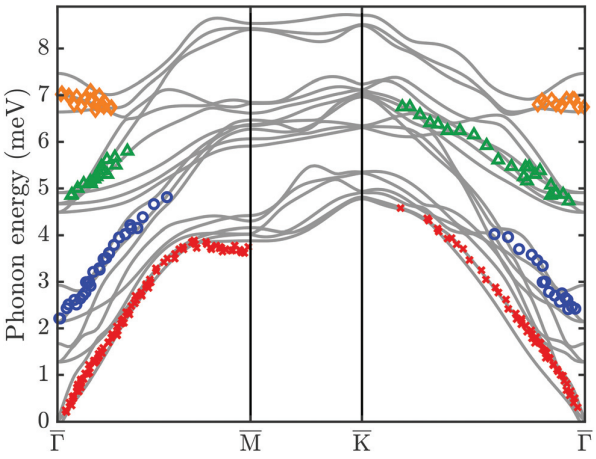

Fig. 4 Comparison of the measured phonon dispersion relation with DFPT calculations using the vdW-DF2-C09 functional for 3 QLs. The solid gray lines represent the DFPT calculation while different symbols for the experimentally determined points correspond to different phonon modes.

lying optical phonon modes (green triangles and orange diamonds). In general the DFPT calculations show excellent agreement with the experimental data points. Note that the inclusion of vdW interactions in the DFPT calculations is particularly important in order to correctly reproduce the longitudinal resonance (blue circles). The role of vdW interactions and SOC will be discussed in greater detail below.

Interestingly there is no evidence for a strong Kohn anomaly as reported by Howard *et al.*[22] According to Howard *et al.* an optical phonon branch originating at 5.8 meV at the Γ̄-point shows a strong V-shaped indentation at $\Delta K \approx 0.08$ Å^{-1}, reaching a minimum of about 4 meV. One reason for the absence of this phonon mode might be the rather low beam energy (8 meV) used in our study. While it is impossible to create phonons with a higher energy than 8 meV, peaks on the annihilation side tend to become weaker with increasing energy. On the other hand, one would expect an indication for this phonon mode for a momentum transfer close to the nesting condition of the Kohn anomaly.

Note that the nesting condition $\Delta K = 2k_F$ for the Kohn anomaly depends on the exact electronic structure, *i.e.* the position where the Dirac cone crosses the Fermi level E_F which determines k_F. In the experiment, the doping of a specific sample plays an important role since the position of the Dirac point with respect to E_F is shifted depending on the doping level. From angle resolved photoemission spectroscopy (ARPES) of the current sample[4] we know that the Fermi level is 0.35 eV above the Dirac point and the Dirac cone crosses E_F at $k_F = 0.14$ Å^{-1}. Hence the nesting condition for the current sample is $\Delta K = 2k_F = 0.28$ Å^{-1} compared to $\Delta K \approx 0.08$ Å^{-1} in the study by Howard *et al.*[22] Moreover, due to the hexagonal warping of the surface state Fermi contour, the nesting should be enhanced when the doping of the sample increases.[63] Nevertheless there is no evidence for such a Kohn anomaly in our experimental data. In particular since a Kohn anomaly becomes typically more pronounced with decreasing temperature (measurements at 115 K in our study *versus* room temperature measurements in ref. 22). We can only speculate whether the nesting becomes less likely with increasing ΔK, where a spin-flip of the electron is needed, which can be provided by the SO part of the electron–phonon interaction.[64] Or whether the absence of the Kohn anomaly has to do with some fundamentally different properties of the investigated samples, *e.g.* the different doping level and possibly different charge carrier densities of the samples.

The absence of a Kohn anomaly in our measurements is also in accordance with our DFPT calculations, as shown in Fig. 5(d) where we report the phonon frequencies at $q_{Nest} = 2k_F = 0.28$ Å^{-1} obtained with a particularly careful sampling of the SBZ as described in the computational details. Similar results have been obtained in a recent work by Heid *et al.*[24] from first principles, who could neither find a large e–ph coupling constant nor the presence of a Kohn anomaly. Hence they suggested that the Kohn anomaly observed in ref. 22 may be connected to a strong e–ph interaction in the doped bulk material rather than a surface state.

Furthermore, a connection with the recently observed acoustic surface plasmon (ASP) on Bi_2Se_3 is also a possible scenario. The dispersion slope of the ASP on Bi_2Se_3 was found to be similar to the group velocity of the surface acoustic mode of an Mn doped crystal[65] as well as the group velocity of the RW mode in our study. Inelastic scattering events associated with such an ASP are likely to appear at a similar energy as the reported Kohn anomaly[22] making a distinction between different inelastic processes difficult.

Finally, upon close inspection there appears to be a small indentation for the L-branch at $\Delta K \approx 0.35$ Å^{-1} along $\overline{\Gamma M}$. The evidence is not particularly strong based on the number of data points in Fig. 4 but is better seen in the intensity plot (see the red arrow in Fig. 3 at 0.35 Å^{-1}). Since in the present Bi_2Te_3 sample the Fermi level is above the bulk conduction band minimum,[4] the impinging ^{3}He atom detects some mixing of the Dirac states with bulk states, thus relaxing the spin selection rule and making such a transition possible. As the Dirac states are 2D they do not depend on k_z, but their ARPES intensity strongly depends on k_z, depending on the Fourier components of the Dirac wave function in the z-direction.[4,34] As can be seen from ARPES data of the current sample (Fig. 4 of ref. 4), the Fermi level is above the minimum of the conduction band and the minimum in the k_z direction occurs at $k_z = 0.31$ Å^{-1}, where the Dirac cone intersects the Fermi level at $2k_F \approx 0.35$ Å^{-1}. Thus the intensification of the Dirac state at the Fermi level is probably due to the resonance (mixing) of this state with bulk states. If this is the case the spin selection rule is considerably relaxed, which explains why the electron–hole excitation is detected by HeSE, though it is rather weak.

The role of vdW interactions and SOC

After this ample discussion about possible anomalies in the vibrational modes of Bi_2Te_3 we will now address the question

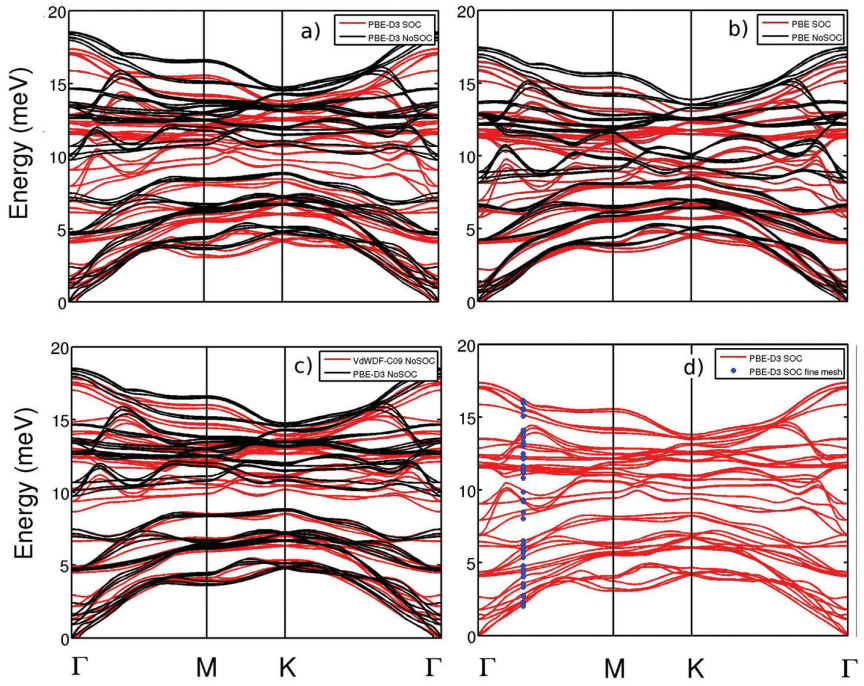

Fig. 5 (a) Phonon dispersions computed using PBE with the inclusion of the vdW PBE-D3 correction including (red) and neglecting (black) SOC. (b) Phonon dispersion computed using bare PBE including (red) and neglecting (black)SOC. (c) Comparison between phonon dispersion computed with two different vdW corrections PBE-D3 (red) and non-local functional vdW-DF2-C09 (black) without SOC. (d) Phonon dispersion computed with PBE-D3 with SOC on a standard mesh (red lines) and phonon frequencies computed at a q-point corresponding to the nesting vector of the Fermi surface (blue dots) for a system slightly doped in order to reproduce the experimental position of the Dirac cone. The calculation has been carried out with a very fine grid around the Γ-point and a small smearing in order to allow a proper description of a potential Kohn anomaly.

to what degree DFPT calculations reproduce specific phonon energies. Therefore, we performed calculations including different vdW corrections and, where possible, both including and neglecting SOC.

Firstly, we start with a short discussion regarding the equilibrium lattice parameters as obtained with different theoretical methods since changes in the equilibrium geometry will lead to different phonon spectra. Table 1 shows the obtained theoretical equilibrium in-plane lattice parameter a as well as the vertical distances Δz between different atoms (see Fig. 1(a)) for different functionals and films with a thickness of N QLs. In terms of the in-plane lattice parameter a, all functionals perform well and agree with the experimentally determined parameters up to the second decimal place, except for the PBE functional without dispersion corrections which gives a slightly larger a. The vertical distances within one QL are reproduced very well by all functionals. However, the vdW gap between the QLs (Te2–Te2 distance in Table 1) is described most accurately with the vdW-DF2-C09 functional while PBE tends to give larger distances which becomes at most 0.5 Å larger than the experimental one if neither SOC nor vdW are accounted for. Hence we can already anticipate that the vdW-DF2-C09 functional, which gives the best agreement for the vdW gap, will also provide a good description of the low-energy acoustic phonon modes. Moreover, we have also performed calculations with the vdW-DF2-C09 functional for a number of different QLs N = 1,2,3 and 5, which are shown in Table 1. It can be seen that changes on the equilibrium geometry are already minor when going from 2 to 3 QLs while there are no significant differences when going from 3 to 5 QLs, suggesting that a DFPT calculation for 3 QLs is sufficient for an accurate mapping of the entire phonon dispersion relation.

Table 1 shows a comparison for the experimentally determined energy of the lowest lying surface phonon mode at the $\bar{M}$ and $\bar{K}$-point with several calculations. Note that the experimental value for the $\bar{K}$ point has been extrapolated using a sine fit to the experimental points shown in Fig. 4. Our results show generally a good agreement with the experimentally measured lowest lying surface phonon mode except for the PBE functional when including both vdW corrections and SOC which tends to give rise to softer phonon energies at the Brillouin zone boundary. Table 1 reveals a rather feeble dependence with respect to vdW correction or SOC. The comparison shows that DFPT (without SOC, considering only 1 QL[15]) tends to overestimate the vibrational energies. On the other hand Huang[66] uses up to 5 QLs for DFPT calculations based on the PBE approximation with SOC but obtains smaller energies than compared to the experiment. However, in ref. 66 the in-plane lattice parameter was fixed at the experimental one. Based on the above described calculations with increasing

Table 1 Energy (meV) of the lowest lying surface phonon mode at selected high-symmetry points of Bi_2Te_3(111) together with a comparison of the theoretically obtained equilibrium geometry of the crystal. The second and third column state whether spin–orbit coupling (SOC) and van der Waals (vdW) interactions where included in the theoretical calculations, respectively. The theoretically obtained values are for films with a thickness of N QLs at a theoretical equilibrium in-plane lattice parameter a (Å). The average vertical distances Δz between different atoms are also reported. Here Te2 indicates the outermost Te atom in a QL and Te1 the central one (see Fig. 1(a)). The in-plane atomic positions are fixed due to symmetry

Method	SOC	vdW	N	a (Å)	Δz Te2–Te2 (Å)	Δz Te2–Bi (Å)	Δz Te1–Bi (Å)	$\bar{M}$	$\bar{K}$
Theory (DFPT)[15]	No	No	1	4.40				4.5	5.6
Theory (vdW-DF2-C09)[a]	No	Yes	1	4.389	—	1.730	2.049	3.70	4.78
Theory (vdW-DF2-C09)[a]	No	Yes	2	4.389	2.688	1.740	2.037	3.79	4.79
Theory (vdW-DF2-C09)[a]	No	Yes	3	4.389	2.681	1.736	2.036	3.9	4.80
Theory (vdW-DF2-C09)[a]	No	Yes	5	4.389	2.682	1.736	2.036	3.9	4.80
Theory (PBE + D3)[a]	No	Yes	3	4.324	2.868	1.761	2.049	3.59	4.76
Theory (PBE + D3)[a]	Yes	Yes	3	4.333	2.736	1.780	2.061	3.08	4.12
Theory (PBE)[a]	Yes	No	3	4.468	2.759	1.744	2.063	3.39	4.40
Theory (PBE)[a]	No	No	3	4.446	3.091	1.723	2.055	3.81	4.96
Theory (PBE)[66]	Yes	No	5	4.386[b]				2.95	4.00
Experiment (HAS)[a]	—	—	—	4.36	—	—	—	3.7	4.7
Experiment (X-ray)[67]	—	—	—	4.386	2.613	1.743	2.033		

[a] Value obtained from current study. [b] Fixed at experimental value.

number of QLs it is more likely that the reported soft phonon energies for 5 QLs[66] are a consequence of the fixed lattice parameter rather than the number of QLs. Indeed we see from our DFPT calculations with the vdW-DF2-C09 functional for N = 1,2,3 and 5 in Table 1 that the influence of the number of QLs on the phonon energies at the Brillouin zone boundaries ($\bar{M}$,$\bar{K}$) is very weak. The reason can be found in the weak vdW coupling between the layers, so that particularly at the zone boundaries where only short-range interactions are important, the phonons of a single QL resemble closely the ones of multiple slabs. On the other hand the vdW interaction is crucial in order to obtain the proper geometry as stated above.

In terms of the lattice vibrations, vdW interactions are instead much more important close to $\bar{\Gamma}$ where long-range interactions are important for the phonon frequencies. Here two effects of the vdW interaction play an important role: the first one is again for obtaining the right equilibrium geometry, the second one is the direct contribution of the vdW interactions to the force constants. This is particularly important in order to obtain the correct longitudinal resonance (blue circles of the experimental data, with about 2 meV at $\bar{\Gamma}$) which is further described below.

The influence of vdW corrections and SOC on the phonon energies can be best seen by a direct comparison of the phonon dispersion obtained with different theoretical methods (for 3 QLs) as plotted in Fig. 5. First of all, we note that the agreement with experiments is marginally better without the inclusion of SOC, likely due to a compensation of errors between the under binding problem that often characterises the PBE functional and the contribution of SOC. The effect of SOC is generally weak for all low energy modes while it becomes increasingly important for the high-energy optical phonons where it is responsible for a softening of up to 13% (see Fig. 5(a) and (b)).

As might be expected, vdW corrections are instead crucial for a good description of the low energy optical modes (particularly the ones starting at around 2 and 5 meV at Γ) involving a modulation of the inter-QL distance as can be inferred by comparing Fig. 5(b) reporting the results of bare PBE without vdW corrections with Fig. 5(a) and (c) in which two different types of vdW corrections are considered. In particular, the non-local exchange–correlation functional vdW-DF2-C09 appears to be the most accurate in describing the weak coupling between the QLs since it is the only one that reproduces the experimental mode at 2 meV (see Fig. 4).

Polarisation of the surface phonon modes

Finally, we turn to the polarisation analysis of the surface phonon modes. The full set of calculated dispersion relations along the symmetry directions is shown in Fig. 6 together with the corresponding phonon densities projected onto the first, second and third layer for shear vertical (SV1, SV2, SV3), longitudinal (L1, L2, L3) and shear horizontal (SH1, SH2, SH3) polarisations. Since the optical modes inside the QLs are weakly affected by the surface, at $\Delta K = 0$ they retain an approximate gerade or ungerade symmetry with respect to the central Te layer. They can then be easily recognised from their third-layer intensity (Fig. 6: SV3, L3, SH3), which is comparatively large for quasi-ungerade and almost vanishing for quasi-gerade modes.

Based on the DFPT calculations, the polarisation of the experimentally observed, particularly intense, RW mode is a combination of shear vertical and shear horizontal, which is however only possible along $\overline{\Gamma\bar{K}}$. Interestingly the largest intensity comes from the SH2 mode (central panel at the bottom of Fig. 6). Note that if the scattering plane, defined by the incoming and scattered He beam, coincides with a mirror plane of the surface, the detection of purely SH modes is in principle forbidden due to symmetry reasons.[68] However, while the atomic displacement is largest for the SH2 polarisation, we see from Fig. 6 that the mode always retains an SV polarisation component as well. Moreover, even a purely SH mode may give

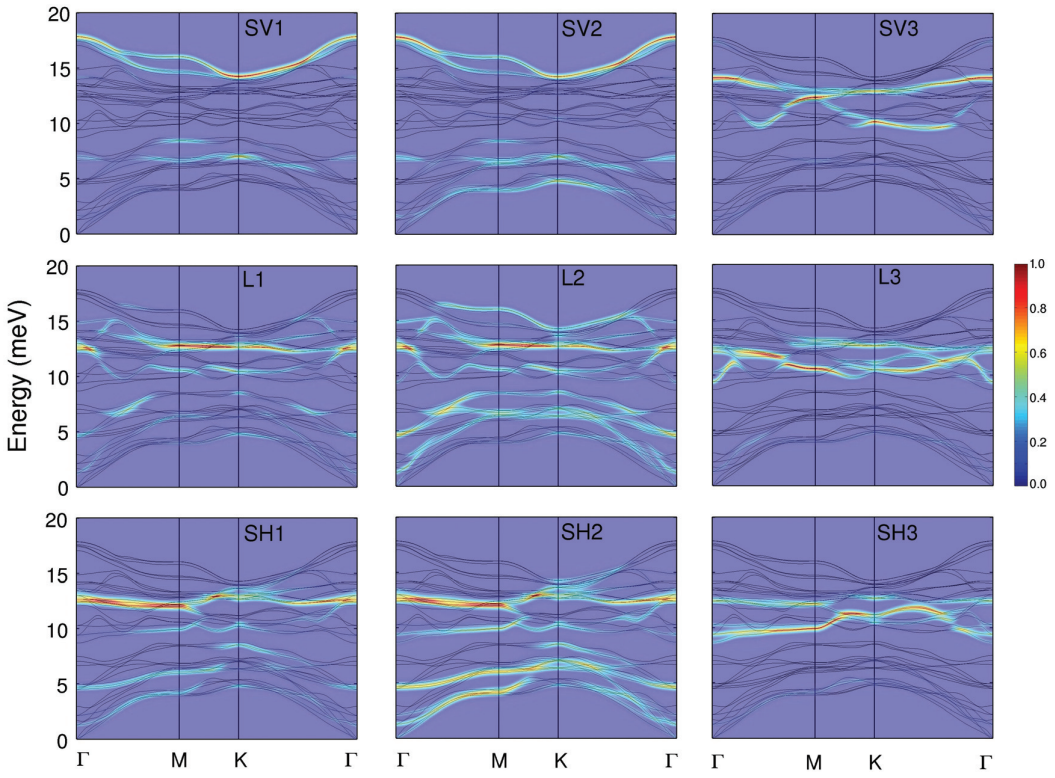

Fig. 6 Polarisation of the calculated phonon dispersion. The intensity corresponds to shear vertical (SV), longitudinal (L) and shear horizontal (SH) polarisation projected onto the first or top-most atomic layer (1), second layer (2) and third layer (3), respectively.

rise to CDOs above the first atomic layer which are eventually observed in inelastic He atom scattering.

The phonon mode at 2 meV is likely ascribable to a shear vertical mode in which the entire outermost QL vibrates rigidly against the inner ones at the Γ-point which then enters a longitudinal resonance when moving towards the zone border. The mode at 5 meV is instead related mainly to a longitudinal vibration of the first and second atomic layer moving in anti-phase with the fourth and fifth layer while the 8 meV mode is characterised by a shear vertical vibration involving the same pair of atoms with a similar anti-phase pattern.

Summary and conclusion

Due to being very low in energy the acoustic phonon modes on topological insulator surfaces are difficult to address and resolve experimentally. However, a precise knowledge of the surface dynamical properties is one of the key ingredients to understand fundamental properties of archetypal topological insulators at elevated temperatures (where electron–phonon scattering processes may become important) as well as for the use of Bi_2Te_3 as one of the most efficient thermoelectric materials in nanoscale devices.[10,11]

We have measured the surface lattice vibrations of $Bi_2Te_3(111)$ in the low energy region using high-resolution helium-3 spin-echo spectroscopy. The low energy region of the surface phonons is mainly dominated by the Rayleigh wave which has been found to be absent in previous experimental studies. The appearance of the RW is consistent with previous bulk lattice dynamics studies as well as theoretical predictions of the surface phonon modes. The speed of sound of the RW is between 1300 m s^{-1} and 1600 m s^{-1} along the $\overline{\Gamma M}$ and $\overline{\Gamma K}$ directions, respectively. Furthermore, our results do not support the presence of a Kohn anomaly, connected with a surface phonon mode, as inferred from a previous study.

The surface phonon dispersion for 3 quintuple layers has been calculated with vdW corrected DFPT calculations (without SOC). Comparison between the experimentally determined values and the calculations show excellent agreement. We have also compared the experimentally determined phonon energies at a number of high symmetry points with calculations using different functionals for the treatment of SOC and vdW interactions. Our results suggest that in order to calculate the surface lattice vibrations of three-dimensional topological insulators with their layered structure, the inclusion of vdW interactions is essential. Within the methods used in our study, the non-local exchange–correlation functional vdW-DF2-C09 appears to be the most accurate one in

describing the coupling between the layers since it provides the right distance for the vdW gap and is the only method that correctly reproduces the experimentally observed longitudinal resonance.

While the performance of the vdW-DF2-C09 functional in terms of an accurate description of the lattice vibrations of Bi_2Te_3 is excellent, it should be noted that one shortcoming is the currently missing implementation of SOC. For now, it may be advocated for further first-principles vibrational investigations of layered TI materials while other methods may be more appropriate when it comes to calculations of the electronic structure, in particular, if they involve non-adiabatic processes within the context of electron–phonon interaction. Future efforts towards a correct description of both vdW interactions as well as SOC may provide significant insight into such complex mechanisms in TI materials.

The observation of a prominent surface acoustic may have important implications in particular for thin-film and nanoscale devices: the thermal conductivity of such devices may be strongly influenced by the contribution of the observed acoustic mode. Moreover, the improved accuracy when including vdW interactions shows that these are possibly crucial for an exact theoretical description of application-relevant issues like the thermal conductivity of layered structures in general.

Author contributions

E.M.J.H. and M. Bremholm synthesised and characterised the samples. A.T. performed the experimental measurements with support from M. Bianchi for the sample preparation. A.T. and G.B carried the analysis of the experimental data out while D.C. performed the DFPT calculations. A.T., D.C. and G.B. wrote the paper, and all authors contributed to the discussion and preparation of the manuscript.

Conflicts of interest

There are no conflicts to declare.

Acknowledgements

One of us (A. T.) acknowledges financial support provided by the FWF (Austrian Science Fund) within the projects J3479-N20 and P29641-N36. The authors are grateful for financial support by the Aarhus University Research Foundation, VILLUM FOUNDATION *via* the Centre of Excellence for Dirac Materials (Grant No. 11744) and the SPP1666 of the DFG (Grant No. HO 5150/1-2). M. B., E. M. J. H. and B. B. I. acknowledge financial support from the Center of Materials Crystallography (CMC) and the Danish National Research Foundation (DNRF93).

References

1 Y. L. Chen, J. G. Analytis, J.-H. Chu, Z. K. Liu, S.-K. Mo, X. L. Qi, H. J. Zhang, D. H. Lu, X. Dai, Z. Fang, S. C. Zhang, I. R. Fisher, Z. Hussain and Z.-X. Shen, *Science*, 2009, **325**, 178–181.

2 M. Z. Hasan and C. L. Kane, *Rev. Mod. Phys.*, 2010, **82**, 3045–3067.

3 J. Moore, *Nat. Phys.*, 2009, **5**, 378–380.

4 A. Tamtögl, P. Kraus, N. Avidor, M. Bremholm, E. M. J. Hedegaard, B. B. Iversen, M. Bianchi, P. Hofmann, J. Ellis, W. Allison, G. Benedek and W. E. Ernst, *Phys. Rev. B: Condens. Matter Mater. Phys.*, 2017, **95**, 195401.

5 J. A. Sobota, S.-L. Yang, D. Leuenberger, A. F. Kemper, J. G. Analytis, I. R. Fisher, P. S. Kirchmann, T. P. Devereaux and Z.-X. Shen, *Phys. Rev. Lett.*, 2014, **113**, 157401.

6 C. Howard and M. El-Batanouny, *Phys. Rev. B: Condens. Matter Mater. Phys.*, 2014, **89**, 075425.

7 T. Kondo, Y. Nakashima, Y. Ota, Y. Ishida, W. Malaeb, K. Okazaki, S. Shin, M. Kriener, S. Sasaki, K. Segawa and Y. Ando, *Phys. Rev. Lett.*, 2013, **110**, 217601.

8 L. Barreto, L. Kühnemund, F. Edler, C. Tegenkamp, J. Mi, M. Bremholm, B. B. Iversen, C. Frydendahl, M. Bianchi and P. Hofmann, *Nano Lett.*, 2014, **14**, 3755–3760.

9 A. J. Minnich, M. S. Dresselhaus, Z. F. Ren and G. Chen, *Energy Environ. Sci.*, 2009, **2**, 466–479.

10 J. Liang, L. Cheng, J. Zhang, H. Liu and Z. Zhang, *Nanoscale*, 2016, **8**, 8855–8862.

11 M. Muñoz-Rojo, B. Abad, V. C. Manzano, P. Torres, X. Cartoixà, F. X. Alvarez and M. Martín-Gonzalez, *Nanoscale*, 2017, **9**, 6741–6747.

12 F. Rittweger, N. F. Hinsche, P. Zahn and I. Mertig, *Phys. Rev. B: Condens. Matter Mater. Phys.*, 2014, **89**, 035439.

13 G. J. Snyder and E. S. Toberer, *Nat. Mater.*, 2008, **7**, 105–114.

14 H. Shi, D. Parker, M.-H. Du and D. J. Singh, *Phys. Rev. Appl.*, 2015, **3**, 014004.

15 V. Chis, I. Y. Sklyadneva, K. A. Kokh, V. A. Volodin, O. E. Tereshchenko and E. V. Chulkov, *Phys. Rev. B: Condens. Matter Mater. Phys.*, 2012, **86**, 174304.

16 C. Wang, X. Zhu, L. Nilsson, J. Wen, G. Wang, X. Shan, Q. Zhang, S. Zhang, J. Jia and Q. Xue, *Nano Res.*, 2013, **6**, 688–692.

17 P. R. Kole, A. P. Jardine, H. Hedgeland and G. Alexandrowicz, *J. Phys.: Condens. Matter*, 2010, **22**, 304018.

18 D. Farías and K.-H. Rieder, *Rep. Prog. Phys.*, 1998, **61**, 1575.

19 E. Frantzeskakis, S. V. Ramankutty, N. de Jong, Y. K. Huang, Y. Pan, A. Tytarenko, M. Radovic, N. C. Plumb, M. Shi, A. Varykhalov, A. de Visser, E. van Heumen and M. S. Golden, *Phys. Rev. X*, 2017, **7**, 041041.

20 M. Mayrhofer-Reinhartshuber, P. Kraus, A. Tamtögl, S. Miret-Artés and W. E. Ernst, *Phys. Rev. B: Condens. Matter Mater. Phys.*, 2013, **88**, 205425.

21 J. R. Manson, G. Benedek and S. Miret-Artés, *J. Phys. Chem. Lett.*, 2016, **7**, 1016–1021.

22 C. Howard, M. El-Batanouny, R. Sankar and F. C. Chou, *Phys. Rev. B: Condens. Matter Mater. Phys.*, 2013, **88**, 035402.
23 V. Parente, A. Tagliacozzo, F. von Oppen and F. Guinea, *Phys. Rev. B: Condens. Matter Mater. Phys.*, 2013, **88**, 075432.
24 R. Heid, I. Y. Sklyadneva and E. V. Chulkov, *Sci. Rep.*, 2017, **7**, 1095.
25 A. M. Reilly and A. Tkatchenko, *Phys. Rev. Lett.*, 2014, **113**, 055701.
26 G. Folpini, K. Reimann, M. Woerner, T. Elsaesser, J. Hoja and A. Tkatchenko, *Phys. Rev. Lett.*, 2017, **119**, 097404.
27 T. Björkman, A. Gulans, A. V. Krasheninnikov and R. M. Nieminen, *Phys. Rev. Lett.*, 2012, **108**, 235502.
28 T. Q. P. Vuong, S. Liu, A. Van der Lee, R. Cuscó, L. Artús, T. Michel, P. Valvin, J. H. Edgar, G. Cassabois and B. Gil, *Nat. Mater.*, 2017, **17**, 152–158.
29 R. Cuscó, L. Artús, J. H. Edgar, S. Liu, G. Cassabois and B. Gil, *Phys. Rev. B: Condens. Matter Mater. Phys.*, 2018, **97**, 155435.
30 M. Birowska, M. Marchwiany and J. A. Majewski, 2017, arXiv preprint arXiv:1707.09795.
31 E. Bahn, A. Tamtögl, J. Ellis, W. Allison and P. Fouquet, *Carbon*, 2017, **114**, 504–510.
32 G. Alexandrowicz and A. P. Jardine, *J. Phys.: Condens. Matter*, 2007, **19**, 305001.
33 A. Jardine, H. Hedgeland, G. Alexandrowicz, W. Allison and J. Ellis, *Prog. Surf. Sci.*, 2009, **84**, 323.
34 M. Michiardi, I. Aguilera, M. Bianchi, V. E. de Carvalho, L. O. Ladeira, N. G. Teixeira, E. A. Soares, C. Friedrich, S. Blügel and P. Hofmann, *Phys. Rev. B: Condens. Matter Mater. Phys.*, 2014, **90**, 075105.
35 A. Tamtögl, E. A. Carter, D. J. Ward, N. Avidor, P. R. Kole, A. P. Jardine, J. Ellis and W. Allison, *Rev. Sci. Instrum.*, 2016, **87**, 066108.
36 S. Baroni, S. de Gironcoli, A. Dal Corso and P. Giannozzi, *Rev. Mod. Phys.*, 2001, **73**, 515–562.
37 P. Giannozzi, S. Baroni, N. Bonini, M. Calandra, R. Car, C. Cavazzoni, D. Ceresoli, G. L. Chiarotti, M. Cococcioni, I. Dabo, A. D. Corso, S. de Gironcoli, S. Fabris, G. Fratesi, R. Gebauer, U. Gerstmann, C. Gougoussis, A. Kokalj, M. Lazzeri, L. Martin-Samos, N. Marzari, F. Mauri, R. Mazzarello, S. Paolini, A. Pasquarello, L. Paulatto, C. Sbraccia, S. Scandolo, G. Sclauzero, A. P. Seitsonen, A. Smogunov, P. Umari and R. M. Wentzcovitch, *J. Phys.: Condens. Matter*, 2009, **21**, 395502.
38 J. Perdew, K. Burke and M. Ernzerhof, *Phys. Rev. Lett.*, 1996, **77**, 3865.
39 S. Grimme, J. Antony, S. Ehrlich and S. Krieg, *J. Chem. Phys.*, 2010, **132**, 154104.
40 M. Dion, H. Rydberg, E. Schroeder, D. Langreth and B. Lundqvist, *Phys. Rev. Lett.*, 2004, **92**, 246401.
41 K. Lee, E. Murray, L. Kong, B. Lundqvist and D. Langreth, *Phys. Rev. B: Condens. Matter Mater. Phys.*, 2010, **82**, 081101.
42 V. Cooper, *Phys. Rev. B: Condens. Matter Mater. Phys.*, 2010, **81**, 161104.
43 J. Hermann, R. A. DiStasio and A. Tkatchenko, *Chem. Rev.*, 2017, **117**, 4714–4758.
44 H. Monkhorst and J. D. Pack, *Phys. Rev. B: Solid State*, 1976, **13**, 5188.
45 G. Benedek, *Phys. Rev. Lett.*, 1975, **35**, 234–237.
46 G. Benedek, M. Bernasconi, V. Chis, E. Chulkov, P. M. Echenique, B. Hellsing and J. P. Toennies, *J. Phys.: Condens. Matter*, 2010, **22**, 084020.
47 A. Jones, A. Tamtögl, I. Calvo-Almazán and A. Hansen, *Sci. Rep.*, 2016, **6**, 27776.
48 W. Kullmann, G. Eichhorn, H. Rauh, R. Geick, G. Eckold and U. Steigenberger, *Phys. Status Solidi B*, 1990, **162**, 125–140.
49 J. O. Jenkins, J. A. Rayne and R. W. Ure, *Phys. Rev. B: Solid State*, 1972, **5**, 3171–3184.
50 Y. C. Akgöz, G. A. Saunders and Z. Sümengen, *J. Mater. Sci.*, 1972, **7**, 279–288.
51 S. Giraud, A. Kundu and R. Egger, *Phys. Rev. B: Condens. Matter Mater. Phys.*, 2012, **85**, 035441.
52 W. Richter and C. R. Becker, *Phys. Status Solidi B*, 1977, **84**, 619–628.
53 W. Kullmann, J. Geurts, W. Richter, N. Lehner, H. Rauh, U. Steigenberger, G. Eichhorn and R. Geick, *Phys. Status Solidi B*, 1984, **125**, 131–138.
54 V. Wagner, G. Dolling, B. Powell and G. Landweher, *Phys. Status Solidi B*, 1978, **85**, 311–317.
55 A. A. Taleb and D. Farrías, *J. Phys.: Condens. Matter*, 2016, **28**, 103005.
56 G. W. Farnell, *Physical Acoustics*, Academic Press, 1970, vol. 6, pp. 109–166.
57 G. W. Farnell, *Acoustic surface waves*, 1978, pp. 13–60.
58 O. Hellman and D. A. Broido, *Phys. Rev. B: Condens. Matter Mater. Phys.*, 2014, **90**, 134309.
59 X. Chen, D. Parker and D. J. Singh, *Phys. Rev. B: Condens. Matter Mater. Phys.*, 2013, **87**, 045317.
60 D. Bessas, I. Sergueev, H.-C. Wille, J. Perßon, D. Ebling and R. P. Hermann, *Phys. Rev. B: Condens. Matter Mater. Phys.*, 2012, **86**, 224301.
61 M. Wiesner, A. Trzaskowska, B. Mroz, S. Charpentier, S. Wang, Y. Song, F. Lombardi, P. Lucignano, G. Benedek, D. Campi, M. Bernasconi, F. Guinea and A. Tagliacozzo, *Sci. Rep.*, 2017, **7**, 16449.
62 B.-L. Huang and M. Kaviany, *Phys. Rev. B: Condens. Matter Mater. Phys.*, 2008, **77**, 125209.
63 L. Fu, *Phys. Rev. Lett.*, 2009, **103**, 266801.
64 V. Chis, G. Benedek, P. M. Echenique and E. V. Chulkov, *Phys. Rev. B: Condens. Matter Mater. Phys.*, 2013, **87**, 075412.
65 X. Jia, S. Zhang, R. Sankar, F.-C. Chou, W. Wang, K. Kempa, E. W. Plummer, J. Zhang, X. Zhu and J. Guo, *Phys. Rev. Lett.*, 2017, **119**, 136805.
66 G. Q. Huang, *EPL*, 2012, **100**, 17001.
67 S. Nakajima, *J. Phys. Chem. Solids*, 1963, **24**, 479–485.
68 A. Tamtögl, E. Bahn, J. Zhu, P. Fouquet, J. Ellis and W. Allison, *J. Phys. Chem. C*, 2015, **119**, 25983–25990.

6.10 Publication J

Tamtögl, A., Pusterhofer, M., Bremholm, M., Hedegaard, E. M., Iversen, B. B., Hofmann, P., Ellis, J., Allison, W., Miret-Artés, S. & Ernst, W. E. A Helium-Surface Interaction Potential of Bi_2Te_3(111) from Ultrahigh-Resolution Spin-Echo Measurements. *Surf. Sci.* **678,** 25–31 (2018)

contributions	
funding	A. Tamtögl, W. Allison, J. Ellis, P. Hofmann, W. E. Ernst
sample synthesis	E. M. J. Hedegaard, M. Bremholm, B. B. Iversen
preparation / setup	A. Tamtögl
data acquisition	A. Tamtögl
data analysis	A. Tamtögl, M. Pusterhofer
interpretation	A. Tamtögl, M. Pusterhofer, S. Miret-Artés
publication writing	A. Tamtögl, M. Pusterhofer

Tamtögl, A., Pusterhofer, M., Bremholm, M., Hedegaard, E. M., Iversen, B. B., Hofmann, P., Ellis, J., Allison, W., Miret-Artés, S. & Ernst, W. E. A Helium-Surface Interaction Potential of Bi_2Te_3(111) from Ultrahigh-Resolution Spin-Echo Measurements. *Surf. Sci.* **678,** 25–31 (2018)

Surface Science 678 (2018) 25–31

Contents lists available at ScienceDirect

Surface Science

journal homepage: www.elsevier.com/locate/susc

A Helium-Surface Interaction Potential of Bi_2Te_3(111) from Ultrahigh-Resolution Spin-Echo Measurements

Anton Tamtögl[a,b,*], Michael Pusterhofer[a], Martin Bremholm[c], Ellen M.J. Hedegaard[c], Bo B. Iversen[c], Philip Hofmann[d], John Ellis[b], William Allison[b], S. Miret-Artés[e], Wolfgang E. Ernst[a]

[a] Institute of Experimental Physics, Graz University of Technology, Petersgasse 16, Graz, 8010, Austria
[b] Cavendish Laboratory, University of Cambridge, J. J. Thomson Avenue, CB3 0HE, Cambridge, United Kingdom
[c] Center for Materials Crystallography, Department of Chemistry and iNANO, Aarhus University, Denmark
[d] Department of Physics and Astronomy, Interdisciplinary Nanoscience Center (iNANO), Aarhus University, Denmark
[e] Instituto de Física Fundamental (IFF-CSIC), Serrano 123, Madrid, 28006, Spain

ARTICLE INFO

Keywords:
Bi2Te3
Topological insulator
Atom-surface interaction
Atom scattering
Bound states
Adsorption

ABSTRACT

We have determined an atom-surface interaction potential for the He–Bi_2Te_3(111) system by analysing ultrahigh resolution measurements of selective adsorption resonances. The experimental measurements were obtained using ^{3}He spin-echo spectrometry. Following an initial free-particle model analysis, we use elastic close-coupling calculations to obtain a three-dimensional potential. The three-dimensional potential is then further refined based on the experimental data set, giving rise to an optimised potential which fully reproduces the experimental data. Based on this analysis, the He–Bi_2Te_3(111) interaction potential can be described by a corrugated Morse potential with a well depth $D = (6.22 \pm 0.05)$ meV, a stiffness $\kappa = (0.92 \pm 0.01)$ Å^{-1} and a surface electronic corrugation of (9.6 ± 0.2)% of the lattice constant. The improved uncertainties of the atom-surface interaction potential should also enable the use in inelastic close-coupled calculations in order to eventually study the temperature dependence and the line width of selective adsorption resonances.

1. Introduction

Bi_2Te_3 is classified as a topological insulator (TI)[1], a class of materials which exhibit protected metallic surface states and an insulating bulk electronic structure[2–4]. The modification of the electronic structure of topological surfaces upon adsorption of atoms and molecules has been subject to several studies[5–8]. However, the interaction of topological insulator surfaces with its environment, including the atom-surface interaction potential is largely unexplored by experiment.

Information about the detailed shape of the interaction potential can be gained from atom scattering experiments. In favourable cases the hard wall of the potential can be studied through the profile of the specular lattice rod, a form of interference in Δk_z[9,10]. However, such methods are relatively insensitive to the form of the attractive interaction, which is the main concern in the present work. Here, we analyse observations of resonant scattering using ^{3}He spin-echo spectroscopy measurements in combination with elastic close-coupling scattering calculations to determine the He–Bi_2Te_3(111) interaction potential. Atom-surface potentials can be measured to an extremely high accuracy by using selective adsorption resonances (SAR) in atom-surface scattering via the technique of ^{3}He spin-echo spectrometry[11,12].

A detailed study of the atom-surface interaction on topological insulators is particularly interesting from a fundamental point of view. Precise measurements of atom-surface potentials offer a high-resolution window into the atom-surface interaction dynamics within the van der Waals regime, a field of intense theoretical interest in testing the ability of density functional theory calculations to simulate nonlocal interactions[13–15]. Hence the experimental data may assist in bench-marking of current theoretical approaches for the description of van der Waals forces. Such approaches become even more complicated for nanostructured surfaces[16]. On topological insulator surfaces with their peculiar electronic surface effects our data and experimental approach may also help to understand the above mentioned influence of adsorption upon the electronic structure, where in particular the long-range part of the potential is responsible for band bending effects[17].

Selective adsorption phenomena appear in atom-molecule scattering off periodic surfaces due to the attractive part of the atom-surface interaction potential. According to Bragg's law, when an atom is scattered

* Corresponding author. Tel: +43 316 873 8143, +436803171626.
E-mail address: at677@cantab.net (A. Tamtögl).

https://doi.org/10.1016/j.susc.2018.02.006
Received 9 January 2018; Received in revised form 6 February 2018; Accepted 12 February 2018
Available online 13 February 2018
0039-6028/

by a periodic surface, the change in the wavevector component parallel to the surface, **K**, must be equal to a surface reciprocal lattice vector, **G**. In the case of elastic scattering, the wavevector component perpendicular to the surface, $k_{f,z}$, is given via the conservation of energy and the kinematically-allowed **G**-vectors for scattering are those for which $k^2_{f,z}$ is positive.

SARs occur when a He atom is diffracted into a channel which is kinematically disallowed ($k^2_{f,z} < 0$) whilst simultaneously dropping into a bound state of the atom-surface potential. The kinematics of a SAR, involving a bound state of energy $-|\epsilon_n|$, is defined by the simultaneous conservation of energy and parallel momentum. The corresponding process can only take place if the difference between the energy of the incident atom and the kinetic energy of the atom moving parallel to the surface matches the binding energy ϵ_n of the adsorbed atom[18]:

$$E = \frac{\hbar^2 \mathbf{k}_i^2}{2m} = \frac{\hbar^2(\mathbf{K}_i + \mathbf{G})^2}{2m} + \epsilon_n(\mathbf{K}_i, \mathbf{G}). \quad (1)$$

Since SARs correspond to the specific bound state energies ϵ_n, of the He-surface interaction potential, the phenomenon provides a natural approach for studies of the atom-surface potential. It has only recently been shown that SARs in He scattering can even be used to reveal the degree of proton order in an ice surface[19]. However, the majority of experimentally measured SARs is based on salts with the NaCl structure[11,12,18,20–23] with some exceptions such as, adsorbate systems[24,25], stepped metal surfaces[20,26] or the semimetal surfaces of Bi(111) and Sb(111)[27,28] and the semiconductor Si(111)-H[29].

2. Experimental Details

In the present work we use ^{3}He–Bi_2Te_3(111) selective adsorption data obtained with the Cambridge helium-3 spin-echo spectrometer[30]. A nearly monochromatic beam of ^{3}He is scattered off the sample surface in a fixed 44.4° source-target-detector geometry. A detailed setup of the apparatus has been described in greater detail elsewhere[30,31].

Bi_2Te_3 exhibits a rhombohedral crystal structure which consists of quintuple layers bound to each other through weak van der Waals forces giving easy access to the (111) surface by cleavage[32,33] (see Michiardi *et al.*[33] for details on the crystal growth procedure). The (111) cleavage plane is terminated by Te atoms with a hexagonal structure ($a = 4.386$ Å)[34]. The Bi_2Te_3 single crystal used in the study was attached onto a sample holder using electrically and thermally conductive epoxy. The sample holder was then inserted into the chamber using a load-lock system[35] and cleaved *in-situ*. The sample holder can be heated using a radiative heating filament on the backside of the crystal or cooled down to $\approx$100 K using liquid nitrogen. The sample temperature was measured using a chromel-alumel thermocouple.

A measurement which can be used to identify SARs, is the so called ϑ-scan, where the scattered beam intensity is measured as a function of the incident angle ϑ_i, while the total scattering angle is fixed. In doing so, the momentum transfer parallel to the surface, given by $|\Delta\mathbf{K}| = |\mathbf{k_i}|(\sin(\vartheta_f) - \sin(\vartheta_i))$, is varied by changing the incident angle ϑ_i. A typical diffraction scan for the $\overline{\Gamma M}$ azimuth is shown in the lower panel of Figure 1. In between the diffraction peaks, there may appear small peaks or dips in the scattered intensity which can be assigned to SARs, with the position of the peaks given by equation (1). By changing the beam energy and the azimuthal angle, different SAR conditions can be met.

In Figure 1 rapid variations in scattered intensity have been identified with particular resonances. The resonance positions are indicated by vertical lines in Figure 1, with annotations indicating the diffraction channel and bound-state index. In identifying particular resonances, we have assumed the free atom approximation, where the binding energy ϵ_n, in Equation 1, is taken as a constant and is independent of $\mathbf{K}_i$ and **G**. The approximation is valid in the limit of zero corrugation and is a useful starting point for the more detailed analysis performed below. A

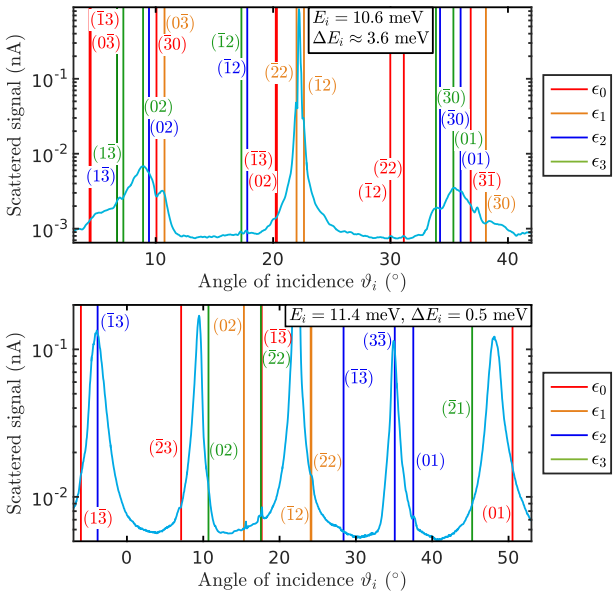

Fig. 1. Scattered He intensities (logarithmic scale) for Bi_2Te_3(111) versus incident angle ϑ_i along the $\overline{\Gamma M}$ azimuth and at a sample temperature of 107 K. The central beam energy E_i is 10.6 and 11.4 meV while the energy spread ΔE_i (full width at half maximum) is 3.6 and 0.5 meV in the top and bottom panels, respectively. In addition to the diffraction peaks, further peaks and dips corresponding to selective adsorption processes are identifiable. The vertical lines illustrate the kinematic conditions for four bound-state energies $\epsilon_0 - \epsilon_3$. Each line is labelled with the Miller indices of the associated **G** vector for the resonance condition.

corrugated potential creates a more complex band-structure for the resonances where the dispersion is no longer that of a free-atom and nearby resonances may interact. Such effects are visible in a 3-D plot of scattered intensity against energy and azimuthal angle. The spin-echo spectrometer enables such plots from measurements of the specular intensity against azimuthal angle, as we describe below. We will only briefly summarise the measurement of such a two-dimensional scan here, since a more detailed description can be found elsewhere[11]. We use the Fourier transform nature of the spectrometer to analyse the intensity distribution as a function of energy within the specularly scattered helium beam, to produce a complete data set of SARs for the particular scattering geometry used. Selective adsorption features were measured by performing a series of spin precession scans on the specularly scattered helium beam using one of the instruments spin-precession coils. The results were Fourier transformed onto an energy scale[30], where selective adsorption processes appear as dips or peaks in the scattered intensity at specific characteristic energies.

To probe as many selective adsorption processes as possible, we used ^{3}He nozzle conditions which gave a wide energy spread in the incident beam. Two sets of measurements were performed, one with the central beam energy at 8 meV and a full width at half maximum of 1.66 meV and one with the central beam energy around 11 meV and a width of 3.80 meV. Figure 2 shows an example of such a scan with the raw and Fourier transformed data.

The spin precession measurements used precession solenoid currents between −400 and +400 mA in 0.33 mA steps. The complete data set was built up from a series of 130 scans (65 at each nozzle temperature), taken at an azimuthal angle spacing of 0.5°, to encompass the entire region within the $\overline{\Gamma M}$ and $\overline{\Gamma K}$ azimuthal directions. The scans at both beam energies were then combined into one plot. To further increase the visibility of bound state resonance features the scattered intensity was subtracted from the beam profile as given without the effect of bound state resonances. We use the average of the whole data set along the

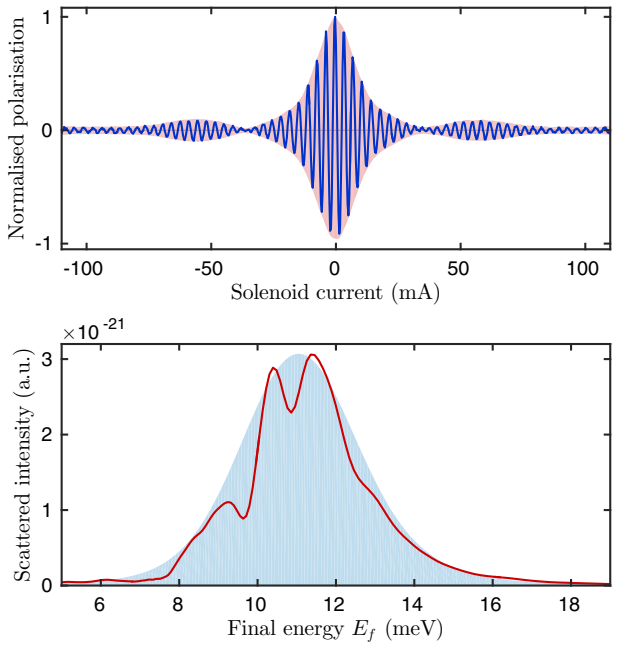

Fig. 2. Example of a typical measurement that includes selective adsorption resonances. The upper panel shows the detector signal for different currents in the incoming solenoid, which is proportional to the magnetic field. The overall decay envelope is due to the energy spread of the beam. The beating effect is an interference pattern due to the existence of multiple energy peaks within the overall beam energy distribution which are a consequence of SARs. The lower panel shows the signal after transformation to the energy scale (red solid line). The distribution of energy in the incident beam is approximately Gaussian and is illustrated by the shaded background. Resonances are evident in the difference between the line and the smooth background. Note that, in contrast to conventional experiments, the energy width of the resonances is given by their natural width and is much less than the energy spread in the beam.

azimuthal direction as a measure of the beam profile[25,29] and the whole data set was then normalised after subtraction from the beam profile.

In Fig. 3a the final data set is shown as a function of φ (the azimuthal angle relative to the $\overline{\Gamma K}$ azimuth) and E_f. A number of lines of high and low intensities, which we identify as SAR features, can be seen to run across the data set.

3. Analysis

For the atom-surface interaction we assume a corrugated Morse potential (CMP). Strictly speaking, the Morse potential does not exhibit the right z^{-3} asymptotic behaviour and the long-range interaction may be described more accurately by modified versions of the interaction potential. However, as shown recently, Morse- or Morse-like potential functions are perfectly suitable for representing the bound state energies of semimetal surfaces[36,37] and the use of the Morse potential allows to solve several steps within the close-coupling (CC) algorithm analytically, which greatly simplifies the computational cost.

For a three-dimensional atom-surface interaction potential the potential is written in terms of the lateral position $\mathbf{R}$ on the surface and the distance z with respect to the surface:[38]

$$V(\mathbf{R}, z) = D\left[\frac{1}{v_{0,0}} e^{-2\kappa[z-\xi(\mathbf{R})]} - 2e^{-\kappa z}\right] \tag{2}$$

where κ is the stiffness parameter, D is the depth of the potential well and $v_{0,0}$ is the surface average of the exponent of the corrugation function. The electronic surface corrugation is given by $\xi(\mathbf{R})$ where $\mathbf{R}$ is the lateral position in the surface plane describing a periodically modulated surface with constant total electron density. $\xi(\mathbf{R})$ is described by the summation of cosine terms obtained from a Fourier series expansion based on a hexagonal unit cell[28,36]:

$$\xi(x,y) = \xi_0 \left\{\cos\left[\frac{2\pi}{a}\left(x - \frac{y}{\sqrt{3}}\right)\right] + \cos\left[\frac{2\pi}{a}\left(x + \frac{y}{\sqrt{3}}\right)\right] + \cos\left[\frac{2\pi}{a}\frac{2y}{\sqrt{3}}\right]\right\} + h.o. \tag{3}$$

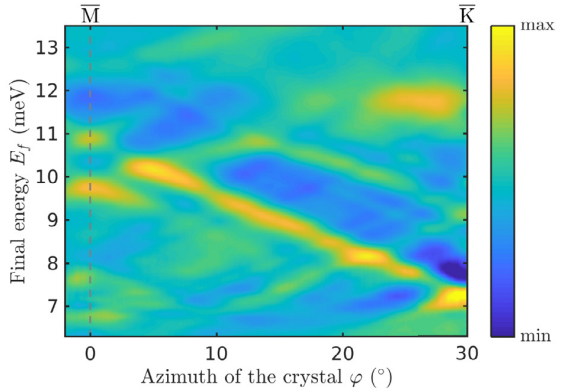

(a) Measured specular scattering intensity as a function of φ and E_f, for ^{3}He scattering from Bi_2Te_3(111) surface, where the colour scale corresponds to the intensity. The crystal was held at 110 K during the measurement and the underlying beam profile of the incoming He beam has been removed to obtain a spectrum of the bound state resonances. A number of lines of high and low intensities, which we identify as selective adsorption resonances features, can be seen to run across the data set.

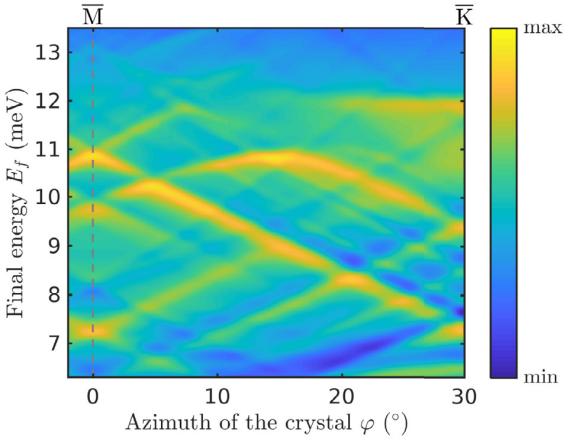

(b) Contour plot of the simulated data set based on the optimised three-dimensional parameters. To obtain the same contour plot as in the experiment (Fig. 3a) the beam profile is included and a small Gaussian blur is introduced which accounts for inelastic effects that are present in the experimental data (measurement at finite temperature).

Fig. 3. Experimental data set as a function of (φ, E_f) together with the simulated data set based on the optimised atom-surface interaction potential.

with ξ_0 the corrugation amplitude. The magnitude of the corrugation is typically given in terms of the peak-to-peak corrugation ξ_{pp} of (3).

The laterally averaged surface potential V_0 of (2) is then given via:

$$V_0(z) = D\left[e^{-2\kappa z} - 2e^{-\kappa z}\right] \tag{4}$$

and the corresponding couplings can be found in[28,36,37]. The bound states of the averaged potential are described by an analytical expression:

$$\epsilon_n = -D + \hbar\omega(n+0.5)\left(1 - \frac{n+0.5}{2\gamma}\right) \tag{5}$$

with a positive integer n, $\omega = \kappa\sqrt{\frac{2D}{m}}$ and $\gamma = \frac{2D}{\hbar\omega}$, where m is the mass of the impinging ^{3}He atom.

In order to determine the best three-dimensional potential, we go through the following three-step process, starting with a laterally averaged atom-surface interaction potential followed by refining the three-dimensional potential via comparison of close-coupled calculations with the experimental data:

1. Obtain an approximate, surface-averaged potential using the free-atom model (Figure 1).
2. Determine the corrugation amplitude ξ_0 of the potential from diffraction measurements to acquire a three-dimensional potential.
3. Simulate the experimental measurements using the corrugated potential and further improve the potential by comparison of the simulation with the experimental data.

The process is described in detail below.

3.1. Comparison with the free atom model

The free atom approximation (for parallel motion) assumes that the surface potential is adequately described simply by the laterally averaged component of the interaction potential. It corresponds to the case where the surface corrugation approaches zero, which is not possible in reality, since corrugation is necessary to provide the corresponding **G**-vector for the resonance processes.

In particular for strongly corrugated systems the free atom approximation is no longer valid. Based on the diffraction peak intensities a peak-to-peak corrugation of 9% of the surface lattice constant was found for Bi_2Te_3[34] and about 5% in the case of Bi(111)[36]. Though still smaller than the corrugation of several semiconductor and insulating surfaces[20,34] these are rather large values. Hence one would expect that band structure effects play a significant role.

Nevertheless, despite its limitations and simplifying nature, the free atom approximation provides a good starting point to understand selective adsorption phenomena. To calculate the positions, the kinematic condition from (1) is written in terms of the incident angle ϑ_i and the incident wave vector k_i, which corresponds to the beam energy as well as the components of the scattering vector $\mathbf{G} = (G_\parallel, G_\perp)$:

$$-\cos^2(\vartheta_i)k_i^2 + 2\sin(\vartheta_i)G_\parallel k_i + G_\parallel^2 + G_\perp^2 - \frac{2m}{\hbar^2}|\epsilon_n| = 0 \tag{6}$$

Here **G** is split into the components $G_\parallel$ and $G_\perp$ parallel and normal to the incidence plane, respectively. Diffraction scans with some SARs are useful in order to obtain a first idea about the bound state energies: Solving (6) provides an estimate of the bound state energy ϵ_n associated with a peak or dip at a certain ϑ_i in the diffraction scan.

The lower panel of Figure 1 shows a diffraction scan for the $\overline{\Gamma M}$ azimuth with an incident beam energy of 11.4 meV. A couple of small peaks and some shoulders at the diffraction peak positions, which may be caused by SARs, are visible in the scan. The upper panel of Figure 1 shows a diffraction scan along $\overline{\Gamma M}$ with a wide energy spread giving rise to the much broader diffraction peaks. SARs sitting on the diffraction peak positions are now much more evident, however, it complicates the analysis since the incoming beam energy E_i and consequently k_i in Equation 6 is no longer clearly defined.

Nevertheless, we can use the positions of the peaks and dips in Figure 1 to get a first idea about the bound state energies ϵ_n and the associated laterally averaged potential. The vertical lines in Figure 1 display the SAR conditions based on Equation 6 for four bound state energies $\epsilon_0 - \epsilon_3$ and the reciprocal lattice vectors **G** as labelled in the graph. Based on these SAR features, there appear to be four bound state energies with $\epsilon_0 \approx 4.5$ meV, $\epsilon_1 \approx 1.9$ meV, $\epsilon_2 \approx 0.3$ meV and $\epsilon_3 \approx 0.05$ meV.

The bound state energies ϵ_n of the laterally averaged potential can be calculated analytically using (5). Using an optimisation routine based on the four bound state energies, we obtain a potential with the parameters $D = (6.4 \pm 0.3)$ meV and $\kappa = (0.94 \pm 0.06)$ Å^{-1}

3.2. Comparison with elastic close-coupled calculations

While in the free atom approximation the coupling term vanishes, the band structure diagram in such a situation would consist entirely of parabolic bands. For strongly corrugated systems, contributions of the higher-order Fourier components in the surface potential become significant and can no longer be neglected. Hence resonance positions calculated using a corrugated surface potential give rise to a substantial deviation from the free atom parabolic bands in analogy to the occurrence of energy gaps in the electronic band structure at the Brillouin zone boundary. Similarly a splitting of parabolic bands and the development of energy gaps at zones of degeneracy may occur due to the spatial periodicity of the atom-surface interaction potential. These effects have been highlighted in the past[39–43] and an exact description of the measured data is only possible by exact quantum mechanical calculations based on the three-dimensional potential.

In a purely elastic scattering scheme, scattering of a He atom with incident wavevector $\mathbf{k}_i$, is described by the time-independent Schrödinger equation with the potential as given by Equation 2. Together with a Fourier expansion of the wave function it gives rise to a set of coupled equations for the diffracted waves which are solved for in the close-coupling algorithm using a finite set of closed channels[27,44].

In a first step the corrugation amplitude of the three-dimensional potential needs to be determined. Therefore the elastic peak intensities are simulated using the close-coupling algorithm, starting with the parameters of the laterally averaged potential obtained in the previous section. The calculated purely elastic intensities are corrected with the Debye-Waller attenuation and compared with the experimentally determined peak areas[34]. The peak-to-peak corrugation ξ_{pp} was varied, over a range of 0.005 – 0.7 Å with a step width of 0.005 Å giving rise to a best fit with the experimentally determined peak areas at $\xi_{pp} = 0.45$ Å.

Once a starting point for the parameters of the three-dimensional potential (2) is known, the close-coupling algorithm is used to calculate a data-set similar to the measurement in Fig. 3a. Therefore the elastically scattered intensity for the secular scattering condition is calculated for a set of different beam energies and for different azimuthal orientations of the crystal. The scattered intensity for each set of (φ, E_f) is shown in the contour plot of Fig. 4a.

Several SARs features appear either as local maxima or minima in the contour plot. The dotted and dash-dotted lines which are superimposed onto the contour plot illustrate a number of kinematic conditions, Equation 6, based on the laterally averaged potential. Note that in regions where there are several resonances based on the free atom model, it is not always possible to identify a clear line shape in the simulated data. In particular, several of the kinematic conditions show a strong deviation with respect to the lines running through the simulated data. There are also several lines in the simulated data which are not matched by any of the kinematic conditions. It illustrates that the above mentioned band structure effects play a significant role and hence the coupling between the scattering channels as present in the close-coupling simulation is essential[44].

Since the deviations of the kinematic conditions from the full quantum-mechanical calculation depend strongly on the potential parameters, the best three-dimensional potential is hard to find. Further-

more, the kinematic conditions do not predict whether a resonance condition gives rise to a maximum or minimum. Therefore, a self-consistency cycle or a method which does not use the kinematic condition has to be evaluated to avoid this problem. The latter can be achieved by comparing the SAR positions obtained from the close-coupling calculation directly to the experimental data, which requires the simulation of data sets for a high number of parameter sets. To make this option viable, the search space has to be reduced, so that it can be scanned in a reasonable amount of time. Therefore, we start with the potential found in 3.1 as the centre of the parameter space and create a parameter grid around it, which reduces the number of simulations and enables the application of parallel computation. In the case of the corrugated Morse potential, the parameter space can be reduced to two dimensions since the corrugation ξ_{pp} can be determined beforehand via comparison with the experimentally determined peak areas.

To quantify the quality of the resulting simulation, a χ^2-test is used, testing that the positions (φ, E_f) of the SARs in the simulated data set coincide with the positions in the experimental data set. It leads to an equation for the χ^2 sum, which adds the squares of the difference between the position of the resonances from the simulation $\epsilon_{i,s}$ and the position seen in the experimental data $\epsilon_{i,m}$ divided by the sum of the standard deviations of the experiment $\sigma_{i,m}$ and the simulated data $\sigma_{i,s}$:

$$\chi^2 = \sum_i \left(\frac{\epsilon_{i,s} - \epsilon_{i,m}}{\sigma_{i,m} + \sigma_{i,s}} \right)^2 \tag{7}$$

Here we assume that the resonance positions follow a normal distribution, since they were measured by hand using the image analysis tool called Fiji[45] on a graphical representation of the simulation. To obtain the standard deviation, a cut at a fixed azimuthal angle φ was taken and the half width at half maximum of the resonance signal was used, after subtracting the background.

The calculation of the χ^2 value is done on a grid with the potential depth D spanning from 5.9 to 6.4 meV with a step width of 0.05 meV and the potential stiffness κ spanning from 0.88 to 1.00 Å^{-1} with a step width of 0.005 Å^{-1} resulting in 143 potentials. For the calculation of the cost function we have used three resonances, associated with ϵ_0, ϵ_1 and ϵ_2 which is illustrated in Figure 4: The kinematic conditions for these resonances are illustrated as dash-dotted lines on top of the experimental as well as the simulated data.

The result of the optimisation is plotted in Figure 5 as a colour-map plot, showing the regions for three different significance levels α of 1%, 2% and 5% (corresponding to a confidence interval of 99%, 98% and 95%), respectively.

Once the best-fit potential parameters D and κ have been found, the corrugation ξ_{pp} is further refined using again a comparison with the experimentally determined diffraction peak areas. Following this approach, the parameters of the best-fit three-dimensional potential based on a significance level of $\alpha = 2\%$ are:

$$D = (6.22 \pm 0.05) \text{ meV}$$
$$\kappa = (0.92 \pm 0.01) \text{ Å}^{-1}$$
$$\xi_{pp} = (0.42 \pm 0.01) \text{ Å}$$

Compared to the results from 3.1, the well depth D and the corrugation are now somewhat smaller while the stiffness κ increased. While the well depth and stiffness obtained from the free particle model may be used as a reasonable estimate, the uncertainties of all three potential parameters are significantly reduced by comparison with the close-coupling calculations. More importantly, the free particle model can only provide an estimate for the position of the resonances but cannot reproduce the shape of the resonances, in particular whether there appear maxima or minima, which is inherently obtained from the close-coupling calculations.

A simulated data set based on the same conditions as the experimental data set with the optimised three-dimensional parameters is shown in Fig. 3a. To obtain the same contour plot as in the experiment (Fig. 3b) the beam profile is included: The simulated data is first multiplied with the beam profile to account for the energy distribution of the incoming He beam after which the data is again subtracted from the beam profile to follow the same procedure as for the treatment of the experimental data. Finally a Gaussian blur with a standard deviation of 80 μeV in energy is introduced. The blur is a measure of the average linewidth of the resonances and accounts for the fact that our purely elastic analysis with the corrugated Morse potential fails to reproduce the linewidths of the resonances as measured in the experiment. Several factors may contribute to a resonance linewidth[29] including inelasticity, disorder and the distribution of the corrugation between the attractive and repulsive parts of the potential. A comparison of the simulated data including the Gaussian blur with the experimental data (Figure 3) shows that all main features are very well reproduced and appear at the right position in terms of φ and E_f.

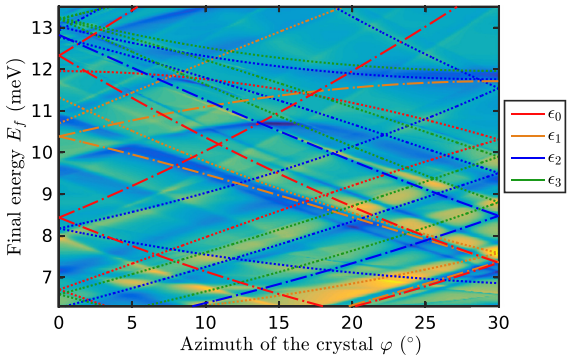

(a) Close coupled calculations of the ^{3}He–Bi_2Te_3(111) specular scattering intensity for the same conditions as the experimental data, using the potential parameters obtained in 3.1. The dotted and dash-dotted lines show a number of kinematic conditions (Equation 6) based on the laterally averaged potential.

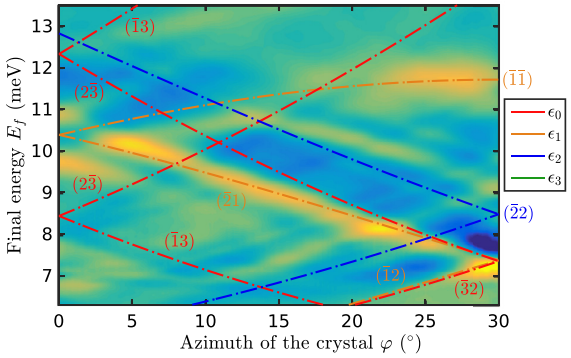

(b) Experimental data from Fig. 3a with several kinematic conditions (Equation 6) of the laterally averaged potential plotted as dash-dotted lines.

Fig. 4. (Same colormap as Fig. 3) A comparison of the resonance positions visible in the simulated data with the kinematic conditions of the laterally averaged in (a) illustrates that band structure effects play a significant role, giving rise to strong deviations. In order to further refine the three-dimensional potential we have picked a number of specific resonances of which the kinematic conditions are illustrated as dash-dotted lines. We then minimise the deviation in terms of the (φ, E_f) position of these specific resonances between the experimental data in (b) and the simulation in (a) to obtain a best-fit three-dimensional potential.

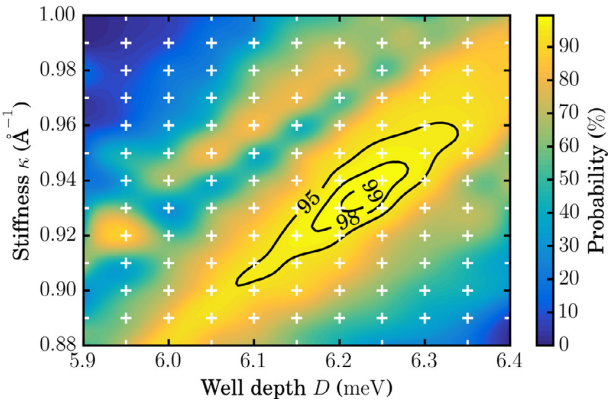

Fig. 5. The probability that the three resonances ϵ_0 - ϵ_2, associated with specific reciprocal lattice vectors (see Figure 4) appear at the same position in the experimental and the simulated data. The white crosses show the evaluated points on the parameter grid and the contour lines show regions for α-values of 1%, 2% and 5% (corresponding to a confidence interval of 99%, 98% and 95%, respectively).

For a rough estimate of the potential depth D, the ratio between the potential depth and the average atomic mass of the sample can be used. It gives rise to a value of 0.039 meV u^{-1} for the Bi_2Te_3(111) surface, which is in good agreement with similar material surfaces such as Sb(111) (0.035 meV u^{-1})[37] and Bi(111) (0.038 meV u^{-1})[36]. The value of the well depth D itself, is between those found for Sb(111)(4.3 meV)[37] and Bi(111) (7.9 meV)[36] while being considerably lower than the one found for graphite(0001)($\approx$16 meV)[40,46].

The stiffness κ of the He–Bi_2Te_3(111) potential is much larger compared to the He–Sb(111) potential (0.39 Å^{-1})[27] and indeed rather comparable to the He–LiF(001) potential[18]. On the one hand this could be connected with the insulating interior and polarisability of the topological material. On the other hand the He–Bi(111) potential has a similar stiffness (0.88 Å^{-1})[36] and it seems to be difficult to identify a general trend based on the stiffness κ.

The peak-to-peak corrugation of the final optimised potential is (9.6 ± 0.2)% relative to the lattice constant and hence only slightly larger compared to a first analysis based on a rough estimate of the potential[34]. This surface electronic corrugation is larger than the ones found for low-index metal surfaces[20,46] while being similar to the corrugation of semimetals such as Bi(111)(5%)[36], graphite(0001)(8.6%)[47,48] and Sb(111)($\approx$15%)[37].

Finally, inelastic processes and phonon mediated SARs have been identified in experiments and proven to play important roles[18,20], also for similar systems as in our study, e.g. for helium scattering of the Bi(111) surface[27]. However, from a theoretical point of view, these effects have been mainly considered in the limit of low corrugated surfaces[49–52]. Since the inelastic scattering amplitudes involving bound states depend sensitively on both the repulsive and attractive parts of the potential they provide a discriminating test of the atom-surface interaction potential and we hope that our work will initiate further theoretical investigations in this direction.

Summary and Conclusion

In summary, we have determined an atom-surface interaction potential for the He–Bi_2Te_3(111) system by analysing selective adsorption resonances. Following an initial free-particle model analysis, we use elastic close-coupling calculations to obtain an exact three-dimensional potential based on ultrahigh resolution ^{3}He spin-echo spectroscopy measurements. Based on this analysis, the He–Bi_2Te_3(111) interaction potential is best described by a corrugated Morse potential with a well depth D = (6.22 ± 0.05) meV, a stiffness κ = (0.92 ± 0.01) Å^{-1} and a surface electronic corrugation of (9.6 ± 0.2)% of the lattice constant.

To our knowledge, this work describes for the first time the determination of a high precision empirical atom-surface interaction potential of a topological insulator. The potential found in our study may assist in the development of first-principles theory where van der Waals dispersion forces play an important role and the improved uncertainties of the potential should also enable the use in inelastic close-coupled calculations. While the calculation of the scattered intensities including inelastic resonances requires the numerical solution of a large set of close-coupling equations which must be sufficiently large to assure convergence, with an exact potential at hand this should eventually allow to study the temperature dependence and the line width of selective adsorption resonances.

Acknowledgement

Upon his retirement from Freie Universität Berlin, Karl-Heinz Rieder enabled the transfer of his last He atom scattering machine to Graz. W. E. E. and the Graz group are grateful for his encouragement to start the investigation of semimetal surfaces which later broadened towards the class of topological materials.

We would like to thank P. Kraus for many helpful discussions. One of us (A.T.) acknowledges financial support provided by the FWF (Austrian Science Fund) within the project J3479-N20. The authors gratefully acknowledge support by the FWF within the project P29641-N36 and financial support by the Aarhus University Research Foundation, VILLUM FONDEN via the Centre of Excellence for Dirac Materials (Grant No. 11744) and the SPP1666 of the DFG (Grant No. HO 5150/1-2). E.M.J.H. and B.B.I. acknowledge financial support from the Center of Materials Crystallography (CMC) and the Danish National Research Foundation (DNRF93). S. M.-A. is grateful for financial support by a grant with Ref. FIS2014-52172-C2-1-P from the Ministerio de Economía y Competitividad (Spain).

References

[1] Y.L. Chen, J.G. Analytis, J.H. Chu, Z.K. Liu, S.K. Mo, X.L. Qi, et al., Experimental realization of a three-dimensional topological insulator, Bi2Te3, Science 325 (5937) (2009) 178–181, doi:10.1126/science.1173034. http://science.sciencemag.org/content/325/5937/178.
[2] J.E. Moore, The birth of topological insulators, Nature 464 (7286) (2010) 194–198, doi:10.1038/nature08916.
[3] M.Z. Hasan, C.L. Kane, Colloquium: Topological insulators, Rev Mod Phys 82 (2010) 3045–3067, doi:10.1103/RevModPhys.82.3045.
[4] X.L. Qi, S.C. Zhang, Topological insulators and superconductors, Rev Mod Phys 83 (2011) 1057–1110, doi:10.1103/RevModPhys.83.1057.
[5] D. Hsieh, Y. Xia, D. Qian, L. Wray, J.H. Dil, F. Meier, et al., A tunable topological insulator in the spin helical dirac transport regime, Nature 460 (7259) (2009) 1101–1105, doi:10.1038/nature08234.
[6] L.A. Wray, S.Y. Xu, Y. Xia, D. Hsieh, A.V. Fedorov, Y.S. Hor, et al., A topological insulator surface under strong coulomb, magnetic and disorder perturbations, Nat Phys 7 (1) (2011) 32–37. 10.1038/nphys1838
[7] E. Wang, P. Tang, G. Wan, A.V. Fedorov, I. Miotkowski, Y.P. Chen, et al., Robust gapless surface state and rashba-splitting bands upon surface deposition of magnetic Cr on Bi_2Se_3, Nano Lett 15 (3) (2015) 2031–2036, doi:10.1021/nl504900s.
[8] M. Caputo, M. Panighel, S. Lisi, L. Khalil, G.D. Santo, E. Papalazarou, et al., Manipulating the topological interface by molecular adsorbates: Adsorption of co-phthalocyanine on Bi_2 Se_3, Nano Lett 16 (6) (2016) 3409–3414, doi:10.1021/acs.nanolett.5b02635.
[9] C. Huang, D.A. MacLaren, J. Ellis, W. Allison, Experimental determination of the helium-metal interaction potential by interferometry of nanostructured surfaces, Phys Rev Lett 96 (2006) 126102, doi:10.1103/PhysRevLett.96.126102.
[10] J. Ellis, K. Hermann, F. Hofmann, J.P. Toennies, Experimental determination of the turning point of thermal energy helium atoms above a Cu(001) surface, Phys Rev Lett 75 (1995) 886–889, doi:10.1103/PhysRevLett.75.886.
[11] A.P. Jardine, S. Dworski, P. Fouquet, G. Alexandrowicz, D.J. Riley, G.Y.H. Lee, et al., Ultrahigh-resolution spin-echo measurement of surface potential energy landscapes, Science 304 (5678) (2004) 1790. http://www.sciencemag.org/content/304/5678/1790.abstract.
[12] D.J. Riley, A.P. Jardine, S. Dworski, G. Alexandrowicz, P. Fouquet, J. Ellis, et al., A refined He-LiF(001) potential from selective adsorption resonances measured with high-resolution helium spin-echo spectroscopy, J Chem Phys 126 (10) (2007) 104702, doi:10.1063/1.2464087.

[13] G.P. Brivio, M.I. Trioni, The adiabatic molecule–metal surface interaction: Theoretical approaches, Rev Mod Phys 71 (1999) 231–265. http://journals.aps.org/rmp/abstract/10.1103/RevModPhys.71.231.

[14] X. Wu, M.C. Vargas, S. Nayak, V. Lotrich, G. Scoles, Towards extending the applicability of density functional theory to weakly bound systems, J Chem Phys 115 (2001) 8748–8757, doi:10.1063/1.1412004.

[15] N. Jean, M.I. Trioni, G.P. Brivio, V. Bortolani, Corrugating and anticorrugating static interactions in helium-atom scattering from metal surfaces, Phys Rev Lett 92 (2004) 013201. http://journals.aps.org/prl/abstract/10.1103/PhysRevLett.92.013201.

[16] A. Ambrosetti, N. Ferri, R.A. DiStasio, A. Tkatchenko, Wavelike charge density fluctuations and van der Waals interactions at the nanoscale, Science 351 (6278) (2016) 1171–1176, doi:10.1126/science.aae0509. http://science.sciencemag.org/content/351/6278/1171.

[17] T. Förster, P. Krüger, M. Rohlfing, *Ab initio* studies of adatom- and vacancy-induced band bending in Bi_2Se_3, Phys Rev B 91 (2015) 035313, doi:10.1103/PhysRevB.91.035313.

[18] H. Hoinkes, H. Wilsch, Resonances in Helium Scattering from Surfaces, Springer Berlin Heidelberg, Berlin, Heidelberg, 1992, pp. 113–172.

[19] N. Avidor, W. Allison, Helium diffraction as a probe of structure and proton order on model ice surfaces, J Phys Chem Lett 126 (2016) 4520–4523, doi:10.1021/acs.jpclett.6b02221.

[20] D. Farías, K.H. Rieder, Atomic beam diffraction from solid surfaces, Rep Prog Phys 61 (12) (1998) 1575. http://stacks.iop.org/0034-4885/61/1575.

[21] D. Eichenauer, J.P. Toennies, Pairwise additive potential models for the interaction of He atoms with the (001) surfaces of LiF, NaF, NaCl and LiCl, Surf Sci 197 (1988) 267–276.

[22] G. Benedek, G. Brusdeylins, V. Senz, J.G. Skofronick, J.P. Toennies, F. Traeger, et al., Helium atom scattering study of the surface structure and dynamics of in situ cleaved MgO(001) single crystals, Phys Rev B 64 (2001) 125421, doi:10.1103/PhysRevB.64.125421.

[23] M. Debiossac, A. Zugarramurdi, P. Lunca-Popa, A. Momeni, H. Khemliche, A.G. Borisov, et al., Transient quantum trapping of fast atoms at surfaces, Phys Rev Lett 112 (2014) 023203, doi:10.1103/PhysRevLett.112.023203.

[24] E. Kirsten, G. Parschau, K. Rieder, He diffraction and resonant scattering studies of Rh(110)(1 × 1)-2H, Chem Phys Lett 181 (6) (1991) 544–548, doi:10.1016/0009-2614(91)80310-T.

[25] D.J. Riley, A.P. Jardine, G. Alexandrowicz, H. Hedgeland, J. Ellis, W. Allison, Analysis and refinement of the Cu(001)c(2 × 2)CO-He potential using he3 selective adsorption resonances, J Chem Phys 128 (15) (2008) 154712, doi:10.1063/1.2897921.

[26] R. Apel, D. Farías, H. Tröger, E. Kirsten, K. Rieder, Atomic beam diffraction and resonant scattering studies of clean Rh(311) and the c(1 × 1)H phase, Surf Sci 364 (3) (1996) 303–311, doi:10.1016/0039-6028(96)00640-1.

[27] P. Kraus, A. Tamtögl, M. Mayrhofer-Reinhartshuber, G. Benedek, W.E. Ernst, Resonance-enhanced inelastic he-atom scattering from subsurface optical phonons of Bi(111), Phys Rev B 87 (2013) 245433, doi:10.1103/PhysRevB.87.245433.

[28] M. Mayrhofer-Reinhartshuber, P. Kraus, A. Tamtögl, S. Miret-Artés, W.E. Ernst, Helium-surface interaction potential of Sb(111) from scattering experiments and close-coupling calculations, Phys Rev B 88 (2013) 205425, doi:10.1103/PhysRevB.88.205425.

[29] F.E. Tuddenham, H. Hedgeland, J. Knowling, A.P. Jardine, D.A. MacLaren, G. Alexandrowicz, et al., Linewidths in bound state resonances for helium scattering from Si(111)-(1 × 1)H, J Phys: Condens Matter 21 (26) (2009) 264004. http://stacks.iop.org/0953-8984/21/i=26/a=264004.

[30] A. Jardine, H. Hedgeland, G. Alexandrowicz, W. Allison, J. Ellis, Helium-3 spin-echo: principles and application to dynamics at surfaces, Prog Surf Sci 84 (11-12) (2009) 323, doi:10.1016/j.progsurf.2009.07.001. http://www.sciencedirect.com/science/article/B6TJF-4X0MP7F-1/2/4b3a9cac32140a526ede2c1e79325b49.

[31] G. Alexandrowicz, A.P. Jardine, Helium spin-echo spectroscopy: studying surface dynamics with ultra-high-energy resolution, J Phys: Cond Matt 19 (30) (2007) 305001. http://stacks.iop.org/0953-8984/19/i=30/a=305001.

[32] C. Howard, M. El-Batanouny, R. Sankar, F.C. Chou, Anomalous behavior in the phonon dispersion of the (001) surface of Bi_2Te_3 determined from helium atom-surface scattering measurements, Phys Rev B 88 (2013) 035402, doi:10.1103/PhysRevB.88.035402.

[33] M. Michiardi, I. Aguilera, M. Bianchi, V.E. de Carvalho, L.O. Ladeira, N.G. Teixeira, et al., Bulk band structure of Bi_2Te_3, Phys Rev B 90 (2014) 075105, doi:10.1103/PhysRevB.90.075105.

[34] A. Tamtögl, P. Kraus, N. Avidor, M. Bremholm, E.M.J. Hedegaard, B.B. Iversen, et al., Electron-phonon coupling and surface debye temperature of Bi_2Te_3(111) from helium atom scattering, Phys Rev B 95 (2017) 195401, doi:10.1103/PhysRevB.95.195401.

[35] A. Tamtögl, E.A. Carter, D.J. Ward, N. Avidor, P.R. Kole, A.P. Jardine, et al., Note: A simple sample transfer alignment for ultra-high vacuum systems, Rev Sci Instrum 87 (2016) 066108, doi:10.1063/1.4954728.

[36] P. Kraus, A. Tamtögl, M. Mayrhofer-Reinhartshuber, F. Apolloner, C. Gösweiner, S. Miret-Artés, et al., Surface structure of Bi(111) from helium atom scattering measurements. inelastic close-coupling formalism, J Phys Chem C 119 (30) (2015) 17235–17242, doi:10.1021/acs.jpcc.5b05010.

[37] P. Kraus, M. Mayrhofer-Reinhartshuber, C. Gösweiner, F. Apolloner, S. Miret-Artés, W.E. Ernst, A comparative study of the He-Sb(111) interaction potential from close-coupling calculations and helium atom scattering experiments, Surf Sci 630 (2014) 208–215, doi:10.1016/j.susc.2014.08.007. http://www.sciencedirect.com/science/article/pii/S0039602814002325.

[38] G. Armand, J. Manson, Scattering of neutral atoms by a periodic potential : the morse corrugated potential, J Phys France 44 (4) (1983) 473–487, doi:10.1051/jphys:01983004404047300.

[39] H. Chow, E. Thompson, Bound state resonances in atom-solid scattering, Surf Sci 59 (1) (1976) 225–251, doi:10.1016/0039-6028(76)90303-4.

[40] H. Hoinkes, The physical interaction potential of gas atoms with single-crystal surfaces, determined from gas-surface diffraction experiments, Rev Mod Phys 52 (1980) 933–970, doi:10.1103/RevModPhys.52.933.

[41] J. Manson, G. Armand, Band structure of an atom adsorbed on a surface; application to the He/Cu (113) system, Surf Sci 126 (1) (1983) 681–688, doi:10.1016/0039-6028(83)90774-4.

[42] M. Vargas, W. Mochán, Bound state spectroscopy of He adsorbed on NaCl(001): band structure effects, Surf Sci 355 (1) (1996) 115–126, doi:10.1016/0039-6028(95)01367-9.

[43] V. Subramanian, R.T. Skodje, Characterization of selective adsorption resonances for helium scattering from a highly corrugated surface using quantum wave packet dynamics, J Chem Phys 111 (11) (1999) 5167–5180, doi:10.1063/1.479771.

[44] A. Sanz, S. Miret-Artés, Selective adsorption resonances: Quantum and stochastic approaches, Phys Rep 451 (2–4) (2007) 37–154. http://www.sciencedirect.com/science/article/pii/S0370157307003250.

[45] J. Schindelin, I. Arganda-Carreras, E. Frise, V. Kaynig, M. Longair, T. Pietzsch, et al., Fiji: an open-source platform for biological-image analysis, Nat Methods 9 (7) (2012) 676–682, doi:10.1038/NMETH.2019.

[46] A. Tamtögl, E. Bahn, J. Zhu, P. Fouquet, J. Ellis, W. Allison, Graphene on Ni(111): Electronic corrugation and dynamics from helium atom scattering, J Phys Chem C 119 (46) (2015) 25983–25990, doi:10.1021/acs.jpcc.5b08284.

[47] G. Boato, P. Cantini, R. Tatarek, Study of gas-graphite potential by means of helium atom diffraction, Phys Rev Lett 40 (13) (1978) 887–889, doi:10.1103/PhysRevLett.40.887.

[48] G. Boato, P. Cantini, C. Guidi, R. Tatarek, G.P. Felcher, Bound-state resonances and interaction potential of helium scattered by graphite (0001), Phys Rev B 20 (1979) 3957–3969, doi:10.1103/PhysRevB.20.3957.

[49] S. Miret-Artés, Resonant inelastic scattering of atoms from surfaces, Surf Sci 339 (1) (1995) 205–220, doi:10.1016/0039-6028(95)00632-X.

[50] W. Brenig, Multiphonon resonances in the Debye-Waller factor of atom surface scattering, Phys Rev Lett 92 (2004) 056102, doi:10.1103/PhysRevLett.92.056102.

[51] A. Šiber, B. Gumhalter, Phonon-mediated bound state resonances in inelastic atomsurface scattering, J Phys: Condens Matter 20 (22) (2008) 224002. http://stacks.iop.org/0953-8984/20/i=22/a=224002.

[52] R. Martinez-Casado, D. Usvyat, L. Maschio, G. Mallia, S. Casassa, J. Ellis, et al., Approaching an exact treatment of electronic correlations at solid surfaces: The binding energy of the lowest bound state of helium adsorbed on MgO(100), Phys Rev B 89 (2014) 205138, doi:10.1103/PhysRevB.89.205138.

6.11 Publication K

Hofmann, P., Ugeda, M. M., Tamtögl, A., Ruckhofer, A., Ernst, W. E., Benedek, G., Martínez-Galera, A. J., Stróżecka, A., Gómez-Rodrıguez, J. M., Rienks, E., Jensen, M. F., Pascual, J. I. & Wells, J. W. Strong-coupling charge density wave in a one-dimensional topological metal. *Phys. Rev. B* **99,** 035438 (2019)

contributions	
funding	P. Hofmann, W. E. Ernst
data acquisition (HAS)	A. Tamtögl, A. Ruckhofer
data analysis (HAS)	A. Tamtögl
data acquisition and analysis (ARPES, LEED & STM)	E. Rienks, E., M. F. Jensen, J. W. Wells, M. M. Ugeda, J. I. Pascual A. J. Martínez-Galera, A. Stróżecka, J. M. Gómez-Rodríguez
interpretation	A. Tamtögl, P. Hofmann, G. Benedek
publication writing	A. Tamtögl, P. Hofmann

Hofmann, P., Ugeda, M. M., Tamtögl, A., Ruckhofer, A., Ernst, W. E., Benedek, G., Martínez-Galera, A. J., Stróżecka, A., Gómez-Rodrıguez, J. M., Rienks, E., Jensen, M. F., Pascual, J. I. & Wells, J. W. Strong-coupling charge density wave in a one-dimensional topological metal. *Phys. Rev. B* **99,** 035438 (2019)

PHYSICAL REVIEW B **99**, 035438 (2019)

Strong-coupling charge density wave in a one-dimensional topological metal

Philip Hofmann,[1,*] Miguel M. Ugeda,[2,3] Anton Tamtögl,[4] Adrian Ruckhofer,[4] Wolfgang E. Ernst,[4] Giorgio Benedek,[2,5] Antonio J. Martínez-Galera,[6] Anna Stróżecka,[7] José M. Gómez-Rodríguez,[6,8,9] Emile Rienks,[1] Maria Fuglsang Jensen,[1] José I. Pascual,[10,3] and Justin W. Wells[11]

[1]*Department of Physics and Astronomy, Interdisciplinary Nanoscience Center (iNANO), Aarhus University, 8000 Aarhus C, Denmark*
[2]*Donostia International Physics Center, DIPC, 20018 San Sebastian-Donostia, Spain*
[3]*Ikerbasque, Basque Foundation for Science, 48011 Bilbao, Spain*
[4]*Institute of Experimental Physics, Graz University of Technology, 8010 Graz, Austria*
[5]*Dipartimento di Scienza dei Materiali, Universitá di Milano-Bicocca, Via Roberto Cozzi 55, 20125 Milano, Italy*
[6]*Department Física de la Materia Condensada, Universidad Autónoma de Madrid, Madrid 28049, Spain*
[7]*Institut für Experimentalphysik, Freie Universität Berlin, 14195 Berlin, Germany*
[8]*Instituto Nicolas Cabrera, Universidad Autónoma de Madrid, 28049 Madrid, Spain*
[9]*Condensed Matter Physics Center (IFIMAC), Universidad Autónoma de Madrid, 28049 Madrid, Spain*
[10]*CIC nanoGUNE, 20018 San Sebastián-Donostia, Spain*
[11]*Department of Physics, Center for Quantum Spintronics, Norwegian University of Science and Technology, NO-7491 Trondheim, Norway*

(Received 12 July 2017; published 25 January 2019)

Scanning tunneling microscopy, low-energy electron diffraction, and helium atom scattering show a transition to a dimerizationlike reconstruction in the one-dimensional atomic chains on Bi(114) at low temperatures. One-dimensional metals are generally unstable against such a Peierls-like distortion, but neither the shape nor the spin texture of the Bi(114) Fermi contour favors the transition: Although the Fermi contour is one dimensional and thus perfectly nested, the very short nesting vector $2k_F$ is inconsistent with the periodicity of the distortion. Moreover, the nesting occurs between two Fermi contour branches of opposite spin, which is also expected to prevent the formation of a Peierls phase. Indeed, angle-resolved photoemission spectroscopy does not reveal any change in the electronic structure near the Fermi energy around the phase transition. On the other hand, distinct changes at higher binding energies are found to accompany the structural phase transition. This suggests that the transition of a strong-coupling type and that it is driven by phonon entropy rather than electronic entropy. This picture is supported by the observed short correlation length of the pairing distortion, the second-order-like character of the phase transition, and pronounced differences between the surface phonon spectra of the high- and low-temperature phases.

DOI: 10.1103/PhysRevB.99.035438

I. INTRODUCTION

The experimental realization of systems with reduced dimensions has often been the key to the discovery of fundamentally new physics. Of particular importance is the situation in one dimension (1D) with its drastically enhanced significance of electronic correlations and electron-phonon coupling [1,2]. An attractive path to studying systems of reduced dimensionality is to create them on the surfaces of semiconducting or semimetallic substrates as this opens the possibility to employ powerful spectroscopic techniques, such as scanning tunneling microscopy (STM), angle-resolved photoemission (ARPES), and surface-sensitive transport measurements [3,4]. Many systems have been realized and studied in this way, such as metallic chains or graphene nanoribbons on semiconductors, see, e.g., Refs. [5–11].

A particularly intriguing situation arises when low dimensionality is combined with an unconventional spin texture of the electronic states as this imposes a number of restrictions on the allowed electronic instabilities [8,12]. This combination is realized on the (114) [13,14] and (441) [15] vicinal surfaces of Bi where strongly Rashba-split surface states span the gap of a semimetallic substrate. Moreover, due to the similarity of Bi to the topological insulator $Bi_{1-x}Sb_x$ [16,17], all Bi surfaces have metallic surface states with a spin texture similar to that of topological insulators [18,19] and several hallmark features of these states, such as the lack of backscattering [20], were first observed on Bi surfaces. It was also pointed out that a Fermi contour with a chiral spin texture should not lead to charge density wave (CDW) formation even in the presence of perfect nesting [12].

The fundamental difference between a conventional one-dimensional metal at half-filling and the electronic surface state on Bi(114) is illustrated in Fig. 1. A conventional electronic state in a lattice with spacing a and half-filling is unstable with respect to the formation of a one-dimensional CDW also called a Peierls distortion. Figure 1(a) illustrates this situation of ideal nesting with a nesting vector length of $2k_F = \pi/a$ as indicated by the arrow in Fig. 1(a). As this corresponds to a real-space periodicity of $2a$, a Peierls-type distortion involving a periodicity doubling via pairing of the

*philip@phys.au.dk

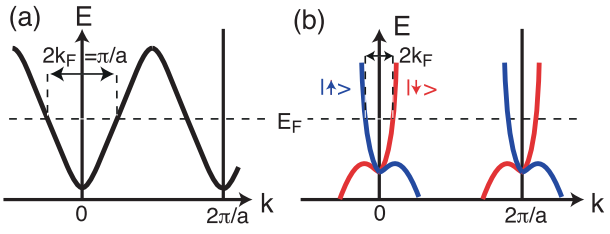

FIG. 1. (a) Conventional one-dimensional electronic state at half-filling. The black dispersion is spin degenerate. This system is sensitive to a Peierls-type instability due to the perfect nesting and the fact that the nesting vector's length corresponds to a real-space periodicity of $2a$. (b) Situation on Bi(114). The spin degeneracy of the bands is lifted, and although perfect nesting is still present, it takes place for a very short nesting vector and between states of opposite spin (indicated by the color of the bands and the arrows), thus protecting against a Peierls-type instability.

atoms in a chain leads to a new Brillouin zone boundary at the Fermi-level crossings of the unreconstructed phase, a gap opening, and hence to an electronic energy gain in the occupied states. The situation is quite different for the surface state on Bi(114) shown in Fig. 1(b). Here, the state is no longer spin degenerate, and the spin texture (indicated by red and blue) and dispersion closely resemble that of a one-dimensional edge state of a two-dimensional topological insulator, the so-called quantum spin Hall effect [21–24]. It is for this reason that Bi(114) has been called a "one-dimensional topological metal" [13]. Although perfect nesting is retained, as for any one-dimensional structure, $2k_F \ll \pi/a$ and a pairing-type reconstruction would not be expected to open a gap at the Fermi-level crossing. More importantly, the spin texture prevents the singularity in the electronic susceptibility required to drive the instability [12], an effect closely related to the forbidden backscattering for such a one-dimensional state [20]. A Peierls distortion would thus not be expected for the case of Bi(114).

Surprisingly, as we report here, such a pairing distortion is nevertheless observed at low temperature on the quasi-one-dimensional Bi(114) surface. Temperature-dependent measurements of the electronic structure by ARPES do not show any signs of a Fermi-surface change as expected from the arguments above but do show some clear spectral changes at higher binding energy. STM, low-energy electron diffraction (LEED), and helium atom scattering (HAS), on the other hand, provide evidence that this transition is a strong-coupling CDW [25], driven by phonon entropy. Strong-coupling CDWs that are not based on Fermi-surface nesting are common for two-dimensional CDW systems [25–31], consistent with strong sensitivity of the electronic susceptibility towards small deviations from ideal nesting conditions [32]. In one dimension, there is always perfect nesting, but in the present case, the nested Fermi surface is irrelevant for the phase transition.

II. EXPERIMENTAL DETAILS

The Bi(114) surface was cleaned by sputtering with noble gas ions and annealing between 300 and 400 K. STM measurements were performed both at a fixed temperature (5 K) and at variable temperatures between 40 and 300 K in two different setups. LEED and ARPES data were collected on the SGM-3 end station of ASTRID [33] between 50 and 300 K. The energy resolution varied between 25 meV for the measurements at low photon energies and 65 meV for the large-scale Fermi-surface maps collected with high photon energies. The angular resolution was better than 0.2°. For the HAS measurements, a nearly monochromatic beam of He ($\Delta E/E \approx 2\%$) was scattered off the sample surface in a fixed 91.5° source-sample-detector geometry. Energy dispersive measurements for inelastic scattering were performed using a time-of-flight (TOF) technique with a pseudorandom chopper disk [34]. The momentum transfer parallel to the surface was calculated from the kinematic scattering conditions [35].

III. RESULTS AND DISCUSSION

The atomic structure of Bi(114) consists of parallel atomic rows with an interatomic spacing of 4.54 Å along the rows [13]. A unit cell comprises several of these rows at different heights, and the periodicity of the unreconstructed surface perpendicular to the rows is 14.20 Å. For the clean surface, a reconstruction-induced doubling of this periodicity has been reported [13] such that the actual periodicity perpendicular to the rows is twice this value. Figure 2(a) shows a closeup STM image of the surface at 5 K. Due to the strong corrugation, the periodicity of 28.40 Å perpendicular to the atomic rows is immediately visible. On close inspection, it becomes clear that the periodicity along the rows is also doubled, i.e., the atoms in the rows are not equally spaced, but most of them appear dimerized. A few of these dimers are emphasized in the figure by red frames. This reconstruction does not only affect the atoms in the top row, but also those in deeper-lying rows. The average interatomic distance in the dimers is 4.15 ± 0.1 Å, thus corresponding to $\sim$0.2 Å atomic displacement from the equilibrium position. This is a substantial fraction of the equilibrium spacing, larger than typically found in Peierls systems [37]. Although dimerization is dominant on a short length scale, long-range ordering is poor. Indeed, defects, such as trimers, are found every few dimers in the row (also indicated by a blue frame in the figure). Moreover, the dimerization appears to be a strongly local phenomenon within each row as no correlations between dimer positions in neighboring atomic rows are evident.

We explored the temperature dependence of the dimerization along the atomic rows. Figures 2(b) and 2(c) compare STM images and height profiles measured at increasing temperatures. Although at 40 K the dimerization is still fully intact, at 150 K it starts vanishing and is nearly absent at 195 K with the exception of the immediate vicinity of structural defects (indicated by an arrow) that appear to serve as a seed for the dimerization. Thus, the dimerization is a low-temperature phase with an apparent transition temperature somewhere between 150 and 195 K.

The reconstruction is also observable in diffraction experiments, even though the coherence length is very short as seen from the STM data. Figure 3 shows LEED data taken at 250 and 55 K, i.e., well above and below the transition temperature range determined by STM. The LEED patterns consist of well-separated rows of closely placed sharp spots.

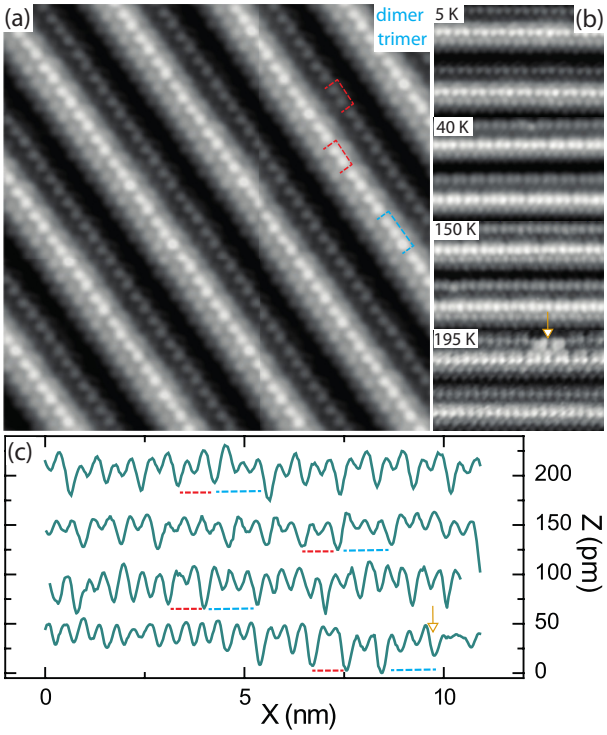

FIG. 2. Dimerization distortion of the quasi-one-dimensional lattice structure of Bi(114). (a) STM image taken at 5 K showing dimer formation in some of the protruding atomic rows (red dashed frames) with frequently appearing defects, such as trimers (blue dashed frame). (b) STM images at higher temperatures and (c) profiles along the protruding atomic rows, measured at the indicated temperatures. At 195 K, the dimerization is lifted and only observed in the immediate vicinity of defects. Tunneling parameters: (a) $U = 0.2$ V and $I = 0.1$ nA and (b) $U = 0.2,\ 1.0,\ -0.1,\ 0.25$ V and $I = 0.1,\ 4.0,\ 2.0,\ 4.0$ nA. All STM data were processed with the WSXM software [36].

The distance between the spots along the rows corresponds to the reciprocal lattice distance perpendicular to the chains ($2\pi/28.4$ Å^{-1}), whereas the distance between the rows corresponds to the interatomic distance in the (unreconstructed)

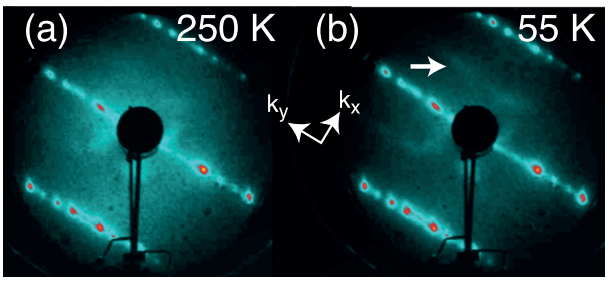

FIG. 3. (a) and (b) LEED patterns collected above and below, respectively, the temperature of the phase transition observed by STM. The arrow in (b) shows the additional streaks induced by the periodicity doubling along the atomic chains. The electron kinetic energy is 27.2 eV.

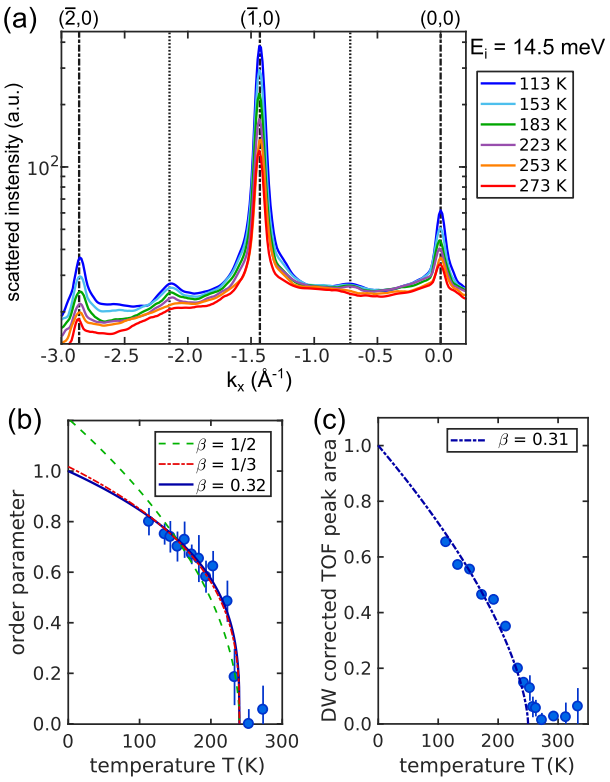

FIG. 4. (a) Scattered He intensities (logarithmic scale) versus parallel momentum transfer k_x (crystal azimuth aligned along $\overline{\Gamma} - \overline{X}$) for various sample temperatures T. A small vertical offset between the individual scans was added for better visibility. The vertical dotted lines illustrate the position of the CDW superlattice peaks due to the doubled periodicity. (b) Normalized square root of the CDW superlattice peak's integrated intensity (peak at $k_x = -2.15$ Å^{-1}), which is proportional to the CDW order parameter. The lines represents fits to Eq. (1) for different choices of the critical exponent β. (c) Peak area of the CDW superlattice peak when integrated over energy in the energy-resolved TOF measurements.

chains ($2\pi/4.54$ Å^{-1}). In the low-temperature image, weak streaks of intensity are observed halfway between the rows (indicated by an arrow) (see the Supplemental Material [38]) and thus consistent with a dimerized structure. The width of streaks along k_x reflects the short coherence of the CDW within the atomic rows, and the (much larger) width along k_y is due to the lack of coherence between these rows. These findings are consistent with the STM results.

A more detailed picture of the phase transition is provided by HAS. Figure 4(a) displays the scattered He intensity versus momentum transfer k_x for various sample temperatures T using an incident beam energy E_i of 14.5 meV. At low temperatures, a small enhancement of the scattered intensity appears halfway between the diffraction peaks which is consistent with a superstructure based on a doubled periodicity along the rows as observed by the LEED and STM measurements. Scans with different beam energies show that this cannot be due to any resonance effect and is indeed caused by a reconstruction [39].

Figure 4(b) shows the temperature dependence of the square root of the integrated intensity for the CDW superlattice peak halfway between the $(\bar{2}, 0)$ and the $(\bar{1}, 0)$ Bragg peaks [see Fig. 4(a)]. In order to access the intensity change relevant to the critical fluctuations of the CDW [40,41] as opposed to the intensity changes due to the Debye-Waller factor [42], the integrated intensity $I(T)$ shown in the figure has been normalized to that of the specular beam (see the Supplemental Material [38]) for more details on the procedure). This correction is particularly necessary in view of the low surface Debye temperature of Bi ($\Theta_D = 85$ K $< T_c$ [43,44], where T_c is the CDW transition temperature). The square root of the resulting $I(T)$ can then be viewed as the order parameter of the CDW [45,46]. $I(T)$ shows a sharp onset below approximately 250 K, followed by a continuous rise at lower temperatures.

The temperature dependence of the order parameter $\sqrt{I(T)}$ can be used to determine T_c and the critical exponent β belonging to the phase transition [40,41,47–49]. This is achieved by fitting the power law,

$$\sqrt{\frac{I(T)}{I(0)}} = \left(1 - \frac{T}{T_c}\right)^{\beta} \tag{1}$$

to the data in Fig. 4(b) [$I(0)$ is the extrapolated intensity at 0 K], resulting in $T_c = (242 \pm 7)$ K and $\beta = (0.32 \pm 0.02)$. The fit is represented by the blue solid line in Fig. 4(b).

Our finding of $\beta = (0.32 \pm 0.03)$ is very close to the universal exponent of $1/3$ as predicted in the presence of fluctuations [49], in agreement with the findings of other CDWs in layered chalcogenides and quasi-1D systems [41,50–53]. On the other hand, using mean-field theory where fluctuations are neglected ($\beta = 1/2$), results in the green dashed curve which does not represent a satisfactory fit to the data. When fitting the data under the constraint that $\beta = 1/3$, we obtain the red dashed curve in Fig. 4(b) and a transition temperature of $T_c = (245 \pm 8)$ K.

At first glance, the transition temperature determined from HAS appears to be inconsistent with the STM data that does not show any short-range order above 195 K. We must keep in mind, however, that strong fluctuations are to be expected and that STM, being a slow technique, only measures the *average* position of the atomic motion and might thus not be able to show the preserved local dimerization at high temperatures. This actually explains why close to defects, dimerization can still be observed frozen in the 195-K images. Indeed, LEED patterns taken at 200 and even 250 K do still show very weak signatures of the superstructure {see Fig. 3(a) and the Supplemental Material [38]}.

Energy-resolved scans performed at the position of the CDW superlattice peak confirm that the enhanced elastic intensity is indeed due to a static change in the structure and cannot be caused by any inelastic effects, such as kinematical focusing [39]. Figure 4(c) shows the TOF peak intensity versus surface temperature which was obtained by fitting the energy-resolved scans with a single Gaussian and applying a correction for the Debye-Waller attenuation (for the original TOF data, see the Supplemental Material [38]). The temperature range where the peak intensity shows a strong rise is consistent with T_c as determined from the data in Fig. 4(b),

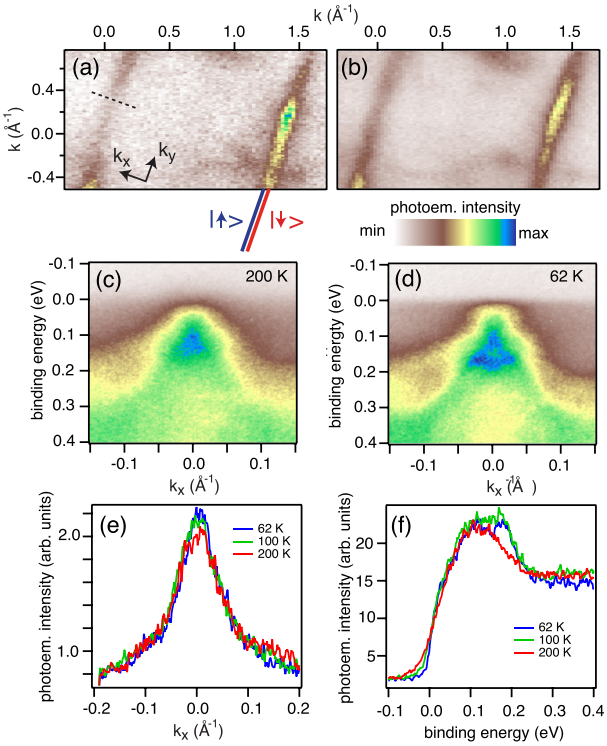

FIG. 5. (a) and (b) Photoemission intensity in the low-temperature phase at $T = 60$ K in a 20-meV window around the Fermi energy and a binding energy of 170 meV, respectively. The sketched continuation of the Fermi surface illustrates that the observed linelike intensity is composed of two unresolved spin-polarized Fermi-level crossings [13], see also Fig. 1(b). The photon energy is $h\nu = 70$ eV. The dashed line shows the direction of the data in (c) and (e). (c) and (d) Photoemission intensity close to and below the CDW transition (at $T = 200$ and 62 K), respectively, along the dashed black line in (a). (e) Momentum distribution curves at the Fermi energy along the dashed line in (a) as a function of temperature. (f) Energy distribution curves along the crossing point of the dashed line in (a) and the Fermi surface at $k_x = 0$, i.e., through the center of the images in (c) and (d). $h\nu = 17$ eV in (c)–(f).

and fitting a critical exponent gives rise to $\beta = (0.31 \pm 0.04)$, also consistent with the data in Fig. 4(b).

After characterizing the phase transition using structural techniques, we now move to the spectroscopic characterization of the electronic and vibrational states by ARPES and HAS. Figure 5(a) shows the $k_\parallel$-dependent photoemission intensity at the Fermi level at 60 K. It is dominated by intense lines in the direction perpendicular to the atomic rows. As has been shown by spin-resolved photoemission, these intense lines are actually caused by the two unresolved spin-polarized Fermi-surface elements due to the spin-split surface state in Fig. 1(b) [13]. This unresolved Fermi contour is indicated as a sketch, extending the observed Fermi contour in the figure. Apart from the intense linear features, the photoemission intensity shows some weak structures that can be assigned to bulk states. A projection of the (small) bulk Fermi surface of Bi onto the (114) surface is given in Ref. [13].

Since the Fermi surface of Fig. 5(a) is measured in the dimerized phase, one might expect replicas of the Fermi-surface lines in between the two intense lines, similar to the additional weak streaks in between the lines of densely spaced spots in the LEED image of Fig. 3(b). Such replicas are not observed, neither at the Fermi surface in Fig. 5(a) nor for the higher binding energy of 170 meV in Fig. 5(b). Note that the lack of replica bands in a CDW is also found for many two-dimensional CDW systems where the spectral weight in the CDW phase tracks that of the normal phase [27]. Hence the CDW period observed in direct space may not correspond to nesting, i.e., to the $2k_F$ measured with high-resolution ARPES in reciprocal space.

Figures 5(c) and 5(d) show the electronic structure of the one-dimensional states above and below, respectively, the dimerization transition temperature as a function of binding energy in the k_x direction perpendicular to the one-dimensional Fermi surface along a cut indicated by the black dashed line in Fig. 5(a). No spectroscopic signature of the transition is observed near the Fermi energy. Indeed, when taking momentum distribution curves (MDCs) through a temperature-dependent series of similar data sets, no significant changes can be observed [see Fig. 5(e)] except for a minor sharpening of the MDC peak at low temperatures as expected due to electron-phonon coupling [54,55].

However, there is a significant change in the electronic structure rather far away from the Fermi energy at around 150 meV where a single intense feature at 110 meV in the high-temperature phase of Fig. 5(c) splits into two peaks, one essentially staying at the same binding energy and one moving to a higher energy of 175 meV. This spectral change is especially well seen in energy distribution curves through the center of a series of temperature-dependent data (see the Supplemental Material [38]) shown in Fig. 5(f). These changes in the electronic structure at high binding energy do not lead to observable replicas in the constant energy surfaces either as seen in Fig. 5(b) which shows the photoemission intensity at a binding energy of 170 meV.

The observation of spectral changes only at high binding energy rules out that the transition is due to a nesting-driven weak CDW, such as the Peierls distortion in Fig. 1(b), as this would require a gap opening at the Fermi energy. On the other hand, an electronic structure change in which states are shifted to a substantially higher binding energy can certainly explain the stabilization of the reconstructed phase. This gives a qualitative explanation for the stability of the pairing distortion at low temperatures, but it does not explain why the pairing should be lifted at higher temperatures. In a conventional Peierls scenario, the transition from the CDW state to the normal state is driven by electronic entropy when the thermal energy becomes comparable to the gap energy. This cannot be the case here. We also note that the CDW is unlikely to be caused by bulk states because of the extremely small density of bulk states at E_F and because of the absence of a CDW in bulk Bi.

A plausible alternative scenario is that the transition is a strong-coupling CDW, driven by phonon entropy [25,29,45,56], and this is supported by several experimental facts, such as the short coherence length and considerable atomic displacements observed here. A strong-coupling

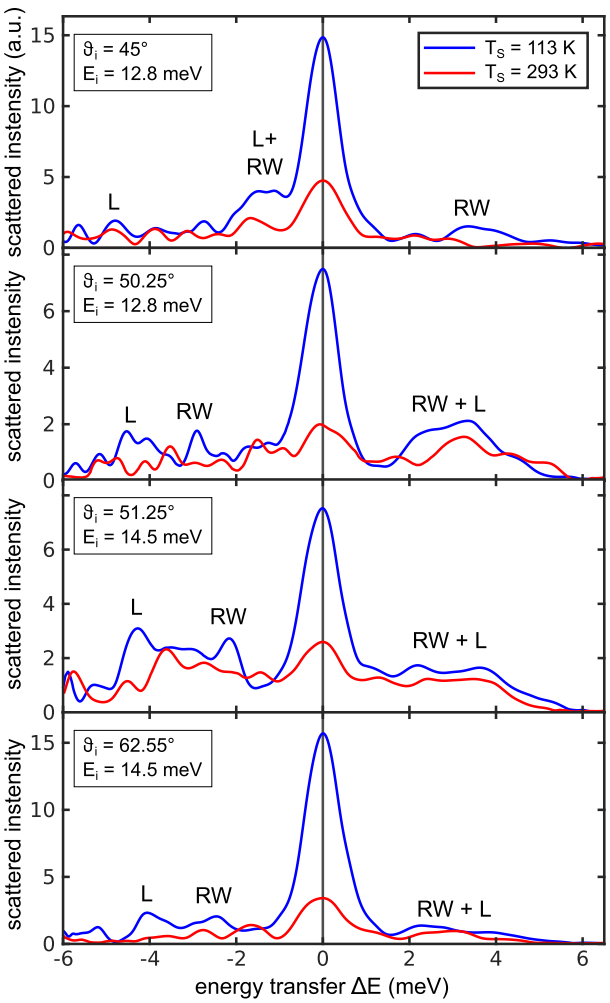

FIG. 6. Comparison of several TOF spectra for the cooled sample and the sample at room temperature, transformed to energy transfer spectra $\Delta E = E_f - E_i$. Energy loss ($\Delta E < 0$) corresponds to the creation of a phonon with phonon energy $\Delta E = \hbar\omega$, and energy gain ($\Delta E > 0$) corresponds to the annihilation of a phonon. RW and L stand for the Rayleigh wave and longitudinal phonon modes, respectively.

CDW would not be uncommon for a one-dimensional surface structure. A similar mechanism has also been suggested for the CDW of In nanowires on Si(111) [57] which, however, also shows a pronounced gap opening at the Fermi energy [5,58]. Most importantly, the strong-coupling picture would explain why a temperature-dependent distortion can appear in a system with this particular spin texture for which it would otherwise not be expected.

A phonon entropy driven phase transition typically gives rise to a change in the phonon density of states, as recently observed for the metal insulator transition in VO_2 [56]. HAS can, in principle, be used to map the full surface phonon dispersion and is especially valuable because its high resolution gives access to low-energy phonons. In the case of Bi(114), the cross section for inelastic phonon scattering turned out to be extremely small such that only spectra at a few values

of the momentum transfer could be measured. TOF spectra were recorded along the $\overline{\Gamma} - \overline{X}$ azimuth with the sample at room temperature and $T = 113$ K. The TOF spectra were then transformed to energy transfer spectra which allows inelastic- (phonon) scattering events to be determined. The energy transfer $\Delta E = E_f - E_i$ was determined by the initial energy E_i, and final energy E_f of the helium atom, energy loss ($\Delta E < 0$), and gain peaks ($\Delta E > 0$) correspond to the creation and annihilation of a phonon, respectively [35].

Figure 6 gives a selection of inelastic spectra measured at different incident energies and angles. The most prominent inelastic features are labeled as RW and L, based on the experimentally and theoretically determined surface phonon dispersion of Bi(111) along $\overline{\Gamma} - \overline{M}$ [35]. Although the data do not give the full surface phonon dispersion, two important conclusions can be drawn: First, we observe a significant change in the phonon spectrum between the two phases. Although the Jacobian scaling upon transforming from TOF to energy transfer increases the height of the experimental noise on the phonon creation side of the spectrum ($\Delta E < 0$), this can be clearly seen on the loss side by comparing the most pronounced peaks at the two temperatures. Second, the low-temperature phase generally shows more intense features on the gain side (phonon annihilation) of the elastic peak, consistent with a higher phonon occupation in the low-temperature phase. Since the Bose factor for the low-energy acoustic modes is not substantially different between both temperatures, it indicates that the phonon density of states changes below T_c. Hence the observation of an enhanced intensity of the low-energy acoustic surface phonon modes below T_c is in line with a strong phonon contribution to the transition entropy.

IV. CONCLUSION

In conclusion, we have reported the observation of a dimerization transition below (245 ± 8) K on Bi(114). Such a transition is highly unexpected even in the presence of a perfectly nested one-dimensional Fermi contour because it appears to be forbidden by the spin texture of the states and the nonmatching nesting vector $2k_F$. Indeed, the transition does not involve the states near the Fermi energy, but spectral changes at higher binding energy are observed. This, as well as the short coherence length and significant changes in the phonon spectrum, support the interpretation of the low-temperature state as a strong-coupling CDW, illustrating that such transitions are still possible in topological systems.

More detailed insight into the driving force of the phase transition could, in principle, be gained by first-principles calculations of the electronic structure, vibrational properties, and electron-phonon coupling in the system, similar to the work that has been carried out for In on Si(111) [57]. In the present case, such calculations are extremely challenging due to the large unit cell, the need to include the spin-orbit interaction for an adequate description of the electronic states and the need for a thick slab in the calculation in order to decouple the deeply penetrating surface states. However, such calculations could give unprecedented insight into role of the spin-split surface states (if any) in a surface CDW of a topological material.

ACKNOWLEDGMENTS

We gratefully acknowledge stimulating discussions with K. Rossnagel, M. Hengsberger, and J. Osterwalder. This work was supported by the Danish Council for Independent Research, Natural Sciences under the Sapere Aude Program (Grant No. DFF-4002-00029) and by VILLUM FONDEN via the center of Excellence for Dirac Materials (Grant No. 11744). J.W.W. acknowledges support from the Institute for Storage Ring Facilities, Aarhus University during the beam time for this project and from the Research Council of Norway through its Centres of Excellence funding scheme, Project No. 262633 "QuSpin" as well as via the Fripro Program, Project No. 250985 "FunTopoMat." A.J.M.-G. acknowledges funding from the Spanish MINECO through the Juan de la Cierva Program (ref. IJCI-2014-19209). J.M.G.-R acknowledges financial support from the Spanish MINECO under Project No. MAT2016-77852-C2-2-R. A.T. and W.E.E. acknowledge financial support provided by the FWF (Austrian Science Fund) within Project No. P29641-N36.

[1] R. E. Peierls, *Quantum Theory of Solids* (Oxford University Press, Oxford, 1955).
[2] J. M. Luttinger and J. C. Ward, Phys. Rev. **118**, 1417 (1960).
[3] P. Hofmann and J. W. Wells, J. Phys.: Condens. Matter **21**, 013003 (2009).
[4] J. W. Wells, K. Handrup, J. F. Kallehauge, L. Gammelgaard, P. Boggild, M. B. Balslev, J. E. Hansen, P. R. E. Petersen, and P. Hofmann, J. Appl. Phys. **104**, 053717 (2008).
[5] H. W. Yeom, S. Takeda, E. Rotenberg, I. Matsuda, K. Horikoshi, J. Schaefer, C. M. Lee, S. D. Kevan, T. Ohta, T. Nagao, and S. Hasegawa, Phys. Rev. Lett. **82**, 4898 (1999).
[6] J. N. Crain, A. Kirakosian, K. N. Altmann, C. Bromberger, S. C. Erwin, J. L. McChesney, J. L. Lin, and F. J. Himpsel, Phys. Rev. Lett. **90**, 176805 (2003).
[7] C. Tegenkamp, T. Ohta, J. L. McChesney, H. Dil, E. Rotenberg, H. Pfnur, and K. Horn, Phys. Rev. Lett. **100**, 076802 (2008).
[8] C. Tegenkamp, D. Lükermann, H. Pfnür, B. Slomski, G. Landolt, and J. H. Dil, Phys. Rev. Lett. **109**, 266401 (2012).
[9] J. Park, S. W. Jung, M.-C. Jung, H. Yamane, N. Kosugi, and H. W. Yeom, Phys. Rev. Lett. **110**, 036801 (2013).
[10] J. Baringhaus, M. Ruan, F. Edler, A. Tejeda, M. Sicot, T.-I. Amina, A.-P. Li, Z. Jiang, E. H. Conrad, C. Berger *et al.*, Nature (London) **506**, 349 (2014).
[11] S. Cheon, T.-H. Kim, S.-H. Lee, and H. W. Yeom, Science **350**, 182 (2015).
[12] T. K. Kim, J. Wells, C. Kirkegaard, Z. Li, S. V. Hoffmann, J. E. Gayone, I. Fernandez-Torrente, P. Haberle, J. I. Pascual, K. T. Moore *et al.*, Phys. Rev. B **72**, 085440 (2005).
[13] J. W. Wells, J. H. Dil, F. Meier, J. Lobo-Checa, V. N. Petrov, J. Osterwalder, M. M. Ugeda, I. Fernandez-Torrente, J. I. Pascual, E. D. L. Rienks *et al.*, Phys. Rev. Lett. **102**, 096802 (2009).
[14] D. Leuenberger, H. Yanagisawa, S. Roth, J. H. Dil, J. W. Wells, P. Hofmann, J. Osterwalder, and M. Hengsberger, Phys. Rev. Lett. **110**, 136806 (2013).

[15] M. Bianchi, F. Song, S. Cooil, A. F. Monsen, E. Wahlström, J. A. Miwa, E. D. L. Rienks, D. A. Evans, A. Strozecka, J. I. Pascual *et al.*, Phys. Rev. B **91**, 165307 (2015).

[16] J. C. Y. Teo, L. Fu, and C. L. Kane, Phys. Rev. B **78**, 045426 (2008).

[17] D. Hsieh, D. Qian, L. Wray, Y. Xia, Y. S. Hor, R. J. Cava, and M. Z. Hasan, Nature (London) **452**, 970 (2008).

[18] P. Hofmann, Prog. Surf. Sci. **81**, 191 (2006).

[19] X.-L. Qi and S.-C. Zhang, Rev. Mod. Phys. **83**, 1057 (2011).

[20] J. I. Pascual, G. Bihlmayer, Y. M. Koroteev, H. P. Rust, G. Ceballos, M. Hansmann, K. Horn, E. V. Chulkov, S. Blugel, P. M. Echenique *et al.*, Phys. Rev. Lett. **93**, 196802 (2004).

[21] C. L. Kane and E. J. Mele, Phys. Rev. Lett. **95**, 226801 (2005).

[22] S. Murakami, Phys. Rev. Lett. **97**, 236805 (2006).

[23] B. A. Bernevig and S.-C. Zhang, Phys. Rev. Lett. **96**, 106802 (2006).

[24] M. Konig, S. Wiedmann, C. Brune, A. Roth, H. Buhmann, L. W. Molenkamp, X.-L. Qi, and S.-C. Zhang, Science **318**, 766 (2007).

[25] W. L. McMillan, Phys. Rev. B **16**, 643 (1977).

[26] M. D. Johannes, I. I. Mazin, and C. A. Howells, Phys. Rev. B **73**, 205102 (2006).

[27] K. Rossnagel, J. Phys.: Condens. Matter **23**, 213001 (2011).

[28] M. Calandra, I. I. Mazin, and F. Mauri, Phys. Rev. B **80**, 241108 (2009).

[29] X. Zhu, Y. Cao, J. Zhang, E. W. Plummer, and J. Guo, Proc. Natl. Acad. Sci. **112**, 2367 (2015).

[30] U. Chatterjee, J. Zhao, M. Iavarone, R. Di Capua, J. P. Castellan, G. Karapetrov, C. D. Malliakas, M. G. Kanatzidis, H. Claus, J. P. C. Ruff *et al.*, Nat. Commun. **6**, 6313 (2015).

[31] C.-W. Chen, J. Choe, and E. Morosan, Rep. Prog. Phys. **79**, 084505 (2016).

[32] M. D. Johannes and I. I. Mazin, Phys. Rev. B **77**, 165135 (2008).

[33] S. V. Hoffmann, C. Søndergaard, C. Schultz, Z. Li, and P. Hofmann, Nucl. Instrum. Methods Phys. Res., Sect. A **523**, 441 (2004).

[34] A. Tamtögl, M. Mayrhofer-Reinhartshuber, N. Balak, W. E. Ernst, and K. H. Rieder, J. Phys.: Condens. Matter **22**, 304019 (2010).

[35] A. Tamtögl, P. Kraus, M. Mayrhofer-Reinhartshuber, D. Campi, M. Bernasconi, G. Benedek, and W. E. Ernst, Phys. Rev. B **87**, 035410 (2013).

[36] I. Horcas, R. Fernández, J. M. Gómez-Rodríguez, J. Colchero, J. Gómez-Herrero, and A. M. Baro, Rev. Sci. Instrum. **78**, 013705 (2007).

[37] J.-P. Pouget, C. R. Phys. **17**, 332 (2016); physique de la matière condensée au {XXIe} siècle: l'héritage de Jacques Friedel.

[38] See Supplemental Material at http://link.aps.org/supplemental/10.1103/PhysRevB.99.035438 for LEED and ARPES data taken at different temperatures as well as additional information on the HAS measurement and analysis.

[39] M. Mayrhofer-Reinhartshuber, P. Kraus, A. Tamtögl, S. Miret-Artés, and W. E. Ernst, Phys. Rev. B **88**, 205425 (2013).

[40] S. Girault, A. H. Moudden, and J. P. Pouget, Phys. Rev. B **39**, 4430 (1989).

[41] H. Requardt, M. Kalning, B. Burandt, W. Press, and R. Currat, J. Phys.: Condens. Matter **8**, 2327 (1996).

[42] P. Kraus, A. Tamtögl, M. Mayrhofer-Reinhartshuber, F. Apolloner, C. Gösweiner, S. Miret-Artés, and W. E. Ernst, J. Phys. Chem. C **119**, 17235 (2015).

[43] H. Mönig, J. Sun, Y. M. Koroteev, G. Bihlmayer, J. Wells, E. V. Chulkov, K. Pohl, and P. Hofmann, Phys. Rev. B **72**, 085410 (2005).

[44] M. Mayrhofer-Reinhartshuber, A. Tamtögl, P. Kraus, K. H. Rieder, and W. E. Ernst, J. Phys.: Condens. Matter **24**, 104008 (2012).

[45] G. Grüner, *Density Waves in Solids*, Frontiers in Physics Vol. 89 (Perseus, Cambridge, MA, 1994).

[46] G. Grüner, Rev. Mod. Phys. **60**, 1129 (1988).

[47] H. Nishimori and G. Ortiz, *Elements of Phase Transitions and Critical Phenomena* (Oxford University Press, Oxford, 2010).

[48] R. K. Pathria and P. D. Beale, *Statistical Mechanics*, 3rd ed. (Elsevier, Amsterdam, 2011).

[49] T. Ma and S. Wang, *Phase Transition Dynamics* (Springer, New York, 2014).

[50] G. Brusdeylins, C. Heimlich, J. G. Skofronick, J. P. Toennies, R. Vollmer, and G. Benedek, Europhys. Lett. **9**, 563 (1989).

[51] G. Brusdeylins, C. Heimlich, J. G. Skofronick, J. P. Toennies, R. Vollmer, G. Benedek, and L. Miglio, Phys. Rev. B **41**, 5707 (1990).

[52] J. E. Lorenzo, R. Currat, P. Monceau, B. Hennion, H. Berger, and F. Levy, J. Phys.: Condens. Matter **10**, 5039 (1998).

[53] M. Hoesch, A. Bosak, D. Chernyshov, H. Berger, and M. Krisch, Phys. Rev. Lett. **102**, 086402 (2009).

[54] J. E. Gayone, S. V. Hoffmann, Z. Li, and P. Hofmann, Phys. Rev. Lett. **91**, 127601 (2003).

[55] P. Hofmann, I. Y. Sklyadneva, E. D. L. Rienks, and E. V. Chulkov, New J. Phys. **11**, 125005 (2009).

[56] J. D. Budai, J. Hong, M. E. Manley, E. D. Specht, C. W. Li, J. Z. Tischler, D. L. Abernathy, A. H. Said, B. M. Leu, L. A. Boatner *et al.*, Nature (London) **515**, 535 (2014).

[57] S. Wippermann and W. G. Schmidt, Phys. Rev. Lett. **105**, 126102 (2010).

[58] T. Frigge, B. Hafke, T. Witte, B. Krenzer, C. Streubühr, A. Samad Syed, V. Mikšić Trontl, I. Avigo, P. Zhou, M. Ligges *et al.*, Nature (London) **544**, 207 (2017).

6.12 Publication L

Ruckhofer, A., Tamtögl, A., Pusterhofer, M., Bremholm, M. & Ernst, W. E. Helium-Surface Interaction and Electronic Corrugation of Bi_2Se_3(111). *J. Phys. Chem. C* **123,** 17829–17841 (2019)

contributions	
funding	A. Tamtögl, W. E. Ernst
sample synthesis	M. Bremholm
preparation / setup	A. Tamtögl
data acquisition	A. Ruckhofer
data analysis	A. Tamtögl, A. Ruckhofer, M. Pusterhofer
interpretation	A. Tamtögl, A. Ruckhofer
publication writing	A. Tamtögl, A. Ruckhofer

Reprinted from:

Ruckhofer, A., Tamtögl, A., Pusterhofer, M., Bremholm, M. & Ernst, W. E. Helium-Surface Interaction and Electronic Corrugation of Bi_2Se_3(111). *J. Phys. Chem. C* **123,** 17829–17841 (2019)

THE JOURNAL OF PHYSICAL CHEMISTRY C

Article

Cite This: J. Phys. Chem. C 2019, 123, 17829−17841

pubs.acs.org/JPCC

Helium−Surface Interaction and Electronic Corrugation of Bi_2Se_3(111)

Adrian Ruckhofer,*[,†] Anton Tamtögl,*[,†] Michael Pusterhofer,[†] Martin Bremholm,[‡] and Wolfgang E. Ernst[†]

[†]Institute of Experimental Physics, Graz University of Technology, Graz 8010, Austria

[‡]Centre for Materials Crystallography, Department of Chemistry and iNANO, Aarhus University, Aarhus 8000, Denmark

ABSTRACT: We present a study of the atom−surface interaction potential for the He−Bi_2Se_3(111) system. Using selective adsorption resonances, we are able to obtain the complete experimental band structure of atoms in the corrugated surface potential of the topological insulator Bi_2Se_3. He atom scattering spectra show several selective adsorption resonance features that are analyzed, starting with the free-atom approximation and a laterally averaged atom−surface interaction potential. Based on quantum mechanical calculations of the He−surface scattering intensities and resonance processes, we are then considering the three-dimensional atom−surface interaction potential, which is further refined to reproduce the experimental data. Following this analysis, the He−Bi_2Se_3(111) interaction potential is best represented by a corrugated Morse potential with a well depth of $D = (6.54 \pm 0.05)$ meV, a stiffness of $\kappa = (0.58 \pm 0.02)$ Å^{-1}, and a surface electronic corrugation of (5.8 ± 0.2)% of the lattice constant. The experimental data may also be used as a challenging benchmark system to analyze the suitability of several van der Waals approaches: the He−Bi_2Se_3(111) interaction captures the fundamentals of weak adsorption systems where the binding is governed by long-range electronic correlations.

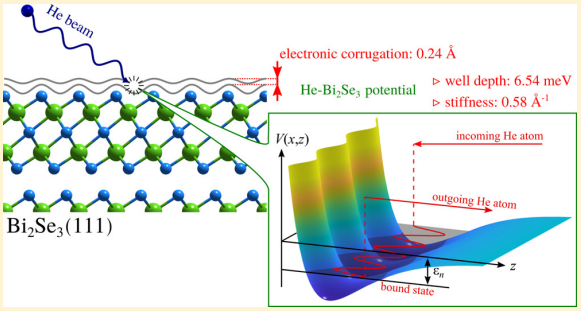

INTRODUCTION

The material class of topological insulators (TIs) has lately received broad attention[1−6] due to their protected metallic surface states and the insulating bulk electronic structure.[7,8] An archetypal TI and one of the most studied examples is the here presented Bi_2Se_3.[9,10] Topological surfaces show modifications of their electronic structure upon adsorption of atoms and molecules.[11−14] However, the interaction of TI surfaces with their environment, that is, atom−surface interaction potentials are barely investigated by the experiment despite the fact that topology can have implications far beyond electronic transport properties and topological materials, provides a perfect platform for studying phenomena such as heterogeneous catalysis or sensing applications.[15,16]

Understanding the atom−surface interaction on topological insulators is interesting from a fundamental point of view and may help to obtain a deeper understanding of the interaction with gases and molecules in the physisorption regime.[17,18] For example, as shown recently, the long-range part of the potential can be responsible for band bending effects upon adsorption.[19]

Here, we present a study of the atom−surface interaction potential for the He−Bi_2Se_3(111) system. The shape of the interaction potential between the surface and atoms can be extracted from atom−surface scattering experiments, and we follow this approach using helium atom scattering from the surface of Bi_2Se_3(111). Helium atom scattering (HAS) is strictly surface-sensitive and allows the investigation of surface structure and dynamics of conducting as well as insulating materials.[20] The technique permits measurements of the atom−surface interaction potential to a very high accuracy via selective adsorption resonances (SARs).[21,22] Studying SARs provides access to the bound-state energies ϵ_n, which are supported by the atom−surface interaction potential, and more importantly, to the atom−surface interaction potential itself. Previous experimental studies of SARs have mainly been performed on salts with the NaCl structure,[20−26] while only recently, semimetals and semiconductors have been studied using this approach.[27−29]

In addition to experimental measurements of SARs, ab initio approaches have been employed to determine a numerical atom−surface interaction potential.[30−32] On the one hand, the extremely small adsorption energies of He atoms on surfaces (in the few meV region) and the delocalized nature and mobility of electrons on conducting surfaces make such systems particularly challenging even for state-of-the-art van der Waals (vdW)-corrected density functional theory (DFT) approaches.[32] On the other hand, since measurements of the atom−surface potential give insight into the atom−surface

Received: April 12, 2019
Revised: June 13, 2019
Published: June 14, 2019

DOI: 10.1021/acs.jpcc.9b03450
J. Phys. Chem. C 2019, 123, 17829−17841

interaction dynamics within the vdW regime, experimental results can be used to test the ability of dispersion-corrected DFT approaches to simulate nonlocal interactions.[30,33,34]

The atom−surface interaction potential is also a necessary ingredient for quantum mechanical calculations of elastic scattering intensities,[35−37] allowing for a comparison with experimentally observed He diffraction peak intensities. In this context, the influence of vdW forces in atom−surface scattering calculations of noble gases has recently been studied,[35,38] and the experimental diffraction intensities may even be used as a benchmark to test the performance of different vdW-corrected DFT approaches.[39]

However, the comparison with diffraction intensities merely considers a small number of diffraction channels, which are accessible in the experiment, and thus, a comparison of quantum mechanical scattering calculations with SARs provides an even more rigorous test in terms of the sought atom−surface interaction potential. Following this approach, we use experimental SARs together with quantum mechanical He−surface scattering calculations to determine an accurate three-dimensional atom−surface interaction potential. Herein, experimental data from complex surfaces such as TIs may be especially valuable, in particular since it was shown only recently that, for an accurate theoretical description of the layered structure of TIs, the inclusion of vdW corrections is essential.[40]

EXPERIMENTAL DETAILS

The experimental data in this work was obtained at the HAS apparatus in Graz, which is able to generate a nearly monochromatic beam of ^{4}He. The scattering geometry is defined by a fixed source-sample-detector angle with 91.5° (for a description in greater detail, see ref 41). Briefly, the He beam is generated via a supersonic expansion from a base pressure of 50 bar to 10^{-6} mbar through a cooled nozzle of 10 μm. The central part is selected with a skimmer (310 μm orifice), creating a He beam with an energy spread of $\Delta E/E \approx 2\%$. By varying the nozzle temperature, the beam energy can be tuned between 9 and 20 meV. The beam then hits the sample in the main chamber under ultrahigh-vacuum (UHV) conditions ($p \leq 2 \times 10^{-10}$ mbar) and is further detected using a quadrupole mass analyzer. For varying the incident angle ϑ_i in the fixed source-sample-detector geometry, the sample can be rotated.

For a detailed description of the sample growth procedure, see the study of Bianchi et al.[42] After in situ cleavage of the sample in a load-lock chamber,[43] the cleanness and purity of the sample can be further studied using low-energy electron diffraction (LEED) and Auger electron spectroscopy (AES). The rhombohedral crystal structure of Bi_2Se_3 is built of quintuple layers (QL), which are bound to each other through weak van der Waals forces.[42] The unit cell consists of three QLs and shows Se termination upon cleavage. The surface along the (111) cleavage plane has a lattice constant of a = 4.14 Å at room temperature.[44] The sample was fixed on a sample holder using thermally conductive epoxy.

The intensity of the specular reflection throughout the measurements typically reached values with a signal-to-noise ratio of 10^3 above the diffuse elastic background (Figure 3), while the full width at half maximum (FWHM) was typically about 0.015 Å^{-1}. Hence, the angular broadening of the specular peak is mainly limited by the angular broadening of the apparatus, giving rise to an estimate (lower limit) for the quality of the crystal[45] with domain sizes larger than 1000 Å.

The sample temperature was varied between cryogenic temperatures (113 K, via a thermal connection to a liquid nitrogen reservoir) and room temperature (300 K). For the first characterization, the scattered specular intensity was measured in dependence of the sample temperature to determine the surface Debye temperature (Θ_D = 122 K[46]). All scattering calculations presented in this work have been corrected by the corresponding Debye−Waller attenuation based on the experimentally determined Debye temperature.

After the first characterization of the crystal, various elastic diffraction scans at 113 K and room temperature were collected in both high-symmetry directions and at different incident energies. Furthermore, measurements of the specular reflection in dependence of the beam energy (measured at 113 K) allow us to obtain further details of the SARs and the atom−surface interaction potential (see Refinement of the Interaction Potential).

RESULTS AND DISCUSSION

After an introduction to the atom−surface interaction potential and the kinematic analysis, we begin our analysis of the SAR features following the free-atom model. Based on the approximate surface-averaged potential, we are then determining the corrugation amplitude of the potential from diffraction measurements to acquire a three-dimensional potential. Finally, we are going to compare the experimental SARs with quantum mechanical scattering calculations to further refine the three-dimensional atom−surface interaction potential.

Atom−Surface Interaction Potential. As stated by Bragg's law, if an atom is scattered by a periodic surface, the change of the wavevector component parallel to the surface, $\mathbf{K}$, must be equal to a surface reciprocal lattice vector, $\mathbf{G}$.

Here, we present mainly measurements where the polar (incident) angle ϑ_i is varied around the corresponding axis, while the scattered beam intensity is detected. For elastic scattering, the momentum transfer parallel to the surface, $\Delta\mathbf{K}$, is then given by

$$|\Delta\mathbf{K}| = |\mathbf{K}_f - \mathbf{K}_i| = |\mathbf{k}_i|(\sin\vartheta_f - \sin\vartheta_i) \quad (1)$$

where $\mathbf{k}_i$ is the incident wavevector, and ϑ_i and ϑ_f are the incident and final angles with respect to the surface normal, respectively.

Selective adsorption phenomena, which may appear upon scattering of atoms from a periodic surface, occur due to the attractive part of the atom−surface interaction potential. For an elastic process, the kinematically allowed $\mathbf{G}$-vectors are those for which the wavevector component perpendicular to the surface $k_{f,z}^2$ is positive. If an incident He atom hits the surface, it can undergo a transition into a bound state on the surface with $-|\epsilon_n|$. The process happens while the He atom is diffracted into a channel, which is kinematically disallowed ($k_{f,z}^2 < 0$). Such SARs can only happen if the difference between the energy of the incident atom and the kinetic energy of the atom moving parallel to the surface matches the binding energy ϵ_n of the adsorbed atom[23]

$$E_i = \frac{\hbar^2\mathbf{k}_i^2}{2m} = \frac{\hbar^2(\mathbf{K}_i + \mathbf{G})^2}{2m} + \epsilon_n(\mathbf{K}_i, \mathbf{G}) \quad (2)$$

where m is the He mass. From eq 2, it is clear that studying SARs provides access to the bound-state energies $\epsilon_n(\mathbf{K}_i, \mathbf{G})$ and, more importantly, to the atom−surface interaction potential.

DOI: 10.1021/acs.jpcc.9b03450
J. Phys. Chem. C 2019, 123, 17829−17841

In this work, we have analyzed SARs upon scattering of He from Bi_2Se_3 using a corrugated Morse potential (CMP). Despite the deviation of the CMP from the expected z^{-3} asymptotic behavior, it has been shown that the overall shape of the CMP represents the measured bound states well enough. A comparative study of various potentials with different asymptotic behavior has shown a similar outcome when subsequently used in close-coupling calculations.[37,47] Likewise, the validity of this potential for TI surfaces[48] and other layered materials such as transition metal dichalcogenides[49] has been proven. In addition, the CMP greatly simplifies the treatment of several steps within the close-coupling (CC) algorithm, allowing for an analytical solution in those cases, which leads to a reduced computational cost.

The three-dimensional CMP, written in dependence of the lateral position $\mathbf{R}$ on the surface and the distance z with respect to the surface, is[50]

$$V(\mathbf{R}, z) = D\left[\frac{1}{\nu_{0,0}} e^{-2\kappa[z-\xi(\mathbf{R})]} - 2e^{-\kappa z}\right] \tag{3}$$

with κ being the stiffness parameter, D being the depth of the potential well, and $\nu_{0,0}$ being the surface average of the exponent of the corrugation function. The electronic surface corrugation is described by $\xi(\mathbf{R})$, where $\mathbf{R}$ describes a periodically modulated surface corresponding to a constant total electron density.

For $\xi(\mathbf{R})$, a two-parameter Fourier ansatz was used, which is described by a summation of cosine terms. The Fourier series expansion is based on the sixfold symmetry of the topmost layer of the surface (see eq 14 in the Appendix), which is the only relevant layer when considering the energies of the impinging He atoms used in this study.[29,37] The corrugation magnitude is then typically given in terms of the peak-to-peak value ξ_{pp} of $\xi(\mathbf{R})$.

The laterally averaged surface potential V_0 (i.e., without corrugation) of eq 3 is given via

$$V_0(z) = D[e^{-2\kappa z} - 2e^{-\kappa z}] \tag{4}$$

The bound states can be described analytically by

$$\epsilon_n = -D + \hbar\omega\left(n + \frac{1}{2}\right)\left(1 - \frac{n + \frac{1}{2}}{2\gamma}\right) \tag{5}$$

where n depicts a positive integer, $\omega = \kappa\sqrt{\frac{2D}{m}}$ is the Debye frequency, with m being the mass of the impinging He atom, and $\gamma = \frac{2D}{\hbar\omega}$.

To determine the three-dimensional potential, we start first with the laterally averaged atom−surface interaction potential, trying to identify SARs in various diffraction scans. After determining a laterally averaged atom−surface interaction potential based on the SAR positions and the free-atom model, we determine the corrugation amplitude ξ_0 of the potential by comparison of the diffraction intensities based on close-coupled calculations with the experimentally determined diffraction intensities. We are then further refining the potential using close-coupled calculations of the resonance positions, optimizing the agreement with the experimental measurements of SARs. The whole procedure is described in more detail below.

Determination of SARs in the Elastic Scans. In a first step of determining the atom−surface interaction potential, the laterally averaged atom−surface interaction potential is used to identify the SARs in various elastic scans. When performing a diffraction scan according to eq 1, the kinematic condition (eq 2) can be fulfilled for specific values of ϑ_i. Two typical diffraction scans for the high-symmetry direction $\overline{\Gamma M}$ are shown in Figure 1. The x-axis has been transformed to parallel momentum transfer using eq 1. In addition to the diffraction peaks, smaller features caused by SARs can be seen.

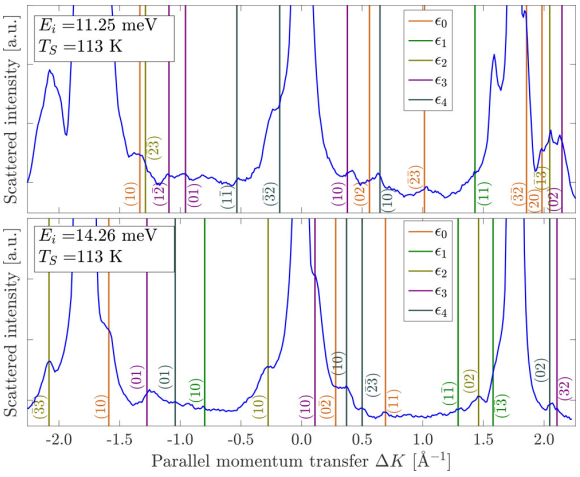

Figure 1. Scattered He intensities for $Bi_2Se_3(111)$ versus parallel momentum transfer $\Delta\mathbf{K}$ along the $\overline{\Gamma M}$ azimuth with a sample temperature of 113 K. The incident beam energy E_i is 11.25 and 14.26 meV in the top and bottom panels, respectively. The intensity scale has been expanded, and in addition to the diffraction peaks that are cut off due to their high intensity, small peaks and dips corresponding to selective adsorption processes can be seen. The vertical lines in various colors illustrate the kinematic conditions for five bound-state energies ϵ_0−ϵ_4 according to eq 6. Each line is labeled with the Miller indices of the associated $\mathbf{G}$-vector for the particular resonance condition.

First, we will restrict the kinematic condition given in eq 2 to the free-atom approximation, which assumes that the surface potential is adequately described by the laterally averaged interaction potential (eq 4). Strictly speaking, it holds only in the case where the surface corrugation approaches zero, which is not possible in reality, since corrugation is necessary to provide the $\mathbf{G}$-vector for the resonance processes. We will then use and refine the full three-dimensional atom−surface interaction potential at a later point within the formalism of close-coupled calculations.

Nevertheless, the free-atom approximation is useful for a first identification of SARs as it treats the binding energies $\epsilon_n(\mathbf{K}_i, \mathbf{G})$ in eq 2 as constants and is therefore independent of $\mathbf{K}_i$ and $\mathbf{G}$. The introduction of a corrugation may give rise to changes in the resonance positions, which tend to become more important with increasing surface electronic corrugation. Since the peak-to-peak corrugation of similar materials is in the region of 5 − 9% of the lattice constant,[37,45] one needs to keep in mind that considerable shifts of the resonance positions may occur.

Using the free-atom model as a starting point, the position of the SARs (eq 2) can be rewritten in terms of the incident angle

DOI: 10.1021/acs.jpcc.9b03450
J. Phys. Chem. C 2019, 123, 17829−17841

ϑ_i and the incident wavevector k_i. The latter is given by the beam energy, which is determined by the nozzle temperature. The scattering vector **G** can be separated into two parts **G** = ($G_\parallel$, $G_\perp$) normal and parallel to the incidence plane

$$k_i^2 = (k_i \sin\vartheta_i + G_\parallel)^2 + G_\perp^2 - \frac{2m}{\hbar^2}|\epsilon_n| \tag{6}$$

The peaks or dips at a particular incident angle ϑ_i in the scans can be associated with a certain bound state energy ϵ_n and scattering channel using eq 6. The position of several SARs is indicated by vertical lines (based on solving eq 6 for ϑ_i) in Figure 1 and labeled according to their diffraction channel **G**, while the different colors correspond to different bound states ϵ_n. For better visibility of the SARs, the sample was cooled down to 113 K to minimize the inelastic background as well as the linewidth of the resonances. The scan in the upper panel was measured with an incident beam energy of 11.25 meV and the lower panel at 14.26 meV. The vertical lines are according to the first five bound-state energies ϵ_0–ϵ_4 of the later determined laterally averaged interaction potential defined by their color, while the numbers next to the lines denote the corresponding reciprocal lattice vectors.

It becomes immediately evident that the assignment of resonances in a single diffraction scan such as Figure 1 is quite ambiguous since numerous combinations of ϵ_n and **G** can be thought of to fulfill eq 6. For a better assignment of the bound states and **G**-vectors, a collection of numerous scans was put together, as shown in the contour plot of Figure 2. To monitor the drift of the resonances versus the incident beam energy, many diffraction scans with various E_i were performed. Putting this collection of measurements together allows us to identify the bound-state resonances much easier. In particular, the curvature of a certain resonance feature allows us to determine the corresponding **G**-vector, which greatly simplifies the search for the associated bound state ϵ_n, which fulfills eq 6.

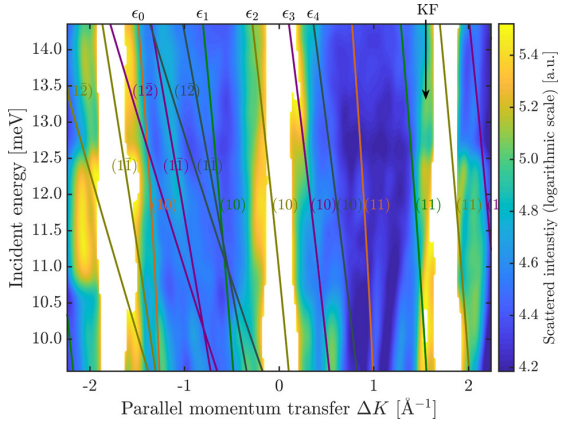

Figure 2. Contour plot of the scattered He intensities (logarithmic scale) versus parallel momentum transfer and incident energy of the He atom along the $\overline{\Gamma M}$ azimuth and at a sample temperature of 113 K. The superimposed solid lines correspond to the resonance conditions calculated with the free-atom approximation. Each line is labeled with the Miller indices of the associated **G**-vector for the resonance condition. The labels $\epsilon_0 - \epsilon_4$ at the top abscissa denote the series of eigenvalues associated with the (10) **G**-vector. Scattered intensities (mainly the diffraction peaks) exceeding a certain value have been cut off to increase the visibility of the resonance effects. The black arrow labeled with KF indicates a region of increased intensity, which is likely to correspond to kinematic focusing (KF) rather than a resonance effect.

A total of 27 ϑ-scans at incident energies ranging from 9.5 to 14.5 meV was collected to construct the contour plot. The *x*-axis in Figure 2 corresponds to the parallel momentum transfer and the *z*-axis to the scattered intensity. The *y*-axis is formed by plotting the scans with various incident energies; that is, a cut at *y* = constant would result in a graph such as Figure 1. The plot was constructed by connecting the individual scans on a two-dimensional grid using a linear interpolation, while the intensity (*z*-axis) is plotted on a logarithmic scale. Scattered intensities (mainly the diffraction peaks) that exceed a certain value have been cut off to increase the visibility of the resonance effects. The superimposed solid lines correspond to identified bound states according to the free-atom approximation (eq 2), with the color coding and associated **G**-vectors labeled in the same way as in Figure 1. A number of lines of high and low intensities, which we identify as selective adsorption resonances features, can be seen to run across the data set.

Following the described approach in analyzing the position of these SARs, a set of five distinct eigenvalues of the laterally averaged potential is obtained (Table 1). The experimentally found bound states are then used to determine the laterally averaged potential (eq 5) by minimizing σ_ϵ

Table 1. Experimentally Determined Bound State Values for the Laterally Averaged He–Bi_2Se_3(111) Interaction Potential[a]

bound state	ϵ_n [meV]	$\Delta\epsilon_n$ [meV]	τ_n [ps]
ϵ_0	5.6	0.39	1.7
ϵ_1	3.8	0.33	2.0
ϵ_2	2.3	0.30	2.2
ϵ_3	1.2	0.27	2.4
ϵ_4	0.5	0.13	4.9

[a]The corresponding internal linewidths $\Delta\epsilon_n$ of the bound states (based on the experimental width of the resonances) and their lifetimes τ_n are also given.

$$\sigma_\epsilon = \frac{1}{N}\sqrt{\sum_{n=0}^{N-1} |\epsilon_n^{\mathrm{exp}} - \epsilon_n^{\mathrm{pot}}|^2} \tag{7}$$

with *N* being the number of bound states included. In doing so, a laterally averaged potential with the parameters *D* = (6.6 ± 0.2) meV and κ = (0.58 ± 0.07) Å^{-1} is determined. The obtained potential supports a total of seven bound states, with ϵ_5 and ϵ_6 being quite close to zero, that is, to the threshold condition.

Note that not all lines of high and low intensities can be explained using SARs based on the free-atom approximation. We will later see that using a three-dimensional potential will give rise to shifts compared to the free-atom approximation, while considering inelastic channels can give rise to changes from maxima to minima and vice versa.[51] There are also some features present that cannot be explained by SARs even when considering a full three-dimensional potential. The features we are referring to show only a weak dependence of ΔK with respect to the incident energy E_i, and thus, no associated **G**-vector can be found that would explain such a curvature. One of these features, indicated by the black arrow labeled with KF

DOI: 10.1021/acs.jpcc.9b03450
J. Phys. Chem. C 2019, 123, 17829–17841

in Figure 2, is likely to correspond to a kinematic focusing (KF) effect (see ref 29).

Moreover, there appear to be features with increased intensity next to the first-order diffraction peaks (see, e.g., the top panel in Figure 1). Additional features in diffraction scans due to spin-conserving electronic interpocket transitions have been observed for the semimetal Sb(111),[52] and the observability of similar transitions in the TI Sb_2Te_3 has been suggested by theory.[53] The observation of additional dispersion curves in Bi_2Se_3[54] in analogy to Sb(111) suggests a similar assignment of the additional peaks in the diffraction spectra. On the other hand, the surface electronic structures of both Sb(111) and Sb_2Te_3 exhibit narrow electron pockets, while the situation for Bi_2Se_3 is different, with a single Dirac cone close to $\bar{\Gamma}$ that typically evolves into multiple states due to the formation of quantum well states. For the latter case, it is still under debate whether both storage in the UHV chamber and exposure to intense ultraviolet light are necessary ingredients.[42,55] The distance of the above-mentioned features in terms of ΔK with respect to the diffraction peaks would make an electronic transition induced by the helium atom possible (via scattering from $-k$ to $+k$). However, the question remains whether this would be a spin-conserving transition, for example, between the Rashba spin-split quantum well states, or whether, for example, a phonon would be required in the process to allow for a spin-flip. In any case, since we can exclude the fact that these features are related to SARs, their origin is not relevant for a determination of the atom−surface interaction potential. Hence, the assignment and discussion about these features are beyond the scope of this work and will be treated separately.[54]

Calculation of the Scattering Intensities. Once a first estimate of the laterally averaged atom−surface interaction potential has been established, we are going to consider the three-dimensional CMP (eq 3). A comparison of quantum mechanical calculations of the scattered intensities with the experimentally found ones yields a value for the corrugation ξ_{pp}. The process of elastically scattering a He atom from a surface can be described by the time-independent Schrödinger equation together with the CMP. In the exponential term of the potential (eq 3), the Fourier series expansion (see eq 14) is used, which yields a set of coupled equations for the outgoing waves. These waves are solved using the close-coupling algorithm for a finite set of closed channels[28,56] (see Details on the Close-Coupling Calculations). The corresponding coupling terms for the CMP can be found in several references.[29,37,47]

To determine the corrugation of the sample surface, the elastic peak intensities are calculated with the close-coupling algorithm and compared with the experimentally measured values of the peak areas.[45] The calculated values of the diffraction peak intensities are corrected with the Debye−Waller attenuation (Θ_D = 122 K[46]), while the measured intensities are determined from the peak area using a fitted Voigt profile.[37] The reason for using the measured peak areas rather than the peak heights is the need to account for the broadening due to the energy spread of the He beam and additional broadening of the diffraction peaks caused by the angular resolution of the apparatus as well as domain size effects of the crystal surface. While the values for D and κ of the potential were held constant, the corrugation ξ_{pp} was varied between 0.01 and 0.6 Å with a step width of 0.001 Å. The corrugation amplitude ξ_{pp}, which describes the best correspondence between measured (I_G^{exp}) and calculated diffraction intensities (I_G^{sim}), is found by minimizing a measure of the deviation R

$$R = \frac{1}{N}\sqrt{\sum_G (I_G^{exp} - I_G^{sim})^2} \tag{8}$$

with N being the number of experimentally measured diffraction peaks.[20]

For the analysis, we used a total of 35 elastic scans at various incident energies, trying to minimize eq 8, that is, searching for the global minimum of R in dependence of ξ_{pp}. In Figure 3, two of these diffraction scans along the two high-symmetry directions of Bi_2Se_3(111) are shown together with the measured and calculated peak areas (symbols in the figure).

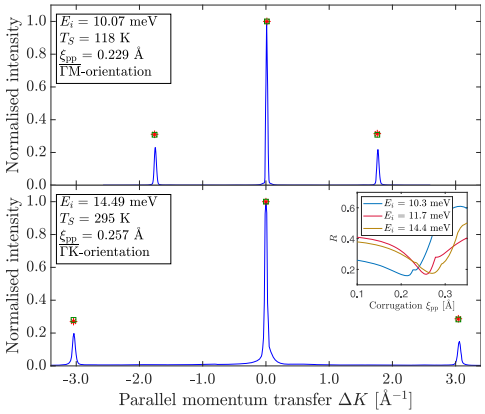

Figure 3. Scattered He intensities for Bi_2Se_3(111) versus parallel momentum transfer. In the top (bottom) panel, the elastic scan taken along the $\overline{\Gamma M}$ ($\overline{\Gamma K}$) azimuth with a sample temperature of 113 K (room temperature) and an incident energy E_i of 10.07 meV (14.49 meV) is plotted. The green squares show the area of the measured diffraction peaks, while the red stars depict the calculated values. The inset shows the R-factor (eq 8) for different values of the corrugation amplitude ξ_{pp} using diffraction data at three different incident energies. The minimum of R shifts to higher values of ξ_{pp} with increasing E_i.

The equipotential surface describing the electronic corrugation $\xi(\mathbf{R})$ corresponds to the classical turning points of the potential, that is, the locus of all points for which $V(\mathbf{R}, z) = E_i$ holds. Hence, one may expect that, with increasing beam energy, the turning point shifts to distances closer to the ion cores and the scattered He atoms experience a larger corrugation amplitude ξ_{pp}. The corrugation then shows a dependence on the incident energy of the molecular beam, typically following a monotonic increase with E_i.[57] Therefore, the above-described optimization routine was repeated by taking into account several experimental spectra recorded around three specific incident energies E_i, as shown in the inset of Figure 3. Indeed, when only diffraction scans taken at the lowest incident energy are considered in the analysis explained above, the best fit value of ξ_{pp} decreases. For medium incident energies (E_i = 10.3 meV), the minimum of R is found with ξ_{pp} = 0.21 Å, while for higher incident energies (E_i = 14.4 meV), it increases to ξ_{pp} = 0.27 Å. Optimizing eq 8 based on all recorded diffraction spectra yields ξ_{pp} = 0.25 Å, which is thus an average corrugation over the whole range of beam energies considered in this study. We will later observe (see Refinement

DOI: 10.1021/acs.jpcc.9b03450
J. Phys. Chem. C 2019, 123, 17829−17841

of the Interaction Potential) that, for the SARs, small changes in terms of ξ_{pp} are much less important compared to changes of the well depth D and the stiffness κ.

As mentioned above, the free-atom approximation used in the first approach (see Determination of SARs in the Elastic Scans) of determining a potential neglects the corrugation of the surface, meaning that the coupling term vanishes and the band structure would solely consist of parabolic bands. In considering surfaces with larger corrugations, higher-order Fourier components of the surface potential have to be considered. The three-dimensional corrugated surface potential (eq 3) may then give rise to substantial deviations from the free-atom parabolic bands. Hence, we will use again quantum mechanical calculations to accurately describe the resonance positions and, in doing so, refine the full three-dimensional potential in the following. We will also rerun the optimization routine for the electronic corrugation ξ_{pp}, which was, at first, determined using D and κ as obtained from the averaged potential, with the refined three-dimensional potential.

Refinement of the Interaction Potential. In addition to elastic ϑ-scans, the intensity of the specular peak can be measured as a function of the incident wavevector k_i. Such a so-called drift spectrum shows again SARs at places where the kinematic condition (eq 2) is fulfilled. As can be seen in Figure 2, the SAR conditions "move through" the specular condition and cause the intensity to change. However, in contrast to the ϑ-scans where most SARs appear as weak features in between the diffraction peaks, a measurement, while staying at the specular reflection, allows for the highest signal-to-noise ratio in the experiment. The top panel in Figure 4 shows such a drift scan along the $\overline{\Gamma K}$ azimuth where a multitude of broad and narrow peaks and dips is visible. Hence, such a measurement gives access to the detailed shape of the potential, and by comparison with calculations, we will further refine the potential, looking into shifts with respect to the free-atom approximation.

At the same time, additional effects may complicate the analysis of SARs in a drift scan. First, the incident beam intensity decreases with increasing nozzle temperature T_N since the He flow through the nozzle is proportional to $1/\sqrt{T_N}$. The effect can however be easily accounted for by correcting the scattered He intensity in the measurement with the corresponding factor (as done in the top panel of Figure 4). Second, surface imperfections such as terraces and steps can give rise to variations of the scattered intensity: The interference of outgoing waves, which are scattered from different terraces, can cause periodic oscillations of the detected signal as a function of k_i.[20,29] From the major peaks and dips of these oscillations, the terrace height(s) of the investigated sample can be calculated.[20,29] These peaks are typically much broader than the peaks and dips caused by SARs, and we will attempt to analyze those in the Appendix.

Moreover, the energy distribution of the incident beam will give rise to a broadening of the natural linewidths of SARs, which can be incorporated by numerically convoluting the elastic intensity with the appropriate distribution in incident energy (see the turquoise dash-dotted curve in the bottom panel of Figure 4[##]). Finally, SARs tend to become less pronounced and broader with increasing sample temperature due to a linewidth broadening and the increasing importance of inelastic effects, as can be seen when comparing Figure 4 with Figure 9.

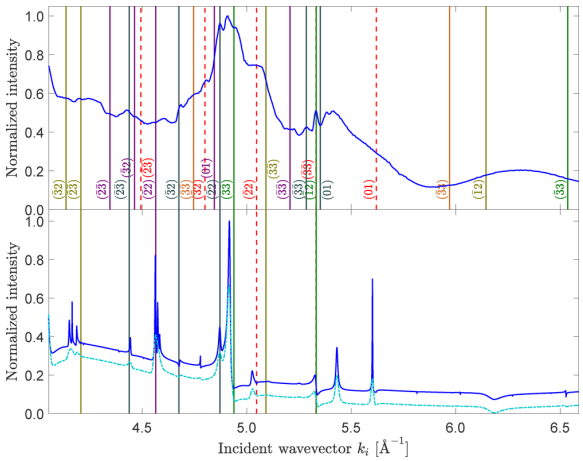

Figure 4. Normalized intensity of the specular peak in dependence of the incident wavevector k_i. Top: Measured drift spectrum along $\overline{\Gamma K}$ with a sample temperature of 113 K and corrected for the He flux through the nozzle. The vertical lines show the predicted positions of the SARs using the free-atom approximation. The colors symbolize the different bound-state energies (same nomenclature as used in Figure 1), with the dashed lines illustrating the threshold energy. The number next to the lines corresponds to the specific interacting **G**-vector. Bottom: Simulated drift spectrum using elastic close-coupled calculations with the optimized three-dimensional potential after multiplication with the corresponding Debye−Waller factor. A few vertical lines from the top panel have been extended as a guide to the eye. The turquoise dash-dotted curve illustrates the experimental broadening due to a convolution of the energy distribution in the incident beam with the SARs.

We turn now to the refinement of the interaction potential based on the drift scan (top panel of Figure 4), which shows the measured specular intensity as a function of the incident wavevector k_i. The sample was aligned along the $\overline{\Gamma K}$ azimuth and held at a sample temperature of 113 K while changing the nozzle temperature from 44 to 100 K. The colored lines display the SAR positions according to the free-atom approximation using the optimized surface potential. The numbers next to the lines denote the corresponding reciprocal lattice vectors following the same nomenclature as for Figure 1. In cases where several **G**-vectors lead to the same solution of the kinematic equation, the Miller indices of only one **G**-vector are given. In addition, the vertical dashed lines correspond to the threshold energies of the surface potential. In principle, threshold resonances can also give rise to intensity variations, which have been predicted to be experimentally detectable for scattering of atoms from highly corrugated surfaces.[56,58] On the other hand, threshold resonances have only been observed experimentally for scattering He from a ruled grating upon grazing incidence.[59]

The measured drift spectrum can be simulated using calculations based on the elastic close-coupling formalism. The simulated spectra can then be compared to the SAR positions in the experimental data, and in doing so, the surface potential can be further refined. For these calculations, the corrugation values from above were used, while the values of D and κ were varied in the neighborhood of the first estimated values. After the potential parameters D and κ, which describe the closest agreement with the measurements, have been found, the corrugation ξ_{pp} is further refined by minimizing eq

DOI: 10.1021/acs.jpcc.9b03450
J. Phys. Chem. C 2019, 123, 17829−17841

8. In the bottom panel of Figure 4, the result of the simulation using the close-coupling formalism is plotted, which has further been multiplied with the corresponding Debye−Waller factor (see Close-Coupling Formalism for further details about the calculations).

Note that, due to the above-described additional effects, it is not possible to resemble the actual shape of the whole measured drift spectrum using the elastic close-coupling simulation since, at finite temperature, the linewidth and shape of the SARs will be influenced by inelastic channels, while at the same time, the oscillations caused by terraces are superimposed onto the experimental spectrum. From a theoretical point of view, these effects have been mainly considered in the limit of low corrugated surfaces,[60−62] but it is well known that inelastic events are expected to account for the attenuation of the line shapes as observed in the experiment and can even turn maxima into minima.[51,61] In the elastic theory of resonant scattering, it has been shown that the occurrence of minima, maxima, and mixed extrema can be explained and predicted by establishing some general rules. However, in many cases, their applicability is limited since these were derived for weak coupling conditions and hard model potentials.[60] Thus, we will mainly concentrate our analysis on the position of the SARs in terms of k_i, as described below. Despite the complications caused by linewidth broadening and the additional oscillations caused by the terraces, most peaks and dips of the measured data can be identified in the simulated drift scan. The position of the SARs based on the free-atom approximation, denoted by the colored lines, are shifted with respect to the peaks of the quantum mechanical calculations using the full three-dimensional potential. Generally, resonances with higher corresponding **G**-vectors tend to show a larger shift compared to those with lower indices (see Close-Coupled Calculations of the Drift Scan for a set of simulated curves showing how the SARs change upon variation of D, κ, and ξ_{pp}). However, it is hard to assign each peak in the calculation to the corresponding resonance condition of the free-atom approximation.

Instead of defining a global χ^2 parameter for the goodness of fit that would not distinguish between different aspects, we will concentrate on optimizing the position of a number of specific features. Due to the above-described broadening effects and superimposed oscillations from the terraces, it is impossible to define a simple parameter that adequately describes the overall agreement between the experiment and simulation. An approach that considers a global χ^2 parameter will be highly sensitive to unimportant aspects such as the energy broadening of the incident beam or the described oscillations due to the terraces that modulate the intensities. Hence, we concentrate on optimizing the position of a number of specific "target" features, which can be identified directly in the experimental measurement and are then checked qualitatively to give an improvement over the entire data set. Target features should be representative of the entire potential, that is, being associated with different **G**-vectors and bound states. Furthermore, for practical purposes, we choose features that can be unambiguously identified, clearly above the background and preferably with no other resonances close enough to cause confusion with a different SAR channel or an intersection with another feature. Finally, SARs leading to peaks are generally preferred to those leading to dips.[21] We concentrate on testing the positions k_i of the SARs in the simulated data compared to the peak positions in the experimental spectrum

$$R_p^2 = \frac{1}{N^2}\sum_{i=1}^{N}\left(\frac{k_i^{sim} - k_i^{exp}}{\sigma_i}\right)^2 \tag{9}$$

where k_i^{exp} are the experimental data values with uncertainties σ_i ($\sigma_i \approx 0.02$ Å^{-1}), and k_i^{sim} are the calculated peak positions. Figure 5 shows the effect on R_p^2 if the potential well depth D

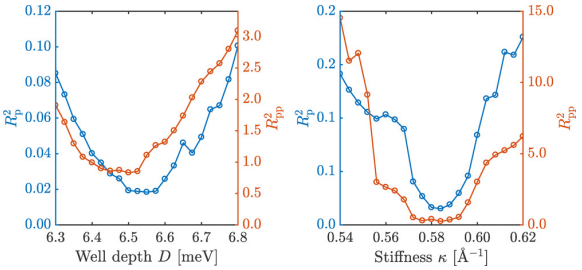

Figure 5. Effect of varying the potential well depth D and stiffness κ around the optimized potential parameters. The left panel shows a measure of the agreement between the simulations and experimental data, while D is varied using eq 9 on the left ordinate and eq 10 on the right ordinate, respectively. The right panel shows the same reliability factors, now varying κ, while D is held constant.

and stiffness κ are varied around the optimized parameters. The whole set of simulated drift spectra for this purpose can be found in Close-Coupled Calculations of the Drift Scan. Note that the effect of varying ξ_{pp} (Figure 8) on the resonance positions is rather small, with the main effect being the changes in the shape and amplitude of the resonances. Thus, ξ_{pp} is better determined in comparison with the diffraction peak intensities, and we concentrate on a refinement of D and κ based on the position of the SARs in the drift scan. Figure 5 clearly illustrates that the final optimized values of D and κ correspond to a minimum in terms of R_p^2.

Another possibility for a measure of the agreement between the simulation and experiment is to try and adopt an R-factor in analogy to what has been used in LEED in experiments. According to Pendry,[63] a good R-factor for comparison with calculated LEED experiments should be sensitive to the peak position. It should not be sensitive to the absolute intensities but take into account the relative intensities of features that are close in energy. Based on those criteria, an R-factor for SARs can be defined by considering a measure of the curvature, that is, the second derivative of the intensity I''_{exp} in the drift scan according to

$$R_{pp}^2 = \frac{1}{\int (I''_{exp})^2 dk}\int (I''_{exp} - c\cdot I''_{sim})^2 dk \tag{10}$$

where the scaling constant $c = \int I_{exp} dk / \int I_{sim} dk$ is used to normalize the experimental and simulated curves with respect to each other.[63,64] Unfortunately, the number of additional effects in the experimental spectrum makes such an approach quite difficult. We can restrict the approach to certain regions in the calculated and simulated spectra, for example, considering the region between k_i = 5.1 and 5.4 Å^{-1}. We see in Figure 5 that the overall trend is the same compared to using R_p as a measure, although the latter seems to be more robust in the present case.

DOI: 10.1021/acs.jpcc.9b03450
J. Phys. Chem. C 2019, 123, 17829−17841

Following this optimization process, the parameters of the final refined three-dimensional atom−surface interaction potential are found as

$$D = (6.54 \pm 0.05)\ \text{meV}$$

$$\kappa = (0.58 \pm 0.02)\ \text{Å}^{-1}$$

Compared to the results from Determination of SARs in the Elastic Scans, the well depth D decreased, while the stiffness κ showed only a subtle change. By using this optimization process, we can define a measure for the agreement between the close-coupled calculations and the experiment. With respect to the first approach based on the free-atom approximation, the uncertainties of all values are significantly reduced.

In comparison to previously studied systems, the value of the well depth D is between those found for $Bi_2Te_3(111)$ (6.22 meV)[48] and Bi(111) (7.9 meV),[37] while the stiffness κ of the He−$Bi_2Se_3(111)$ potential is significantly smaller than for $Bi_2Te_3(111)$ and for the Bi(111) single crystal, although larger compared to Sb(111).[47]

Because Bi_2Se_3 has a smaller vdW gap than Bi_2Te_3 and Sb_2Te_3,[40,42,65] a different interaction of the outermost layer in the weak vdW regime might be expected, and indeed, this is confirmed by the determined potential in terms of the different stiffness κ. Due to the polarizability of both Bi and Se, one would expect a "soft" potential with a significant long-range attractive part. On the other hand, the determined potential parameters indicate that the potential is actually "stiffer" than the typical potential of a simple flat metallic surface. Detailed simulations will be required to resolve the importance of the above-mentioned effects, and the presented data may provide a benchmark to test challenging vdW approaches in DFT.

Finally, revisiting the calculation of the diffraction peak intensities with the refined potential parameters yields a peak-to-peak corrugation

$$\xi_{pp} = (0.26 \pm 0.01)\ \text{Å}$$

for an incident beam energy E_i = 11.7 meV. The average overall beam energies considered in this study correspond to a surface electronic peak-to-peak corrugation of (5.8 ± 0.2)% of the surface lattice constant. The value is similar to the semimetal Bi(111) (5%)[37] while being smaller than the reported 9.6% for Bi_2Te_3.[48]

Since the spin−orbit coupling in Bi_2Se_3 is stronger than in Bi_2Te_3, giving rise to a different electronic structure of the topological surface states,[9,66] this may also cause a different electronic surface corrugation, although it is of course difficult to make any connections between the localized electronic bands in terms of k-space and the "global" surface electronic corrugation. At the same time, the work functions of Bi_2Se_3 and Bi_2Te_3 are quite similar,[45,67] and hence one might not expect large differences in terms of the surface electronic corrugation. Nevertheless, we can certainly conclude that the surface electronic corrugation of both Bi_2Se_3 and Bi_2Te_3 is of the same order of magnitude and the charge smoothing due to the Smoluchowski effect is definitely less pronounced for both TIs compared to the observations of flat metal surfaces.[20]

Linewidth and Lifetime of SARs. The angular broadening of SARs in experimental measurements is related to the lifetime of the corresponding bound state, that is, the time that the He atom spends in the bound state before it leaves the surface. The experimentally determined (external) width has to be corrected for resolution aspects of the apparatus to determine the internal or natural linewidth of the bound state.[56,68] The external full width at half maximum (FWHM) was determined by fitting the SAR features in several angular diffraction scans with a Gaussian function. The external width $\Delta\vartheta_{total}$ is corrected for the resolution aspects based on the convolution of two Gaussian distributions, yielding an internal angular width $(\Delta\vartheta_{res})^2 = (\Delta\vartheta_{total})^2 - (\Delta\vartheta_{app})^2$. $\Delta\vartheta_{app}$ accounts for the angular resolution of the apparatus as well as the energy spread in the beam and was obtained from the FWHM of the associated diffraction channel. The natural linewidth $\Delta\epsilon_n$ of the bound state in terms of energy is then given via[68]

$$\Delta\epsilon_n = \left|\frac{\partial\epsilon}{\partial\vartheta_i}\right|\Delta\vartheta_i \text{ with } \left|\frac{\partial\epsilon}{\partial\vartheta_i}\right| = \frac{\hbar^2}{m}k_i\cos\vartheta_i(k_i\sin\vartheta_i + G_{\parallel}) \tag{11}$$

where $G_{\parallel}$ is the parallel component of the **G**-vector associated with the resonance. Finally, the lifetime τ of the bound states can be established from the uncertainty principle using $\tau_n = \hbar/\Delta\epsilon_n$.[56]

The natural linewidths and corresponding lifetimes of all bound states are listed in Table 1. The lifetimes increase with increasing quantum number n of the bound state. The trend is expected since bound states with a higher n are further away from the surface and thus experience less of the surface corrugation, decreasing also the probability of scattering events that would cause the He atom to leave the surface.

In general, various factors will affect and limit the lifetime of a bound state. For elastic scattering, the lifetime is limited by the probability of being scattered out of the bound-state channel, which relates to the form and amplitude of the lateral corrugation in the atom−surface potential. Considering inelastic processes, the natural lifetime will be further reduced by factors such as defect or phonon scattering, with the latter becoming more important with increasing temperature.[27,56]

Due to the required high experimental resolution, information about the linewidth and lifetime of SARs is limited to a very small number of systems.[27,47,68,69] Direct experimental information is only available for the He−LiF(001) system[68] and the He−Sb(111) system.[47] The internal linewidths of the He−LiF(001) system are comparable to those found for He−Bi_2Se_3 in Table 1. Based on elastic scattering events and the similarity of the atom−surface interaction potentials (similar depth although larger corrugation in the case of He−LiF(001)), one would expect similar linewidths in both cases, and indeed, this is confirmed by the measurements. On the one hand, with increasing surface temperature (room temperature in ref 68 compared to 113 K in our study), inelastic events may become more important; on the other hand, the higher Debye temperature of LiF compared to Bi_2Se_3 suggests that phonon scattering will again be similar when comparing both studies.

The influence of different atom−surface interaction potentials on the linewidth has also been subject to previous studies. As noted by Tuddenham et al.,[27] based on close-coupled calculations, a Morse potential with the same corrugation as a corresponding reference potential gives features whose linewidth is similar to those seen in the experiment. Hence, we hope that the experimental determination of the linewidths presented in this study will initiate further work in this direction and, for example, in comparison with inelastic close-coupled calculations, eventually allow to

DOI: 10.1021/acs.jpcc.9b03450
J. Phys. Chem. C 2019, 123, 17829−17841

rule out whether elastic or inelastic scattering channels are mainly responsible for the lifetime of bound states.

SUMMARY AND CONCLUSIONS

In summary, we have determined an atom−surface interaction potential for the He−Bi_2Se_3(111) system by analyzing selective adsorption resonances in helium atom scattering spectra. For a first approximation, we start with the free-atom approximation and a laterally averaged atom−surface interaction potential, which is then further improved and refined based on close-coupled calculations to obtain an accurate three-dimensional atom−surface interaction potential. The free-atom approximation cannot provide information about the shape of the resonances, and by comparison with close-coupled calculations, we are able to obtain the complete experimental band structure of atoms in the corrugated surface potential. Following a systematic analysis, the He−Bi_2Se_3(111) potential is best represented by a corrugated Morse potential, which exhibits a well depth of $D = (6.54 \pm 0.05)$ meV and a stiffness of $\kappa = (0.58 \pm 0.02)$ Å^{-1}. The surface electronic corrugation varies slightly depending on the incident beam energy with an average of (5.8 ± 0.2)% of the lattice constant.

Inelastic processes and phonon-mediated resonances have been proven to play important roles, and a precise atom−surface interaction potential as determined in this study is a necessary ingredient to investigate the effects such as the temperature dependence and linewidth of selective adsorption resonances. From the angular width of selective adsorption resonances in the scattering spectra, we are able to obtain the natural linewidth of the resonances and an estimate for the lifetime of the bound states. Moreover, since a meV He beam is scattered in the low-density region dominated by the tails of Fermi-level surface states, studying selective adsorption resonances provides access to the interaction of TI surfaces within the weak adsorption regime. Hence, we hope that the present data will encourage future ab initio studies to test the ability of vdW corrections on the current system.

As a side note, in the Appendix, we use intensity oscillations due to the interference of the He beam being scattered from different terraces to analyze the step heights of the cleaved crystal surface. The analysis confirms the existence of steps with a quintuple layer height with an indication that subquintuple layer steps may exist also. Despite the existence of terraces, the angular broadening in the diffraction spectra speaks for the high quality of the cleaved sample with domain sizes larger than 1000 Å.

APPENDIX

Details on the Close-Coupling Calculations

Close-Coupling Formalism. Considering the periodicity of the surface lattice, both the surface potential $V(\mathbf{r})$ and wave function $\psi(\mathbf{r})$ can be written as a Fourier series

$$V(\mathbf{r}) = \sum_{\mathbf{G}} V_{\mathbf{G}}(z)\exp(\mathrm{i}\mathbf{G}\cdot\mathbf{R})$$
$$\psi(\mathbf{r}) = \sum_{\mathbf{G}} \psi_{\mathbf{G}}(z)\exp(\mathrm{i}(\mathbf{G}+\mathbf{K}_i)\cdot\mathbf{R}) \quad (12)$$

Inserting the latter into the time-independent Schrödinger equation yields

$$\left[\frac{d^2}{dz^2} + \mathbf{k}_{\mathbf{G},z}^2 - V_0(z)\right]\psi_{\mathbf{G}}(z) = \sum_{\mathbf{G}'\neq\mathbf{G}} V_{\mathbf{G}-\mathbf{G}'}(z)\psi_{\mathbf{G}'}(z) \quad (13)$$

for the z-direction, where $\mathbf{k}_{\mathbf{G},z}^2$ is the z-component of the particles kinetic energy after the surface interaction, and V_0 is the laterally averaged interaction potential.

Equation 13 is a set of coupled equations, with $V_{\mathbf{G}-\mathbf{G}'}$ being the coupling terms, which can be written in a matrix form, since the close-coupling method treats each $\psi_{\mathbf{G}}$ as a scattering channel. Finally, the matrix equation is solved by using a Numerov algorithm.[29,56]

The two-parameter Fourier ansatz used for the corrugation function $\xi(\mathbf{R})$ is

$$\xi(x,y) = \xi_0\left\{\cos\left[\frac{2\pi}{a}\left(x - \frac{y}{\sqrt{3}}\right)\right] + \cos\left[\frac{2\pi}{a}\left(x + \frac{y}{\sqrt{3}}\right)\right] + \cos\left[\frac{2\pi}{a}\frac{2y}{\sqrt{3}}\right]\right\} + \text{h. o.} \quad (14)$$

where x and y depict the coordinates, and ξ_0 determines the corrugation amplitude. The value of the corrugation is determined by the peak-to-peak corrugation ξ_{pp} of eq 14.

For all close-coupled calculations presented in this work, all open channels were considered in the simulations. The number of closed channels was adjusted until the error was determined to be $<10^{-4}$. In the drift simulations, a value of less than 100 closed channels was sufficient, while for the calculation of the diffraction intensities, a minimum of 150 channels was required for the result to converge. For the drift spectrum calculated in Figure 3, 100 closed channels were used, and the integration boundaries in terms of z were set to $[-9, 20]$ Å with an energy resolution of $dE = 0.001$ meV.

As mentioned in the main part of the paper, the value of the corrugation ξ_{pp} exhibits a feeble dependence on the incident energy E_i. Therefore, the best fit value of ξ_{pp} was determined for several sets of diffraction spectra, with each set taken at a different incident energy. In a first approximation, we assume that the corrugation increases linearly within the considered energy region, according to

$$\xi_{pp}\,[\text{Å}] = 0.013 \times E_i\,[\text{meV}] + 0.092 \quad (15)$$

which is further used for the CC calculations of the drift spectra in Close-Coupled Calculations of the Drift Scan.

Close-Coupled Calculations of the Drift Scan. Figures 6−8 show the complete sets of close-coupled calculations used for comparison with the experimental drift scan. Figures 6 and 7 are used in Refinement of the Interaction Potential for the refinement of the potential and the calculation of the reliability factors. For these simulations, the corrugation magnitude was varied according to the incident energy, following eq 15.

In Figure 6, the well depth D is varied within a range of 6.3 to 6.8 meV, which clearly shows different shifts of the individual features in the drift spectrum depending on D. With increasing well depth, the peaks wander toward lower incident energies E_i. In addition, it becomes clear that certain features shift at various "speeds" upon varying the well depth. For instance, the position of the sharp feature at $E_i \approx 5.6$ meV barely changes along the calculated range of D. Therefore, this feature might be caused by a threshold condition. In general peaks originating from lower index, **G**-vectors show a slower shift, as already mentioned in the main part of the paper.

DOI: 10.1021/acs.jpcc.9b03450
J. Phys. Chem. C 2019, 123, 17829−17841

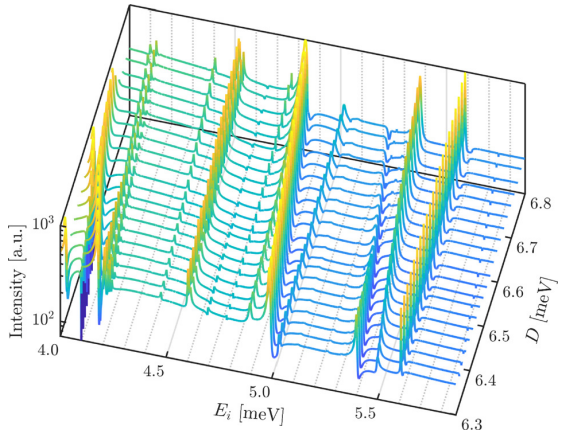

Figure 6. Simulation of the drift scan using elastic close-coupled calculations for various values of D with κ = 0.58 Å^{-1} and ξ_{pp} according to eq 15.

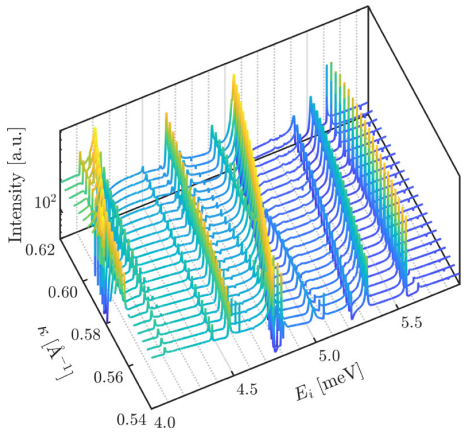

Figure 7. Simulation of the drift scan using elastic close-coupled calculations for various values of κ with D = 6.54 meV and ξ_{pp} according to eq 15.

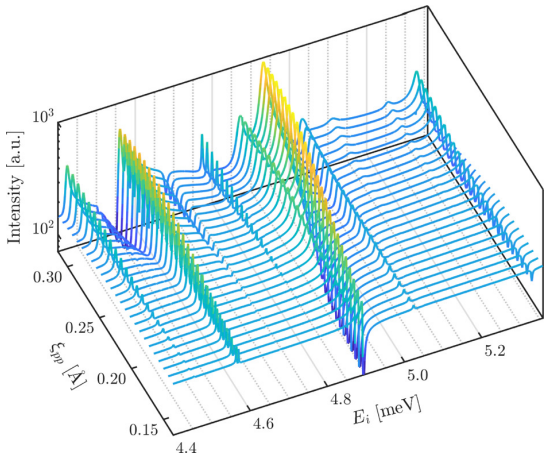

Figure 8. Simulation of the drift scan using elastic close-coupled calculations for various values of ξ_{pp} with D = 6.54 meV and κ = 0.58 Å^{-1}.

In the next step, the well depth was held constant, while the stiffness κ was varied in a range from 0.54 to 0.62 Å^{-1}. The peaks in Figure 7 tend to shift to higher incident energies with increasing stiffness. The most prominent feature changes its position rapidly from 4.7 to 5.1 meV over the whole calculated range of κ.

Finally, the corrugation ξ_{pp} was varied from 0.14 to 0.32 Å. In Figure 8, it becomes clear that the influence of the corrugation within the considered range of ξ_{pp} is much more subtle in terms of the position of the peaks. However, ξ_{pp} significantly changes the shape and intensity of the individual features. For example, the peak at $E_i \approx 4.9$ meV changes its shape from a minimum to a pronounced maximum when increasing ξ_{pp}. In addition, some features might not even be visible at lower values of the corrugation, changing to sharp maxima at higher values of ξ_{pp}.

Detailed Analysis of the In-Phase/Anti-Phase Conditions due to Steps

If the specular intensity is dominated by interference of waves scattered from different terraces, the drift spectrum can also be used to determine the terrace height(s) of the investigated sample surface.[20,29,70] When changing the incident wavevector k_i, the specular intensity shows oscillations due to constructive (in-phase) and destructive (antiphase) interference of the outgoing waves. The phase difference φ upon scattering from two terraces separated by a step height h is given by[29,70]

$$\varphi = 2hk_i\cos\vartheta_i = 2hk_{iz} = h\Delta k_z \qquad (16)$$

where Δk_z is the momentum transfer perpendicular to the surface. In Figure 9, the specular intensity is plotted as a function of the incident wavevector k_i for both high-symmetry directions $\overline{\Gamma M}$ and $\overline{\Gamma K}$ with the sample held at room temperature. The measured intensity has again been corrected for the decreasing He flux with increasing nozzle temperature T_N.[29] The variation of the intensity can then be described by a simple model that overlaps the plane waves that are reflected of the different terraces from the sample. The intensity as a function of Δk_z is described as

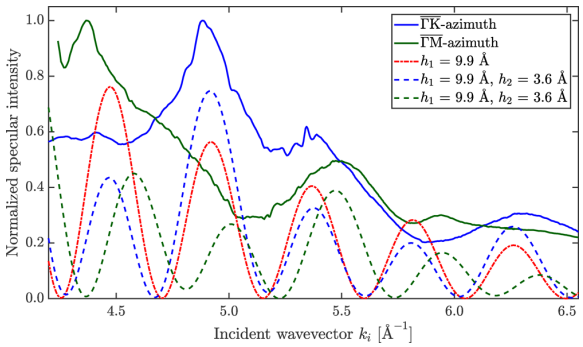

Figure 9. Determination of the step heights from the oscillations present in the drift scan. The solid lines show the measured specular intensity as a function of the incident wavevector k_i measured at room temperature with the crystal aligned along the $\overline{\Gamma M}$ and $\overline{\Gamma K}$ azimuths, respectively. The red dash-dotted line shows intensity oscillations (eq 17), which are expected in the presence of terraces separated by steps with a quintuple layer height. The dashed lines show oscillations for quintuple and subquintuple layer steps, with a different number of subquintuple layer steps for $\overline{\Gamma M}$ and $\overline{\Gamma K}$.

DOI: 10.1021/acs.jpcc.9b03450
J. Phys. Chem. C 2019, 123, 17829−17841

$$I(\Delta k_z) = I_0 e^{-2W} \left| 1 + \sum_{j=0}^{N} a_j e^{-ih_j \Delta k_z} \right|^2 \quad (17)$$

for N different step heights h_j with a probability a_j. I_0 is the intensity of an ideal surface without any steps, and the exponential prefactor accounts for the Debye−Waller attenuation, with W being the Debye−Waller factor.[29,70] The latter considers that the Debye−Waller factor changes with increasing perpendicular incident momentum k_{iz}[29] during a drift scan.

The individual QLs in Bi_2Se_3 as well as other layered TIs are bound to each other through weak vdW forces, which gives easy access to the (111) surface by cleavage.[42,48] Hence, steps that occur upon cleaving are expected to correspond to the QL distance along the c-axis of the conventional hexagonal unit cell (9.6 Å at room temperature[44]). Indeed, the main oscillation in Figure 9 suggests a step height of 9.9 Å (red dash-dotted curve according to eq 9) in good agreement with the separation between the Se termination layers of a QL.[71] The small deviation from the theoretical QL distance may be due to electron spill-out, that is, the fact that the electronic step height observed in HAS does not necessarily correspond to the crystallographic one as measured, for example, with LEED.[72] On the other hand, it appears in Figure 9 that an additional oscillation, giving rise to a further modulation of the intensities from the QL steps and according to a smaller step height, is present also. Sub-QL steps have previously been observed during thin-film growth of TIs,[73,74] while different terminations have also been found for cleaved single crystals depending on the sample treatment.[75,76] Inclusion of a second step height (h_2 = 3.6 Å, dashed curves in Figure 9) seems to improve the agreement with the experimental data, which suggests that terraces with the internal Se layer exist in some cases.[76] Here, considering a different number of steps along $\overline{\Gamma K}$ and $\overline{\Gamma M}$ gives a better agreement with the experimental data, which would imply that the orientation of the terraces is not completely random and depends on the crystal orientation. The fact that Bi_2Se_3 has a smaller vdW gap than Bi_2Te_3 and Sb_2Te_3 might explain the existence of sub-QL steps of the cleaved samples.

Note, however, that the number of parameters in eq 17 and the overlapping with SARs makes an exact determination of the step height difficult. While some of the peaks appear in the $\overline{\Gamma K}$ direction as well as in the $\overline{\Gamma M}$ direction, the peak at around k_i = 4.9 Å^{-1} can only be found in the $\overline{\Gamma K}$ direction. It should also be considered that SARs with lower interacting **G**-vector "move" slower across the specular peak, which may lead to peaks that look like oscillations caused by the steps. From the above analysis, it is clear that oscillations due the QL spacing are present, while there is also a hint toward sub-QL steps. At the same time, we would like to stress that, during such a drift scan, HAS is particularly sensitive to single defects, and hence the appearance of sub-QL steps is likely to be negligible. In fact, as mentioned in Experimental Details, the small width of the specular and diffraction peaks in the elastic scans suggests a very high quality of the cleaved crystals.

Finally, as already mentioned above, the measurements at room temperature (Figure 4) show quite nicely upon comparison with the low temperature measurements (Figure 9) that the resonance effects are more pronounced for the latter. At higher temperatures, the natural linewidth of the SARs increases, which makes it harder to distinguish them from noise. At lower temperature, mainly elastic scattering channels need to be considered, while at elevated temperatures, the inelastic channels become important also, making the inclusion of these channels in the quantum mechanical calculations necessary.

AUTHOR INFORMATION

Corresponding Authors

*E-mail: ruckhofer@tugraz.at (A.R.).
*E-mail: tamtoegl@gmail.com (A.T.).

ORCID

Adrian Ruckhofer: 0000-0003-4368-8207
Anton Tamtögl: 0000-0001-9590-6224
Martin Bremholm: 0000-0003-3634-7412
Wolfgang E. Ernst: 0000-0001-8849-5658

Notes

The authors declare no competing financial interest.

ACKNOWLEDGMENTS

We would like to thank G. Benedek for many helpful discussions. The authors gratefully acknowledge support by the FWF within projects J3479-N20 and P29641-N36 as well as financial support by the Aarhus University Research Foundation, Villum Fonden, via the Centre of Excellence for Dirac Materials (grant no. 11744) and the SPP1666 of the DFG (grant no. HO 5150/1-2). M.B. acknowledges financial support from the Center of Materials Crystallography (CMC) and the Danish National Research Foundation (DNRF93).

ADDITIONAL NOTE

[#]In reality, the broadening changes with E_i, but the convolution with a single Gaussian presents a simple illustration of the general effect.

REFERENCES

(1) Bradlyn, B.; Elcoro, L.; Cano, J.; Vergniory, M. G.; Wang, Z.; Felser, C.; Aroyo, M. I.; Bernevig, B. A. Topological Quantum Chemistry. *Nature* **2017**, *547*, 298−305.
(2) Bansil, A.; Lin, H.; Das, T. Colloquium: Topological Band Theory. *Rev. Mod. Phys.* **2016**, *88*, No. 021004.
(3) Hasan, M. Z.; Xu, S.-Y.; Bian, G. Topological Insulators, Topological Superconductors and Weyl Fermion Semimetals: Discoveries, Perspectives and Outlooks. *Phys. Scr.* **2015**, *T164*, No. 014001.
(4) Ando, Y. Topological Insulator Materials. *J. Phys. Soc. Jpn.* **2013**, *82*, 102001.
(5) Qi, X.-L.; Zhang, S.-C. Topological Insulators and Superconductors. *Rev. Mod. Phys.* **2011**, *83*, 1057−1110.
(6) Hasan, M. Z.; Kane, C. L. Colloquium: Topological Insulators. *Rev. Mod. Phys.* **2010**, *82*, 3045−3067.
(7) Moore, J. E. The Birth of Topological Insulators. *Nature* **2010**, *464*, 194−198.
(8) Chen, Y. L.; Analytis, J. G.; Chu, J.-H.; Liu, Z. K.; Mo, S.-K.; Qi, X. L.; Zhang, H. J.; Lu, D. H.; Dai, X.; Fang, Z.; et al. Experimental Realization of a Three-Dimensional Topological Insulator, Bi_2Te_3. *Science* **2009**, *325*, 178−181.
(9) Zhang, H.; Liu, C.-X.; Qi, X.-L.; Dai, X.; Fang, Z.; Zhang, S.-C. Topological Insulators in Bi_2Se_3, Bi_2Te_3 and Sb_2Te_3 with a Single Dirac Cone on the Surface. *Nat. Phys.* **2009**, *5*, 438.
(10) Xia, Y.; Qian, D.; Hsieh, D.; Wray, L.; Pal, A.; Lin, H.; Bansil, A.; Grauer, D.; Hor, Y. S.; Cava, R. J.; et al. Observation of a Large-Gap Topological-Insulator Class with a Single Dirac Cone on the Surface. *Nat. Phys.* **2009**, *5*, 398.
(11) Hsieh, D.; Xia, Y.; Qian, D.; Wray, L.; Dil, J. H.; Meier, F.; Osterwalder, J.; Patthey, L.; Checkelsky, J. G.; Ong, N. P.; et al. A

DOI: 10.1021/acs.jpcc.9b03450
J. Phys. Chem. C 2019, 123, 17829−17841

Tunable Topological Insulator in the Spin Helical Dirac Transport Regime. *Nature* **2009**, *460*, 1101−1105.
(12) Wray, L. A.; Xu, S.-Y.; Xia, Y.; Hsieh, D.; Fedorov, A. V.; Hor, Y. S.; Cava, R. J.; Bansil, A.; Lin, H.; Hasan, M. Z. A Topological Insulator Surface under Strong Coulomb, Magnetic and Disorder Perturbations. *Nat. Phys.* **2011**, *7*, 32−37.
(13) Wang, E.; Tang, P.; Wan, G.; Fedorov, A. V.; Miotkowski, I.; Chen, Y. P.; Duan, W.; Zhou, S. Robust Gapless Surface State and Rashba-Splitting Bands upon Surface Deposition of Magnetic Cr on Bi_2Se_3. *Nano Lett.* **2015**, *15*, 2031−2036.
(14) Caputo, M.; Panighel, M.; Lisi, S.; Khalil, L.; Santo, G. D.; Papalazarou, E.; Hruban, A.; Konczykowski, M.; Krusin-Elbaum, L.; Aliev, Z. S.; et al. Manipulating the Topological Interface by Molecular Adsorbates: Adsorption of Co-Phthalocyanine on Bi_2Se_3. *Nano Lett.* **2016**, *16*, 3409−3414.
(15) Schoop, L. M.; Pielnhofer, F.; Lotsch, B. V. Chemical Principles of Topological Semimetals. *Chem. Mater.* **2018**, *30*, 3155−3176.
(16) Kong, D.; Dang, W.; Cha, J. J.; Li, H.; Meister, S.; Peng, H.; Liu, Z.; Cui, Y. Few-Layer Nanoplates of Bi_2Se_3 and Bi_2Te_3 with Highly Tunable Chemical Potential. *Nano Lett.* **2010**, *10*, 2245−2250.
(17) Otrokov, M. M.; Chulkov, E. V.; Arnau, A. Breaking Time-Reversal Symmetry at the Topological Insulator Surface by Metal-Organic Coordination Networks. *Phys. Rev. B* **2015**, *92*, 165309.
(18) Pia, A. D.; Lisi, S.; Luca, O. D.; Warr, D. A.; Lawrence, J.; Otrokov, M. M.; Aliev, Z. S.; Chulkov, E. V.; Agostino, R. G.; Arnau, A.; et al. TCNQ Physisorption on the Topological Insulator Bi_2Se_3. *ChemPhysChem* **2018**, *19*, 2405−2410.
(19) Förster, T.; Krüger, P.; Rohlfing, M. Ab initio Studies of Adatom- and Vacancy-Induced Band Bending in Bi_2Se_3. *Phys. Rev. B* **2015**, *91*, No. 035313.
(20) Farias, D.; Rieder, K.-H. Atomic Beam Diffraction from Solid Surfaces. *Rep. Prog. Phys.* **1998**, *61*, 1575.
(21) Riley, D. J.; Jardine, A. P.; Dworski, S.; Alexandrowicz, G.; Fouquet, P.; Ellis, J.; Allison, W. A Refined He-LiF(001) Potential from Selective Adsorption Resonances Measured with High-Resolution Helium Spin-Echo Spectroscopy. *J. Chem. Phys* **2007**, *126*, 104702.
(22) Jardine, A. P.; Dworski, S.; Fouquet, P.; Alexandrowicz, G.; Riley, D. J.; Lee, G. Y. H.; Ellis, J.; Allison, W. Ultrahigh-Resolution Spin-Echo Measurement of Surface Potential Energy Landscapes. *Science* **2004**, *304*, 1790.
(23) Hoinkes, H. The Physical Interaction Potential of Gas Atoms with Single-Crystal Surfaces, Determined from Gas-Surface Diffraction Experiments. *Rev. Mod. Phys.* **1980**, *52*, 933−970.
(24) Eichenauer, D.; Toennies, J. P. Pairwise Additive Potential Models for the Interaction of He Atoms with the (001) Surfaces of LiF, NaF, NaCl and LiCl. *Surf. Sci.* **1988**, *197*, 267−276.
(25) Benedek, G.; Brusdeylins, G.; Senz, V.; Skofronick, J. G.; Toennies, J. P.; Traeger, F.; Vollmer, R. Helium Atom Scattering Study of the Surface Structure and Dynamics of in situ Cleaved MgO(001) Single Crystals. *Phys. Rev. B* **2001**, *64*, 125421.
(26) Debiossac, M.; Zugarramurdi, A.; Lunca-Popa, P.; Momeni, A.; Khemliche, H.; Borisov, A. G.; Roncin, P. Transient Quantum Trapping of Fast Atoms at Surfaces. *Phys. Rev. Lett.* **2014**, *112*, No. 023203.
(27) Tuddenham, F. E.; Hedgeland, H.; Knowling, J.; Jardine, A. P.; MacLaren, D. A.; Alexandrowicz, G.; Ellis, J.; Allison, W. Linewidths in Bound State Resonances for Helium Scattering from Si(111)-(1×1)H. *J. Phys.: Condens. Matter* **2009**, *21*, 264004.
(28) Kraus, P.; Tamtögl, A.; Mayrhofer-Reinhartshuber, M.; Benedek, G.; Ernst, W. E. Resonance-Enhanced Inelastic He-Atom Scattering from Subsurface Optical Phonons of Bi(111). *Phys. Rev. B* **2013**, *87*, 245433.
(29) Mayrhofer-Reinhartshuber, M.; Kraus, P.; Tamtögl, A.; Miret-Artés, S.; Ernst, W. E. Helium-Surface Interaction Potential of Sb(111) from Scattering Experiments and Close-Coupling Calculations. *Phys. Rev. B* **2013**, *88*, 205425.
(30) Brivio, G. P.; Trioni, M. I. The Adiabatic Molecule−Metal Surface Interaction: Theoretical Approaches. *Rev. Mod. Phys.* **1999**, *71*, 231−265.
(31) Martínez-Casado, R.; Usvyat, D.; Maschio, L.; Mallia, G.; Casassa, S.; Ellis, J.; Schütz, M.; Harrison, N. M. Approaching an Exact Treatment of Electronic Correlations at Solid Surfaces: The Binding Energy of the Lowest Bound State of Helium Adsorbed on MgO(100). *Phys. Rev. B* **2014**, *89*, 205138.
(32) de Lara-Castells, M. P.; Fernández-Perea, R.; Madzharova, F.; Voloshina, E. Post-Hartree-Fock Studies of the He/Mg(0001) Interaction: Anti-Corrugation, Screening, and Pairwise Additivity. *J. Chem. Phys* **2016**, *144*, 244707.
(33) Wu, X.; Vargas, M. C.; Nayak, S.; Lotrich, V.; Scoles, G. Towards Extending the Applicability of Density Functional Theory to Weakly Bound Systems. *J. Chem. Phys.* **2001**, *115*, 8748−8757.
(34) Jean, N.; Trioni, M. I.; Brivio, G. P.; Bortolani, V. Corrugating and Anticorrugating Static Interactions in Helium-Atom Scattering from Metal Surfaces. *Phys. Rev. Lett.* **2004**, *92*, No. 013201.
(35) Martinez-Casado, R.; Usvyat, D.; Mallia, G.; Maschio, L.; Casassa, S.; Ellis, J.; Schütz, M.; Harrison, N. M. Diffraction of Helium on MgO(100) Surface Calculated from First-Principles. *Phys. Chem. Chem. Phys.* **2014**, *16*, 21106−21113.
(36) Tamtögl, A.; Bahn, E.; Zhu, J.; Fouquet, P.; Ellis, J.; Allison, W. Graphene on Ni(111): Electronic Corrugation and Dynamics from Helium Atom Scattering. *J. Phys. Chem. C* **2015**, *119*, 25983−25990.
(37) Kraus, P.; Tamtögl, A.; Mayrhofer-Reinhartshuber, M.; Apolloner, F.; Gösweiner, C.; Miret-Artés, S.; Ernst, W. E. Surface Structure of Bi(111) from Helium Atom Scattering Measurements. Inelastic Close-Coupling Formalism. *J. Phys. Chem. C* **2015**, *119*, 17235−17242.
(38) del Cueto, M.; Muzas, A. S.; Füchsel, G.; Gatti, F.; Martín, F.; Díaz, C. Role of van der Waals Forces in the Diffraction of Noble Gases from Metal Surfaces. *Phys. Rev. B* **2016**, *93*, No. 060301.
(39) del Cueto, M.; Maurer, R.; Taleb, A. A.; Farías, D.; Martín, F.; Díaz, C. Performance of van der Waals DFT approaches for helium diffraction on metal surfaces. *J. Phys.: Condens. Matter* **2019**, *31*, 135901.
(40) Tamtögl, A.; Campi, D.; Bremholm, M.; Hedegaard, E. M. J.; Iversen, B. B.; Bianchi, M.; Hofmann, P.; Marzari, N.; Benedek, G.; Ellis, J.; et al. Nanoscale Surface Dynamics of $Bi_2Te_3(111)$: Observation of a Prominent Surface Acoustic Wave and the Role of van der Waals Interactions. *Nanoscale* **2018**, *10*, 14627−14636.
(41) Tamtögl, A.; Mayrhofer-Reinhartshuber, M.; Balak, N.; Ernst, W. E.; Rieder, K. H. Elastic and Inelastic Scattering of He Atoms from Bi(111). *J. Phys.: Condens. Matter* **2010**, *22*, 304019.
(42) Bianchi, M.; Hatch, R. C.; Guan, D.; Planke, T.; Mi, J.; Iversen, B. B.; Hofmann, P. The Electronic Structure of Clean and Adsorbate-Covered Bi_2Se_3: an Angle-Resolved Photoemission Study. *Semicond. Sci. Technol.* **2012**, *27*, 124001.
(43) Tamtögl, A.; Carter, E. A.; Ward, D. J.; Avidor, N.; Kole, P. R.; Jardine, A. P.; Ellis, J.; Allison, W. Note: A Simple Sample Transfer Alignment for Ultra-High Vacuum Systems. *Rev. Sci. Instrum.* **2016**, *87*, No. 066108.
(44) Chen, X.; Zhou, H. D.; Kiswandhi, A.; Miotkowski, I.; Chen, Y. P.; Sharma, P. A.; Lima Sharma, A. L.; Hekmaty, M. A.; Smirnov, D.; Jiang, Z. Thermal Expansion Coefficients of i_2Se_3 and Sb_2Te_3 Crystals from 10 K to 270 K. *Appl. Phys. Lett.* **2011**, *99*, 261912.
(45) Tamtögl, A.; Kraus, P.; Avidor, N.; Bremholm, M.; Hedegaard, E. M. J.; Iversen, B. B.; Bianchi, M.; Hofmann, P.; Ellis, J.; Allison, W.; et al. Electron-Phonon Coupling and Surface Debye Temperature of $Bi_2Te_3(111)$ from Helium Atom Scattering. *Phys. Rev. B* **2017**, *95*, 195401.
(46) Ruckhofer, A. Surface Dynamics of the Topological Insulator Bi_2Se_3 from Helium Atom Scattering. M.Sc. Thesis, Graz University of Technology, 2017.
(47) Kraus, P.; Mayrhofer-Reinhartshuber, M.; Gösweiner, C.; Apolloner, F.; Miret-Artés, S.; Ernst, W. E. A Comparative Study of the He-Sb(111) Interaction Potential from Close-Coupling Calcu-

DOI: 10.1021/acs.jpcc.9b03450
J. Phys. Chem. C 2019, 123, 17829−17841

lations and Helium Atom Scattering Experiments. *Surf. Sci.* **2014**, *630*, 208−215.
(48) Tamtögl, A.; Pusterhofer, M.; Bremholm, M.; Hedegaard, E. M. J.; Iversen, B. B.; Hofmann, P.; Ellis, J.; Allison, W.; Miret-Artés, S.; Ernst, W. E. A Helium-Surface Interaction Potential of Bi_2Te_3(111) from Ultrahigh-Resolution Spin-Echo Measurements. *Surf. Sci.* **2018**, *678*, 25−31.
(49) Anemone, G.; Taleb, A. A.; Benedek, G.; Castellanos-Gomez, A.; Farías, D. Electron−Phonon Coupling Constant of 2H-MoS_2(0001) from Helium-Atom Scattering. *J. Phys. Chem. C* **2019**, *123*, 3682−3686.
(50) Armand, G.; Manson, J. R. Scattering of Neutral Atoms by a Periodic Potential : the Morse Corrugated Potential. *J. Phys. France* **1983**, *44*, 473−487.
(51) Hutchison, J. S. Effect of Inelastic Scattering on the Resonance Line Shapes in He-Graphite. *Phys. Rev. B* **1980**, *22*, 5671−5678.
(52) Tamtögl, A.; Kraus, P.; Mayrhofer-Reinhartshuber, M.; Benedek, G.; Bernasconi, M.; Dragoni, D.; Campi, D.; Ernst, W. E. Statics and Dynamics of Multivalley Charge Density Waves in Sb(111). *npj Quantum Mater.* **2019**, *4*, 28.
(53) Campi, D.; Bernasconi, M.; Benedek, G. Ab-Initio Calculation of Surface Phonons at the Sb_2Te_3(111) Surface. *Surf. Sci.* **2018**, *678*, 46−51.
(54) Ruckhofer, A.; Campi, D.; Pusterhofer, M.; Bremholm, M.; Hofmann, P.; Benedek, G.; Ernst, W. E.; Tamtögl, A. THz Surface Modes and Electron-Phonon Coupling in Bi_2Se_3(111). 2019, unpublished.
(55) Frantzeskakis, E.; Ramankutty, S. V.; de Jong, N.; Huang, Y. K.; Pan, Y.; Tytarenko, A.; Radovic, M.; Plumb, N. C.; Shi, M.; Varykhalov, A.; et al. Trigger of the Ubiquitous Surface Band Bending in 3D Topological Insulators. *Phys. Rev. X* **2017**, *7*, No. 041041.
(56) Sanz, A.; Miret-Artés, S. Selective Adsorption Resonances: Quantum and Stochastic Approaches. *Phys. Rep.* **2007**, *451*, 37−154.
(57) Martínez-Casado, R.; Meyer, B.; Miret-Artés, S.; Traeger, F.; Wöll, C. Diffraction Patterns of He Atoms from the MgO(100) Surface Calculated by the Close-Coupling Method. *J. Phys.: Condens. Matter* **2007**, *19*, 305006.
(58) Guantes, R.; Borondo, F.; Margalef-Roig, J.; Miret-Artés, S.; Manson, J. R. Threshold Resonances in Classical Chaotic Atom-Surface Scattering. *Surf. Sci.* **1997**, *375*, L379−L384.
(59) Zhao, B. S.; Zhang, W.; Schöllkopf, W. Universal diffraction of Atoms and Molecules from a Quantum reflection Grating. *Sci. Adv.* **2016**, *2*, No. e1500901.
(60) Miret-Artés, S. Resonant Inelastic Scattering of Atoms from Surfaces. *Surf. Sci.* **1995**, *339*, 205−220.
(61) Miret-Artés, S. Elementary Resonance Processes in Atom-Surface Scattering. *Surf. Sci.* **1996**, *366*, L735−L741.
(62) Šiber, A.; Gumhalter, B. Phonon-Mediated Bound State Resonances in Inelastic Atom−Surface Scattering. *J. Phys.: Condens. Matter* **2008**, *20*, 224002.
(63) Pendry, J. B. Reliability Factors for LEED Calculations. *J. Phys. C* **1980**, *13*, 937−944.
(64) Lee, G. Y. H. Resonant Scattering of Helium Atoms from Corrugated Surfaces. Ph.D. Thesis, University of Cambridge, 2004.
(65) Anderson, T. L.; Krause, H. B. Refinement of the Sb_2Te_3 and Sb_2Te_2Se Structures and their Relationship to Nonstoichiometric $Sb_2Te_{3-y}S_{ey}$ compounds. *Acta Crystallgr., Sect. B: Struct. Crystallogr. Cryst. Chem.* **1974**, *30*, 1307−1310.
(66) West, D.; Sun, Y. Y.; Wang, H.; Bang, J.; Zhang, S. B. Native Defects in Second-Generation Topological Insulators: Effect of Spin-Orbit Interaction on Bi_2Se_3. *Phys. Rev. B* **2012**, *86*, 121201.
(67) Suh, J.; Fu, D.; Liu, X.; Furdyna, J. K.; Yu, K. M.; Walukiewicz, W.; Wu, J. Fermi-Level Stabilization in the Topological Insulators Bi_2Se_3 and Bi_2Te_3: Origin of the Surface Electron Gas. *Phys. Rev. B* **2014**, *89*, 115307.
(68) Brusdeylins, G.; Doak, R. B.; Toennies, J. P. Observation of Selective Desorption of One-Phonon Inelastically Scattered He atoms from a LiF Crystal Surface. *J. Chem. Phys* **1981**, *75*, 1784−1793.
(69) Hernández, M. I.; Campos-Martínez, J.; Miret-Artés, S.; Coalson, R. D. Lifetimes of Selective-Adsorption Resonances in Atom-Surface Elastic Scattering. *Phys. Rev. B* **1994**, *49*, 8300−8309.
(70) Pan, F. M.; Pflitsch, C.; David, R.; Verheij, L. K.; Franchy, R. Reconstruction of the CoGa(100) Surface Studied by Thermal-Energy Helium-Atom Scattering, LEED, and AES. *Phys. Rev. B* **2001**, *63*, 125414.
(71) Jeon, J. H.; Jang, W. J.; Yoon, J. K.; Kahng, S.-J. Metal-Supported High Crystalline Bi_2Se_3 Quintuple Layers. *Nanotechnology* **2011**, *22*, 465602.
(72) Benedek, G.; Toennies, J. P. *Atomic Scale Dynamics at Surfaces: Theory and Experimental Studies with Helium Atom Scattering*; Springer Berlin Heidelberg: Berlin, Heidelberg, 2018, pp 441−486.
(73) Zhang, G.; Qin, H.; Teng, J.; Guo, J.; Guo, Q.; Dai, X.; Fang, Z.; Wu, K. Quintuple-Layer Epitaxy of Thin Films of Topological Insulator Bi_2Se_3. *Appl. Phys. Lett.* **2009**, *95*, No. 053114.
(74) Borisova, S.; Kampmeier, J.; Luysberg, M.; Mussler, G.; Grützmacher, D. Domain Formation Due to Surface Steps in Topological Insulator Bi_2Te_3 Thin Films Grown on Si (111) by Molecular Beam Epitaxy. *Appl. Phys. Lett.* **2013**, *103*, No. 081902.
(75) Hewitt, A. S.; Wang, J.; Boltersdorf, J.; Maggard, P. A.; Dougherty, D. B. Coexisting Bi and Se Surface Terminations of Cleaved Bi_2Se_3 Single Crystals. *J. Vac. Sci. Technol.* **2014**, *32*, No. 04E103.
(76) Hermanowicz, M.; Koczorowski, W.; Bazarnik, M.; Kopciuszyński, M.; Zdyb, R.; Materna, A.; Hruban, A.; Czajka, R.; Radny, M. W. Stable Bismuth Sub-Monolayer Termination of Bi_2Se_3. *Appl. Surf. Sci.* **2019**, *476*, 701−705.

DOI: 10.1021/acs.jpcc.9b03450
J. Phys. Chem. C 2019, 123, 17829−17841

6.13 Publication M

Tamtögl, A., Kraus, P., Mayrhofer-Reinhartshuber, M., Benedek, G., Bernasconi, M., Dragoni, D., Campi, D. & Ernst, W. E. Statics and dynamics of multivalley charge density waves in Sb(111). *npj Quantum Mater.* **4,** 28 (2019)

contributions	
funding	G. Benedek, W. E. Ernst
preparation / setup	A. Tamtögl, M. Mayrhofer-Reinhartshuber
data acquisition	A. Tamtögl, M. Mayrhofer-Reinhartshuber
data analysis	A. Tamtögl, P. Kraus
interpretation	A. Tamtögl, P. Kraus, G. Benedek
theory (*ab initio*) calculations	D. Dragoni, D. Campi, M. Bernasconi
publication writing	A. Tamtögl, G. Benedek

Reprinted from:

Tamtögl, A., Kraus, P., Mayrhofer-Reinhartshuber, M., Benedek, G., Bernasconi, M., Dragoni, D., Campi, D. & Ernst, W. E. Statics and dynamics of multivalley charge density waves in Sb(111). *npj Quantum Mater.* **4,** 28 (2019)

npj | Quantum Materials

www.nature.com/npjquantmats

ARTICLE OPEN

Statics and dynamics of multivalley charge density waves in Sb (111)

Anton Tamtögl[1], Patrick Kraus[1], Michael Mayrhofer-Reinhartshuber[1], Giorgio Benedek[2,3], Marco Bernasconi[3], Daniele Dragoni[3], Davide Campi[3,4] and Wolfgang E. Ernst[1]

Charge density waves (CDWs), periodic modulations of the charge density, are among the most abundant and non-trivial ordered phases in condensed matter. Here we demonstrate the occurrence of multi-valley charge density waves (MV-CDW) on the semimetal Sb(111), a phenomenon previously observed at semiconductor surface inversion layers. The topological nature of the pocket surface states in Sb(111) ensures perfect nesting conditions giving rise to sharp peaks in helium atom scattering (HAS) diffraction spectra. The peculiar temperature dependence permits to distinctly associate the diffraction peaks with surface electron and hole-pocket states due to the non-trivial surface electronic band structure known from recent experimental data and present ab-initio calculations. Inelastic HAS spectra, besides providing the surface phonon dispersion curves in agreement with density functional perturbation theory calculations, reveal two additional dispersion curves of elementary excitations in the gap well below Rayleigh waves. They are attributed to collective excitations of the quasi-commensurate MV-CDWs associated with the surface electron M-pocket states at the Fermi level. These findings suggest that HAS can be regarded as a choice spectroscopy for the investigation of surface electronic excitations in the THz domain, opening up a new window for the search of collective phases at surfaces.

npj Quantum Materials (2019)4:28 ; https://doi.org/10.1038/s41535-019-0168-x

INTRODUCTION

Fermi level multivalley states occurring around distinct wavevectors of some semimetal surfaces provide a basis for the occurrence of charge density waves (CDWs).[1–3] The mechanism of multivalley CDWs at semiconductor surfaces, first described by Kelly and Falicov in the 70 s is conceptually similar to that of 1D Peierls CDWs.[4] Both mechanisms are based on an almost perfect nesting between states with wavevectors **k** concentrated around well-defined values at the Fermi level. In the ordinary two (three)-dimensional case, where nesting is defined by stationary diameters across the Fermi contour (surface), fluctuations admix states with any Δ**k** connecting the continuum of states at the Fermi level. In multivalley systems with narrow pockets, fluctuations can only mix states with Δ**k** either very small or close to the intervalley nesting vectors, thus making intervalley CDWs more robust against fluctuations. Notably, in semiconductors and semimetals the Fermi level shifts substantially with temperature, so that the critical behaviour of a multivalley CDW is not just a matter of fluctuations as for ordinary CDWs. In addition, multivalley CDWs are generally, albeit not necessarily, stabilised by electron–phonon (e–ph) interaction.[3,5–7]

Helium atom scattering (HAS) has been recently recognised as a powerful tool to investigate the mode-selected e–ph interaction at the surface of conducting or highly polarisable surfaces.[8–10] The ability relies on the fact that the exchange of energy and parallel momentum between the neutral probe atom and the atoms of the solid can only occur via the interposed surface electrons whose wave functions extend outward up to the scattering atom turning point. More precisely the inelastic-scattering amplitudes from surface phonons are proportional to the phonon-induced surface charge density oscillations, and therefore to the mode-selected e–ph interaction.[9,11]

Given this mechanism, a natural question is whether the energy and parallel momentum provided by the atom can be retained by low-energy surface electronic excitations, rather than being transmitted to phonons, and reveal their dispersion curves. Since the band structure at the Fermi level of semimetal surfaces like Bi (111) and Sb(111) is characterised by sets of narrow surface electron and hole pockets in the reciprocal space,[12–14] multivalley CDWs are expected to be observed in HAS diffraction patterns.

The high sensitivity of HAS to CDWs as compared to other surface probes allowing for a precise determination of the transition temperatures and critical exponents was demonstrated long ago for layered chalcogenides[15,16] as well as recently for the 1D topological metal Bi(114).[17] The observation of phason dispersion curves with HAS was previously reported for the long-period reconstruction of the Au(111) $23\times\sqrt{3}$ surface[18] and another hint comes from the non-adiabatic Kohn-anomalies observed for Mo(110):H and W(110):H[19–22] which are associated with electron–hole pair excitations. However, a signature of collective surface electronic excitations in elastic atom–surface scattering spectra has remained missing up to date.

With regard to the ideal surfaces, there is some consensus about whether CDWs can exist in Bi(111),[12,13] whereas they seemed to be excluded in Sb(111).[13] On the other hand the

[1]Institute of Experimental Physics, Graz University of Technology, Graz, Austria; [2]Donostia International Physics Center (DIPC), Donostia/San Sebastián, Spain; [3]Dipartimento di Scienza dei Materiali, Università degli Studi di Milano-Bicocca, Milano, Italy and [4]Theory and Simulation of Materials (THEOS) and National Centre for Computational Design and Discovery of Novel Materials (MARVEL), École Polytechnique Fédérale de Lausanne, CH-1015 Lausanne, Switzerland
Correspondence: Anton Tamtögl (tamtoegl@gmail.com)

Received: 23 April 2018 Accepted: 22 May 2019
Published online: 12 June 2019

Published in partnership with Nanjing University

npj nature partner journals

spin–orbit (SO) coupling, which makes Sb(111) a weak topological insulator with spin-split bands around the zone centre,[23] can in principle support a spin-density wave.[14]

Here we show that the spin-selected nesting between the states of narrow pockets at the Fermi level, peculiar of topological semimetals, yields sharp features in the HAS diffraction spectra corresponding to multivalley CDWs, and clear signatures of collective phase and amplitude CDW excitations in the THz spectral region. Inelastic HAS measurements on Sb(111) at two different temperatures reveal two additional branches in the gap below the Rayleigh wave branch. On the basis of density functional perturbation theory (DFPT) calculations of the surface phonon dispersion curves of Sb(111),[23] it appears that the two low-energy branches cannot be attributed to any possible phonon branch of the ideal surface. Their dispersion curves appear to be compatible with the Brillouin zone (BZ) of the commensurate surface electron CDW lattice, which suggests their assignment to a phason/ampliton pair.

Sb(111) exhibits a rhombohedral crystal structure (A7, space group $R\bar{3}m$), where atoms are arranged in bilayers normal to the [111]-direction.[24,25] Intralayer bonding is mostly covalent, whereas bilayers are held together by weaker interactions which permits an easy cleavage, giving rise to the hexagonal surface unit cell of Sb(111) with a lattice constant $a = 4.308$ Å[26] (see Fig. 1b).

There are no significant changes in terms of the structure upon truncation of bulk Sb,[26,27] in contrast to the electronic properties, which change significantly depending on the crystal thickness. While bulk Sb(111) is a topological semimetal,[28,29] Sb thin films are predicted to become a topological insulator at a thickness under 22 layers, to exhibit a quantum spin Hall phase below 8 layers[28,30] and finally to be a semiconductor at bilayer thickness.[31,32] For a bismuth monolayer lattice on top of an insulator, a quantum spin hall phase at room temperature has also been recently predicted.[33]

A previous HAS analysis of the surface structure, step height, and terrace distribution of Sb(111) provided a surface corrugation of about 13% of the lattice constant, and confirmed the occurrence of bilayer steps, with 14% of specular reflection from surface portions including one-bilayer step, and only 2% from two-bilayer steps.[34] For a HAS coherence length of the order of 50 Å the terrace width can be estimated based on the width of the specular peak, with 40–80 nm throughout several scans.[35]

RESULTS

Elastic scattering

Figure 1c shows three HAS diffraction patterns of Sb(111) plotted versus the parallel momentum transfer ΔK. For elastic scattering ΔK is given by:

$$\Delta K = |\mathbf{k_i}|(\sin\vartheta_f - \sin\vartheta_i) \quad (1)$$

with $\mathbf{k_i}$, the incident wave vector, and ϑ_i and ϑ_f the incident and final angle with respect to the surface normal, respectively (see Fig. 1a). Figure 1c shows scans along the $\overline{\Gamma K}$ azimuth plotted versus ΔK, measured for an incident energy E_i varying between 11.85 and 22 meV and three different surface temperatures T_S from 121 to 405 K. The intensity scale has been expanded to show additional features with smaller intensity. Besides some features assigned to bound-state resonances (e.g. the peak R) and kinematical focusing (KF), which are easily recognised due to the strong dependence of their position on the incident energy,[36] there are features that occur at fixed values of ΔK, independently of the incident energy, and are therefore assigned to elastic diffraction processes, just as the two main diffraction peaks at $\Delta K = \pm 2.90$ Å^{-1} corresponding to the periodicity of the surface atomic lattice. The additional weaker diffraction peaks occur at $\Delta K = \pm 1.45$ Å^{-1} and $\Delta K = \pm 0.3$ Å^{-1} (with an uncertainty of about ± 0.04 Å^{-1}).

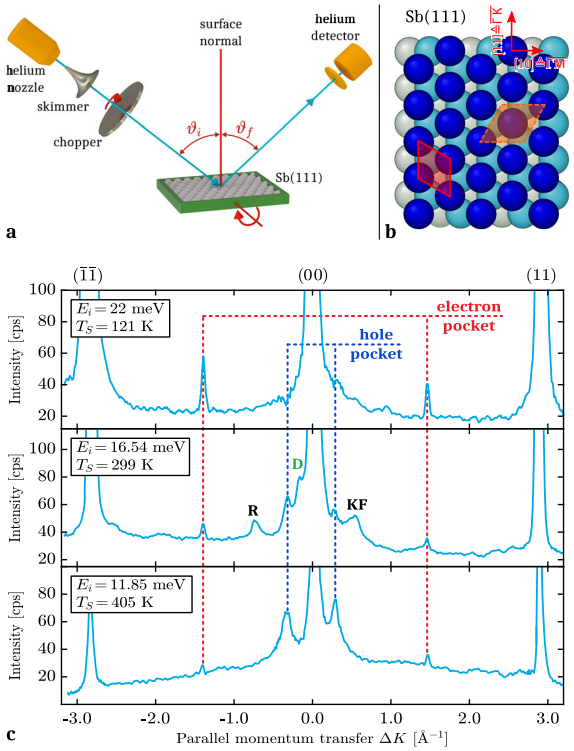

Fig. 1 Measurement principle and diffraction scans showing the CDW periodicity. **a** Schematic overview of the apparatus. A supersonic helium beam is produced in a source chamber, before scattering from the Sb(111) sample. The scattered beam is detected in a mass-spectrometer detector. Momentum transfer ΔK occurs due to scattering of the He beam from the crystal, at a certain incident angle ϑ_i, through a fixed total scattering angle. Energy resolution is optionally added by chopping the He beam with a chopper and measuring the time-of-flight. **b** The crystal structure of Sb(111) showing the first bilayer (dark and light blue atoms) and the first atomic plane of the second bilayer (grey atoms), with the surface unit cell (full line; lattice constant $a = 4.308$ Å) and the $(2/\sqrt{3} \times 2/\sqrt{3})$R30° surface unit cell of the electron pocket multi-valley CDW (broken line; CDW lattice constant $a_{CDW} = 2a/\sqrt{3}$). **c** Diffraction scans for Sb(111) along the $\overline{\Gamma K}$ azimuth for different surface temperatures and beam energies. The vertical-dashed lines show the momentum transfers corresponding to the interpocket transitions as illustrated in Fig. 2. Note the slight shift to smaller absolute values of ΔK of the hole-pocket peaks with increasing T_S. The small peak D corresponds to transitions between equivalent spots on the Dirac ring

The intensity of the sharp peaks at $\Delta K = \pm 1.45$ Å^{-1} falling at one half of the **G**-vector along $\overline{\Gamma K}$ decreases rapidly with temperature, faster than for the ordinary specular and diffraction peaks[37] (see also the SI for an analysis of the temperature dependence). It might also be associated with a surface reconstruction disappearing above a certain temperature, however, the temperature dependence in Fig. 1c is inconsistent with that scenario. The intensity of the satellite diffraction peaks at ± 0.3 Å^{-1} increases with temperature, contrary to the expected Debye–Waller attenuation. Since HAS is basically diffracted by the surface electron charge density, the interpretation of such superstructure should be searched for in the peculiar surface electronic structure of Sb(111) which is characterised by narrow electron and hole pockets at the Fermi level,[13,38] potentially responsible for the presence of CDWs.

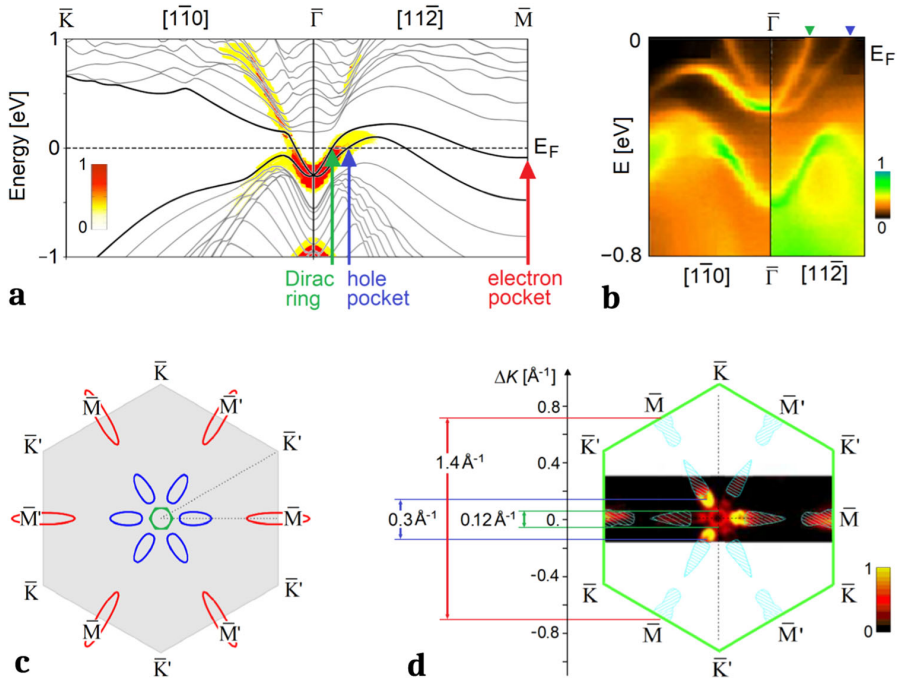

Fig. 2 Surface electronic band structure of Sb(111) together with an illustration of the interpocket transitions. **a** Details of the surface electronic band structure of Sb(111) calculated with DFT-SO showing the two surface spin-split bands in the $\overline{\Gamma M}$ direction and a portion along $\overline{\Gamma K}$. The colour shadows give the degree of surface localisation and linewidths. At the Fermi level the surface bands form a quasi-isotropic electron pocket at $\bar{\Gamma}$ (Dirac ring) and along $\overline{\Gamma M}$ an elongated hole pocket, with a pronounced surface character at small wavevectors, and another electron pocket centred at the $\bar{M}$-point. **b** Laser-based ARPES band profiles measured by Xie et al.[39] show excellent agreement with the calculated band structure in a. **c** Calculated pocket Fermi contours: The orientations of pocket hole and electron spins depend on whether pockets are in the $\overline{\Gamma M}$ or the $\overline{\Gamma M}'$ direction. The removal of spin degeneracy lowers the surface hexagonal symmetry to trigonal. **d** ARPES data by Sugawara et al.[13] (reproduced with permission, copyright 2006 by the American Physical Society). Pockets with the same spin show intense spots, reflecting the trigonal symmetry, in closer agreement with the theoretical positions, and shapes shown in c than with bulk LAPW-LDA calculations reported by Sugawara et al.[13] (light blue contours shown in panel d). Similar results have been reported by Xie et al.[39] The interpocket transitions in the $\overline{\Gamma K}$ direction and the respective ΔK values corresponding to the peaks in the diffraction spectrum of Fig. 1c are indicated as double arrows in **d**

The diffraction patterns along the $\overline{\Gamma M}$ direction[36] (not reported here) show prominent features, besides the specular and diffraction peaks, which can all be assigned to bound-state resonances or kinematical focusing, from their dependence on the incident energy. Only a weak feature at $-3G/2 \approx -2.6$ Å^{-1} (but not at $+3G/2$) appears to be persistent for varying incident energy, and is also vanishing for increasing temperature like that at $G/2$ along $\overline{\Gamma K}$. The following analysis shows that the peculiar surface electronic structure of Sb(111) explains the HAS diffraction patterns measured at different surface temperatures in the $\overline{\Gamma K}$ direction.

Surface electronic structure of Sb(111)

The electronic surface states of Sb(111) have been analysed previously by Höchst and Ast[38] and by Sugawara et al.[13] with angle-resolved photoemission spectroscopy (ARPES) and later by Xie et al. with laser-based ARPES.[39] Sb(111) exhibits a non-trivial surface electronic structure as seen in the DFT calculations including SO coupling of the band structure around the Fermi level depicted in Fig. 2a. It appears that, starting from a Dirac point at the zone centre ($\bar{\Gamma}$), two spin-split surface bands generate a narrow electron pocket at $\bar{\Gamma}$, a hole pocket in each of the six $\overline{\Gamma M}$ directions and another electron pocket at the six $\bar{M}$ symmetry points. The corresponding Fermi contours at the Fermi level are shown in Fig. 2c. They are found in excellent agreement with Xie et al. laser-based ARPES[39] (Fig. 2b) and Sugawara et al. ARPES data[13] (Fig. 2d).

As seen in Fig. 2d, in addition to the quasi-hexagonal Dirac ring around $\bar{\Gamma}$ (radius ≈0.07 Å^{-1}), high-intensity spots from the pocket states crossing the Fermi level are observed in the $\overline{\Gamma M}$ directions as described by DFT calculations, corresponding to hole pockets and electron pockets with maximum intensity at $\bar{M}$. As appears in Fig. 2a the hole-pocket states have a prominent surface density of states (DOS) around the edge at $K_h \approx 0.15$ Å^{-1} in good agreement with ARPES observation in Fig. 2d.

The presence of electron pockets at the $\bar{M}$-points and of hole-pockets at $\approx \overline{\Gamma M}/4$, and the close correspondence between the positions of the additional diffraction peaks and the corresponding intervalley separations ΔK in the $\overline{\Gamma K}$ direction is a compelling evidence for multi-valley CDWs. As shown by Kelly and Falicov[1], this is possible, provided the electron–phonon contribution to the intervalley exchange interaction is sufficiently strong. The authors remark that "the electron–electron interaction, via phonons is known to be the dominant intervalley exchange effect; it leads to superconductivity in some many-valley degenerate semiconductors,[40] but is large and attractive even in materials which are not superconducting". The antimony (111) surface clearly belongs to this family.

The basic mechanism for the formation of a multivalley CDW associated with the electron pockets at the $\bar{M}$-points ($K = G/2$) can be understood by considering the three degenerate free-electron pocket states of equal spin at the Fermi level exp[iKx] and exp[iK

$(x/2 \pm \sqrt{3}y/2)]$ with $K = G/2$ and their three linear combinations A, E_1, and E_2 dictated by the crystal point symmetry. The density associated to each linear combination shows a CDW modulation, whereas their sum with equal weights gives a uniform density. Any perturbation, e.g. electron–phonon interaction causing a splitting of the states, and their different population at finite temperature yields a CDW. A totally symmetric ground state, would give a CDW shape:

$$|\psi_A|^2 \propto \sin^2\left(\tfrac{3Gx}{4}\right) + \left[\cos\left(\tfrac{3Gx}{4}\right) + 2\cos\left(\tfrac{\sqrt{3}Gy}{4}\right)\right]^2. \quad (2)$$

Equation (2) defines a hexagonal surface CDW lattice rotated 30° with respect to the crystal lattice and a lattice constant $a_{CDW} = 2a/\sqrt{3} = 4.97$ Å (Fig. 1b). A similar argument holds for a CDW associated with the hole states, where $K = G/2$ is replaced by K_h. The construction of a CDW originating from the superposition of free-electron waves from electron- and hole-pockets would lead of course to a more complex CDW lattice and a larger period. However, the temperature dependence of the diffraction spectra indicates that at low temperature the hole-pocket states play a negligible role.

The association of the additional diffraction peaks to the electron and hole-pockets stems from the peculiar temperature dependence of their intensities. On the one hand, the hole-pocket peaks increase with surface temperature, unlike ordinary diffraction peak intensities which decrease with increasing T_S. On the other hand, the $\overline{M}$ electron pocket peaks decrease faster than the ordinary diffraction peaks, possibly disappearing at ≈450 K. An analysis of the temperature dependence and the critical exponent based on the corresponding order parameter can be found in the SI. Such an anomalous temperature dependence may be attributed to a downward shift of the Fermi energy for increasing T_S, which has the effect of increasing the DOS in the hole pocket and decreasing that of the $\overline{M}$ electron pockets.

The DFT calculation tells that both pockets are already there at 0 K and the $\overline{M}$ electron pocket minimum is at about −0.1 eV below the Fermi level (Fig. 2a). Thus a temperature increase of ≈450 K which gives rise to the disappearance of the $\overline{M}$ electron pocket peaks, corresponds to a work function change rate of $d\phi/dT_S \approx 0.22$ meV K^{-1}. The value of $d\phi/dT_S$ falls just in the range of other p-band metals, e.g. 0.22 meV K^{-1} for Sn and 0.20 meV K^{-1} for Bi[41] and agrees with measurements of ϕ for Sb thin films at 77 and 300 K giving $d\phi/dT_S \approx 0.18$ meV K^{-1}.[42] The downward shift of the Fermi level is also responsible for the slight shift of the hole-pocket peaks to smaller absolute values of ΔK with increasing temperature (see Fig. 1c).

The above described analysis makes the CDW scenario the most plausible, despite previous indications that no CDW occurs in Sb (111). The fact that the presence of a CDW in Sb(111) has so far gone unnoticed in investigations with other experimental techniques may be explained by the higher sensitivity of HAS to charge density modulations. The smallest charge density modulation Δn detectable with HAS can be estimated based on an energy resolution $\Delta E \approx 1$ meV divided by the Esbjerg–Nørskov constant for low-energy He atoms, $A = 750$ eV/a.u.,[43] yielding $\Delta n \approx 1.3 \times 10^{-6}$ atomic units. Nevertheless, a very recent scanning tunnelling microscopy study[44] has revealed for Sb(111) at a temperature of about 5 K a (2×2) surface structure, which is the minimum periodicity common to the $(2/\sqrt{3} \times 2/\sqrt{3})$R30° CDW and the Sb (111)(1×1) lattice (for a short discussion see the SI, in particular Fig. S5). It follows from the above, that experimental techniques which distinctly probe the charge density over the topmost atomic layer seem to be better suited for the search of surface CDWs compared to techniques which imply some penetration depth into the bulk.

There is however, another possible explanation of the observed diffraction spectra not requiring CDWs: the quasi-elastic collisions of pocket electrons with the flying-by He atom and consequent spin-conserving intervalley transitions. A simple classical calculation conserving total energy and parallel momentum (the atom normal momentum change is as usual absorbed by the crystal center of mass) shows that for an incident He-atom energy of 15 meV, the electron energy for the $\Delta K = \pm 1.4$ Å^{-1} transitions changes by −6.0 and +5.0 meV, respectively. These are small amounts as compared to the Fermi energy relative to the $\overline{M}$-pocket bottom, at least at low temperature, but cause some asymmetry in the two diffraction amplitudes. Some asymmetry is noticed in Fig. 1c, but not at high temperature, where it should be more pronounced. The hole intervalley transitions would imply a much smaller energy transfer of the order of ±1 meV, whereas in the $\overline{\Gamma M}$ direction the $-3G/2$ inter-pocket transition with larger energy transfer would cause large asymmetry, perhaps explaining the absence of the $+3G/2$ spot. It should be noted that in this direction the shortest inter-pocket transitions $\Delta K = \pm G/2$ would be spin forbidden and the same would hold for $\Delta K = \pm 3G/2$ (the $\Delta K = \pm G$ transition is covered by the lattice diffraction). Hence, since $\Delta K = \pm 3G/2$ is just the shortest reciprocal vector G_{CDW} of the CDW lattice in its $[110]_{CDW}$ direction the observation of a feature at $-3G/2$ supports the CDW scenario.

Moreover, for the alternative scenario without a CDW, inelastic transitions at special values of ΔK corresponding to single-particle inter-pocket transitions would be detected in time-of-flight (TOF) measurements. On the contrary, as shown in the following section, TOF spectra give, besides a complete set of surface phonon dispersion curves, two low-energy branches which can be assigned to the expected ampliton and phason excitations of the electron CDW lattice.[45–47] The ability of inelastic HAS in its high-resolution ^{3}He spin-echo version to observe phasons associated with misfit dislocations in the long-period $23 \times \sqrt{3}$ reconstructed Au(111) surface was demonstrated by McIntosh et al.[18] recently, while here CDW phasons and amplitons are observed with ordinary HAS spectroscopy.

Dispersion curves

The dispersion curves of elementary excitations have been obtained by transforming TOF spectra of the scattered He atoms to energy transfer spectra (see Fig. S2 in the Supplementary Information). The experimental dispersion curves of surface phonons and the two additional low-energy branches assigned to phasons and amplitons measured at both 170 (only acoustic region) and 300 K (whole spectrum) are plotted in Fig. 3. The symbols represent the experimental data while the background lines correspond to the DFPT calculations. The colour scale of the DFPT calculations corresponds to the intensity of the phonon modes projected onto the first surface layer. The experimental data points are labelled according to their proximity to the calculated phonon modes, with either prominently shear vertical (SV) or longitudinal (L) polarisation on the first or third atomic layer, respectively.

As already observed in the surface phonon dispersion of Bi (111),[10] the e–ph interaction on Sb(111) is sufficiently large to make vibrational modes that are mainly localised at the third layer (SV3, L3) visible for HAS. Due to the e–ph interaction, large modulations of the surface charge density are induced,[10] which is also important in observing comparatively large inelastic intensities from surface optical modes.[48] The property is common to other layered structures, as recently shown theoretically[49] and experimentally[50,51] for Bi_2Te_3(111) and Bi_2Se_3(111). In general the overall agreement of the measurements with the calculations is very good.

In addition to the data points which are reproduced by the DFPT calculations, there are data points plotted as grey stars in Fig. 3, which cannot be assigned to any surface vibrational mode. These data points form two separate branches, the aforementioned phasons and amplitons, which becomes particularly

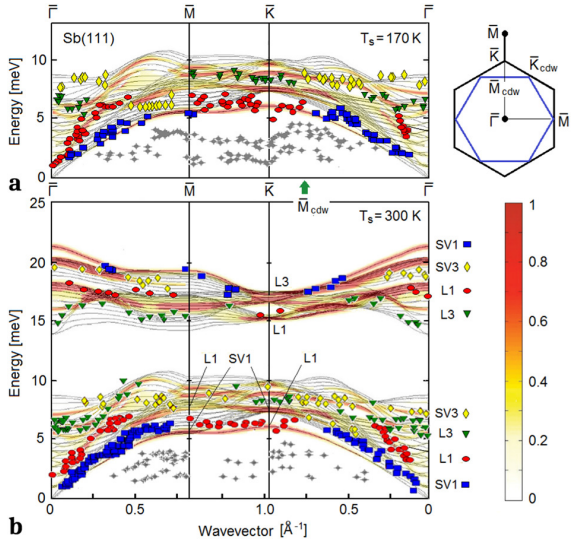

Fig. 3 Measured surface phonon dispersion of Sb(111) in comparison with DFPT calculations. The data points have been extracted from measurements at 170 K in (**a**) and at 300 K in (**b**). They are plotted on top of the theoretical DFPT dispersion curves, with the corresponding DOS projected onto the first surface layer and given by colour code. All phonon polarisations accessible using the present scattering geometry are superimposed and the measured data points are labelled by proximity to the calculated phonon modes. SV1 or SV3 denote surface (quasi-) shear-vertical modes with the largest amplitudes at the surface layer (bilayer) or at the third layer (second bilayer), respectively. Similarly L1 (L3) denote surface (quasi-) longitudinal modes with the largest amplitude on the first (second) bilayer. Shear-horizontal modes are not plotted. The grey data points (crosses) are attributed to phasons and amplitons of the multi-valley CDW associated with the Fermi surface $\overline{\mathrm{M}}$-point electron pockets. The inset at the top-right shows the BZ of the surface CDW lattice inscribed into the crystallographic surface BZ. The CDW symmetry point $\overline{\mathrm{M}}_{\mathrm{CDW}}$ corresponds to a maximum in the phason/ampliton branches (green arrow in **a**)

evident for the measurements at $T_S = 170$ K along the $\overline{\Gamma\mathrm{KM}}$ direction. The features leading to these modes are small in intensity but consistently present over the whole measuring range as can be seen in the SI (Figs. S2 and S3). The broad maximum, falling in both branches at one half of the $\overline{\Gamma\mathrm{KM}}$ segment, is seen to occur at 0.7 Å^{-1} (green arrow in Fig. 3a), which is the $\overline{\mathrm{M}}_{\mathrm{CDW}}$ symmetry point of the CDW BZ (Fig. 3, inset). This correspondence and the approximate specularity of the branches with respect to $\overline{\mathrm{M}}_{\mathrm{CDW}}$ suggest to assign the two branches to CDW excitations, i.e. phasons and amplitons. Note that the commensurate excitations of a commensurate electron CDW have a finite energy at $\Delta K = 0$ (here also at the $\overline{\mathrm{M}} \equiv \overline{\Gamma}_{\mathrm{CDW}}$ point) due to the pinning to the lattice.

For a phenomenological description of CDW excitations the multipole expansion (ME) model[52] is applied to the M-electron CDW lattice, viewed as a 2D periodic lattice of electron shells subject to dynamical multipolar deformations. In the simplest picture the latter are restricted to dipolar deformations (rigid displacements) either normal (amplitons) or parallel longitudinal (phasons) to the surface. While the corresponding degrees of freedom are endowed with an effective inertial mass μ, the atomic lattice is assumed to be rigid (infinite mass) so as to ensure adiabaticity, and to exert on the electron shells an isotropic pinning force constant f_0 (see "CDW structure and dynamics within the ME model" in the SI). The two dispersion curves can then be fairly well reproduced with just nearest neighbour (nn) and next nn (2n) force constants for normal (ampliton) and parallel longitudinal (phason) shell (dipolar) displacements, $f_{1\alpha}$ and $f_{1\varphi}$,

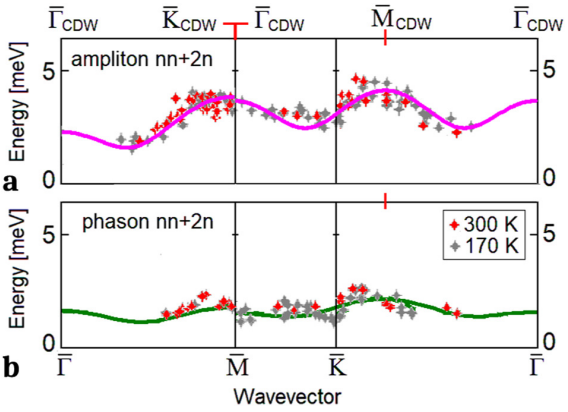

Fig. 4 The measured low-energy branches fitted with the ME model. The additional low-energy branches measured with HAS in Sb(111) at two different surface temperatures are attributed to the elementary excitations of the commensurate electron multi-valley CDW: **a** amplitons, **b** phasons. The upper abscissa shows the symmetry points of the CDW lattice. The full lines show fits based on the ME model with dipolar coordinates and nearest (nn) and next-nearest (2n) interactions (see SI)

and $f_{2\alpha}$ and $f_{2\varphi}$, respectively. The fit shown in Fig. 4 (effective masses = 1) is obtained (see SI) with $f_0 = 12$, $f_{1\alpha} = 3$, $f_{2\alpha} = -2$ and $f_{1\varphi} = 1$, $f_{2\varphi} = -1$, all in meV^2/μ units.

The deviations, notably the small dips at $\overline{\mathrm{K}}$ may be due to the coupling either with the hole pockets, which would introduce short-period oscillations in the dispersion curves, or with phonons. A possible coupling to phonons as the cause of dips at $\overline{\mathrm{K}}$ in the CDW branches (and apparently also in the lowest phonon branch) deserves further investigation. The physical meaning of the fitting parameter values does not seem to be trivial, especially the fact that the 2n force constants remain comparable to the nn ones, while having opposite signs. For a pure dipole–dipole interaction $f_{1\alpha}$ and $f_{2\alpha}$ should both be positive with a ratio $f_{1\alpha}/f_{2\alpha} = \sqrt{27}$, while $f_{1\varphi}$ and $f_{2\varphi}$ should be negative and in the same ratio. Pauli repulsion for in-plane shell displacements, many-body effects and dispersion forces, as well as the amplification/depression of interactions at different distances due to the interference of the electron CDW with that of the pocket holes (see "CDW structure and dynamics within the ME model" in the SI), are expected to play a role in the effective force constants of the ME model—an issue worth being investigated from first principles.

DISCUSSION

In summary, we have shown that additional elastic peaks which are observed in HAS diffraction spectra from Sb(111) can be assigned, on the basis of their peculiar temperature dependence, to electron and hole multi-valley CDWs. The multi-valley structure at the Fermi level consists of six electron pockets at the $\overline{\mathrm{M}}$ symmetry points of the surface BZ, and six hole pockets at about 1/5 of the $\overline{\mathrm{KM}}$ segments of alternate spins, as found in existing ARPES data and present DFT calculations including SO coupling.

Furthermore, inelastic HAS spectra, besides providing the surface phonon dispersion curves in agreement with DFPT + SOC calculations, reveal two additional dispersion curves of elementary excitations in the energy region well below the Rayleigh mode. They can be associated to phasons and amplitons of the multi-valley CDW associated with the electron pockets. The fact that inelastic HAS from surface phonons exclusively occurs, for a conducting surface, through the e–ph interaction[8–11] implies that also the dispersion of low-energy surface electron collective excitations can be measured by HAS. It is expected that ordinary

HAS, as well as its ultrahigh-resolution ^{3}He spin-echo version,[53,54] will be regarded as a choice spectroscopy for the investigation of surface electronic excitations in the THz domain.

METHODS

Experimental details

The experiments were carried out on the helium-atom-scattering apparatus H.A.N.S which has been described in greater detail in earlier publications.[55] Figure 1a shows a schematics of the experimental setup. The energetically narrow He-atom beam ($\Delta E/E \approx 2\%$) is created by a supersonic expansion of He-gas and scattered off the surface in a fixed 91.5° source-sample-detector geometry. Energy dispersive measurements for inelastic scattering are performed using TOF measurements with a pseudo-random chopper disc.

The sample under investigation was an antimony (Sb) single crystal cleaved in the (111) direction in shape of a disc of 15 mm diameter and 2 mm thickness. The crystal was cleaned by several cycles of Ar^+ sputtering and subsequent annealing at 475 K. The contamination and cleanness were checked by auger electron spectroscopy and the intensity of the diffuse elastic peak. The sample holder can be cooled using liquid nitrogen and heated using a button heater while the temperature is measured by a type K thermocouple. The used He beam energies range from 11.8 to 36.6 meV and the experiments were carried out at constant surface temperatures between 120 and 405 K.

Computational details

Calculations have been performed within DFT by using a norm conserving fully relativistic pseudopotential and the Perdew–Burke–Ernzerhof generalised gradient approximation for the exchange and correlation functional.[56] SO coupling effects are taken into account self-consistently with the formalism of non-collinear spin magnetisation as implemented in the QE distribution.[57] The Kohn–Sham wave functions are expanded in plane waves up to a kinetic-energy cutoff of 45 Ry. A Gaussian smearing of 0.01 Ry is used to deal with the metallic character of Sb.

In accordance with Campi et al.,[23] the Sb(111) surface is modelled by a slab geometry with a single atom per layer and 24 layers. The periodic images of the slab are separated by a vacuum region 12 Å wide. The band structure and the Fermi energy are calculated for the optimised slab geometry.[23] To resolve the fine details of the electronic properties of interest, we first performed a self-consistent calculation with integration of the BZ over a $(48 \times 48 \times 1)$ Monkhorst–Pack[58] mesh followed by non self-consistent calculations over highly dense meshes.

DATA AVAILABILITY

The data that support the findings of this study are available from the corresponding author upon reasonable request.

ACKNOWLEDGEMENTS

This research was supported by the European Commission and the Styrian Government within the ERDF program. A.T. acknowledges financial support provided by the FWF (Austrian Science Fund) within the project J3479-N20. A.T. and W.E.E. gratefully acknowledge support by the FWF within the project P29641-N36, as well as by NAWI Graz.

AUTHOR CONTRIBUTIONS

A.T., P.K. and M.M.-R. performed the experimental measurements under the supervision of W.E.E. The analysis of the experimental data was carried out by A.T., P.K. and G.B. D.D. and M.B. performed the DFT calculations while D.C. ran the DFPT calculations and G.B. implemented the ME model. G.B. co-wrote the paper with A.T. and all authors contributed to the discussion and preparation of the manuscript.

ADDITIONAL INFORMATION

Supplementary information accompanies the paper on the *npj Quantum Materials* website (https://doi.org/10.1038/s41535-019-0168-x).

Competing interests: The authors declare no competing interests.

REFERENCES

1. Kelly, M. J. & Falicov, L. M. Electronic structure of inversion layers in many-valley semiconductors. *Phys. Rev. Lett.* **37**, 1021–1024 (1976).
2. Kelly, M. J. & Falicov, L. M. Electronic ground state of inversion layers in many-valley semiconductors. *Phys. Rev. B* **15**, 1974–1982 (1977).
3. Kelly, M. J. & Falicov, L. M. Optical properties of charge-density-wave ground states for inversion layers in many-valley semiconductors. *Phys. Rev. B* **15**, 1983–1987 (1977).
4. Grüner, G. *Density Waves in Solids*, vol. 89 of *Frontiers in Physics* (Perseus Publishing, Cambridge, Massachusetts, 1994).
5. Aruga, T. Charge-density waves on metal surfaces. *J. Phys. Condes. Matter* **14**, 8393 (2002).
6. Zhu, X., Cao, Y., Zhang, J., Plummer, E. W. & Guo, J. Classification of charge density waves based on their nature. *Proc. Natl Acad. Sci. USA.* **112**, 2367–2371 (2015).
7. Xi, X. et al. Strongly enhanced charge-density-wave order in monolayer $NbSe_2$. *Nat. Nanotechnol.* **10**, 765 (2015).
8. Sklyadneva, I. Y. et al. Mode-selected electron-phonon coupling in superconducting Pb nanofilms determined from He atom scattering. *Phys. Rev. Lett.* **107**, 095502 (2011).
9. Benedek, G. et al. Unveiling mode-selected electron-phonon interactions in metal films by helium atom scattering. *Phys. Chem. Chem. Phys.* **16**, 7159–7172 (2014).
10. Tamtögl, A. et al. Surface and subsurface phonons of Bi(111) measured with helium atom scattering. *Phys. Rev. B* **87**, 035410 (2013).
11. Manson, J. R., Benedek, G. & Miret-Artés, S. Electron-phonon coupling strength at metal surfaces directly determined from the helium atom scattering Debye-Waller Factor. *J. Phys. Chem. Lett.* **7**, 1016–1021 (2016).
12. Ast, C. R. & Höchst, H. Indication of charge-density-wave formation in Bi(111). *Phys. Rev. Lett.* **90**, 016403 (2003).
13. Sugawara, K. et al. Fermi surface and anisotropic spin-orbit coupling of Sb(111) studied by angle-resolved photoemission spectroscopy. *Phys. Rev. Lett.* **96**, 046411 (2006).
14. Koroteev, Y. M. et al. Strong spin-orbit splitting on Bi surfaces. *Phys. Rev. Lett.* **93**, 046403 (2004).
15. Benedek, G. et al. Shifted surface-phonon anomaly in 2H-$TaSe_2$. *Phys. Rev. Lett.* **60**, 1037–1040 (1988).
16. Brusdeylins, G. et al. Determination of the critical exponent for a charge density wave transition in 2H-$TaSe_2$ by helium atom scattering. *EPL* **9**, 563 (1989).
17. Hofmann, P. et al. Strong-coupling charge density wave in a one-dimensional topological metal. *Phys. Rev. B* **99**, 035438 (2019).
18. McIntosh, E. M. et al. Measurement of the phason dispersion of misfit dislocations on the Au(111) Surface. *Phys. Rev. Lett.* **110**, 086103 (2013).
19. Hulpke, E. & Lüdecke, J. Hydrogen-induced phonon anomaly on the W(110) surface. *Phys. Rev. Lett.* **68**, 4 (1992).
20. Hulpke, E. & Lüdecke, J. The giant surface phonon anomaly on hydrogen saturated W(110) and Mo(110). *Surf. Sci.* **287**, 837–841 (1993).
21. Plummer, E., Shi, J., Tang, S.-J., Rotenberg, E. & Kevan, S. Enhanced electron-phonon coupling at metal surfaces. *Prog. Surf. Sci.* **74**, 251–268 (2003).
22. Kröger, J. Electron-phonon coupling at metal surfaces. *Rep. Prog. Phys.* **69**, 899 (2006).
23. Campi, D., Bernasconi, M. & Benedek, G. Phonon and electron-phonon interaction at the Sb(111) surface. *Phys. Rev. B* **86**, 7 (2012).
24. Barrett, C. S., Cucka, P. & Haefner, K. The crystal structure of antimony at 4.2, 78 298° K. *Acta Crystallogr.* **16**, 451–453 (1963).
25. Schiferl, D. & Barrett, C. S. The crystal structure of arsenic at 4.2, 78 and 299 °K. *J. Appl. Crystallogr.* **2**, 30–36 (1969).
26. Bengió, S. et al. The structure of Sb(111) determined by photoelectron diffraction. *Surf. Sci.* **601**, 2908–2911 (2007).
27. Stegemann, B., Ritter, C., Kaiser, B. & Rademann, K. Characterization of the (0001) cleavage surface of antimony single crystals using scanning probe microscopy: atomic structure, vacancies, cleavage steps, and twinned interlayers. *Phys. Rev. B* **69**, 155432 (2004).
28. Zhang, P., Liu, Z., Duan, W., Liu, F. & Wu, J. Topological and electronic transitions in a Sb(111) nanofilm: the interplay between quantum confinement and surface effect. *Phys. Rev. B* **85**, 201410 (2012).
29. Soumyanarayanan, A. & Hoffman, J. E. Momentum-resolved STM studies of Rashba-split surface states on the topological semimetal Sb. *J. Electron Spectrosc. Relat. Phenom.* **201**, 66–73 (2015).
30. Kim, S. H. et al. Topological phase transition and quantum spin Hall edge states of antimony few layers. *Sci. Rep.* **6**, 33193 (2016).

31. Wang, G., Pandey, R. & Karna, S. P. Atomically thin group V elemental films: theoretical investigations of antimonene allotropes. *ACS Appl. Mater. Interfaces* **7**, 11490–11496 (2015).
32. Fortin-Deschênes, M. et al. Synthesis of antimonene on germanium. *Nano Lett.* **17**, 4970–4975 (2017).
33. Reis, F. et al. Bismuthene on a SiC substrate: a candidate for a high-temperature quantum spin Hall material. *Science* **357**, 287–290 (2017).
34. Mayrhofer-Reinhartshuber, M., Tamtögl, A., Kraus, P. & Ernst, W. E. Helium atom scattering investigation of the Sb(111) surface. *J. Phys.* **25**, 395002 (2013).
35. Farías, D. & Rieder, K.-H. Atomic beam diffraction from solid surfaces. *Rep. Prog. Phys.* **61**, 1575 (1998).
36. Mayrhofer-Reinhartshuber, M., Kraus, P., Tamtögl, A., Miret-Artés, S. & Ernst, W. E. Helium-surface interaction potential of Sb(111) from scattering experiments and close-coupling calculations. *Phys. Rev. B* **88**, 205425 (2013).
37. Tamtögl, A., Mayrhofer-Reinhartshuber, M., Kraus, P. & Ernst, W. E. Surface Debye temperature and vibrational dynamics of Antimony(111) from helium atom scattering measurements. *Surf. Sci.* **617**, 225–228 (2013).
38. Höchst, H. & Ast, C. R. The Fermi surfaces of thin Sb(111) films. *J. Electron Spectrosc. Relat. Phenom.* **137-140**, 441–444 (2004).
39. Zhuo-Jin, X. et al. Weak electron-phonon coupling and unusual electron scattering of topological surface states in Sb(111) by laser-based angle-resolved photoemission spectroscopy. *Chin. Phys. Lett.* **31**, 067305 (2014).
40. Cohen, M. L. Superconductivity in many-valley semiconductors and in semimetals. *Phys. Rev.* **134**, A511–A521 (1964).
41. Ibragimov, K. I. & Korol'kov, V. A. Temperature dependence of the work function of metals and binary alloys. *Inorg. Mater.* **37**, 567–572 (2001).
42. Fahrenbruch, A. L. *Photoelectric Properties Of Evaporated Antimony Films As A Function Of Film Thickness*. Master's thesis (Oregon State University, Corvallis, 1967).
43. Esbjerg, N. & Nørskov, J. K. Dependence of the He-scattering potential at surfaces on the surface-electron-density profile. *Phys. Rev. Lett.* **45**, 807–810 (1980).
44. Yam, Y. -C. et al. Unexpected zero bias conductance peak on the topological semimetal Sb (111) with a broken bilayer. Preprint at https://arxiv.org/abs/1810.13390 (2018).
45. Vallade, M., Dvorak, V. & Lajzerowicz, J. Amplitudons and phasons in the triple-k incommensurate phase of quartz-type crystals. *J. de. Phys.* **48**, 1171–1179 (1987).
46. Grüner, G. The dynamics of charge-density waves. *Rev. Mod. Phys.* **60**, 1129–1181 (1988).
47. Torchinsky, D. H., Mahmood, F., Bollinger, A. T., Božović, I. & Gedik, N. Fluctuating charge-density waves in a cuprate superconductor. *Nat. Mater.* **12**, 387–391 (2013).
48. Kraus, P., Tamtögl, A., Mayrhofer-Reinhartshuber, M., Benedek, G. & Ernst, W. E. Resonance-enhanced inelastic He-atom scattering from subsurface optical phonons of Bi(111). *Phys. Rev. B* **87**, 245433 (2013).
49. Heid, R., Sklyadneva, I. Y. & Chulkov, E. V. Electron-phonon coupling in topological surface states: the role of polar optical modes. *Sci. Rep.* **7**, 1095 (2017).
50. Tamtögl, A. et al. Electron-phonon coupling and surface Debye temperature of Bi_2Te_3(111) from helium atom scattering. *Phys. Rev. B* **95**, 195401 (2017).
51. Tamtögl, A. et al. Nanoscale surface dynamics of Bi_2Te_3 (111): observation of a prominent surface acoustic wave and the role of van der Waals interactions. *Nanoscale* **10**, 14627–14636 (2018).
52. Jayanthi, C. S., Bilz, H., Kress, W. & Benedek, G. Nature of surface-phonon anomalies in noble metals. *Phys. Rev. Lett.* **59**, 795–798 (1987).
53. Jardine, A., Hedgeland, H., Alexandrowicz, G., Allison, W. & Ellis, J. Helium-3 spin-echo: principles and application to dynamics at surfaces. *Prog. Surf. Sci.* **84**, 323 (2009).
54. Jones, A., Tamtögl, A., Calvo-Almazán, I. & Hansen, A. Continuous compressed sensing for surface dynamical processes with helium atom scattering. *Sci. Rep.* **6**, 27776 (2016).
55. Tamtögl, A., Mayrhofer-Reinhartshuber, M., Balak, N., Ernst, W. E. & Rieder, K. H. Elastic and inelastic scattering of He atoms from Bi(111). *J. Phys. Condes. Matter* **22**, 1–6 (2010).
56. Perdew, J. P., Burke, K. & Ernzerhof, M. Generalized gradient approximation made simple. *Phys. Rev. Lett.* **77**, 3865–3868 (1996).
57. Giannozzi, P. et al. QUANTUM ESPRESSO: a modular and open-source software project for quantum simulations of materials. *J. Phys. Condes. Matter* **21**, 395502 (2009).
58. Monkhorst, H. J. & Pack, J. D. Special points for Brillouin-zone integrations. *Phys. Rev. B* **13**, 5188–5192 (1976).

6.14 Publication N

Tamtögl, A., Sacchi, M., Avidor, N., Calvo-Almazán, I., Townsend, P. S. M., Bremholm, M., Hofmann, P., Ellis, J. & Allison, W. Nanoscopic diffusion of water on a topological insulator. *Nat. Commun.* **11,** 278 (2020)

contributions	
funding	A. Tamtögl, W. Allison, J. Ellis, P. Hofmann
sample synthesis	M. Bremholm
preparation / setup	A. Tamtögl
data acquisition	A. Tamtögl, N. Avidor, I. Calvo-Almazán, P. Townsend
theory (*ab initio*) calculations	M. Sacchi
data analysis	A. Tamtögl
interpretation	A. Tamtögl, N. Avidor, W. Allison
publication writing	A. Tamtögl, W. Allison

Reprinted from:

Tamtögl, A., Sacchi, M., Avidor, N., Calvo-Almazán, I., Townsend, P. S. M., Bremholm, M., Hofmann, P., Ellis, J. & Allison, W. Nanoscopic diffusion of water on a topological insulator. *Nat. Commun.* **11,** 278 (2020)

nature COMMUNICATIONS

ARTICLE

https://doi.org/10.1038/s41467-019-14064-7 OPEN

Nanoscopic diffusion of water on a topological insulator

Anton Tamtögl [1,2*], Marco Sacchi [3], Nadav Avidor [2], Irene Calvo-Almazán[2,4], Peter S.M. Townsend[2,5], Martin Bremholm [6], Philip Hofmann[7], John Ellis[2] & William Allison[2]

The microscopic motion of water is a central question, but gaining experimental information about the interfacial dynamics of water in fields such as catalysis, biophysics and nanotribology is challenging due to its ultrafast motion, and the complex interplay of intermolecular and molecule-surface interactions. Here we present an experimental and computational study of the nanoscale-nanosecond motion of water at the surface of a topological insulator (TI), Bi_2Te_3. Understanding the chemistry and motion of molecules on TI surfaces, while considered a key to design and manufacturing for future applications, has hitherto been hardly addressed experimentally. By combining helium spin-echo spectroscopy and density functional theory calculations, we are able to obtain a general insight into the diffusion of water on Bi_2Te_3. Instead of Brownian motion, we find an activated jump diffusion mechanism. Signatures of correlated motion suggest unusual repulsive interactions between the water molecules. From the lineshape broadening we determine the diffusion coefficient, the diffusion energy and the pre-exponential factor.

[1] Institute of Experimental Physics, Graz University of Technology, 8010 Graz, Austria. [2] Cavendish Laboratory, J. J. Thompson Avenue, Cambridge CB3 0HE, UK. [3] Department of Chemistry, University of Surrey, Guildford GU2 7XH, UK. [4] Material Science Division, Argonne National Laboratory, Argonne 60439 IL, USA. [5] Department of Chemistry and Chemical Biology, Rutgers University, 123 Bevier Road, Piscataway, NJ 08854, USA. [6] Center for Materials Crystallography, Department of Chemistry and iNANO, Aarhus University, 8000 Aarhus, Denmark. [7] Department of Physics and Astronomy, Interdisciplinary Nanoscience Center (iNANO), Aarhus University, 8000 Aarhus C, Denmark. *email: tamtoegl@gmail.com

Water is ubiquitous in everyday life, yet its nanoscale motion at surfaces is a major challenge to theory, which suffers from the lack of experimental insight[1–9]. The motion of protons, the vibrational dynamics and electronic transitions of water at surfaces usually happens at ultrafast time scales (in the order of femtoseconds)[10]. These processes are accessible with ultrafast optical spectroscopy[11–13], whereas the interfacial diffusion of molecules typically occurs in the pico- to nanosecond regime and is monitored either in real space using microscopic techniques or in reciprocal space using scattering techniques. However, to make these fast diffusive motions accessible to microscopy studies, the process typically needs to be considerably slowed down. At the same time an intrinsic problem of scanning probe microscopy is that the probes inevitably induce perturbation to the fragile water structure, due to the excitation of tunnelling electrons and the tip–water interaction forces[10,14].

The studied Bi_2Te_3 surface is classified as a topological insulator (TI)[15], a class of materials which exhibit topologically protected metallic surface states (TSS) and an insulating bulk electronic structure[16–18]. The distinct properties of their surface states make TIs promising candidates for possible applications in spintronics and quantum information[17–19], while surface-dominated transport is currently one of the major objectives on the way to technical applications[20,21]. However, topology can have implications far beyond electronic transport properties and topological materials provide a perfect platform for studying phenomena such as heterogeneous catalysis. Since the TSSs are insensitive to details of the surface such as defects or other kinds of disorder, in contrast to trivial surface states, TIs allow to study processes such as the catalytic activity where the condition of the surface is one of the most important, but also most difficult to describe parameters[22].

The stability of the electronic structure of TI surfaces upon adsorption has been widely studied due to being crucial for future TI based devices[23–29], including also the modification of the electronic structure upon adsorption and doping[30–35]. On the one hand, Bi_2Se_3 reacts with water vapour giving rise to an *n*-doping of the surface[23]. In the case of Bi_2Te_3 on the other hand, it was shown that water adsorption is less pronounced than the adsorption of oxygen[26,36], even though the reactivity of water with Bi_2Te_3 is still under debate[26,27,37]. Except for the influence of adsorbates on the electronic structure, chemistry on TI surfaces has been largely ignored, even though it was shown that TIs hold great potential for sensing applications[38,39] and exfoliation in liquid environment has been used to obtain nanosheets with unique properties[40–42]. With respect to catalysis, the existence of TSS can modify the catalyst–adsorbate interactions[43], e.g. acting on the adsorption energy of small molecules irrespective of surface modifications[22], and effect processes sensitive to the adsorbate binding strength such as hydrogen evolution reactions[44]. It has been suggested that the TSSs can be used as an additional parameter to adjust the catalyst–adsorbate interactions, with the TSS acting as a tunable electron bath[22].

Given such implications a thorough investigation addressing the interaction of TI surfaces with water is overdue, as is an experimental study about the dynamics and diffusion of adsorbates on TI surfaces in general. Up to now studies about the diffusion and mobility of adsorbates on TI surfaces are solely based on theoretical methods and include the diffusion of metal and alkali metal atoms on Bi_2Se_3[45,46] and the diffusion of Pb[47]. Since the kinetics of surface chemical reactions and epitaxial processes used to build advanced TI based structures depends on the mobility of adsorbates, an accurate characterisation of these phenomena and a precise understanding of the diffusion mechanism is crucial.

In this work we provide a detailed insight into the atomic-scale motion of water on the TI surface of $Bi_2Te_3(111)$. Our experiments provide a unique insight into wetting, friction and physisorption for an important class of materials. Therefore, we use helium-3 spin-echo (HeSE) spectroscopy[48] which allows to follow the atomic-scale motion of atoms and molecules on surfaces, resolving diffusion processes on timescales from ns to sub-ps. The experimental data is analysed in terms of an analytical model for adsorbate diffusion and compared with density functional theory (DFT) calculations including dispersion corrections. The data provides a measure of the diffusion barrier and coefficient and shows that the motion of water molecules on $Bi_2Te_3(111)$ occurs by activated hopping on a hexagonal lattice. Our results illustrate that the structure and dynamics of water is determined by an intricate interplay of intermolecular interactions and molecule-surface interactions with signatures of correlated motion due to repulsive interactions between the individual water molecules as further detailed in kinetic Monte Carlo (MC) simulations. Finally, since HeSE is capable of delivering detailed information on the energy landscape during diffusion[49,50], it allows us to elucidate the physics of energy dissipation at solid–liquid interfaces i.e. the mechanisms in which vibrational (e.g. phonons) and electronic energy (e.g. electron–hole pairs) is transferred between the adsorbates and the surface which eventually governs tribology. We conclude from the observed motion that energy dissipation in nanoscale motion of water on TI surfaces lies in the medium to low-friction regime.

Results

Water uptake and dynamics measurements. The tendency of water to aggregate upon adsorption on metallic surfaces is well documented in the literature[4–7,51]. After dosing water on Bi_2Te_3 at 105 K (to different coverages), diffraction scans do not show any sharp peaks, indicating the absence of long range order and the adsorption of water as amorphous multilayers. Between 105 and 130 K (where desorption starts to become significant, see Supplementary Figs. 2 and 3), we could not detect a diffusion signature. Hence, our diffusion measurements were performed in a temperature range of 135–160 K where dynamics could be clearly resolved, while maintaining a small equilibrium water pressure (around 10^{-9} mbar) against desorption and ensuring small water densities which allows interpretation of the dynamics observed.

The dynamics of H_2O adsorbed on Bi_2Te_3 were studied experimentally by measuring the intermediate scattering function (ISF), using a HeSE spectrometer[48]. The ISF, $I(\Delta\mathbf{K}, t)$, describes the correlation at the surface after time t, for the scattering condition of the helium beam, $\Delta\mathbf{K}$—the parallel momentum transfer. Loss of correlation (dephasing) at $(t_1, \Delta\mathbf{K}_1)$, as manifested in the helium beam intensity, is a measure for the dynamics at the surface during time t_1, with the characteristic periodic length scale $2\pi/\Delta\mathbf{K}_1$. When the adsorbate dynamics are well described as hopping between adsorption sites that form a Bravais lattice, the ISF is known analytically and for a fixed $\Delta\mathbf{K}$ consists of an exponential decay in t with a rate that depends on $\Delta\mathbf{K}$[52]. Allowing for a static offset due to surface defects, $I(\Delta\mathbf{K}, t)$ can then be written as:[48,53]

$$I(\Delta\mathbf{K}, t) = I_0(\Delta\mathbf{K}, 0) \cdot e^{-\alpha(\Delta\mathbf{K})\cdot t} + C(\Delta\mathbf{K}) \quad (1)$$

where α is the dephasing rate and I_0 the amplitude at $t = 0$ (see Fig. 1(c) for a typical ISF). The dynamics can then be extracted from the form of $I(\Delta\mathbf{K}, t)$ and the functional dependence of $\alpha(\Delta\mathbf{K})$ on $\Delta\mathbf{K}$.

Most dynamics measurements were performed at 150 K at a specular attenuation of $I_0/3$ and $I_0/5$ which corresponds to a

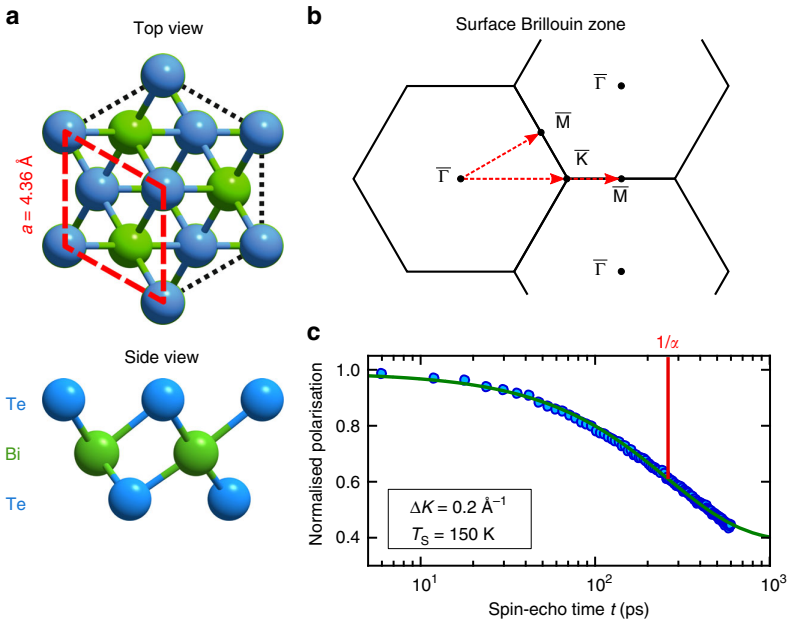

Fig. 1 Bi_2Te_3 structure and dynamics measurements from the lineshape broadening. a Top and side view of the (111) surface of Bi_2Te_3. The surface layer is terminated by a Te layer and the red rhombus highlights the hexagonal surface unit cell. **b** Surface Brillouin zone with the corresponding scanning directions. **c** A typical intermediate scattering function (ISF) showing the normalised polarisation versus spin-echo time t. The measured data (filled circles) is fitted with a single exponential decay ((1), solid green line) characterised by the dephasing rate α. The logarithmic time axis shows that a single exponential provides a good description of the experimental data.

coverage of 0.05 and 0.08 monolayer (ML), respectively (see Supplementary Methods). The motion of H_2O on Bi_2Te_3(111) was then extracted from HeSE measurements based on a single exponential fit of the experimentally measured ISF according to (1).

At short times, the data shows the expected deviation from a single exponential and we use an iterative routine to optimise the range for inclusion (see Supplementary Methods and Supplementary Fig. 4). Note that the intermediate scattering function may contain information about dynamical processes at different timescales. In particular, the short-range limit typically includes signatures from substrate phonons or may also contain information about intra-cell diffusion[48]. However, in the present work we concentrate on the longer times which are related to the long-range part in diffusion—i.e. the translational part of the diffusion mechanism. The data points within the time-window related to the long-range (translational) diffusion are best fitted with a single-exponential decay and there is no evidence for a double-exponential decay[53] within this window.

Diffusion mechanism of H_2O. The atomic-scale diffusion of molecules on surfaces is typically described by molecules moving or hopping along the surface while the substrate provides the thermal energy for the motion[48,55–57]. For an activated diffusion process, motion of the adsorbates is governed by the interaction of the molecule with a corrugated potential energy surface (PES). Information about the PES and the hopping motion of the molecule can be obtained from the temperature dependence and the functional form of $\alpha(\Delta\mathbf{K})$[48].

First, the activation energy for the diffusion of H_2O on Bi_2Te_3 (111) can be obtained via temperature dependent measurements at a fixed momentum transfer $\Delta K = |\Delta\mathbf{K}|$. On a not-too-weakly corrugated surface, adsorbate diffusion proceeds by thermally activated hopping whose rate is given by an Arrhenius relation[48,56,58,59]. We will shortly see that α at a fixed ΔK is proportional to a hopping rate (Fig. 3). Therefore, as long as the diffusion mechanism does not change significantly with temperature, $\alpha(T_S)$ at a fixed ΔK is also expected to follow an Arrhenius relation:

$$\alpha = \alpha_0 \exp\left(-\frac{E_a}{k_B T_S}\right) \quad (2)$$

where α_0 is the pre-exponential factor describing the jump attempt frequency, E_a is the activation energy for diffusion, k_B the Boltzmann constant and T_S the temperature of the sample surface.

Figure 2(a) shows an Arrhenius plot for two different momentum transfers ($\Delta K = 0.22$ Å^{-1} and $\Delta K = 0.55$ Å^{-1} along $\overline{\Gamma M}$) over a temperature range from 130 to 160 K. The plot of $\ln(\alpha)$ clearly shows a linear dependence upon $1/T_S$ as expected for activated motion. To ensure a constant H_2O coverage of 0.05 ML at all temperatures, the over-pressure at each temperature was adjusted to maintain an attenuation of the specularly reflected signal by a factor of 3. The uncertainties are the corresponding confidence bounds (1σ) of the single-exponential fit and the activation energy E_a is then obtained from the slope of a weighted fit to the Arrhenius plot (Fig. 2(a), see Supplementary Methods for more details), whereupon the intercept gives α_0. Based on both data sets shown in Fig. 2(a) we obtain an activation energy E_a of:

$$E_a = (34 \pm 4)\,\mathrm{meV}.$$

While the temperature range of the measurements is limited by the timescale accessible to the instrument, the range is greater than achieved for water diffusion by some other techniques[2]. There is no evidence of a curvature, which would indicate a temperature dependence of the pre-exponential factor (see Supplementary Note and Supplementary Fig. 6). Only a pathological coincidence where the diffusion mechanism changes in the experimental temperature window would lead to any

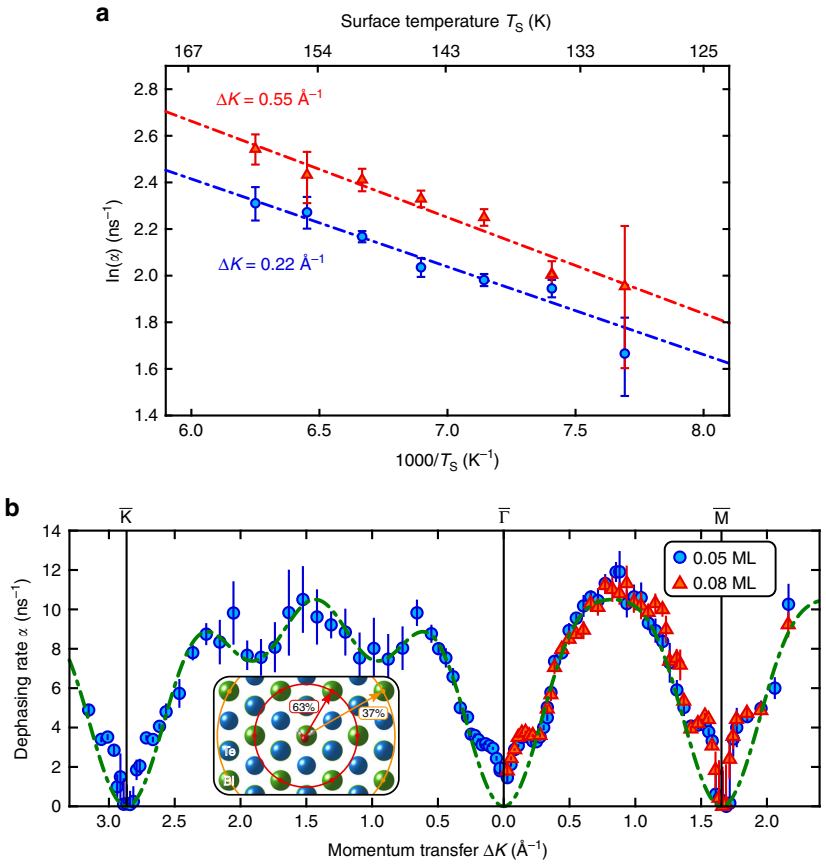

Fig. 2 Dephasing rates $\alpha(\Delta K)$ as determined from measurements of $I(\Delta\mathbf{K}, t)$. a Arrhenius plot showing the temperature dependence at two different momentum transfers along the $\overline{\Gamma M}$-azimuth for the diffusion of water on Bi_2Te_3(111). The measurements were taken at an H_2O coverage of 0.05 ML. **b** Momentum transfer dependence for the diffusion of H_2O on Bi_2Te_3(111) at a fixed temperature. The measurements were taken at a constant surface temperature of $T_S = 150$ K and a water coverage of 0.05 ML (blue circles) and 0.08 ML (red triangles), respectively. The dash-dotted line corresponds to the analytic model for jump-diffusion with jumps on a hexagonal lattice to nearest and next-nearest sites as illustrated in the small inset. The red and yellow circles illustrate the jump distance to the next and next nearest sites, respectively. The extracted barriers E_a and pre-exponential factors α_0 for two different momentum transfers ΔK as well as the pre-exponential hopping rate Γ_0 for the diffusion process at 150 K are given in Table 1. The error bars correspond to the confidence bounds (1σ) upon determination of $\alpha(\Delta K)$ from the measurements of $I(\Delta\mathbf{K}, t)$—see text.

systematic error in terms of the activation energy or pre-exponential factor.

Having established the diffusion barrier for the motion we now turn to the spatial correlation of the motion. The characteristics of the dephasing rate α versus the momentum transfer ΔK reflects the underlying energy landscape. The dependence of $\alpha(\Delta K)$ on the momentum ΔK for the diffusion of H_2O on Bi_2Te_3(111) ($T_S = 150$ K) is shown in Fig. 2(b) for both high symmetry crystal directions (see Fig. 1(b) for the scanning directions).

Simple hopping motions of an adsorbate can be described by an analytical model, the Chudley–Elliott (CE) model[48,52,55]. It assumes that a particle rests for the mean residence time τ between motion from one adsorption site to the other. In the case of motion on a Bravais lattice, the dephasing rate $\alpha(\Delta K)$ becomes:

$$\alpha(\Delta K) = \frac{2}{\tau}\sum_n p_n \sin^2\left(\frac{\Delta\mathbf{K}\cdot\mathbf{l}_n}{2}\right) \qquad (3)$$

where $\mathbf{l}_n$ are the corresponding jump vectors and p_n is the probability that a jump to the corresponding site occurs.

Figure 2(b) shows that the experimental data can be very well described using a CE model (green dash-dotted line). The best fit using (3) corresponds to jumps on a simple hexagonal Bravais lattice ($a = 4.36$ Å) with nearest and next-nearest neighbour jumps, respectively ($p_1 = 63\%$, $p_2 = 37\%$). Based on the momentum transfer dependence (Fig. 2(b)), the hopping motion of the water molecules occurs between equivalent adsorption sites, on a hexagonal Bravais lattice with the substrate spacing a (see (Fig. 1(a)).

Any hopping motion between inequivalent adsorption sites would lead to additional decaying exponential components in the tail of the ISF[53]. There is no direct evidence for multi-exponential components in our data, and the fitted $\alpha(\Delta K)$ shows clear zeros at the Bragg condition along both high symmetry directions, where

Table 1 Diffusion parameters as determined from the experimental data in Fig. 2.

ΔK (Å^{-1})	E_a (meV)	α_0 (ns^{-1})
0.22	32 ± 4	107 ± 45
0.55	36 ± 4	171 ± 72

Extracted diffusion barriers E_a and pre-exponential factors α_0 for two different momentum transfers ΔK. The pre-exponential hopping rate Γ_0 for the diffusion process at 150 K is then $\Gamma_0 = (1.7 \pm 0.6) \cdot 10^{11}$ s^{-1}

a faster second exponential component would be clearly seen if present[53]. Therefore, the data is entirely consistent with a single relevant adsorption site per primitive cell. In accordance with the results from the vdW corrected DFT calculations (see "DFT Results"), we conclude that jumps occur between the adsorption site above the second layer Bi atoms as shown in the inset of Fig. 2 (b).

The corresponding mean residence time of the water molecules in the adsorption sites is $\tau \approx 95\,\mathrm{ps}$ based on the CE model. Together with the temperature dependent data (α_0 from (2)), the hopping rate from the CE model at 150 K can be related to a pre-exponential factor, now also in terms of a hopping rate $\Gamma_0 = (1.7 \pm 0.6) \cdot 10^{11}\,\mathrm{s}^{-1}$. Note that compared to the diffusion of water on other substrates this is at least an order of magnitude smaller[2,60].

In the region of ΔK close to zero and around the diffraction peak positions (vertical lines in Fig. 2(b)), the experimental data points lie above the analytical CE model. This is likely to be due to adsorbate-adsorbate interactions which will be discussed below (see "Adsorbate Interactions"). Furthermore, the diffusion coefficient D for two-dimensional motion can be calculated from the hopping rate as determined from the CE model using:

$$D = \frac{1}{4}\langle l \rangle^2 \Gamma \qquad (4)$$

where Γ is the hopping rate and $\langle l \rangle$ the mean jump length[48,55]. Using the hopping rate at 150 K (Fig. 2(b), $\Gamma = 1.05 \cdot 10^{10}\,\mathrm{s}^{-1}$) together with the mean jump length of 5.6 Å we obtain a diffusion coefficient of $D = 8.2 \cdot 10^{-10}\,\mathrm{m}^2\,\mathrm{s}^{-1}$.

Compared to the surface diffusion of other small molecules this is rather slow, especially when compared to the diffusion of NH_3 on graphite, where an ultra-fast diffusion with $D = 3.9 \cdot 10^{-8}\,\mathrm{m}^2\,\mathrm{s}^{-1}$ was observed at a temperature of 94 K[61]. On the other hand, theoretical studies predict a generally quite small diffusivity on TI surfaces[45]. The reported (ab-initio) diffusion barriers for metal atoms on TI surfaces are typically much larger, in the range of 110–320 meV depending on the adsorbate[45–47], in line with the predicted small diffusivity. The alkali metal Rb is the only studied adsorbate which shows a diffusivity (as extracted from a kinetic Monte Carlo approach—although at higher temperature[45]) comparable to the one of water found in our study.

DFT results. We have studied the adsorption of H_2O on Bi_2Te_3 for a number of different adsorption geometries and initial water configurations using van der Waals (vdW) corrected DFT calculations (see "DFT Methods" and Supplementary Fig. 5 for the setup of the supercell). The initial water configurations include both OH bonds pointing down or up, a single OH bond pointing down and a horizontal configuration.

The adsorption energy of a single water molecule is 271 meV with the H_2O molecule at a distance of about 4 Å from the surface. The optimised structures for the minimum energy configuration on the three considered adsorption sites are shown in Fig. 3. The most favourable adsorption site is on top of the second layer Bi atom (Fig. 3a), followed by adsorption above the third layer Te atom (Fig. 3b) with an energy difference of only 21 meV. The first layer Te atom is the least favourable for adsorbing H_2O, being 100 meV higher in energy than the absolute minimum. Yashina et al.[26] reported the third layer Te atom as the most favourable adsorption site, however, they did not consider adsorption above the second layer Bi atom in their study, where we find the largest adsorption energy. In addition, we obtain the same adsorption site and optimised configuration for a (2×2) supercell as shown in Fig. 3(d), i.e. when considering a smaller coverage of water molecules on the surface.

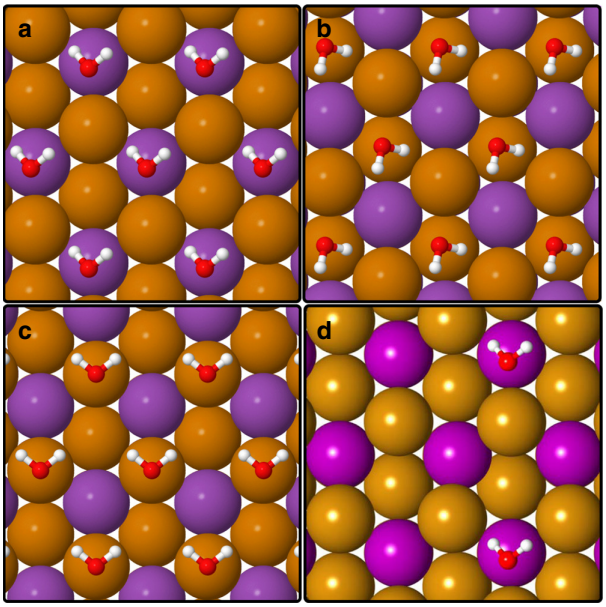

Fig. 3 Van der Waals corrected DFT calculations of the adsorption site for H_2O on Bi_2Te_3(111). The Bi and Te atoms are illustrated as purple and brown spheres, respectively. The energetically most favourable adsorption site is on top of the second layer Bi atom (**a**), followed by adsorption on top of the third layer Te atom (**b**) with a difference of 21 meV. Adsorption on top of the first layer Te atom (**c**) is the least favourable adsorption geometry, being 100 meV higher in energy than the absolute minimum. The optimised configuration of the water molecules for a (2×2) supercell in **d** is essentially the same as for the higher coverage in **a**.

Table 2 Adsorption energies and orientations for water at different adsorption sites on Bi_2Te_3.

Position	Orientation	E_a (eV)	ΔE_a (meV)
1-Te	ho	−0.171	100
1-Te	ld	−0.158	113
2-Bi	skew	−0.271	0
2-Bi	ho	−0.225	46
3-Te	skew	−0.250	21
3-Te	ho	−0.241	29

The adsorption energy E_a and the energy difference ΔE_a relative to the most favourable adsorption site for H_2O on Bi_2Te_3. The table shows adsorption on top of the first layer Te atom (1-Te), the second layer Bi atom (2-Bi) and the third layer Te atom (3-Te). The optimised orientations of the H_2O molecule on the according positions are horizontal (ho), with a single OH bond pointing down (ld) or at an intermediate angle (skew)—i.e. with the OH bond being neither perpendicular nor horizontal to the surface

Table 2 summarises different orientations of the molecule for adsorption on top of the second layer Bi atom and on the third layer Te atom (for the complete set of DFT calculations including all considered adsorption geometries please refer to the Supplementary Tables 1 and 2). We conclude from Fig. 2 that the optimal orientation of the water molecule on both adsorption sites is at an intermediate angle (skew), i.e. with the OH bond being neither perpendicular nor horizontal to the surface.

The second most stable adsorption site is where we would approximately localise the diffusion barrier. Based on the results of these static vdW corrected DFT calculations (the temperature

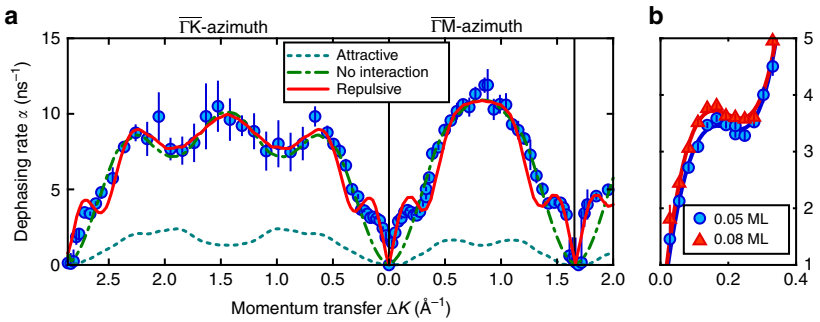

Fig. 4 Comparison of the experimental dephasing rates $\alpha(\Delta K)$ with kinetic Monte Carlo simulations and the coverage dependence of $\alpha(\Delta K)$. **a** Momentum transfer dependence $\alpha(\Delta K)$ for the diffusion of H_2O on Bi_2Te_3(111) at 150 K. Experimental results for a coverage of 0.05 ML are shown as discrete points. The red solid line shows $\alpha(\Delta K)$ as extracted from a kinetic Monte Carlo simulation where repulsive dipole–dipole forces between the individual water molecules are included. Attractive interactions (turquoise dashed line) give dephasing rates much lower than the experiment, while diffusion without forces (green dash-dotted line) does not reproduce the structure around the zone centre (see text). **b** A close-up of the experimental dephasing rates in Fig. 2 (b) along the $\overline{\Gamma M}$-direction for two coverages: 0.05 ML, (red line and points), and 0.08 ML (blue line and points). The observed increase in dephasing rate below 0.3 Å^{-1} confirms the presence of repulsive interactions. The error bars correspond to the confidence bounds (1σ) of $\alpha(\Delta K)$.

of the system is ignored) using the energy differences between the adsorption sites (Fig. 2) would result in a diffusion barrier of about 20 meV, which is in excellent agreement with the value found in the experiment.

As shown in Fig. 3(d), calculations using a (2×2) supercell give rise to the same adsorption site as for the (1×1) supercell. As can also be seen by a comparison with further results in the Supplementary Table 2, the relative energies and therefore the diffusion barrier do not significantly depend on the water coverage used for the calculations. Hence the experimentally determined barrier for H_2O diffusion as well as the one found via vdW corrected DFT are significantly smaller compared to the diffusion barriers of metal atoms on TI surfaces as found by DFT calculations[45–47].

Since the DFT calculations are static (essentially corresponding to an ideal state at a temperature of 0 K), more evolved theoretical studies such as ab-initio molecular dynamics simulations could address phonons and molecular vibration/rotation effects at finite temperatures but they are computationally extremely demanding for the current system. Furthermore, in most weakly-bound supramolecular systems, zero-point energy effects do not affect substantially the magnitude of the barrier height and are usually ignored since the weak frustrated translation and out-of-plane bending modes are extremely difficult to accurately calculate[61,62]. Hence while the DFT calculations provide a good measure for the energetics of adsorption sites and configurations, for further dynamic properties we rely on other computationally less expensive theoretical approaches as explained below.

Adsorbate interactions. One reason for the steep rise of $\alpha(\Delta K)$ at small ΔK values, which is not reproduced by the analytic CE model, may be repulsive interactions between the adsorbates. The characteristic shape of the curve for such a case, with a peak at small ΔK values followed by a de Gennes narrowing dip, has been described theoretically and observed experimentally for surface diffusion[48,56,58]. The location of the dip corresponds to a peak in the static structure factor[63], verifies the repulsive nature of the force and allows also a coverage estimation of the adsorbates (see Supplementary Methods).

The momentum transfer dependence for two different coverages along $\overline{\Gamma M}$ is shown in Fig. 2(b). α increases slightly when increasing the coverage from 0.05 to 0.08 ML (blue circles vs. red triangles). The difference is quite subtle but seen when zooming into the region at small ΔK as plotted in Fig. 4(b).

The repulsive nature of the interactions can be verified by a simple kinetic Monte Carlo (MC) simulation, which is illustrated by the red solid line in Fig. 4(a). Therein, we assume that the water molecules move on a hexagonal grid between adjacent sites (based on the results of the analytical model above). Repulsive/attractive inter-adsorbate interactions were included with a pairwise dipole–dipole potential. Using the trajectories of the MC simulation, the dephasing rate α is then determined from the calculated ISFs (see Supplementary Methods for more details). For no interaction between the molecules we obtain the same $\alpha(\Delta K)$ from the MC simulation as the CE model (green dash-dotted line). Attractive interactions between the molecules cannot explain the de Gennes dip (turqouise dashed line). Only the introduction of repulsive forces in the MC simulation can reproduce the experimental data including also the de Gennes dip at small ΔK and around the diffraction peaks as illustrated by the red solid line in Fig. 4(a). The effect is however much less pronounced compared to other systems e.g. to Na on Cu(001)[58] and to the diffusion of water on the hydrophobic graphene surface[60].

The repulsive forces will increase the hopping rate in the long-range limit (for $|\Delta K \pm G|$ approaching 0), i.e. if one adsorbate moves it pushes the other ones in the vicinity due to the repulsive forces, thus increasing the overall hopping rate. The situation of the individual water molecules depends on the distance between the adsorbates and the actual configuration at the surface. Consequently, the dipole moment associated with an adsorbate used in the simulations that describe the experimental data provides a good measure of the interactions. Using a dipole moment of about 2 debye in the MC simulations provides a good description of the experimental data, which corresponds roughly to the dipole moment of an isolated water molecule and is by a factor of three smaller than compared to the Na/Cu(001) system[58].

Energy dissipation and atomic-scale friction. Based on the low corrugation of the PES (from experiment and DFT calculations) in combination with the rather small diffusion constant we may already anticipate that the system exhibits an unusual atomic-scale friction. Friction in surface diffusion processes can be caused by a variety of dissipative mechanisms, interactions with phonons and electrons in the substrate[54] as well as interactions between adsorbates[64] and coupling of the internal molecular degrees of freedom with the motion of the centre of mass[65]. For Brownian

motion, the atomic-scale friction η can be directly extracted with Einstein's relation[61,66], while it is not possible for hopping motion. In principle the CE model for hopping motion contains Brownian diffusion as a long range diffusion limit (for $\Delta K \rightarrow 0$, $\alpha(\Delta K)$ converges to a parabola), but this approach is problematic[61], in particular for the interacting case. Furthermore, we are not able to resolve any frustrated translational vibration of the water molecule, thus allowing conclusions about the friction force from the broadening of the vibrational mode[56].

Instead, we base our analysis on the rate of barrier crossing obtained from a Langevin description of the dynamics, where the friction is a direct measure of the coupling between the centre-of-mass motion and the heat-bath of the substrate[67]. Friction has a direct influence on the diffusion as it affects the rate of energy transfer between the adsorbate and the substrate. In the present study we seek to understand the relatively low rate of diffusion noted above. In ideal Brownian diffusion, where there are no barriers, the rate decreases as the friction increases. However, if the diffusion is activated, as in the present case, then there exists also a low-friction regime where the rate decreases as the friction is reduced.

The phenomenology is well understood from a theoretical perspective, where it is known as Kramer's turnover theory[68]. Motion in the high-friction regime is dominated by single-jumps, while behaviour in the low-friction regime includes both single- and multiple-jumps, though single-jumps always dominate. Comparison with the analysis in Fig. 2(b), and in particular the significant fraction of double jumps, suggest that the observed motion lies in the low-friction regime. Notably, the finding differs from the observation of other molecular adsorbates which generally showed a higher friction[65].

Understanding the energy dissipation channels during diffusion on TI surfaces is interesting due to their insulating interior, so that the only contribution to electronic friction arises from the metallic surface state. There is no simple way to disentangle the electronic from the phononic contribution to the friction[54] but it is noteworthy that Bi_2Te_3 has a low Debye temperature with phonons having correspondingly low frequencies[69,70]. The energy mismatch between the acoustic phonons and the internal modes of a water molecule, together with a mismatch between the mass of the water molecule and the heavy substrate atoms, suggests that phononic friction will occur predominantly through multi-phonon processes (see also Supplementary Discussion and Supplementary Table 3). The likely absence of single-phonon coupling suggests that electronic friction may therefore be a significant contribution. Electron–hole excitation in a metallic band is the predominant mechanism for electronic friction[54]. In the present instance any contribution is restricted to the density of surface states arising from the topological character of the substrate.

Taken together, these observations are suggestive of a system where both the phonon and electron contributions are limited. The picture is consistent with the experimental results in Fig. 2 (b), where a high proportion of multiple-jumps is required to explain the data. The newly available data may provide the necessary experimental benchmarks in order to study these effects from a theoretical point of view.

Future work will be required to resolve the importance of the above mentioned effects towards energy dissipation and to explain the measurements fully; in particular considering the full-dimensional potential of the diffusing molecule together with possible internal degrees of freedom of the H_2O molecules[65,71]. Other routes for first-principle theoretical calculations regarding the frictional forces are possible within the harmonic approximation and have been applied in the past for calculations, especially for atomic self-diffusion. However, its validity for weakly-bonded supramolecular systems is questionable, especially in the context of a well-known multidimensional and temperature-dependent contribution to the friction force from surface phonons, excitons and other non-adiabatic effects[72]. Furthermore, more evolved theoretical studies such as ab-intio molecular dynamics simulations are on the verge of what is currently possible in terms of computing time considering the observed relatively slow diffusion process on a rather complex surface.

Discussion

In summary, to our knowledge, this work reveals for the first time the mechanism of water diffusion on a TI surface based on experiments. Our analysis and understanding of the correlated motion of H_2O on Bi_2Te_3(111) provides a more general insight into the mobility of small molecules at TI surfaces. The diffusion of water molecules on Bi_2Te_3(111) follows an activated hopping motion on a corrugated potential energy surface, with a diffusion barrier of 34 meV, in good agreement with the results of vdW-corrected DFT calculations. Jumps of the water molecules occur on a hexagonal lattice corresponding to the substrate lattice spacing, with a significant fraction of longer jumps (37%).

The mechanism is remarkable as it shows signatures of repulsive interaction between the individual water molecules. The experimentally determined diffusion coefficient is 2–3 orders of magnitude larger than the theoretically calculated atomic mobilities of most metal atoms on TI surfaces, yet slower than the diffusion of small molecules on flat metal surfaces. In addition to the experimental insight into wetting, friction and physisorption of water on an important class of materials, the hereby studied system provides also a special platform for an atomic level investigation in what ways kinetic and chemical energy is transferred between adsorbates and the substrate—not least due to the insulating interior and the existence of topologically protected metallic surface states on TIs.

The observed diffusive properties differ strongly from those at low-index metal surfaces for molecular diffusion on solid surfaces. The experimental data obtained during this study provides the necessary benchmarks for further theoretical progress since experimental and theoretical findings suggest that energy dissipation between the water adsorbates and surface atoms governs the diffusion mechanism.

Methods

Experimental details. All measurements were performed on the Cambridge helium-3 spin-echo apparatus which generates a nearly monochromatic beam of ^{3}He that is scattered off the sample surface in a fixed 44.4° source–target–detector geometry. The detailed setup of the apparatus has been described in greater detail elsewhere[48,50]. The crystal structure of Bi_2Te_3 is rhombohedral, consisting of quintuple layers bound to each other through weak van der Waals forces which gives easy access to the (111) surface by cleavage[15]. The (111) cleavage plane (Fig. 1a) is terminated by Te atoms and exhibits a hexagonal structure ($a = 4.386$ Å[21]). The Bi_2Te_3 single crystals used in the study were attached onto a sample holder using electrically and thermally conductive epoxy. The sample holder was then inserted into the chamber using a load-lock system[73] and cleaved in situ. The sample holder can be heated using a radiative heating filament on the backside of the crystal or cooled down to 105 K via thermal connection to a liquid nitrogen cooling reservoir. The sample temperature was measured using a chromel-alumel thermocouple.

Water was dosed onto the sample with a microcapillary array beam doser which was brought close to the surface. Previous to the dynamics measurement H_2O is dosed up to a certain attenuation (corresponding to a certain H_2O coverage, see Supplementary Fig. 1) of the specularly reflected helium signal. Therefore the partial pressure of water in the scattering chamber is adjusted using an automatic leak valve and the reflected helium signal is monitored until equilibrium is obtained.

The dynamics of H_2O adsorbed on Bi_2Te_3(111) were extracted from helium spin-echo measurements, via the intermediate scattering function (ISF), $I(\Delta\mathbf{K}, t)$ with a single exponential decay according to (1). While a signal exponential decay provides the best fit to the data throughout the experiments presented here, note that for different types of motion occurring on different timescales $I(\Delta\mathbf{K}, t)$ will

deviate from the single exponential form in (1) and is better fitted using multiple exponential decays[48].

Computational details. For the DFT calculations presented in this work we employed CASTEP[74], a plane wave, periodic boundary condition code. The plane wave basis set is truncated at an electron energy cut-off of 1000 eV and we employ fully-relativistic pseudopotentials. The Brillouin zone was sampled with a $(5\times5\times1)$ Monkhorst–Pack k-point mesh. The Perdew–Burke–Ernzerhof (PBE) exchange-correlation functional[75] was applied in combination with the Tkatchenko–Scheffler (TS) dispersion correction method[76]. The electronic structure was minimised to the ground state energy by fully including spin-orbit coupling (SOC) and non-collinear spin treatment. Due to the topologically non-trivial nature of Bi_2Te_3 the inclusion of SOC leads to the formation of the TSS, i.e. the Dirac cones in the surface electronic structure[69]. The Bi_2Te_3 substrate was modelled with a single quintuple layer in a (1×1) supercell, and an additional 25 Å vacuum layer for separating the periodically repeated supercells in the z-direction. The positions of the atoms in the substrate and adsorbate were left fully unconstrained, except for the set of calculations with the frozen substrate. For the structural optimisations, the force tolerance was set to 0.05 eVA^{-1}.

Data availability

The data that support the findings of this study are available from the corresponding author upon reasonable request.

Code availability

The code for the kinetic Monte Carlo simulations is available from https://doi.org/10.5281/zenodo.3531646 under the GNU/GPL-3.0 license.

Received: 26 February 2019; Accepted: 13 December 2019;
Published online: 14 January 2020

References

1. Björneholm, O. et al. Water at Interfaces. *Chem. Rev.* **116**, 7698–7726 (2016).
2. Heidorn, S.-C., Bertram, C., Cabrera-Sanfelix, P. & Morgenstern, K. Consecutive mechanism in the diffusion of D_2O on a NaCl(100) Bilayer. *ACS Nano* **9**, 3572–3578 (2015).
3. Mitsui, T., Rose, M. K., Fomin, E., Ogletree, D. F. & Salmeron, M. Water diffusion and clustering on Pd(111). *Science* **297**, 1850–1852 (2002).
4. Maier, S. & Salmeron, M. How does water wet a surface? *Acc. Chem. Res.* **48**, 2783–2790 (2015).
5. Carrasco, J., Hodgson, A. & Michaelides, A. A molecular perspective of water at metal interfaces. *Nat. Mater.* **11**, 667–674 (2012).
6. Hodgson, A. & Haq, S. Water adsorption and the wetting of metal surfaces. *Surf. Sci. Rep.* **64**, 381–451 (2009).
7. Verdaguer, A., Sacha, G. M., Bluhm, H. & Salmeron, M. Molecular structure of water at interfaces: wetting at the nanometer scale. *Chem. Rev.* **106**, 1478–1510 (2006).
8. Ma, M., Tocci, G., Michaelides, A. & Aeppli, G. Fast diffusion of water nanodroplets on graphene. *Nat. Mater.* **15**, 66–71 (2016).
9. Avidor, N. & Allison, W. Helium diffraction as a probe of structure and proton order on model ice surfaces. *J. Phys. Chem. Lett.* **7**, 4520–4523 (2016).
10. Guo, J., Li, X.-Z., Peng, J., Wang, E.-G. & Jiang, Y. Atomic-scale investigation of nuclear quantum effects of surface water: experiments and theory. *Prog. Surf. Sci.* **92**, 203–239 (2017).
11. Nihonyanagi, S., Yamaguchi, S. & Tahara, T. Ultrafast dynamics at water interfaces studied by vibrational sum frequency generation spectroscopy. *Chem. Rev.* **117**, 10665–10693 (2017).
12. Smit, W. J. & Bakker, H. J. The surface of ice is like supercooled liquid water. *Angew. Chem.* **129**, 15746–15750 (2017).
13. Thämer, M., De Marco, L., Ramasesha, K., Mandal, A. & Tokmakoff, A. Ultrafast 2D IR spectroscopy of the excess proton in liquid water. *Science* **350**, 78–82 (2015).
14. Lin, C. et al. Ice nucleation on a corrugated surface. *J. Am. Chem. Soc.* **140**, 15804–15811 (2018).
15. Chen, Y. L. et al. Experimental realization of a three-dimensional topological insulator, Bi_2Te_3. *Science* **325**, 178–181 (2009).
16. Moore, J. E. The birth of topological insulators. *Nature* **464**, 194–198 (2010).
17. Hasan, M. Z. & Kane, C. L. Colloquium: topological insulators. *Rev. Mod. Phys.* **82**, 3045–3067 (2010).
18. Qi, X.-L. & Zhang, S.-C. Topological insulators and superconductors. *Rev. Mod. Phys.* **83**, 1057–1110 (2011).
19. Beenakker, C. & Kouwenhoven, L. A road to reality with topological superconductors. *Nat. Phys.* **12**, 618–621 (2016).
20. Barreto, L. et al. Surface-dominated transport on a bulk topological insulator. *Nano Lett.* **14**, 3755–3760 (2014).
21. Tamtögl, A. et al. Electron-phonon coupling and surface Debye temperature of Bi_2 Te_2 (111) from helium atom scattering. *Phys. Rev. B* **95**, 195401 (2017).
22. Schoop, L. M., Pielnhofer, F. & Lotsch, B. V. Chemical principles of topological semimetals. *Chem. Mater.* **30**, 3155–3176 (2018).
23. Benia, H. M., Lin, C., Kern, K. & Ast, C. R. Reactive chemical doping of the Bi_2Se_3 topological insulator. *Phys. Rev. Lett.* **107**, 177602 (2011).
24. Bianchi, M. et al. Robust surface doping of Bi_2Se_3 by rubidium intercalation. *ACS Nano* **6**, 7009–7015 (2012).
25. Kong, D. et al. Rapid surface oxidation as a source of surface degradation factor for Bi2Se3. *ACS Nano* **5**, 4698–4703 (2011).
26. Yashina, L. V. et al. Negligible surface reactivity of topological insulators Bi_2Se_2 and Bi_2Te_2 towards oxygen and water. *ACS Nano* **7**, 5181–5191 (2013).
27. Zhang, K.-W. et al. Real-space characterization of reactivity towards water at the Bi_2 Te_2 (111) surface. *Phys. Rev. B* **93**, 235445 (2016).
28. Volykhov, A. A. et al. Rapid surface oxidation of Sb_2Te_3 as indication for a universal trend in the chemical reactivity of tetradymite topological insulators. *Chem. Mater.* **28**, 8916–8923 (2016).
29. Su, S. H. et al. Selective hydrogen etching leads to 2D Bi(111) bilayers on Bi_2 Se_2: large rashba splitting in topological insulator heterostructure. *Chem. Mater.* **29**, 8992–9000 (2017).
30. Hsieh, D. et al. A tunable topological insulator in the spin helical dirac transport regime. *Nature* **460**, 1101–1105 (2009).
31. Wray, L. A. et al. A topological insulator surface under strong Coulomb, magnetic and disorder perturbations. *Nat. Phys.* **7**, 32–37 (2011).
32. Roy, S. et al. Tuning the Dirac point position in Bi_2Se_3(0001) via surface carbon doping. *Phys. Rev. Lett.* **113**, 116802 (2014).
33. Wang, E. et al. Robust gapless surface state and Rashba-splitting bands upon surface deposition of magnetic Cr on Bi_2Se_2. *Nano Lett.* **15**, 2031–2036 (2015).
34. Caputo, M. et al. Manipulating the topological interface by molecular adsorbates: adsorption of Co-phthalocyanine on Bi_2Se_2. *Nano Lett.* **16**, 3409–3414 (2016).
35. Martínez-Velarte, M. C. et al. Chemical disorder in topological insulators: a route to magnetism tolerant topological surface states. *Nano Lett.* **17**, 4047–4054 (2017).
36. Haneman, D. Adsorption and bonding properties of cleavage surfaces of bismuth telluride. *Phys. Rev.* **119**, 567 (1960).
37. Netsou, A.-M. et al. Scanning probe microscopy induced surface modifications of the topological insulator Bi_2Te_2 in different environments. *Nanotechnology* **28**, 335706 (2017).
38. Kong, D. et al. Few-layer nanoplates of Bi_2Se_2 and Bi_2Te_2 with highly tunable chemical potential. *Nano Lett.* **10**, 2245–2250 (2010).
39. Liu, B. et al. Surrounding sensitive electronic properties of Bi_2Te_2 nanoplates—potential sensing applications of topological insulators. *Sci. Rep.* **4**, 4639 (2014).
40. Ambrosi, A., Sofer, Z., Luxa, J. & Pumera, M. Exfoliation of layered topological insulators Bi_2 Se_2 and Bi_2 Te_2 via electrochemistry. *ACS Nano* **10**, 11442–11448 (2016).
41. Ludwig, T. et al. Mechanism of bismuth telluride exfoliation in an ionic liquid solvent. *Langmuir* **31**, 3644–3652 (2015).
42. Guo, L. et al. Selective adsorption of bismuth telluride nanoplatelets through electrostatic attraction. *Phys. Chem. Chem. Phys.* **16**, 11297–11302 (2014).
43. Thomas, C. R. et al. Surface oxidation of Bi2(Te,Se)$_3$ topological insulators depends on cleavage accuracy. *Chem. Mater.* **28**, 35–39 (2016).
44. Xiao, J., Kou, L., Yam, C.-Y., Frauenheim, T. & Yan, B. Toward rational design of catalysts supported on a topological insulator substrate. *ACS Catal.* **5**, 7063–7067 (2015).
45. Gosálvez, M. A. et al. Low-coverage surface diffusion in complex periodic energy landscapes: analytical solution for systems with symmetric hops and application to intercalation in topological insulators. *Phys. Rev. B* **93**, 075429 (2016).
46. Ryabishchenkova, A. G., Otrokov, M. M., Kuznetsov, V. M. & Chulkov, E. V. Ab initio study of the adsorption, diffusion, and intercalation of alkali metal atoms on the (0001) surface of the topological insulator Bi_2Se_2. *J. Exp. Theor. Phys.* **121**, 465–476 (2015).
47. Huang, W.-K. et al. Tailoring kinetics on a topological insulator surface by defect-induced strain: Pb mobility on Bi_2Te_3. *Nano Lett.* **16**, 4454–4461 (2016).
48. Jardine, A., Hedgeland, H., Alexandrowicz, G., Allison, W. & Ellis, J. Helium-3 spin-echo: principles and application to dynamics at surfaces. *Prog. Surf. Sci.* **84**, 323 (2009).
49. Jardine, A. P. et al. Ultrahigh-resolution spin-echo measurement of surface potential energy landscapes. *Science* **304**, 1790 (2004).
50. Alexandrowicz, G. & Jardine, A. P. Helium spin-echo spectroscopy: studying surface dynamics with ultra-high-energy resolution. *J. Phys.: Condens. Matter* **19**, 305001 (2007).
51. Shiotari, A. & Sugimoto, Y. Ultrahigh-resolution imaging of water networks by atomic force microscopy. *Nat. Commun.* **8**, 14313 (2017).

52. Chudley, C. T. & Elliott, R. J. Neutron scattering from a liquid on a jump diffusion model. *Proc. Phys. Soc.* **77**, 353 (1961).
53. Tuddenham, F. E. et al. Lineshapes in quasi-elastic scattering from species hopping between non-equivalent surface sites. *Surf. Sci.* **604**, 1459–1475 (2010).
54. Rittmeyer, S. P. et al. Energy dissipation during diffusion at metal surfaces: disentangling the role of phonons versus electron-hole pairs. *Phys. Rev. Lett.* **117**, 196001 (2016).
55. Barth, J. Transport of adsorbates at metal surfaces: from thermal migration to hot precursors. *Surf. Sci. Rep* **40**, 75–149 (2000).
56. Ala-Nissila, T., Ferrando, R. & Ying, S. C. Collective and single particle diffusion on surfaces. *Adv. Phys.* **51**, 949–1078 (2002).
57. Calvo-Almazán, I. et al. Ballistic diffusion in poly-aromatic hydrocarbons on graphite. *J. Phys. Chem. Lett.* **7**, 5285–5290 (2016).
58. Alexandrowicz, G., Jardine, A. P., Hedgeland, H., Allison, W. & Ellis, J. Onset of 3D collective surface diffusion in the presence of lateral interactions: Na/Cu(001). *Phys. Rev. Lett.* **97**, 156103 (2006).
59. Hänggi, P., Talkner, P. & Borkovec, M. Reaction-rate theory: fifty years after Kramers. *Rev. Mod. Phys.* **62**, 251–341 (1990).
60. Tamtögl, A. et al. Dynamics of water monomers on a hydro-phobic surface (2019). Preprint at https://arxiv.org/abs/1810.00650.
61. Tamtögl, A. et al. Ultrafast molecular transport on carbon surfaces: the diffusion of ammonia on graphite. *Carbon* **126**, 23–30 (2018).
62. Lechner, B. A. J. et al. Quantum influences in the diffusive motion of pyrrole on Cu(111). *Angew. Chem. Int. Ed.* **52**, 5085–5088 (2013).
63. Serra, A. & Ferrando, R. An efficient method for computing collective diffusion in a strongly interacting lattice gas. *Surf. Sci.* **515**, 588–596 (2002).
64. Martínez-Casado, R., Vega, J. L., Sanz, A. S. & Miret-Artés, S. Line shape broadening in surface diffusion of interacting adsorbates with quasielastic he atom scattering. *Phys. Rev. Lett.* **98**, 216102 (2007).
65. Lechner, B. A. J. et al. Atomic scale friction of molecular adsorbates during diffusion. *J. Chem. Phys.* **138**, 194710 (2013).
66. Hedgeland, H. et al. Measurement of single-molecule frictional dissipation in a prototypical nanoscale system. *Nat. Phys.* **5**, 561–564 (2009).
67. Miret-Artés, S. & Pollak, E. The dynamics of activated surface diffusion. *J. Phys.: Condens. Matter* **17**, S4133–S4150 (2005).
68. Ianconescu, R. & Pollak, E. A study of Kramers' turnover theory in the presence of exponential memory friction. *J. Chem. Phys.* **143**, 104104 (2015).
69. Tamtögl, A. et al. Nanoscale surface dynamics of Bi_2Te_2 (111): observation of a prominent surface acoustic wave and the role of van der Waals interactions. *Nanoscale* **10**, 14627–14636 (2018).
70. Chis, V. et al. Vibrations in binary and ternary topological insulators: first-principles calculations and Raman spectroscopy measurements. *Phys. Rev. B* **86**, 174304 (2012).
71. Alexandrowicz, G. et al. Observation of microscopic CO dynamics on Cu(001) using ^{3} He spin-echo spectroscopy. *Phys. Rev. Lett.* **93**, 156103 (2004).
72. Hutson, J.M. An introduction to the dynamics of Van der Waals molecules. in *Advances in Molecular Vibrations and Collision Dynamics*, 1 (JAI Press, Greenwich, CT, 1991).
73. Tamtögl, A. et al. Note: a simple sample transfer alignment for ultra-high vacuum systems. *Rev. Sci. Instrum.* **87**, 066108 (2016).
74. Clark, S. J. et al. First principles methods using CASTEP. *Z. Kristallogr. Cryst. Mater.* **220**, 567–570 (2005).
75. Perdew, J. P., Burke, K. & Ernzerhof, M. Generalized gradient approximation made simple. *Phys. Rev. Lett.* **77**, 3865–3868 (1996).
76. Tkatchenko, A. & Scheffler, M. Accurate molecular van der Waals interactions from ground-state electron density and free-atom reference data. *Phys. Rev. Lett.* **102**, 073005 (2009).

Acknowledgements

A.T. would like to thank G. Benedek, G. Alexandrowicz, D. J. Ward, A. P. Jardine, M. Alducin and J.I. Juaristi for many helpful discussions. The publication has been supported by the TU Graz Open Access Publishing Fund. The authors are grateful for financial support by the Aarhus University Research Foundation, VILLUM FONDEN and the SPP1666 of the DFG (Grant No. HO 5150/1-2). One of us (A.T.) acknowledges financial support provided by the FWF (Austrian Science Fund) within the projects J3479-N20 and P29641-N36. I. C-A. is grateful to the Ramón Areces foundation for financial support and N.A. gratefully acknowledges the Blavatnik Foundation. M.B. acknowledges financial support from the Center of Materials Crystallography (CMC) and the Danish National Research Foundation (DNRF93).

Author contributions

A.T. conducted the majority of the experimental measurements with some additional measurements by N.A., I.C-A. and P.T. The vdW corrected DFT calculations were performed by M.S. The analysis of the experimental data as well as the kinetic MC were carried out by A.T. The topological insulator samples were synthesised and characterised by M.B. and A.T., N.A., M.S. and W.A. interpreted the data and wrote the manuscript. J.E. and P.H. contributed to the conception of the project and all authors contributed to the discussion and preparation of the manuscript.

Competing interests

The authors declare no competing interests.

Additional information

Supplementary information is available for this paper at https://doi.org/10.1038/s41467-019-14064-7.

Correspondence and requests for materials should be addressed to A.T.

Peer review information Nature Communications thanks Richard Catlow, and other, anonymous, reviewer(s) for their contribution to the peer review of this work.

Reprints and permission information is available at http://www.nature.com/reprints

Publisher's note Springer Nature remains neutral with regard to jurisdictional claims in published maps and institutional affiliations.

6.15 Publication O

Benedek, G., Miret-Artés, S., Manson, J. R., Ruckhofer, A., Ernst, W. E. & Tamtögl, A. Origin of the Electron-Phonon Interaction of Topological Semimetal Surfaces Measured with Helium Atom Scattering. *J. Phys. Chem. Lett.* **11,** 1927–1933 (2020)

contributions	
funding	A. Tamtögl, W. E. Ernst
preparation / setup	A. Tamtögl, A. Ruckhofer
data acquisition	A. Tamtögl, A. Ruckhofer
theory	G. Benedek, S. Miret-Artés, J. R. Manson
data analysis	A. Tamtögl, G. Benedek
interpretation	A. Tamtögl, G. Bendek
publication writing	A. Tamtögl, S. Miret-Artés, G. Bendek, J. R. Manson

Reprinted from:

Benedek, G., Miret-Artés, S., Manson, J. R., Ruckhofer, A., Ernst, W. E. & Tamtögl, A. Origin of the Electron-Phonon Interaction of Topological Semimetal Surfaces Measured with Helium Atom Scattering. *J. Phys. Chem. Lett.* **11,** 1927–1933 (2020)

THE JOURNAL OF PHYSICAL CHEMISTRY Letters

pubs.acs.org/JPCL Letter

Origin of the Electron–Phonon Interaction of Topological Semimetal Surfaces Measured with Helium Atom Scattering

Giorgio Benedek, Salvador Miret-Artés,* J. R. Manson, Adrian Ruckhofer, Wolfgang E. Ernst, and Anton Tamtögl*

Cite This: J. Phys. Chem. Lett. 2020, 11, 1927–1933 Read Online

ACCESS | Metrics & More | Article Recommendations

ABSTRACT: He atom scattering has been demonstrated to be a sensitive probe of the electron–phonon interaction parameter λ at metal and metal-overlayer surfaces. Here it is shown that the theory linking λ to the thermal attenuation of atom scattering spectra (the Debye–Waller factor) can be applied to topological semimetal surfaces, such as the quasi-one-dimensional charge-density-wave system Bi(114) and the layered pnictogen chalcogenides. The electron–phonon coupling, as determined for several topological insulators belonging to the class of bismuth chalcogenides, suggests a dominant contribution of the surface quantum well states over the Dirac electrons in terms of λ.

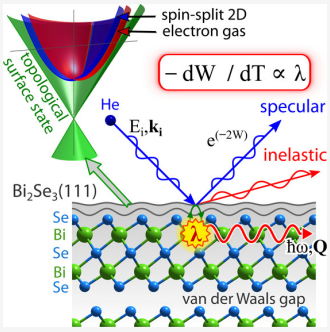

Knowledge of the electron–phonon (e–ph) interaction at conducting surfaces and the specific role of dimensionality are of great relevance both from a fundamental point of view as well as for various applications, such as two-dimensional (2D)[1] and quasi-1D superconductivity[2] in nanotechnology. Similarly, the e–ph interaction plays a relevant role in other transport properties, e.g., thermoelectricity, in low-dimensional systems such as layered Bi and Sb chalcogenides[3] and in quasi-crystalline materials which are often viewed as periodic solids in higher dimensions.[4]

In a series of recent experimental and theoretical works, it was shown that the e–ph coupling constants for individual phonons $\lambda_{Q,\nu}$ as well as their average λ (also known as the mass-enhancement parameter or factor)[5−7] can be measured directly with helium atom scattering (HAS).[8−11] In particular, the study of multilayer metallic structures[8,11] has shown that HAS can detect subsurface phonons as deep as those that contribute to the e–ph interaction. For example, HAS can detect phonons spanning as many as 10 atomic layers in Pb films[8,9] (known as the *quantum sonar effect*), thus providing the individual $\lambda_{Q,\nu}$ values for phonons which provide the dominant contributions to λ. The values of λ are obtained directly from the temperature dependence of the HAS Debye–Waller (DW) exponent, and the interaction range can be assessed from the number of layers, n_{sat}, above which the measured λ becomes thickness-independent. In that analysis, the conducting surface region of a 3D material could be viewed as a stack of (interacting) 2D electron gases (2DEGs), allowing for the simpler formalism characterizing the 2DEG.[11] Due to the appreciable depth explored by the e–ph interaction, the values of λ obtained from HAS (hereafter called λ_{HAS}) generally are close to the most reliable values found in the literature,[10,11] thus allowing one to assess the validity of the new method.

In this work, we investigate the specific role of dimensionality in the e–ph mass-enhancement factor λ_{HAS} as derived from HAS. The method is shown to be particularly suitable for different classes of conducting 2D materials, such as the layered chalcogenides, topological insulators, and systems characterized by a quasi-1D free electron gas, including Bi(114). The present analysis shows that the charge density wave (CDW) transition in Bi(114), recently observed with HAS,[12] is sustained by multivalley e–ph interaction with a pronounced 1D character. In the case of topological materials, the present analysis of previous HAS data on $Bi_2Te_3(111)$[13] and $Bi_2Se_3(111)$[14] as well as new experimental data on $Bi_2Te_2Se(111)$ indicates the overwhelming contribution to λ_{HAS} from the surface quantum well states as compared to that of the Dirac states.

The DW factor describes the attenuation due to the thermal atomic motion of the elastically scattered intensity $I(T)$ observed at temperature T, with respect to the elastic intensity

Received: December 23, 2019
Accepted: February 7, 2020
Published: February 7, 2020

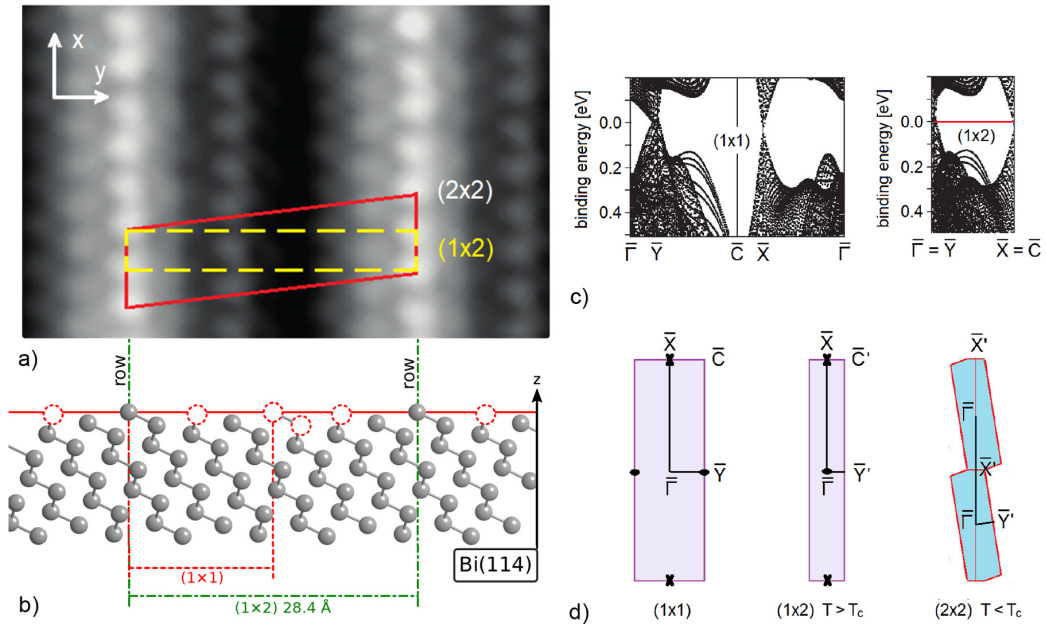

Figure 1. (a) The Bi(114) surface is characterized by parallel atomic rows due to a (1 × 2) surface reconstruction as visualized in STM images[30] (reproduced with permission, copyright 2009 by the American Physical Society). (b) Side view of the ideal (114) truncation of bismuth (including the red dashed circles) and the actual (1 × 2) surface reconstruction (circles removed), giving rise to the parallel atomic rows with an inter-row distance of 28.4 Å and an interatomic distance of 4.54 Å. The corresponding (1 × 2) electronic structure (c) is schematically represented as a folding of the calculated electronic structure[30] for the truncated Bi(114) (1 × 1) surface, with the corresponding surface BZ shown in (d) (reproduced with permission, copyright 2009 by the American Physical Society). In particular, the cones of electronic states occurring at the Fermi level at the $\bar{X}$ and $\bar{Y}$ symmetry points turn out to be aligned in the $\bar{\Gamma}\bar{X}$ direction after the (1 × 2) folding [panel d]. It allows for a multivalley 1D CDW instability along the rows leading to a (2 × 2) dimerization below ∼280 K and a corresponding CDW observed with HAS.[12] The (2 × 2) surface portion reproduced in (a)[30] shows a π dephasing of two adjacent rows so as to give a rhombohedric cell, with the corresponding BZ shown in (d).

of the corresponding rigid surface I_0. It is a multiplicative factor usually written as an exponential function, $\exp\{-2W(\mathbf{k}_f, \mathbf{k}_i, T)\}$, of the final ($\mathbf{k}_f$) and incident ($\mathbf{k}_i$) wavevectors of the scattered atom,

$$I(T) = I_0 e^{-2W(T)} \tag{1}$$

where it is implicit that all quantities in eq 1 depend on the scattering wavevectors ($\mathbf{k}_f$, $\mathbf{k}_i$). For a two-body collision model, where the incident atom directly interacts with the surface target, the DW exponent is simply expressed by $2W(\mathbf{k}_f, \mathbf{k}_i, T) = \langle(\Delta\mathbf{k}\cdot\mathbf{u})^2\rangle_T$, where $\Delta\mathbf{k} = (\mathbf{k}_f - \mathbf{k}_i)$ is the scattering vector, $\mathbf{u}$ is the phonon displacement experienced by the projectile atom upon collision, and $\langle\cdots\rangle_T$ indicates a thermal average. However, atoms incident on a conducting surface with energies generally well below 100 meV are scattered exclusively by the surface free-electron density, a few ångströms away from the first atomic layer so that the exchange of energy with the phonon gas occurs only via the phonon-induced modulation of the surface free-electron gas, i.e., via the e−ph interaction. Therefore, it is logical that $2W(\mathbf{k}_f, \mathbf{k}_i, T)$, which originates from the integrated action of all phonons weighted by their respective Bose factors, turns out to be directly proportional, under reasonable approximations, to the mass-enhancement factor λ.

The expression of λ_{HAS} derived in refs 10 and 15 for a 3D free-electron gas is readily extended to any dimension d

$$\lambda_{HAS}^{(d)} = -\frac{\phi\gamma_d}{(k_F r_0)^d}\frac{{k_F}^2}{{k_{iz}}^2}\frac{\partial \ln\{I(T)\}}{k_B \partial T} \tag{2}$$

where r_0 is a lattice distance (${r_0}^2 \equiv A_c$ for the surface unit cell area in 2D; ${r_0}^3 \equiv V_c$, the unit cell volume in 3D), ϕ is the work function, k_F is the Fermi wavevector, k_{iz} is the perpendicular component of the incident wave vector, k_B is the Boltzmann constant, $I(T)$ is the diffraction peak intensity, and $\gamma_d \equiv 2^{d-1}\pi^{d/2}\Gamma\left(\frac{d}{2}\right)$,[16] with Γ being the Gamma function. As mentioned above and discussed in ref 11, the 3DEG of a thick slab can be viewed as a stack of n_{sat} 2DEGs, where n_{sat} is the number above the one at which the HAS reflectivity becomes independent of thickness. This yields the definition $n_{sat} = c^* k_{F\perp}/\pi$, where $k_{F\perp}$ is the Fermi wavevector normal to the surface and c^* is the e−ph interaction range normal to the surface, i.e., the maximum depth beneath the surface from where phonon displacements can modulate the surface charge density. Note that $\pi/k_{F\perp}$ is the wavelength of the Fermi-level charge density $\cos^2 k_{F\perp}z$, i.e., the nominal thickness of a single 2DEG.

In this way, the 2D expression of the e−ph coupling constant for a three-dimensional crystal is obtained,[11] which is reproduced here for the special case of measurements at the specular condition:

$$\lambda_{HAS}^{(2D)} = \frac{\pi}{2n_{sat}}\alpha,\ \alpha \equiv -\frac{\phi}{A_c {k_{iz}}^2}\frac{\partial \ln\{I(T)\}}{k_B \partial T} \tag{3}$$

https://dx.doi.org/10.1021/acs.jpclett.9b03829
J. Phys. Chem. Lett. 2020, 11, 1927−1933

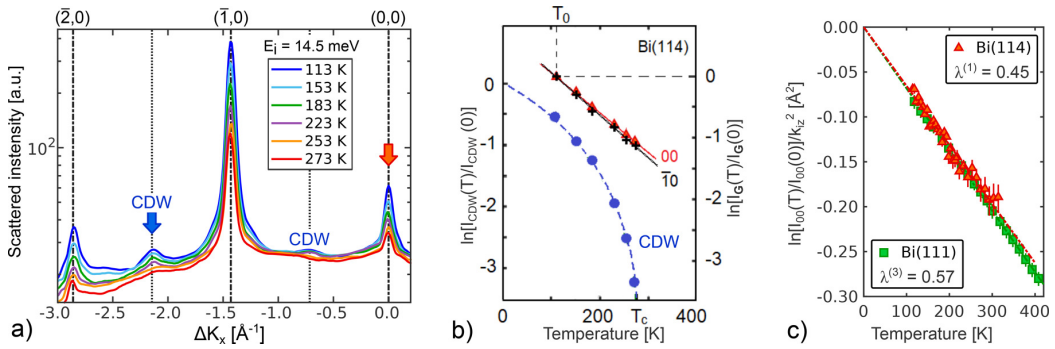

Figure 2. Helium atom scattering data from Bi(114): (a) HAS angular distributions for several different temperatures, ranging from 113 to 273 K as marked, showing both diffraction peaks of the (1×2) reconstruction and the appearance of the CDW feature according to a (2×2) superstructure. (b) Temperature dependence of the $(\bar{3}/2, 0)$ CDW peak (left ordinate scale) and of the (0, 0) (specular) and $(\bar{1}, 0)$ (diffraction) peak DW exponents (right ordinate scale) referred to the lowest temperature measured, T = 113 K. (c) The DW exponents of the Bi(114) and Bi(111) specular peaks, when divided by the respective squared perpendicular wavevector transfers, show similar slopes but lead to different e−ph coupling strengths.

When applying eq 3, it is important to distinguish between metallic surfaces, which present to the He atoms a soft repulsive potential plus a weak long-range attractive well and layered semimetal surfaces, where the free electron gas is protected by an anion surface layer that results in a hard-wall potential plus a comparatively deep attractive van der Waals potential. In the latter case, k_{iz}^2 needs to be corrected due to the acceleration that the He atom undergoes when entering the attractive well, before being repelled by the hard wall (Beeby correction[17]). This is made with the substitution $k_{iz}^2 \rightarrow k_{iz}^2 + 2mD/\hbar^2$, where m is the He atom mass and D is the attractive potential depth (generally derived from He-surface bound-state resonances). In many experiments, the incident energy E_i is generally much larger than D, so the Beeby correction may be neglected but not, for example, in ^{3}He spin−echo experiments, where E_i is low and comparable to D.[18]

Low-dimensional free electron gases are often characterized by a CDW instability below a critical temperature T_c, generally induced by e−ph interaction via the Fröhlich−Peierls[19,20] or the Kelly−Falicov multivalley mechanism,[21−23] the former typically applying to metal surfaces with a CDW wavevector corresponding to some nesting wavevectors between the Fermi contours and the latter more appropriate to semimetal surfaces with pocket states at the Fermi level.[24] The phonon-induced transitions between narrow pockets (nests) realize what is meant as perfect nesting. Since He atoms scattered from a conducting surface probe the surface charge density directly, the occurrence of a CDW below T_c yields additional T-dependent diffraction peaks in the elastic scattering angular distribution at parallel wavevector transfers $\Delta K = |\Delta \mathbf{K}|$ equal or close to the nesting vectors Q_c (i.e., $Q_c = 2k_F$ for the 1D Peierls mechanism). It should be noted that the high sensitivity of HAS permits the detection of weak surface CDWs that are difficult to detect with other methods. An interesting question is whether the temperature dependence of the CDW diffraction peaks carries additional information on the e−ph interaction which sustains the CDW transition.

When considering the temperature dependence of a diffraction peak intensity for a wavevector transfer $\Delta \mathbf{K}$ equal to either a $\mathbf{G}$ vector of the unreconstructed surface lattice ($\Delta \mathbf{K} = \mathbf{G}$) or to a CDW wavevector Q_c, the DW exponent also involves the longitudinal mean-square phonon displacement. For an isotropic mean-square displacement, eq 2 also can be applied to diffraction peaks by replacing $4k_{iz}^2$ with $\Delta k_z^2 + \Delta \mathbf{K}^2$, calculated at the actual scattering geometry at which the diffraction peak is observed. In most HAS experiments, the condition $\Delta \mathbf{K}^2 \ll \Delta k_z^2$ holds, so little difference is expected between the T dependence of the diffraction and specular peaks, provided λ_{HAS} is independent, as it should be, of the scattering channel chosen in the experiment.

There is, however, a caveat for the use of a CDW diffraction intensity $I_{CDW}(T)$. In eq 1, it has been assumed implicitly that $W(T)$ includes all of the temperature dependence of $I(T)$ and that this originates exclusively from thermal vibrations. This is clearly not true for the diffraction from a surface CDW which forms below T_c from a Fermi surface instability and has the temperature-dependent population of electron states near the Fermi level according to Fermi statistics. In this case, I_0 has an implicit dependence on T, which generally is negligible with respect to that of $W(T)$, except near T_c: here its square root $\sqrt{I_0}$ works as an order parameter[25,26] and vanishes for increasing $T \rightarrow T_c$ as $(1 - T/T_c)^{\beta}$, where β is the order-parameter critical exponent (typically $\beta = 1/3$,[12,27−29] while $T_c \approx 280$ K in the present case[12]).

As a good 1DEG example, it is shown that a CDW diffraction peak also may be used to extract λ_{HAS} away from the critical region. The ideal (114) truncation of bismuth (Figure 1) is characterized by parallel atomic rows along the $x \equiv [1\bar{1}0]$ direction, separated by 7.1 Å in the normal direction $y \equiv [22\bar{1}]$, with a unit cell including two rows (b = 14.2 Å) and one atom per row (atom spacing along the rows a = 4.54 Å). At room temperature, the Bi(114) surface is reconstructed in a (1×2) fashion with three missing rows out of four so as to have one row per unit cell (b = 28.4 Å) and one atom per row (Figure 1a,b). The electronic structure, calculated by Wells et al.[30] for the (1×1) phase (Figure 1c, left), shows cones centered at the $\bar{X}$ and $\bar{Y}$ points (Figure 1c,d) at the Fermi level. Those at $\bar{Y}$ are folded into $\bar{\Gamma}$ in the (1×2) reconstructed phase. Both electronic structures allow for a multivalley CDW via e−ph interaction, the former with 2D character and the latter with pure 1D character due to the cone alignment along $\bar{\Gamma}\bar{X}$ with $G/2$ spacing. HAS angular distributions along $\bar{\Gamma}\bar{X}$[12] (Figure 2a) show the growth of additional peaks at $\pm G/2$ and $\pm 3G/2$ below $T \approx 280$ K, indicating the formation of a surface-commensurate CDW.[12] The associated (2×2) reconstruction

https://dx.doi.org/10.1021/acs.jpclett.9b03829
J. Phys. Chem. Lett. 2020, 11, 1927−1933

consists of a dimerization along the rows. The portion of the Bi(114)-(2 × 2) STM image reproduced in Figure 1b from Hofmann et al.[12,31] suggests a phase correlation between rows, giving an oblique (2 × 2) unit cell and a corresponding elongated hexagonal Brillouin zone (BZ) (Figure 1d).

The HAS DW exponents for the specular $\mathbf{G}$ = (0, 0), diffraction $G = (\bar{1}, 0)$ and CDW $(\overline{3/2}, 0)$ peaks measured as a function of temperature below T_c are plotted in Figure 2b. The specular and diffraction DW exponents have almost the same slopes, with the small difference being compensated for by the ratio $(\Delta {k_{iz}}^2)_{(0,0)}/[\Delta {k_z}^2 + \Delta \mathbf{K}^2]_{(\bar{1},0)}$, resulting in the same values of $\lambda_{HAS}^{(1D)}$ within less than 1%. The input data in eq 2 for d = 1 are ϕ = 4.23 eV,[32] $2k_F = G/2 = 0.7$ Å^{-1}, $r_0(2 \times 2) = 9.08$ Å, incident energy E_i = 14.5 meV, and fixed scattering angle 91.5°, so $(\Delta {k_{iz}}^2)_{(0,0)} = 54.3$ Å^{-2}. The $(\bar{1}, 0)$ diffraction occurs at the incident angle of 51.2°, which gives $(\Delta {k_{iz}}^2)_{(\bar{1},0)} = 53.8$ Å^{-2}, and the resulting e−ph coupling constant is $\lambda_{HAS}^{(1D)} = 0.45 \pm 0.03$, being the same value for both specular and diffractive channels.

The CDW $(\bar{3}/2, 0)$ peak intensity (Figure 2b) shows the expected critical behavior with $\beta \cong 1/3$, so that a value of $\lambda_{HAS}^{(1D)}$ can be estimated only from the slope at the lowest temperatures. This is smaller than that for the specular peak by ≈5% and is compensated for approximately the same amount by the correcting factor $(\Delta {k_{iz}}^2)_{(0,0)}/[\Delta {k_z}^2 + \Delta \mathbf{K}^2]_{(\bar{3}/2,0)}$ = 1.047, with the incident angle for the CDW peak at $(\bar{3}/2, 0)$ being 62.75°. Thus, it is reasonable to conclude that consistent values of $\lambda_{HAS}^{(1D)}$ can be extracted from the T dependence of the CDW peaks.

It is interesting to compare the value $\lambda_{HAS}^{(1D)} = 0.45$ for Bi(114) to that previously derived for Bi(111), either treated as a 3D system where $\lambda_{HAS}^{(3D)} = 0.57$,[10] in agreement with the value of $\lambda = 0.60$ in Hofmann's review,[31] or as a 2D system with n_s = 2 (a single bilayer), where it is found that $\lambda_{HAS}^{(2D)} = 0.40$, in fair agreement with a recent ab initio calculation by Ortigoza et al. for Bi(111)[33] which yielded $\lambda = 0.45$, just as found here for Bi(114). As seen in Figure 2c), the DW exponent has about the same slope for Bi(111) and Bi(114), when it is divided by ${k_{iz}}^2$, in order to account for the different incident energies used in HAS experiments. The fact that $\lambda_{HAS}^{(1D)}$ [Bi(114)] < $\lambda_{HAS}^{(3D)}$ [Bi(111)] reflects the dimensionality effect of γ_d in the prefactor of eq 2. Incidentally, we note that treating Bi(114) as a 2D system would yield a 5-fold smaller, probably unphysical, value for λ_{HAS} due to the large surface unit cell area.

Layered chalcogenides, such as 2D topological materials, with strong intralayer and weak interlayer forces form a wide class of quasi-2D materials with a conducting surface. Some transition-metal dichalcogenides (TMDC) have been investigated with HAS since the late 1980s in connection with CDW transitions, related Kohn anomalies in the bulk, and surface phonon dispersion curves.[34−38] More recently, HAS studies have been extended to the surfaces of other TMDCs such as 2H-MoS_2(0001)[39] and 1T-$PtTe_2$[40] as well as to pnictogen chalcogenides with surface topological electronic bands at the Fermi level, such as Bi_2Te_3[13,41,42] and Bi_2Se_3.[14,43] The 2D expression for the e−ph coupling constant $\lambda_{HAS}^{(2D)}$ in eq 3 is the one to be used for these systems. When dealing with the e−ph coupling constant λ_{HAS} expressed as an average over the whole phonon spectrum and over all electronic transitions across the Fermi level, natural questions are (a) which phonons contribute most and (b) which electronic states at the Fermi level are more important.

The theoretical analysis by Heid et al.[47] of the mode-selected e−ph coupling constants $\lambda_{\mathbf{Q},\nu}$ shows that in pnictogen chalcogenides, optical phonons give the major contribution to the e−ph interaction and therefore to the DW exponent. Both Bi_2Se_3(111)[14] and Bi_2Te_3(111)[42] exhibit two highly dispersed optical branches with deep minima at $\bar{\Gamma}$ for third-layer longitudinal polarization and at ∼$\overline{\Gamma M}/2$ for (mostly) third-layer shear-vertical (SV3) polarization. Their optical character and largest amplitude at the central chalcogen layer of the quintuple layer endow these modes with dipolar character and therefore a large e−ph interaction is consistent with Heid et al.'s theoretical analysis.[47] Spin−echo ^{3}He scattering data from Bi_2Te_3(111)[42] suggest a Kohn anomaly also in the longitudinal acoustic branch corresponding to a nesting across the Dirac cone above the surface conduction-band minimum. As discussed in ref 47, the interband e−ph coupling occurring when the Fermi level is above the surface conduction-band minimum is enhanced largely by the involvement of surface quantum-well states. This conclusion is confirmed by the following analysis of $\lambda_{HAS}^{(2D)}$ in Bi chalcogenides as a function of the Fermi-level position.

The temperature dependence of HAS specular reflectivity from the three Bi chalcogenide surfaces Bi_2Se_3(111), Bi_2Te_3(111), and $Bi_2Te_{3-x}Se_x$(111) (phase II with $x \approx 1$,[48,49] hereafter approximated by Bi_2Te_2Se(111)) has been measured for three samples whose surface electronic states near the Fermi level, in particular, the topological Dirac states and the quantum-well states above the surface conduction-band minimum, are known from angle-resolved photoemission spectroscopy (ARPES) data.[44−46,50] As seen in Figure 3 (top panel), the binding energy of the Dirac point (D) with respect to the Fermi energy E_F decreases in the sequence Bi_2Se_3(111) > Bi_2Te_3(111) > Bi_2Te_2Se(111), as does the surface conduction-band minimum (from 0.15 to 0.08 eV and ≈0, respectively). Correspondingly, the DW exponent slope derived from the HAS specular intensity as a function of temperature also decreases. A similar behavior is expected for the e−ph coupling constant $\lambda_{HAS}^{(2D)}$, which is shown in Table 1. The latter is derived from eq 3 by setting $n_{sat} = 2\lambda_{TF}/c_0$, where c_0 is the quintuple layer (QL) thickness and λ_{TF} is the Thomas−Fermi screening length, accounting for the surface band-bending extension in degenerate semiconductors and semimetals.[51] The factor of 2 in the above expression of n_{sat} accounts for the fact that each QL contains two metal (Bi) layers. Note that the Fermi-level density of states includes the factor of 2 for spin multiplicity, and this is appropriate for the quantum-well states above the surface conduction-band minimum that mostly contribute to $\lambda_{HAS}^{(2D)}$. On the other hand, no factor of 2 in n_{sat} is necessary when only the Dirac states are involved, due to their multiplicity of 1. The uncertainties (±) given for λ_{HAS} in the following text are based on the confidence bounds of the DW slope. Other sources in terms of the uncertainty are A_c, ϕ, and λ_{TF}, with the largest contribution likely to be due to λ_{TF}. Taken together, it is safe to assume a relative uncertainty of about 10% for λ_{HAS} as shown in Table 1.

With the input data collected in Table 1 and the DW exponent slopes displayed in Figure 3 (bottom panel), it is found that $\lambda_{HAS}^{(2D)} = 0.23 \pm 0.01$ for Bi_2Se_3(111), 0.19 ± 0.01 for Bi_2Te_3(111), and 0.080 ± 0.004 for Bi_2Te_2Se(111), in good agreement with selected results from other sources (Table 1, last column). This clearly indicates the dominant role of surface quantum-well (QW) states over the modest contribution of Dirac electrons. The enhancement effect of QW states and related interband transitions has been investigated

https://dx.doi.org/10.1021/acs.jpclett.9b03829
J. Phys. Chem. Lett. 2020, 11, 1927−1933

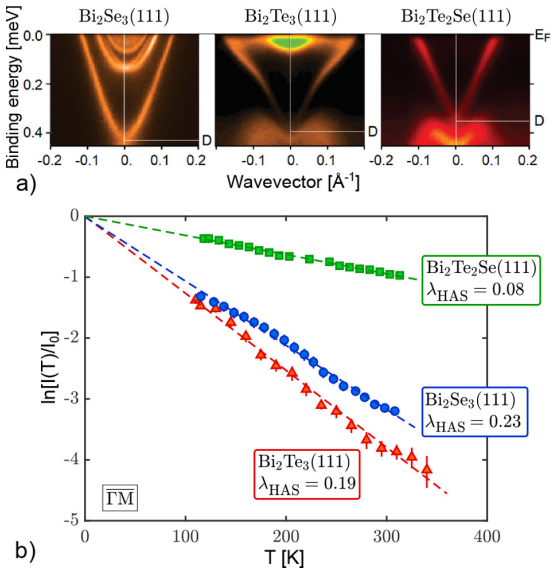

Figure 3. Three different Bi chalcogenides Bi_2Se_3, Bi_2Te_3, and Bi_2Te_2Se: (a) ARPES data for the (111) surface of three Bi chalcogenides with decreasing binding energy of the Dirac point (D) and of the surface conduction-band minimum [from 0.15 eV in Bi_2Se_3[44] (reproduced with permission, copyright 2012 by the Institute of Physics) to 0.08 eV in Bi_2Te_3[45] (reproduced with permission, copyright 2014 by the American Physical Society) and ≈0 in Bi_2Te_2Se[46] (reproduced with permission, copyright 2014 by the American Chemical Society]. (b) DW exponent slopes from HAS specular intensity measured as functions of temperature with the scattering plane in the $\overline{\Gamma M}$ direction for the same samples. Corresponding e−ph coupling constants λ_{HAS} decrease from $Bi_2Se_3(111)$ to $Bi_2Te_2Se(111)$, suggesting a dominant role in the e−ph interaction of the conduction band quantum-well electronic states over the Dirac electrons.

thoroughly by Chen et al.[52] with high-resolution ARPES for the family $Bi_2Te_{3-x}Se_x(111)$ ($0 \le x \le 3$), including n-type $Bi_2Te_3(111)$, and theoretically for $Bi_2Se_3(111)$ and $Bi_2Te_3(111)$ by Heid et al.[47] As shown by Pan et al.,[60] in accurate ARPES studies on bulk $Bi_2Se_3(111)$ samples, where only Dirac topological states are involved because the Fermi level is less than 0.3 eV above the Dirac point, the e−ph coupling constant turns out to be quite small, ranging from 0.076 ± 0.007 to 0.088 ± 0.009, similar to that found with HAS in $Bi_2Te_2Se(111)$ under similar conditions.

Since the surface QW states extend into the bulk on the order of λ_{TF}, i.e., much longer than the penetration of surface Dirac states, it is interesting to compare the above results for $\lambda_{HAS}^{(2D)}$ with the corresponding values of $\lambda_{HAS}^{(3D)}$ when these materials are treated as 3D materials. The ratio $\lambda_{HAS}^{(3D)}/\lambda_{HAS}^{(2D)} = \pi/(k_F\lambda_{TF})$, with $k_F \approx 0.1$ Å^{-1} (Figure 3, top) and λ_{TF} representing the 3DEG thickness, turns out to be ≈1.

Unlike Bi(114), where the quasi-1D character of the electron gas is quite evident, in layered pnictogen chalcogenides the considerable penetration of the QW states gives $\lambda_{HAS}^{(2D)} \approx \lambda_{HAS}^{(3D)}$. This is consistent with the fact that the QW states are the surface states which provide the major contribution to the e−ph interaction. Information about which phonons contribute most to λ can also be obtained from inelastic HAS intensities, as explained in the introduction. The Kohn anomalies reported in the lower part of the phonon spectrum[41−43] are indicative of a strong e−ph coupling for specific wavevectors and frequencies, though it has been predicted that the major contribution in these materials comes from polar optical modes.[47] Indeed, this is in agreement with recent HAS measurements of the phonon dispersion curves in $Bi_2Se_3(111)$,[14] which indicate the longitudinal optical branch L3 (with the largest displacement on the third (Se) atomic plane) as the one having the largest mode-selective e−ph coupling.

In conclusion, it has been shown that the temperature dependence of HAS specular reflectivity allows for the determination of the electron−phonon coupling constant of topological semimetal surfaces. In the case of the quasi-1D Bi(114) surface, the DW factor from the CDW diffraction peak yields an e−ph coupling constant $\lambda_{HAS}^{(1D)}$ consistent with that derived from the reflectivity. Therefore, the e−ph interaction acts as the driving mechanism for the observed multivalley CDW transition. In the absence of spin−orbit coupling, the phonon angular momentum cannot convert to an electron spin-flip, so no good nesting would be allowed across the Dirac cone and only the strong spin−orbit coupling occurring in topological materials allows for a comparatively weak e−ph intracone interaction. The multivalley mechanism at the zone boundary overcomes the nesting problem because with more Dirac cones separated by less than a **G** vector there is always a good intercone (i.e., multivalley) nesting, even for opposite chiralities. Such a favorable circumstance, allowing for a substantial $\lambda_{HAS}^{(1D)}$ in Bi(114) and a CDW transition, does not occur in pnictogen chalcogenides due to the single Dirac cone location in the center of the BZ. Most of their appreciable e−ph interaction is provided by the QW states, as long as they are located at the Fermi level. The present extension of HAS λ-analysis from metal surfaces[9,10] and thin metal films[11] to topological semimetal surfaces qualifies He atom scattering as a universal tool for the measurement of electron−phonon coupling in conducting low-dimensional systems.

EXPERIMENTAL METHODS

The experimental data in this work was obtained on the HAS apparatus in Graz[61] and the ^{3}He spin−echo scattering apparatus in Cambridge.[18] In both cases, the scattering intensity of a nearly monochromatic He beam in the range

Table 1. Input Data for the Calculation from the HAS DW Exponent and Results for the e−ph Coupling Constant $\lambda_{HAS}^{(2D)}$ (with a Relative Uncertainty of about 10%) in Comparison with Values from Other Sources

surface	k_{iz}^2 [Å^{-2}]	ϕ [eV]	λ_{TF} [Å]	A_c [Å^2]	c_0 [Å]	D [meV]	$\lambda_{HAS}^{(2D)}$	λ (other refs)
$Bi_2Se_3(111)$	10.1[14]	4.9[53]	≈60[50]	14.92	9.60	6.54[54]	0.23	0.17,[52] 0.25,[55] 0.26[56]
$Bi_2Te_3(111)$	9.9[13]	4.9[53]	≈100[57]	16.46	10.16	6.22[58]	0.19	0.19[52]
$Bi_2Te_2Se(111)$	10.71[a]	4.9[53]	≈100[59]	16.09	10.0	6.4[b]	0.08	0.12[52]

[a]This work. [b]Average over $Bi_2Se_3(111)$ and $Bi_2Te_3(111)$.

https://dx.doi.org/10.1021/acs.jpclett.9b03829
J. Phys. Chem. Lett. 2020, 11, 1927−1933

of 8−15 meV is monitored as a function of incident angle ϑ_i and at various surface temperatures. The DW measurement of Bi_2Te_3 can be found in ref 13, while the DW data of Bi_2Se_3 is reported in ref 14. Most of the Bi(114) data has been published in the work of Hofmann et al.,[12] whereas the Bi_2Te_2Se experimental data is presented here for the first time.

AUTHOR INFORMATION

Corresponding Authors

Salvador Miret-Artés − *Donostia International Physics Center (DIPC), 20018 Donostia-San Sebastian, Spain; Instituto de Física Fundamental, Consejo Superior de Investigaciones Científicas, 28006 Madrid, Spain;* orcid.org/0000-0002-4056-376X; Email: s.miret@iff.csic.es

Anton Tamtögl − *Institute of Experimental Physics, Graz University of Technology, 8010 Graz, Austria;* orcid.org/0000-0001-9590-6224; Email: tamtoegl@gmail.com

Authors

Giorgio Benedek − *Donostia International Physics Center (DIPC), 20018 Donostia-San Sebastian, Spain; Dipartimento di Scienza dei Materiali, Università di Milano-Bicocca, 20125 Milano, Italy*

J. R. Manson − *Donostia International Physics Center (DIPC), 20018 Donostia-San Sebastian, Spain; Department of Physics and Astronomy, Clemson University, Clemson, South Carolina 29634, United States*

Adrian Ruckhofer − *Institute of Experimental Physics, Graz University of Technology, 8010 Graz, Austria;* orcid.org/0000-0003-4368-8207

Wolfgang E. Ernst − *Institute of Experimental Physics, Graz University of Technology, 8010 Graz, Austria;* orcid.org/0000-0001-8849-5658

Complete contact information is available at: https://pubs.acs.org/10.1021/acs.jpclett.9b03829

Notes

The authors declare no competing financial interest.

ACKNOWLEDGMENTS

G.B. thanks Profs. M. Bernasconi (Milano-Bicocca), E. V. Chulkov, and P. M. Echenique (DIPC, San Sebastian) for many helpful discussions. This work is partially supported by a grant with ref. FIS2017-83473-C2-1-P from the Ministerio de Ciencia Universidades e Innovación (Spain). A.R., W.E.E., and A.T. acknowledge financial support provided by the FWF (Austrian Science Fund) within projects J3479-N20 and P29641-N36. G.B. gratefully acknowledges the Italian Ministry of University and Research (MIUR) for financial support through grant "Dipartimenti di Eccellenza-2017 Materials for Energy". We thank Martin Bremholm, Ellen M. J. Hedegaard, and Bo B. Iversen for the synthesis of the samples, Marco Bianchi for his advice and help in terms of the sample preparation, and Philip Hofmann as well as the aforementioned people for many helpful discussions and additional characterizations of the samples.

REFERENCES

(1) Saito, Y.; Nojima, T.; Iwasa, Y. Highly Crystalline 2D Superconductors. *Nat. Rev. Mater.* **2017**, *2*, 16094.

(2) Zhang, W.; Melo, C. A. R. S. D. *Quasi-One-Dimensional Organic Superconductors*; Zhang, W., Ed.; Advanced Physics Series; World Scientific Publishing: Singapore, 2018; Vol. 5.

(3) Liang, J.; Cheng, L.; Zhang, J.; Liu, H.; Zhang, Z. Maximizing the Thermoelectric Performance of Topological Insulator Bi_2Te_3 Films in the Few-Quintuple Layer Regime. *Nanoscale* **2016**, *8*, 8855−8862.

(4) Dolinsek, J.; Smontara, A.; Barišíc, O. S.; Gille, P. Phonon-Enhanced Thermoelectric Power of Y-Al-Ni-Co Decagonal Approximant. *Z. Kristallogr. - Cryst. Mater.* **2009**, *224*, 64.

(5) McMillan, W. L. Transition Temperature of Strong-Coupled Superconductors. *Phys. Rev.* **1968**, *167*, 331.

(6) Grimvall, G. *The Electron-Phonon Interaction in Metals*; North-Holland: New York, 1981.

(7) Allen, P. B. Neutron Spectroscopy of Superconductors. *Phys. Rev. B* **1972**, *6*, 2577.

(8) Sklyadneva, I. Y.; Benedek, G.; Chulkov, E. V.; Echenique, P. M.; Heid, R.; Bohnen, K.- P.; Toennies, J. P. Mode-Selected Electron-Phonon Coupling in Superconducting Pb Nanofilms Determined from He Atom Scattering. *Phys. Rev. Lett.* **2011**, *107*, No. 095502.

(9) Benedek, G.; Bernasconi, M.; Bohnen, K.-P.; Campi, D.; Chulkov, E. V.; Echenique, P. M.; Heid, R.; Sklyadneva, I. Y.; Toennies, J. P. Unveiling Mode-Selected Electron-Phonon Interactions in Metal Films by Helium Atom Scattering. *Phys. Chem. Chem. Phys.* **2014**, *16*, 7159.

(10) Manson, J. R.; Benedek, G.; Miret-Artés, S. Electron-Phonon Coupling Strength at Metal Surfaces Directly Determined from the Helium Atom Scattering Debye-Waller Factor. *J. Phys. Chem. Lett.* **2016**, *7*, 1016.

(11) Benedek, G.; Miret-Artés, S. S.; Toennies, J. P.; Manson, J. R. The Electron-Phonon Coupling Constant of Metallic Overlayers from Specular He Atom Scattering. *J. Phys. Chem. Lett.* **2018**, *9*, 76−83.

(12) Hofmann, P.; Ugeda, M. M.; Tamtögl, A.; Ruckhofer, A.; Ernst, W. E.; Benedek, G.; Martínez-Galera, A. J.; Stróżecka, A.; Gómez-Rodríguez, J. M.; Rienks, E.; et al. Strong-Coupling Charge Density Wave in a One-Dimensional Topological Metal. *Phys. Rev. B: Condens. Matter Mater. Phys.* **2019**, *99*, No. 035438.

(13) Tamtögl, A.; Kraus, P.; Avidor, N.; Bremholm, M.; Hedegaard, E. M. J.; Iversen, B. B.; Bianchi, M.; Hofmann, P.; Ellis, J.; Allison, W.; et al. Electron-Phonon Coupling and Surface Debye Temperature of Bi_2Te_3(111) from Helium Atom Scattering. *Phys. Rev. B: Condens. Matter Mater. Phys.* **2017**, *95*, 195401.

(14) Ruckhofer, A.; Campi, D.; Bremholm, M.; Hofmann, P.; Benedek, G.; Bernasconi, M.; Ernst, W. E.; Tamtögl, A. THz Surface Modes and Electron-Phonon Coupling in Bi_2Se_3(111). *Phys. Rev. Res.* **2020**, arXiv:1907.01864.

(15) Manson, J. R.; Benedek, G.; Miret-Artés, S. Correction to "Electron-Phonon Coupling Strength at Metal Surfaces Directly Determined from the Helium Atom Scattering Debye-Waller Factor. *J. Phys. Chem. Lett.* **2016**, *7*, 1691−1691.

(16) Coxeter, H. S. M. *Introduction to Geometry*, 2nd ed.; John Wiley and Sons: New York, 1969.

(17) Beeby, J. L. Scattering of Helium Atoms from Surfaces. *J. Phys. C: Solid State Phys.* **1971**, *4*, L359.

(18) Jardine, A.; Hedgeland, H.; Alexandrowicz, G.; Allison, W.; Ellis, J. Helium-3 SpinEcho: Principles and Application to Dynamics at Surfaces. *Prog. Surf. Sci.* **2009**, *84*, 323−379.

(19) Peierls, R. E. *Quantum Theory of Solids*; Oxford University Press: Oxford, 1955.

(20) Fröhlich, H. On the Theory of Superconductivity: The One-Dimensional Case. *Proc. R. Soc. Lond* **1954**, *223*, 296.

(21) Kelly, M. J.; Falicov, L. M. Electronic Ground-State of Inversion Layers in Many-Valley Semiconductors. *Phys. Rev. B* **1977**, *15*, 1974.

(22) Kelly, M. J.; Falicov, L. M. Optical-Properties of Charge-Density-Wave Ground-States for Inversion Layers in Many-Valley Semiconductors. *Phys. Rev. B* **1977**, *15*, 1983.

(23) Kelly, M. J.; Falicov, L. M. Electronic Structure of Inversion Layers in Many-Valley Semiconductors. *Phys. Rev. Lett.* **1976**, *37*, 1021.

(24) Tamtögl, A.; Kraus, P.; Mayrhofer-Reinhartshuber, M.; Benedek, G.; Bernasconi, M.; Dragoni, D.; Campi, D.; Ernst, W. E. Statics and Dynamics of Multivalley Charge Density Waves in Sb(111). *npj Quantum Mater.* **2019**, *4*, 18.

https://dx.doi.org/10.1021/acs.jpclett.9b03829
J. Phys. Chem. Lett. 2020, 11, 1927−1933

(25) Liu, R.; Ma, T.; Wang, S.; Yang, J. Thermodynamical Potentials of Classical and Quantum Systems. *Discrete Contin. Dyn. Syst. Ser. B* **2019**, *24*, 1411.
(26) Ma, T.; Wang, S. Cahn-Hilliard Equations and Phase Transition Dynamics for Binary Systems. *Discrete Contin. Dyn. Syst. Ser. B* **2009**, *11*, 741.
(27) Ge, Y.; Liu, A. Y. Phonon-Mediated Superconductivity in Electron-Doped Single-Layer MoS_2: A First-Principles Prediction. *Phys. Rev. B: Condens. Matter Mater. Phys.* **2013**, *87*, 241408.
(28) Liu, A. Y. Electron-Phonon Coupling in Compressed 1T-TaS_2: Stability and Superconductivity from First Principles. *Phys. Rev. B: Condens. Matter Mater. Phys.* **2009**, *79*, 220515.
(29) Benedek, G.; Hofmann, F.; Ruggerone, P.; Onida, G.; Miglio, L. Surface Phonons in Layered Crystals - Theoretical Aspects. *Surf. Sci. Rep.* **1994**, *20*, 1.
(30) Wells, J. W.; Dil, J. H.; Meier, F.; Lobo-Checa, J.; Petrov, V. N.; Osterwalder, J.; Ugeda, M. M.; Fernandez-Torrente, I.; Pascual, J. I.; Rienks, E. D. L.; et al. Nondegenerate Metallic States on Bi(114): A One-Dimensional Topological Metal. *Phys. Rev. Lett.* **2009**, *102*, No. 096802.
(31) Hofmann, P. The Surfaces of Bismuth: Structural and Electronic Properties. *Prog. Surf. Sci.* **2006**, *81*, 191.
(32) Michaelson, H. B. The Work Function of the Elements and its Periodicity. *J. Appl. Phys.* **1977**, *48*, 4729.
(33) Ortigoza, M. A.; Sklyadneva, I. Y.; Heid, R.; Chulkov, E. V.; Rahman, T. S.; Bohnen, K.-P.; Echenique, P. M. *Ab initio* Lattice Dynamics and Electron-Phonon Coupling of Bi(111). *Phys. Rev. B: Condens. Matter Mater. Phys.* **2014**, *90*, 195438.
(34) Benedek, G.; Miglio, L.; Skofronick, J. G.; Brusdeylins, G.; Heimlich, C.; Toennies, J. P. Surface Phonon Dynamics in 2H-$TaSe_2$(001). *J. Vac. Sci. Technol., A* **1987**, *5*, 1093.
(35) Benedek, G.; Brusdeylins, G.; Heimlich, C.; Miglio, L.; Skofronick, J.; Toennies, J. P. Shifted Surface Phonon Anomaly in 2H-$TaSe_2$. *Phys. Rev. Lett.* **1988**, *60*, 1037.
(36) Brusdeylins, G.; Heimlich, C.; Skofronick, J. G.; Toennies, J. P.; Vollmer, R.; Benedek, G. Determination of the Critical Exponents for a Charge Density Wave Transition in 2H-$TaSe_2$ by Helium Atom Scattering. *Europhys. Lett.* **1989**, *9*, 563.
(37) Benedek, G.; Miglio, L.; Seriani, G. In *Helium Atom Scattering from Surfaces*; Hulpke, E., Ed.; Springer: Heidelberg, 1992.
(38) Benedek, G.; Brusdeylins, G.; Hofmann, F.; Ruggerone, P.; Toennies, J.; Vollmer, R.; Skofronick, J. Strong Coupling of Rayleigh Phonons to Charge Density Waves in 1T-TaS_2. *Surf. Sci.* **1994**, *304*, 185−190.
(39) Anemone, G.; Taleb, A. A.; Benedek, G.; Castellanos-Gomez, A.; Farías, D. Electron-Phonon Coupling Constant of 2H-MoS_2(0001) from Helium-Atom Scattering. *J. Phys. Chem. C* **2019**, *123*, 3682−3686.
(40) Anemone, G.; Garnica, M.; Zappia, M.; Aguilar, P. C.; Taleb, A. A.; Kuo, C.-N.; Lue, C. S.; Politano, A.; Benedek, G.; de Parga, A. L. V. Experimental Determination of Surface Thermal Expansion and Electron-Phonon Coupling Constant of 1T-$PtTe_2$. *2D Mater.* **2020**, *7*, No. 025007.
(41) Howard, C.; El-Batanouny, M.; Sankar, R.; Chou, F. C. Anomalous Behavior in the Phonon Dispersion of the (001) Surface of Bi_2Te_3 Determined from Helium AtomSurface Scattering Measurements. *Phys. Rev. B: Condens. Matter Mater. Phys.* **2013**, *88*, No. 035402.
(42) Tamtögl, A.; Campi, D.; Bremholm, M.; Hedegaard, E. M. J.; Iversen, B. B.; Bianchi, M.; Hofmann, P.; Marzari, N.; Benedek, G.; Ellis, J.; et al. Nanoscale Surface Dynamics of Bi_2Te_3(111): Observation of a Prominent Surface Acoustic Wave and the Role of van der Waals Interactions. *Nanoscale* **2018**, *10*, 14627−14636.
(43) Zhu, X.; Santos, L.; Sankar, R.; Chikara, S.; Howard, C.; Chou, F. C.; Chamon, C.; El-Batanouny, M. Interaction of Phonons and Dirac Fermions on the Surface of Bi_2Se_3: A Strong Kohn Anomaly. *Phys. Rev. Lett.* **2011**, *107*, 186102.
(44) Bianchi, M.; Hatch, R. C.; Guan, D.; Planke, T.; Mi, J.; Iversen, B. B.; Hofmann, P. The Electronic Structure of Clean and Adsorbate-Covered Bi_2Se_3: an Angle-Resolved Photoemission Study. *Semicond. Sci. Technol.* **2012**, *27*, 124001.
(45) Michiardi, M.; Aguilera, I.; Bianchi, M.; de Carvalho, V. E.; Ladeira, L. O.; Teixeira, N. G.; Soares, E. A.; Friedrich, C.; Blügel, S.; Hofmann, P. Bulk Band Structure of Bi_2Te_3. *Phys. Rev. B: Condens. Matter Mater. Phys.* **2014**, *90*, No. 075105.
(46) Barreto, L.; Kühnemund, L.; Edler, F.; Tegenkamp, C.; Mi, J.; Bremholm, M.; Iversen, B. B.; Frydendahl, C.; Bianchi, M.; Hofmann, P. Surface-Dominated Transport on a Bulk Topological Insulator. *Nano Lett.* **2014**, *14*, 3755−3760.
(47) Heid, R.; Sklyadneva, I. Y.; Chulkov, E. V. Electron-Phonon Coupling in Topological Surface States: The Role of Polar Optical Modes. *Sci. Rep.* **2017**, *7*, 1095.
(48) Mi, J.-L.; Bremholm, M.; Bianchi, M.; Borup, K.; Johnsen, S.; Søndergaard, M.; Guan, D.; Hatch, R. C.; Hofmann, P.; Iversen, B. B. Phase Separation and Bulk p-n Transition in Single Crystals of Bi_2Te_2Se Topological Insulator. *Adv. Mater.* **2013**, *25*, 889−893.
(49) According to the surface lattice constant (a = 4.31 Å as determined by HAS) and Figure 1b in ref 48, $x \approx 1$ for the present sample.
(50) Bianchi, M.; Guan, D.; Bao, S.; Mi, J.; Iversen, B. B.; King, P. D.; Hofmann, P. Coexistence of the Topological State and a two-dimensional Electron Gas on the Surface of Bi_2Se_3. *Nat. Commun.* **2010**, *1*, 128.
(51) Shklovskii, B. I.; Efros, A. E. *Electronic Properties of Doped Semiconductors*; Springer: Heidelberg, 1984.
(52) Chen, C.; Xie, Z.; Feng, Y.; Yi, H.; Liang, A.; He, S.; Mou, D.; He, J.; Peng, Y.; Liu, X.; et al. Tunable Dirac Fermion Dynamics in Topological Insulators. *Sci. Rep.* **2013**, *3*, 2411.
(53) Suh, J.; Fu, D.; Liu, X.; Furdyna, J. K.; Yu, K. M.; Walukiewicz, W.; Wu, J. Fermi-Level Stabilization in the Topological Insulators Bi_2Se_3 and Bi_2Te_3: Origin of the Surface Electron Gas. *Phys. Rev. B: Condens. Matter Mater. Phys.* **2014**, *89*, 115307.
(54) Ruckhofer, A.; Tamtögl, A.; Pusterhofer, M.; Bremholm, M.; Ernst, W. E. Helium-Surface Interaction and Electronic Corrugation of Bi_2Se_3(111). *J. Phys. Chem. C* **2019**, *123*, 17829−17841.
(55) Hatch, R. C.; Bianchi, M.; Guan, D.; Bao, S.; Mi, J.; Iversen, B. B.; Nilsson, L.; Hornekær, L.; Hofmann, P. Stability of the Bi_2Se_3(111) Topological State: Electron-Phonon and Electron-Defect Scattering. *Phys. Rev. B: Condens. Matter Mater. Phys.* **2011**, *83*, 241303.
(56) Zeljkovic, I.; Scipioni, K. L.; Walkup, D.; Okada, Y.; Zhou, W.; Sankar, R.; Chang, G.; Wang, Y. J.; Lin, H.; Bansil, A.; et al. Nanoscale Determination of the Mass Enhancement Factor in the Lightly Doped Bulk Insulator Lead Selenide. *Nat. Commun.* **2015**, *6*, 6559.
(57) Pettes, M. T.; Maassen, J.; Jo, I.; Lundstrom, M. S.; Shi, L. Effects of Surface Band Bending and Scattering on Thermoelectric Transport in Suspended Bismuth Telluride Nanoplates. *Nano Lett.* **2013**, *13*, 5316.
(58) Tamtögl, A.; Pusterhofer, M.; Bremholm, M.; Hedegaard, E. M.; Iversen, B. B.; Hofmann, P.; Ellis, J.; Allison, W.; Miret-Artés, S.; Ernst, W. E. A Helium-Surface Interaction Potential of Bi_2Te_3(111) from Ultrahigh-Resolution Spin-Echo Measurements. *Surf. Sci.* **2018**, *678*, 25−31.
(59) Gehring, P.; Gao, B. F.; Burghard, M.; Kern, K. Growth of High-Mobility Bi_2Te_2Se Nanoplatelets on hBN Sheets by van der Waals Epitaxy. *Nano Lett.* **2012**, *12*, 5137.
(60) Pan, Z.-H.; Fedorov, A. V.; Gardner, D.; Lee, Y. S.; Chu, S.; Valla, T. Measurement of an Exceptionally Weak Electron-Phonon Coupling on the Surface of the Topological Insulator Bi_2Se_3 Using Angle-Resolved Photoemission Spectroscopy. *Phys. Rev. Lett.* **2012**, *108*, 187001.
(61) Tamtögl, A.; Mayrhofer-Reinhartshuber, M.; Balak, N.; Ernst, W. E.; Rieder, K. H. Elastic and Inelastic Scattering of He Atoms from Bi(111). *J. Phys.: Condens. Matter* **2010**, *22*, 304019.

https://dx.doi.org/10.1021/acs.jpclett.9b03829
J. Phys. Chem. Lett. 2020, 11, 1927−1933

6.16 Publication P

Ruckhofer, A., Campi, D., Bremholm, M., Hofmann, P., Benedek, G., Bernasconi, M., Ernst, W. E. & Tamtögl, A. Terahertz surface modes and electron-phonon coupling on Bi_2Se_3(111). *Phys. Rev. Research* **2,** 023186 (2020)

contributions	
funding	A. Tamtögl, W. E. Ernst, P. Hofmann
sample synthesis	M. Bremholm
preparation / setup	A. Tamtögl, A. Ruckhofer
data acquisition	A. Tamtögl, A. Ruckhofer
theory (*ab initio*) calculations	D. Campi, M. Bernasconi
data analysis	A. Tamtögl, A. Ruckhofer
interpretation	A. Tamtögl, G. Benedek
publication writing	A. Tamtögl, A. Ruckhofer, G. Benedek

Reprinted from:

Ruckhofer, A., Campi, D., Bremholm, M., Hofmann, P., Benedek, G., Bernasconi, M., Ernst, W. E. & Tamtögl, A. Terahertz surface modes and electron-phonon coupling on Bi_2Se_3(111). *Phys. Rev. Research* **2,** 023186 (2020)

PHYSICAL REVIEW RESEARCH **2**, 023186 (2020)

Terahertz surface modes and electron-phonon coupling on Bi_2Se_3(111)

Adrian Ruckhofer [1,*] Davide Campi [2] Martin Bremholm [3] Philip Hofmann [4] Giorgio Benedek [5,6] Marco Bernasconi [5] Wolfgang E. Ernst [1] and Anton Tamtögl [1,†]

[1]*Institute of Experimental Physics, Graz University of Technology, Graz, Austria*
[2]*THEOS and MARVEL, École Polytechnique Fédérale de Lausanne, Lausanne, Switzerland*
[3]*Center for Materials Crystallography, Department of Chemistry and iNANO, Aarhus University, 8000 Aarhus, Denmark*
[4]*Department of Physics and Astronomy, Aarhus University, Aarhus, Denmark*
[5]*Dipartimento di Scienza dei Materiali, Università degli Studi di Milano-Bicocca, Milano, Italy*
[6]*Donostia International Physics Center (DIPC) and University of the Basque Country, 20018 Donostia / San Sebastian, Spain*

(Received 13 August 2019; accepted 13 April 2020; published 19 May 2020)

We present a combined experimental and theoretical study of the surface vibrational modes of the topological insulator Bi_2Se_3 with particular emphasis on the low-energy region below 10 meV that has been difficult to resolve experimentally. By applying inelastic helium atom scattering (HAS), the entire phonon dispersion was determined and compared with density functional perturbation theory (DFPT) calculations. The intensity of the phonon modes is dominated by a strong Rayleigh mode, in contrast to previous experimental works. Moreover, also at variance with recent reports, no Kohn anomaly is observed. These observations are in excellent agreement with DFPT calculations. Besides these results, the experimental data reveal—via bound-state resonance enhancement—two additional dispersion curves in the gap below the Rayleigh mode. They are possibly associated with an excitation of a surface electron density superstructure that we observe in HAS diffraction patterns. The electron-phonon coupling parameter $\lambda = 0.23$, derived from our temperature-dependent Debye-Waller measurements, compares well with values determined by angular resolved photoemission or Landau level spectroscopy. Our work opens up a new perspective for terahertz (THz) measurements on two-dimensional (2D) materials as well as the investigation of subtle details (band bending, the presence of a 2D electron gas) with respect to the electron-phonon coupling.

DOI: 10.1103/PhysRevResearch.2.023186

I. INTRODUCTION

Bi_2Se_3 (Fig. 1) is categorized as a three-dimensional topological insulator (TI), a new state of quantum matter with a bulk gap and spin-orbit split surface states forming a Dirac cone across the gap [1,2]. The interaction of electrons with surface phonons in Bi_2Se_3 has been studied intensively due to its important role in transport properties and possible constraints for potential applications in a variety of nanotechnologies [3–9]. Bismuth selenide as well as telluride alloys are classical thermoelectric materials [10,11] with a large Seebeck coefficient and, as such, they have been used in thermoelectric refrigeration for a long time [12]. However, to fully understand the thermoelectric properties of Bi_2Se_3 thin films and nanoscale devices [13,14], information on the surface phonon dispersion curves and the electron-phonon (e-ph) interaction is crucial [13,15,16].

So far experimental information about the surface phonon dispersion curves of Bi_2Se_3(111) was limited to previous helium atom scattering (HAS) studies by Zhu *et al.* [7,17], in the low-energy part of the phonon spectrum. These studies suggested the presence of a deep Kohn anomaly (KA) in the 7.5 meV optical phonon branch (S2) coupled to the electronic (spin-forbidden) transition across the Dirac cone [17]. However, existing first-principle calculations of Bi_2Se_3(111) phonon dispersion curves, do not show any evidence of KAs in the S2 branch [18].

A convenient parameter to characterize the e-ph coupling strength is the mass-enhancement λ [21] and in recent years it was demonstrated that HAS from conducting surfaces can directly measure the mode-selected e-ph coupling constants $\lambda_{\mathbf{Q},j}$ [22,23], besides the surface phonon dispersion curves [24]. Moreover the temperature-dependence of the HAS Debye-Waller factor was shown to provide the global e-ph coupling constant λ at the surface of thin metal films [24,25] and topological insulators [26,27]. Yet the large λ as estimated based on the KA [7] is at odds with theoretical findings that indicate that the major contribution to λ comes from the higher optical phonon branches [18], especially when the Fermi level crosses the surface quantum-well states above the conduction band minimum [see Fig. 1(c)]. The situation is actually met in recent high-resolution ^{3}He-spin scattering studies on Bi_2Te_3(111), where the weak signature of a KA

*ruckhofer@tugraz.at
†tamtoegl@gmail.com

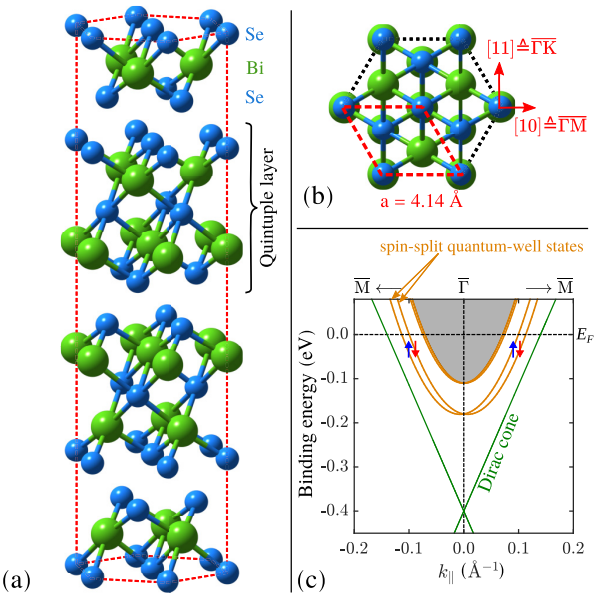

FIG. 1. (a) Crystal structure of Bi_2Se_3 based on the conventional hexagonal unit cell. The unit cell consists of three quintuple layers of which each one is terminated by a Se layer. (b) Top view of the (111) surface with the red rhombus illustrating the hexagonal surface unit cell with lattice constant a. The two high-symmetry scanning directions are indicated by the red arrows. (c) Illustration of the electronic dispersion around the $\overline{\Gamma}$ point (see Refs. [19,20]). Despite the Dirac cone, quantum-well states as illustrated by the orange lines exist on the surface as well. The quantum-well states are split due to Rashba coupling, thus making the previously degenerate spin states (illustrated by the red and blue arrows) separate into an inner and outer branch, each having a spin texture with opposite chirality.

is detected in the surface longitudinal acoustic resonance [28], also not found in adiabatic *ab initio* calculations of the phonon branches.

In order to elucidate these conflicting results, we have undertaken a HAS study of the surface phonon dispersion curves and the e-ph interaction of Bi_2Se_3(111). Supersonic neutral He atom beams with incident energies in the range $\leqslant$20 meV have been used to probe low-energy surface excitations with the best available resolution, while being an inert completely nondestructive probe [24,29]. The technique allows to measure most of the surface phonon branches in the acoustic and optical regions. Low-energy He atoms impinging on a conducting surface are exclusively scattered by the surface charge density [23,30] and inelastic scattering from surface phonons only occurs via the phonon-induced charge density oscillations, i.e., via the e-ph interaction. It is in this way that inelastic HAS provides a first-hand information on the e-ph interaction, with the neutral He atoms acting as a sort of local mechanical probe on the electron density.

Energy and momentum, inelastically exchanged by He atoms with the surface can, however, be retained by the electron system in the form of low-energy collective excitations. In principle, the HAS signal from this kind of excitations is expected to be quite small. Nevertheless, an increased e-ph interaction due to surface quantum-well states [31] in combination with an enhancement from HAS bound-state resonances [32], suggests to assign two branches of low-energy modes in the gap well below the Rayleigh waves (RW) to some sort of collective electronic excitations. Actually anomalous acoustic plasmons have been recently reported in Bi_2Se_3(111) by Jia *et al.* [33], from high-resolution electron energy-loss spectroscopy, although these modes turn out to be superimposed in the first Brillouin zone onto the RW branch.

Plasmons in a two-dimensional electron gas (2DEG) with a $\sqrt{Q}$ dispersion in dependence of a parallel wave vector Q (2D plasmons) have been predicted long ago by Frank Stern [34,35]. Later it was shown that the coupling of 2DEG plasmons arising from two different quantum-well minibands, as found in semiconductor surface accumulation layers, yields a surface plasmon pair: a 2D plasmon and an acoustic surface plasmon (ASP) with a linear dispersion above the upper edge of the single-particle excitation spectrum [36,37]. Similarly the coupling of a 2DEG at a metal surface coupled to the underlying 3D electron gas yields an ASP in addition to the ordinary surface plasmon [31,38–40]. As discussed below, the assignment of the two additional low-energy branches as collective polaron excitation recently suggested by Shvonski *et al.* [36], although plausible in semimetals with a large dielectric constant, definitely requires further *ad hoc* studies, possibly with even higher resolution as available, e.g., with ^{3}He spin-echo spectroscopy [28,41].

II. EXPERIMENTAL AND COMPUTATIONAL DETAILS

a. Experimental details. The reported measurements were performed on a HAS apparatus which generates a nearly monochromatic beam ($\Delta E/E \approx 2\%$) of ^{4}He that is scattered off the sample surface in a fixed 91.5° source-sample-detector geometry. The beam is produced in a supersonic expansion of He through a 10 μm nozzle followed by sampling the core of the supersonic expansion via a 310 μm skimmer. For a detailed description of the apparatus please refer to Ref. [42].

Energy dispersive measurements for inelastic scattering can be performed using time-of-flight (TOF) measurements with a pseudorandom chopper disk. After deconvolution with the pseudo random chopper sequence, the TOF signal is further transformed to an energy transfer scale which allows to determine inelastic (phonon) scattering events [42]. The scattering spectra were mainly taken with the crystal at room temperature, while a few spectra were taken with the sample cooled down to 115 K. The incident He beam energy was varied between 10 and 18 meV.

The crystal structure of Bi_2Se_3 is rhombohedral, formed of quintuple layers (QLs) which are bound to each other through weak van der Waals forces [43]. The hexagonal unit cell of the Bi_2Se_3 crystal, shown in Fig. 1, consists of three QLs. Each QL is terminated by Se atoms, giving rise to the (111) cleavage plane that exhibits a hexagonal structure [a = 4.14 Å at room temperature [44], see Fig. 1(b)]. The Bi_2Se_3 crystal was attached onto a sample holder using thermally conductive epoxy. The sample holder was then inserted into the transfer chamber using a load-lock system and cleaved *in situ* [45]. The sample can be heated using a button heater on the backside of the crystal or cooled down to 115 K

via a thermal connection to a liquid nitrogen reservoir. The sample temperature was measured using a chromel-alumel thermocouple.

b. Computational details. The surface dynamical properties of Bi_2Se_3 were studied using density functional perturbation theory (DFPT) calculations [46] within the QUANTUM ESPRESSO package [47]. Norm-conserving pseudopotentials and the Perdew-Burke-Ernzerhof (PBE) approximation [48] for the exchange and correlation functional were used as implemented in the QUANTUM ESPRESSO package. The surface phonon dispersion was calculated using a slab consisting of 3 QLs separated from its periodic replica by 20 Å of vacuum, without the inclusion of spin-orbit corrections (SOC) (see also Appendix A for calculations with SOC). For an accurate calculation of the surface lattice vibrations, in principle, both SOC and van der Waals (vdW) corrections are necessary, both due to the presence of heavy elements in the compound and the latter to fully account for the weak bonds between the individual quintuple layers. However, as thoroughly discussed for Bi_2Te_3(111) [28], it appears that for layered crystals with heavy elements SOC alone gives a general softening of the phonon spectrum, compensated by the inclusion of vdW corrections, so that satisfactory results are obtained at a minor computational cost without both SOC and vdW corrections and with a better agreement with experiment [23,49]. Also for Bi_2Se_3 better agreement with the experiment is achieved with no SOC and no vdW corrections (see Sec. III A), likely due to a compensation of errors between the underbinding often characterising PBE functionals and SOC contributions and the overbinding due to vdW forces [28]. More precisely, the effect of SOC was found however to be weak for the low-energy surface vibrational modes of typical TIs such as Bi_2Te_3 and Sb_2Te_3 [28,50], while on the other hand, it was shown that vdW corrections become important for an exact description of the low-energy optical modes of Bi_2Te_3 [28].

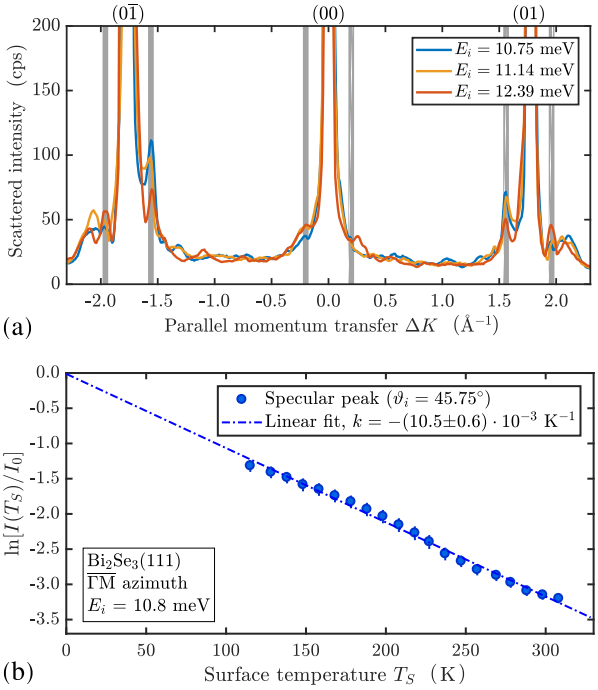

FIG. 2. (a) HAS diffraction scans for Bi_2Se_3(111) measured at various incident energies with the sample at 113 K, aligned along the $\bar{\Gamma}\bar{M}$ azimuth. The smaller features between the specular and the two diffraction peaks are due to bound-state resonances and kinematic focusing [51]. The vertical shaded regions next to the diffraction peaks illustrate additional features which appear to be independent of E_i, at a distance of about 0.2 Å^{-1} form the specular and first order diffraction peaks. (b) The temperature dependence of the Debye-Waller exponent of Bi_2Se_3(111) for the specular peak with the sample aligned along $\bar{\Gamma}\bar{M}$.

III. RESULTS AND DISCUSSION

Figure 2(a) shows several diffraction scans along the $\bar{\Gamma}\bar{M}$ azimuth plotted versus momentum transfer $\Delta K = |\Delta\mathbf{K}|$ parallel to the surface, while in Fig. 2(b), the temperature dependence of the specular peak intensity is plotted, which can be used to extract the e-ph coupling constant λ (Sec. III C). The diffraction scans in Fig. 2(a) have been measured at three different incident energies E_i, at a sample temperature of 113 K. The intensity scale has been scaled to show additional features with smaller intensity. Besides some features assigned to bound-state resonances and kinematic focusing, which are easily recognized due to the strong dependence of their position on the incident energy [30], there are features that occur at fixed values of ΔK, independently of E_i with a distance of about 0.2 Å^{-1} from the specular and first-order diffraction peaks, as indicated by the vertical shaded regions (further diffraction scans, including also the $\bar{\Gamma}\bar{K}$ azimuth can be found in Appendix B).

We recently observed with HAS a multivalley charge density wave (CDW) in Sb(111) originating from the $\bar{M}$-point electron pockets giving rise to additional peaks in the diffraction pattern [52]. In Bi_2Se_3(111), however, no carrier pockets exist besides the Dirac cone and the quantum-well minibands occurring around the zone center [see Fig. 1(c)]. The latter provide nesting wave vectors of about 0.2 Å^{-1} between states of equal spin, which correspond fairly well to the parallel momentum transfers of the satellites observed aside the $(0, \pm1)$ peaks in HAS diffraction spectra (and likely also aside the specular peak, despite the coincidence with bound-state resonances) [Fig. 2(a)]. Charge density structures typically show a strong temperature-dependent behavior and vanish when the temperature approaches T_c. In the present work, we performed full angular scans at 113 K and room temperature (see Fig. 10 in Appendix B). In comparison, the satellite peaks become smaller at room temperature but are still discernible above the inelastic background. While we do not have a full temperature-dependent measurement at hand which would allow a determination of, e.g., the critical exponent, it appears from the comparison that any transition temperature would be above room temperature, as we did not go to much higher temperatures due to the low melting point of the material and the risk of degrading the sample at those temperatures.

It should be noted, however, that the observation of satellite peaks whose position is independent of the HAS incident energy is by itself indicative of a long-period superstructure of the electron density, possibly incommensurate or weakly

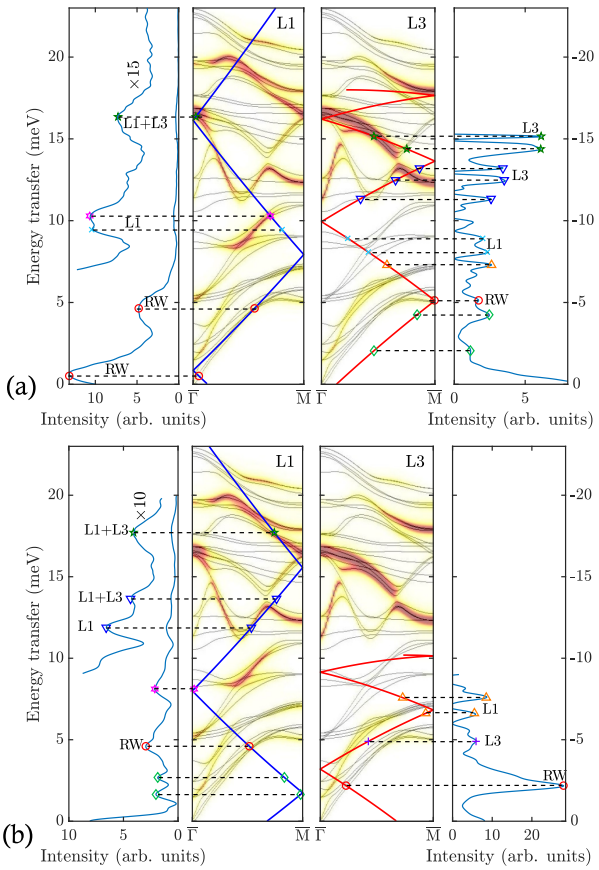

FIG. 3. Plot of two typical TOF measurements with the sample along $\overline{\Gamma M}$ and at room temperature. In (a), the incident energy is $E_i = 17.97$ meV with $\vartheta_i = 34.25°$ while in (b) $E_i = 10.19$ meV and $\vartheta_i = 40.25°$. The left and right-most panels show the TOF spectrum after conversion to energy transfer. The blue (phonon annihilation, $\Delta E > 0$) and red (phonon creation, $\Delta E < 0$) lines in the center panels show the scan curves superimposed onto the calculated dispersion using DFPT (The color code giving the intensity of the longitudinal L1 and L3 modes projected onto the first and third surface layer, respectively, is that of Fig. 5). The symbols denote peaks in the TOF spectrum which have been assigned to phonon events (RW = Rayleigh wave). The two distinct low-energy peaks (green diamonds) observed on the creation (a) and annihilation (b) sides in the phonon gap below the RW are tentatively assigned to low-energy collective surface electronic excitations, associated with the long-period surface superstructure and revealed through HAS bound-state resonance enhancement.

commensurate with the surface atomic lattice. Charge density oscillations as low as 10^{-6} atomic units, presently accessible to HAS, can in principle sustain very low-energy collective phase and amplitude excitations in the meV spectral range [52], and suggest an assignment of the present low-energy branches (Sec. III B).

A. Time-of-flight measurements and phonon dispersion curves

The phonon energies were determined by performing TOF measurements over a wide range of incident angles between the first-order diffraction peaks and at various beam energies. The phonon dispersion was then obtained by calculating the parallel momentum transfer ΔK for each extracted phonon energy from the conservation laws of energy and parallel momentum providing the so-called scan curve for planar scattering (see Eq. (C1) in Appendix C and Refs. [23,53]).

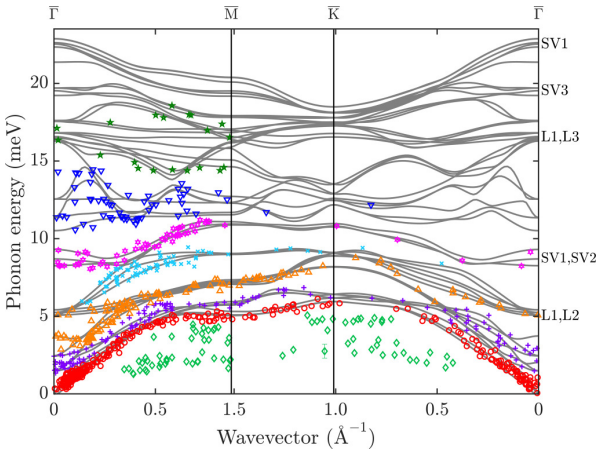

FIG. 4. Comparison of the measured phonon dispersion relation with DFPT calculations for three quintuple layers. The solid grey lines represent the DFPT calculation while different symbols for the experimentally determined points correspond to different phonon modes. The assignment of the symbols is based on the proximity to particular modes.

In Fig. 3(a), an example of a TOF spectrum after conversion to the energy transfer scale is shown. The measurement was taken in the high-symmetry direction $\overline{\Gamma M}$ with an incident beam energy $E_i = 17.97$ meV and at an incident angle of $\vartheta_i = 34.25°$. The TOF spectrum consists of several peaks which are located on the creation ($\Delta E < 0$) as well as the annihilation ($\Delta E > 0$) side. The peak at zero energy transfer corresponds to elastically scattered helium atoms [28,29]. The scan curve, shown in the two center panels of Fig. 3 for phonon annihilation (blue) and creation (red) events, associates each phonon event with a specific momentum transfer ΔK. The scan curve has been backfolded into the irreducible part of the Brillouin zone and is plotted on top of the calculated dispersion. The different symbols on the scan curves, marking the main inelastic features, have been associated to phonons of different character and polarization.

The large peaks in the TOF spectra marked with the red circles in Fig. 3, correspond to the Rayleigh wave (RW) as seen in the DFPT calculations. Note that in the present TOF spectra, the RW exhibits typically the largest intensity of all inelastic events [cf. the intensities in Fig. 3(a)]. There is a fair correspondence between the present HAS data and those previously reported by Zhu *et al.* [17]. Curiously Zhu *et al.* stated that the RW is not observed, whereas it appears in their plot, though with only a few data points, in reasonable agreement with the present one in the $\overline{\Gamma K}$ direction; it also occurs in the $\overline{\Gamma M}$ direction, once it is recognized that there is an avoided crossing, so that the RW at $\overline{M}$ is not the lowest mode. There is however an important difference with respect to Zhu *et al.* [17]: Present HAS data do not show any evidence

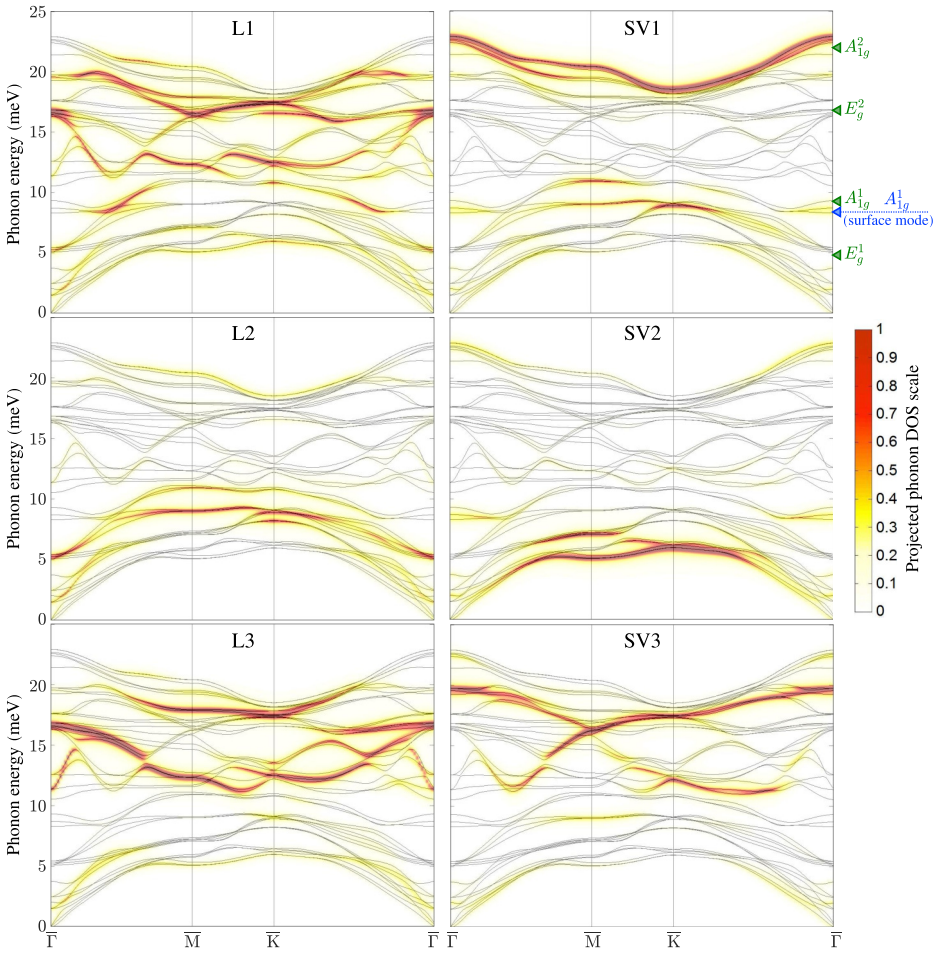

FIG. 5. Polarisation of the calculated phonon dispersion of Bi_2Se_3 from DFPT. The left column shows longitudinal polarization for the topmost three atomic layers (L1-L3). The right column shows shear vertical polarization (SV1-SV3). The color code bar on the right-hand side gives the intensity of the mode projected onto the corresponding layer. The green triangles at the top-right ordinate indicate the experimental energies of bulk Raman active modes according to Ref. [54], while the blue triangle shows the surface phonon softening according to Ref. [55].

of a KA in the ≈ 8 meV branch for wave vectors around 0.2 $Å^{-1}$ (see also Fig. 12 in Appendix C) and associated with the nesting at the Fermi level across the Dirac cone (or more likely across the parabolic dispersion of surface quantum-well states [19,20]).

Figure 4 shows the entire experimental surface phonon dispersion (symbols) superimposed onto the DFPT calculations (grey lines). The different symbols have been associated to phonons of different character and polarization based on the proximity to particular modes of the DFPT calculations. In total, we are able to distinguish at least eight different branches.

The polarization analysis of the calculated surface phonon modes can be found in Fig. 5 where the intensity of each polarization projected onto the corresponding layer is given by the color code. The left column shows the longitudinal polarisations for the first (L1), second (L2), and third (L3) layers. The right column shows the shear vertical polarization for the first three layers (SV1–SV3), while the shear horizontal polarization can be found in Fig. 9 of Appendix A. The theoretical dispersion curves are seen to agree quite well with the HAS data and also with the experimental Raman-active modes at $\overline{\Gamma}$ (green triangles in Fig. 5 according to [54]).

A closer comparison of the experimental data points in Fig. 4 with Fig. 5 shows that mainly phonon events with the largest amplitude in the two topmost layers of the sample are observed in the experiment. In particular in the low-energy region (<10 meV), most contributions come from phonons with the largest amplitude in the second layer (L2, SV2), which is a Bi layer and therefore about 2.5 times heavier than the first Se layer. The most prominent mode in the TOF spectra, the RW, corresponds predominantly to L and SV polarisations, due to its elliptical polarization, with a particularly strong SV2 component at the Brillouin zone boundary.

Note that the calculation does not reproduce the KA reported by Zhu *et al.* [17] (see Appendix A for calculations with SOC), in agreement with other recent *ab initio* calculations including SOC by Heid *et al.* [18] as well as with the

experimental and theoretical studies of $Bi_2Te_3(111)$ [28]. Heid *et al.* [18] suggested that the KA observed by Zhu *et al.* [7,17] may be connected to a strong e-ph interaction in the doped bulk material rather than to a surface state. According to their calculations, the largest contribution to the e-ph coupling comes from an in-plane polar-type branch in the optical region between 10 and 18 meV [18].

In fact, the strong dispersion of the optical phonon modes (Fig. 5), also found in Bi and Sb tellurides [28,50] may already be regarded as a manifestation of a significant e-ph interaction. In addition, Sobota *et al.* [55] reported a strong coupling of the A_{1g}^1 mode at a phonon energy of 8.48 meV which manifests itself in time-dependent renormalisations of the Dirac cone in angle-resolved photoemission spectroscopy (ARPES) measurements. The excellent quality of the DFPT calculations is further confirmed upon comparison with the experimentally observed softening of the A_{1g}^1 phonon mode at the surface, as reported by Sobota *et al.* [55] and as shown by the blue triangle in Fig. 5: The softening becomes apparent for the two lower branches of the DFPT calculations for three QLs.

We note that in the region around 15 meV the number of experimental data points is small and any mode assignment is probably accompanied by a large uncertainty, due to the strong dispersion and the avoided crossings of the calculated curves. Nevertheless it appears from the DFPT calculations that the optical phonon branch starting at about 16.5 meV at the $\overline{\Gamma}$ point softens to about 11 meV along $\overline{\Gamma M}$, in particular when considering the strong longitudinal character of this mode on the first atomic layer as shown in the top-left panel of Fig. 5. Such a softening could be caused by a screening of the quantum well electrons in analogy to the electron screening manifest as phonon softening of the optical phonon mode at 8.48 meV in the work of Sobota *et al.* [55], although in the latter case coupling appears mainly to the electrons of the Dirac cone rather than the quantum well states. It is also in accordance with our findings about the e-ph coupling (Sec. III C) which appears to be larger in the presence of a 2DEG upon comparison with systems that exhibit exclusively the Dirac topological states [27].

We turn now to the acoustic energy region and in particular the group velocity of the RW. In the long wavelength limit (close to $\overline{\Gamma}$) the dispersion relation of the RW is linear. Its slope provides the RW group velocity in the two symmetry directions $\overline{\Gamma M}$ and $\overline{\Gamma K}$:

$$\overline{\Gamma M} : v_{\mathrm{RW}}(112) = (1.63 \pm 0.07)\ \mathrm{km/s},$$
$$\overline{\Gamma K} : v_{\mathrm{RW}}(110) = (1.80 \pm 0.15)\ \mathrm{km/s}\ .$$

In order to appreciate the degree of localisation of the RW in the two symmetry directions, these values are to be compared with the corresponding speeds of sound. The present DFPT values (compared with values in parentheses derived from the available elastic constants [56]) are

$$\begin{aligned} \overline{\Gamma M}: \quad & v_{T,SV} = 1.757\ (1.91)\ \mathrm{km/s}, \\ & v_{T,SH} = 2.290\ (2.24)\ \mathrm{km/s}, \\ \overline{\Gamma K}: \quad & v_{T,SV} = 3.227\ (2.93)\ \mathrm{km/s}, \\ & v_{T,SH} = 1.416\ (1.22)\ \mathrm{km/s}\ . \end{aligned}$$

It appears that the RW has a velocity in the $\overline{\Gamma M}$ direction smaller than both transverse bulk values and is therefore a localized surface wave, whereas in the $\overline{\Gamma K}$ direction it has a velocity larger than that of the SH transverse sound, and is therefore a pseudosurface wave [57,58]. Actually in the absence of mirror symmetry for the sagittal plane in this direction, the RW is a resonance. The fact may have suggested (see Zhu *et al.* [7,17]) that in $Bi_2Se_3(111)$ the RW is suppressed but the present comparison with the DFPT calculation confirms that the RW is actually observed in both directions, though as a resonance along $\overline{\Gamma K}$. Values for the bulk longitudinal ($v_L = 2.9$ km/s) and transverse ($v_T = 1.7$ km/s) group velocities of Bi_2Se_3 have also been reported in the framework of the isotropic elastic continuum theory [8,59]. In this approximation, the corresponding RW velocity, obtained by solving the cubic Rayleigh equation [60], would be $v_{\mathrm{RW}} = 1.56$ km/s in any direction.

B. Low-energy branches

The measured HAS-TOF spectra displayed in Fig. 3 show also distinct peaks yielding two branches of elementary excitations with an energy below the RW branch (green diamonds in Fig. 4). On the basis of present DFPT surface phonon dispersion curves, they cannot be attributed to any possible phonon branch of the ideal surface. HAS from conducting surfaces exclusively occurs through the interaction (mostly Pauli repulsion) with the surface electron density, and therefore also electronic excitations in the THz range can be observed by HAS, with a 0.5 meV resolution and sensitivity to charge density oscillations in the 10^{-6} atomic units range.

Actually the observed low-energy branches are reminiscent of those recently observed with HAS in Sb(111), which have been attributed to elementary excitations (phasons/amplitons) of a multivalley CDW [52]. The concomitant presence of a commensurate component associated with the $\overline{M}$-point electron pockets at the Fermi level, and an incommensurate one due to the hole pockets along the $\overline{\Gamma M}$ direction, allows for collective excitations with a comparatively small gap at $Q = 0$. On the other hand no low-energy phason/ampliton modes have been detected with HAS for the perfectly commensurate multivalley CDW reported in the quasi-1D surface Bi(114) [61], discommensuration being a requisite for depinning and a vanishing/small gap at $\overline{\Gamma}$. $Bi_2Se_3(111)$ has no pocket states at the Fermi level, besides the rings around $\overline{\Gamma}$ of the surface topological Dirac and the quantum-well states [19,20]. The satellites near the HAS diffraction peaks [see Fig. 2(a)] suggest some long-period charge-density structures and possibly low-energy collective excitations. In order to detect the associated, seemingly small inelastic features in the TOF spectra, we rely on the bound-state resonance enhancement method (Ref. [32] and Chap. 10 of Ref. [24]), applicable to highly corrugated surfaces and successfully used to detect with HAS high-energy optical surface modes in ionic crystals [24,62]. The complete set of He-surface bound states has been measured previously [51].

Bound-state inelastic resonances occur in the HAS-TOF spectrum, with a possibly large enhancement of the inelastic intensities, at the locus of intersections of the scan curve (1) [23] with the inelastic bound-state resonance condition (2)

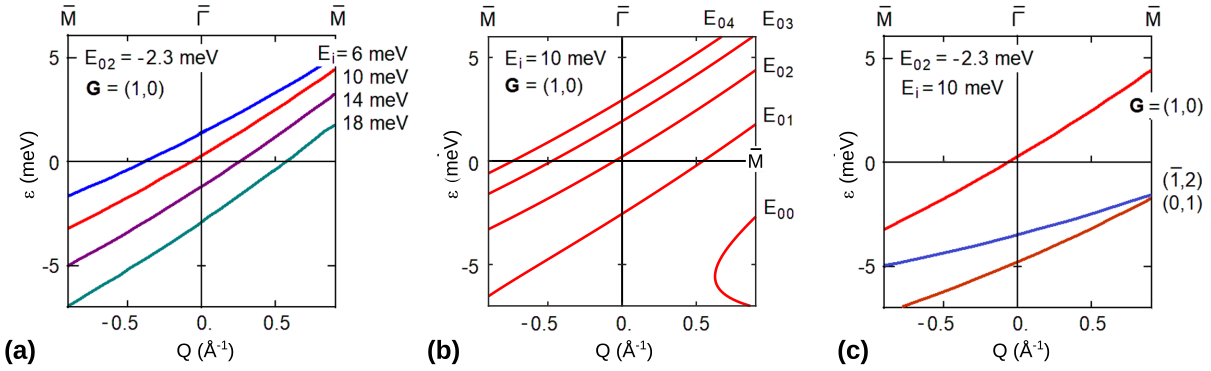

FIG. 6. Inelastic bound-state resonance conditions along the $\overline{\Gamma M}$ direction in the first Brillouin zone: (a) for $\mathbf{G} = (1, 0) \equiv (1.76, 0)$ Å^{-1}, the bound state $n = 2$ and different incident energies; (b) for a given $E_i = 10$ meV, $\mathbf{G} = (1,0)$ and the different bound states $n = 0, 1, \ldots, 4$; (c) for $E_i = 10$ meV, the bound state $n = 2$ and three different $\mathbf{G}$ vectors $(1, 0)$, $(\bar{1}, 2) \equiv (0, 3.05)$ Å^{-1}, $(0, 1) \equiv (0.88, 1, 53)$ Å^{-1}. Here, the integer indices refer to the hexagonal reciprocal lattice base, while the components in Å^{-1} units are those of $\mathbf{G} = (G_\parallel, G_\perp)$. Other $\mathbf{G}$-values yield inelastic resonances in the low-energy range $|\varepsilon| < 5$ meV only for wave vectors Q outside the first BZ. Suitable combinations of E_i, E_{0n}, and of the $\mathbf{G}$-vector permit to scan the phonon gap region below the RW branch, which can be used to tune the conditions for localized excitations, to detect those via a resonance enhancement.

(see Chap. 30 of Ref. [24]). For elementary excitations with an energy $\Delta E = \varepsilon$ and wave vector $\Delta K = Q$ the equations become

$$k_i \sin\vartheta_i + Q = \sin\vartheta_f \sqrt{2m(E_i + \varepsilon)/\hbar}, \tag{1}$$

$$E_i + \varepsilon = -|E_{0n}| + \frac{\hbar^2}{2m}\left[(k_i \sin\vartheta_i + Q + G_\parallel)^2 + G_\perp^2\right]. \tag{2}$$

At the mentioned intersection of (1) and (2), an elementary excitation with (ε, Q) assists the selective adsorption of the atom of mass m, incident energy E_i, wave vector k_i, and angle ϑ_i into a bound state of energy $-|E_{0n}|$, via the exchange of a surface reciprocal lattice vector $\mathbf{G} = (G_\parallel, G_\perp)$. On returning the $\mathbf{G}$ vector to the surface lattice, the atom is selectively desorbed from the bound state into the final angle ϑ_f. In (2), the vector $\mathbf{G}$ has been conveniently expressed via its components parallel and orthogonal to the scattering plane, respectively. In $Bi_2Se_3(111)$, the measured He-surface bound-state energies [51] are $E_{0n} = -5.6, -3.8, -2.3, -1.2, -0.5$ meV for $n = 0$, 1, 2, 3, 4, respectively. For a fixed scattering geometry $\vartheta_i + \vartheta_f = \vartheta_{SD}$ (here $\vartheta_{SD} = 91.5°$), Eqs. (1) and (2) provide, via the elimination of $\vartheta_i = \vartheta_{SD} - \vartheta_f$, the locus of intersections $\varepsilon = \varepsilon_{E_i,n;\mathbf{G}}(Q)$ for any incident energy E_i, bound state n and reciprocal surface vector $\mathbf{G}$.

The three panels of Fig. 6 show some plots of $\varepsilon = \varepsilon_{E_i,n;\mathbf{G}}(Q)$ in the $\overline{\Gamma M}$ direction for: (a) different values of the incident energy E_i at a given bound state ($n = 2$) and $\mathbf{G} = (1, 0)$; (b) different bound state energies at a given incident energy $E_i = 10$ meV; (c) several different $\mathbf{G}$ vectors at a given incident energy $E_i = 10$ meV and for the bound state $n = 2$. The functions $\varepsilon = \varepsilon_{E_i,n;\mathbf{G}}(Q)$ cross the phonon gap below the RW in the first BZ. In practice the phonon gap can be fully scanned by the resonance curves $\varepsilon = \varepsilon_{E_i,n;\mathbf{G}}(Q)$ upon varying the incident energy, so as to detect, via resonance enhancement, weak elementary excitations.

Since the low-energy data points appear to align along two dispersion curves, independently of the incident energy, as well as of n and $\mathbf{G}$, rather than being spread over the entire gap, they cannot be attributed to a resonance-enhanced many-phonon background. Furthermore, frustrated translational modes of adsorbates like CO would show no dispersion and would appear at higher vibrational energies [63]. More likely these points indicate two branches of low-energy excitations associated with the surface charge-density superstructure observed in the diffraction spectra, as anticipated above.

In this respect, it is worth mentioning a recent work by Shvonski *et al.* [36] where it is argued that a strong e-ph interaction affecting the surface 2DEG of a 3D topological crystal allows for collective polaron excitations (plasmon-polarons). Their dispersion is predicted to be that of an acoustic plasmon running below the single-particle excitation spectrum as an effect of the polaron-polaron attractive interaction. The theoretical analysis by Shvonski *et al.* [36] is actually interpreting the recent observation with high-resolution electron energy loss spectroscopy (HREELS) by Jia *et al.* [33] of an anomalous acoustic plasmon (AAP) mode from the topologically protected states of $Bi_2Se_3(111)$, with energy between 0 and 6.5 meV (and its continuation in the second zone up to ≈10 meV). The present HAS data do not permit to identify this AAP due to its superposition with the RW in the first BZ and in part with other phonon branches in its continuation.

C. Electron-phonon coupling

As shown in recent papers [25–27], the temperature dependence of the Debye-Waller (DW) exponent plotted in Fig. 2(b) permits to extract for a conducting surface the mass-enhancement parameter λ expressing the electron-phonon coupling strength. It is related to the DW exponent by the equations:

$$\lambda = \frac{\pi}{2n_s}\alpha\,, \quad \alpha \equiv \frac{\phi}{A_c\, k_{iz}^2}\frac{\partial \ln I(T_S)}{k_B\, \partial T_S}\,, \tag{3}$$

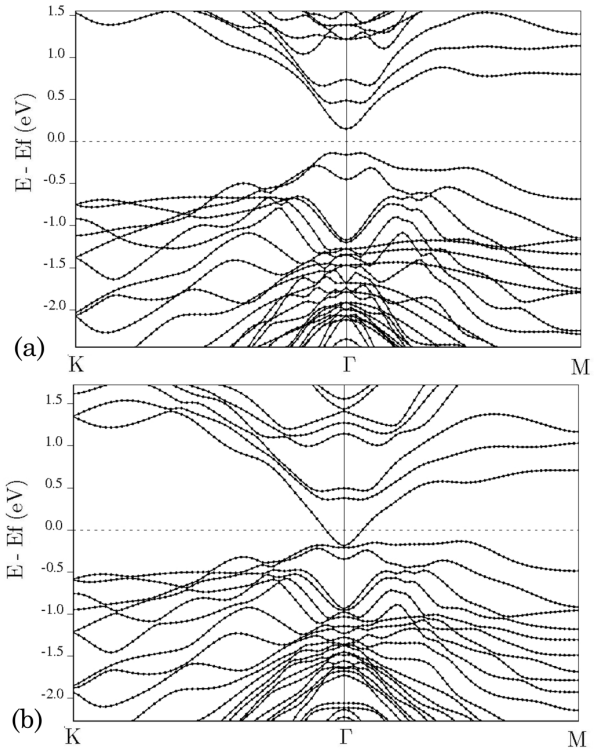

FIG. 7. Surface electronic band structure of Bi_2Se_3(111) omitting SOC (a). The topological surface states appear when SOC is included as shown in (b).

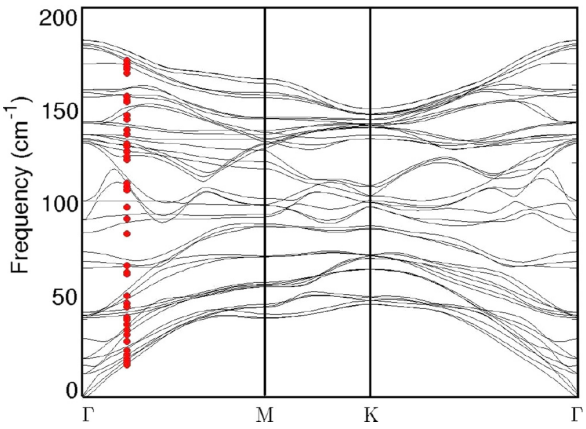

FIG. 8. Surface phonon dispersion of Bi_2Se_3 omitting (black continuous line) and including SOC (red dots) at a Q vector corresponding to the nesting vector $2k_F$. The inclusion of SOC gives rise to a softening of the phonon modes but no evidence for a KA is found.

where $\phi = 4.9$ eV is the work function [64], $A_c = 14.92$ Å^2 the unit cell area, $I(T_S)$ the He-beam specular intensity, T_S the surface temperature, $k_{iz} = 3.18$ Å^{-1} the normal component of the incident wave vector, and n_s the number of conducting layers which contribute to the phonon-induced modulation of the surface charge density.[1] The latter is estimated to be $n_s = 2\lambda_{TF}/c_0$, where λ_{TF} is the Thomas-Fermi screening length characterising the surface band-bending region (here ≈6 nm) [19], $c_0 = 9.6$ Å the QL thickness, and the factor 2 indicates the 2DEG multiplicity as observed with ARPES in the current Bi_2Se_3 sample [19]. With these values and the experimental DW derivative with respect to T_S from Fig. 2(b), we obtain $\lambda = 0.51$.

We note that there appear to be weak oscillations in the temperature-dependent data of Fig. 2(b). While deviations from a linear behavior could occur due to anharmonic effects at higher temperatures, or due to phonon-phonon coupling events, it appears from the experimental uncertainties that a linear regression provides still an accurate approximation in the present case. It should also be mentioned that, unlike in the case of low-index metal surfaces, characterized by a soft-wall repulsive potential and negligible corrugation, here the large electronic corrugation [51] implies a hard-wall potential. In this case, one needs to correct k_{iz}^2 so as to account for the acceleration impressed by the attractive part of the potential on the He atom when approaching the surface turning point (Beeby correction [29]). Therefore k_{iz}^2 is replaced by $k_{iz}'^2 = k_{iz}^2 + 2mD/\hbar^2$, where m is the He mass and $D = 6.54$ meV the He-surface potential well depth [51]. With the Beeby correction it is found $\lambda = 0.23$.

The value compares quite well with values in the literature derived from other experiments, e.g., $\lambda = 0.25$ [3], and $\lambda = 0.17$ [5] from ARPES measurements and $\lambda = 0.26$ [65] from Landau level spectroscopy. A theoretical study by Giraud *et al.* [8] with phonons calculated in the isotropic continuum limit gives $\lambda = 0.42$, whereas for other ARPES measurements, where only Dirac states appear to be involved, values of λ as low as 0.076 to 0.088 have been found [4].

From the comparison, it appears that the presence of a 2DEG due to quantum-well minibands (at least two in the present analysis) plays an important role in raising the e-ph coupling strength, which is quite small when exclusively due to the Dirac topological states, to values in the range of 0.2–0.4. It seems to be a general phenomenon for TIs belonging to the class of bismuth chalcogenides as reported by Benedek *et al.* [27]. The same conclusion follows from the theoretical analysis by Heid *et al.* [18], who showed that raising the Fermi level from the Dirac point to above the conduction band minimum gives a corresponding increase of λ from values well below 0.1 to values in the range above 0.2, with a substantial contribution from interband coupling and in very good agreement with the present analysis. The role of n-type doping contributing to the formation of the surface quantum-well 2DEG is quite clear in the analysis of the e-ph coupling strength in Cu-doped Bi_2Se_3, where an analysis

[1]The (bulk) carrier concentration as extracted from Hall measurements of the current sample is in the region $(1.75–1.8) \times 10^{18}$ cm^{-3}, i.e., a particularly small conductivity in the bulk suggesting that the carrier concentration at the surface may even be larger, compared to the first generation samples [19] which had a much larger bulk charge carrier concentration.

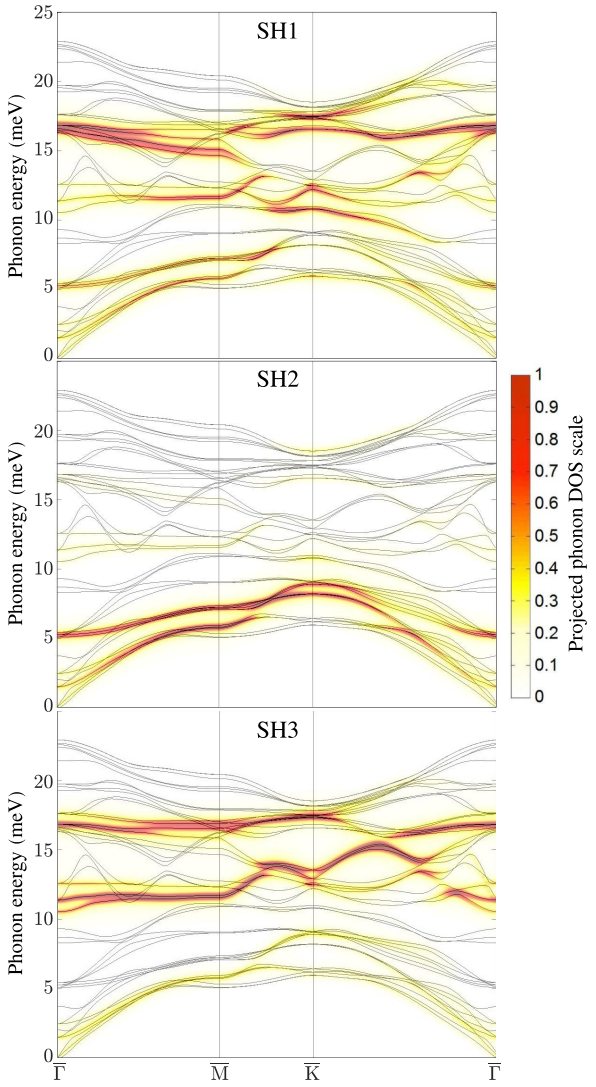

FIG. 9. Shear horizontal (SH) polarization of the calculated phonon dispersion of Bi_2Se_3 for the topmost three atomic layers (SH1-SH3) from DFPT without SOC. The color code bar on the right-hand side gives the intensity of the mode projected onto the corresponding layer.

based on the McMillan formula [66], indicates a value for λ as large as 0.62 [4].

IV. CONCLUSIONS

In summary, we have determined the surface phonon dispersion curves of Bi_2Se_3 along both high-symmetry directions, where the largest inelastic scattering intensity is provided by the Rayleigh wave. Thus our measurements show in contrast to previous studies that the Rayleigh mode exists and is a localized surface mode in one of the high-symmetry directions ($\overline{\Gamma M}$), while in the other high-symmetry direction it is actually a pseudo-surface wave ($\overline{\Gamma K}$). Comparison with density functional perturbation theory calculations shows

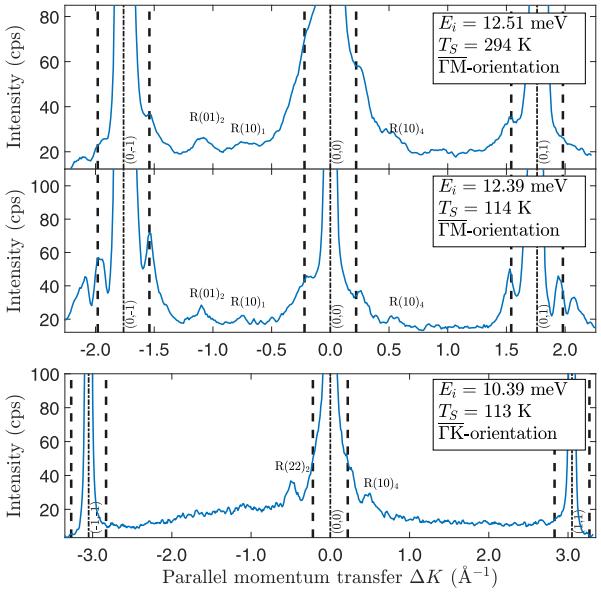

FIG. 10. HAS diffraction scans for Bi_2Se_3(111) measured at room temperature and 113 K along the high-symmetry direction $\overline{\Gamma M}$ and at low temperature along $\overline{\Gamma K}$. The smaller features between the specular and the two diffraction peaks are due to bound-state resonances and kinematical focusing [51].

excellent agreement with the experimental data. In addition to the phonon-related losses, we observe two additional dispersion curves in the gap well below the Rayleigh mode. These two low-energy branches may correspond to collective low-energy excitations of surface electrons. The appearance of these collective electronic excitations in an unprecedentedly low-energy region is probably associated with a small surface charge density and an appreciable electron-phonon coupling ($\lambda = 0.23$). However, much more detailed experiments and theoretical analysis will be needed in order to fully understand these excitations; e.g., what is the influence of the carrier concentration upon doping and what is the role of both the Dirac and the quantum-well states, with the latter providing a much larger electron-phonon interaction than the former. The analysis advocates for a more systematic study by means of elastic and inelastic HAS spectroscopy of the surface structure, the low-energy collective excitations, and the electron-phonon interaction of interesting 2D materials, where the superior space and energy resolution of HAS is hardly attainable with other current surface probes.

ACKNOWLEDGMENTS

We are grateful to Evgueni V. Chulkov (DIPC) and Krzysztof Kempa (Boston College) for useful discussions. The authors are grateful for financial support by the FWF (Austrian Science Fund) within the project P29641-N36 and A.T acknowledges financial support within the project J3479-N20. We would like to thank the Aarhus University Research Foundation, VILLUM FOUNDATION via the Centre of Excellence for Dirac Materials (Grant No. 11744) and the

SPP1666 of the DFG (Grant No. HO 5150/1-2) for financial support. M. Bremholm acknowledges financial support from the Center of Materials Crystallography (CMC) and the Danish National Research Foundation (DNRF93).

APPENDIX A: ADDITIONAL CALCULATIONS AND THE EFFECT OF SOC

Without SOC, Bi_2Se_3 exhibits a band gap, not only in the bulk but also at the surface with a band gap of 0.35 eV as evident from density functional theory (DFT) calculations [Fig. 7(a)]. By including SOC as shown in Fig. 7(b), the electronic band dispersion becomes gapless, with spin-polarized and Dirac cone shaped surface bands around the $\overline{\Gamma}$ point in the typical manner of 3D topological insulators.

The topologically protected Dirac cone forms a small Fermi circle around the $\overline{\Gamma}$ point which cannot be properly described with a coarse mesh and a large smearing resulting in the impossibility to capture subtle effects, such as the proposed KA [17] with a standard calculation. In order to verify the effect of such states on surface phonons, we repeated the phonon calculations at the Q point corresponding to the nesting vector ($2k_F$) by including SOC. We compared the result with that obtained by omitting the SOC.

To perform these calculations we had to improve the sampling of the Brillouin zone close to the Fermi surface which is particularly important to resolve a possibly existing anomaly. Given the peculiar shape of the Fermi surface in the Bi_2Se_3(111) slabs consisting of a ring around the $\overline{\Gamma}$ point, we used a graded k-point mesh (equivalent to a $50 \times 50 \times 1$ uniform mesh) near the $\overline{\Gamma}$ point and a coarser one (equivalent to a $8 \times 8 \times 1$ mesh) near the zone boundary. The results are reported in Fig. 8. A one to one comparison between phonon modes calculated with and without SOC shows that there is no evidence of a KA induced by the presence of the surface metallic states, involving any of the surface phonon modes. The spin-orbit coupling results merely in an overall softening of the phonon modes of at most 6%.

In addition to the shear vertical and shear horizontal phonon densities shown in the main part of the paper, Fig. 9 shows the shear horizontal polarisations projected onto the first, second and third layer (SH1, SH2, SH3). If the scattering plane, defined by the incoming and scattered He beam, coincides with a mirror plane of the surface, the detection of purely SH modes is, in principle, forbidden due to symmetry reasons [67] and we show the calculations of the SH modes here for completeness. However, phonon modes often exhibit a mixing of polarization components and even a purely SH mode may give rise to charge density oscillations above the first atomic layer which are eventually observed in inelastic He atom scattering.

APPENDIX B: ADDITIONAL DIFFRACTION SCANS

A comparison of two angular scans with 113 K and room temperature in the $\overline{\Gamma M}$ azimuth can be seen in Fig. 10. It shows that at higher temperatures the satellite peaks at constant momentum transfer are still present even though they are much smaller and sometimes appear as mere shoulders close to the diffraction peaks. In addition to the diffraction scans along $\overline{\Gamma M}$ which are already shown in the main part of the paper, Fig. 10 shows a diffraction scan along the $\overline{\Gamma K}$ azimuth.

Note that along $\overline{\Gamma K}$ there is no evidence for additional peaks close to the diffraction peaks, despite two small features close to the specular reflection which can be assigned to resonances [51]. The fact that these peaks appear only along $\overline{\Gamma M}$ is indicative of the hexagonal shape of the quantum well states giving rise to a multitude of connecting vectors with similar momentum transfer between the flat sides of the hexagon and thus along the $\overline{\Gamma M}$ azimuth.

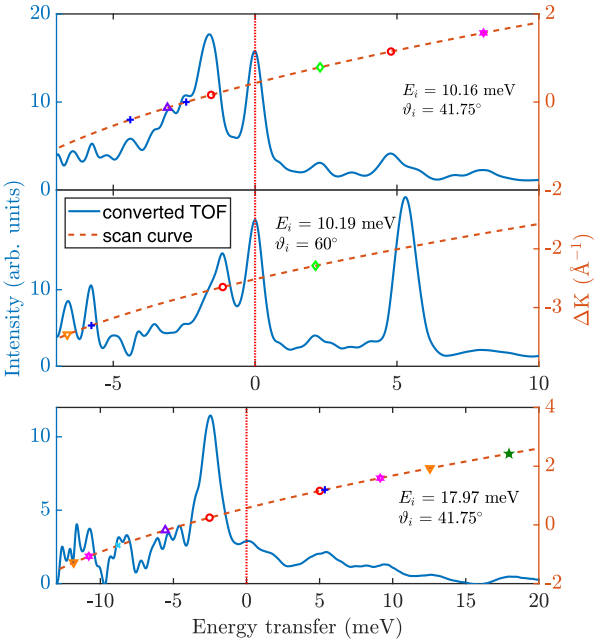

FIG. 11. Comparison of different TOF spectra in the $\overline{\Gamma M}$ direction with various incident Energies E_i and angles ϑ_i. For the two upper graphs the nozzle temperature was set to 50 K and for the bottom one to 80 K, while the sample was held at room temperature. The vertical red dotted line corresponds to elastically scattered atoms. The dashed line describes the scan curve which connects energy transfer with momentum transfer (y axis on the right-hand side). The symbols denote peaks in the TOF spectrum which have been assigned to phonon events (same symbols as the main part of the article).

APPENDIX C: FROM TOF MEASUREMENTS TO THE PHONON DISPERSION AND ADDITIONAL TOF DATA

The phonon energies were determined by performing TOF measurements over a wide range of incident angles between the first-order diffraction peaks and at various beam energies. The phonon dispersion was then obtained by calculating the parallel momentum transfer $\Delta K = |\Delta \mathbf{K}|$ for each extracted phonon energy ΔE from the conservation laws of energy and parallel momentum providing the so-called scan curve for

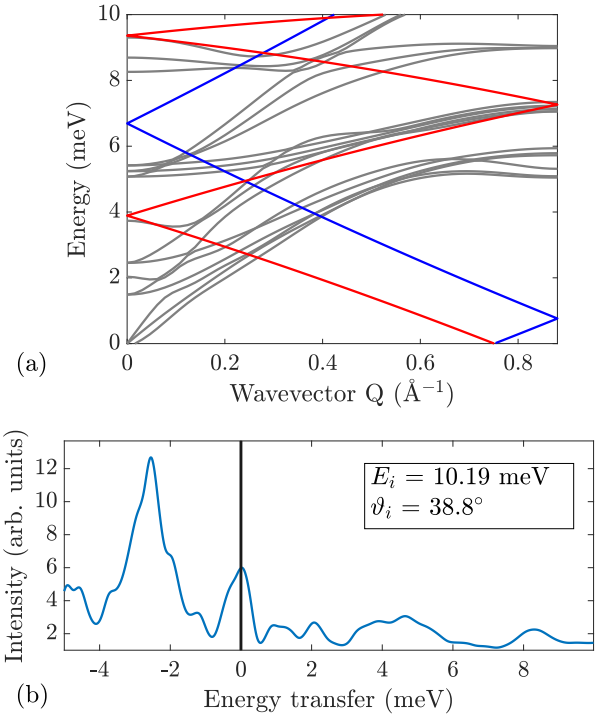

FIG. 12. In (b), the TOF spectrum with the x axis converted to energy transfer is shown. (a) depicts the corresponding scan curve [Eq. (C1)], backfolded into the first Brillouin zone and superimposed onto the results of the DFPT calculation (grey lines).

planar scattering [23,53]:

$$\frac{\Delta E}{E_i} + 1 = \frac{\sin^2 \vartheta_i}{\sin^2 \vartheta_f}\left(1 + \frac{\Delta \mathbf{K}}{\mathbf{K}_i}\right)^2, \tag{C1}$$

where E_i is the energy of the incident beam, $\mathbf{K}_i$ is the parallel component of the incident wave vector, and ϑ_i and ϑ_f are the incident and final angle, respectively.

Figures 11 and 12 show some further examples of measured TOF spectra along the $\overline{\Gamma M}$ azimuth and the sample at room temperature. Each TOF spectrum consists of various peaks which are located on the creation (negative x axis, $\Delta E < 0$) as well as the annihilation (positive x axis, $\Delta E > 0$) side. The peak at zero energy transfer corresponds to elastically scattered helium atoms due to the diffuse elastic peak which is caused by scattering from surface imperfections such as steps [28,29]. The scan curve associates each phonon event with a specific momentum transfer ΔK based on [Eq. (C1)], since the incoming helium atom looses or gains momentum via inelastic scattering from a phonon.

Figure 11 shows an additional set of TOF spectra along the $\overline{\Gamma M}$ direction. Most measurements covering the low-energy region with the acoustic phonon modes where performed with a ≈10 meV beam (top and center panel in Fig. 11), while for the optical phonon modes higher incident beam energies (bottom panel in Fig. 11) were used, in order to cover the optical energy region on the creation side. Note that the particularly strong peak at around 5.5 meV in the center panel is not assigned to a phonon event. This seemingly inelastic feature originates from elastic scattering and is caused by the outer tails of the velocity distribution in the incident beam. These so-called deceptons or spurions occur within the vicinity of the diffraction peaks and give rise to a large intensity in the inelastic spectra due to their elastic nature [68].

As mentioned in the main part of the article, there is no evidence for a strong KA in our measurements as reported by Zhu *et al.* [7,17], who observed a strong V-shaped indentation at $\Delta K \approx 0.25$ Å^{-1} for an optical phonon branch originating at 7.4 meV at the $\overline{\Gamma}$ point. The scan curve on the phonon annihilation side (blue curve) in Fig. 12(a) covers exactly the 6–8 meV close to the $\overline{\Gamma}$ point. Neither the DFPT calculations [grey lines in Fig. 12(a)] support such a KA nor does the experimental data which in turn even shows a minimum of the scattered inelastic intensity in the 6–8 meV region of the $\Delta E > 0$ side [Fig. 12(b)].

[1] M. Z. Hasan and C. L. Kane, Colloquium: Topological insulators, Rev. Mod. Phys. **82**, 3045 (2010).

[2] J. Moore, Topological insulators: The next generation, Nat. Phys. **5**, 378 (2009).

[3] R. C. Hatch, M. Bianchi, D. Guan, S. Bao, J. Mi, B. B. Iversen, L. Nilsson, L. Hornekær, and P. Hofmann, Stability of the Bi_2Se_3(111) topological state: Electron-phonon and electron-defect scattering, Phys. Rev. B **83**, 241303(R) (2011).

[4] Z.-H. Pan, A. V. Fedorov, D. Gardner, Y. S. Lee, S. Chu, and T. Valla, Measurement of an Exceptionally Weak Electron-Phonon Coupling on the Surface of the Topological Insulator Bi_2Se_3 Using Angle-Resolved Photoemission Spectroscopy, Phys. Rev. Lett. **108**, 187001 (2012).

[5] C. Chen, Z. Xie, Y. Feng, H. Yi, A. Liang, S. He, D. Mou, J. He, Y. Peng, X. Liu *et al.*, Tunable Dirac fermion dynamics in topological insulators, Sci. Rep. **3**, 2411 (2013).

[6] T. Kondo, Y. Nakashima, Y. Ota, Y. Ishida, W. Malaeb, K. Okazaki, S. Shin, M. Kriener, S. Sasaki, K. Segawa, and Y. Ando, Anomalous Dressing of Dirac Fermions in the Topological Surface State of Bi_2Se_3, Bi_2Te_3, and Cu-Doped Bi_2Se_3, Phys. Rev. Lett. **110**, 217601 (2013).

[7] X. Zhu, L. Santos, C. Howard, R. Sankar, F. C. Chou, C. Chamon, and M. El-Batanouny, Electron-Phonon Coupling on the Surface of the Topological Insulator Bi_2Se_3 Determined from Surface-Phonon Dispersion Measurements, Phys. Rev. Lett. **108**, 185501 (2012).

[8] S. Giraud, A. Kundu, and R. Egger, Electron-phonon scattering in topological insulator thin films, Phys. Rev. B **85**, 035441 (2012).

[9] P. Di Pietro, M. Ortolani, O. Limaj, A. Di Gaspare, V. Giliberti, F. Giorgianni, M. Brahlek, N. Bansal, N. Koirala, S. Oh, P. Calvani, and S. Lupi, Observation of Dirac plasmons in a topological insulator, Nat. Nanotechnol. **8**, 556 (2013).

[10] K. Kadel, L. Kumari, W. Li, J. Y. Huang, and P. P. Provencio, Synthesis and thermoelectric properties of Bi_2Se_3 nanostructures, Nanoscale Res. Lett. **6**, 57 (2011).

[11] S. K. Mishra, S. Satpathy, and O. Jepsen, Electronic structure and thermoelectric properties of bismuth telluride and bismuth selenide, J. Phys.: Condens. Matter **9**, 461 (1997).

[12] H. J. Goldsmid, *Thermoelectric Refrigeration* (Springer, 1964).

[13] J. Liang, L. Cheng, J. Zhang, H. Liu, and Z. Zhang, Maximizing the thermoelectric performance of topological insulator Bi_2Te_3 films in the few-quintuple layer regime, Nanoscale **8**, 8855 (2016).

[14] H. Tang, X. Wang, Y. Xiong, Y. Zhao, Y. Zhang, Y. Zhang, J. Yang, and D. Xu, Thermoelectric characterization of individual bismuth selenide topological insulator nanoribbons, Nanoscale **7**, 6683 (2015).

[15] A. J. Minnich, M. S. Dresselhaus, Z. F. Ren, and G. Chen, Bulk nanostructured thermoelectric materials: Current research and future prospects, Energy Environ. Sci **2**, 466 (2009).

[16] T.-C. Hsiung, C.-Y. Mou, T.-K. Lee, and Y.-Y. Chen, Surface-dominated transport and enhanced thermoelectric figure of merit in topological insulator $Bi_{1.5}Sb_{0.5}Te_{1.7}Se_{1.3}$, Nanoscale **7**, 518 (2015).

[17] X. Zhu, L. Santos, R. Sankar, S. Chikara, C. Howard, F. C. Chou, C. Chamon, and M. El-Batanouny, Interaction of Phonons and Dirac Fermions on the Surface of Bi_2Se_3: A Strong Kohn Anomaly, Phys. Rev. Lett. **107**, 186102 (2011).

[18] R. Heid, I. Y. Sklyadneva, and E. V. Chulkov, Electron-phonon coupling in topological surface states: The role of polar optical modes, Sci. Rep. **7**, 1095 (2017).

[19] M. Bianchi, D. Guan, S. Bao, J. Mi, B. B. Iversen, P. D. King, and P. Hofmann, Coexistence of the topological state and a two-dimensional electron gas on the surface of Bi_2Se_3, Nat. Commun. **1**, 128 (2010).

[20] P. D. C. King, R. C. Hatch, M. Bianchi, R. Ovsyannikov, C. Lupulescu, G. Landolt, B. Slomski, J. H. Dil, D. Guan, J. L. Mi, E. D. L. Rienks, J. Fink, A. Lindblad, S. Svensson, S. Bao, G. Balakrishnan, B. B. Iversen, J. Osterwalder, W. Eberhardt, F. Baumberger, and P. Hofmann, Large Tunable Rashba Spin Splitting of a Two-Dimensional Electron Gas in Bi_2Se_3, Phys. Rev. Lett. **107**, 096802 (2011).

[21] G. Grimvall, *The Electron-Phonon Interaction in Metals* (North-Holland, Amsterdam, 1981).

[22] I. Y. Sklyadneva, G. Benedek, E. V. Chulkov, P. M. Echenique, R. Heid, K.-P. Bohnen, and J. P. Toennies, Mode-Selected Electron-Phonon Coupling in Superconducting Pb Nanofilms Determined from He Atom Scattering, Phys. Rev. Lett. **107**, 095502 (2011).

[23] A. Tamtögl, P. Kraus, M. Mayrhofer-Reinhartshuber, D. Campi, M. Bernasconi, G. Benedek, and W. E. Ernst, Surface and subsurface phonons of Bi(111) measured with helium atom scattering, Phys. Rev. B **87**, 035410 (2013).

[24] G. Benedek and J. P. Toennies, *Atomic Scale Dynamics at Surfaces* (Springer, Berlin, Heidelberg, 2018).

[25] G. Benedek, S. Miret-Artés, J. P. Toennies, and J. R. Manson, Electron-phonon coupling constant of metallic overlayers from specular he atom scattering, J. Phys. Chem. Lett. **9**, 76 (2018).

[26] A. Tamtögl, P. Kraus, N. Avidor, M. Bremholm, E. M. J. Hedegaard, B. B. Iversen, M. Bianchi, P. Hofmann, J. Ellis, W. Allison, G. Benedek, and W. E. Ernst, Electron-phonon coupling and surface Debye temperature of Bi_2Te_3(111) from helium atom scattering, Phys. Rev. B **95**, 195401 (2017).

[27] G. Benedek, S. Miret-Artés, J. R. Manson, A. Ruckhofer, W. E. Ernst, and A. Tamtögl, Origin of the electron-phonon interaction of topological semimetal surfaces measured with helium atom scattering, J. Phys. Chem. Lett. **11**, 1927 (2020).

[28] A. Tamtögl, D. Campi, M. Bremholm, E. M. J. Hedegaard, B. B. Iversen, M. Bianchi, P. Hofmann, N. Marzari, G. Benedek, J. Ellis, and W. Allison, Nanoscale surface dynamics of Bi_2Te_3(111): Observation of a prominent surface acoustic wave and the role of van der Waals interactions, Nanoscale **10**, 14627 (2018).

[29] D. Farías and K.-H. Rieder, Atomic beam diffraction from solid surfaces, Rep. Prog. Phys. **61**, 1575 (1998).

[30] M. Mayrhofer-Reinhartshuber, P. Kraus, A. Tamtögl, S. Miret-Artés, and W. E. Ernst, Helium-surface interaction potential of Sb(111) from scattering experiments and close-coupling calculations, Phys. Rev. B **88**, 205425 (2013).

[31] V. M. Silkin, A. García-Lekue, J. M. Pitarke, E. V. Chulkov, E. Zaremba, and P. M. Echenique, Novel low-energy collective excitation at metal surfaces, Europhys. Lett. **66**, 260 (2004).

[32] D. Evans, V. Celli, G. Benedek, J. P. Toennies, and R. B. Doak, Resonance-Enhanced Atom Scattering from Surface Phonons, Phys. Rev. Lett. **50**, 1854 (1983).

[33] X. Jia, S. Zhang, R. Sankar, F.-C. Chou, W. Wang, K. Kempa, E. W. Plummer, J. Zhang, X. Zhu, and J. Guo, Anomalous Acoustic Plasmon Mode from Topologically Protected States, Phys. Rev. Lett. **119**, 136805 (2017).

[34] F. Stern, Polarizability of a Two-Dimensional Electron Gas, Phys. Rev. Lett. **18**, 546 (1967).

[35] T. Ando, A. B. Fowler, and F. Stern, Electronic properties of two-dimensional systems, Rev. Mod. Phys. **54**, 437 (1982).

[36] A. Shvonski, J. Kong, and K. Kempa, Plasmon-polaron of the topological metallic surface states, Phys. Rev. B **99**, 125148 (2019).

[37] H. Yu and J. C. Hermanson, Subband structure and plasmon-phonon coupled excitations in the accumulation layer of ZnO, Phys. Rev. B **41**, 5991 (1990).

[38] J. M. Pitarke, V. M. Silkin, E. V. Chulkov, and P. M. Echenique, Theory of surface plasmons and surface-plasmon polaritons, Rep. Prog. Phys. **70**, 1 (2006).

[39] Y. Wang, E. W. Plummer, and K. Kempa, Foundations of plasmonics, Adv. Phys. **60**, 799 (2011).

[40] B. Diaconescu, K. Pohl, L. Vattuone, L. Savio, P. Hofmann, V. M. Silkin, J. M. Pitarke, E. V. Chulkov, P. M. Echenique, D. Farías, and M. Rocca, Low-energy acoustic plasmons at metal surfaces, Nature (London) **448**, 57 (2007).

[41] A. Tamtögl, M. Sacchi, N. Avidor, I. Calvo-Almazán, P. S. M. Townsend, M. Bremholm, P. Hofmann, J. Ellis, and W. Allison, Nanoscopic diffusion of water on a topological insulator, Nat. Commun. **11**, 278 (2020).

[42] A. Tamtögl, M. Mayrhofer-Reinhartshuber, N. Balak, W. E. Ernst, and K. H. Rieder, Elastic and Inelastic Scattering of He Atoms from Bi(111), J. Phys.: Condens. Matter **22**, 304019 (2010).

[43] M. Michiardi, I. Aguilera, M. Bianchi, V. E. de Carvalho, L. O. Ladeira, N. G. Teixeira, E. A. Soares, C. Friedrich, S. Blügel, and P. Hofmann, Bulk band structure of Bi_2Te_3, Phys. Rev. B **90**, 075105 (2014).

[44] X. Chen, H. D. Zhou, A. Kiswandhi, I. Miotkowski, Y. P. Chen, P. A. Sharma, A. L. L. Sharma, M. A. Hekmaty, D. Smirnov, and Z. Jiang, Thermal expansion coefficients of Bi_2Se_3 and Sb_2Te_3 crystals from 10 K to 270 K, Appl. Phys. Lett. **99**, 261912 (2011).

[45] A. Tamtögl, E. A. Carter, D. J. Ward, N. Avidor, P. R. Kole, A. P. Jardine, J. Ellis, and W. Allison, Note: A simple sample transfer alignment for ultra-high vacuum systems, Rev. Sci. Instrum. **87**, 066108 (2016).

[46] S. Baroni, S. de Gironcoli, A. Dal Corso, and P. Giannozzi, Phonons and related crystal properties from density-functional perturbation theory, Rev. Mod. Phys. **73**, 515 (2001).

[47] P. Giannozzi, S. Baroni, N. Bonini, M. Calandra, R. Car, C. Cavazzoni, D. Ceresoli, G. L. Chiarotti, M. Cococcioni, I. Dabo, A. D. Corso, S. de Gironcoli, S. Fabris, G. Fratesi, R. Gebauer, U. Gerstmann, C. Gougoussis, A. Kokalj, M. Lazzeri, L. Martin-Samos, N. Marzari, F. Mauri, R. Mazzarello, S. Paolini, A. Pasquarello, L. Paulatto, C. Sbraccia, S. Scandolo, G. Sclauzero, A. P. Seitsonen, A. Smogunov, P. Umari, and R. M. Wentzcovitch, QUANTUM ESPRESSO: A modular and open-source software project for quantum simulations of materials, J. Phys.: Condens. Matter **21**, 395502 (2009).

[48] J. P. Perdew, K. Burke, and M. Ernzerhof, Generalized Gradient Approximation Made Simple, Phys. Rev. Lett. **77**, 3865 (1996).

[49] M. Alcántara Ortigoza, I. Y. Sklyadneva, R. Heid, E. V. Chulkov, T. S. Rahman, K.-P. Bohnen, and P. M. Echenique, *Ab initio* lattice dynamics and electron-phonon coupling of Bi(111), Phys. Rev. B **90**, 195438 (2014).

[50] D. Campi, M. Bernasconi, and G. Benedek, *Ab-initio* calculation of surface phonons at the Sb_2Te_3(111) surface, Surf. Sci. **678**, 46 (2018).

[51] A. Ruckhofer, A. Tamtögl, M. Pusterhofer, M. Bremholm, and W. E. Ernst, Helium-surface interaction and electronic corrugation of Bi_2Se_3(111), J. Phys. Chem. C **123**, 17829 (2019).

[52] A. Tamtögl, P. Kraus, M. Mayrhofer-Reinhartshuber, G. Benedek, M. Bernasconi, D. Dragoni, D. Campi, and W. E. Ernst, Statics and dynamics of multivalley charge density waves in Sb(111), npj Quantum Mater. **4**, 28 (2019).

[53] S. A. Safron, High-resolution helium atom scattering as a probe of surface vibrations, Adv. Chem. Phys. **95**, 129 (1996).

[54] I. Boulares, G. Shi, E. Kioupakis, P. Lošt'ák, C. Uher, and R. Merlin, Surface phonons in the topological insulators Bi_2Se_3 and Bi_2Te_3, Solid State Commun. **271**, 1 (2018).

[55] J. A. Sobota, S.-L. Yang, D. Leuenberger, A. F. Kemper, J. G. Analytis, I. R. Fisher, P. S. Kirchmann, T. P. Devereaux, and Z.-X. Shen, Distinguishing Bulk and Surface Electron-Phonon Coupling in the Topological Insulator Bi_2Se_3 Using Time-Resolved Photoemission Spectroscopy, Phys. Rev. Lett. **113**, 157401 (2014).

[56] X. Gao, M. Zhou, Y. Cheng, and G. Ji, First-principles study of structural, elastic, electronic and thermodynamic properties of topological insulator Bi_2Se_3 under pressure, Philos. Mag. **96**, 208 (2016).

[57] G. W. Farnell, Properties of elastic surface waves, in *Physical Acoustics*, Vol. 6, edited by W. P. Mason and R. N. Thurston (Academic Press, 1970), Vol. 6, pp. 109–166.

[58] G. W. Farnell, Types and properties of surface waves, in *Acoustic Surface Waves*, edited by A. A. Oliner, Topics in Applied Physics Vol. 24 (Springer-Verlag, Berlin, Heidelberg, 1978), pp. 13–60.

[59] Y. D. Glinka, S. Babakiray, T. A. Johnson, M. B. Holcomb, and D. Lederman, Acoustic phonon dynamics in thin-films of the topological insulator Bi_2Se_3, J. Appl. Phys. **117**, 165703 (2015).

[60] A. A. Maradudin and G. I. Stegeman, Surface acoustic waves, in *Surface Phonons*, edited by F. W. W. Kress (Springer, Heidelberg, 1991), pp. 5–35.

[61] P. Hofmann, M. M. Ugeda, A. Tamtögl, A. Ruckhofer, W. E. Ernst, G. Benedek, A. J. Martínez-Galera, A. Stróżecka, J. M. Gómez-Rodríguez, E. Rienks, M. F. Jensen, J. I. Pascual, and J. W. Wells, Strong-coupling charge density wave in a one-dimensional topological metal, Phys. Rev. B **99**, 035438 (2019).

[62] G. Bracco, R. Tatarek, S. Terreni, and F. Tommasini, Surface optical phonons in LiF(001) observed by inelastic helium scattering, Phys. Rev. B **34**, 9045 (1986).

[63] A. P. Graham, The low energy dynamics of adsorbates on metal surfaces investigated with helium atom scattering, Surf. Sci. Rep. **49**, 115 (2003).

[64] J. Suh, D. Fu, X. Liu, J. K. Furdyna, K. M. Yu, W. Walukiewicz, and J. Wu, Fermi-level stabilization in the topological insulators Bi_2Se_3 and Bi_2Te_3: Origin of the surface electron gas, Phys. Rev. B **89**, 115307 (2014).

[65] I. Zeljkovic, K. L. Scipioni, D. Walkup, Y. Okada, W. Zhou, R. Sankar, G. Chang, Y. J. Wang, H. Lin, A. Bansil, F. Chou, Z. Wang, and V. Madhavan, Nanoscale determination of the mass enhancement factor in the lightly doped bulk insulator lead selenide, Nat. Commun. **6**, 6559 (2015).

[66] W. L. McMillan, Transition temperature of strong-coupled superconductors, Phys. Rev. **167**, 331 (1968).

[67] A. Tamtögl, E. Bahn, J. Zhu, P. Fouquet, J. Ellis, and W. Allison, Graphene on Ni(111): Electronic corrugation and dynamics from helium atom scattering, J. Phys. Chem. C **119**, 25983 (2015).

[68] W. Allison, R. F. Willis, and M. Cardillo, Origin of the anomalous low-frequency losses observed in the inelastic scattering of He atoms from LiF(001), Phys. Rev. B **23**, 6824 (1981).

Acknowledgements

It has been almost exactly 8 years since I wrote my last acknowledgements for a thesis and while many things changed some things just stayed the same. To my parents and my sister Magdalena, no matter how long I had been away, as soon as I enter your house I feel at home again and I thank you all for your support over the years. Dear Manu, meeting you was a stroke of luck, well and maybe a sip of whisky was involved as well. With all the differences we share, I never felt closer to being met at equal footing: Thank you for loving me the way I am.
I am grateful to all of my friends - after returning to Graz from two years abroad you made it feel like I had never left. In addition to my friends, music has always been a companion throughout my life and also helped me through some hard times. As soon as I started to play music myself more actively again, it has always been a pleasure to do that together with friends.
I would also like to take the opportunity and thank all friends I found as a postdoc in Cambridge. Our times together were short and I left with a heavy heart but also with beautiful memories collected.

These experiences would not have been possible without my academic mentor and supervisors Bill Allison. What makes him stand out, besides his scientific curiosity and love for science, is the way he always tries to be supportive, friendly and encouraging to the group and other researchers around him.
Among the many people I met in Cambridge I would like to thank I. Calvo-Almazán who introduced me into the field of neutron scattering as well as N. Avidor, J. Ellis and A. P. Jardine for letting my stay in Cambridge grow into a fruitful collaboration which still continuous.

Many thanks go to all my colleagues in Cambridge and Graz and the valuable discussions during coffee/tea breaks as well as after-work pub evenings, where eventually some of these colleagues have become friends over the years.

There are many other people on the road and I believe that (in particular) experimental works are nowadays never the output of one individual. I cannot mention each single person here but their contributions should be obvious from the reproduced papers in this work and I would like to thank all of them again at this point.
A lot of the published manuscripts build upon work started by excellent students such as A. Ruckhofer as well as previous members of the group in Graz such as P. Kraus and M. Mayrhofer-Reinhartshuber, to mention a few.
In terms of several collaborative efforts I would like to thank M. Sacchi, D. Campi, Ph. Hofmann, M. Bermholm and P. Fouquet.
There are also a couple of people involved who usually go unnoticed and those are, in addition to the administrative staff, when it comes to experimental works, the mechanical and electronic workshops both in Cambridge and in Graz. Without their help the realisation of these projects would not have been possible.

Dear G. Benedek, S. Miret Artés and D. Manson, I am grateful for having had the opportunity to visit you and to learn from you, not just about science, but also about how to inspire others and create such a productive environment for joint research. In particular Giorgio has taught me many times how to interpret and understand the experimental results. It has also been an honour to work with A. Sabik and G. Antczak.

Finally, I am grateful to Prof. W. E. Ernst, who has accompanied me throughout my academic career, starting from my dissertation. Having introduced me to professional research, he has never failed to guide me ever since. And last but not least I would like to thank Prof. A. Winkler who introduced me into the field of surface science.